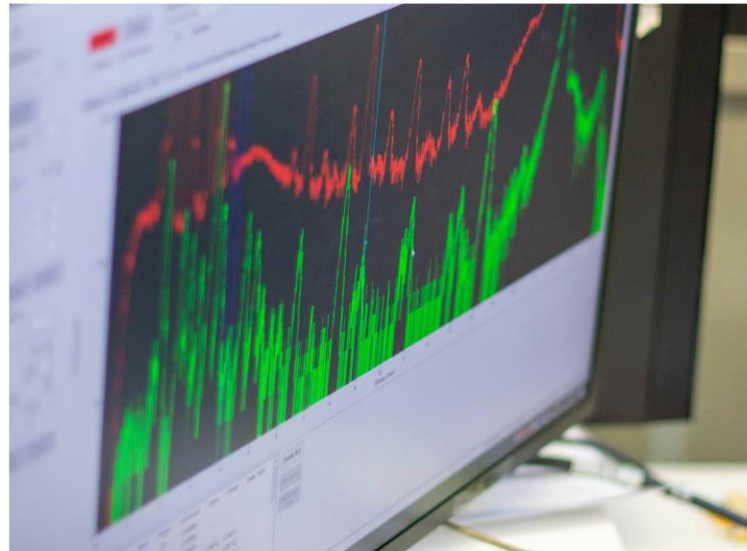


HUN REN



Centre for
Energy Research



Progress Report on Research Activities 2023

HUN-REN CENTRE FOR ENERGY RESEARCH

29-33 KONKOLY-THEGE MIKLÓS ÚT
1121 BUDAPEST, HUNGARY

PROGRESS REPORT
ON RESEARCH ACTIVITIES
IN 2023

DEAR READER

Welcome to the 2023 yearbook published by the HUN-REN Centre for Energy Research (EK), summarising the scientific achievements of its three institutions and highlights in 2023. This booklet summarises the research done, and the personnel and equipment of departments or research groups working in the Centre.

The ELKH - Hungarian Research Network (HUN-REN) - Steering Board renewed from September 1, 2023, at the joint proposal of the Minister of Culture and Innovation János Csák and Tamás Freund, President of the Hungarian Academy of Sciences. Balázs Gulyás has been selected to be the president of HUN-REN. The steering board, which previously consisted of 13 people, will continue its work with 9 people in the future. The appointment of the new members is for 6 years. The main task of the renewed Steering Board is to increase the measurable effectiveness of the Hungarian scientific research network and position it in the international research area, too.

The head of the Steering Board of the Hungarian Research Network is the president, Balázs Gulyás, who has been the head of the research network since May 1, 2023. He worked and researched abroad for more than 41 years - among others at the Karolinska Institute in Sweden and then at the Nanyang Technological University in Singapore. He has enormous achievements as a scientist and science organizer.

The energy crisis that started in 2022 still influenced the research in the whole world. Nevertheless, research in our centre has a significant influence on everyday life. Out of these results, three were selected:

i). HUN-REN EK researchers developed [novel nanostructures for electronics manufacturing and hydrogen catalysis](#). The researchers at the Institute of Technical Physics and Materials Science and the Institute for Energy Security and Environmental Safety are developing advanced semiconductor materials and technologies with a strong emphasis on energy efficiency and sustainability within an ongoing Thematic Program of Excellence. These materials and processes can be utilized for manufacturing more efficient light sources (LED) and electronic devices, and for electrocatalytic systems for water splitting.

ii) As a significant stride towards realising the potential of fusion energy, the joint [European and Japanese effort has reached a landmark milestone with the successful operation of JT-60SA](#), the most advanced experimental fusion device to date. This achievement underscores the strong commitment of both regions to develop efficient, safe, and sustainable fusion technology. The HUN-REN Centre for Energy Research (HUN-REN EK-CER) Institute for Atomic Energy Research has played a pivotal role in this project. Their researchers and engineers developed an innovative video camera system called EDICAM (Event Detection Intelligent Camera). This high-speed digital technology is designed for diagnostic purposes and is crucial for observing and recording the million-degree plasmas within the fusion device. The EDICAM system's ability to capture and analyse these extreme conditions is fundamental in advancing our understanding of fusion processes.

iii) Researchers from the Institute of Technical Physics and Materials Science of the HUN-REN Centre for Energy Research (HUN-REN EK-CER) have developed methods based on optical and electrochemical sensors applicable in a microscopic environment, in collaboration with Aedus Space Ltd. and the Dutch company Micronit B.V. under the umbrella of the Moore4Medical ECSEL project. [The new technology facilitates the direct mapping of the chemical environment and metabolism of cell cultures](#) established in microfluidic Organ-on-Chip systems, thereby aiding in understanding the mechanisms of diseases and therapies. The results can significantly contribute to the acceleration of drug active ingredient testing and the replacement of animal experiments.

In 2023 besides many national and international projects EK was also successful in winning EU-funded projects. These are the NEPHEWS 101131414, QuKiT 101115315, PowerizeD 101096387, SolarHyValue 101103762, SELFAQUASENS 101131379. Details about these projects can be found at [Projects & results | CORDIS | European Commission \(europa.eu\)](#) by searching for the short name and/or ID number listed above.

Ákos Horváth
Director General
horvath.akos@ek.hun-ren.hu

CONTENTS

Dear Reader.....	2
Contents.....	3
Mission Statement of the HUN-REN Centre for Energy Research	7
Organization Structure of the HUN-REN Centre for Energy Research (2023).....	8
Quality Management	9
Budapest Research Reactor	13
Environmental Protection Service.....	15
I. RESEARCH ACTIVITIES SUPPORTED BY DOMESTIC AND INTERNATIONAL PUBLIC AGENCIES.....	16
ALLEGRO Design Development.....	17
Simulating the Doses from Radon Progeny Decay in Rat Airways.....	19
Evaluation of Radiation Protection Issues by Assessing the Opinions of Stakeholders Based on a PIANOFORTE Partnership Survey	21
DELISA-LTO: International Project Proposal for Researching the AGING of Reactor Parts.....	22
Accelerator and Research Reactor Infrastructures for Education and Learning, EURATOM ARIEL Project.....	23
DMS Fast Shutter Prototype Development.....	24
Fusion Research and Development in the EUROFUSION Program	25
Remote Maintenance Related Tasks within the DEMO Project	28
Establishing Weights for Country-Specific Criteria in Long-Term Energy Planning Across Europe.....	30
X-ray Spectrometry Characterization of Size-Fractionated Aerosol Particles	33
Calculations on High Pu Content MOX Fuel in Fast Reactors	35
Support Laboratory for the ITER Disruption Mitigation System.....	36
STRUMAT: Structural Materials Research for Safe Long Term Operation of Light Water Reactor Nuclear Power Plants.....	38
Towards Optimized Use of Research Reactors in Europe	39
FRACTESUS: Fracture Mechanics Testing of Irradiated RPV Steels by Means of Sub-Sized Specimens.....	40
Fast Valve for Nuclear Fusion Applications	41
Medical Radioisotope Production Study at the Budapest Research Reactor – the WP2 of the SECURE Project.....	43
II. RESEARCH AND DEVELOPMENT RELATED TO NUCLEAR POWER PLANTS.....	44
Activities of HUN-REN EK as Main Consultant of Paks Nuclear Power Plant.....	45
New Verification and Validation Results of the Neutronic/Thermal-hydraulic Codes Applied at Reactor Analysis Department	46
Mechanical Tests with Slim Fuel Cladding.....	48
Subchannel Analysis in VERONA Core Monitoring System	49
Investigation of Flows in a Core Comprised of Multiple Types of Fuel Assemblies	51
Accounting of Burnup in the Criticality Calculation of Storage and Transport Facilities - Investigating the Similarity between HZP States and Storage Facilities	52
Mechanical Testing of Cladding Materials for Accident Tolerant Fuel.....	53
Integral Test with Accident Tolerant Fuel.....	54
The Experiences of NPP Operation with Identified Defective Fuel Assemblies.....	55
Creep and Burst Tests with Slim Fuel Cladding Tubes.....	56
Measurement of Fuel Element Burst and Leakage by Acoustic Emission.....	57

Optimal Control of Power Plant Load Changes.....	58
Burnup-dependent Group Constant Parametrization by Applying Different Machine Learning Methodologies.....	59
Innovative Experimental and Numerical Tools in Materials Testing.....	60
Improving the Structural Integrity Computation Methodology.....	62
Pre-Test Simulation of RIA Experiments on Fresh Rodlets with Hydrided Cladding in the HERA Exercise.....	63
Fusion Material Science Research: Material Development, Irradiation and Radiation Damage Testing.....	65
Test Technology Standardization of Miniaturized Fracture Mechanics Specimens for Fusion Applications.....	67
III. NUCLEAR SECURITY, DOSIMETRY AND SPACE RESEARCH.....	68
Gamma-ray Measurement and Analysis of Spent Fuel Assemblies of Paks NPP, 2023 (I) & Development of New Model and Nuclear Measuring Procedure for Determination of Burnup History of Nuclear Fuels for Safeguards and Forensic Analytical Investigations (II).....	69
Development of a New Model and Nuclear Measuring Procedure for Determination of the Burnup History of Nuclear Fuels for Safeguards and Forensic Analytical Investigations.....	72
Development of Nuclear Forensic Analytical Methods for Determining the Origin of Smuggled Materials.....	74
Experimental Implementation of Wide-Scale Tuned Pulsed Photon Radiation Fields, Development of Measurement Techniques from the Dosimetric and Scientific Point of View, Related Detector and Detector-Application Development.....	77
Regional Training Course on Gamma Radiation Processing Dosimetry.....	85
Development of a Method for Wound Measurement and Dose Assessment in the EK - Part 1.....	86
Assessment of the Characteristics of Radionuclides and Determination of Key Nuclides for Radiation Protection Calculations: Part 2.....	88
Developments in Personal Dosimetry: Part 1.....	89
Training and Tutoring for Experts of the NRAs and their TSOs for Developing or Strengthening their Regulatory and Technical Capabilities.....	91
Developing Dose Map Calculation Methods for Off-normal NPP Operations.....	92
Development of Space Research Instruments.....	93
Radiation Monitoring with the RadMag (RM-S) Space Weather Instrument.....	96
Detailed Design of the Internal Dosimetry Array for Gateway, the Space Station of the Artemis Program.....	98
IV. ENERGY SECURITY AND ENVIRONMENTAL STUDIES.....	99
New (Photo)Electrocatalytic Systems for Water Splitting.....	100
Hydrogen or Syngas by Catalytic Methane Conversion.....	102
Examination of the Recyclability of Electronic Waste Using Nuclear Analytical and Imaging Methods.....	103
Effect of the Energy-efficient High Energy Ionizing Radiation Treatment on Degradation of Metoprolol and Oxacillin Focusing on the Removal Rate and Antimicrobial Activity.....	105
Examination of Electrochemical Reduction Processes (Hydrogen Development and CO ₂ Reduction).....	107
Power Production from Low-Temperature Heat Sources.....	108
Energy Strategy and Environmental Effects.....	110
Chemical Evolution and Radionuclide Retention Studies for High-Level Radioactive Waste Disposal.....	116
Methodology Development for the Investigation of the Elemental and Organic Carbon Content of Size-Fractionated Environmental Aerosol Samples.....	124
Integrated Methodology for Distributed Geothermal Co-Heat and -Power Production.....	127
Catalytic Methane Pyrolysis Combined with Microcombinatorial TEM Studies.....	134
Tracking Surface Processes on Water Oxidizing Anodes using High-sensitivity Operando Ellipsometry.....	139
Modelling the Airborne Transmission of SARS-CoV-2 in a Hospital Ward During Nursing Care Activities.....	143
Increasing the Stability of Power Systems with High Renewable Energy Share by the use of Coupled Oscillators.....	145
V. NUCLEAR ANALYSIS AND CHEMISTRY.....	146
The Renewed Cold Neutron Imaging Facility, NORMA.....	147

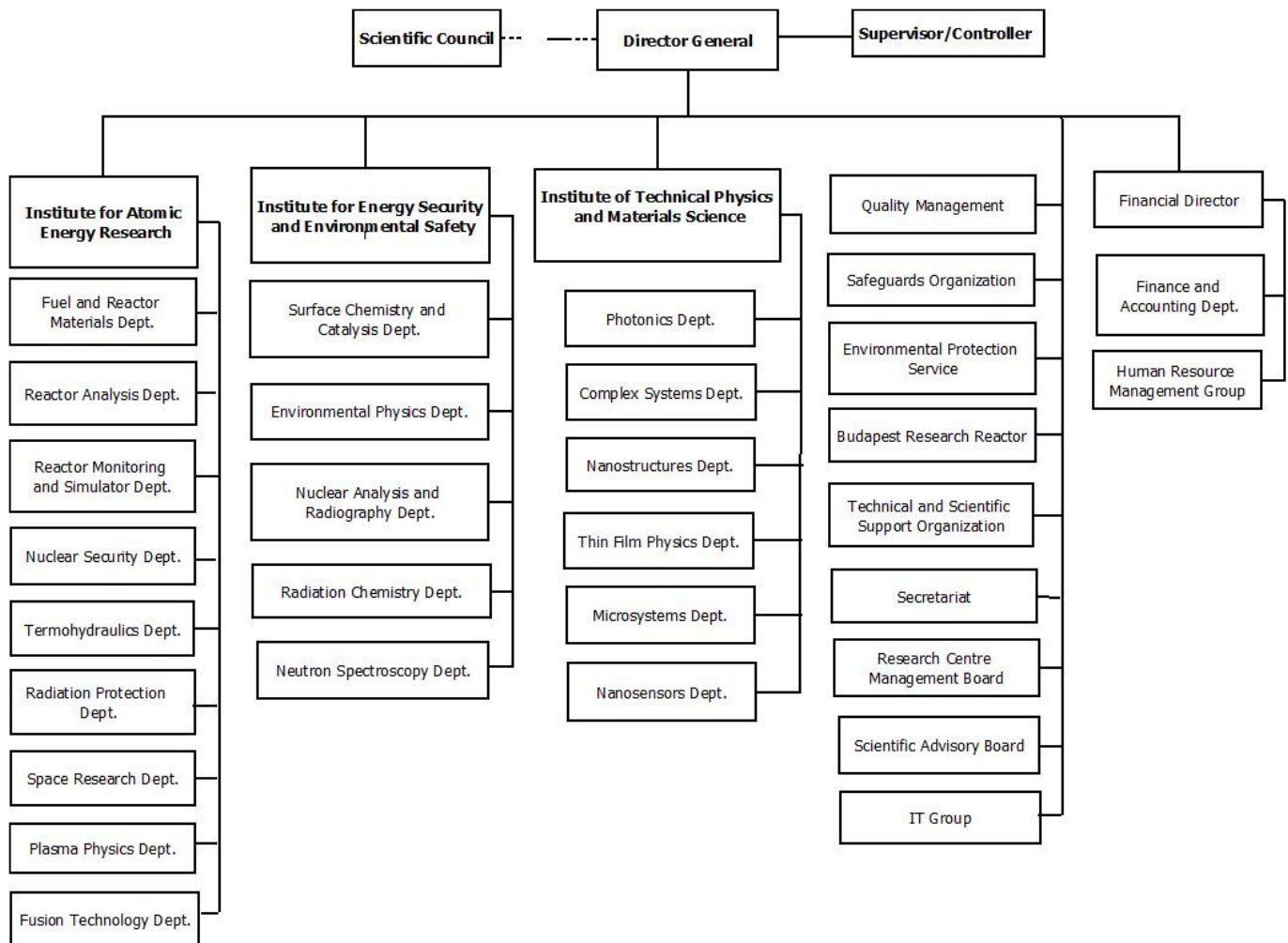
Performance Testing of Low-dimensional Cold Neutron Moderators at the Budapest Research Reactor	148
Results of the HUN-REN EK Electron Cyclotron Resonance Proton Ion Source.....	149
Hybrid Photonic Nanoarchitectures Based on Butterfly Wings and In situ Grown Metallic Nanoparticles	151
Materials Science Applications of Neutron Scattering	154
Functional Silica Materials for Environmental and Medical Applications	157
Heritage Science Applications of Nuclear Analytical and Structural Studies.....	159
Applications of Nuclear and X-ray Analytical Techniques to Chemistry, Material and Nuclear Sciences.....	161
Structural Aspects of Iron-, Tin- and Gold-based Material Systems Studied by Mössbauer Spectroscopy and Other Methods	163
Neutron and X-ray Radiography and Tomography at the Budapest Neutron Centre	165
Preparation and Characterization of Glasses in the ZnO - B ₂ O ₃ - Bi ₂ O ₃ - WO ₃ System.....	167
Preparation and Characterization of Glasses in the ZnO - B ₂ O ₃ - Bi ₂ O ₃ - WO ₃ :Eu ₂ O ₃ System.....	169
VI. RESEARCH AND DEVELOPMENT IN INSTITUTE OF TECHNICAL PHYSICS AND MATERIAL SCIENCES.....	171
Identification of Graphite with Perfect Rhombohedral Stacking by Electronic Raman Scattering	172
Stabilizing Giant Moiré Superlattices in Twisted Bilayer Graphene	174
2D MoS ₂ Crystals can Stabilize Semiconducting Pt Structures	176
Hybrid Bio-Nanocomposites by Integrating Nanoscale Au in Butterfly Scales Coloured by Photonic Nanoarchitectures	178
Photocatalytic Dye Degradation with Biotemplated ZnO Photonic Nanoarchitectures Based on Morpho Butterfly Wings.....	180
Contact Angle Determination by the Capillary Bridge Probe and Sessile Drop Method on PTFE Surfaces.....	182
Surface Sodification and Self-assembly of Gold Nanoprisms	184
Multicomponent Heteronanoparticles for Photocatalytic Application	186
3-colour Ellipsometric Mapping Tool without Moving Components	188
Nanoscale Monitoring of Water Condensation in Electrochemical Migration-Induced Printed Circuit Board (PCB) Failure.....	193
Investigation of Electrochromic, Combinatorial TiO ₂ -SnO ₂ Mixed Layers.....	194
Reactive Sputter Deposition of Ga ₂ O ₃ Thin Films Using Liquid Ga Target	196
Resonance-based Kretschmann-Raether Ellipsometry Utilizing Plasmonic and Periodic Nanostructures at Solid-liquid Interfaces.....	198
Makyoh Imaging and Topography	200
TEM of Innovatively Used of PtSi Contact Material.....	202
Reactive Sputter Deposition of Ga ₂ O ₃ Thin Films using Liquid Ga Target	204
Industrially Deposited Hard and Damage Resistant W-B-C Coatings.....	206
Effect of Nb Incorporation in Mo ₂ BC Coatings on Structural and Mechanical Properties - Ab Initio Modelling and Experiment	207
Composition Dependent Structure, Morphology and Mechanical Properties of the Al _{1-x} Cu _x Thin Film System.....	209
Combinatorial Characterisation of the Complete Y-Ti-O Thin Layer System; Issues of DC and HIPIMS Sputtering Processes	211
Catalytic Methane Pyrolysis Combined with Microcombinatorial TEM Studies	213
Reductive Treatment of Ti _{0.8} Sn _{0.2} O ₂ -C Composite Supported Pt	215
Microstructure and Growth of α -Mn(Cu) Solid Solution Films	217
Multifunctional Biomineralized Calcium Phosphate-loaded Biopolymer Composites as Biodegradable Coatings on Implants	218
R+D+I Development and Utilization of High-Performance Electronic Chips "CHIPCER" Phase 1	221
Digitalization of Power Electronic Applications within Key Technology Value Chains.....	222
Quantification of Piezoresponse Force Microscopy for Thin Al _(1-x) Sc _x N Film.....	223
A Rutherford Backscattering/Channelling and Spectroscopic Ellipsometry study of ϵ -Ga ₂ O ₃	225

He ⁺ Ion Beam-Induced Luminescence from Defect Centres in α -Al ₂ O ₃	227
Enhancing the Nucleation in Atomic Layer Deposition: A Study on Vanadium Sulphide and Oxide Layers.....	229
Resistor Network Simulation of VO ₂ Nanogaps	231
AlGa _N /Ga _N Heterostructure Based Frequency Selective Vibration Sensor	233
Smart Scalpel – a Novel Force-Sensor-Based Surgery Hand Tool	235
First Steps Toward Kitaev Transmon Generation.....	237
Wearable Gas Sensors for Emergency and Extreme Conditions.....	238
3D MEMS Force Sensor for Tissue Recognition	240
Microfluidic Methods for Particle and Cell Manipulation and Analysis.....	242
Small Scale Production and Development of Near Infrared LEDs for Spectroscopic Applications.....	246
Cell Culture Media Analysis in Organ-on-Chip Applications	247
Dean-flow Affected Lateral Focusing and Separation of Particles and Cells in Periodically Inhomogeneous Microfluidic Channels	249
Label-free Biosensing of Lignans for Therapeutics using Engineered Model Surfaces	250
Design, Fabrication, and Characterization of Picowell Arrays on Cyclic Olefin Copolymer Surfaces Generated with a 10.5 MeV N ⁴⁺ Ion Microbeam.....	251
Nanoinjection of Extracellular Vesicles to Single Live Cells by Robotic Fluidic Force Microscopy.....	252
Polysaccharide-based Nano-engineered Multilayers for Controlled Cellular Adhesion in Label-free Biosensors.....	253
The Competition of Alliances with Inner Blocking Mechanism.....	254
Revisiting and Modelling Power-Law Distributions in Empirical Outage Data of Power Systems	256
Scaling Laws of Failure Dynamics on Complex Networks.....	258
Spontaneous Symmetry-breaking in Spatial Evolutionary Games.....	259
An Investigation of Evolutionary Potential Games Using the Tensor Renormalization Group Method	260
Evolutionarily Stable Payoff Matrix in Hawk–Dove Games	262
ABBREVIATIONS	263

MISSION STATEMENT OF THE HUN-REN CENTRE FOR ENERGY RESEARCH

- Research and development in the field of nuclear science and technology for facilitating the adoption and the safe use of nuclear technology in Hungary.
- To participate in international research effort aiming at the establishing a new generation of nuclear power plants and closing the fuel cycle.
- Maintaining and improving competence in nuclear science and technology, especially in the field of nuclear safety, security, health physics, nuclear and isotope chemistry.
- To guarantee the safe operation of Budapest Research Reactor (BRR), and to ensure the open access to the research facilities around the reactor operated by the Budapest Neutron Centre.
- Research activities to improve nuclear analytical and imaging methods and their applications for energy and materials science.
- Perform studies in the field of environmental physics related to energy generation, renewable energies, energy storage and their impact on public health, and on environmental safety.
- Research and development in the field of low-carbon energy technologies and of energy saving in industrial technologies.
- Development of nuclear energy production processes based on nuclear fusion, research and development of related technological and physical issues.
- Development of manned mission space dosimetry and space weather measurement systems, furthermore, improvement of devices for space-biological, -chemical and -material science experiments.
- Interdisciplinary research on complex functional materials and nanometer-scale structures, exploration of their physical, chemical, and biological principles, exploitation their operations in integrated micro- and nanosystems, and in the development of characterization techniques.
- Dissemination of the results in international programs, education and industrial research.

ORGANIZATION STRUCTURE OF THE HUN-REN CENTRE FOR ENERGY RESEARCH (2023)



QUALITY MANAGEMENT

In order to achieve the highest quality of research, development, design, condition monitoring and valuation, engineering, contracting and managing in design, production, implementation and inspection, the Research Centre's quality management system has continuously been upgraded by the recommendations of ISO 9001 standard since 1994. Reviewing our QM system by integral audits and management reviews, evaluating improvement opportunities, maintaining project documentation, infrastructure, supporting communication, ensuring the competence of workers the management improves the Centre's QM system. For the new organization structure, our Quality Policy has been renewed. Many new employees induced a need to upgrade our QM tuition practice. We organized the work and fire safety educations. Our QM system has been certified by Hungarian Standards Institution, IQNet and MVM Paks NPP.





Building
trust
together.

Certificate

MSZT has issued an IQNET recognized certificate that the organization:

Centre for Energy Research (except Institute of Technical Physics and Materials Science (MFA) and Reactor Department (Reaktorüzem))

**Certified headquarters: Konkoly-Thege Miklós út 29-33.
HU-1121 Budapest Hungary**

has implemented and maintains a
Quality Management System

for the following scope:

research, development, design, condition monitoring and valuation, engineering, contracting and managing in design, production, implementation and inspection, independent technological expert activity in the field of application of nuclear energy

which fulfils the requirements of the following Standard:

ISO 9001:2015

Issued on: **2023-06-23**
First issued on: **1999-06-22**
Expires on: **2026-06-22**

Registration Number: **HU-MSZT-503/0309(8)-097(8)**




Alex Stoichitoiu
President of IQNET


György Pónyai
general director



This attestation is directly linked to the IQNET Member's original certificate and shall not be used as a stand-alone document.

IQNET Members*:

AENOR Spain **AFNOR Certification** France **APCER** Portugal **CCC** Cyprus **CISQ** Italy **CQC** China **CQM** China **CQS** Czech Republic
Cro Cert Croatia **DQS Holding GmbH** Germany **EAGLE Certification Group** USA **FCAV** Brazil **FONDONORMA** Venezuela **ICONTEC**
Colombia **ICS** Bosnia and Herzegovina **Inspecta Sertifointi Oy** Finland **INTECO** Costa Rica **IRAM** Argentina **JOA** Japan **KFQ** Korea
LSQA Uruguay **MIRTEC** Greece **MSZT** Hungary **Nemko AS** Norway **NSAI** Ireland **NYCE-SIGE** Mexico **PCBC** Poland **Quality Austria**
Austria **SII** Israel **SIO** Slovenia **SIRIM QAS International** Malaysia **SOS** Switzerland **SRAC** Romania **TSE** Türkiye **YUQS** Serbia

*The list of IQNET Members is valid at the time of issue of this certificate. Updated information is available under www.iqnet-certification.com



Building
trust
together.

Annex 1 to IQNET Certificate Number
HU-MSZT-503/0309(8)-097(8)

**Centre for Energy Research (except Institute of Technical
Physics and Materials Science (MFA) and Reactor
Department (Reaktorüzem))**

Certified headquarters: Konkoly-Thege Miklós út 29-33.
HU-1121 Budapest

Scope

kutatás, fejlesztés, tervezés, állapotfelmérés és szakvéleményezés, mérnökszolgálat, fővállalkozási tevékenység tervezési, gyártási, kivitelezési és vizsgálati munkák irányítására, atomenergia alkalmazása körében eljáró független műszaki szakértői tevékenység

..... This annex is only valid in connection with the original certificate number mentioned above.

IQNET Members*:

AENOR Spain **AFNOR Certification** France **APCER** Portugal **CCC** Cyprus **CISO** Italy **CQC** China **COM** China **CQS** Czech Republic **Cro Cert** Croatia **DQS Holding GmbH** Germany **EAGLE Certification Group** USA **FCAV** Brazil **FONDONORMA** Venezuela **ICONTEC** Colombia **ICS** Bosnia and Herzegovina **Inspecta Sertifointi Oy** Finland **INTECO** Costa Rica **IRAM** Argentina **JQA** Japan **KFQ** Korea **LSQA** Uruguay **MIRTEC** Greece **MSZT** Hungary **Nemko AS** Norway **NSAI** Ireland **NYCE-SIGE** Mexico **PCBC** Poland **Quality Austria** Austria **SII** Israel **SIQ** Slovenia **SIRIM QAS International** Malaysia **SQS** Switzerland **SRAC** Romania **TSE** Turkey **YUQS** Serbia

* The list of IQNET Members is valid at the time of issue of this certificate. Updated information is available under www.iqnet-certification.com



AZ MVM PAKSI ATOMERŐMŰ ZRT. IGAZOLJA, HOGY
KÖVETELMÉNYEINEK AZ

ENERGIATUDOMÁNYI KUTATÓKÖZPONT

MINŐSÉGIRÁNYÍTÁSI RENDSZERE

M E G F E L E L.

MINŐSÍTETT TERÜLET:

ABOS 1, 2, 3 biztonsági osztályokba sorolt technológiai rendszerek és rendszerelemek átalakításával, javításával, karbantartásával és üzemeltetésével összefüggően főkonzulensi, tervezői, szakértői, valamint független műszaki szakértői tevékenységek végzése.

A MINŐSÍTÉS ÉRVÉNYESSÉGI IDEJE: 2026.08.31.

A MINŐSÍTÉS SZÁMA: KM 55/2023

EZEN MINŐSÍTŐ LAP A MELLÉKLETTEL EGYÜTT ÉRVÉNYES.

Paks, 2023. augusztus 18.

PUSKÁS LÁSZLÓ
főosztályvezető

REPOVSZKI GÁBOR
osztályvezető



Certifications by Hungarian Standards Institution, IQNet and MVM Paks NPP

Centre for Energy Research has complied with the requirements of the Hungarian Academy of Sciences which follow international standards. In 2019, the Hungarian Academy of Sciences thereby authorized the Centre for Energy Research to use the label MTA Centre of Excellence. This certificate was extended annually in 2020, 2021, 2022 and 2023.

BUDAPEST RESEARCH REACTOR

One of Hungary's most important strategic large-scale research facilities is the Budapest Research Reactor (BRR). It serves the needs of an extensive and diverse scientific community by supporting R&D opportunities, helping innovation and providing a strong foundation for training and education.



Renovated building of the Budapest Research Reactor

BRR is a VVR-type reactor that uses light water as moderator and cooling fluid. The power of the reactor is 10 MW provided from low enrichment uranium fuel, and its main purposes – as established during the feasibility/functionality study – are radioisotope production, production of thermal and cold neutron beams for research and applications in many areas of development of material sciences and nuclear physics.

The core is designed to have about 120 reactor days per year, having a time span of 4 days a week. We are committed to long-term safety and responsible operations, taking care of the wastes from the spent fuel coming from the reactor. Besides the temporary spent fuel storage pool, we also operate a long-term spent fuel storage building for the physical and environmental separation between the reactor and the spent fuel storage.



Top view of the research reactor



Layout of the BRR's facilities

The reactor hosts three kinds of activities: research activities utilizing neutron beams, production of radioisotopes for industrial, medical and research purposes, and providing national and international training. We are proud of our innovative flagship research topics, which are carried out by a network of neutron beam stations, including beam lines of thermal neutrons, experiments on powder and residual stress diffractometry, TOF neutron spectroscopy, radiography, biological irradiations, and beam lines of cold neutrons for experiments on small angle neutron scattering, reflectometry, prompt gamma activation analysis and nuclear data measurements. In accordance with recent worldwide trends, we are open to establishing new industrial relations and supporting innovation. The BRR's experimental facilities are open to science based on excellence for researchers from all around the world. We aim to increase our competence on special topics, implement new technologies and develop new materials, to promote and exploit our R&D capacity at the national, regional, as well as international levels. During the past years, BRR hosted several international schools on various technical and research topics, special trainings in the field of reactor physics, reactor operation, nuclear measurement techniques, and safety and environmental issues. Typical research fields are physics, chemistry, material sciences, engineering, life sciences and biotech.

BRR is used by groups of different scientific communities from medical, environmental, material, archaeological, nuclear sciences, and industry, as well as several Hungarian Universities. Neutron beams are uniquely suited to study the structure and dynamics of materials at the atomic level. The Budapest Neutron Centre (BNC) coordinates the scientific utilization of the research reactor. Some of the main research topics currently are as follows.

- Neutron scattering is used to examine changes in sample properties under different conditions such as variations in vacuum or pressure, high and low temperature and magnetic field, modelling real-world conditions.
- Using prompt and delayed neutron activation analysis makes it possible to measure the concentration of elements in ppm and ppb levels even for small samples. They decay by gamma-rays characteristic for each element that can be detected by suitable detectors.
- Neutron activation to produce different radioisotopes are widely used in industry and medicine production. For example, Y-90 microspheres to treat liver cancer are produced by bombarding Y-89 with neutrons, which capture them. Radioisotopes are produced for different applications such as medicine, sterilization and industrial use.
- Testing reactor materials are subjected to intense neutron irradiation, which causes radiation damage to their crystalline structure. For instance, some steels become brittle. Thus, the so-called high-entropy alloys resisting embrittlement are to be used in nuclear reactors instead.
- Applied research using neutron beams produce images of the material interior. Examples are the visualization of porosities in materials or changes of density inside the sample. Dynamic neutron radiography is capable of visualizing motion in materials. Examples are the viewing bubble forming in the cooling system of a refrigerator or the visualization of fuel burn in the engine system of a car.

BNC provides researchers with 15 neutron instruments; 13 of them are installed directly on the horizontal beam ports of the reactor or to the thermal and cold neutron guides, while the other 2 are placed at the vertical irradiation channels. The instruments are supported by a variety of sample environments, data acquisition hardware, analysis software, and visualization tools.

BNC provides access to the international neutron user community through a peer-review system. Local scientists assist researchers and industrial users in finding the appropriate neutron techniques that meet their research needs. The various neutron scattering instruments in BNC cater to a large number of users from Europe and have grown in strength over the years. Since the COVID-19 pandemic, BNC accepts so-called remote users as well, which means that samples are sent by mail and the measurements are performed by the instrument scientists without the user and the results are forwarded to the users via electronic ways.

BNC is a member of the League of advanced European Neutron Sources (LENS) and CERIC-ERIC, and a partner in recent EU Framework Programme projects (H2020 IPERION HS, EURIZON, ARIEL, ReMade@ARI, EASI-STRESS, SECURE, and TOURR).

BNC is strongly committed to the training of future professionals inland and all over the world in co-operation with the International Atomic Energy Agency. We cooperate with several Hungarian universities (Budapest University of Technology and Economics, Eötvös Loránd University (ELTE), Pannon University, Óbuda University, Moholy-Nagy University of Art and Design, and University of Pécs). BNC accommodates students for laboratory practice for studying nuclear-based techniques. A specialized course was developed for geology students of ELTE to introduce nuclear analytical techniques into their education. BNC organizes the Central European Training School on Neutron Scattering biannually. The school provides insight into neutron scattering, element analysis and imaging techniques and their applications to study the structure and dynamics of condensed matter.

Other courses were ELTE TTK PHD Doctor of Earth Sciences 2 semesters lecture and practice "Nuclear element analytical methods and their applications in earth science and archeometric research I. and II." BME, Doctoral School of Physics "Advanced neutron techniques of material characterization" Budapest Neutron Center staff at ELTE, Doctoral School of Physics. "Advanced neutron techniques of material characterization, Historical and modern materials science III. Historical and contemporary building materials III" Budapest Neutron Center staf, Breuer Marcell Doctoral School, PTE ". The Budapest Research Reactor is open to the public. Members of the local communities and high school and university students visit us regularly and learn more about the amazing nuclear science possibilities available at BRR.

ENVIRONMENTAL PROTECTION SERVICE

The main task in the Environmental Protection Service of the HUN-REN Centre for Energy Research (EK) is the environmental control of radiation protection of the KFKI Site.



The building of Environmental Protection Service

Our Environmental Policy, developed on the basis of the relevant legislation, describes in detail that with what frequency and to what characteristics we have to examine the various sample types. These tests include monitoring of airborne gamma radiation, examinations of atmospheric fallout, and gamma spectrometry and total-beta activity of air aerosol particles. By the use of our own resources and tenders, we intend to develop our equipment and instrumentation in order to perform our tasks with high reliability.



Berthold LB790-5L-Lead type alpha-beta counting device

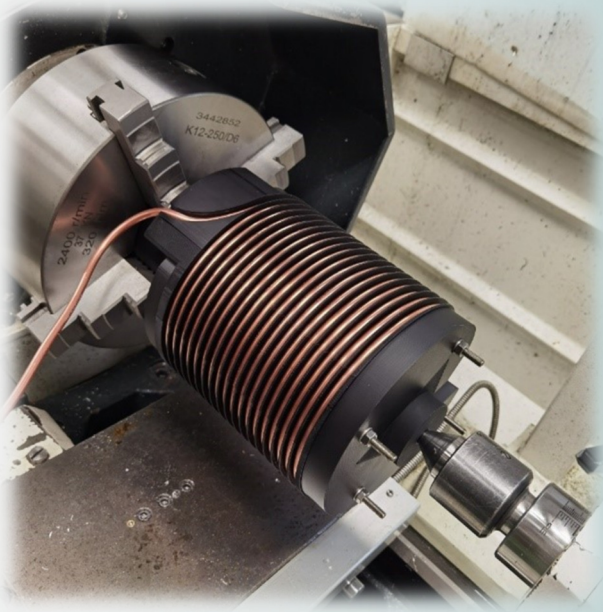


Environmental dose rate measuring probe

In addition to checking the external environment, we also monitor the external and internal radiation exposure of employees exposed to radiation. In addition to official TLD tests, the external radiation exposure is checked with the RADOS type thermoluminescent dosimeters used by the Service.

A detailed report of the work of the Service carried out in each year is available on the HUN-REN EK website.

Gáborné, Endródi
Head of Service
endrodi.gaborne@ek.hun-ren.hu



I. RESEARCH ACTIVITIES SUPPORTED BY DOMESTIC AND INTERNATIONAL PUBLIC AGENCIES



ALLEGRO DESIGN DEVELOPMENT

Gusztáv Mayer, János Gadó, Bálint Batki, Zsombor Bali, Petra Pónya, István Pataki, István Panka, Attila Guba

Objective

The European SAFEG project ensures four-year-long financial support for Gas-cooled Fast Reactor (GFR) technology development in which HUN-REN EK actively participates through neutronic and thermal-hydraulic calculations. In 2023 the main aims were to check the performance of the new Main Heat Exchanger (MHX) and Decay Heat Removal (DHR) design of the Czech ÚJV Řež, a. s. and to propose a new, optimized refractory core configuration extended by a study on reflector and shielding.

Methods

For thermal hydraulics calculation, the French CATHARE system code was used. The previously developed ALLEGRO input was modified according to the ÚJV's proposal for the DHR. Concerning the MHX, ÚJV proposed a new gas-gas main heat exchanger to foster the possibility of electricity generation by gas turbines and to eliminate the water ingress into the core by design. To achieve this MHX design option, a new model was created by replacing the water with a helium-nitrogen mixture at the main secondary loops and by increasing the core outlet temperature up to 800 C. To assess the capability of the new models transient calculations have been elaborated.

The new refractory core was optimized by a genetic algorithm using the KIKO3DMG nodal code which was validated previously [1]. As a first step, the maximum linear heat rate was determined by transient calculations for the selected transients at lower core power using the CATHARE code. The fuel assembly geometry remained unchanged, preserving the well-studied reference fuel. In the optimization process, the primary goal was to maintain the refractory core power at 75 MW_{th}. Achieving the reduced maximum linear heat rate involves a combination of lower average power density and a more evenly distributed radial power. Introducing additional fuel sub-assemblies is unavoidable to lower power density, even though it results in a larger core, which we aimed to minimize for economic reasons. Using profiled fuel sub-assemblies with different Pu content helped to achieve a more even radial power distribution.

Potential reflector materials, including Silicon Carbide (SiC), Zirconium Carbide (ZrC), Zirconium Silicide (Zr₃Si₂), and stainless-steel alloy (15-15Ti), were analyzed and compared using the SERPENT Monte Carlo code [2].

We investigated the following promising shielding materials: 'B₄C-(15-15Ti)', a homogeneous mixture of 70 vol% B₄C, 10 vol% 15-15Ti, and 20 vol% He', 'Graphite' and 'C-B₄C'.

Results

The CATHARE calculations showed that in the case of Station Blackout Transient (SBO), the investigated ÚJV DHR concept ensures sufficient core cooling. Concerning the new preconceptual gas-gas MHX device designed by ÚJV, the calculation showed that the vast majority of the investigated transients do not satisfy the corresponding safety criteria, indicating the need for further design iteration in the MHX and the secondary gas parameters. The study suggests that special attention is needed to check the validity of the heat transfer correlations at lower Reynolds numbers.

As a result of the core optimization, a new REFRACTORY2 core was proposed by HUN-REN EK as a promising future core configuration, see below (Fig. 1). It satisfies several safety constraints such as maximum fuel sub-assembly power (< 0.801 MW) limit, core shut down with a positive margin at the hot zero power state using the primary (SD1) and secondary (SD2) shutdown systems, and using the Control and Shutdown Devices (CSD) and Diverse Shutdown Devices (DSD), assuming that the absorber with the largest reactivity worth is not inserted. The consequence of an inadvertent rod withdrawal transient is mitigated by the relatively low maximum reactivity increase (480 pcm) and the Third Shutdown System (TSD), which can also shut down the reactor at full power. The core can also be safely shut down in cold states, with a large positive margin even in the case of severe fuel handling errors. The new core can operate at full power for about 700 days, and the End of Cycle (EOC) average burnup is 19.6 MWday/kgHM. The peak burnup value (29.4 MWday/kgHM) is well below the preliminary limit (48 MWday/kgHM).

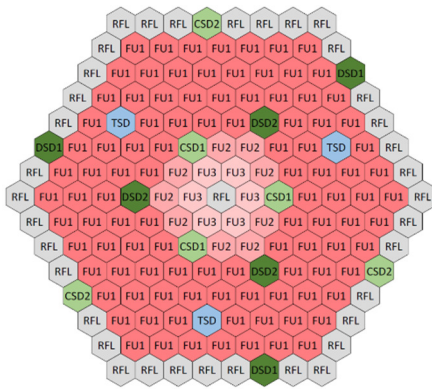


Figure 1: Radial layout of the optimized refractory core.
 RFL –reflector, TSD third diverse shutdown device,
 CSD control and shutdown system, DSD diverse shutdown
 system, FU1 reference, FU2 -20%Pu, FU3 -20%Pu

Based on the performed analysis of the reactor performance parameters, it was concluded that ZrC is a promising reflector material for gas-cooled fast reactors. The application of the ZrC reflector exhibits high reserve reactivity, relatively flat power and neutron flux distribution, and a reasonable Doppler reactivity coefficient. It also helps to achieve low displacements per atom (dpa) in the fuel cladding. Furthermore, the application of ZrC results in a relatively low fast neutron flux on the inner surface of the Reactor Pressure Vessel (RPV) wall.

The shielding material 'C-B₄C' exhibits superior performance in reducing fast neutron flux on the internal RPV wall surface, while all examined materials ensure a fast neutron fluence for 30 Effective Full Power Year (EFPY) of operation below 10²⁰ cm⁻².

Remaining work

In the Euratom TREASURE project, the fuel cycle will be optimized for better utilization of the fissile material aiming to reach the maximum discharge burnup of the reference “refractory core” configuration while staying in compliance with key safety-related criteria. Existing ALLEGRO models devoted to safety analyses will be updated by utilizing the proposed heat storage system in TREASURE.

Related publications

- [1] I. Pataki, B. Batki, M. Tóth, I. Panka: *Validation of the KIKO3DMG neutronics code on the CEFR start-up test*, Annals of Nuclear Energy **180**, 109493 (2023) <http://dx.doi.org/10.1016/j.anucene.2022.109493>
- [2] P. Pónya, C. Ding, Sz. Czifrus, E. Schwageraus: *ALLEGRO-reaktor reflector optimalizációja*, MNT szimpózium, Siófok, 2023

SIMULATING THE DOSES FROM RADON PROGENY DECAY IN RAT AIRWAYS

Szilvia Kugler, Péter Fűri, Árpád Farkas, Balázs Madas

Objective

The RadoNorm project under EURATOM Horizon 2020 aims at managing risk from radon and Naturally Occurring Radioactive Materials (NORM) exposure situations to assure effective radiation protection based on improved scientific evidence and social considerations. Establishment of relationships between the irradiation dose and the related biological outcome is one of the tasks of this project. In the frame of this task the rat lung, as a surrogate of the human lung, is applied to estimate hazards following exposure to ambient aerosols and radon progeny. However, this requires the exact knowledge of radiation doses absorbed by rat epithelial cells. The goal of this work was to calculate the deposition distribution of attached and unattached radon progeny in rat airways and as the next step, to calculate the radiation burden in the nuclei of the basal and secretory cells of the rat epithelium.

Methods

Besides the physical properties of the inhaled particles like diameter, shape, and density, the main factors that influence particle deposition in both human and rat airways are the airway geometry and the breathing pattern (minute ventilation, inhalation and exhalation times) of the subject. While there are similarities between the airways of rats and humans, there is an important difference in the structure of the airways (monopodial branching in rats versus dichotomic branching in humans). In addition, the dimensions of the airways (length, diameter, branching and gravitational angles) are also quite different for rats compared to humans. The breathing pattern is also strongly different. The tidal volume for a sitting adult man is about 750 cm³, while the breathing frequency is around 12 min⁻¹. In case of rats, the tidal volume is about 2 cm³ and the breathing frequency is around 117 min⁻¹.

To determine the deposited amount of radon progeny in rat airways, an aerosol particle deposition model (Specific Lung Model - SLM Rat) was developed and used. The model takes into account the primary deposition mechanisms (diffusion, sedimentation and impaction) in the rat airways. As the next step, a clearance and dosimetry model simulated the movement and decay of radon progeny. Finally, from the distribution of ²¹⁸Po and ²¹⁴Po decays in the airways alpha-tracks were generated, and the absorbed energy in the nuclei of the radiation sensitive basal and secretory cells was calculated.

Results

Figure 1A shows that the inhaled attached radon progeny is deposited mainly in the acinar airways and to a less extent in the bronchial airways. However, due to the smaller central airways of rats, the bronchial deposition of attached progeny is still high in the first three-four airway generations compared to an adult man with breathing mode characteristic of sitting.

The extrathoracic deposition is around 3% for the attached progeny. The unattached progeny, however, has a high deposition fraction both in the upper airways (~98%) and in the first six to seven bronchial airway generations of the rats.

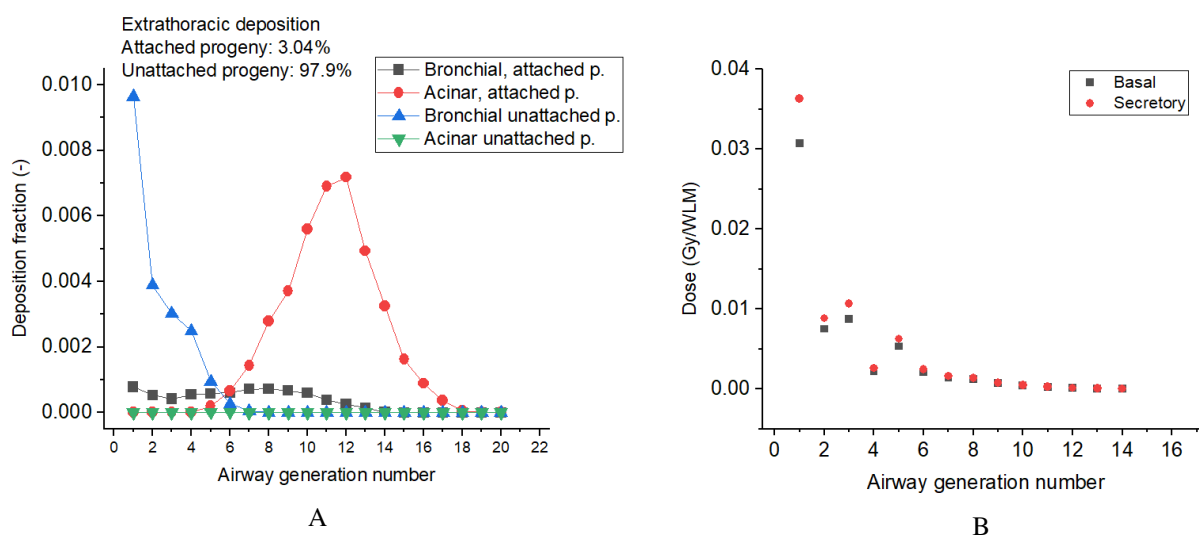


Figure 1: (A) Deposition fractions of attached and unattached progeny in the extrathoracic, bronchial and acinar airways of rats
(B) Absorbed doses in the nuclei of the basal and secretory cells for 1 Working Level Month (WLM) exposure

Figure 1B represents mean absorbed doses in the nuclei of the basal and secretory cells of the rat epithelium. Absorbed doses are strongly inhomogeneous along the bronchial airway generations of rats. The highest doses can be found in the first five airway generations.

The average absorbed dose for the whole bronchial region of rats assuming equal weighting of basal and secretory cells was 4.72 mGy/WLM. This is in good agreement with the average absorbed doses in the bronchial region of rats calculated by Winkler-Heil et al. (2015), which was 4.89 mGy/WLM.

Based on the deposition distribution of radon progeny in rat airways calculated by the SLM Rat, absorbed doses in radiation sensitive target cells were calculated considering the effect of small airways and the shallower depth distribution of the basal and secretory cells for rats. For this, a new mucociliary clearance and radon dosimetry model was also developed. It was found that the spatial distribution of the absorbed doses in the nuclei of the basal and secretory cells is strongly inhomogeneous for the rats, and the highest dose can be found in the first few airway generations. Now, the above presented doses can be used for *in vivo* measurements with rats in the RadoNorm project and other projects in the future.

Remaining work

Next year in the project, we plan to compare the deposition hot spots in the lungs of rats with the location of radiation induced tumors.

Related publication

- [1] G. Albrecht, Á. Farkas, P. Fűri, U. Giesen, B. Madas: *Report on results of computational microdosimetry supporting the preparation and evaluation of experiments*, Final version as of 31.08.2023 of deliverable D3.5 of project RadoNorm. (2023)

EVALUATION OF RADIATION PROTECTION ISSUES BY ASSESSING THE OPINIONS OF STAKEHOLDERS BASED ON A PIANOFORTE PARTNERSHIP SURVEY

Veronika Groma, Balázs Madas

Objective

The fundamental objective of the PIANOFORTE partnership is to provide support and facilitate the consolidation of research and development within the domain of radiation protection. Equally important, the Partnership aims to bridge existing knowledge gaps, address societal concerns, and face new problems related to radiation protection. To actively engage stakeholders, one of the few key components is to collect their opinions about the radiation protection system, existing criticisms, considerations and expectations on possible improvements and to track this stakeholder engagement in time.

Methods

The PIANOFORTE partnership developed an online questionnaire to map stakeholders and to prepare these networks for direct engagement by getting their opinions on different radiation protection topics. In the survey, by assessing their opinion, which may include their preferences for future R&D projects or their views on health and radiation protection topics, the main objective was to identify where networking and communication should be enhanced.

Initially, the responses to the questions were evaluated individually, analyzing each answer separately. Subsequently, our objective was also to identify opinion groups based on the collected data. By employing a clustering approach, we can identify groups of individuals with similar attitudes and preferences and measure the prevalence and significance of these clusters within the respondent pool. For this, the Positive Matrix Factorization (PMF) method was chosen, which is a widely used data evaluation technique.

Results

We received feedback from nearly every European country, along with participation from five other nations, which means that a broad international response sample has been collected. A total of 440 respondents answered the survey, however, keeping in mind that not all stakeholders would find our sample to be representative, it did manage to capture a large amount of input from stakeholders (70 %) who had not previously participated in such surveys.

The survey showed that PIANOFORTE is well known also by many stakeholders from outside the Partnership, suggesting that the Partnerships' dissemination and communication activities from the first project months have been fruitful. By including informative content about the Partnership and its activities, the survey has increased awareness of PIANOFORTE and radiation protection related issues and leveraged the number of officially registered stakeholders. The survey respondents' feedback on which research topics should be prioritized should have a high priority for the PIANOFORTE Open Calls and have already been used within the prioritization process of the topics of the first PIANOFORTE Open Call. Responses were diverse, as anticipated, because of the diverse structure and varying professional background of the survey participants. As a whole, the research topics in the field of health and medical use of ionizing radiation were considered as having a slightly higher priority.

Going from research to implementation, an important finding from the survey is the substantial heterogeneity in the perception of EU Basic Safety Standards Directive (BSS) implementation. This highlights the imperative for a comprehensive follow-up analysis in this domain.

We could successfully apply the PMF method to group respondents and attitudes. As a result, we identified 4 distinct opinion clusters. Interestingly, despite the fact that only a small number of respondents identified themselves as non-professionals in the field of radiation protection, they predominantly clustered within just two groups (1&2). Given that improving radiation protection is relevant to the broader society, it is crucial to explore the areas of interest and concerns specific to these groups. Members of group 1 frequently responded with 'I don't know' to several questions, indicating a lack of decisive opinions. On the other hand, those in group 2, which as the only one includes members of the broader public (however only 17 individuals) among other stakeholders, exhibited a higher degree of concern. This group displayed the strongest disapproval of nuclear facilities, and notably, radon measurement was infrequently observed among its members. Members of these opinion clusters expressed low satisfaction with the availability of information and the implementation of measures in accordance with the EU BSS. Notably, a significant number of respondents either chose not to answer or lacked a clear opinion on these matters, indicating a potential information gap that needs to be addressed.

Regarding groups 3 and 4, we were able to identify stakeholder groups with a notably positive attitude towards nuclear facilities. A substantial portion (65 %) of these individuals have actively conducted radon measurements in their homes, reflecting a higher level of awareness and engagement in this regard.

Related publication

- [1] V. Groma, B. Madas, F. Rauser, M. Birschwilks, A. Blume, A. Real, R. Murakas, B. Michalik, I. Paiva, TM. Sjømoen, A. Tkaczyk, JM. Popic: *Quantitative stakeholder-driven assessment of radiation protection issues via a PIANOFORTE online survey*, submitted to Radiation and Environmental Biophysic

DELISA-LTO: INTERNATIONAL PROJECT PROPOSAL FOR RESEARCHING THE AGING OF REACTOR PARTS

*Balázs Hargitai, Dávid Cinger, Andor Kristóf Csikós, Ildikó Szenthe,
Márta Horváth, Ferenc Gillemot*

Objective

The examination of the materials of the primary circuit equipment and structures is an essential condition for the long-term operation of pressurized water reactors, with an operating time of more than 60 years. DELISA-LTO (DEscription of the extended LIfetime and its influence on the SAfety operation and construction materials performance – Long Term Operation with no compromises in the safety), a project started in June 2022 with the support of the European Union, wants to give an answer for engineering material science challenges of long-term operation beyond 60 years.

One of the goals of the project is to determine the most affected and endangered components in terms of long-term operation, to describe the changes in the material properties after 60 years; specifically focusing on the swelling that occurs during ageing and the degradation mechanisms caused by thermal ageing.

During the work, after selecting the appropriate heat treatment parameters, the selected primary circuit materials must be thermally aged at a temperature and duration that can be used to examine the effect of thermal ageing on the materials of the primary circuit components and pipelines offered by the participating institutes and institutions, in the event of operation exceeding 60 years.

During the period of project preparation, the institutes applying for the project assessed the available materials suitable for further examination. The most affected components in terms of service life beyond 60 years include the heat exchanger tubes of the steam generators, typically with cyclic thermal stress, and the internal parts of the reactor vessel in terms of swelling. We needed materials that were already available at the partner institutes, that had spent at least 20-30 years in operation, under recorded conditions, and their original material certificate before installation were also available. Finally, among the available materials, the decommissioned Jaslovské Bohunice Nuclear Power Plant (WWER 440 V230 type, Slovakia - block 1 and block 2), the Paks Nuclear Power Plant in Hungary and WWER 1000 type reactors in Ukraine, mainly of reactor internal and primary circuit origin materials were chosen.

Methods

The obtained materials must be divided into two, one must be examined in its current state, and the other half is simulated with the help of accelerated thermal aging for the long-term operation of more than 60 years, after which it is examined using the same material's testing methods.

The project participants chose the following mechanical testing methods: Charpy impact test, static fracture toughness test, tensile test, hardness measurement, and microstructural investigations with the help of optical and scanning electron microscopy, Positron Annihilation Spectroscopy (PAS), and other methods.

From the test results of the materials in their as received state and thermally aged state, we can draw conclusions about the degradations that occur during the long-term operation.

Results

The project is currently in the first third of its 4-year duration. The participating institutes have just started processing the materials and examining the received conditions. Heat treatment of materials intended for thermal ageing has started. The examination of the received materials is expected to be completed by the end of 2024. Testing of thermally aged materials is expected to be completed in December 2025.

The first results are expected to be presented at the end of summer 2024.

Remaining work

Our institute will perform various material testings of the received parts, completion of thermal ageing and its evaluation. Collecting all test results and analyzing them from the point of view of long-term operation will follow it.

ACCELERATOR AND RESEARCH REACTOR INFRASTRUCTURES FOR EDUCATION AND LEARNING, EURATOM ARIEL PROJECT

Tamás Belgya and László Szentmiklósi

Objective

Integration of access to neutron facilities with education and training. Experiments in international teams. Hands-on training for students at the graduate and postgraduate level - lead to PhD and master theses.

Methods

Teaching and training of students using the Prompt-gamma Neutron Activation Analysis (PGAA) facility of Budapest Neutron Centre (BNC), which can provide important nuclear data for applications. In addition, provision of measuring possibility for young students for their work to increase the competence in the field of nuclear data production and applications. Organizing hands-on school for young students and post-docs together with Budapest University of Technology and Economics Nuclear Technology Institute (BMGE NTI).

Results

After the COVID-19 pandemic, hands-on work could begin from the end of 2022, thus most of our work was concentrated into the year 2023. Tamara Milanovic, PhD Student at Faculty of Science, University of Novi Sad Vinca Institute of Nuclear Sciences Faculty of Science Serbia, and David Knežević PhD student, Institute of Physics Belgrade were the trainees in the 3 week-long $^{107}\text{Ag}(n,\gamma\gamma)$ coincidence experiments, in which 800 GB of list-mode data were acquired. Stefan Oberstedt of EU JRC Institute for Reference Materials and Measurements (IRMM) provided us with a ^{107}Ag target of 99.07% enrichment. Preliminary analysis shows that enough coincidences were collected throughout the campaign and that it will be possible to determine the nuclear decay scheme of ^{107}Ag as well as its gamma-strength functions using the two-step method.

At the end of September, the H2020 ARIEL nuclear data school, entitled "Hands-on school on nuclear data from Research Reactors" was held. 25 students were selected from 58 applicants from 27 countries all over the world. More information can be found on the web page of the school: <https://indico.cern.ch/event/1290109/>.



Figure 1: The students of the school before the teaching reactor of BMGE NTI.

Remaining work

The collaboration is planned to continue with the Faculty of Science, University of Novi Sad, but the ARIEL project has ended.

Related publications

- [1] N. Jovancevic, D. Knezevic, et al.: MLZ User Meeting 2023, Talk.
- [2] D. Knežević, N. Jovančević, C. Stieghorst, T. Milanović, L. Szentmiklósi, Z. Révay, T. Belgya: *Radiative capture study of silver γ -decay spectra using $\gamma\gamma$ -coincidences*, ARIEL Final Workshop, Paris (2024) Talk

DMS FAST SHUTTER PROTOTYPE DEVELOPMENT

András Zsákai, Dániel Réfy, Erik Walcz, Domonkos Nagy, Dénes Zoltán Oravecz, László Richárd Csiszár, Sándor Zoletnik

Objective

The project started at the beginning of 2022 to develop a fast shutter prototype that can effectively close off a 40 mm aperture in under a few milliseconds. The shutter will be part of the Disruption Mitigation System (DMS) which is for the protection from the consequences of plasma disruptions during high-power operations. This works on the basic principle of a cryogenic pipe gun with a several-meter-long barrel. It is important to avoid any contact between the pellet and the internal surfaces of the flight line to minimize the risk of premature pellet breakage. Therefore, the internal dimensions of the flight tube of the Shattered Pellet Injection (SPI) are relatively large compared to the pellet, hence providing a bypass for propellant gas to pass the pellet resulting in a significant quantity of propellant arriving in the plasma ahead of the pellet. This will cause undesirable instability in the plasma and compromise the effectiveness of disruption mitigation. One possible solution for this issue is the use of a fast-acting shutter in the flight line, which will close after the pellet has passed through it to hold back the propellant gas, therefore the need to build and test a prototype has arisen.

Methods

During 2023, the main aim of the research was to confirm the chosen concept of the fast shutter [1] which consists of an eddy current based accelerator (copper coil – copper ring pair) and an eddy current based decelerator (conductive plate – magnet stack pair). Based on previous tests on a simpler test bench [2], a new concept has been designed [3] with more capabilities in terms of acceleration and deceleration while being also vacuum-tight and using the same diagnostics method (optical LEDs) [2] as before. The design has been tested for various conductor plate materials and various accelerating plate materials. Additionally, cycle testing software has been built up for the design to be able to run the shutter for 10.000 cycles.

Results

The new design performed flawlessly and a minimum of 2 ms closing time was reachable using an 800 μF capacitor with a 2kV voltage source, while using an aluminium secondary coil and an aluminium conductor plate (Al Al Al case). Alternatively, an aluminium secondary coil with a copper conductor and titanium casing setup was also tested (Al Cu Ti case) and compared.

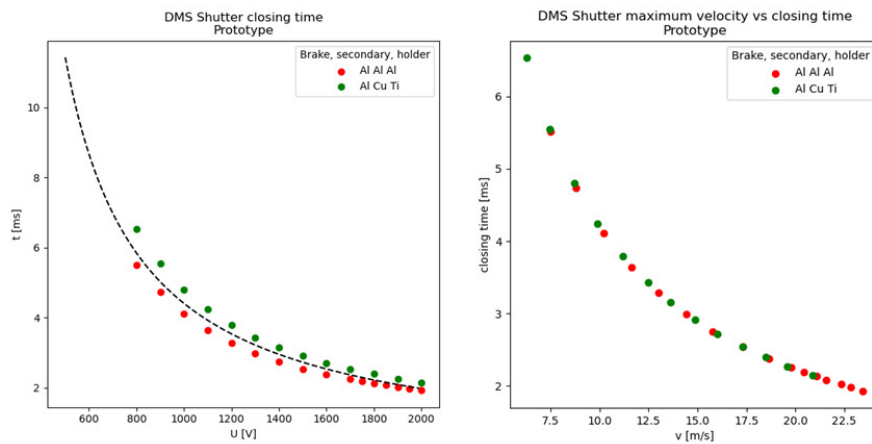


Figure 1: Results for the Al, Al, Al (red) and the Al, Cu, Ti (green) setup: closing time as a function of capacitor voltage (left) and closing time as a function of maximum shutter head velocity (right)

After proving that the concept could meet the strict closing time requirements, we started to modify the system to run the 10.000 cycle tests to show the sturdiness of the system. The first cycle tests were conducted in December.

Remaining work

The cycle testing of the shutter needs to be finished while performing a leak rate analysis of the shutter during the cycle testing.

Related publications

- [1] A. Zsákai et al.: *Fast Shutter optioneering study for the ITER Disruption Mitigation System*, DOI: 10.1016/j.fusengdes.2024.114324
- [2] D. I. Réfy et al.: *ITER DMS Fast Shutter development and laboratory testing*, DOI: 10.1016/j.fusengdes.2024.114156
- [3] L. R. Csiszár et al.: *Mechanical design of a Fast Shutter for the Disruption Mitigation System*, DOI: 10.1016/j.fusengdes.2024.114330
- [4] D. I. Réfy et al.: *ITER DMS Fast Shutter Laboratory Prototype Testing*, abstract sent to SOFT 2024 conference

FUSION RESEARCH AND DEVELOPMENT IN THE EUROFUSION PROGRAM

Sándor Zoletnik

Objective

A coordinated research program is being conducted in the European Union for the development of nuclear fusion energy production. It is managed by the Eurofusion consortium, which includes participants from each Member State. From Hungary, the HUN-REN Centre for Energy Research is the member of Eurofusion, and the HUN-REN Wigner Research Centre for Physics and the Budapest University of Technology and Economics participate with some contributions as an "Affiliated Entity". The Eurofusion work program comprises two main elements: plasma physics research on existing experiments and development of the EU Demonstration Fusion Power Plant (DEMO) conceptual design.

Methods

In 2023 the Fusion Plasma Physics Department (FPL) participated in experiments on the Joint European Torus (JET, Culham, UK) by operating and analysing data [1-4] of the Lithium-beam diagnostic, on the MAST Upgrade tokamak (Culham, UK) by measurements with the Beam Emission Spectroscopy (BES) diagnostic [5], on the Wendelstein 7-X stellarator (Greifswald, Germany) by video and alkali beam diagnostics [6-10]. After several years of delay the joint EU-Japan tokamak experiment, JT-60SA performed its first plasma experiment in December 2023. The first EU diagnostic was the EDICAM camera system developed and operated by the FPL team. Besides observing the plasma shape and other discharge properties a study was done for the possibility of detecting high-energy (runaway) electrons in the discharge [11]. Data from earlier experiments on COMPASS [12,13] and ASDEX Upgrade [14] were also evaluated and results were published.

The experimental work with beam-based diagnostics is supported by modelling activities [15].

Work continued on the design of the DONES irradiation facility. System engineering studies and design of the test system are being done by engineers of FPL. Several other elements of the device are being designed by involving C3D Kft. as subcontractor.

In the conceptual design work of the EU DEMO fusion reactor, the remote handling concept of the internal blanket modules is being designed with contributions from FPL. The conceptual design work of the DEMO visible and infrared diagnostic is led by Daniel Dunai from FPL with contributions from various EU laboratories. This work is closely related to the Eurofusion Engineering Grant of Imre Katona. The Fusion Technology Department (FTL) contributes to the DEMO design work by studying and testing methods for in-situ joining of cooling pipes.

Results

On the JET tokamak, the Li-beam diagnostic provides edge plasma density profiles and fluctuation data related to plasma turbulence. This is important information, therefore used in the study of various phenomena [1-4]. On the MAST-Upgrade tokamak, the upgraded BES diagnostic was installed in 2022. In 2023, systematic measurements were done and the data evaluation software was further developed. The Wendelstein 7-X stellarator finished its Op2.1a campaign in March 2023. The video camera system and the alkali beam diagnostic was operated by the staff of FPL. Data evaluation continued for the earlier campaign. A statistical study was completed on edge plasma turbulence [6] revealing similarities and differences to edge plasma turbulence in tokamaks. To complement this one-dimensional study edge plasma turbulence was also investigated in 2D by video cameras [16], which revealed the poloidal movement of structures and spatial variations in turbulence activity.

Preparations were continued to develop our diagnostic techniques to provide data for real-time control systems. The software integration of EDICAM into the MARTE framework was completed [17], and work started for the application of artificial intelligence methods for swift calculation of alkali beam light emission from plasma parameters. This, and similar methods are considered for the real-time calculation of edge plasma density profiles from alkali beam measurements. The alkali beam diagnostic on the Wendelstein 7-X stellarator was upgraded with a second optical observation, which is devoted to spectroscopic measurements [19]. The possibilities were explored by evaluating trial measurements in the Op.2.1b campaign which revealed that the diagnostic can provide plasma ion temperature data in the plasma edge with about one s time resolution.

The DONES design work concentrated on the mechanical and neutron shielding optimization and tolerance analysis of the concrete shielding of the test cell [20]. Optimization was done for the lithium target, and thermo-mechanical optimization of the liquid lithium storage vessel under the device was completed. An additional work was the design of remote maintenance procedures and system engineering [21].

In the EU DEMO design the concept of a manipulator system has been developed [21,22] which can precisely move the several ten ton weight blanket modules in the tight spaces. The DEMO optical diagnostic design focussed on two elements. The divertor observation system used modelling of the divertor plasma to optimize the viewing range of the diagnostic, while for the pellet observation the consequences of the possible pellet injector technologies were explored. Engineering modelling and experiments were done for the brazing technologies of large diameter cooling pipes.

Remaining work

The JET tokamak performed its final experimental campaign with Deuterium-Tritium mixture fuel and achieved record fusion energy production. The accumulated experimental data will be processed and published in the coming years. The MAST Upgrade tokamak will continue operation in 2024, and the BES diagnostic will be used for plasma turbulence measurements. The JT-60SA tokamak will remain in shutdown for 2 years, when the heating systems and more diagnostics will be installed. Discussions started whether additional EDICAM systems should be built and installed. The next experimental campaign of the Wendelstein 7-X stellarator will start in September 2024, when the video and alkali beam diagnostic will be operated. Data evaluation from previous campaigns is still ongoing.

The design work for the DONES irradiation facility will continue within Eurofusion until 2025, but it is gradually taken over by the new established DONES legal entity. The DEMO design activities will also continue until 2025 when the conceptual design should be finished.

Related publications

- [1] L. Frassinetti, C. Perez von Thun, B. Chapman-Oplopoiou, H. Nyström, M. Poradzinski, J.C. Hillesheim, L. Horvath, C.F. Maggi, S. Saarelma, A. Stagni, G. Szepesi, A. Bleasdale, A. Chomiczewska, R.B. Morales, M. Brix, P. Carvalho, D. Dunai, A.R. Field, J.M. Fontdecaba, H.J. Sun, D.B. King, D. Kos, E. Kowalska, B. Labit, M. Lennholm, S. Menmuir, E. Rachlew, D.I. Refy, P.A. Schneider, E.R. Solano, N. Vianello, M. Vécsei and JET Contributors: *Nuclear fusion effect of the isotope mass on pedestal structure, transport and stability in D, D/T and T plasmas at similar β_N and gas rate in JET-ILW type I ELMs H-modes*, Nuclear Fusion **63**, 112009 (2023) <http://dx.doi.org/10.1088/1741-4326/acf057>
- [2] E. Solano, ... D. Refy...: *L-H transition studies in tritium and deuterium-tritium campaigns at JET with Be wall and W divertor*, Nuclear Fusion **63**, 112011 (2023) <http://dx.doi.org/10.1088/1741-4326/acee12>
- [3] L. Horvath, B. Lomanowski, J. Karhunen, M. Maslov, P. A. Schneider, J. Simpson, M. Brix, B. Chapman-Oplopoiou, G. Corrigan, L. Frassinetti, M. Groth, K. Lawson, C. F. Maggi, S. Menmuir, R. B. Morales, D. Moulton, O. Myatra, D. Nina, T. Pereira, D. I. Réfy, S. Saarelma, M. Vécsei and JET Contributors, *Pedestal particle balance studies in JET-ILW H-mode plasmas*, Plasma Physics and Controlled Fusion **65**, 044003 (2023) <http://dx.doi.org/10.1088/1361-6587/acbb23>
- [4] I Balboa, ..., G. Kocsis, ...: *Remote Infrared View of JET divertor compatible with D-T operations*, Plasma Physics and Controlled Fusion **65**, 094002 (2023) <https://doi.org/10.1088/1361-6587/ace6d3>
- [5] A. Sladkomedova, I. Cziegler, A.R. Field, A.A. Schekochihin, D. Dunai, P.G. Ivanov: *Intermittency of density fluctuations and zonal-flow generation in MAST edge plasmas*, Journal of Plasma Physics **89**, 905890614 (2023) <http://dx.doi.org/10.48550/arXiv.2306.06704>
- [6] B. Csillag, S. Zoletnik, C. Killer, M. Vécsei, G. Anda, D. Dunai, S. Hegedus, D. Refy, D. Nagy, M. Otte and the W7-X Team: *Statistical analysis of plasma filaments in the island divertor of Wendelstein 7-X*, Nuclear Fusion **64**, 016017 (2023) <http://dx.doi.org/10.1088/1741-4326/ad0af7>
- [7] H.M. Xiang, A. Krämer-Flecken, X. Han, T. Windisch, G. Weir, K. Rahbarnia, J. Schilling, H. Thomsen, S.vaz Mendes, A. Knieps, M. Vécsei, M. Otte, S. Zoletnik, G. Anda, D. Dunai, D. Zhang, P. Kornejew, J. Huang, T. Zhang, X.D. Lin, X. Gao, Y. Liang and the W7-X team: *Investigation of a low frequency coherent mode in Wendelstein 7-X with island divertor*, Nuclear Fusion **63**, 126050 (2023) <http://dx.doi.org/10.1088/1741-4326/ad0415>
- [8] E. Maragkoudakis¹, D. Carralero, T. Estrada, T. Windisch, Y. Gao, C. Killer, M. Jakubowski, A. Puig Sitjes, F. Pisano, H. Sándor, M. Vecsei, S. Zoletnik, A. Cappa and the W7-X Team: *On the interaction between the island divertor heat fluxes, the scrape-off layer radial electric field and the edge turbulence in Wendelstein 7-X plasmas*, Nuclear Fusion **63**, 026011 (2023) <https://doi.org/10.1088/1741-4326/aca6fa>
- [9] A Tancetti, S K Nielsen, J Rasmussen, D Moseev, T Stange, S Marsen, M Vecs ei, C Killer, G A Wurden, T Jensen, M Stejner, G Anda, D Dunai, S Zoletnik, K Rahbarnia, C Brandt, H Thomsen, M Hirsch, U Hoefel, N Chaudhary, V Winters, P Kornejew, J Harris, H P Laqua and The W7-X Team: *Inhibition of parametric decay in heating microwave beams during fluctuations of the density profile in the edge island of Wendelstein 7-X*, Plasma Physics and Controlled Fusion **65**, 015001 (2023) <http://dx.doi.org/10.1088/1361-6587/aca121>
- [10] D. Naujoks, ... G. Cseh, ..., G. Kocsis,...: *Performance of tungsten plasma facing components in the stellarator experiment W7-X: Recent results from the first OP2 campaign*, Nuclear Materials and Energy **37**, 101514 (2023) <http://dx.doi.org/10.1016/j.nme.2023.101514>
- [11] S. Olasz, M. Hoppe, T. Szepesi, K. Kamiya, P. Balazs, G. I. Pokol, *Feasibility of the EDICAM camera for runaway electron detection in JT-60SA disruptions*, Fusion Engineering and Design **195**, 113940 (2023) <http://dx.doi.org/10.1016/j.fusengdes.2023.113940>
- [12] J. Adamek, J. Cavalier, D. Tskhakaya, B. Csillag, L. Cinnirella, J. Lips, D. Lopez-Rodriguez, D. Sosa, D. Medina, P. Vondracek, L. Kripner, M. Komm, M. Sos, H. Lindl and the COMPASS Team, *Temporal characteristics of ELMs on the COMPASS divertor*, Nuclear Fusion **63**, 086009 (2023) <http://dx.doi.org/10.1088/1741-4326/acdd10>
- [13] O. Grover, P. Manz, A. Yashin, D. Réfy, J. Seidl, N. Vianello, G. Birkenmeier, E. Solano, M. Šos, P. Boehm, P. Bilkova, M. Hron, R. Panek, JET Contributors, ASDEX Upgrade Team, COMPASS Team, Globus-M Team: *Experimentally*

- corroborated model of pressure relaxation limit cycle oscillations in the vicinity of the transition to high confinement in tokamaks*, Nuclear Fusion **64**(2), 026001 (2024) <http://dx.doi.org/10.1088/1741-4326/ad0eae>
- [14] J. Galdon-Quiroga, G. Birkenmeier, P. Oyola, H. Lindl, A.Rodriguez-Gonzalez, G.Anda, M.Garcia-Munoz, A.Herrmann, J.Kalis, K.Kaunert, T.Lunt, D.Refy, V.Rohde, J.Rueda-Rueda, M.Sochor, B.Tal, M.Teschke, M.Videla, E.Viezzler, S.Zoletnik, and ASDEX Upgrade Team, *First measurements of an imaging heavy ion beam probe at the ASDEX Upgrade tokamak*, Review of Scientific Instruments **95**(1), 013504 (2024) <http://dx.doi.org/10.1063/5.0175720>
- [15] C. Hill, Dipti, K. Heinola, A. Dubois, N. Sisourat, A. Taoutioui, H. Agueny, K. Tokési, I. Ziaeian, C. Illescas, A. Jorge, L. Méndez, A.S. Kadyrov, N.W. Antonio, A.M. Kotian, T. Kirchner, A.C.K. Leung, J. Ko, J.K. Lee, O. Marchuk, M.G. O'Mullane, E. Litherland-Smith, G.I. Pokol, O. Aszталos, P. Balazs, Y. Wu, C.C. Jia, L. Liu and J.G. Wang: *Atomic collisional data for neutral beam modelling in fusion plasmas*, Nuclear Fusion **63**, 125001 (2023) <https://doi.org/10.1088/1741-4326/acf5da>
- [16] A. Buzás, G. Kocsis, C. Biedermann, G. Cseh, T. Szepesi, M. Szűcs and the W7-X Team: *A study of turbulent filaments in the edge plasma of the Wendelstein 7-X stellarator*, Nuclear Fusion, submitted (2023)
- [17] G. Cseh, G. Kocsis, B. Kovács, E. Skáre, T. Szepesi: *Integrating EDICAM into the MARTE framework*, Fusion Engineering and Design **191**, 113516 (2023) <http://dx.doi.org/10.1016/j.fusengdes.2023.113516>
- [18] M. Karacsonyi, O. Aszталos, A. Jalalvand, D.I. Réfy and G.I. Pokol: *Application of neural networks in beam emission spectroscopy modelling*, 49th European Conference on Plasma Physics, poster (2023)
- [19] D. Nagy, S. Zoletnik, M. Otte, M. Vécsei, M. Krychowiak, R. König, D. Dunai, G. Anda, S. Hegedűs, B. Csillag, I. Katona and W7-X Team: *Development of the W7-X Alkali Metal Beam Diagnostic Observation System for OP2*, Journal of Nuclear Engineering **142-151**, 4 (2023) <http://dx.doi.org/10.3390/jne4010010>
- [20] D. Oravecz, A. Zsákai, C. Melendez, T. Dézsi, S. Becerril, J. Castellanos, A. Ibarra, Y. Qiu: *Updates of the Removable Biological Shielding Blocks inside of the Test Cell, part of the Test Systems of IFMIF-DONES*, Fusion Engineering and Design **200**, 114179 (2023) <https://doi.org/10.1016/j.fusengdes.2024.114179>
- [21] C. Torregrosa-Martin, ... , A. Zsakai: *Overview of IFMIF-DONES diagnostics: Requirements and techniques*, Fusion Engineering and Design **191**, 113556 (2023) <https://doi.org/10.1016/j.fusengdes.2023.113556>
- [22] L. Poszovecz, I. Katona, B. Longauer, S. Budden, O. Crofts, J. Szymanowski, K. Grodzicki: *Assessment of architectural changes that benefit remote maintenance structural feasibility for Large Port-Based Tokamaks focusing on the study of the aspect ratio and the inboard blanket segmentation*, ISFNT conference poster (2023)
- [23] M.Málics, L. Poszovecz, A. Sinha, I. Chiang, I. Katona: *Development of lower manipulator system for breeding blanket maintenance within large port-based tokamaks*, Fusion Engineering and Design **202**, 114398 (2024) <https://doi.org/10.1016/j.fusengdes.2024.114256>

REMOTE MAINTENANCE RELATED TASKS WITHIN THE DEMO PROJECT

*Attila Bóhm, Baross Tétény, Fruzsina Darányi, Jenő Kádi, József Szóke,
Márton Gregor, Miklós Palánkai*

Objective

DEMO is set to be the first example of a commercial fusion power plant (Tokamak type) using the heat produced in the reactor to generate electricity. To successfully produce a fully operational, commercially viable Demonstration Fusion Power Plant (DEMO), the maintenance of the plant must be considered as an integral part of the overall design. Due to the nature of fusion reactors, almost all maintenance will, by necessity, be remote.

Methods

Within the Work Package Remote Maintenance (WPRM) project our tasks cover 2 different topics:

1. Due to the thermal and nuclear loading on the first wall (closest to the plasma), the components will need to be removed and replaced periodically. Installation of new blankets requires the joining of their service pipes. Brazing is one of the alternatives that are being considered for joining the service pipes of the DEMO breeding blankets.
2. The work for 2023 advanced the development of welding, repair, and Non-Destructive Testing (NDT) techniques to be used ex-vessel in DEMO, as part of a program of work that will achieve a validated concept design by the end of Framework Program 9 (FP9).

Results

The results obtained in the topics above:

1. To realize in-bore brazing within DEMO, 2023's work focused on finishing the test rig, on the production of the custom induction coil, and on the preliminary tests aimed at understanding the behaviour of Microbraz 10 and 152, the best candidates for the brazing task so far. Previously, the support structure of the pipes was to be heated and the DN200 samples were manufactured and assembled. Preliminary tests of the induction power generator have been conducted, with the 3-phase electrical and cooling water supply installed. Electromagnetic (EM) 3D / 2D calculations were performed in ANSYS Maxwell as steady-state Eddy Current simulations. The ohmic loss distribution was close-to-axisymmetric, so the 2D model was used. The excitation on the copper coil was 200 A at 50 kHz. The ohmic loss can be seen in Fig. 1. The estimated coil electric power was 22.8 kW, where the total useful ohmic loss was 11.59 kW. Based on the results, the ideal shape of an induction heating coil was designed. A special tool was developed to bend the coil to the proper diameter. (See Fig. 2 and 3.) To avoid the electrical contact between the environment and the copper coil, an aluminium silicate insulation was used. (See Figure 4.)

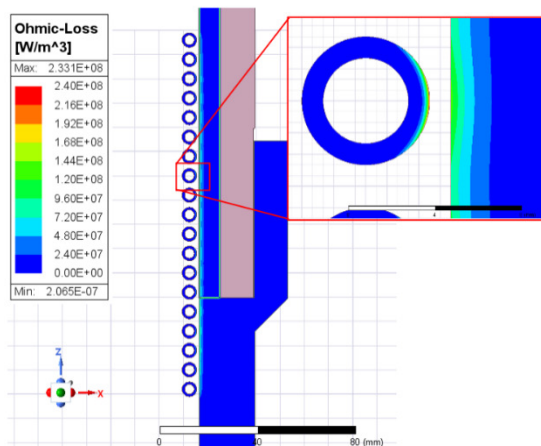


Figure 1: Ohmic loss distribution in the cross-section

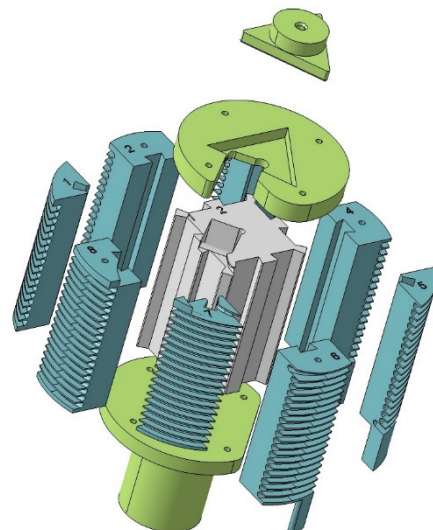


Figure 2: Sliced induction coil bender exploded view

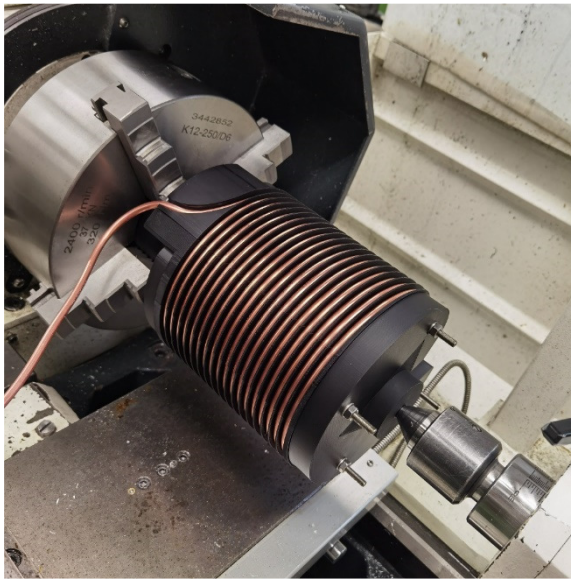


Figure 3: Copper pipe wound on the bending tool



Figure 4: Test induction coil placed in the DN 200 pipe

2. Welding and NDT technologies were examined for remote maintenance operations inside the bio-shield, from which the most viable technologies were selected, and their commercially available alternatives were compared to our assumptions and requirements. The technologies were selected into Datasheet groupings. These groups were created by choosing one attribute about the technologies which can be true for each of them. This could have been size, function, compatibility etc. From this information, sets of System Requirement Documents (SRD) and Context Definition Documents (CDD) were created, finally culminating in the creation of a risk register, which examined the gaps between current and expected technological capabilities and the reality of the assumption that discrepancies between the two could be bridged, given our current timeframe and resources. A successful final review meeting was held about the grouped technologies and discussed the future possibilities.

Remaining work

In the following years our tasks will include:

1. conducting experiments regarding the heating of 2 different pipe sizes, DN80 and DN200. The most important thing would be to find out whether it is possible to heat the brazing filler metal between the pipes to a mostly uniform temperature of around 1000 °C. The type of the brazing filler metal is just as important, potential candidates need to be tested.
2. studying the remaining open questions related to the maintenance of the ex-vessel welds of the DEMO tokamak to obtain a concept design by the end of FP9. New form of documentation has been put into action by DEMO, so the created System Requirement Documents (SRD's) must be transferred into these new documentation forms which observes the readiness and the equipment capability levels. Research in scientific journals have been examined to look for possibilities of the technologies developments in the future, but this work should continue for the next year as well.

Related publication

- [1] J. Kádi, M. Palánkai, M. Gregor, J. Szóke, T. Baross, G. Veres, O. Crofts, T. Tremethick: *Induction brazing of DEMO's large bore cooling pipes*, *Fusion Engineering and Design* **202**, 114379 (2024) ISSN 0920-3796, <https://doi.org/10.1016/j.fusengdes.2024.114379>

ESTABLISHING WEIGHTS FOR COUNTRY-SPECIFIC CRITERIA IN LONG-TERM ENERGY PLANNING ACROSS EUROPE

Endre Börcsök, Veronika Groma

Objective

The goal of the research was to establish country-specific weights for selected criteria based on historical electricity generation data for European countries. These results aim to be a realistic starting point for predictive calculations and to contribute to the development of long-term energy scenarios by adding environmental and social criteria to the commonly used economic and climate impact-focused criteria.

Methods

A novel approach was developed within the Multi-Criteria Decision Analysis (MCDA) framework to determine decision criteria and their importance weights. Historical energy production and consumption data were used as a foundation for long-term energy strategy modelling for various countries. The model included 33 electricity generation technologies and considered the hourly data from ENTSO-E database for four one-week periods from different seasons of the year 2019. Through the modelling, we optimized the hourly production data as variables based on objective functions formulated with various criteria. The variables are constrained by the installed capacities, which are set as the upper limits to ensure that hourly electricity generation values are within realistic limits.

Seven criteria were evaluated: climate effect, air pollution, geopolitical factors, flexibility, risk of accident, and fixed and variable costs.

First, a Linear Programming (LP) model was used to balance the energy produced and consumed at each point in time, optimizing an objective function. Then Monte Carlo simulations were conducted to optimize the importance weights, with the best results being selected based on minimizing the distance to historical data. The simulations performed using an in-house developed energy system model were performed in the GAMS environment.

The study introduces $w(s; c)$ importance weights of criteria (s) for each country (c), the scores of alternatives were determined according to criteria based on data from the literature: installed capacities $CP(s; c; p)$, hourly electricity generation $CE(s; c; a)$, and cross-border electricity exchanges ($CB(s; c; b)$). The hourly electricity generation ($s; a; d$), the installed capacities $x(s; p; d)$ and the cross-border electricity exchanges $x(s; b; d)$ optimized as variables, whilst the objective function to be minimized is formalized as follows:

$$\sum_d \sum_c \sum_s w(s; c) (\sum_a CE(s; c; a)x(s; a; d) + \sum_p CP(s; c; p)x(s; p; d) + \sum_b CB(s; c; b)x(s; b; d)) = z(\min).$$

This linear programming optimization problem is a type of fixed cost distribution problem, with production constraints summarized by the equation:

$$\sum_{a_h} x(s; a; d) + \sum_{b_h} x(s; b; d) - \sum_{b'_h} x(s; b; d) = dem(s; h)$$

where a_h is the hourly value of the electricity generation time series of a country, while b_h is the hourly value of electricity imports and b'_h is the hourly value of electricity exports. Furthermore, the parameter $dem(s; h)$ is the hourly electricity demand of a country.

For the thermal power plants, two artificial variables were introduced to account for the hourly increase and decrease in production:

$$x(s; a_{th}; d) + x(s; a_{uh}; d) - x(s; a_{dh}; d) = x(s; a_{t(h+1)}; d),$$

where production data of alternatives are $x(s; a_{th}; d)$ for the hour h of each day d , the hourly increase in production $x(s; a_{uh})$, and the hourly decrease in production $x(s; a_{dh})$.

Similarly, for energy storage, the recursive conditions were given by:

$$x(s; a_{qh}; d) + x(s; a_{ih}; d) - x(s; a_{oh}; d) = x(s; a_{q(h+1)}; d),$$

where $x(s; a_{qh})$ is the stored energy value for the given hour, while the $x(s; a_{ih})$ and $x(s; a_{oh})$ values are the amounts of the charged and discharged energy.

Constraints corresponding to the installed capacities and the potential constraint of the annual maxima of alternatives related to variable renewable energy sources were also applied:

$$x(s; a_{ph}; d) \leq \delta_{sph} x(s; p; d),$$

$$x(s; b_{ph}; d) \leq x(s; p; d), \text{ where } b_{ph} \text{ is the electricity imports and exports for each hour, and country-specific, seasonal hourly profiles for the variable renewable energy sources } 0 \leq \delta_{sph} \leq 1.$$

The model incorporated the impact of seasonality and constrained the generation of different energy sources by gradients. Hourly gradients were set to specific percentages to reflect the variability in production capacity.

The uniformized criteria values for the main electricity generation alternatives are presented in Table 1.

Table 1: Uniformed criteria values for aggregated alternatives

Alternatives	Criterion						
	Fix Cost	Variable Cost	Climate Change Effect	Air Pollution	Geo-Political Factors	Flexibility	Risk of Accident
Biomass	84.50	135.22	22.90	331.88	0.00	37.03	0.00
Fossil Gas	48.59	203.97	214.06	64.19	479.61	0.00	8.80
Fossil Hard coal	70.83	114.89	440.89	173.66	82.10	37.03	0.00
Geothermal	198.04	64.02	16.30	9.88	0.00	37.03	0.00
Hydro	67.12	48.81	9.25	6.42	0.00	40.79	43.99
Nuclear	127.53	62.86	5.73	18.90	194.99	22.50	703.89
Solar	41.00	58.57	18.94	15.07	0.00	359.72	0.00
Waste	59.52	19.17	22.90	126.81	0.00	37.03	0.00
Wind On-shore	59.56	49.18	5.73	9.88	0.00	185.59	0.02

To obtain the optimum set of importance weights, Monte Carlo simulations were performed. This involved unbiased random sampling and the analysis of the differences in the historical production time series. After an iterative process, the best 10% of the importance weights were grouped into 10 clusters.

Results

Our method has the opportunity to involve additional environmental and social criteria into the traditionally used economic and climate impact-focused criteria, employing multi-objective optimization. We have determined the importance weights of seven distinct criteria for 28 European countries, and these weights were normalized and categorized for comparison purposes (see results in Table 2) [1].

Table 2: Normalized importance weight for each studied criteria for selected European countries

Importance weight/criteria	Very low	Low	Lower Medium	Higher Medium	High	Very high
Fix cost	FR, DK	NL, CH	BE, AT	GR, FI	BG, HU	PT, PL
Variable cost	UK, GR	HR, SL	AT, SE	IT, SK	FR, FI	NL, RO
Climate change	CZ, NL	PL, BG	RO, IT	AT, FR	DE, LV	NO, DK
Air pollution	PL, BG	HU, UK	AT, CZ	ES, BE	SE, SK	LT, GR
Geopolitical factors	PT, SE	SL, SK	FR, GR	ES, DK	CH, DE	NO, IE
Flexibility	IT, NO	RO, HR	IE, CH	FR, LU	FI, HU	SE, PL
Risk of accident	SE, UK	RO, HU	LV, PT	LT, NO	IT, AT	EE, DK

The results varied significantly across the countries studied, of which we would highlight the following:

- The Eastern European region showed exceptional sensitivity towards investment costs.
- Countries relying heavily on renewable or nuclear energy, like Denmark, Greece, Norway, Slovenia, Spain, and the United Kingdom, showed a dominant influence of environmental factors.
- Flexibility criteria aligned well with installed generation capacities.
- Geopolitical factors and the risk of accidents criteria revealed complex interactions, indicating diverse national priorities and sensitivities.

The interpretation of these importance weights is nuanced, as they depend not only on the chosen criteria but also on the available potential, generation, and load profiles that significantly influence modelling. If a country's energy generation excels in a specific criterion, such as climate-friendliness, the alternatives favourably evaluated by this criterion will be reflected in both actual generation and modelling results. Criteria that emerge as decisive in the best results tend to dominate a country's outcomes even after normalization and mean value computation.

The study's initial phase involved selecting solutions with the smallest distances between modelling results and actual electricity generation data. Interestingly, the number of solutions within 20% of the mean distance varied significantly from country to country, with some having as few as three and others up to 300. These results were grouped into clusters that typically exhibited distinct characteristics.

In pursuit of greater accuracy, the study generated 1000 additional solutions within the 20% range of the clusters, from which the best results were chosen. However, this process revealed a clear inhomogeneity among the best results, suggesting that different clusters contributed to the solutions. This discovery raises questions about the influence of modelling constraints on results and whether the criteria weights play a significant role in determining the optimum. To investigate this, the study applied potential constraints increased by 20%, but this adjustment did not yield notable differences, calling for a more thorough analysis to provide conclusive answers.

Even after 1000 additional calculations per country in fixed environments of 10 clusters, no significant improvement was observed in the difference between model-based and historical time series. This led to the normalization of the sum of importance weights of the best results to one for each country, and the evaluation of mean values.

The study also faced methodological limitations, such as the exclusion of cross-border exchanges due to computational resource constraints. This limitation notwithstanding, the simplified model's results generally aligned with expectations. However, certain issues were identified for long-term studies, such as the narrow scope of available potentials when constrained by yearly maximum values, and the potential non-impact of a criterion on the results, allowing for a broad variation in its value. The scarcity of comprehensive studies on evaluating various decision criteria further complicates the validation of the study's findings.

Overall, the study's approach provides a data-driven method for defining importance weights for various criteria, which can aid in the development of energy strategies. However, the results suggest that further research is necessary to fully understand the implications of the findings and the influence of modelling constraints on the optimization of energy scenarios. We aim to conduct further studies with the help of a survey prepared by the social science working group.

Remaining work

We would like to compare our results with the help of a database created based on a large international survey conducted during the year 2023 within the EUROfusion project SES WP. During this survey, responses evaluating importance weights of four selected criteria (economy, environmental, safety, reliability) were collected on a representative sample in 21 European countries. The expected results can be utilized in shaping the EU's long-term energy scenarios.

Related publication

- [1] E. Börcsök, V. Groma, Á. Gerse, J. Osán: *Determination of Country-Specific Criteria Weights for Long-Term Energy Planning in Europe*, *Energies* **16**, 4920 (2023) <https://doi.org/10.3390/en16134920>

X-RAY SPECTROMETRY CHARACTERIZATION OF SIZE-FRACTIONATED AEROSOL PARTICLES

János Osán, Csaba Dücső, Ottó Czömpöly, Veronika Groma

Objective

Direct Total-reflection X-Ray Fluorescence analysis (TXRF) of aerosol particles collected with Cascade Impactors (CI) is a valuable method for size-resolved elemental analysis. Detection limits below 100 pg/m^3 can be reached by laboratory or portable equipment for sampling durations of a few hours. With an appropriate size- and time resolution, the combination of CI and TXRF enables to study daily time trends of the size distribution of chemical elements. Internal standardization generally performed for droplet residues is not straightforward for direct TXRF analysis of CI samples, since the deposition pattern of the collected particles is generally different for various impactor types. Within the AEROMET II project, potential reference samples were developed and characterized. The reference samples have known elemental composition and mass distributed along a lateral pattern similar to the aerosol particle deposits expected in the impactors. The objective of the last year of the project was to use the developed reference samples for the calibration of benchtop TXRF systems and the application of the method for size-fractionated atmospheric aerosol samples.

Methods

The reference samples were prepared on 30-mm Si wafers and quartz discs to be suitable for measurements in most commercial TXRF equipment. Round Cr pads of 2-3 μm in diameter and 50-120 nm in height are distributed randomly within the deposited areas using optical lithography [1]. Deposition patterns of thin stripes (May or Sioutas impactor) or a circularly symmetric series of round spots (Dekati impactor) were considered.

Calibration of benchtop TXRF systems were carried out in two different ways. The T-Star system (Bruker Nano, Germany) allows performing angular scans, therefore a full calibration could be performed using a pre-characterized TiCrNi-Trilayer on silicon. The geometrical parameters were optimized using model calculations of the angular dependence of X-ray fluorescence intensities. The newly developed reference was used as an application sample. The low-power TXRF system at EK is a fixed angle equipment, therefore a two-step calibration procedure was used. First, the relative sensitivities for chemical elements were determined using a standard procedure used for measurement of droplet residues. Series of standard solutions of a concentration range of 0.1 - 10 mg/L were prepared, containing a few elements including Cr, with minimal spectral overlap. Droplets of 5 μL dried on quartz or Si substrates were measured and elemental sensitivities relative to Cr were calculated. Next, by measurement of the newly developed reference samples with known deposited mass of Cr (10 - 50 ng), the instrumental response could be determined (absolute sensitivity in cps/ng).

The combined CI-TXRF method was applied to study the elemental composition of size-fractionated aerosol samples collected at Pardubice (Czechia) by a 13-stage Dekati CI (0.03-10 μm diameter range) and at Budapest (Hungary) by a 9-stage May CI (0.07-10 μm diameter range).

Results

An aerosol sample set collected in Budapest using a 9-stage May impactor on 28.8-mm diameter Si wafers was analyzed both by the compact TXRF system of EK and the S4 T-Star system at Bruker Nano GmbH. The comparison of the results indicates a reasonable agreement between the results obtained by the two, differently calibrated TXRF systems.

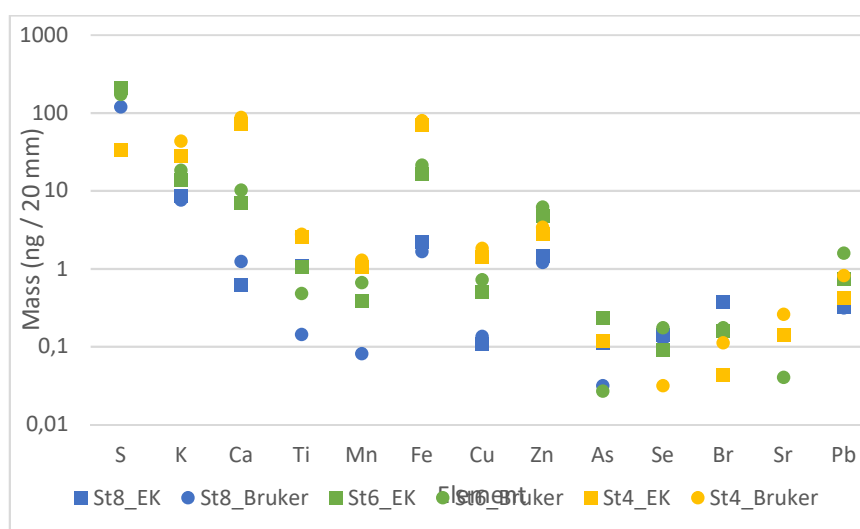


Figure 1: TXRF results expressed as deposited elemental masses, as determined by the compact TXRF system (EK) and the S4 T-Star (Bruker); St8: 0.18–0.3 μm ; St6: 0.6–1.2 μm ; St4: 2.4–4.8 μm fraction

As an example of the results of the aerosol samples collected at Pardubice, normalized elemental size distributions are plotted for sample set PD8 (Stages 1-12, in order to cover the PM_{10} range), which are presented as $\Delta C/\Delta \log d_p/C$ (Fig. 2). As the argument of log function needs to be dimensionless, d_p stands for relative particle diameter (-) and C is the total concentration of the measured size fractions (30 nm - 10 μ m) determined by TXRF in ng/m^3 . This way the areas under the curves are equal to one. The calculated values are plotted in the function of the representative diameter (which is the geometric mean of the cut-off diameters for each stage in our case). The reason for presenting the size distributions normalized to the total concentration is that both major and minor components can be plotted on the same figure, despite that two or even three order of magnitude difference can occur in their concentrations. By presenting all elements on the same figure the differences and similarities in the shape of size distributions are clearly noticeable. Elements having size distribution of similar shape can be assumed to be linked to the same emission sources.

The size distribution of major elements of crustal origin (Ca and Ti) is clearly unimodal covering the coarse fraction. Secondary particles formed from precursor gases (S and Cl) are dominated in the fine fraction. Elements of both crustal and anthropogenic origin (Fe and K) have both modes in their distribution with different proportions. Surprisingly, Mn in Pardubice dominates in the fine fraction, suggesting anthropogenic origin.

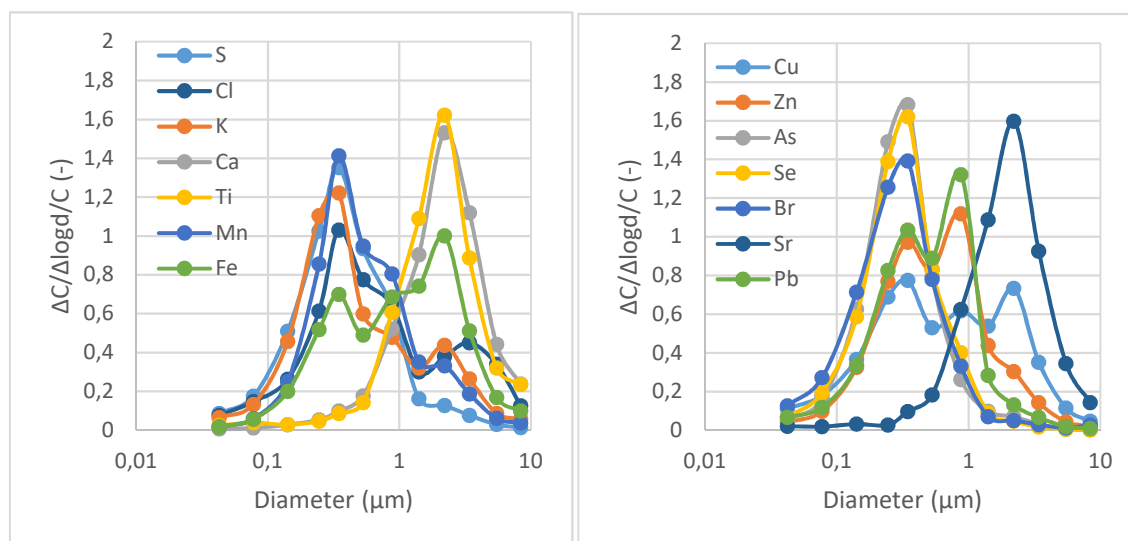


Figure 2: Normalized elemental size distribution of particles for sample set PD8 collected in Pardubice (CZ), for major elements (left), minor and trace elements (right)

Thanks to the high sensitivity of the TXRF method, size distributions for trace elements As, Se, Br, Sr and Pb could be evaluated, which can be informative for sources. The peak overlap between As-K and Pb-L lines could be resolved accurately as it is indicated by the completely different size distribution of the two elements. Zn and Pb show a common bimodal distribution, while As and Se show an unimodal distribution in the fine fraction, indicating common sources of Zn, Pb, and As, Se, respectively.

Related publication

- [1] J. Osán, C. Dücső, O. Czömpöly, M. Gottschalk, S. Seeger, A. Gross, Y. Kayser and B. Beckhoff: *Potential reference samples for TXRF analysis of airborne particulate matter*, 19th International Conference on Total Reflection X-ray Fluorescence Analysis and Related Methods, Clausthal, Germany, 5-8 September 2023, SS-3-06 (2023)

CALCULATIONS ON HIGH PU CONTENT MOX FUEL IN FAST REACTORS

Berta Bürger, János Gadó, Zoltán Hózer, Emese Slonszki

Objective

In the framework of the EU PUMMA project focusing on high-plutonium content Mixed Oxide (MOX) fuels, experts from HUN-REN EK conducted fuel cycle and fuel element behaviour calculations. The objective of fuel behaviour simulation was to enhance the validation range of the codes through inter-code comparison, comparison with experimental data, and, if possible, development/improvement of models. The aim of fuel cycle simulation was to provide detailed data for proliferation analyses.

Methods

Using the FUROM-FBR computer code, the irradiation of three high-plutonium content MOX fuel elements (CAPRIX, TRABANT 1/1, and TRABANT 2/2) was simulated by HUN-REN EK experts. The following institutes participated in this task: KIT (Germany) with the FEMAXI code; PSI (Switzerland) with the FRED code; CEA, EDF, and FRAMATOME (France) with the GERMINAL code; EPFL (Switzerland) with the OFFBEAT code; VTT (Finland) with the TRAFIC code; ENEA, POLIMI (Italy), UJV (Czech), and VUJE (Slovakia) with the TRANSURANUS code; and SCK-CEN (Belgium) with the MACROS code.

In the fuel cycle calculations, thermal Evolutionary Power Reactors (EPR) and Gas-cooled Fast Reactors (GFR) were modelled. Two scenarios were considered: one with a MOX fuel containing 15-16% plutonium, and another with 30-32% plutonium content. The calculations by HUN-REN EK were completed as early as 2022. The results were sent to Finnish VTT experts in 2023, who performed proliferation calculations.

Results

Within the EU PuMMA project a sensitivity task was set up in order to study the effect of various parameters on the results of calculations for the three experimental irradiations (CAPRIX, TRABANT 1/1, TRABANT 2/2). The simulation of three fuel irradiation histories was successfully completed using the FUROM-FBR code. As a summary, one can state that the investigated effects are generally small. The most significant change can be observed in the gap size which is influenced by the fuel thermal expansion coefficient and also the cladding swelling. It leads to changes in the gap conductance and the pellet outer temperature. Fission gas release and internal pressure are influenced by the variation and the switch on/off the increase of the grain size and also by the decrease of cladding swelling (Figure 1).

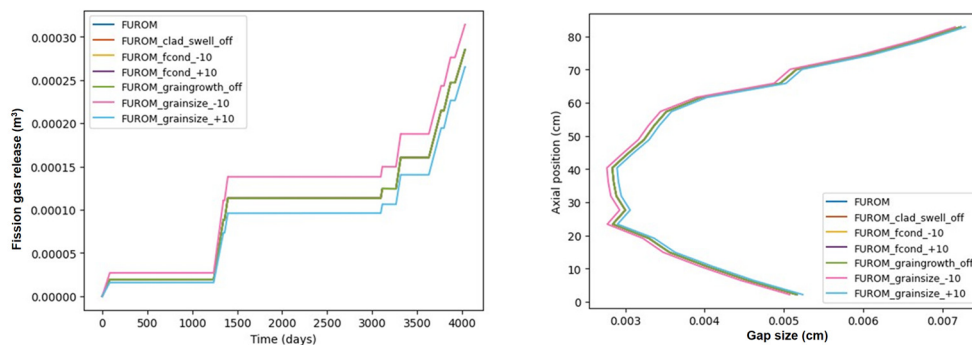


Figure 1: FUROM-FBR calculation of CAPRIX irradiation test

The results of fuel cycle simulations highlighted that reactors and interim storages provided the highest resistance against nuclear proliferation due to the form and inaccessibility of materials. Conversely, the lowest resistance against nuclear proliferation was observed during MOX fuel reprocessing and fresh MOX production, as plutonium separation occurs in processes where the material is easily accessible. According to the analyses, increasing the plutonium concentration in MOX fuel (from approximately 15% to around 30%) does not significantly increase nuclear proliferation risks.

Remaining work

The measurement results of the irradiated fuel elements were only partially available in 2023, limiting the possibilities for comparison between measurements and calculations. Further comparison of measured and calculated data is expected in 2024.

Related publication

- [1] M. Stefanowska-Skrodzka, J. Lavarenne, E. Deveaux, E. Brunetto, D. Jaramillo, V. Matocha, A. Magni, M. Massone, K. Mikityuk, Y. Wang, J. Gado, B. Burger, V. Blanc, V. Dupont, L. Argeles, B. Perrin, G. Michel, C. Fiorina, J. Peltonen, A. del Nevo, L. Luzzi, D. Pizzocri, S. Lemehov, S. Bebjak, T. Chrebet, C. Strmnsky: *Fuel pin behaviour under irradiation with high Pu content: Benchmark exercise*, EU PuMMA Task 2.2. 13-11-2023

SUPPORT LABORATORY FOR THE ITER DISRUPTION MITIGATION SYSTEM

Sándor Zoletnik, Erik Walcz, Tamás Szepesi, et al.

Objective

This project started at the end of 2020 with the aim of setting up a laboratory for the development of a “Shattered Pellet Injection” (SPI) technology for ITER [1]. The equipment consists of a cryogenic pellet injector [2], a flight tube and a shattering plate, where the solid Hydrogen, Deuterium and Neon pellets are broken into pieces, and finally their fragment size and velocity distributions are measured. This solid fragment cloud can inject material into an unstable ITER plasma much faster and deeper than in gaseous form, therefore can more quickly cool the plasma, and prevent damage to the device wall from uncontrolled heat loads. The technology of reproducibly generating a suitable distribution fragment cloud is expected to be provided by the Support Laboratory, so that the 27 SPI injectors for ITER can be built and reliably operated.

The pellet production recipes were developed in 2022. In 2023, the experiments aimed at studying the shattering process and determining the fragment distribution for various pellets and recipes.

Methods

The fragment size, velocity and spatial distribution are measured with the double laser curtain diagnostic [3]. The setup is shown in Figure 1. Two different colour line lasers illuminate two planes in the diagnostic vacuum vessel. The pellet enters through a flight tube and shatters on the angled plate in the shattering head. The fragments fly through the two laser light sheets and scatter light towards the two fast cameras. A dichroic filter separates the two different colour lights to the two cameras. A software was developed to identify fragments in the images. From the fragment size and laser light crossing time the volume, spatial location and arrival time of each fragment are determined. The fragment velocity is determined from the flight time between the arrival of the pellet into the shattering head and detection in the laser curtains. In the design, it was foreseen to measure with two laser curtains as shown in Figure 1. However, it proved to be impossible to identify individual fragments as they crossed the two laser curtains. Therefore, in the final experiments only a single laser curtain was used.

Two different shattering devices were applied in the experiments: an open one where the shattering plate has no surrounding box, and a closed one where the shattering head is located inside a box following the ITER design.

Additionally to the pellet shattering experiments, the ITER Disruption Mitigation System (DMS) Support Laboratory also tested the concept of the Optical Pellet Diagnostic (OPD) developed by Fusion Instrument Kft. in the framework of a separate ITER contract. This diagnostic aims at determining pellet parameters after launch but before shattering.

The “pfreeze” pellet desublimation code developed in 2022 was further developed and systematic runs were done to compare the simulation results to the measurements in the ITER DMS Support Laboratory.

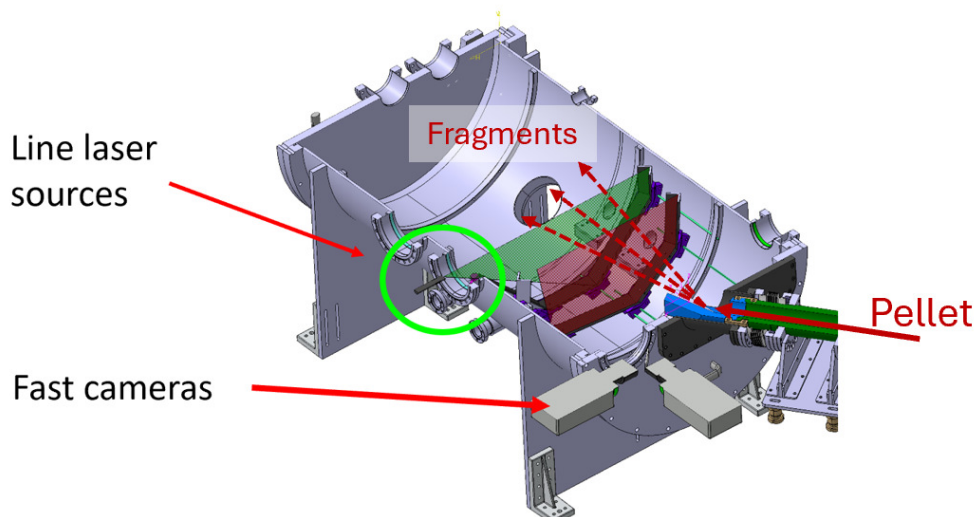


Figure 1: Design of the double laser curtain diagnostic

Results

The fragment distributions were determined for both shattering heads, hydrogen, neon and deuterium pellets with 28.5 mm diameter and 55 mm length. For each pellet material two velocities were measured to see differences in the fragment distribution. At least 5 identical velocity pellets were measured in each case. It was found that fragments larger than about 1

mm can reliably be measured, but the statistics of smaller ones is unreliable. The distributions of the larger fragments were successfully determined. For each pellet material a critical velocity was found below which larger fragments were produced. The fragment distributions were reproducible for identical pellets, statical fluctuations were observed only for the largest fragments around 5 mm, where the number of fragments is small.

The OPD concept was verified with real ITER-size ($d=28.5$ mm) hydrogen and neon pellets. About 40 pellets were measured, processed and the capability of the diagnostic for determining the pellet velocity, 2D passing location, angle and quality was demonstrated.

The comparison between pellet desublimation model results and experiments (gas desublimation rate, pellet production time) shows best agreement when high gas flow rate is applied during pellet production, but the experimental gas desublimation rate falls below modelling for slow gas feed. This is considered the result of nonuniform gas pressure in the pellet production volume, which was verified experimentally. In the modelling uniform gas pressure is assumed.

Remaining work

ITER extended the ITER DSM Support Laboratory contract with a new Task Order. Three aims are defined: measurement of pellet velocity direction scatter using a large diameter flight tube, studying gas flow and retaining of propellant gas in a volume identical with the ITER design, and study of pellet production with a gas system similar to the ITER design. The engineering design of these modifications is ready, manufacturing and experiments will be done in 2024.

An answer to the ITER tender to develop a prototype of the OPD was submitted by a consortium of EK and Fusion Instruments Kft. ITER awarded the tender to this consortium, development will start in 2024 for two years.

Related publications

- [1] S. Zoletnik, et al: *Shattered pellet technology development in the ITER DMS test laboratory*, Fusion Engineering and Design **190**, 113701 (2023) <http://dx.doi.org/10.1016/j.fusengdes.2023.113701>
- [2] E. Walcz, et al: *Development of a Shattered Pellet Injector test bench for the ITER DMS support laboratory*, Fusion Engineering and Design **191**, 113584 (2023) <https://doi.org/10.1016/j.fusengdes.2023.113584>
- [3] G. Kocsis, et al: *Fragment plume diagnostics for cryogenic pellet shattering studies: Development and first experimental results*, Fusion Engineering and Design **190**, 113515 (2023) <http://dx.doi.org/10.1016/j.fusengdes.2023.113515>

STRUMAT: STRUCTURAL MATERIALS RESEARCH FOR SAFE LONG TERM OPERATION OF LIGHT WATER REACTOR NUCLEAR POWER PLANTS

*Ildikó Szenthe, Ferenc Gillemot, Dávid Cinger, Balázs Hargitai,
Kristóf Andor Csikós, Márta Horváth*

Objective

One of the critical issues for the long-term operation of pressurized water reactors is the embrittlement of the reactor pressure vessel wall, caused mainly by neutron irradiation. The goal of the project is to understand the unfavourable synergy between Nickel, Manganese and Silicon on the microstructure and mechanical properties of the reactor pressure vessel at high neutron fluences. This is needed to elucidate the irradiation effects toward the end of the life of the vessel. Existing embrittlement trend equations tend to underpredict the reactor vessel material embrittlement at higher fluence regimes. The suitability of a master curve approach at high fluences, together with the use of small/sub-sized test specimens characterize irradiation induced shifts in reference curves for bulk materials, needs to be further investigated.

Methods

An international collaborative research project with the participation of 17 European countries + Ukraine was set up to study these issues. The project is led by our institute. An irradiation campaign had been performed in the High Flux Reactor, Petten, Netherlands. A variety of different steel reactor vessel samples with systematic variations in Nickel, Manganese and Silicon contents have been irradiated to a high fluence, which resembles reactor operation for greater than 60 years. The materials were coded from A to N for easier identification.

Results

HUN-REN EK undertook the management of the manufacturing and testing of irradiated small specimens. More than three hundred fracture toughness testing specimens were tested from as-received reference and irradiated materials. The results were evaluated together with the results of tensile testing and hardness testing, and compared with microstructural analyses. Figure 1 shows the individual irradiation embrittlement shift of T_0 , the measured reference temperature change, caused by the irradiation in the function of the Mn+Ni+Si content. The tendency is clear, the increasing Mn+Ni+Si content increases the T_0 shift. This result can be used in the development of embrittlement trend evaluation curves.

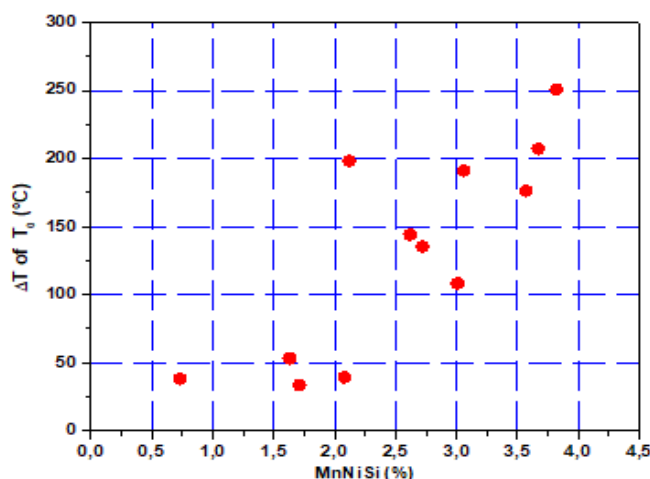


Figure 1: Irradiation-induced shift of T_0 reference temperature vs. the Mn+Ni+Si content of the tested material

Remaining work

Based on the test results the embrittlement evaluation trend curves will be evaluated. The results of the project will be disseminated in several conferences in 2024.

Related publications

- [1] D. Cinger, B. Hargitai, K. A. Csikós, M. Horváth Márta, F. Gillemot: *Small specimen test technics*, OATK (2023)
- [2] F. Gillemot, M. Horváth, D. Cinger, B. Hargitai, I. Szenthe: *Master Curve evaluation on miniaturized CT specimens*, OATK (2023)
- [3] F. Gillemot.: *Partner Project contribution in STRUMAT LTO*, FRACTESUS consortium meeting, MOL (2023)
- [4] D. Cinger: *Microstructural examination of 15H2NMFA RPV steel*, STRUMAT_LTO consortium meeting, Dresden (2023)

TOWARDS OPTIMIZED USE OF RESEARCH REACTORS IN EUROPE

László Szentmiklósi

Objective

The TOURR was a project aiming at proposing a strategy for the optimization of the European Research Reactor (RR) fleet and providing tools to facilitate the achievement of the objective. This initiative is an answer to the challenge to assess the impact of the decreasing number of RRs, identify future needs (including new neutron sources), draw a roadmap for the upgrade of the existing RR fleet, and a model for harmonized resource management. The project is also looking into providing the research community with the opportunity to coordinate the use of the Research Reactors and their facilities in terms of access and experimental opportunities for researchers.

Methods

Work Package 3 members compiled the Strategy for the optimized use of research reactors in Europe. It started from the data collected previously from reactor operators with a questionnaire [1] and relied on the data analysis performed via Gap analysis and SWOT analysis. Further, technical recommendations for planning the refurbishment of existing research reactors or the construction of new ones were drafted.

Results

To facilitate the implementation of the 'optimization strategy', the Towards Optimised Use of Research Reactors in Europe (TOURR) project delivered an online platform, reachable at <https://tourr-platform.eu> and open for everyone to join upon moderated registration. It provides an overview of RR according to capabilities rather than to technical characteristics. This makes it, for example, different from the IAEA RR database. The purpose of the platform is to provide information about the use of RRs in terms of their capacity for science and technology, production of radionuclides, education and training activities.

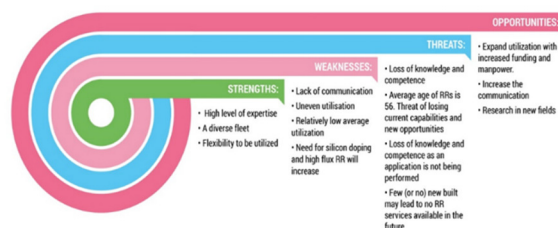


Figure 1: The SWOT analysis of the main challenges of European research reactors

The platform includes a searchable registry of available infrastructures, characterization of these infrastructures as well as a continuously updated overview of the available capacities and corresponding abilities of the participating RR operators. It will be easier to match the capacity 'offer' with the 'demand' on all aspects, once all the information is gathered on the same online tool. It will also facilitate easy contact between potential users and reactor operators [2].

A second activity focused on the future of the European research reactor fleet. A resulting document provides a comprehensive overview of the nuclear fleet as of today. A series of recommendations are issued to plan the refurbishment of the existing RR and also to construct new RRs. Regarding neutron beam applications, the following conclusions could be highlighted:

1. There is a high demand for beam time for neutron science, clearly exceeding capacity.
2. The ILL (Institut Laue-Langevin, Grenoble, France) is currently expected to remain in operation until 2033. By this time, the European Spallation Source (ESS) currently under construction in Lund (Sweden) should be in operation (service entry is expected by 2026).
3. There is a risk of further delays and early commissioning problems in the ESS.
4. The closure of several medium flux facilities in recent years has resulted in the loss of many neutron experimental stations. The concentration of neutron measurement opportunities at a few facilities is more vulnerable to unexpected technical problems. A network of facilities, in contrast, can sustain national or regional neutron scientist communities.
5. Compact Accelerator-based Neutron Sources (CANS) are the preferred options for replacing medium flux reactors for neutron scattering applications.
6. Keeping in operation the ILL until ESS and other alternative neutron sources, which are fully operational, seems the more straightforward way to maintain neutron experimental capacity in Europe.

The results of the project have also been articulated in form of an invited lecture at the RANC-2023 conference [3].

Related publications

- [1] A. Pungerčič, R. Cirillo, J. Walkiewicz, E. Novák, J. Gajewski, L. Szentmiklósi, L. Van Puyvelde, J. Starflinger, D. Cano, G. Pohlner, R. Mikolajczak, G. Pavel, L. Snoj: *Identified Opportunities in Utilization of the European Research Reactor Fleet as a Part of the TOURR Project*, EPJ Web of Conferences 288 04013 (2023) ANIMMA 2023 Proceedings <https://doi.org/10.1051/epjconf/202328804013>
- [2] https://www.tourr.eu/fileadmin/user_upload/TOURR_D3_3_Online_platform_for_optimized_use_of_research.pdf
- [3] L. Szentmiklósi: *Networking activities of European Research Reactors to sustain scientific use, industrial services, and radioisotope supply*, 3rd International Conference on Radioanalytical and Nuclear Chemistry 7-12 May 2023, Budapest

FRACTESUS: FRACTURE MECHANICS TESTING OF IRRADIATED RPV STEELS BY MEANS OF SUB-SIZED SPECIMENS

*Ildikó Szenthe, Ferenc Gillemot, Márta Horváth, Dávid Cinger,
Balázs Hargitai, Kristóf Andor Csikós*

Objective

Safety and operability of any nuclear system heavily rely on a defence in depth strategy where the integrity of structural material plays an essential role. Due to irradiated material availability, the use of small-size specimen to obtain reliable measurement of the resistance to fracture is needed by the nuclear industry to comply with the Nuclear Safety Directive. Attempts to develop small-size specimen fracture toughness measurement (with a ratio of 1:0.16) has already succeeded. However, further efforts are required to validate the results and achieve European regulatory acceptance of this approach. The goal of the project is to develop and demonstrate the procedures necessary to address the various national regulatory authority concerns about data derived from small specimens and, if necessary, to propose changes to current codes and standards to incorporate these procedures. FRACTESUS is involving regulatory bodies, code and standardization committees, the industry and the international community at a very early stage, in order that the consortium can optimize available resources and expertise.

Methods

Un-irradiated and irradiated real- and model Reactor Pressure Vessel (RPV) materials which are representative of nuclear reactor walls had been chosen. The selected materials have to be already well characterized by previously standard tests. Small-scale, compact tension specimens with a 0.16 ratio were fabricated and tested from the original specimen remnants. To enhance the testing quality, benchmark calculation and Round-Robin testing of as received and irradiated materials was initiated.

Results

HUN-REN EK tested irradiated material was produced under the 5th irradiation series in the Heavy-Steel Technology Program conducted in the 80's of the 20th century, and irradiated, annealed and re-irradiated water-water energetic, 440MW reactor vessel steel specimens. The remnants of these specimens and unirradiated pieces were selected as materials for testing the miniaturized specimen technology within the FRACTESUS project. To compare with larger sample behaviour, the range of the measured and calculated values derived from small datasets are similar in large and miniature samples. The applicability of miniaturized specimens for fracture toughness tests under hot cell conditions was demonstrated. Fractography results support the usability of fracture toughness data from miniaturized specimens.

Remaining work

To establish a solid base of small specimen fracture toughness and to achieve change in code and standards at the national regulatory authorities need to compare the results of the standard and miniaturized specimens in a special form. In this task, HUN-REN EK will participate as responsible for the deliverable "Comparison of fracture toughness results from standard and sub-sized specimens". The project will be ended in the second half of 2024.

Related publication

- [1] D. Cinger: *Microstructural examination of 15H2NMFA RPV steel*, STRUMAT_LTO consortium meeting, Dresden (2023)

FAST VALVE FOR NUCLEAR FUSION APPLICATIONS

*Dániel Imre Réfy, Sándor Zoletnik, Erik Walcz, Domonkos Nagy, Tamás Szepesi,
Richárd László Csiszár, Dénes Oravecz, Imre Katona*

Objective

In reactor-sized fusion devices, the uncontrolled collapse of plasma, known as disruption, can damage the structural integrity of the device. To prevent this, introducing a few grams of material into the device is necessary, allowing the plasma to release its energy, which can then be evenly distributed on the device's first-wall in the form of heat radiation.

For the current - smaller - experiments, fast valves are used to introduce several bar-litre of gas into the device on a millisecond time scale (Massive Gas Injection - MGI).

In larger reactor-sized devices, the same amount of material is introduced in the form of cryogenic ice, as it can penetrate deep enough into the device's high-temperature plasma. Frozen hydrogen ice pellets are to be injected, breaking them into smaller pieces before entering the plasma, allowing hundreds of smaller pellet fragments to reach the plasma. The equipment creating this is called Shattered Pellet Injector (SPI), and the EK Fusion Plasma Physics Department (FPL) is building a prototype of such a device in connection with an ITER tender [1][2].

One key element of both MGI and SPI systems is a high-pressure fast gas valve. Although similar valves have been developed by other research institutes, they are not commercially available, and their detailed designs are also not available. Compared to the valves available in publications, the valve developed at EK [3] differs in that there is no mechanical feedthrough between the high-pressure gas chamber and the atmospheric pressure, resulting in a significantly simpler and more durable concept.

Specifications

Valve volume: 1 Litre

Valve fill: hydrogen, deuterium, helium

Maximum pressure: 15 MPa (150 bar)

Opening time: approximately 1 ms from the arrival of the control signal

Force required to open: approximately 20 kN within 600 μ s from the arrival of the control signal

Valve orifice diameter: 20 mm

Volume flow rate: approximately 10 m³/s

Target pressure in the barrel: 50 bar

Maximum leakage into the barrel (critical for pellet freezing): 10⁻⁷ Pa m³/s

Maximum leakage into the atmosphere (critical for hydrogen operation): 10⁻⁶ Pa m³/s

Operating principle

The operation of the valve is based on the principle of eddy currents: according to Lenz's law, a change in the magnetic field generated by the primary coil induces a current in the secondary coil whose field reduces the field created by the primary coil. The fields of currents flowing in opposite directions in the two coils thus repel each other, which force can be used to accelerate a linear actuator. There is a plug at one end of the linear actuator and a secondary coil at the other end, and a fixed primary coil between the two. By connecting a charged capacitor on the primary coil, a rapidly rising primary current can be driven, which induces a current in the secondary coil as described above, creating the desired repulsive force between the primary and secondary coils. The section view of the fast valve is shown in Figure 1.

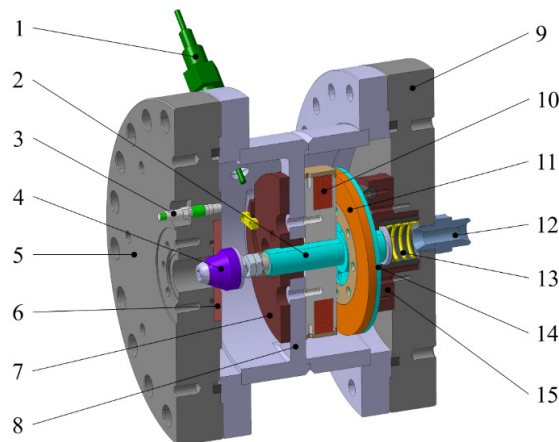


Figure 2: Section view of the fast valve consisting of high-pressure electrical feedthrough (1); shaft (2); fast pressure gauge (3); closure plug (4); front closure flange (5); orifice disc (6); front plain bearing (7); valve body (8); rear closure flange (9); primary coil with housing (10); secondary ring (11); gas inlet connector (12); closure spring (13); secondary ring holder (14); rear plain bearing and bumper (15).

Implementation and Results

Preliminary electromagnetic and gas-dynamics simulations of the system showed that the eddy current-based actuator described above is suitable for our purposes. The pressure vessel and the piston, equipped with the eddy current actuator were designed, based on which the prototype of the valve was manufactured. For the integrated test of the prototype, a test stand with high-voltage electronics with appropriate life protection, high-pressure gas system, barrel mock-up with a vacuum system, mechanical protection, and diagnostics was built. Integrated tests showed that the system meets all technical specifications [3].

The valve was then integrated into the SPI system, and its control was integrated into the SPI control system. Between December 2021 and September 2022 more than 300 hydrogen, deuterium, and neon pellets of relevant size for ITER have successfully been launched with the valve [1], and over 1000 shots were performed with the system. The valve was at TRL 6 (Prototype system verified), and its control system was at TRL 5 (Laboratory testing of integrated system) level at the time.

The development continued in 2022 with the support of the HUN-REN Proof of Concept Funding.

Two fluid dynamics models have been developed and experimentally validated based on the CAD designs of the valve's initial version using the Ansys Fluent system: one aimed at quasi-one-dimensional optimization and the other at detailed examination of flows around the valve seat in an axisymmetric two-dimensional model.

Two new valve mechanical designs have been produced, one of which has been implemented. The version of the valve where the primary coil was placed outside the pressure vessel was not implemented, because mechanical finite element simulation results indicated that the required wall thickness for pressure containment would be too large for efficient operation of the eddy current actuator with the desired efficiency.

However, a new high-pressure fast valve similar to the first version [3] has been implemented. The significant difference compared to the initial valve version lies in the material selection for moving parts: stainless steel components have been replaced with titanium, and copper components with aluminium, thereby halving the mass of moving parts. The other critical component, the plug, which proved to be critical in terms of fatigue fracture, has been redesigned based on new principles.

The new valve has been tested on the SPI system and a dedicated test bench. We examined the quantity of gas released from the valve as a function of pressure and capacitor voltage, which significantly influences the final velocity of the expelled pellet. The valves were tested by shooting into a vacuum, and tests were conducted with both the old and the new valves. The comparative analysis of these valves, along with the valve development results, has been published in a conference paper and a peer-reviewed journal article [4][5].

Based on a detailed technical specification, a high-voltage electronics system and its complete control system have been designed (low and high voltage, as well as mechanical system design), its components have been manufactured or procured, and it has been assembled. The valve control electronics were tested with the new valve on the valve test bench, and they operated as expected: the control system immediately displays signals from the high-voltage electronics on the screen after firing, allowing comparison of their timing with theoretical expectations, showing good agreement.

The advances which were allowed by the HUN-REN Proof of Concept funding led to a system which can be considered Level 7 (System prototype demonstrated in an operational environment) on the Technical Readiness Level scale.

This work was supported by the HUN-REN Proof of Concept Grant [ELKH-PoC-2022-047].

Related publications

- [1] S. Zoletnik, E. Walcz, S. Jachmich, U. Kruezi, M. Lehnen, G. Anda, T. Szabolics, T. Szepesi, G. Bartók, G. Cseh, Z. Boros, D. Dunai, G. Gárdonyi, J. Hakl, S. Hegedűs, I. Katona, A. Kovacs, G. Kocsis, M. Lengyel, S. Mészáros, D. Nagy, D. Oravecz, L. Poszovecz, D. Réfy, K. Vad, M. Vécsei: *Shattered pellet technology development in the ITER DMS test laboratory*, Fusion Engineering and Design **190**, 113701 (2023) <https://doi.org/10.1016/j.fusengdes.2023.113701>
- [2] S. Zoletnik, E. Walcz, D. Dunai, A. Zsákai, S. Jachmich, U. Kruezi, M. Lehnen, M. Kochergin, G. Anda, T. Szabolics, T. Szepesi, G. Bartók, G. Cseh, Z. Boros, G. Gárdonyi, J. Hakl, S. Hegedűs, I. Katona, G. Kocsis, M. Lengyel, M. Málics, S. Mészáros, D. Nagy, D. Oravecz, L. Poszovecz, D. Réfy, K. Vad, M. Vavrik, M. Vécsei: *Shattered Pellet Injection technology development for the ITER Disruption Mitigation System*, in Proceedings of IAEA Fusion Energy Conference (2023)
- [3] D. I. Réfy, S. Zoletnik, E. Walcz, D. Nagy, T. Szepesi, M. Vécsei, D. Oravecz, I. Katona, S. Hegedűs, M. Vavrik, S. Jachmich, U. Kruezi: *Instrumented fast valve for the ITER DMS support laboratory test bench*, Fusion Engineering and Design **194**, 113893 (2023) <https://doi.org/10.1016/j.fusengdes.2023.113893>
- [4] D. Nagy, D. I. Réfy, E. Walcz, S. Zoletnik: *Eddy current actuated fast valve development for disruption mitigation applications*, in Proceedings of 15th International Symposium on Fusion Nuclear Technology, PS2-110 (2023)
- [5] D. Nagy, D. I. Réfy: *Eddy current actuated fast valve development for disruption mitigation applications*, submitted to Fusion Engineering and Design (2023)

MEDICAL RADIOISOTOPE PRODUCTION STUDY AT THE BUDAPEST RESEARCH REACTOR – THE WP2 OF THE SECURE PROJECT

László Szentmiklósi, Boglárka Maróti, Zoltán Kis, Katalin Gméling, Noémi Buczkó

Objective

The aim of the SECURE (Strengthening the European Chain of sUPply for next generation medical RadionuclidEs) project is to make a major contribution to the sustainability of medical isotope production and its safe application in Europe. That includes target development and reliable solutions for production methods of therapeutic and diagnostic radionuclides for α and β emitters. Our group is involved in the task “Feasibility calculation of producing beta-emitting radionuclides via MCNP6 and FISPACT software”. The detailed MCNP6 model of the Budapest Research Reactor and the specific irradiation geometry of three vertical channels were established, and realistic material cards were specified for natural and isotope-enriched targets. The energy- and spatial distributions of the neutron field calculated by MCNP6 were transferred to FISPACT-II, and the resulting activities were validated against those measured using neutron-irradiated targets representing the beta-emitting radioisotopes of interest.

Methods

We applied MCNP6.2 calculations for neutron flux determination, FISPACT II for the radioisotope inventory calculations, while the calculations were validated with Neutron Activation Analysis (NAA).

Results

Three vertical irradiation channels with highly different neutron-energy distributions were selected for the validation experiments (Fig. 1). The MCNP F4 tally output data were tabulated according to the CCFE-709 group energy structure, one of the native energy-bin sets of FISPACT, ranging from 10^{-5} eV to 10^9 eV. Using the neutron field parameters and the composition of the target, a radioisotope inventory for any time instant during and after the irradiation can be obtained by using the FISPACT-II code. Initially, we used the FISPACT’s default TENDL-2017 nuclear data library for our calculations, later the calculations were repeated with the ENSDF/B.VIII data. We identified a few discrepant cases, while most of the results were in good agreement.

Gd, Pd, Pt, and Lu-containing samples were prepared for neutron activation in the Nr. 17, 47, and 72 vertical channels, to produce Tb-161, Ag-111, Au-199, and Lu-177 radionuclides, respectively. The experimental activities of the irradiated samples were measured using well-calibrated HPGe detectors placed inside low-level iron counting chambers. The results were compared with the FISPACT calculations and an agreement within 30% was found. The method can be generalized to assess the yield for any, yet untested irradiation site.

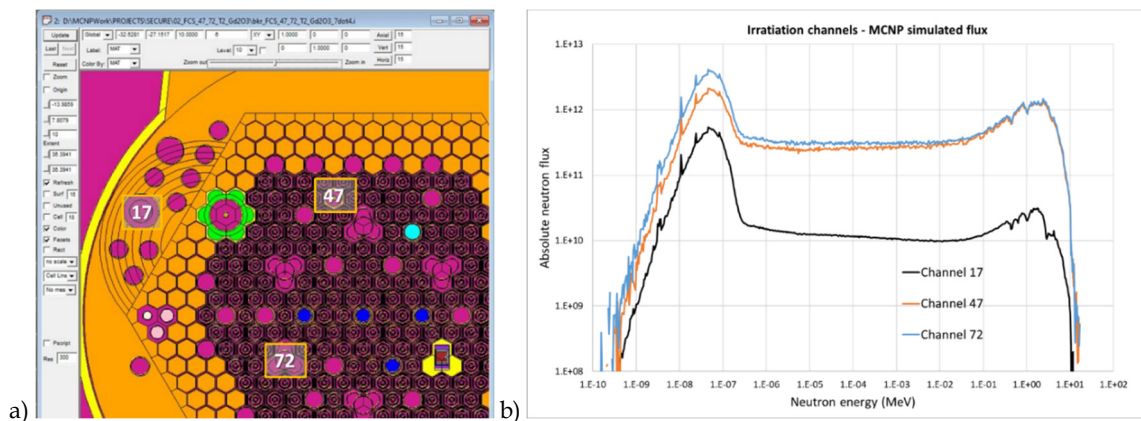


Figure 1: a) MCNP visualization of the reactor core and the selected vertical irradiation channels for the validation experiments. b) Visualization of the neutron energy distribution based on the MCNP F4 tally output data.

The effect of target upscaling was studied by simulating radioisotope yields for increasing masses of the same target material. Due to the lack of isotope-enriched targets, the experimental results for natural targets were, after validation, transferred to the case of enriched targets by computations. The results form a solid basis for designing further experiments to produce novel beta emitter radioisotope in the Budapest Research Reactor in commercial quantities, as well as prepare the documentation requested by the Authorities. The experience gained in this study will also be utilized when the Ac-225 production is being assessed in Task 2.1.

Related publication

- [1] L. Szentmiklósi, B. Maróti, Z. Kis, K. Gméling, N. Buczkó: *Radionuclides production study by a 10 MW reactor*, SECURE Project Report, dated on 23/01/2024



II. RESEARCH AND DEVELOPMENT RELATED TO NUCLEAR POWER PLANTS



ACTIVITIES OF HUN-REN EK AS MAIN CONSULTANT OF PAKS NUCLEAR POWER PLANT

Pál Szentannai, Katalin Kulacsy, Márton Király, Erzsébet Perez-Feró, Tamás Novotny, Attila Guba, István Trosztel, Zsolt Kerner, István Almási, Gergely Dósa, Péter Kirchknopf, Zoltán Kovács, and Boglárka Maróti

Objective

HUN-REN EK, together with NUBIKI (Nuclear Safety Research Institute), has been the main consultant of Paks Nuclear Power Plant (NPP) for many years. The main consultant supports the NPP in solving safety-related technical issues and helping with strategic planning. The work is done by the most experienced and highly qualified members of the staff on the basis of yearly work plans. In 2023, HUN-REN EK undertook the following separate tasks, done by different (groups of) experts:

- preparatory work for simulating western fuel rods;
- small-scale measurements on the cladding of Westinghouse fuel rods;
- revision of the Probabilistic Safety Analysis (PSA) success criteria referring to the hydroaccumulators by means of the ATHLET code;
- expert's report on decreasing the hydrazine-dosing in the primary circuit;
- in-situ X-ray Fluorescence Analysis (XRF) investigation of the heat transfer tubes of the steam generators No. 1 and 4 in block 1.

Methods

Each task required different methods, which are summarized on their specific upcoming sheets.

Results

The individual results of the tasks are summarized on their specific subsequent pages.

Remaining work

The tasks for 2023 have been completed.

Related publications

- [1] K. Kulacsy: *Preparatory work for simulating western fuel rods*, EK TFO-2023-751-04-01-M0, in Hungarian (2023)
- [2] M. Király, E. Perez-Feró, T. Novotny: *Small-scale measurements on the cladding of Westinghouse fuel rods*, EK TFO-2023-751-5-1-M0, in Hungarian (2023)
- [3] A. Guba, I. Trosztel: *Revision of the PSA success criteria referring to the hydroaccumulators, using the ATHLET code*, EK-TFO-2023-751-06-01-M0, in Hungarian (2023)
- [4] Zs. Kerner: *Expert's report on decreasing the hydrazine-dosing in the primary circuit*, EK-TFO-2023-751-07-01-M0, in Hungarian (2023)
- [5] Zs. Kerner, I. Almási, G. Dósa, P. Kirchknopf, Z. Kovács, and B. Maróti: *In-situ XRF investigation of the heat transfer tubes of the steam generators No. 1 and 4 in block 1*, EK-TFO-2023-751-09-01-M0, in Hungarian (2023)

NEW VERIFICATION AND VALIDATION RESULTS OF THE NEUTRONIC/THERMAL-HYDRAULIC CODES APPLIED AT REACTOR ANALYSIS DEPARTMENT

Bálint Batki, Zoltán István Böröczki, György Hegyi, István Panka, István Pataki, Emese Temesvári

Objective

In 2023, three new tasks were considered to further validate the codes we use. In the first case, the main aim was to validate the in-house developed KIKO3DMG nodal multigroup diffusion and Simplified Spherical Harmonics (SPN) code and the ATHLET code developed by GRS (Gesellschaft für Anlagen- und Reaktorsicherheit, Hamburg, Germany) on the OECD NEA WPRS Rostov-2 benchmark problem, which is a commissioning test of reactivity compensation of boron dilution by stepwise insertion of control rod cluster into a VVER-1000 core. In the second case, the criticality calculations concerning the new Paks-2 units were aimed at the in-house developed KARATE-1200 program system. For this purpose, the latest available data from the literature for VVER-1200 Novovoronezh NPP-2 were used: measured critical boron concentration for the first load. Additionally, the planned units are third-generation evolutionary power plants subject to strict international standards. One of them, the value of the so-called recriticality temperature, was examined in detail. The third task is aimed at the further validation and verification of our applied codes for Gen. IV reactors. The South-West Experimental Fast Oxide Reactor (SEFOR) cooled by sodium was selected, where a series of experimental programs from 1969 to 1972 conducted by the American General Electric Company (GE) and the West German Karlsruhe Laboratory (KFK) were performed. The SEFOR benchmark is available through the OECD NEA UAM-SFR platform.

Methods

For the OECD NEA WPRS Rostov-2 benchmark problem, the full-core KIKO3DMG model of the Rostov-2 core was set up, and the thermal-hydraulic modelling of the primary and secondary loops – according to the specification – was modelled with the ATHLET code (version 3.3) and the KIKO3DMG-ATHLET(version 3.0A) coupled code. The calculations were performed with varied make-up flow rates in the range specified. The neutronic model consists of 163 fuel assemblies and the axial and radial reflector regions, the group constant library was calculated by the benchmark team. In the case of Novovoronezh NPP-2, the calculations were performed with the KARATE-1200 stationary program with the ENDF/B-VI. (version 6.) nuclear data library. As before, 163 fuel assemblies and reflectors were modelled for the first load of the nuclear power plant. A special task was the investigation of the value of the SCRAM (emergency shutdown of the reactor) reactivity; several configurations were modelled, including absorber rods stuck in one or two upper positions. In the case of the SEFOR benchmark, during the investigation, the Serpent 2 Monte Carlo code was used to provide a reference solution for the different thermal feedbacks, reactivity worth of two given reflectors, and assembly-wise power distributions. Group constants were generated with the European Cell CODE (ECCO) from the ERANOS in 33 energy groups and with the Serpent 2 code in 24 groups. Currently, the PARTISN discrete ordinates neutron transport code and the KIKO3DMG codes are used as deterministic solvers for the investigations. JEFF 3.1.1. library was used during all simulations.

Results

In the case of the Rostov-2 benchmark, the KIKO3DMG calculations applying average core temperature at static case showed indeed a good match with the measured control rod worth [1].

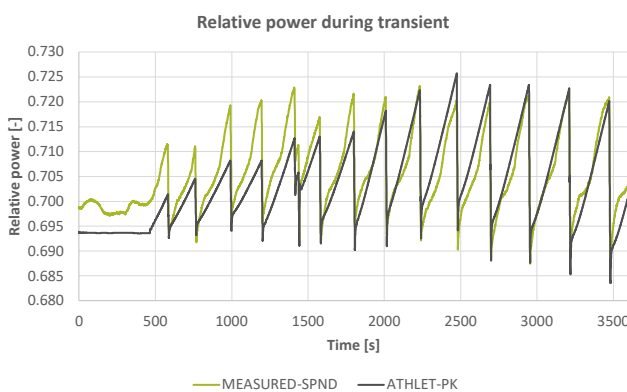


Figure 3: Boron dilution transient in Rostov-2 benchmark, relative power from measured Self Powered Neutron Detector (SPND) and from ATHLET calculation results using point kinetics

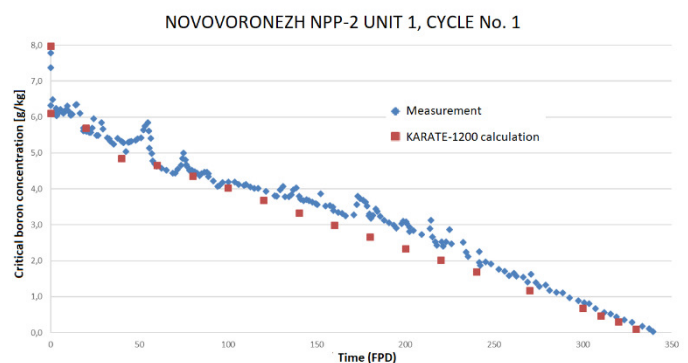


Figure 4: Measured and KARATE-1200 calculated critical boron concentration in the VVER-1200 Novovoronezh NPP-2 during the burnup

The transient results with the developed ATHLET 3.3 model resulted in quite good agreement with the point kinetic approximation, as shown in Figure 1. The coupled KIKO3DMG-ATHLET(3.0A) calculation was also successful, but the differences show that further refinements of the model are needed [1]. Concerning the VVER-1200 reactors, rather good agreement was gained by the KARATE-1200 code system for the critical boron calculation as demonstrated in Figure 2. The detailed investigation of the SCRAM reactivity worth showed that the recriticality temperature is below 100 °C at the equilibrium cycle assuming that the most valuable rod is stuck in the upper position. This case is the accepted conservatism in safety analysis until now. However, if two rods are stuck, the temperature can be much higher than this value [2].

For the OECD NEA WPRS SEFOR benchmark problem, the calculations for the 15 proposed cases for CORE I-E were performed [3, 4]. We mention that the EK also participated in the preparation of the benchmark specification. Calculations with Serpent, KIKO3DMG, and PARTISN (with group constants generated by ECCO and Serpent) have been done for the isothermal test validation cases. The results for the K_{eff} reactivity feedbacks

and power distribution were compared to each other and to the original measurement data. It was found that the reference Serpent calculations give slightly lower K_{eff} values compared to the CEA TRIPOLI-4 results, the deterministic PARTISN and KIKO3DMG codes provide fairly good results, the Doppler and non-Doppler effects agreed well in most cases. The relative differences between the assembly-wise power distributions for the PARTISN code are demonstrated in Figure 3, with the maximum difference being below 3%.

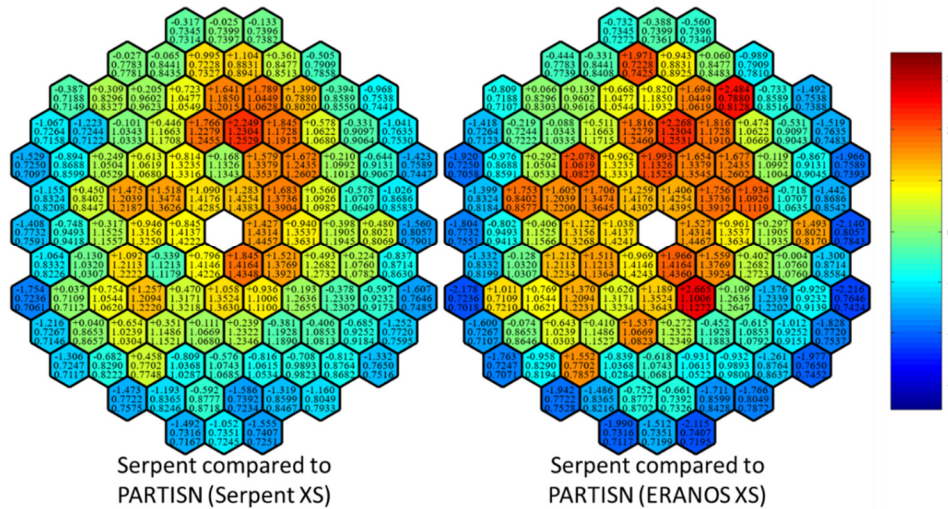


Figure 5: Relative differences between the assembly-wise power distributions. The upper values are the relative differences in percentage, the middle values are the reference Serpent 2 solution, and the bottom values are the results of the PARTISN calculations.

Remaining work

The OECD NEA Rostov-2 benchmark and the SEFOR benchmark series will continue in 2024. The current calculation results are planned to be published in international journals with some additions.

Related publications

- [1] I. Pataki, B. Batki, I. Panka: *Calculation of the Rostov-2 VVER-1000 Benchmark using the KIKO3DMG and ATHLET codes*, OECD NEA WPRS Benchmarks Workshop, Bologna, Italy, 22 - 26 May 2023
- [2] Gy. Hegyi, E. Temesvári: *Criticality calculations for the new Paks units with the KARATE-1200 program system*, Submitted to the journal NUKLEON in 2023 (in Hungarian)
- [3] Z. I. Böröczki: *CER Preliminary results for the SEFOR Benchmark*, OECD NEA WPRS Benchmarks Workshop, Bologna, Italy, 22 - 26 May 2023
- [4] Z. I. Böröczki: *General and SMR-related R&D activities in the Hungarian nuclear industry*, IAEA Interregional Workshop on Safety Analysis for Small Modular Reactors, Ottawa, Canada, 16 - 20 October 2023

MECHANICAL TESTS WITH SLIM FUEL CLADDING

Erzsébet Perez-Feró, Tamás Novotny, Márta Horváth, Márton Király

Objective

The aim of the project was to characterize the mechanical behaviour of the SLIM cladding in different pre-treated (oxidized, heat-treated and hydrogenated) states and to compare the results with measurements on E110 alloy.

Methods

Ring tensile and ring compression tests were carried out by Instron 1195 universal test machine. The load – displacement curves were recorded and evaluated. The purpose of the ring tensile measurements was to determine the effect of steam oxidation, heat-treatment in an inert atmosphere, and hydrogenation on tensile strength. The investigations primarily occurred at 20 °C, but in some cases, measurements were also conducted at 300 °C. Ring compression tests were carried out at 135 °C to investigate the expected ductile-to-brittle transition during a Loss of Coolant Accident (LOCA) event. The tests were performed not only with oxidized samples but also with pre-hydrogenated samples to simulate the effect of accumulated hydrogen in the cladding. Evaluation of cladding ductility was carried out using specific energies at failure derived from force-displacement curves, and the ductile-to-brittle transition region characteristic of SLIM claddings was determined.

Results

The results of the tensile tests performed at room temperature indicated that both heat-treatment and oxidation significantly increase the tensile strength of the cladding. The tensile strength was influenced only by the heat-treatment temperature, the heat-treatment time had little effect on it. In contrast, increasing the oxidation time increased in tensile strength. Comparing the effects of heat-treatment and oxidation, it can be concluded that the effect of oxidation surpasses that of heat-treatment. The low hydrogen content barely affected the tensile strength of the cladding, whereas a higher amount of absorbed hydrogen (600 ppm) increased tensile strength. This latter finding was also true at a temperature of 300 °C; however, the tensile strength values were considerably lower in this case. Results of tensile tests conducted at 20 °C showed significant differences between SLIM and E110 alloys. As-received and oxidized SLIM samples exhibited significantly higher tensile strength than E110 samples. However, the difference between the two alloys was much smaller at 300 °C.

It was found that in the SLIM alloy without hydrogen, the ductile-to-brittle transition occurs at 20% Cathcart-Pawel Equivalent Cladding Reacted (CP-ECR) (Fig. 1), which is much more favourable than the previously determined 7.5% CP-ECR for the E110 alloy. In the case of the SLIM cladding, the embrittlement limit significantly decreases with hydrogen content, while the effect of hydrogen is negligible up to 400 ppm for the E110 alloy.

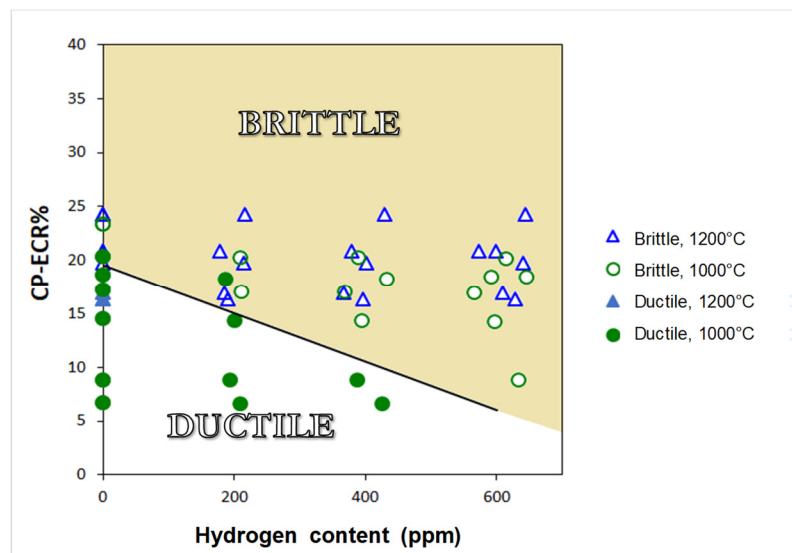


Figure 1: The ductile-to-brittle transition of SLIM alloy oxidized at 1000 °C and 1200 °C

Remaining work

This project has been completed.

Related publication

- [1] E. Perez-Feró, T. Novotny, M. Horváth, M. Király: *Ring tensile and ring compression tests with slim fuel cladding*, EK-FRL-2023-701-1-3-M0, in Hungarian (2023)

SUBCHANNEL ANALYSIS IN VERONA CORE MONITORING SYSTEM

Áron Vécsi, Csaba Horváth, Gábor Házi

Objective

A new type of fuel assembly has been introduced at Paks Nuclear Power Plant (NPP) in order to improve its fuel economy. The reactor thermal power could be increased due to the higher moderating ratio, which is achievable with the thinner fuel rods and claddings in the new design. This is the so-called slim fuel. Seven spacer grids in different axial levels of the assembly are maintained by mixing vane to intensify the mixing in the assembly and to homogenize the coolant temperature, decreasing its maximal value. In line with the new fuel design, the thermohydraulic calculations of VERONA core monitoring system had to be revised, and based on the preliminary results, the decision was made to improve the calculations by introducing a new approach using detailed subchannel thermohydraulic calculations.

Methods

A new subchannel thermohydraulic code called SURET has been developed calculating the major thermohydraulic parameters of a fuel assembly in 258 lateral points and 42 axial levels. The code solves the discretized mass, momentum and energy conservation equations taking into account the lateral mixing between subchannels. Calculations were verified by separate effect tests and validated by comparing SURET's results with the ones obtained by Computational Fluid Dynamics (CFD) calculations. After proving its accuracy, the calculations were parallelized using multi-thread techniques and the code was coupled with the online VERONA core monitoring system and commissioned in the four units of Paks NPP.

Results

Several benchmark calculations were performed comparing the results of SURET and CFD calculations. We have found that the difference in temperature maximum was less than 0.15 °C. Also, the distributions of outlet water temperature obtained by SURET fitted CFD data reasonably well as shown in Figure 1.

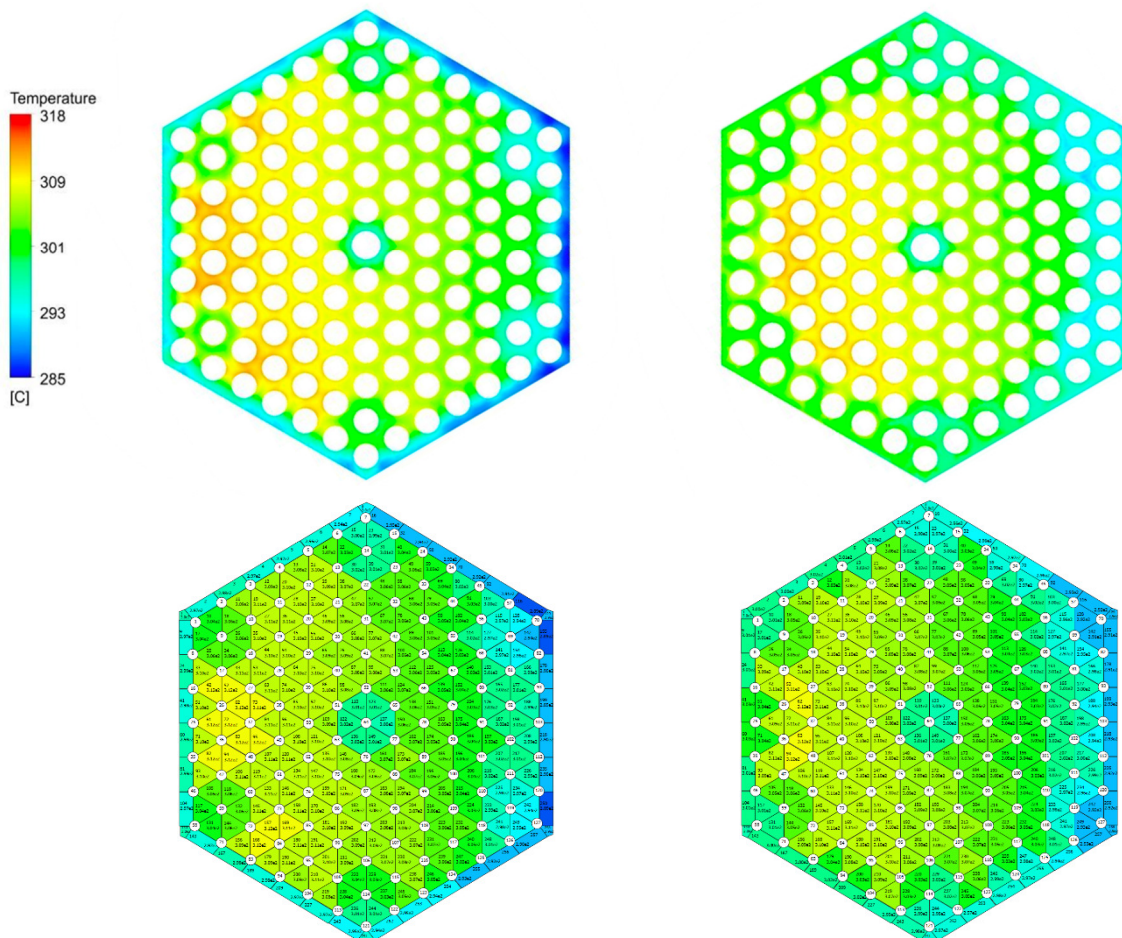


Figure 1: Distributions of outlet temperature (top: CFD; bottom: SURET; left: without mixing vane, right: with mixing vane)

Before we integrated SURET into the VERONA core-monitoring system, there was a campaign with some slim fuel assemblies used for testing purposes. Using the measurements of these assemblies, we performed calculations with SURET in a test VERONA system and evaluated the differences between the measured and calculated outlet water temperature. Comparisons were made not only for the new slim assemblies (Fuel Id: 1014, 1016), but for the standard assemblies (Fuel ID: 1018, 1020), too. As an example, the relative frequency of the differences is shown for different fuel types in Figure 2.

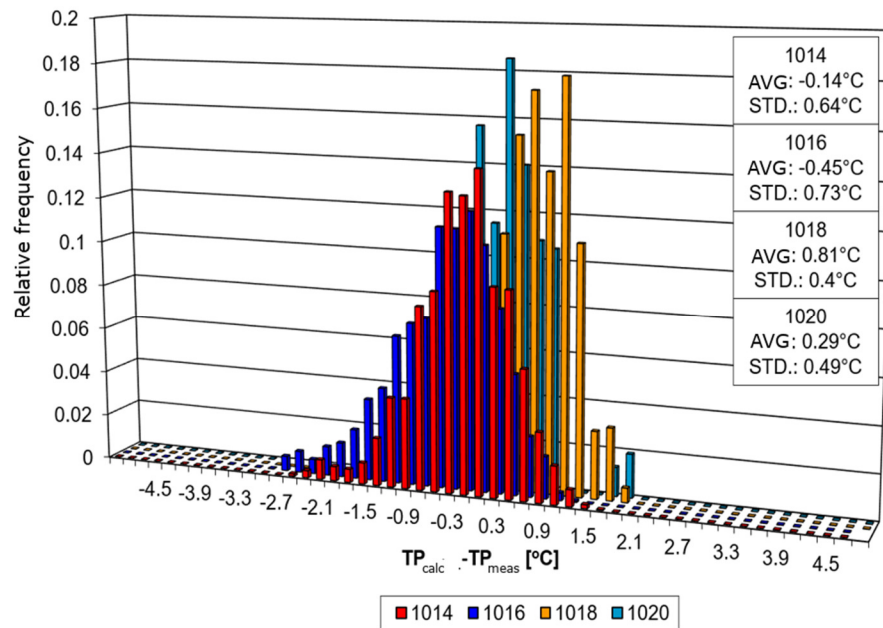


Figure 2: Relative frequency of the difference between the calculated and measured outlet water temperature (TP) for different fuel assembly types

As it can be seen, the average difference between measurements and calculations was less than 0.5 °C for most assembly types, but somewhat higher deviations could also be observed (e.g. for Fuel Id: 1018 in Figure 2), indicating the need for further tuning of SURET's mixing factors.

After tuning, the integration of SURET calculation into the online VERONA core monitoring system of the four units of Paks NPP was finished in 2023.

Remaining work

VVER-440 fuel assemblies are separated from each other by wall, therefore mixing of coolant between fuel assemblies is limited to the upper plenum of the core. Therefore, the calculation of mixing in such reactors can be very efficient by doing it individually for each fuel assembly in a parallel manner. Calculation of fuel assemblies having fuels without wall (e.g. to be used in Paks II NPP) is more challenging and can be really time consuming. However, by extending SURET and using some specific matrix permutation techniques, we have recently been able to reduce significantly the computational costs in such geometries, too. Benchmark calculations will be performed by the extended code, and its development for modelling two-phase flows is also in progress.

Related publication

- [1] Á. Vécsei, G. Házi, Cs. Horváth, I. Pócs, Z. Kálya, T. Parkó, M. Horváth: *SURET is a new form of subchannel thermohydraulic calculations*, 31st International Conference Nuclear Energy for New Europe, Sept. 12-15, Portoroz, Slovenia, No. 401 (2022)

INVESTIGATION OF FLOWS IN A CORE COMPRISED OF MULTIPLE TYPES OF FUEL ASSEMBLIES

Áron Hegedüs, Attila Guba

Objective

To improve the efficiency of fuel utilization at Paks NPP, fuel assemblies containing SLIM fuel pins are gradually being installed in the reactors. The new fuel type has thinner cladding, which leads to somewhat modified flow resistances. The core may be comprised of many different types of fuel assemblies. The objective of the project was producing a software capable of calculating the mass flow distribution inside the core. From these mass flows, the assembly exit temperatures can be calculated and compared with the measured values in Paks NPP.

Methods

A fuel assembly is modelled having three parts: the bundle and bypass channel coupled parallel, and these channels coupled in series with the inlet channel. Many such assemblies (e.g. one sixth of the core or the whole core) are connected in parallel to model the core. To each assembly is assigned a type, and for each such type its hydraulic properties are defined, which are the flow area and Pressure Loss Coefficients (PLC) of the channels. The calculation also requires the primary pressure, the total mass flow and core (or assembly) inlet temperature as input. Using these input parameters, the assembly outlet temperature map is produced.

The program may also be used in „reverse“ mode, that is, given the (measured) assembly outlet temperature map, the channel model's PLC is calculated for each assembly. This result then can be analyzed statistically and compared with the original PLC values.

Results

The program can calculate the core flows - in „forward“ mode, or the PLC values - in „reverse“ mode. Figure 1 shows an example where the core flows are calculated for different total primary mass flows and at different points during a campaign. The grey dotted line denotes the bypass flow value assumed for safety analysis. Using this figure, it is possible to estimate the total core mass flow at different times.

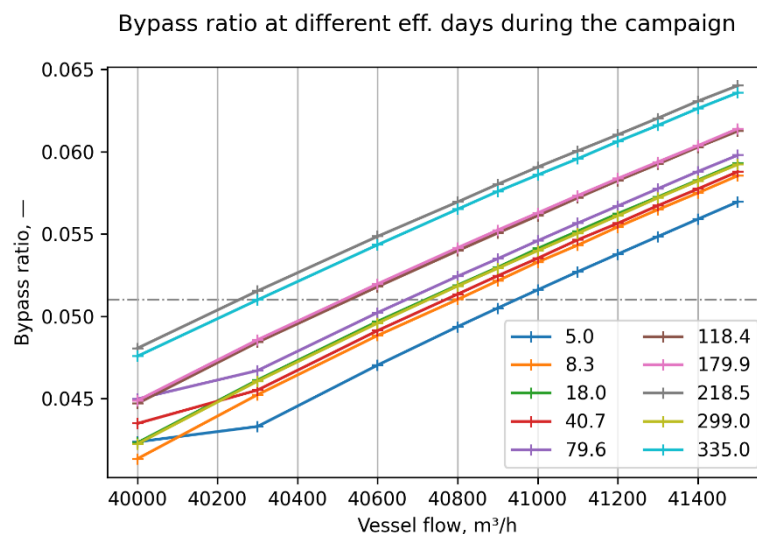


Figure 1: Core bypass flow at different times in the campaign

The software was used to estimate the difference between the old and the new SLIM fuel. It was found that although the flow rates differ slightly, the overall core behaviour does not change. There is no adverse effect of the application of the mixed core.

Remaining work

The project has been completed.

ACCOUNTING OF BURNUP IN THE CRITICALITY CALCULATION OF STORAGE AND TRANSPORT FACILITIES - INVESTIGATING THE SIMILARITY BETWEEN HZP STATES AND STORAGE FACILITIES

István Panka, Gábor Hordósy

Objective

The subcriticality analysis of a spent fuel storage facility is strongly influenced by the uncertainty of the calculated multiplication factor (k_{eff}) due to the uncertainties of nuclear cross section and technological data. When burnup credit is applied in the subcriticality analysis i.e. the change of reactivity due to the change of composition with burnup is considered, the problem arises that there are no such published critical experiments where the fuel composition is similar to the composition of the spent fuel.

A possible solution is to determine the discussed uncertainty by calculation using the covariance data of the cross sections as well as the uncertainties of the technological parameters and use the Hot Zero Power (HZP) states of operated NPP's for checking the calculations. In a previous study, 35 HZP states of Paks NPP were investigated and it was found that, using a methodology based on the statistical version of the KARATE code and Monte Carlo N-Particle Transport (MCNP), the resulting uncertainty values clearly covered the deviation of the calculated multiplication factors from reality in all cases. The aim of the current work was to assess how representative are the considered HZP states for the storage facility in connection with the fuel composition.

Methods

The representativeness of HZP states for storage facilities was characterized by the so-called similarity indices (' c_k ' values). They are integral quantities based on linear perturbation theory and can be derived from the sensitivity vectors of the multiplication factor (in different systems) for each cross section and the related covariance matrices. Its values are between -1 and 1 and characterize the correlation between the two systems in terms of nuclear cross section uncertainties. The closer c_k is to 1, the greater the similarity between the two systems. The similarity indices were calculated by the SCALE and MCNP codes. For isotopic concentrations, the sensitivities by concentration were compared to characterize the similarity between systems.

Results

In 2023, the representativeness of the considered HZP states was investigated for different assembly configurations of the Spent Fuel Pool (SFP) of Paks NPP. The studies were first performed on a simplified SFP model using the SCALE code, then the similarity was tested on a detailed radially infinite model of the SFP, and finally on a finite SFP model using the MCNP code.

Overall, it was found that the results for the lower shelf of SFP show a high degree of similarity to the HZP conditions, as demonstrated in Table 1. For the upper shelf, the similarity was significantly lower. Our present studies have also revealed that the sensitivity of the multiplication factor to isotope concentrations is similar for both the HZP conditions and the shelves of the spent fuel pool. Based on these results, the use of HZP states seems to be suitable for use in subcriticality analysis for the lower shelf of SFP. It is important to highlight that the similarity index of around 0.83 found in the finite model of the upper shelf is also essentially the same as the highest similarity index of 0.82 obtained for about 160 critical experiments selected from the International Handbook of Evaluated Criticality Safety Benchmark Experiments.

Table 1: The c_k similarity index between HZP states and the bottom shelf of the SFP at different temperatures (burnup of the assemblies on shelf is 9.43 MWnap/kgU, radially finite model is used). The isotopes considered for the calculation of the bottom shelf are A_GD: actinides and gadolinium, A_NG: actinides only.

Unit/ Cycle	T = 20 °C		T = 60 °C		T = 100 °C	
	A_GD	A_NG	A_GD	A_NG	A_GD	A_NG
1/38	0,961	0,960	0,963	0,962	0,966	0,966
2/36	0,958	0,957	0,960	0,959	0,962	0,964
3/34	0,955	0,951	0,956	0,953	0,957	0,962
4/34	0,959	0,958	0,962	0,961	0,964	0,964

Remaining work

Investigations will continue to assess the uncertainties of subcriticality calculations of SFP using the methodology based on the HZP states.

Related publication

- [1] G. Hordósy, I. Panka: *Accounting of burnup in the criticality calculation of storage and transport facilities - Investigating the similarity between HZP states and storage facilities No. 2*, EK-RAL-2023-708-01-04-M0, in Hungarian (2023)

MECHANICAL TESTING OF CLADDING MATERIALS FOR ACCIDENT TOLERANT FUEL

Zoltán Hózer, Anna Pintér-Csordás, Levente Illés, Márta Horváth, Zoltán Kovács, Péter Szabó, Dávid Cinger, Barbara Somfai

Objective

In the framework of the IAEA project “Testing and Simulation for Advanced Technology and Accident Tolerant Fuels” (ATF-TS), EK laboratories carried out large number of tests with different cladding materials. The main objective of the test series was the comparison of the new cladding designs with the reference Zr alloy claddings.

Methods

Both ring compression and tensile tests were carried out in an INSTRON 1195 universal tensile test machine. The cross-head speed was 0.5 mm/min and the tests were performed at room temperature (≈ 20 °C). The load-displacement data were recorded with a 0.4 s interval. The tensile tests were continued until the failure (rupture) of the ring sample. The ring compression tests were continued until the failure (fracture) of the brittle ring samples. If the ring sample was ductile, the tests were continued until the total flattening of the sample.

Results

In the tensile tests, the coating on the zirconium alloy samples did not significantly influence the behaviour of the as-received samples. The Zr-based oxidized samples showed brittle behaviour, since two-sided oxidation took place in the pre-oxidation procedure and the inner side of all samples was heavily oxidized. The oxidation had much less effect on FeCrAl samples. The Cr-coated samples failed at a higher load compared to uncoated cladding (Fig. 1).

In the ring compression tests the mechanical behaviour of FeCrAl claddings was not influenced by the long-term oxidation in steam neither at 1000 °C nor at 1200 °C. The TiAl coating did not have a positive effect on the mechanical strength: the coated samples failed at lower loads than that of uncoated Zircaloy-4. The Zr claddings with Cr coating could keep ductility after oxidation at 1000 °C. However, the oxidation at 1200 °C resulted in brittle behaviour and failure at low loads. The CrN coating and the multilayer Cr+CrN coatings improved significantly the cladding behaviour even after oxidation at 1200 °C (Fig. 2).

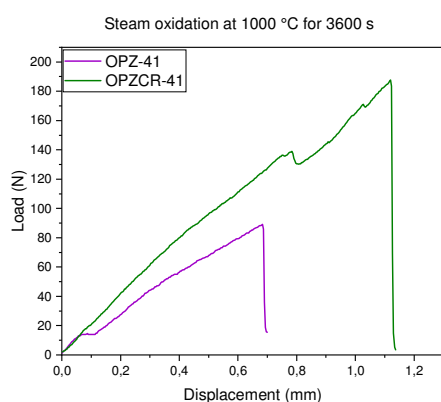


Figure 1: Tensile test load-displacement curves of uncoated (OPZ) and Cr-coated (OPZCR) optZIRLO samples after oxidation at 1000 °C for 3600 s

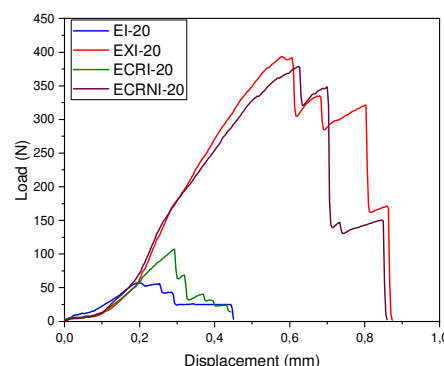


Figure 2: Ring compression load-displacement curves of uncoated (EI), Cr coated (ECRI), CrN coated (ECRNI) and Cr+CrNi coated (EXI) samples after oxidation at 1200 °C for 1800 s

Remaining work

Experimental database will be built and provided for the IAEA ATF-TS project.

Related publications

- [1] M. Horváth, P. Szabó, D. Cinger, Z. Hózer: EK ring tensile tests with cladding samples provided by IAEA ATF-TS partners, EK-FRL-2023-120-1-4-M0
- [2] M. Horváth, P. Szabó, Z. Hózer: EK ring compression tests with cladding samples provided by IAEA ATF-TS partners, EK-FRL-2023-120-1-5-M0
- [3] A. Pintér Csordás, L. Illés, Z. Kovács, B. Somfai: Electron beam studies of Canadian cladding samples, EK-FRL-2023-120-1-6-M0
- [4] A. Pintér Csordás, Z. Kovács, B. Somfai: Electron beam studies of various oxidised cladding samples originated from different countries, EK-FRL-2023-120-1-11-M0

INTEGRAL TEST WITH ACCIDENT TOLERANT FUEL

Róbert Farkas, Zoltán Hózer, Berta Bürger, Nóra Vér

Objective

An integral bundle test was carried out in the framework of the IAEA Testing and Simulation for Advanced Technology and Accident Tolerant Fuels (ATF-TS) project in the CODEX (COre Degradation Experiment) facility in order to directly compare the behaviour of traditional and accident tolerant fuel cladding materials under high-temperature accident conditions.

Methods

The test section included an electrically heated seven-rod bundle composed of 3 pieces uncoated and 4 pieces Cr-coated optZIRLO cladding tubes. The main parameters of the scenario were selected on the basis of pre-test calculations.

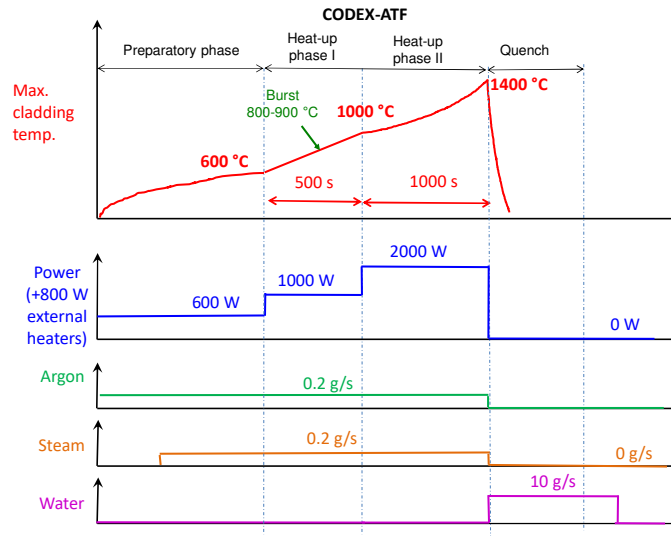


Figure 1: Main parameters of the selected CODEX-ATF scenario

Electrical heating with two tungsten heaters was applied in each rod. The heated length was 650 mm. The rods were pressurized during the test in order to reach ballooning and burst in the early phase of the experiment. The rods in the bundle were fixed by two spacer grids made of Zr1%Nb alloy. The bundle was placed into a hexagonal shroud. The shroud material was Zr2.5%Nb alloy, and the total length of the shroud was 1000 mm. The bundle was heated by direct current power supply units. The steam generator provided hot steam to the test section. The water injection into the steam generator was performed with a precision pump at a constant flow rate. For heating up, argon gas was also injected into the steam generator.

Results

The CODEX-ATF test was successfully performed on 23rd August, 2023.

In the preparatory phase the facility was heated up to 600 °C in 0.2 g/s steam and 0.2 g/s argon flow rates using both external heaters and fuel rod heaters. The heat-up phase continued with the same flow rates and with 1000 W heating power on the rods and 800 W power from external heaters. The rods were pressurized and cladding burst took place at ≈ 900 °C on most of the rods. The temperature increase was very smooth. At the initiation of the water quench, the cladding temperature at the top of the bundle was above 1600 °C. In the upper part of the fuel rods 1400 °C was reached. It is expected that intense Zr-Cr eutectic formation would take place at these temperatures. During the quench phase, room temperature water was injected into the bottom of the test section. The total hydrogen production during the experiment was about 3 g, which indicated significant oxidation of the Zr components.

The database of online measurements is available for the interested partners and was uploaded to the ATF-TS share point.

Remaining work

The post-test examination of the bundle will be carried out using several techniques to characterize the bundle state.

Related publications

- [1] R. Farkas, N. Vér, B. Bürger, Z. Hózer: *The CODEX-ATF experiment*, 28th International QUENCH Workshop Karlsruhe, 5-7 December 2023
- [2] R. Farkas, N. Vér, B. Bürger, Z. Hózer, P. Szabó, Z. Hózer: *The CODEX-ATF integral test simulating a nuclear power plant accident (in Hungarian)*, XXth Symposium of the Hungarian Nuclear Society, Siófok, 23-24 November, 2023.

THE EXPERIENCES OF NPP OPERATION WITH IDENTIFIED DEFECTIVE FUEL ASSEMBLIES

Péter Szabó, Zoltán Hózer, Berta Bürger

Objective

The main objective of this work was to summarize the experience of nuclear power plants with fuel assemblies identified as defective.

Methods

The operational experience of several Nuclear Power Plants (NPPs) was reviewed, and the main conclusions from related documents by the International Atomic Energy Agency (IAEA) and OECD Nuclear Energy Agency (NEA) were summarized. The risks associated with operating with defective fuel assemblies and with replacement assemblies were analyzed, taking into account factors such as primary coolant activity concentrations, contaminations in the primary circuit, development of secondary failures, accumulation of radioactive waste, asymmetric core configurations, operational limitations, and replacement of defective fuel rods.

Results

The main conclusion of the review was that the presence of some leaking fuel elements in the reactor core does not pose a significant safety risk. Operating with leaking assemblies requires certain measures to be taken during the campaign. Continued operation with defective assemblies offers numerous operational and economic advantages. Employing replacement assemblies entails economic disadvantages, and may pose certain risks due to asymmetric power distribution in the core.

The advantages, disadvantages, and risks of operation with defective fuel assemblies and replacement assemblies are summarized in Tables 1 and 2.

Table 1: Operation with defective fuel assembly

advantages	<ul style="list-style-type: none"> • No need for an extended shutdown if the leaking assembly does not need to be selected • The assembly can be operated until the planned burn-up is reached • The campaign can be carried out with the original planned core configuration • No asymmetric power distribution occurs in the reactor core • There is no need to redesign the campaign
disadvantages	<ul style="list-style-type: none"> • High activity concentrations in the primary coolant • More frequent primary circuit sampling, intensive water purification • Iodine spiking during transients • Limited load-follow operation and transients • More radioactive waste generated (water purification filters)
risks	<ul style="list-style-type: none"> • Development of secondary damage on the leaking heating element • Fissile material contamination on primary circuit surfaces

Table 2: Operation with replacement fuel assembly

advantages	<ul style="list-style-type: none"> • Low activity concentrations are in the primary coolant • There is no need for more frequent primary circuit sampling and intensive water purification • There is no iodine spiking during transients • Load-follow operation can be applied • Less radioactive waste is generated (water purification filters)
disadvantages	<ul style="list-style-type: none"> • A longer shutdown is required to select the leaking assembly and the replacement assembly • The leaking assembly does not reach the planned burn-up, hence less energy can be extracted from it • Asymmetric power distribution is in the core, which may cause power limitations • It is necessary to redesign the campaign
risks	<ul style="list-style-type: none"> • The efficiency of the control assemblies may vary

Remaining work

The planned work was completed.

Related publication

- [1] P. Szabó, Z. Hózer, B. Bürger, I. Nagy: *The conditions and risks of NPP operation with defective fuel assemblies*, EK-FRL-2023-251-1-1-M0, in Hungarian (2023)

CREEP AND BURST TESTS WITH SLIM FUEL CLADDING TUBES

Márton Király, Richárd Nagy, Péter Szabó

Objective

In this project, the behaviour of SLIM (0.2 mm smaller outer diameter) fuel cladding tubes was investigated in normal operation conditions. This new fuel type was recently introduced in the MVM Paks NPP.

Methods

The thermo-mechanical creep was investigated using a pressure system and a three-zone tube furnace. The internal pressure of the cladding samples was set to 11 MPa, while the furnace maintained a 400 °C constant temperature in a mostly inert atmosphere. The change in diameter was measured using a custom-built profilometer comprised of a laser micrometre and a linear module. The data was recorded in LabView and in Excel, the data processing was partially automated in Excel.

Results

The creep rate of the new SLIM cladding tube was found to be greater than that of the traditional type E110 cladding material. There were some discrepancies in the measurements, like applying the same pressure to the tubes of different diameters and wall thicknesses resulted in different stress states in the two cladding types. This was done in order to investigate the tubes in the same conditions, as the tests at similar radial stresses was already completed. We have solved the slight oxidation of the surface of the cladding tubes caused by air ingress by constant pressurization of the furnace with argon. The furnace setup and the pressure system were modified to create constant inner pressure, and sacrificial getter materials were inserted to capture the remaining air and water. Control samples with no pressurization were also used to measure the oxidation of the samples.

The samples were taken out of the furnace weekly to measure the change in diameter. The test was concluded after 69.3 effective days. The diameter change due to oxidation was found to be around 5 µm, this was constant after the first two weeks, so no additional oxidation took place during the test. The secondary creep rate was calculated from the measured data. The thermomechanical creep rate of the E110 was 1.14 µm/day, for the SLIM samples it was 3.2 µm/day. While the radial stress on the thinner walled SLIM was 18% higher due to both claddings pressurized to the same 11 MPa, there is a significant discrepancy between the two tested alloys, the creep rate of the SLIM was found to be about 2.8 times greater than for the traditional E110 cladding. This was the third time we tried to verify these data and the results are in agreement.

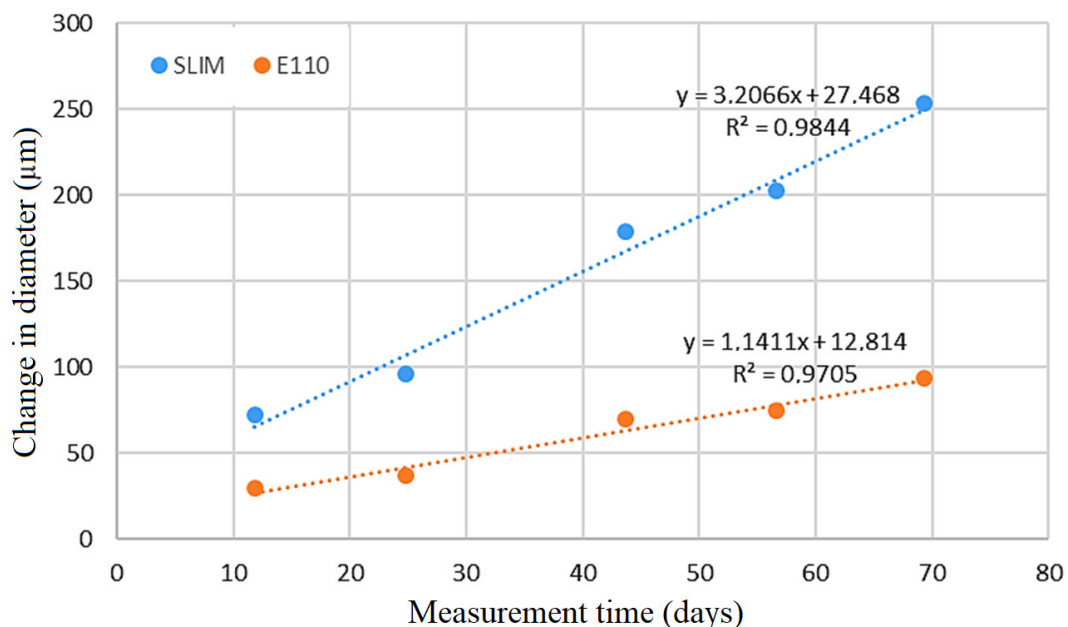


Figure 1: The diameter increase of the SLIM cladding tube and the reference E110 cladding during the creep test

Remaining work

All tests were completed and the results were evaluated, the project is finished.

MEASUREMENT OF FUEL ELEMENT BURST AND LEAKAGE BY ACOUSTIC EMISSION

Attila Gábor Nagy

Objective

Our aim was to apply the acoustic measurement technique to the detection of fuel element bursts and leaks.

Methods



Figure 1: Sensor fixing on the tube

To perform our measurements we had to construct a gripping device for the Acoustic Emission (AE) sensor housing, which we did by drilling through a brick-shaped piece of iron, using acoustic coupling material. The sample to be measured is assembled from several pieces, our preliminary test measurements showed that there is a significant signal loss at the couplings. To avoid this, we constructed acoustic couplings, which could greatly help the AE signal propagation. The next problem to be solved was to have the possibility to use two sensors. In this solution, I asked for the help of colleagues who know the furnace well (Márton Király, Richárd Nagy - thanks for their help). We planned to measure leakage, we had to ensure that the sample would start to leak after reaching the right pressure. We achieved this by modifying the threads of the couplers, and to be able to detect liquid leakage, we solved this by injecting water with a needle. The pressure signals were collected by the AE device itself using appropriate interface electronics.

Results

Firstly, we performed the bursting experiments. Our experience was that as the pressure increases the acoustic signals become more frequent. As the bursting pressure point is approached, the signal density becomes intense; as the sample is opened up, the signal density decreases but does not disappear completely. We performed an experiment without raising the temperature using this method to observe the Kaiser effect. The nature of the acoustic signals can be divided into two groups, we detected burst type signals, which indicate the release of stress in the material, the other type of signals are more similar to noise - but much stronger than normal

noise. These can be caused by the initiation of deformation, the noise generated by the various fasteners under stress. We also observed the possible localizations. Of course, ideally the localization would be on homogeneous material, this was not the situation in this case. In comparison, the localizations were more or less in the same place, to facilitate the localization the sample was exactly in the middle of the two detectors. In our leakage experiments, we've found that a significant effect was obtained above about 40bar pressure. There were also some experiments where the leakage preceded the splitting of the sample (Figure 2). In the liquid leakage experiments, the pressure value at which AE activity was excited was lower than when the sample was filled only with gas. I presented my results at the OATK 2023 conference.

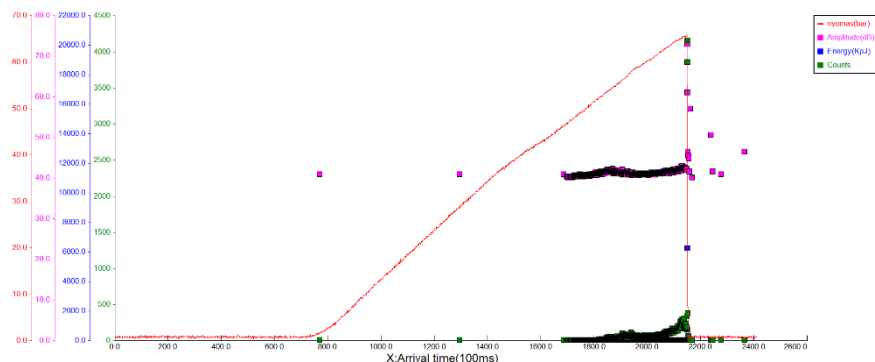


Figure 2: Fuel element bursts and leaks

Remaining work

1. Study the possibility to make these measurements useful in general practice,
2. Publish the results.

OPTIMAL CONTROL OF POWER PLANT LOAD CHANGES

Pál Szentannai, Tamás Fekete, and Bálint Pudleiner

Objective

Increasing the service lifetime of large scale power plants does significantly improve their benefits both from economic and ecological aspects. Life-Time Considering Control (LTCC) is a new approach to optimizing the load changes of power plants, the advantage of which is that it considers also the side effects of the transients. A benchmark for any control realizations is the theoretically possible best control. For setting up this, a methodology was developed by the authors.

Methods

For defining the criteria of optimal control, a cost function (also called target function) was formulated first. This contains, besides the traditionally applied control quality, also the most relevant side-effect, its consequences on Structural Integrity (SI). For finding the minimum of this cost function under any circumstances, modelling the following phenomena is necessary: (i) the power plant process, (ii) the stress-strain consequences, and (iii) material aging in critical points.

Results

The instationary power plant model was extended by a dynamic description of the SI phenomenon. For this, Finite Element Analysis (FEA) was carried out on the most critical part of the pressure vessel of the nuclear power plant, as illustrated in Figure 1.

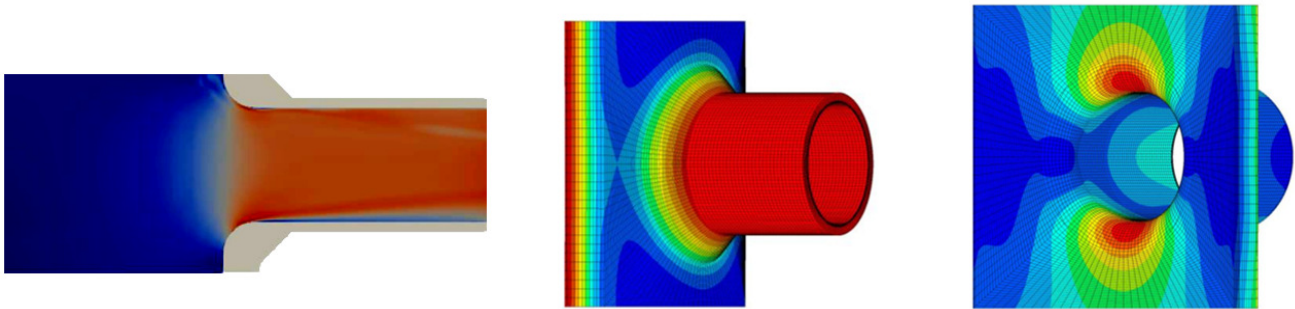


Figure 1: Steps of FEA calculations for modelling the SI consequences of load changes.
Left to right: Fluid mechanics; Heat Transfer; Stress-strain calculation

The FEA results were considered as the outputs of a dynamical process, the description of which had to be formulated in one of its well-known definition methods. The *transfer function* in the s -domain was chosen, which was estimated by a numerical method, the result of which is shown both graphically and numerically in Fig. 2.

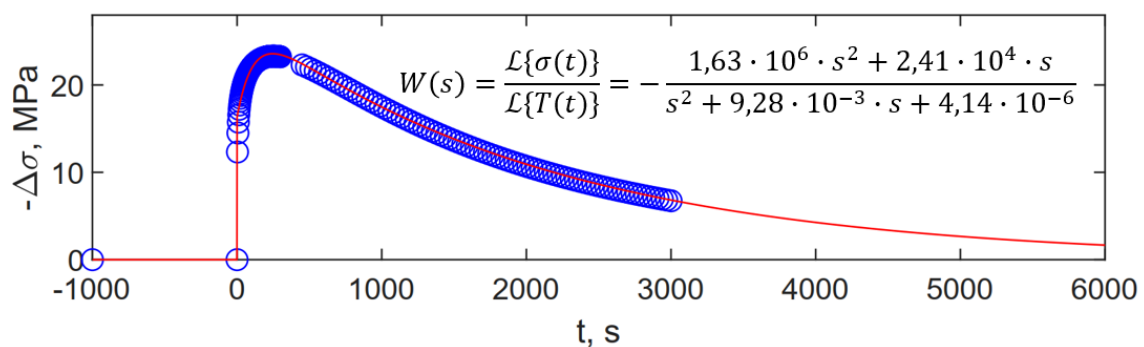


Figure 2: Extension of the dynamical power plant model as identified: the transfer function of the dynamical SI model

Remaining work

For developing the optimal control, several scenarios have to be investigated. Further, the benchmarks generated by this method should be implemented under the given environment of the particular practical cases.

Related publications

- [1] P. Szentannai and T. Fekete: *Optimal Load-control*, 20th MNT Nuclear Symposium, Nov. 23-24, 2023, Siófok
- [2] P. Szentannai, T. Szűcs, B. Pudleiner, and T. Fekete: *Transient phenomena and their consideration in load-following control of nuclear power plants*, Thermal Science (Min.Rev.), p. 13., ThSci2023.187

BURNUP-DEPENDENT GROUP CONSTANT PARAMETRIZATION BY APPLYING DIFFERENT MACHINE LEARNING METHODOLOGIES

Dániel Sebestény, István Panka, Bálint Batki

Objective

The need for group constant parametrization arises from the two-step neutronics calculation schemes. The first code produces few-group constants spatially homogenized to assemblies or nodes, while the second code uses them for full core calculations. These values depend on several properties, including burnup and various operating conditions (e.g., temperature, moderator density, boron concentration), these properties are called features. Since the first code can produce group constant values for a finite number of feature combinations, and the second code may need the values for any feature combination, a predictive model (also called the parametrized group constant library) is needed for each group constant. This study explores the viability of various models for this problem. A fitting and testing code package has been developed that includes hyperparameter optimization and model selection.

Methods

Different mathematical models were applied: linear interpolation, CORK regression which is a novel polynomial regression with square roots, random forest regression, support vector machine, feedforward neural network: a dense net using Keras library. In case of CORK regressor, the hyperparameters are: a number for each feature that denotes the maximum whole degree the feature can appear in any term of the polynomial, a Boolean value for each feature that shows if square roots of the feature can appear in the terms, a maximum degree for any (pure or mixed) term. The physical model was an assembly of the VVER-1200 reactor and the sample points were generated according to five features: burnup, boron concentration, fuel temperature, coolant temperature, and coolant density. Models were trained and evaluated on data for this fuel assembly, calculated using the MULTICELL 2D transport code. Different datasets for training (1211 sample points) were used in case of the validation procedure, for hyperparameter optimization 239 points were selected and for the testing 239 points were applied; random distribution in non-burnup features was considered. For the optimization of the hyperparameters, we used the Optuna framework, which is a flexible framework that can use several algorithms and black-box optimization.

Results

A cross-section fitting and testing code package was implemented, and the various fitting algorithms were compared to each other. It was found that the CORK regressor has the best performance on the used VVER-1200 assembly model with an average RMS error of 0.00073 for the fitted K_{inf} . The method's stable performance is demonstrated by the estimated standard deviation of the error of ~1%. Random forest was found to be ineffective for this problem, while other methods showed suboptimal performance. However, running the pipeline with outputs from other assemblies and fitting different group constants might have slightly different conclusions.

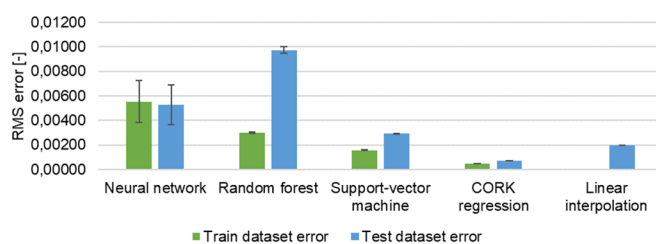


Figure 6: Mean and corrected sample standard deviation of root mean square error at the fitting of the infinite multiplication factor (K_{inf}), shown for different models

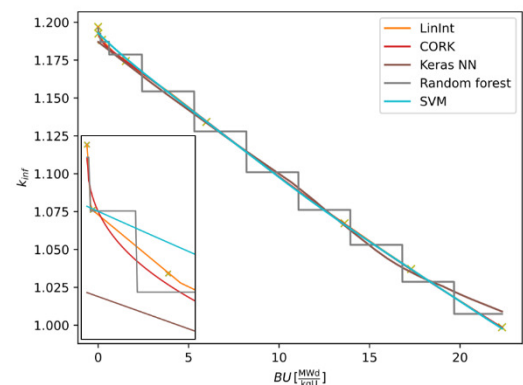


Figure 7: Fitting of each method on points along a burnup (BU) dependent line in the 5-dimensional feature space. The fittings at the beginning are shown enlarged in the bottom left corner.

Remaining work

The presented work has been supplemented by a study of the fitting of group constants and will be published soon.

Related publication

- [1] D. Sebestény, I. Panka, B. Batki: *Burnup-dependent group constant parametrization by applying different machine learning methodologies*, NENE International Conference Nuclear Energy for New Europe, 11–14 September, 2023, Portorož, Slovenia

INNOVATIVE EXPERIMENTAL AND NUMERICAL TOOLS IN MATERIALS TESTING

Tamás Fekete, Dániel Antók, Levente Tatár, Péter Bereczki

Objective

Structural Integrity (SI) is an engineering paradigm that addresses 'the safe operation of engineering components, structures and materials, and addresses the science and technology that is used to assess the margin between safe operation and failure' – as formulated by the European Structural Integrity Society (ESIS).

Supporting the safety of Large-Scale Pressure Systems of Nuclear Power Plants for Long-Term Operation (LTO) is a growing challenge for the scientific and engineering communities; therefore, increasing the reliability of Structural Integrity Computations (SICs) is becoming more pressing. The robustness of outcomes from SICs is heavily dependent on: (1) the forecasting performance of the theoretical and numerical framework underlying the methodology; (2) the information extracted from the material tests to support the calculations, in terms of quantity and quality; (3) the quantity and quality of information evaluated from the material test results.

Methods

The theoretical part of the project is concerned with the development of a state-of-the-art methodology for the measurement and evaluation of material tests. This methodology appears promising for future applications in industrial SI projects. In the practical part, Digital Twins (DTs) for tensile measurements were first developed. The models will further be developed towards other material test setups and advanced material models.

Results

The main outcome of the theoretical part of the project is the new Measurement and Evaluation Framework. The DT concept is at the core of the methodology, which goes beyond a metrology-based understanding of measurements to a process-based understanding that forms the basis of the new SIC Methodology. The test system is built around a Gleeble 3800 thermomechanical simulator. The tensile tests are based on standard test setups using flat 8x2 mm cross-section specimens. Force and crosshead displacements are measured by in-system sensors; standards-compliant elongation is measured by clip-type extensometers. The testing machine is equipped with an optical system that provides spatial geometric images of the test specimens during measurements, allowing beyond-standard measurements to be made. The active part of the test specimens has initially a regular mesh along the gauge length. Before measurements, high-precision coordinate maps were made of the dimensions of each test sample along its gauge length. During measurements, the optical system takes images of the specimen at times synchronized with the sampling, controlled by the machine's trigger signal.

DTs of the tests are implemented using Finite Element (FE) modelling technology, in the Hexagon Marc-Mentat FE system. Corresponding simulations are performed using that system. The specimen's DT is the full 3D geometric model of the realized specimen. The gauge section is meshed with hexahedron elements, based on the high-precision coordinate maps, which have been produced along their gauge lengths during post-production dimension control. Von Mises plasticity theory is used with strain-hardening material response. The material is considered initially homogeneous and isotropic. Boundary conditions are provided by the corresponding kinematic constraints. The calculations use large strain-large displacement kinematics, in updated Lagrangian setting.

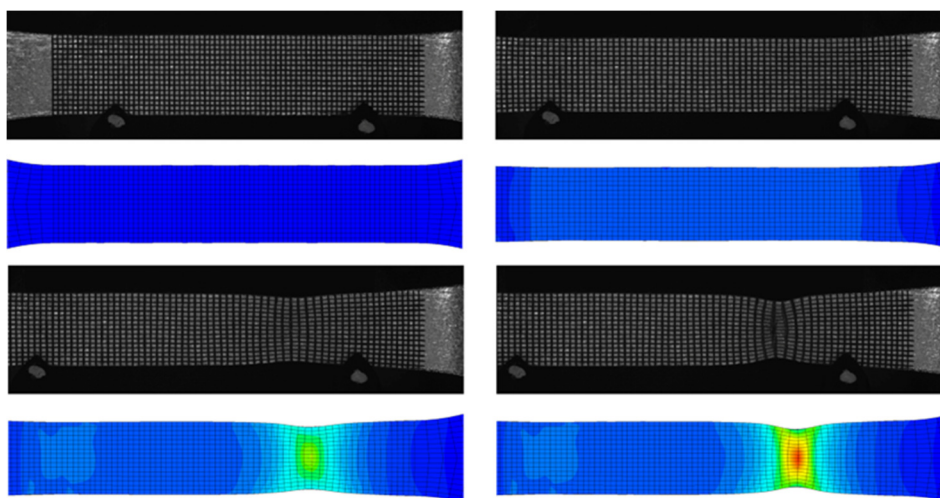


Figure 1: Synchronized results of the F1 specimen tensile test and its Digital Twin simulation

An illustration of the adequacy of the DTs developed for the problem is given in Figures 1 and 2, which show the observed and simulated shapes of two different specimens, which differ only slightly from each other according to the results of the coordinate measurements mentioned above (for F1 specimen in Figure 1, for F2 specimen in Figure 2). The results show that DTs constructed with geometric imperfections are highly effective for simulating the time evolution of the specimen shape and the deformation field, as well as the failure location.

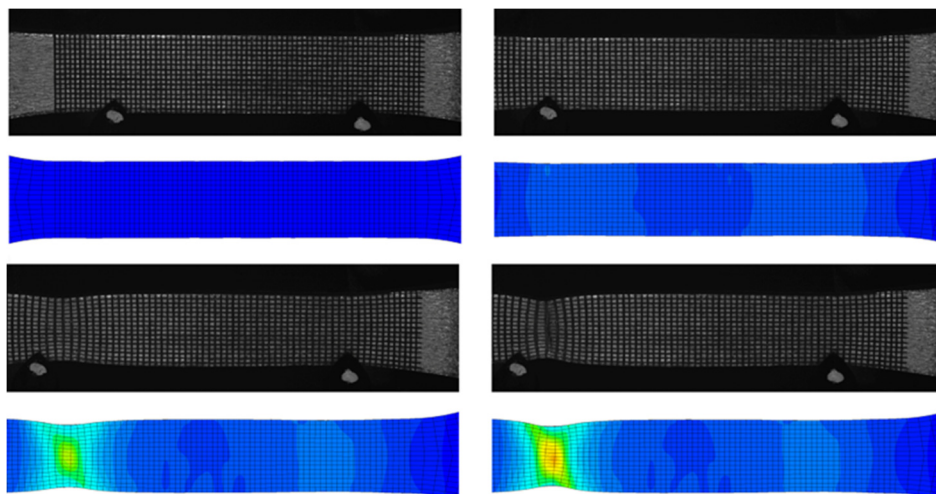


Figure 2: Synchronized results of the F2 specimen tensile test and its Digital Twin simulation

Remaining work

The presented methodology and the models developed for the evaluation of the measurements will further be developed towards more advanced material models and later for industrial applications.

Publications

- [1] T. Fekete, D. Antók, L. Tatár, P. Bereczki: *Investigation on geometric imperfections of tensile test specimens using optical full-field measurements and digital twin-based simulations* In: ICSI 2023 The 5th International Conference on Structural Integrity, Structural Integrity Procedia **54**, 314–321 (2024)
- [2] T. Fekete, D. Antók, L. Tatár, P. Bereczki: *Innovative Experimental, Analytical and Numerical Tools in Fracture Research, Theoretical and Applied Fracture Mechanics* (Submitted)
- [3] Fekete T: *Anyagvizsgálatok és kiértékelésük innovatív módszertana*, Anyagvizsgálók Lapja 2023/III 27–38. (2023)
- [4] Fekete T, Antók D, Tatár L, Bereczki P: *Szakítóvizsgálatok innovatív kiértékelési módszertanáról*, Anyagvizsgálók Lapja 2023/III 39–54. (2023)

IMPROVING THE STRUCTURAL INTEGRITY COMPUTATION METHODOLOGY

Tamás Fekete

Objective

Large-Scale Engineering Systems (LSEs) are planned for a limited Service-Lifetime (SL), called Design Service-Lifetime (DSL). During the third quarter of the 20th century, the DSL of an LSE was generally 30–40 Operating Years (OY); today, the DSL of a new plant – e.g., a Nuclear Power Plant (NPP) –, is 60 OY. The Operating License (OL) of a new plant is usually granted for its DSL. Large-Scale Pressure Systems (LSPs) are of prime importance for the safety of power plants, e.g., NPPs and heavy chemical facilities; the overall plant SL is governed by the SL of their safety critical LSPs. During design, Design Safety Calculations (DSCs) prove the safety of LSPs, at least up to the DSL. During operation, Structural Integrity Calculations (SICs) are performed to robustly assess, under which conditions and for what time – up to the Technically Allowable Lifetime (TAL) – the safety of an LSPs can be expected. An operating plant may be granted an extended OL, if SICs for that plant demonstrate that the TAL of its LSPs is more than the envisaged Extended Operating Time (EOT). Several NPPs, built worldwide in the last third of the 20th century, have already been granted an Extended OL – called first-phase extended OL –, in most cases for 20 OY. Nowadays, NPP owners are preparing for the second phase extended OL, to obtain an additional 20 OY OLs. These NPPs will operate in the Long-Term Operation (LTO) range – i.e., between 50 and 80 OYs –. The methodology of SIC projects during first-phase extended OL procedures was the same as that used for the DSCs. Now, in the preparation for second phase of extended OL, a series of questions are emerging that previously had not been relevant for safety assessment, because the ageing of the LSPs's structural materials over decades of operation has reshaped conditions for safe operation. It seemed therefore worthwhile to rethink the SIC methodology from its foundations.

Methods

The research involved two steps. The first step focused on the critical analysis of the international good practice-based methodology of SICs. The second step attempted to build a new theoretical framework based on modern thermomechanics.

Results

The most fundamental result of the project achieved so far is a paradigm shift that bases the traditional discipline-based methodology of SICs on Modern Thermodynamics, as a holistic, irreversible theory.

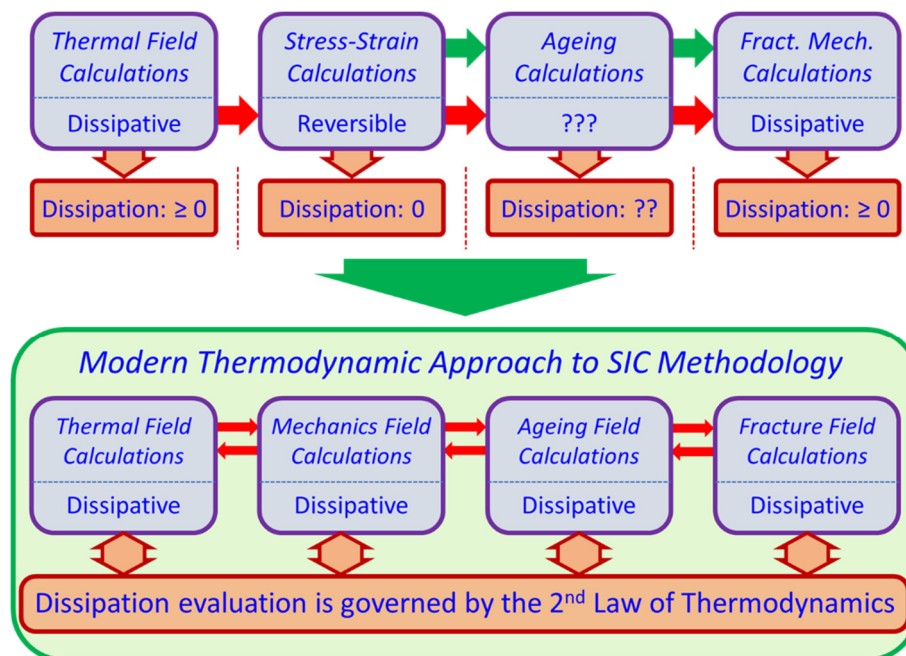


Figure 1: A paradigm shift in the methodology of SICs.

Remaining work

Future work will focus on the questions of industrial applicability of the new theory.

Related publication

- [1] T. Fekete: *Towards new Fundamentals for Structural Integrity Calculations of Large-Scale Pressure Systems*, Procedia Structural Integrity **48**, 302–309 (2023) <https://doi.org/10.1016/j.prostr.2023.07.128>

PRE-TEST SIMULATION OF RIA EXPERIMENTS ON FRESH RODLETS WITH HYDRIDED CLADDING IN THE HERA EXERCISE

Katalin Kulacsy

Objective

The Framework for Irradiation Experiments (FIDES) has been created and is coordinated by the OECD NEA in an effort to make up for the lack of irradiation facilities after the closure of the Halden Reactor. Several projects run in parallel in different reactors, one of them is HERA (High Burnup Experiment in Reactivity Initiated Accident) and includes RIAs carried out in the TREAT reactor in the USA and in the NSRR reactor in Japan. The first series of experiments was performed on fresh fuel rodlets in unirradiated but pre-hydrided Zircaloy-4 cladding. The experiments were preceded by a pre-test modelling and simulation exercise and benchmark to test the effect of pulse width, enthalpy increase, hydrogen content in the cladding and gap width on the predicted failure of the cladding. A total of 14 cases were simulated for the 6 experiments to follow, as shown in Table 1.

Table 1: Cases for the pre-test simulation

Case No.	Experiment identifier	Reactor	Pulse width (ms)	Max. enthalpy increase (J/g)	H content (ppm)	Pellet radius (mm)
1	HERA-PreH-1,2	NSRR	7.5	650	400	4.1605
2				650	200	4.1605
3				650	600	4.1605
4				550	400	4.1605
5				750	400	4.1605
13				650	400	4.1305
6	HERA-PreH-3,4	TREAT	90	650	400	4.1605
7				650	200	4.1605
8				650	600	4.1605
9				550	400	4.1605
10				750	400	4.1605
14				650	400	4.1305
11	HERA-PreH-5,6		50	650	400	4.1605
12	HERA-PreH-5,6		300	650	400	4.1605
13						

Methods

The simulations were done using the code FRAPTRAN-2.0 as released by the developers (Pacific North-West National Laboratory, USA).

The fabrication data of the rodlets, the power history of the power pulse and the parameters of the coolant were given by the benchmark organizers. For those who could not model the behaviour of the coolant, which was stagnant water, they also provided the cladding outer temperatures calculated by a coupled system of a thermohydraulics and a fuel behaviour code.

The outputs were requested in a given format. Among others, they had to include the Cladding Failure Prediction (CFP), which was the ratio of the achieved failure parameter (e.g. cladding strain) to the failure limit (e.g. temperature-dependent failure strain).

Results

All 14 cases were simulated. Only the rods subjected to the very short pulse (7.5 ms), reaching a high enthalpy increase (at least 650 J/g) and with a cladding somewhat embrittled by hydrogen (at least 400 ppm) failed, as shown in Table 2. Case 1 is very interesting, as the cladding practically reached the failure limit, but numerically the code considered it as non-failed. However, realistically, we consider it as failed (Fig. 1).

All the results submitted by the Centre for Energy Research were within the range of the results presented by the majority of the participants, which is a sign that hopefully the code gives good results. However, the post-test simulations will be the real validation.

Table 2: Results of the pre-test simulation

Case No.	Enthalpy increase (J/g)	H content (ppm)	Pellet radius (mm)	Pulse width (ms)	CFP (-)
1	650	400	4.1605	7.5	0.99
2	650	200	4.1605	7.5	0.65
3	650	600	4.1605	7.5	1.00
4	550	400	4.1605	7.5	0.74
5	750	400	4.1605	7.5	1.00
6	650	400	4.1605	90	0.48
7	650	200	4.1605	90	0.44
8	650	600	4.1605	90	0.50
9	550	400	4.1605	90	0.39
10	750	400	4.1605	90	0.55
11	650	400	4.1605	50	0.64
12	650	400	4.1605	300	0.16
13	650	400	4.1305	7.5	0.48
14	650	400	4.1305	90	0.14

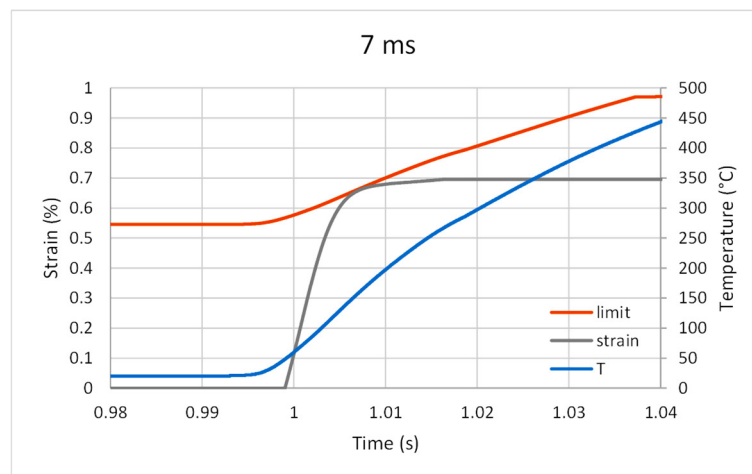


Figure 1: Engineering hoop strain and strain limit for Case 1

Remaining work

The pre-test simulations have been completed, but the modelling and simulation efforts accompanying the experiments continue during the years to come.

FUSION MATERIAL SCIENCE RESEARCH: MATERIAL DEVELOPMENT, IRRADIATION AND RADIATION DAMAGE TESTING

Ildikó Szenthe, Dávid Cinger, Balázs Hargitai, Kristóf Andor Csikós, Szilvia Móritz

Objective

The development of the new enhanced material for fusion reactors is one of the highest research activities of the European Union. HUN-REN EK became a member of these peak-level research groups during the previous years. We would like to save this position in 2024, too. The next step in European fusion research after the ITER reactor is the development of the DEMO fusion reactor. In connection with the DEMO material science research, HUN-REN EK participates in the development of new materials suitable for fusion conditions, their testing, evaluation and summarization of the results. In the design of the DEMO fusion reactor, they want to standardize the use of several materials that cannot yet be produced on an industrial scale, but the aim is to standardize them in the coming years. In the framework of the EUROfusion FP9 project, Reactor Materials research group irradiates the material samples in the BAGIRA irradiation probe and conducts further examination of the irradiated materials in qualified laboratory rooms connected to the reactor's service rooms. We participated in several subprojects of the WPMAT work package fusion materials science research in 2023.

Methods

Mechanical and microstructural research of the ODS (Oxide Dispersion Strength alloy), Eurofer97 steel and CuCrZr alloys in the frame of High Heat Flux Material and Steel Development subtask perform an investigation of mini specimens, whose dimensions are below the standards in the frame of the Small Specimen Test techniques subtask. We perform the continuation of the neutron irradiation of the base metal EUROFER97 to achieve: 1 dpa (displacement per atom) at 300°C, 1 dpa at 350°C, 2 dpa at 300°C, 2 dpa at 350°C. In order to fill the gaps in the database linked to the Tritium Breeder Blanket subtask, tests were performed on the irradiated specimens. In the functional materials subproject, the research group participated in the development of the Materials Property Handbook for materials of the fusion reactor vessel components and aimed at the advancement of the development of Materials Databases on functional materials. The activities include collection and qualification of the data as well as preparation for transferring it into the Materials Database system, and elaboration of the detailed test matrices to close the database gaps for the materials.

Results

At the small specimen test technique subtask, according to the mechanical and connected microstructural test results, the number of the tests defined in the relevant standards is usually not enough and has to be increased to app. 150%. The tested experimental ODS material developed by the fusion research became stringy and the result was not valid. (Fig. 1).

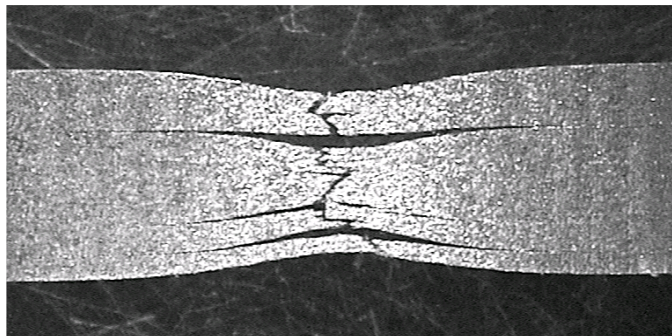


Figure 1: Top view of ODS specimen after tensile test at room temperature

The tested Eurofer97 material as received and after 0.4 dpa at 300°C irradiation shows general yielding at room temperature and at higher temperature testing, in this temperature range no valid fracture toughness value result was measured. It means that at room temperature and over, most probably fracture toughness check at designing is not needed.

At the functional material subtask, dielectrical and physical properties of the materials were collected and evaluated. In 2023, the database extended mainly with new aged material data. The data was uploaded into the database and used for elaboration of the functional material's Material Property Handbook.

Remaining work

It is planned for 2024 to continue participation in the fusion research projects of the different subtasks in the frame of the EUROfusion consortium. We plan the continuation of the mechanical and microstructural testing of other newly developed

structural materials and the irradiated Eurofer 97 steel. We plan to continue the handling of the functional material database and Material Property Handbook, too.

Related publications

- [1] I. Szenthe, D. Cinger, B. Hargitai, K. A. Csikós, Sz. Móritz: *Fusion material sciences research in Hungary*, conference OATK 2023
- [2] D. Cinger, B. Hargitai, K. A. Csikós, M. Horváth Márta¹, F. Gillemot: *Small Specimen Test Technics*, conference OATK 2023
- [3] K. A. Csikós, D. Cinger, B. Hargitai, I. Szenthe, F. Gillemot: *Irradiation of Eurofer97 steel in the BAGIRA irradiation rig*, conference OATK 2023

TEST TECHNOLOGY STANDARDIZATION OF MINIATURIZED FRACTURE MECHANICS SPECIMENS FOR FUSION APPLICATIONS

*Dávid Cinger, Balázs Hargitai, Andor Kristóf Csikós, Ildiko Szenthe,
Márta Horváth, Ferenc Gillemot*

Objective

The Centre for Energy Research undertook to perform the Research Project entitled "Validation of the Use of Small Compact Tension (SCT) Specimens by Incorporation of Experiences for Fusion Use" which forms part of the International Atomic Energy Agency (IAEA) Coordinated Research Project (CRP) "F13021" entitled "Towards the Standardization of Small Specimen Test Techniques for Fusion Applications - Phase II".

On international level the design and construction rules are very much fragmented and aren't conducive for an internationalization of the fusion industry.

Small Specimen Test Techniques (SST) are currently based on the knowledge collected in laboratories and institutions, which have developed their own way for performing mechanical tests. These techniques and practices differ in size (USA, EU, Japan...) and shape of specimen used, measurement techniques, evaluation methodologies and acceptance criteria for valid data.

The fusion community needs guidelines for small specimen testing on main test techniques (tensile, creep, low cycle fatigue, fracture toughness, fatigue crack growth rate) for reference structural fusion materials. This effort already started in the earlier CRP, Towards the Standardization of Small Specimen Test Techniques for Fusion Applications (F13017), which was concluded in 2021.

Methods

To make the results comparable, the research institutes participating in the project chose a dedicated structural material for the fusion power plants, the EUROFER-97 RAFM (Reduced Activation Ferritic Martensitic) steel alloy, as the test material. The test specimens are made from this alloy.

The smaller a test piece, the higher the manufacturing precision required by the standard. This is not accidental, as otherwise it would lead to a large deviation of the results. To achieve the required production precision, our institute has developed a two-step processing, the first element of which is that a wire-EDM (Electric Discharge Machine) processes the test specimens from the block material, and then a CNC (Computer Numerical Control) milling machine prepares the holes with an accuracy of 0.1 mm. Dimensions of the specimen: 10 x 9.6 x 4 mm, with D=2 mm holes.

From the point of view of measurement techniques, there are two schools. One measures the displacement in the load line (LLD - Load Line Displacement) and the other on the front surface (see Figure 1). The advantage of the first version is that we get direct LLD values, in the second case we have to introduce a conversion factor into the calculations, too.

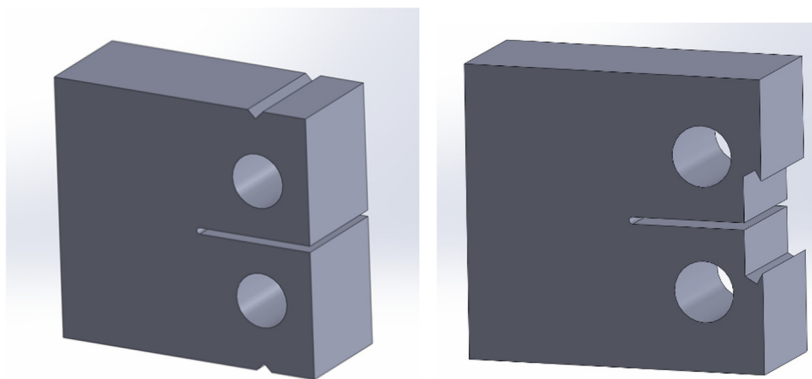


Figure 1: Mini-CT configurations

Results

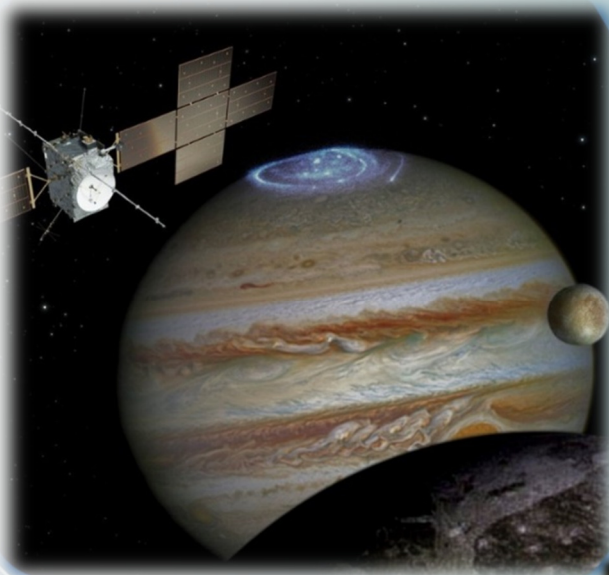
Our results show that although the direct LLD measurement is practical, in many cases the deformation around the holes is also measured in the LLD value, thus falsifying the result. Therefore, we chose the front face measurement approach.

Remaining work

The project lasts 4 years. In the remaining time, we perform fracture mechanics tests on a series of mini-CT samples and compare the results with literature data measured on large samples.



III. NUCLEAR SECURITY, DOSIMETRY AND SPACE RESEARCH



GAMMA-RAY MEASUREMENT AND ANALYSIS OF SPENT FUEL ASSEMBLIES OF PAKS NPP, 2023 (I)

&

DEVELOPMENT OF NEW MODEL AND NUCLEAR MEASURING PROCEDURE FOR DETERMINATION OF BURNUP HISTORY OF NUCLEAR FUELS FOR SAFEGUARDS AND FORENSIC ANALYTICAL INVESTIGATIONS (II)

Péter Kirchknopf, Imre Szalóki, Péter Völgyesi

Section I.

Objective

For safety reasons, the fuel manufacturer must set a maximum burnup limit for its assemblies. To guarantee operational safety, the Nuclear Power Plant (NPP) staff decreases this limit by a so-called 'engineering factor'. This factor accounts for the uncertainty of the NPP's reactor physics calculations. The long-term goal of this project is to prove that the uncertainty of the burnup calculated by the NPP is well within the scope of the currently used engineering factor. This would allow the staff to increase the burnup limit, thus achieving better fuel utilization while maintaining operational safety.

Methods

In-situ High-Resolution Gamma-ray Spectrometry (HRGS) measurements were performed on ten selected spent fuel assemblies with 3.82%, 4.2%, and 4.7% average initial enrichments. All assemblies were measured from three sides that were rotated by an angle of +/-120° relative to each other and they were also scanned axially at 9-10 points to record the approx. 2.4 m long burnup profile. The spectra were collected with an Ortec SGD-GEM-3615 coaxial type 3% relative efficiency High-Purity Germanium (HPGe) detector connected to an Ortec digiDART 16k channel Multi Channel Analyzer (MCA). Isotopic activity ratios of fission products such as $^{134}\text{Cs}/^{137}\text{Cs}$, $^{154}\text{Eu}/^{137}\text{Cs}$, and $^{134}\text{Cs}^2/(^{106}\text{Ru}^{137}\text{Cs})$, which correlate well with the fuel burnup were determined. After calculating the net peak areas with the Ortec GammaVision software, an intrinsic efficiency calibration method was employed to obtain the mentioned activity ratios. Finally, the activity ratio values at the end-of-operation dates were calculated using the known cooling times of the assemblies.

Results

The results (Table 1) were utilized in the Reactor Physics Department at the NPP, so that the reactor physicists could compare them with their burnup calculations. Figure 1 shows this year's measurement results in comparison with fitted curves obtained in earlier measurement campaigns. Large deviations are present between the points and the previously fitted curves, which suggest that a single activity ratio might not be sufficient in all cases for accurate burnup prediction. With the analysis done, our objective for 2023 has been completed.

Table 1: Measured activity ratios calculated at the end-of-operation dates. Each measurement lasted for between 7,500-8,000 s (live time). The 2σ relative uncertainties for $^{134}\text{Cs}/^{137}\text{Cs}$, $^{154}\text{Eu}/^{137}\text{Cs}$, and $^{134}\text{Cs}^2/(^{106}\text{Ru}^{137}\text{Cs})$ are 0.7%, 1.8%, and 3%, respectively.

Assembly ID	Initial Enrichment [%]	Declared Burnup [GWd/MTU]	$^{134}\text{Cs}/^{137}\text{Cs}$			$^{154}\text{Eu}/^{137}\text{Cs}$			$^{134}\text{Cs}^2/(^{106}\text{Ru}^{137}\text{Cs})$		
			-120°	-0°	+120°	-120°	0°	+120°	-120°	0°	+120°
382_1	3.82	37.56	1.82	1.80	1.80	0.047	0.046	0.046	-	-	-
382_2	3.82	38.66	1.86	1.86	1.86	0.047	0.049	0.048	-	-	-
382_3	3.82	41.36	1.46	1.58	1.48	0.048	0.051	0.049	0.67	0.68	0.65
420_1	4.2	47.72	1.62	1.54	1.73	0.067	0.067	0.072	0.84	0.81	0.91
420_2	4.2	47.72	1.74	1.57	1.57	0.070	0.066	0.066	0.91	0.82	0.82
470_1	4.7	51.25	1.67	1.79	1.58	0.070	0.073	0.065	0.94	1.00	0.86
470_2	4.7	52.47	1.76	1.60	1.58	0.071	0.065	0.067	1.01	0.91	0.89
420_3	4.2	52.42	2.05	2.05	2.12	0.070	0.069	0.072	0.97	0.97	1.03
470_3	4.7	51.31	1.81	1.62	1.68	0.070	0.064	0.067	1.00	0.88	0.92
470_4	4.7	48.72	2.03	2.04	2.02	0.070	0.070	0.070	0.89	0.89	0.89

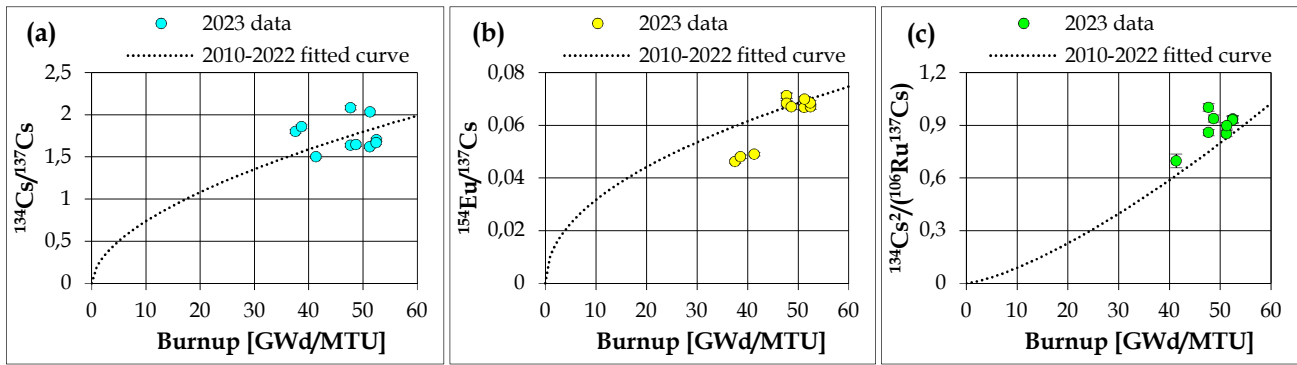


Figure 1: Measurement results for (a) $^{134}\text{Cs}/^{137}\text{Cs}$, (b) $^{154}\text{Eu}/^{137}\text{Cs}$, and (c) $^{134}\text{Cs}^2/(^{106}\text{Ru}^{137}\text{Cs})$ activity ratios compared to previous data

Remaining work

The work for the year 2023 has been completed. A new contract for this project in the year 2024 is in preparation.

Section II.

Objective

The objective of this research is the development of a spent nuclear fuel characterization method that relies on Non-Destructive Assays (NDA), mainly gamma-ray spectrometry. This study encompasses the measurement of power reactor spent fuel assemblies, evaluation of the measured data, and the testing of various data analysis techniques that can be used to predict some of the most important parameters of spent fuels: burnup, cooling time, initial enrichment, and the burnup history profile. The resulting method could be useful for Nuclear Safeguards inspectors, and it could also provide a basis for Nuclear Forensics analysis of irradiated nuclear materials.

The objectives in 2023 included the in-laboratory measurements of several pin configurations using VVER-440 type fresh fuel pins in a mock-up assembly model, which allows partial reconstruction of the spent fuel gamma measurements at Paks NPP, and the study of individual pin contributions to the detector. The other important research goal for this year was the application of Machine Learning (ML) algorithms on the gamma-ray spectrometric dataset collected at Paks NPP between 2010 and 2021, to improve the previously published experimental characterization methods (Kirchknopf et al., *Annals of Nuclear Energy*, 2022).

Methods

The mock-up assembly measurements were carried out using fresh, 4.4% enriched UO_2 fuel pins that were once part of the ZR-6 critical system, a steel barrel filled with water, steel as well as lead shielding elements (to simulate the circumstances at the NPP), and the same HPGe detector that was employed at the NPP. A total of 31 fuel pin gamma-ray spectra were collected during a three-month period using the smallest possible water thickness (7.3 cm), as opposed to the value set at certain spent fuel measurements (33.5 cm) due to the already limiting detection statistics. The 1001 keV gamma peak originating from the decay of ^{238}U was analyzed and the absolute detection efficiencies at this energy for 23 pin positions were calculated.

The dataset used in the ML approach consisted of evaluated fission product activity ratios at the time of measurement as well as at the assembly end-of-life date, and the main fuel parameters: burnup, cooling time, initial enrichment, with an additional calculated parameter: ^{239}Pu concentration, obtained from the KARATE-440 code system at the HUN-REN Centre for Energy Research. The ML models considered were Support Vector Regression (SVR), Random Forest (RF), Multi-Layer Perceptron (MLP), and Convolutional Neural Network (CNN). The CNN model was applied directly to the recorded gamma spectra, thus making characterization possible without any kind of spectrum evaluation. The sample size was 128, which is considered small for the training of artificial neural networks, however, data augmentation using random sampling from the extended measurement uncertainty interval helped to overcome this difficulty. The training process utilized 80-20% train-test splitting and K-fold cross-validation (5-fold used) to increase the robustness of the models. Each model was also subject to hyperparameter optimization prior to training. Implementation was done in the Python 3 environment, utilizing the *scikit-learn* and *keras* ML packages [1].

Results

Following spectrum evaluation, the calculated efficiency values at 1001 keV and the associated uncertainties are presented in Figure 2. Results were derived by subtracting multiple spectra from each other to compensate for the presence of additional fuel pins necessary to model the attenuation of the outer pins. It is determined from the experiments that out of all the measured positions, almost 60% of the counts at this energy originate from the closest two rows in an assembly, with other pins contributing less than 2% individually. Consequently, if pins from the 3rd row or deeper are removed (partial defect scenario), a simple gamma spectrometric measurement might not be adequate to reveal the defect.

The trained ML models all gave satisfactory results for the prediction of burnup, cooling time, initial enrichment, and ^{239}Pu concentration. The reference results obtained with the earlier methodology are denoted by NLR (Non-Linear Regression). A final ensemble model, which utilizes the mean predicted values of all other models, was also calculated, and compared to the

other models (Table 2). In the table, the Mean Absolute Error (MAE) values of the model predictions are displayed separately for the train and test data splits, and for different scenarios which represent the contents of the feature and target vectors. For example, the *BU* scenario has burnup as the target and uses all other available information, including cooling corrected activity ratios and enrichment, while *NF-BU* uses only directly measured information for burnup prediction (NF = Nuclear Forensics). The lowest test MAE values among the individual models are highlighted in green for each scenario. It is worth pointing out that in many cases the ensemble model has the best accuracy. In conclusion, the previously studied fuel parameters could be predicted more accurately with the ML approach, while parameters where the earlier methods failed (initial enrichment and ²³⁹Pu content) could be determined as well. The methodology and result of this work are presented in a paper published in the journal *Annals of Nuclear Energy* [2].

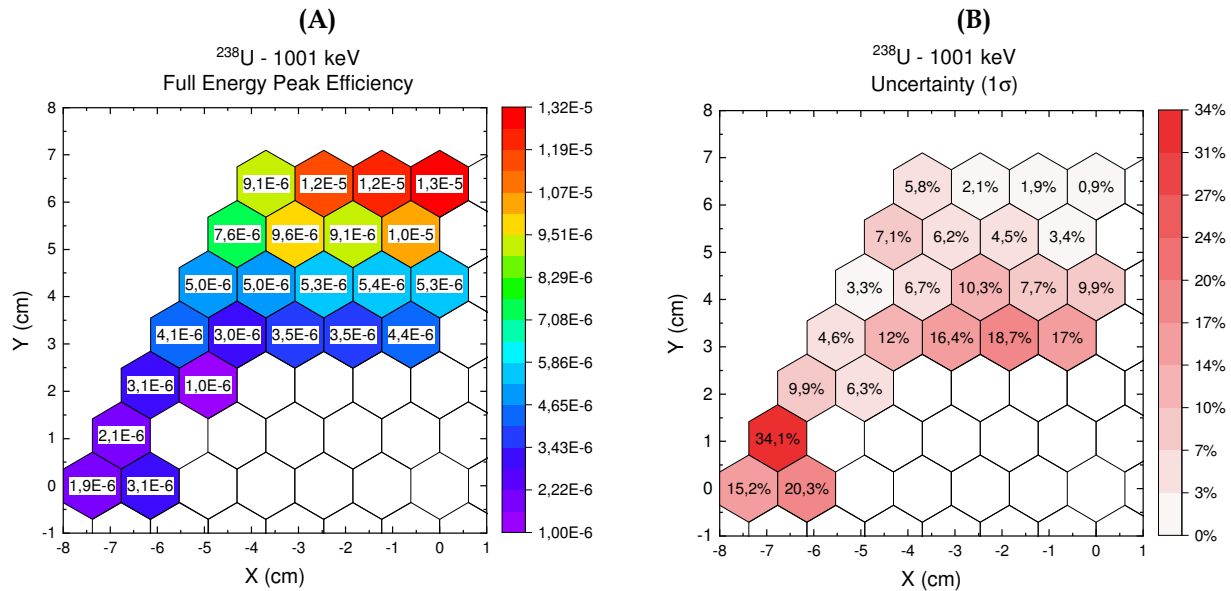


Figure 2: Absolute detection efficiency distribution among the measured fuel pin positions in a VVER-440 assembly lattice, the detector is positioned in the top direction. (A) shows the efficiency values, while uncertainties are displayed in (B).

Table 2: Mean absolute error values of train and test datasets produced by the ML models for all considered scenarios

MAE		NLR		SVR		RF		MLP		CNN		Ensemble	
Target	Scenario	train	test	train	test								
Burnup (GWd/tU)	<i>BU</i>	1.22	1.24	0.40	1.08	0.49	1.27	0.75	1.08	-	-	0.46	0.95
	<i>NF-BU</i>	1.38	1.40	0.79	1.52	0.70	1.54	1.09	1.48	1.18	1.41	0.79	1.23
Cooling time (day)	<i>CT</i>	119.4	120.7	21.9	69.0	18.2	47.4	72.9	80.0	-	-	34.3	56.3
	<i>NF-CT</i>			46.9	76.8	21.4	53.5	38.5	58.7	40.8	45.3	46.9	61.1
Enrichment (%)	<i>IE</i>	-	-	0.04	0.13	0.05	0.14	0.08	0.13	-	-	0.05	0.12
	<i>NF-IE</i>	-	-	0.02	0.15	0.06	0.15	0.13	0.16	0.13	0.17	0.08	0.13
²³⁹ Pu content (10 ¹⁷ /cm ³)	<i>Pu239</i>	-	-	0.74	4.26	1.57	4.26	2.42	3.83	-	-	1.19	3.38
	<i>NF-Pu239</i>	-	-	5.19	10.1	4.62	10.9	9.08	10.9	7.76	8.77	5.88	8.63

Remaining work

The paper containing the results of the spent fuel measurement Monte Carlo simulations is still in preparation and needs to be submitted for review. Additional Monte Carlo simulations need to be carried out for the mock-up assembly measurements as well, to discover the efficiency contributions of the inner fuel pins.

The investigated ML methodology should also be applied to isotopic data of other types of Pressurized Water Reactor (PWR) and possibly Boiling Water Reactor (BWR) spent fuels, utilizing the available NEA SFCOMPO 2.0 database.

Related publications

- [1] P. Kirchknopf, B. Batki: *Machine learning approaches to predict spent fuel parameters based on in-situ gamma spectrometry at Paks NPP*, Oral presentation, The International Conference on Mathematics and Computational Methods Applied to Nuclear Science and Engineering (M&C 2023), Niagara Falls, Canada, 15/8/2023.
- [2] P. Kirchknopf, B. Batki, P. Völgyesi, Z. Kató, I. Szalóki: *Application of machine learning methods for spent fuel characterization based on gamma spectrometry measurements*, *Annals of Nuclear Energy* **205**, 110601 (2024) <https://doi.org/10.1016/j.anucene.2024.110601>

DEVELOPMENT OF A NEW MODEL AND NUCLEAR MEASURING PROCEDURE FOR DETERMINATION OF THE BURNUP HISTORY OF NUCLEAR FUELS FOR SAFEGUARDS AND FORENSIC ANALYTICAL INVESTIGATIONS

Péter Kirchknopf, Imre Szalóki, Péter Völgyesi

Objective

The objective of this research is the development of a spent nuclear fuel characterization method that relies on Non-Destructive Assays (NDA), mainly gamma-ray spectrometry. This study encompasses the measurement of power reactor spent fuel assemblies, evaluation of the measured data, and the testing of various data analysis techniques that can be used to predict some of the most important parameters of spent fuels: burnup, cooling time, initial enrichment, and the burnup history profile. The resulting method could be useful for nuclear safeguards inspectors, and it could also provide a basis for nuclear forensics analysis of irradiated nuclear materials.

The objectives in 2023 included the in-laboratory measurements of several pin configurations using VVER-440 type fresh fuel pins in a mock-up assembly model, which allows partial reconstruction of the spent fuel measurements at Paks Nuclear Power Plant (NPP) and the study of individual pin contributions to the detector. The other important goal for this year was the application of Machine Learning (ML) algorithms on the gamma-ray spectrometric dataset collected at Paks NPP between 2010 and 2021, to improve the previously published experimental characterization methods [1].

Methods

The mock-up assembly measurements were constructed using fresh, 4.4% enriched UO_2 fuel pins that were once parts of the ZR-6 critical system, a steel barrel filled with water, steel and lead shielding elements (to simulate the circumstances at the NPP), and the same HPGe detector that was employed at the NPP. A total of 31 fuel pin gamma-ray spectra were collected during a three-month period using the smallest possible water thickness (7.3 cm), as opposed to the value set at certain spent fuel measurements (33.5 cm) due to the already limiting detection statistics. The 1001 keV gamma peak originating from the decay of ^{238}U was analyzed and the absolute detection efficiencies at this energy for 23 pin positions were calculated.

The dataset used in the ML approach consisted of evaluated fission product activity ratios at the time of measurement as well as at the assembly end-of-life date, and the main fuel parameters: burnup, cooling time, and initial enrichment, with an additional calculated parameter: ^{239}Pu concentration, obtained from the KARATE-440 code system at the HUN-REN Centre for Energy Research. The ML models considered were Support Vector Regression (SVR), Random Forest (RF), Multi-Layer Perceptron (MLP), and Convolutional Neural Network (CNN). The CNN model was applied directly to the recorded gamma spectra, thus making characterization possible without any kind of spectrum evaluation. The sample size was 128, which is considered small for the training of artificial neural networks, however, data augmentation using random sampling from the extended measurement uncertainty interval helped to overcome this difficulty. The training process utilized 80-20% train-test splitting and K-fold cross validation (5-fold was used) to increase the robustness of the models. Each model was also subject to hyperparameter optimization prior to training. Implementation was done in the Python 3 environment, utilizing the *scikit-learn* and *keras* ML packages [2].

Results

Following spectrum evaluation, the calculated efficiency values at 1001 keV and associated uncertainties are presented in Fig. 1. Results were derived by subtracting multiple spectra from each other to compensate for the presence of additional fuel pins necessary to model the attenuation of the outer pins. It is determined from the experiments that out of all the measured positions, almost 60% of the counts at this energy originate from the closest two rows in an assembly, with other pins contributing less than 2% individually. Consequently, if pins from the 3rd row or deeper are removed (partial defect scenario), a simple gamma spectrometric measurement might not be adequate to reveal the defect.

The trained ML models all gave satisfactory results for the prediction of burnup, cooling time, initial enrichment, and ^{239}Pu concentration. The reference results obtained with the earlier methodology in [1] are denoted by NLR (Non-Linear Regression). A final ensemble model, which utilizes the mean predicted values of all other models, was also calculated, and compared to the other models (Table 1). In the table, the Mean Absolute Error (MAE) values of the model predictions are displayed separately for the train and test data splits, and for different scenarios, which represent the contents of the feature and target vectors. For example, the *BU* scenario has burnup as the target and uses all other available information, including cooling corrected activity ratios and enrichment, while *NF-BU* uses only directly measured information for burnup prediction (*NF* = Nuclear Forensics). The lowest test MAE values among the individual models are highlighted in green for each scenario. It is worth pointing out that in many cases the ensemble model has the best accuracy. In conclusion, the previously studied fuel parameters could be predicted more accurately with the ML approach, while parameters, where the earlier methods failed

(initial enrichment and ^{239}Pu content), could be determined as well. The methodology and result of this work are written in an almost complete manuscript that will be submitted for publication in a scientific journal (possible candidates: *Annals of Nuclear Energy, Nuclear Instrumentation and Methods A*) by the end of this year [3].

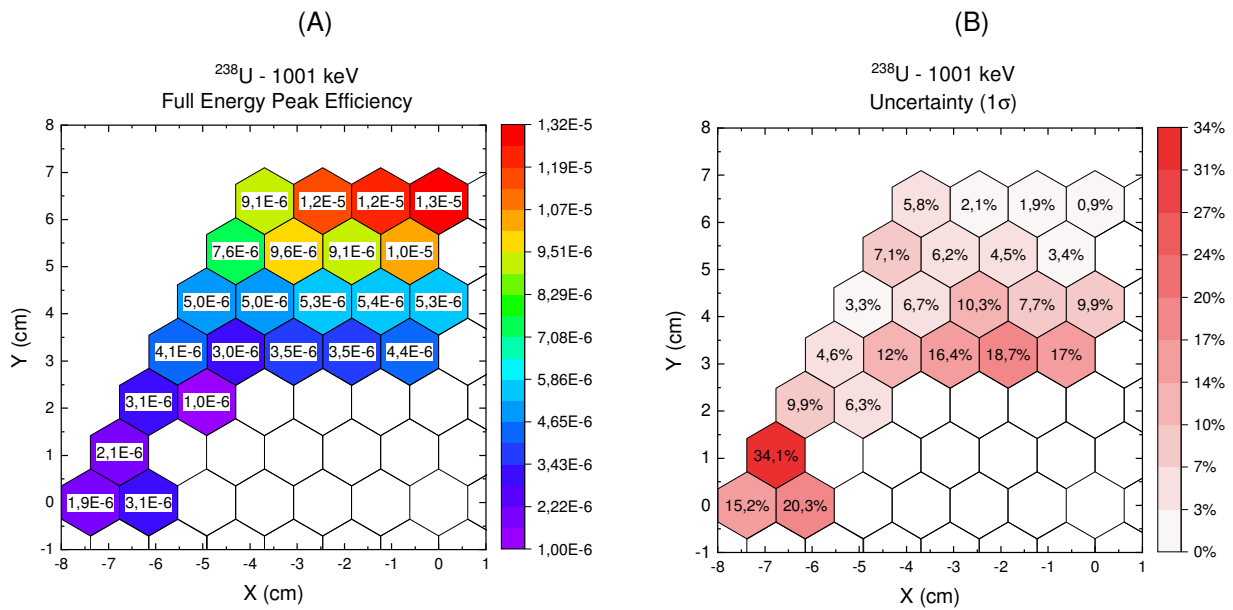


Figure 1: Absolute detection efficiency distribution among the measured fuel pin positions in a VVER-440 assembly lattice, the detector is positioned in the top direction. (A) shows the efficiency values, while uncertainties are displayed in (B).

MAE		NLR		SVR		RF		MLP		CNN		Ensemble	
Target	Scenario	train	test	train	test								
Burnup (GWd/tU)	BU	1.22	1.24	0.40	1.08	0.49	1.27	0.75	1.08	-	-	0.46	0.95
	NF-BU	1.38	1.40	0.79	1.52	0.70	1.54	1.09	1.48	1.18	1.41	0.79	1.23
Cooling time (day)	CT	119.4	120.7	21.9	69.0	18.2	47.4	72.9	80.0	-	-	34.3	56.3
	NF-CT			46.9	76.8	21.4	53.5	38.5	58.7	40.8	45.3	46.9	61.1
Enrichment (%)	IE	-	-	0.04	0.13	0.05	0.14	0.08	0.13	-	-	0.05	0.12
	NF-IE			0.02	0.15	0.06	0.15	0.13	0.16	0.13	0.17	0.08	0.13
^{239}Pu content ($10^{17}/\text{cm}^3$)	Pu239	-	-	0.74	4.26	1.57	4.26	2.42	3.83	-	-	1.19	3.38
	NF-Pu239			5.19	10.1	4.62	10.9	9.08	10.9	7.76	8.77	5.88	8.63

Table 1: Mean absolute error values of train and test datasets produced by the ML models for all considered scenarios

Additionally, yet another set of spent fuel assemblies was successfully measured at Paks NPP in October of this year. Similarly to last year, recently discharged assemblies were selected to strengthen the lower region of the cooling time regime. This additional experimental data will also be useful to validate the trained ML models.

Remaining work

The paper containing the results of the spent fuel measurement Monte Carlo simulations was still in preparation at the end of 2023, and was expected to be submitted for review no later than February 2024. Additional Monte Carlo simulations need to be carried out for the mock-up assembly measurements as well, to discover the efficiency contributions of the inner fuel pins.

The investigated ML methodology should also be applied to isotopic data of other types of PWR and possibly BWR spent fuels, utilizing the available NEA SFCOMPO 2.0 database.

Related publications

- [1] P. Kirchknopf, I. Almási, G. Radócz, I. Nemes, P. Völgyesi and I. Szalóki: *Determining burnup, cooling time and operational history of VVER-440 spent fuel assemblies based on in-situ gamma spectrometry at Paks Nuclear Power Plant*, *Annals of Nuclear Energy* **170**, 108975 (2022) <https://doi.org/10.1016/j.anucene.2022.108975>
- [2] P. Kirchknopf, B. Batki: *Machine learning approaches to predict spent fuel parameters based on in-situ gamma spectrometry at Paks NPP*, Oral presentation, The International Conference on Mathematics and Computational Methods Applied to Nuclear Science and Engineering (M&C 2023), Niagara Falls, Canada, 2023.08.15.
- [3] P. Kirchknopf, P. Völgyesi, Z. Kató, I. Szalóki, B. Batki: *Application of machine learning methods for spent fuel characterization based on gamma spectrometry measurements*, [Journal TBD].

DEVELOPMENT OF NUCLEAR FORENSIC ANALYTICAL METHODS FOR DETERMINING THE ORIGIN OF SMUGGLED MATERIALS

Csaba Tóbi, Péter Völgyesi

Objective

The aims of the PhD research are to determine the origin of nuclear materials, to identify new key parameters for origin assessment as well as to select from the already known parameters those with which a substance can be identified with certainty. It also belongs to the research goal to find novel methodologies for nuclear forensics analysis, to develop new methods and to further improve the existing ones.

Methods

Development of Rare Earth Element (REE) separation method for ICP-MS

REE pattern is a highly confidential signature to determine the origin of uranium-containing materials in the nuclear forensic examination. In the literature, there are many different REE separation techniques in the case of nuclear materials, but reproducibility in the laboratory is usually difficult. The efficiency of the REE separation technique used at the Nuclear Security Department is not completely satisfactory. Therefore, in the method development the digestion of the samples, part was examined based on the following recipe with a UOC reference material, using different digestion solutions:

- Dissolution of the samples in different digestion solutions: 300-500 mg subsample.
 - REE 1 - 9 ml 10M HNO₃ + 150 µl cc. HCl
 - REE 2 - 9 ml 10M HNO₃ + 150 µl HCl + 20 µl cc. HF
 - REE 3 - 9 ml 10M HNO₃ + 150 µl cc. HCl + 500 µl cc. H₂O₂
 - REE 4 - 9 ml 10M HNO₃ + 20 µl cc. HF
 - REE 5 - 9 ml 10M HNO₃
 - REE 6 - 9 ml 10M HNO₃ + 500 µl cc. H₂ODigestion time: 6 hours at 90 °C temperature.
- REE separation method:
 - Samples LOAD: 300 µl sample+ 900 µl MiliQ water.
 - Extraction chromatographic resin: 1.8 ml TRU (Triskem).
 - REE Separation: 1. Condition of the column with 10 ml 2 M HNO₃ 2. Sample upload 3. Washing the column with 2 ml 2M HNO₃ 4. Washing the REE fraction with 1 ml cc. HCl, after that with 4 ml 4M HCl.
 - Evaporation of the samples at 130 °C with 2 ml of cc. HNO₃ and 200 µl H₂O₂.
 - Droplet pick up with 4 ml 1% HNO₃ solution.

Inductively Coupled Plasma Mass Spectrometry (ICP-MS) measurements of the samples.

Nuclear Forensic measurements on nuclear fuel pellets by Atomic Force Microscope

The Atomic Force Microscopy (AFM) has already been used for the examination of various nuclear materials, including nuclear forensic investigations. However, the number of scientific articles dealing with this is very small and few of them have dealt with the comparison of the surface of nuclear fuel pellets. The surface of the tested reference pellets is considered a rough surface for the instrument, thus before the 3D-topographic scanning, the optimal parameters were identified to obtain adequate quality images. After the determination of the optimized settings for the optimal measurement of the instrument, nine nuclear fuel pellets with different enrichments were scanned. These topographic images were taken in a 50x50 µm area on the samples. If the scanning of the smaller area produced adequate results, a 20x20 µm area was scanned in the same way. All of the topographic scan images were edited using Gwyddion, an open-source professional cross-platform modular program for scanning probe microscopy data visualization and analysis.

Results

Development of Rare Earth Element separation method for ICP-MS

Based on the results, the best digestion solution for UOC is REE 2 solution (9 ml 10M HNO₃ + 150 µl HCl + 20 µl cc. HF) (Fig.1).

However, there were other results of the observation of the REE separations with TRU resin:

- In TRU resin separation, the following elements appeared in higher concentrations in the 2nd eluate: Nd, Ce, Pr, Sm, Eu.
- The uranium binding capacity of TRU resin is known, but it is not for REE.
- Probably the reason is that the lighter REE elements can be bound more strongly to the resin than the heavier elements.

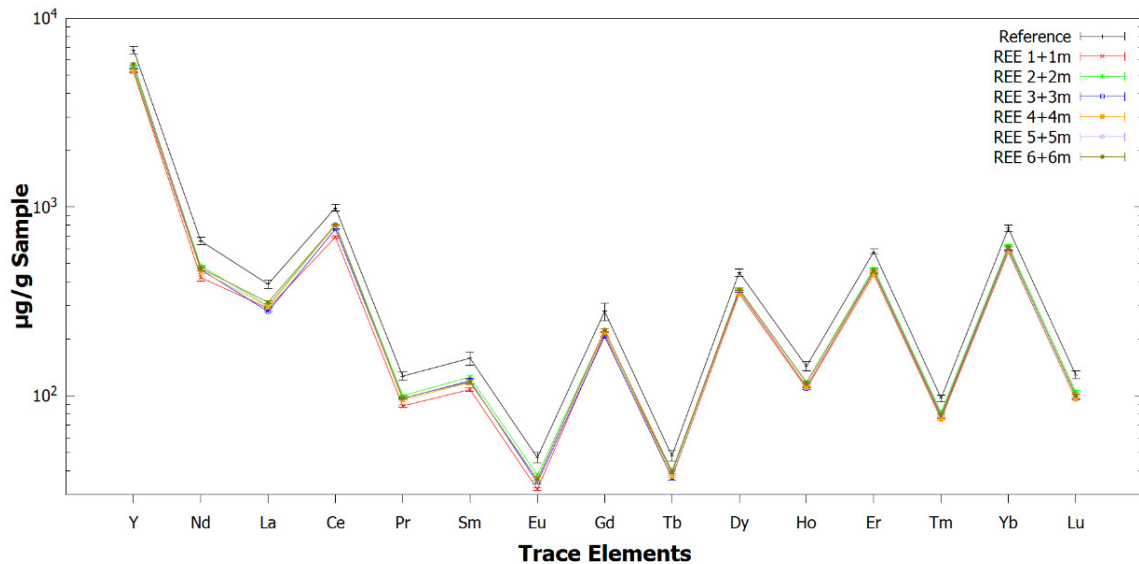
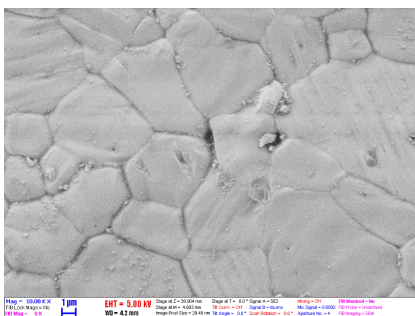


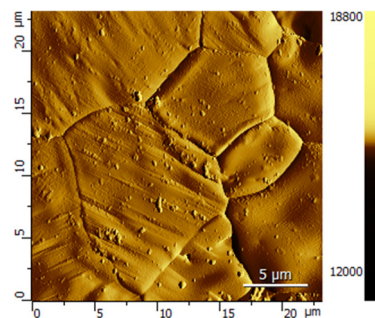
Figure 1: REE pattern of the different digestion solution

Nuclear Forensic measurements on nuclear fuel pellets by Atomic Force Microscope

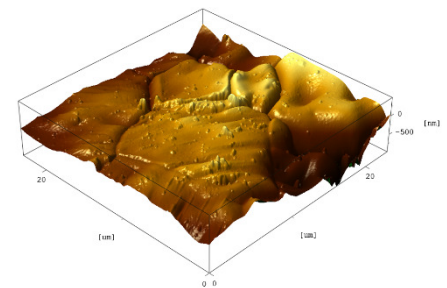
The AFM results were compared with images taken by Scanning Electron Microscopy (SEM) originating from previous measurements (Fig 2). Based on the results, similarly to SEM measurements, AFM is also capable of providing information about the morphology of fuel pellets, however, with higher resolution. Furthermore, the AFM is also capable of producing 3D-topographic images that can be useful for the measurement and determination of the surface roughness. As an advantage, the SEM equipped with Energy Dispersive X-ray Spectroscopy (EDX) is useful for semi-quantitative elemental analysis and elemental mapping. On the other hand, the AFM is also capable of identifying the different material compositions (phases). On the surface of the measured fuel pellets characteristic ridges and/or faceted grain structure of uranium were identified as well as in the previous SEM images. These faceted grains are called hyper-stoichiometric forms of UO_2 in the literature. This form of UO_2 could be identified by both techniques. Although SEM can capture the hyper-stoichiometric form of UO_2 , AFM can demonstrate it with higher resolution and in 3D-topographic form.



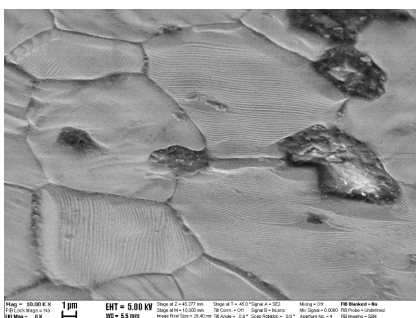
SEM image of CMX4-13-1



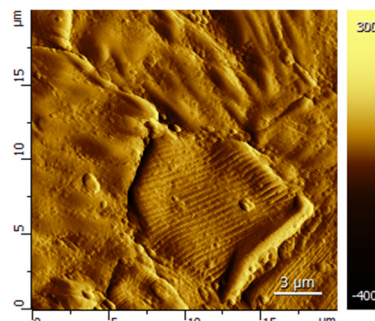
AFM Heights image of CMX4-13-1



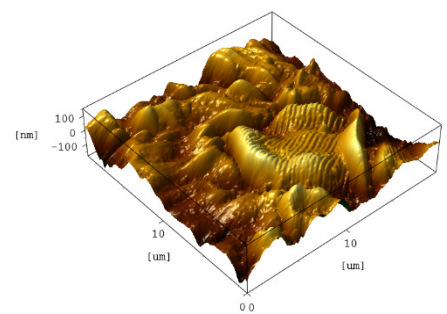
AFM 3D-topographic image of CMX4-13-1



SEM image of CMX5-Hu1b



AFM Heights image of CMX5-Hu1b



AFM 3D-topographic image of CMX5-Hu1b

Figure 2: Comparison of SEM and AFM images of nuclear fuel pellets

Remaining work

Development of Rare Earth Element separation method: The development of the REE separation method is still ongoing. The goal of the separation method development is to achieve a higher extraction level of REE in the case of uranium ore concentrates and uranium fuel pellets. This means the examination of different sample solution techniques and chemical separation methods for REE. Further investigation is needed regarding the bonding characteristics of the REEs to different resins.

Nuclear Forensic measurements on nuclear fuel pellets by Atomic Force Microscope: The AFM and SEM measurements of the nuclear fuel pellets are considered complete. However, the particle size distribution on the SEM and AFM images still needs to be calculated and compared, looking at differences between the fuel pellets. Furthermore, there is a strong consideration to publish the achieved results.

Related publications

- [1] Cs. Tóbi, Z. Homonnay, K. Süvegh: *A possible novel method in nuclear forensics: positron annihilation spectroscopy*, J. of Radioanalytical and Nuclear Chemistry **332**, 2741–2747 (2023) <https://doi.org/10.1007/s10967-023-08926-0>
- [2] Cs. Tóbi, E. Csipa, N. Q. Khánh, Zs. Kovács, Z. Homonnay: *Applicability of Atomic Force Microscopy in Nuclear Forensic Examination*, 3rd International Conference on Radioanalytical and Nuclear Chemistry, 7-12 May 2023, Budapest Hungary <https://doi.org/10.13140/RG.2.2.32072.39686>

EXPERIMENTAL IMPLEMENTATION OF WIDE-SCALE TUNED PULSED PHOTON RADIATION FIELDS, DEVELOPMENT OF MEASUREMENT TECHNIQUES FROM THE DOSIMETRIC AND SCIENTIFIC POINT OF VIEW, RELATED DETECTOR AND DETECTOR-APPLICATION DEVELOPMENT

Attila Gulyás, Károly Bodor, László Takács, Zoltán Szabó, István Kérészy, Zsolt Csalótzky, János Pető, Tünde Tóth, András Kovács, Péter Völgyesi

Objective

Since 2019, the detector testing laboratory of the Nuclear Security Department (NSD) has been dealing with the dosimetry problem of pulsed radiation fields as a continuous research topic. In 2022, the research and development plan was divided into four parts, each concerning the creation of the wide-scale tuned high-energy photon pulse(s) and its measurement technique.

- The first part includes the extension of the capabilities of the already existing rotating dial gamma-chopper with additional structural machine elements in relation to repetitive pulses, and the production of the single pulse and its experimental conditions with a machine where a lead wall equipped with a collimator moves vertically under controlled conditions (linear-chopper).
- The second part aims to include the pulse time range that cannot be reached by mechanical chopping into our dosimetry capabilities by the Linear Electron Accelerator (LINAC) of the Radiation Chemistry Department and to create experimental conditions, as well as to develop experimental dosimetry to LINAC equipment (what was designed and so far used for the rapid dosage of high doses (kGy)) from the point of view of detector testing (to make it suitable for small doses: mSv, μ Sv).
- The third part of the program is to widen the cooperation with research groups investigating gamma/x-ray pulses occurring in nature, terrestrial and space weather.
- The fourth part of the plan is aimed at starting the own detector and detector-application development with the Microsystems Department of the MFA (Institute of Technical Physics and Materials Science), which can soon meet the expectations of the space-time resolution of pulsed radiation fields and other applications.

The developments carried out led to practical research and measurement methods/procedures in this, not yet standardized field. Thus, there is an opportunity for a professional partnership with the Hungarian Atomic Energy Authority (OAH), Government Office of the Capital City Budapest - Metrological and Technical Supervisory Department (BFKH MMFF), German National Metrology Institute (PTB), ELI ALPS Laser Research Institute (ELI), and detector manufacturers to develop calibration and licensing practices.

Methods

The demonstration experimental machines and elements were created partly by modifying existing structural materials and components, and partly by mechanical engineering design, sizing and manufacturing. In the creation of the machines and LINAC experiments, mechanical testing (for example, disk balance analysis and test) was carried out in addition to radiation protection aspects.

Results

Regarding the first part of the topic, in terms of component development, an equipment, that is capable of storage and positioning an approximately 100 GBq activity Cs-137 source and its cantilever, was created and attached to the gamma-chopper (Figure 1). Also thanks to this development, the previous 1:1000 dose rate jump in the pulse (between the levels of the baseline and the pulse peak/plateau) can be changed to 1:100000. The previously produced collimator tunnels in the disks were manufactured in the line of the diameter of the circular sheet. Thus, the radiation attenuates in the line of diameter and not in the line of thickness of the disk. So one full turn of the disk resulted in two pulses, and for a given disk, the frequency of pulses (connection of pulse period and rotation speed) and pulse time (connection of collimator-tunnel diameter and peripheral speed) were data fixed to each other. Short pulses could only be produced with relatively high frequency. The smallest filling factor (pulse time/period) was 1:33 so far, relatively large with respect to the expected characteristics of pulsed fields. This could only be changed by the relation of the diameters of the disk and the collimator tunnel. In order to somewhat separate the previous constraint of pulse frequency and pulse time and decrease the filling factor, a special demonstration experimental disk was created, which gives a pulse only once per one full turn because the collimator tunnel in disk was manufactured in the line of chord (relatively close to the diameter) of the circular sheet (Figure 1).

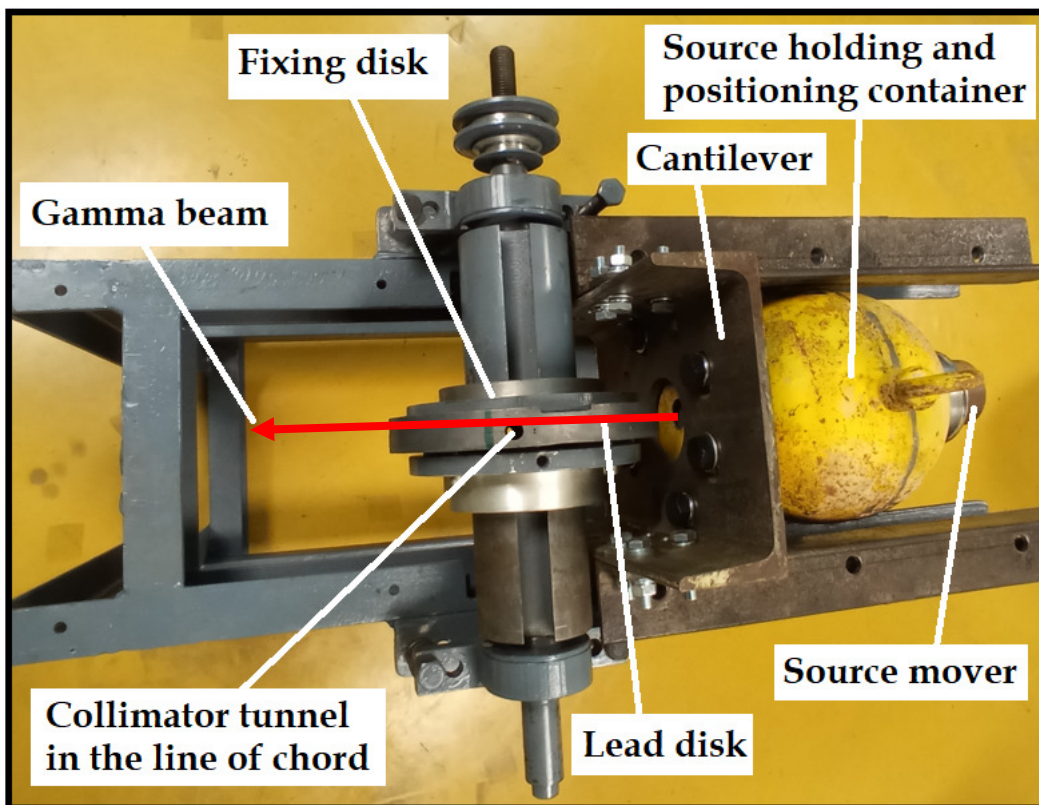


Figure 1: A top view of the gamma-chopper, showing the design of the source holding and positioning equipment, the cantilever and the collimator tunnel in the line of chord in the rotating disk

The upper diagram of Figure 2 shows the continuously repeating pulses with a filling factor of 1:78 (pulse time of 2.2 ms, period of 171 ms). In terms of experimental capability, double field chopping was also demonstrated by generating the so-called pulse train, which contains only a few pulses (1, 3 and 2 needle pulses in the pulse train, Figure 2 - middle diagram). The lowest diagram of Figure 2 shows the relatively good and bad timing of the second chopping: the 2.2 ms needle pulse on the left side is created in a wider base pulse (approx. 150 ms wide thickening of the channel count registration). On the right side, however, no needle pulse can be detected in the basic pulse, i.e. here a bad timing is presented.

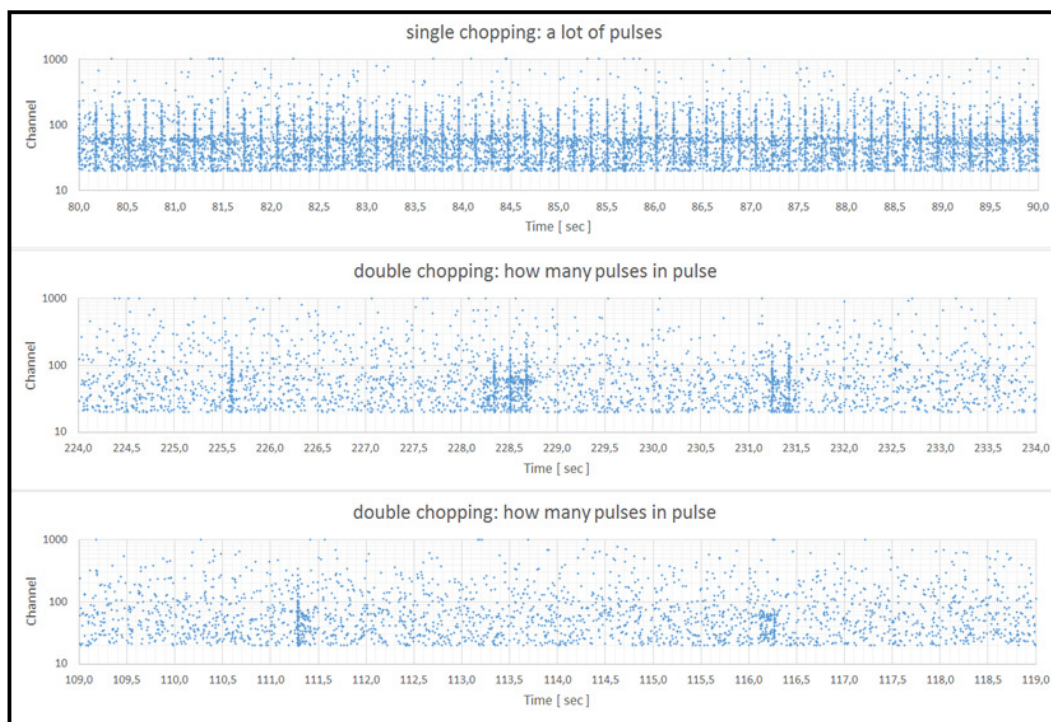


Figure 2: Time diagrams of the channel registration of the scintillation light signals recorded with 100 μ s time resolution by using CsI scintillation "lightning tester" detector at the gamma-chopper demonstration experiments

To create a single pulse formed by the single chopping principle, we created and are continuously developing the linear chopper (so-called gamma-guillotine). In this machine a lead wall is accelerated to a relatively high speed under controlled conditions and then stopped, i.e. the collimator tunnel passes quickly and only once in front of the gamma beam (Figure 3). The formation of a short (a few ms) pulse is created by acceleration (using the force of gravity) and controlled stopping (with kinetic energy absorption system) of the lead wall and collimator. Demonstration experiments (testing with high acceleration, a more mature production lead wall and collimator, chopped radiation detecting with reference and self-developed detector) took place with adequate results.



Figure 3: A side view of the gamma-guillotine, showing the design of the stand, the suspension, the controlled movement of the lead wall with parallel guide rods and winch, as well as the hole of the collimator tunnel

At the same time, the design and production of (high-activity - 2 TBq - source storage) irradiation equipment, source moving mechanics (Figure 4) and the plastic disc for the neutron-chopper were completed.

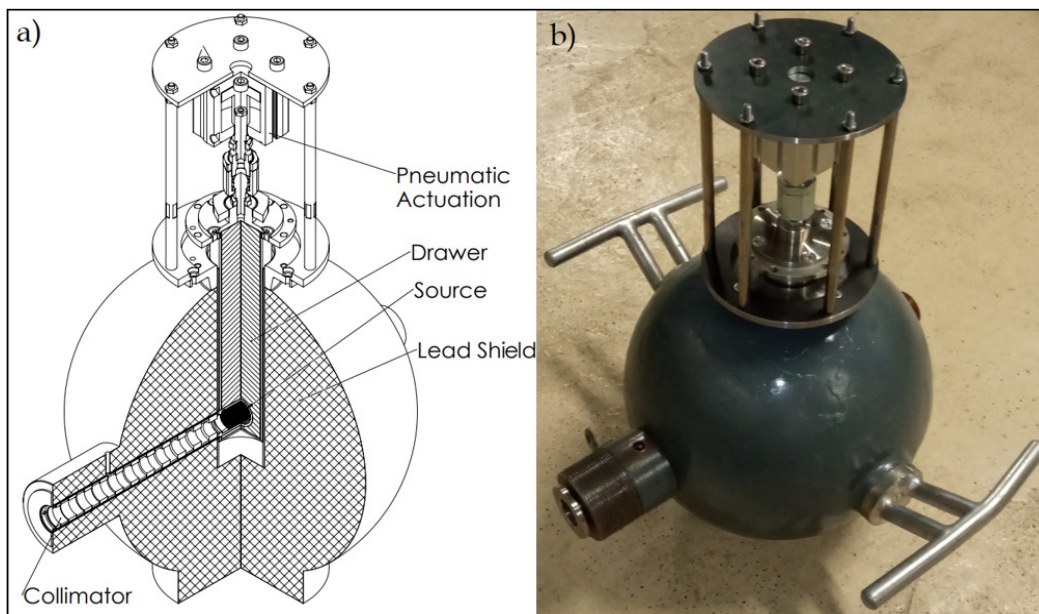


Figure 4: Half-section technical structural drawing of the design a) and implementation picture b) of the irradiation equipment (source is "on" state in figure a)

Regarding the second part of the topic, in terms of creating experimental conditions: in order to weaken the high ionization background radiation generated during operation in the LINAC measurement room (which is the result of the 50 kV pre-acceleration phase of the electrons), an experimental arrangement of a cavity with thick lead walls had to be created. In addition, due to the microwave acceleration of the electrons, the strong microwave background radiation had to be eliminated or significantly weakened. The size and wall thickness of the cavity were sized in several ways (wall thickness: 3, 5 and 10 cm lead, cavity size: 10 cm x 10 cm x 20 cm – 30 cm x 50 cm x 20 cm), depending on placement and movement of the detectors and the level of background radiation. We ensured that the measured signal was output to the operator's room with a suitable detector cable and video image (Figure 5). In the design of the experimental arrangements, the examination of the background radiation level and the formation of the single pulse and its separation from the background noise were the main aspects. According to Figure 5, with the appropriate wall thickness and cavity design, we solved the reduction of the average dose rate of the LINAC background radiation (approx. 10 $\mu\text{Sv/h}$) to about 100 times the level of the natural background radiation (0.13 $\mu\text{Sv/h}$). Just only by changing the average level of the background radiation level, we created a pulsed field of 0.8 and 2.6 μs pulses repeated at the given frequency, whose pulse peak (plateau) dose rate can be controlled in the range (100 - 100000 mSv/h) that can be used to examine adequate measurement capability of the personal and ambient dosimeters.

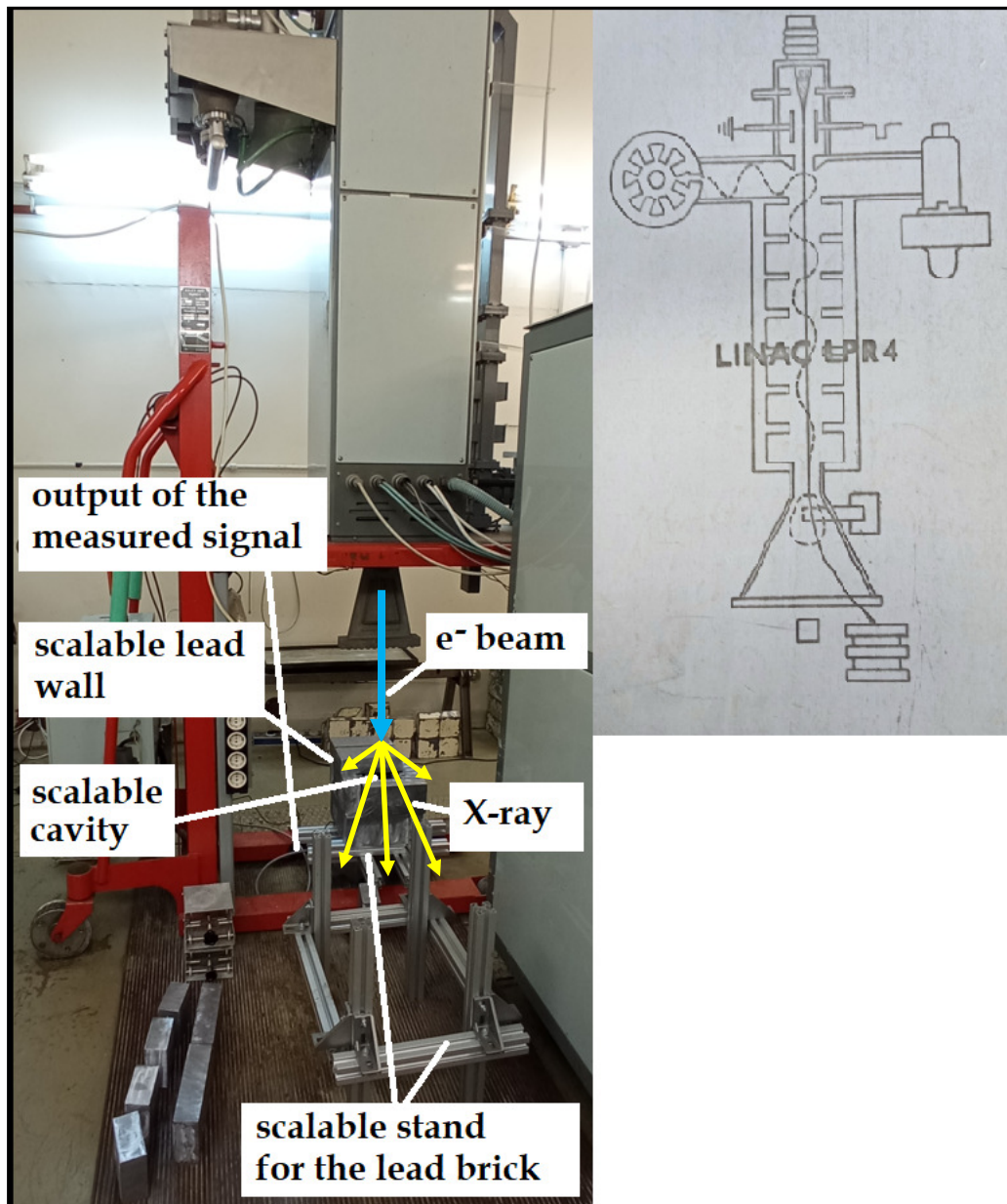


Figure 5: A side view of the LINAC equipment, showing the design of the experimental conditions, the sized cavity and lead wall, output of the measured signal

The single pulse can be created by selecting one of the pre-accelerated phase electron packets at the press of a button and by sending it to the microwave acceleration phase and causing a Bremsstrahlung X-ray pulse on a given target material. This single pulse can stand out from the repetitive background pulses and the average noise level of the background radiation caused by them due to its higher dose and pulse peak dose rate (Figure 6).

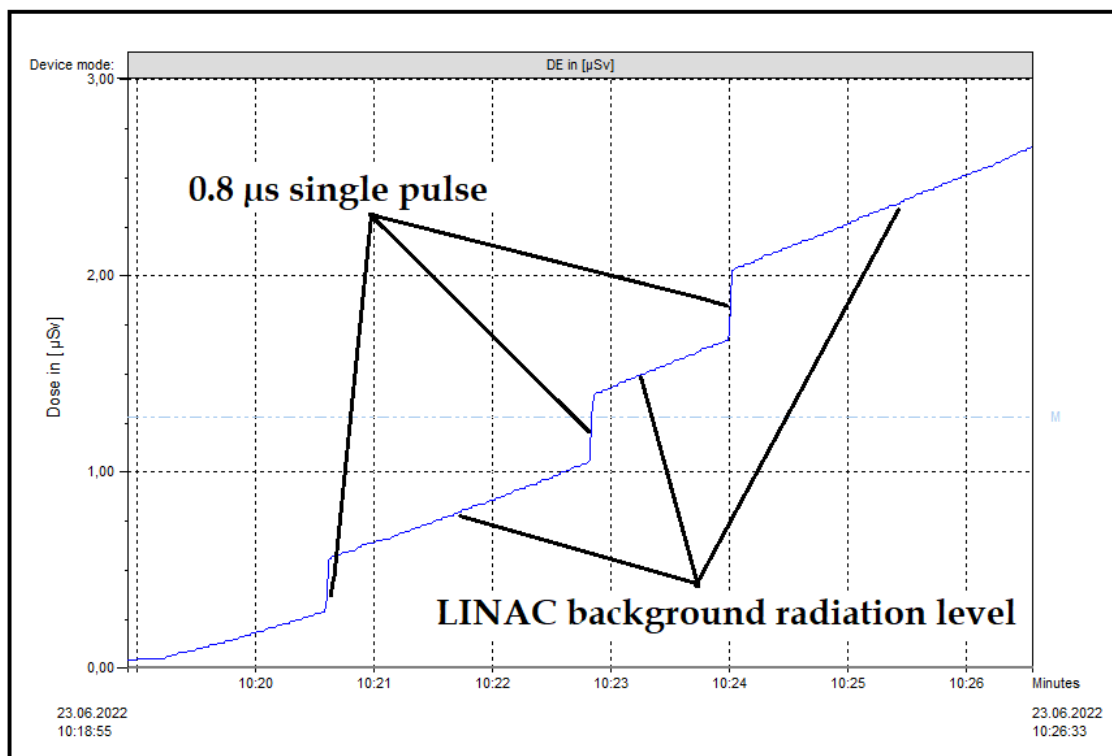


Figure 6: During a LINAC experiment, the dose equivalent accumulation of the STEP OD-02 ionization chamber as a function of time was measured in a lead cavity. The straight line of the constant slope of the background radiation level (constant average dose rate) is broken by the dose step of 0.8 µs single pulse selected by the push of a button.

The dose of the created single pulse (~ 0.3 µSv in Figure 5) and the peak dose rate are several orders of magnitude higher than those of the pulses causing background radiation. This dose of the single pulse is within the principle measurable and displayable range with personal dosimeters, which have the resolution of 0.1 and 1 µSv. At the smallest increase of the cathode current of the LINAC from near zero, the channel registration of the CsI scintillation detector was overloaded at 50 Hz, and only the maximum channel (1024) registration, appearing every 20 ms, was visible. Even at the minimum cathode current, due to the similarity of the pulse time of ~1 µs and the time of 1-10 µs of the scintillation light signal worthwhile spectrometric information cannot be extracted (since it is not known how many photon(counting) impact events produced a given scintillation light signal). That is, even the most reduced background radiation level was too strong for both quantitative and qualitative information. At the same time, the detector gave good information about the time characteristics. From the time dependence of the dose accumulation and the knowledge of the time characteristics of the pulses (pulse time 0.8 µs, pulse frequency 50 Hz), an approximate dose rate-time diagram (Figure 7) can be calculated, which is a basic classification of the pulsed fields. Figure 7 shows a single pulse selected at the press of a button (at the time of 60 ms), which stands out from the pulses of background radiation due to its 4 orders of magnitude higher peak dose rate. The background also consists of 0.8 µs pulses and follows each other with a period of 20 ms and the peak dose rates are six orders of magnitude higher than the average level of natural background radiation (0.13 µSv/h). At the same time, most of the time (between pulses), the background is one order of magnitude smaller than that due to the shielding effect of the lead cavity.

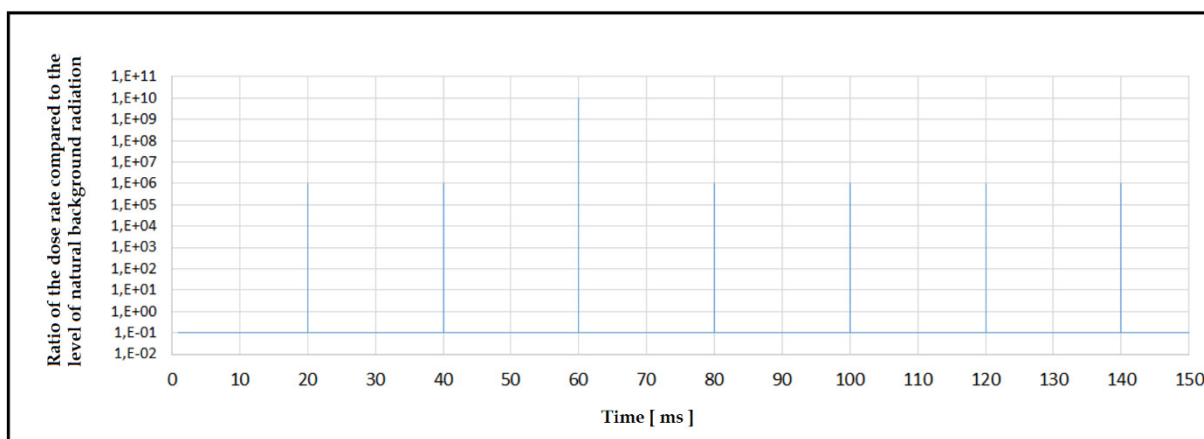


Figure 7: During a dose accumulation experiment, a 150 ms time window containing a single pulse (stands out from the background pulses) is shown and the dose rate as a function of time is calculated in the space of the lead cavity

In terms of the cooperation with the research groups of pulsed fields (third part), the borrowed CsI scintillation detector, developed for examining gamma and X-ray pulses of lightning, was used as a reference detector (radiation characterization in time) in the experiments with LINAC, rotating gamma-chopper and linear-chopper. The implementation of the measurements planned for the aircraft and stormy weather is continuous with the Brazilian Federal Centre for Technological Education of Minas Gerais (CEFET-MG). Description of tasks performed: 1. Fulfilment of comparative calibration measurements between the TERA (Thunderstorm Energetic Radiation Array) detector, which contains a $7.6 \text{ cm} \times 7.6 \text{ cm}$ cylindrical NaI(Tl) scintillator coupled with a photomultiplier tube station and the small self-contained CsI scintillation detector from Kyoto (coupled with photodiode). 2. Installation of both the TERA station and Kyoto CsI detector at the CEFET-MG lightning laboratory to perform simultaneous electromagnetic field, and high-speed video measurements of lightning concurrently with the energetic (X-ray) radiation measurements.

The fourth part of the research topic is the implementation of own detector development and detector application development, where the scintillation signal is measured with a photometer diode (and the amplifier/signal-shaping electronic measuring module produced by Hamamatsu) and not with the commonly used Photomultiplier Tube (PMT). We connected the detector experimental set-up to an oscilloscope and tested it under chopped radiation experimental conditions, and successfully compared it with the so far used reference ($100 \mu\text{s}$ time resolution, CsI lightning tester from Kyoto, Japan) detector (Figure 8). We found that it meets the expectations of the planned space-time resolution. In the applied 1 cm^3 NaI(Ta) crystal, the scintillation light signal takes place in about $0.5 \mu\text{s}$.

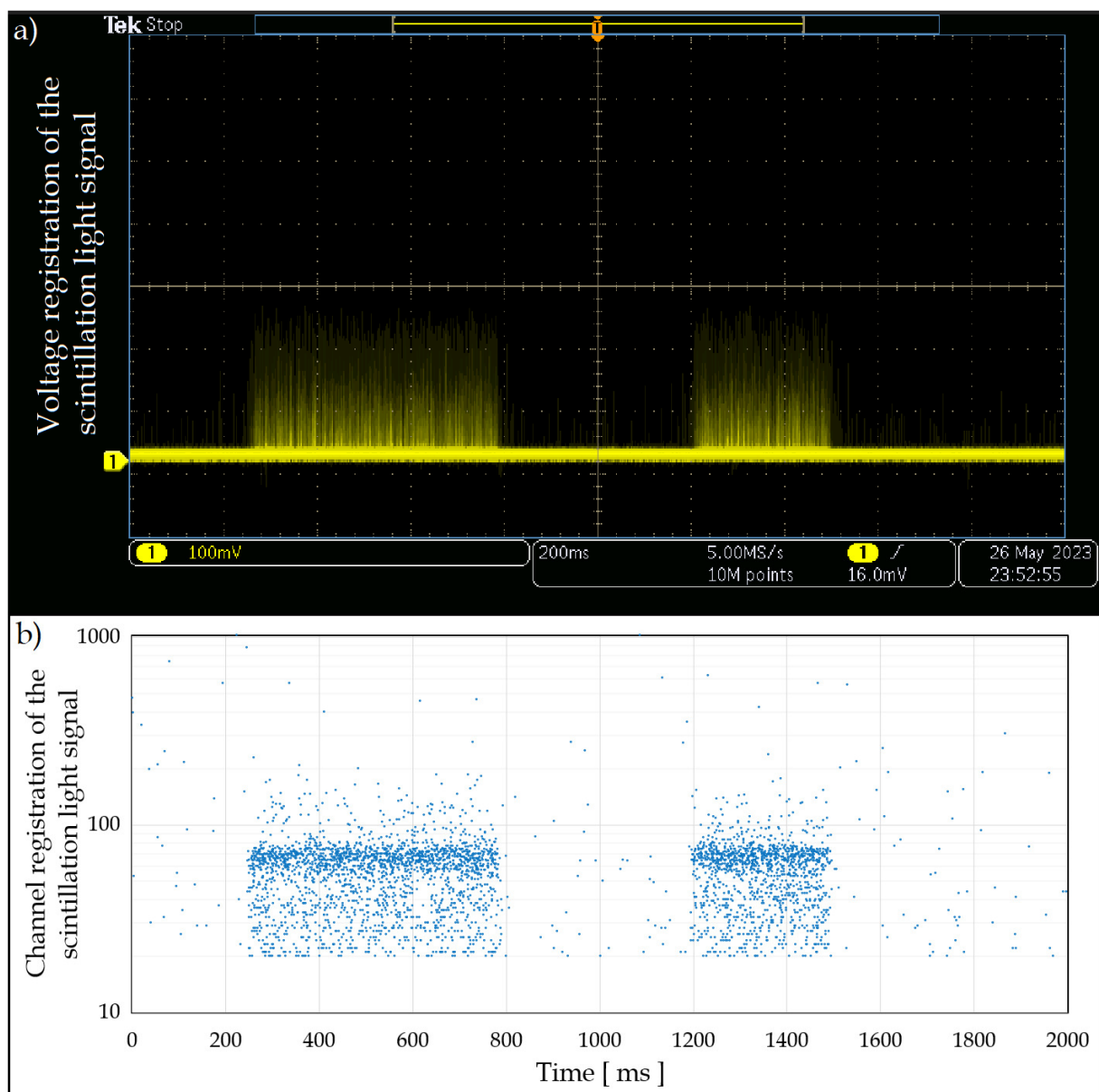


Figure 8: During the comparison of both own detector experimental set-up connected to an oscilloscope and reference detector the same 2 sec time window are shown containing two specially chopped approx. 550 ms and 300 ms radiation pulses (stand out from the "empty zone" background). The same distribution of scintillation light signals as a function of time could be recorded on the oscilloscope screen a) and on the depicted histogram of the CsI reference detector b).

The ThermoFisher TruDose personal dosimeter reader interface developed for the pulsed radiation field and its associated software were purchased, which is an essential requirement for conducting measurements and evaluations with the detector.

Thanks to the improvements, the NSD can contribute to the professional support of official activities of the OAH in the framework of technical foundation activity for the authority control of the safe use of atomic energy (ABA-MMT).

Remaining work

In the experimental conditions of LINAC, a further reduction of the background radiation level, and an increase of the dose represented by the single pulse and the pulse peak dose rate are intended.

Related publications

- [1] K. Bodor, A. Gulyás: *Investigation of the measurement of pulsed fields at the Centre for Energy Research*, 47. Radiation Protection Conference, Szeged 13.09.2022-15.09.2022.
- [2] K. Bodor, A. Gulyás, P. Zagyvai, P. Völgyesi: *Testing measuring devices in well-defined pulsed radiation fields*, RAD Conference Proceedings 7, 40-46 (2023) (11th International Conference on Radiation, Natural Sciences, Medicine, Engineering, Technology and Ecology), ISSN 2466-4626 (online), <https://doi.org/10.21175/RadProc.2023.08>.
<https://www.rad-proceedings.org/proceedings.php?id=7>
- [3] I. Kérészy, V. A. Rakov, A. Gulyás, Z. Ding, T. Enoto, Y. Wada: *A new approach to studying energetic radiation from thunderstorms and lightning*, 36th International Conference on Lightning Protection (ICLP) (2022)
- [4] I. Kereszy, V. A. Rakov, A. Gulyás, Z. Ding, T. Enoto, Y. Wada, L. Araújo, M. Guimarães: *Toward large-scale aircraft-based measurements of energetic radiation from thunderstorms and lightning*, Electric Power Systems Research **233**, 110454 (2024) ISSN 0378-7796, <https://doi.org/10.1016/j.epsr.2024.110454>

REGIONAL TRAINING COURSE ON GAMMA RADIATION PROCESSING DOSIMETRY

András Kovács, András Kelemen, Péter Völgyesi

Objective

Radiation processing is a worldwide applied standardized technology for improving human health and safer food hygiene, production of advanced high-quality materials, preservation and improvement of our environment and protection of archaeological, historical relics and cultural values. Due to its worldwide high importance, the International Atomic Energy Agency (IAEA), through its Regional Technical Cooperation (TC) projects, has continuously been making severe efforts to introduce, develop and/or strengthen these technologies for the improvement of human life conditions. The tool of these efforts is the initiation of regional/interregional cooperation between Member States to facilitate capacity building, knowledge-sharing, partnership building and support for networking. The European IAEA TC projects in radiation processing, ongoing for more than two decades, aim at the safe operation of gamma and electron beam irradiation facilities by applying standardized radiation technologies. This aim can be achieved by the introduction, reliable use and continuous control of national and international (EU, ASTM, ISO, etc.) standards. One of the most important quality control activities includes gamma and electron beam radiation processing dosimetry based on the ISO 11137 international standard. In the frame of the present European Regional TC Project, RER1021 („Enhancing the Use of Radiation Technologies in Industry and Environment”), a „Regional Training Course on Gamma Radiation Processing Dosimetry” was organized and hosted at the Nuclear Security Department of the HUN-REN Centre for Energy Research (15 – 19. May 2023.). The main purpose of the TC was the increased knowledge and experience of irradiation facility staff regarding the regularly used dosimetry systems, as well as the introduction of new dosimetry methods for process control of environmental protection radiation technologies. Although the main topic of the training course was gamma dosimetry, due to the fact, that in four participating laboratories electron irradiation facilities are in operation, a few important aspects of electron beam dosimetry were also discussed and also practised, having in mind, that the other laboratories, using only gamma irradiation facilities at the present also plan the establishment of electron accelerators due to the widening scope of their present irradiation portfolio. In the frame of the training course, 15 scientists – irradiation facility operators and dosimetrists from Azerbaijan, Croatia, Estonia, Kazakhstan, Poland, Portugal, Romania, Russia, Serbia, Turkey and Uzbekistan - participated in the training and gave country presentations about their regular process control activities and related procedures in their relevant irradiation facilities.

Methods

At the beginning of the course, theoretical presentations were given introducing the role, the significance and the main application fields of radiation processing, including the theoretical background of process control activities. Special attention was given to the discussion of the practical use of the most frequently applied liquid and solid dosimetry systems in light of the available international standards, which describe the basic characteristics, advantages, selection criteria, restrictions and application conditions of various reference and routine dosimetry systems. The calibration of the reference and routine dosimeters is of utmost importance, therefore its theoretical and practical introduction and use was one of the most significant tasks and thus in the focus of the course. Besides, similar attention was also paid to the practical training of such basic dosimetry procedures, like the Installation Qualification (IQ), Operational Qualification (OQ) and Performance Qualification (PQ), as described in the relevant ISO 11137 sterilization standard. During the course ethanol-monochlorobenzene (ECB) solution, GEX radiochromic film, Al₂O₃ Thermoluminescent (TL) dosimeters and Polystyrene (PS) calorimeters were applied for the dosimetry procedures mentioned above. The gamma irradiation of the dummy products and the dosimeters was carried out at the ⁶⁰Co gamma irradiation facility of the Institute of Isotopes Co. Ltd., while the electron irradiation investigations were carried out with the LPR-4 linear accelerator of the HUN-REN Centre for Energy Research. The irradiated ECB dosimeters were evaluated by oscillometry, the GEX films by spectrophotometry, and the TL dosimeters with a TL reader and the PS calorimeters by resistance measurements. In order to achieve an efficient practical activity, the participants were divided into three groups, and the exercises were arranged in a “rotating platform” manner. Each team selected a group leader who organized the activities of his group and gave an account of their practical dosimetry activities at the end of the course.

Results

In line with the theoretical and practical background of the course participants, as well as with their expectations in the radiation processing dosimetry field, the following oral presentations were given: “Introduction to Radiation Processing”, “Irradiation Facilities”, “Dosimetry Principles, Procedures and Systems”, “Principles of Thermoluminescence”, “Gamma Radiation Sources for Radiation Processing – Challenges and Solutions”, “Principles of Calibration”, “Influence of Environmental Factors on Dosimetry Systems” and “Role of Dosimetry in IQ, OQ, PQ and Routine Process Control”. Accordingly, the practical exercises involved the calibration of the above dosimeters (except the calorimeters), the transit dose determination at the gamma irradiation facility, the measurement of dose distribution (dose mapping) in various density “dummy” products, and in electron beam processing the measurement of beam homogeneity and nominal dose on the conveyor. At the end of the course, all three working teams gave account on their measurements by evaluating the results achieved, discussed the conclusions and analyzed their potential mistakes. The evaluation of the TC has been completed with a written report of the participants as their feedback on the lessons learnt.

DEVELOPMENT OF A METHOD FOR WOUND MEASUREMENT AND DOSE ASSESSMENT IN THE EK – PART 1

Annamária Pántya, Tamás Pázmándi, Zsófia Rékasi, Péter Zagyzvai

Objective

In the field of wound dosimetry, it is extremely important to develop a suitable measurement protocol and a wound dosimetry model that helps in describing the biokinetics of radioactive material and the effect of radiation on a person. A contaminated wound provides an entry point for the radionuclides into the systemic circulation, which may potentially result in high radiation doses to the whole body or specific organs or tissues. When it comes to wound contamination by ionizing radiation, estimation of the internal radiation exposure caused by the radioactive material that entered the wound is of essential importance. However, our knowledge of the measurement method and protocol is very limited. Our aim was to investigate the options available in the EK for wound dosimetry.

Methods

Initially, we performed a literature review and surveyed the available models, research results, and measurement protocols.

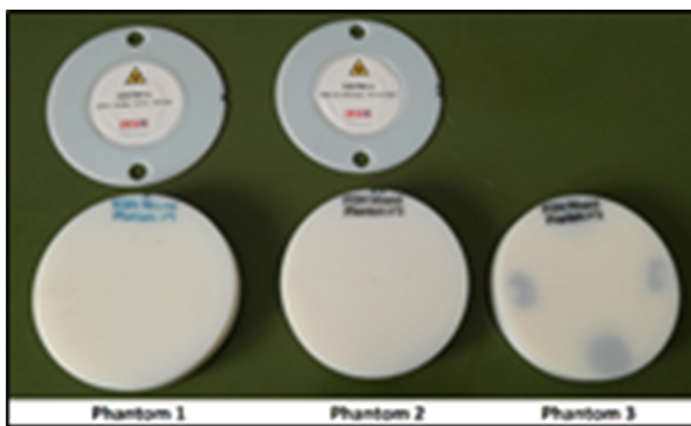


Figure 1: Wound phantom and sources

Subsequently, we assessed the necessary measuring instruments for the measurement process and developed the measurement methodology. Following this, we performed the measurement steps of the intercomparison organized by EURADOS in the field of wound dosimetry. This was the first international intercomparison in this area, and almost 20 countries took part, including EK.

The phantoms were provided by EURADOS, but the measurement protocol was compiled by the participants (the detector type, and the measurement time). The phantoms consisted of plates (made of tissue-equivalent material). The radiation source was placed between the plates. The thickness of the plates was 2 mm and they could be placed on each other. The radioactive source could be placed from 0 to 16 mm depth.

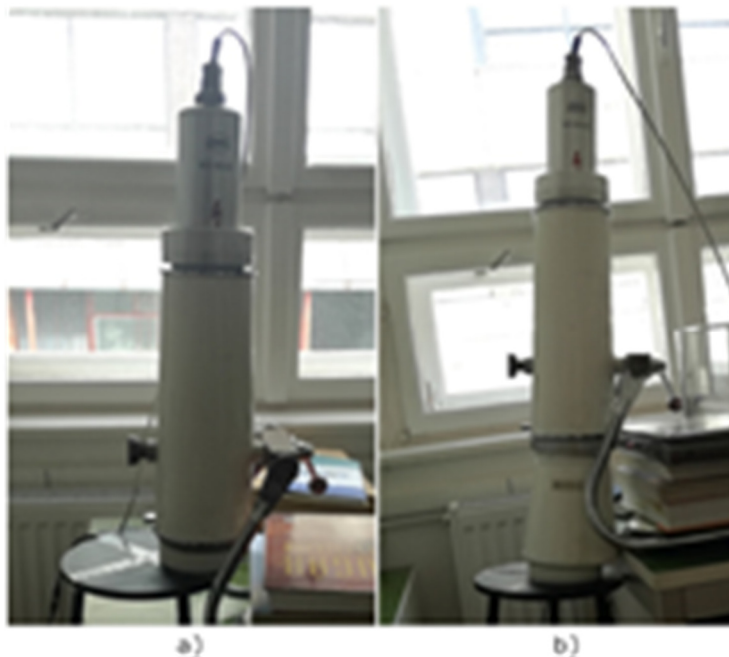


Figure 2: Measurement geometry with the scintillation detector a) without collimator b) with collimator

There were three exercises in the intercomparison. The first one was a calibration exercise, where the composition of the radioactive material and the activity were known. In the second exercise, the composition of the radioactive material and its activity were unknown. The source was placed at the 4 mm and 16 mm positions. In the third exercise, the composition of the radioactive material, the activity and the depth were also unknown.

We used two types of detectors for the measurement. The first one was a NaI(Tl) scintillation detector. The second was an HPGe detector in the whole body counter. For the scintillation detector, the measurement was performed with and without the collimator. The procedure always started with the background measurement. The measurement time with the collimator was 1800 s, but without the collimator, the time was lower in any cases (900 s), and with the HPGe detector it was 600 s. The MultiAct and GSNAL spectrum analyser software, which is well suited to analyzing wound spectra, was used for the evaluation. However, in some cases, manual calculations were necessary.

Results

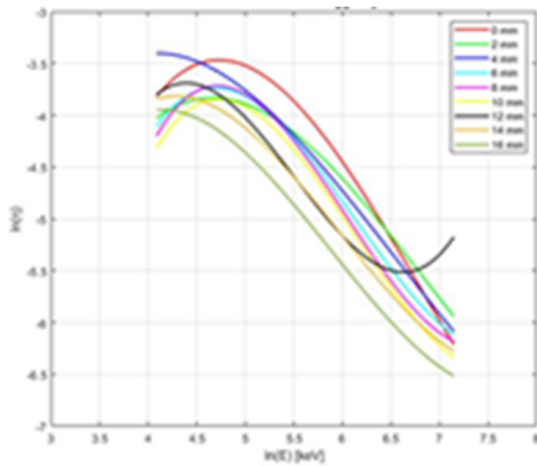


Figure 3: Efficiency calibration curve for each depth with scintillation detector

Our conclusion is that both the NaI(Tl) scintillation detector and the HPGe detector can be used for wound measurement. Both detectors give similar results. However, the resolution and efficiency of the two detector types differ. The scintillation detector has a better efficiency, while the HPGe detector represents the peaks more energy selective. We also found that when we used a collimator, especially at low activity, a significant proportion of the counts were lost due to the increased source-detector distance. However, when there was a high level of activity without a collimator, the dead time increased. This calibration measurement help us to define the activity in the wound and used with the biokinetic and dosimetry model the dose estimation can be performed.

Remaining work

In the second phase of the work, which is planned to last several years, the task is to understand the dose estimation of the substance entering the wound and to define the steps needed for the evaluation. In order to master this method, we will participate in an international comparison.

ASSESSMENT OF THE CHARACTERISTICS OF RADIONUCLIDES AND DETERMINATION OF KEY NUCLIDES FOR RADIATION PROTECTION CALCULATIONS: PART 2

Dorottya Jakab, Annamária Pántya, Tamás Pázmándi, Csilla Rudas, Péter Zagyoai

Objective

The goal of this work is to determine key nuclides contributing significantly to public doses that shall be considered in dose calculations. Based on these results the computational burden of such dose calculations could be reduced. However, for different nuclear facilities, various operation states and release scenarios the key nuclides could be different. These investigations require the work to spread over several years to be able to develop methods for determining the key nuclides for a wide range of circumstances.

Methods

In the second part of the work, the radionuclides that occur/are produced in nuclear facilities such as nuclear power plants or research reactors were characterized based on their physical and chemical properties. These classifications can be combined with the grouping according to radionuclides' contribution to the public dose for a hypothetical Design Basis Accidents (DBA4) release scenario from a nuclear power plant, which was computed in the previous part of the work. Summarizing those results concisely, the nuclides that are responsible for a large part of both the short- and long-term dose are I-131, I-133, I-135, Cs-134, Cs-137, Ce-144, Sr-90, and La-140.

Results

Based on the physical properties, the most commonly used classification of the radionuclides is according to their production method as follows:

- Fission products: Cs, Ba, I, Te, Xe, Mo, Tc, Zr, Nb, Rh, Y, Sr, Pr, Nd, Pm, Sm, Eu
- Neutron activation products
 - in fuel: U, Np, Am, Pu, Bk, Cm
 - in structure: Zn, Co, Fe, Mn, Ni, Cr, Ag, Sb, W, Re, Zr, Mo
 - in primary water: Na, K, H, Ar, F, C.

It should be noted that some nuclides (e.g. nuclides of Mo and Zr) can be in both groups.

A different classification can be made according to the chemical properties of the radionuclides shown below. The representative element for each group is indicated by bold font.

- Noble Gases: He, Ne, Ar, Kr, **Xe**, Rn, H, N
- Alkali Metals: Li, Na, K, Rb, Cs, Fr
- Alkali Earths: Be, Mg, Ca, Sr, **Ba**, Ra,
- Halogens: F, Cl, Br, **I**, At
- Chalcogens: O, S, Se, **Te**, Po
- Platinoids: **Ru**, Rh, Pd, Re, Os, Ir, Pt, Au, Ni
- Early Transition Elements: V, Cr, Fe, Co, Cu, Mn, Nb, **Mo**, Tc, Ta, W
- Tetravalents: Ti, Zr, Hf, **Ce**, Th, Pa, Np, Pu, C
- Trivalents: Al, Sc, Y, **La**, Ac, Pr, Nd, Pm, Sm, Eu, Gd, Tb, Dy, Ho, Er, Tm, Yb, Lu, Am, Cm, Bk, Cf, Es, Fm
- Uranium: **U**
- More volatile main group: **Cd**, Hg, Zn, As, Sb, Pb, Tl, Bi
- Less volatile main group: Ga, Ge, In, **Sn**, Ag
- Boron: **B**, Si, P

This categorization, together with the dose contributions of nuclides as determined in the case studies implemented in the preceding phase of the work, ought to be considered in the classification and identification of key nuclides.

Remaining work

Results for various conditions of nuclear power plants, such as operating states, fuel burn-up, accident conditions as well as source terms for different nuclear facilities (e.g. research reactors) will be investigated and compared. Evaluations of the contribution of different radionuclides to the public dose will be performed in order to identify the key nuclides for different facilities and conditions and to quantify the level of correction that is needed with the omission of a large number of radionuclides. Based on the results, recommendations can be formulated on which nuclides should be included in the assessment and which can be excluded, and a correction factor can be determined to compensate for the nuclides not included.

DEVELOPMENTS IN PERSONAL DOSIMETRY: PART 1

*Dorottya Jakab, Annamária Pántya, Tamás Pázmándi, Zsófia Rékasi,
Csilla Rudas, Márton Zagyvai, Péter Zagyvai*

Objective

The objective is to establish a complex research facility specializing in personal dosimetry. The facility aims to effectively address and solve real-life, practical challenges, investigate events and incidents involving potential exposure risks or actual external or internal exposures, determine the resulting doses or projected doses, and mitigate exposure risks. Additionally, it needs to be designed to allow for fostering international research activities in collaboration with prominent researchers and institutes in the field, occasionally spearheading research initiatives. The resulting infrastructure and expertise will be beneficial and directly applicable to higher education (BSc, MSc and PhD students), as well as providing valuable resources and support for the training and ongoing competence development of professionals in the field.

Methods

- 1) Measurement developments in the field of in-vivo, i.e. whole-body and partial-body measurements: development of numerical and physical phantoms, and methods to take into account the specific characteristics of individuals

In-vivo measurements are used to determine the activity present in certain parts (e.g. organs such as thyroid, lung) or the whole human body and accumulated for a longer period of time. The bodies and their parts may exhibit varying characteristics that should be considered when determining the measurement efficiency for which physical or numerical (virtual) phantoms can be used. In this research, a Monte Carlo transport code was used to create numerical phantoms allowing the consideration of variant geometries of the bodies and the organs and the assessment of the influence of several parameters (e.g. position of the detector relative to the organ, size and shape of the organ) on the measurement results by means of simulations.

- 2) Development of methods for quantifying isotopes relevant to internal exposure but challenging to measure, specifically focusing on the determination of ^{90}Sr from urine samples

Recent developments in the determination of ^{90}Sr from urine samples have been reviewed. The separation methods based on semi-selective precipitation, ion exchange, solvent extraction and extraction chromatography have been thoroughly studied.

- 3) Improvement of measurement techniques for the determination of radioactivity in biological samples

As part of this work, we aimed to develop a unique efficiency calibration method for the Liquid Scintillation Counting (LSC) of ^3H that combines two computational methods, namely the standard addition and the colour quench curve fitting that allows taking the special features of the measured sample into account.

- 4) Evaluation of measurement uncertainty and identification of methods for its mitigation in both active and passive measurement methods used in external personal dosimetry

Measurement uncertainty plays a central role in the quality assessment of measurements by ensuring validity, comparability and metrological traceability of measurement results. In this phase, the applicability of the most commonly used uncertainty evaluation methods (Law of Propagation of Uncertainties - LPU, numerical, Monte Carlo Method - MCM-based approach implementing the propagation of distributions) to external dosimetric measurements has been investigated. Furthermore, the key sources of measurement uncertainty in these measurements have been identified and quantified, which can be focused on to effectively reduce uncertainty.

Results

- 1) We have shown that variations in the thyroid gland's shape had a more pronounced effect on the measurement results when using the physical phantom. The measurement efficiency was more significantly influenced by the thyroid gland's size in the numerical simulations.
- 2) The measurement protocol of the determination of ^{90}Sr from urine samples was developed.
- 3) In the combined calibration method, the efficiencies are calculated by plotting the standard addition against the individual colorimetric values (tSIE) of the samples. We have demonstrated that with the resulting function, the colour quench calibration can be extended to small ranges (10-20 tSIE) compared to the initial full-scale range (250-500 tSIE). Consequently, the detection limit as well as the measurement uncertainty of ^3H determination with LSC can be reduced.
- 4) We have shown that although the LPU-based uncertainty evaluation can reliably be applied to many measurement problems, its adequacy can be compromised if the parameters influencing the measurand and included in the often non-linear or non-linearizable measurement models used in dosimetric measurements have large uncertainties. The LPU-based evaluation is also limited in its ability to consider environmental conditions realistically, which is particularly critical in view of the energy and directional dependence of dose responses, which significantly influences the results and contributes substantially to the uncertainty of dosimetric measurements.

Remaining work

In the next phases of the work, we intend to move forward in the following areas to achieve this goal:

- 1) Development of numerical and physical phantoms, and methods to take into account the specific characteristics of individuals. Optimization of thyroid measurements, further development of measurement methods, development of numerical (and in some specific cases physical) phantoms taking into account individual parameters.
- 2) Development of a method and comparison of the results obtained by the developed method with standard procedures, validation of the methods in a comparative study to identify advantages and disadvantages.
- 3) Enhancement of the gamma spectrometry technique to improve the accuracy and precision in determining radioactivity in biological samples.
- 4) Further investigation of methods for reducing measurement uncertainty in external dosimetry measurement and testing and verification of their practical applicability in real radiation fields.
- 5) Characterization of typical radiation fields to be considered for external occupational exposure and dosimetry, investigation of the influence of real workplace conditions, such as energy distribution and incidence of radiation, on the calibration, measurement and measurement evaluation of external dosimetric measurements.

TRAINING AND TUTORING FOR EXPERTS OF THE NRAs AND THEIR TSOs FOR DEVELOPING OR STRENGTHENING THEIR REGULATORY AND TECHNICAL CAPABILITIES

Dorottya Jakab, Tamás Pázmándi

Objective

The European Union (EU) supports the promotion of the effective nuclear safety and radiation protection culture, the safe management of spent nuclear fuel and radioactive waste, the establishment of efficient safeguards for nuclear materials, and the implementation of the highest related standards in non-EU countries. These objectives are achieved through the external assistance program called European Instrument for International Nuclear Safety Cooperation (INSC). The Training & Tutoring (T&T) Initiative and Program within INSC concerns transferring knowledge, EU expertise and best practices for non-EU countries in need of technical assistance and provides training and education for staff of National Nuclear Regulatory Authorities (NRAs) and Technical Support Organizations (TSOs). Such assistance ultimately supports NRAs in their efforts to become competent, reasonably independent, and self-sufficient concerning their tasks and responsibilities in terms of management and technical means.

This project (MC3.01/20) is the 5th phase of the INSC T&T Initiative, with the main goal of providing training and tutoring (on-the-job training) for the experts of NRAs and TSOs to strengthen their capabilities in the field of nuclear and radiological safety. It aims to assist them in developing and maintaining competencies and skills related to the different areas of regulatory responsibilities and functions, and provide the underlying technical knowledge necessary to comprehend and apply scientific and technological fundamentals and concepts for effective nuclear safety regulation. The aim of the courses is the effective knowledge transfer with reference to EU directives and international safety standards, illustration of the practicalities, such as the application of the state-of-the-art European nuclear safety regulatory approach, with particular attention to the local needs and specificities of the beneficiary countries concerned. This project supports not only the promotion of nuclear safety culture but also the enhancement of global cooperation on nuclear safety regulation.

Methods

The MC3.01/20 project started in January 2022, and is being carried out by a six-member international consortium led by the HUN-REN Centre for Energy Research. The project implementation is based on the activities of 5 tasks (i.e. working groups): alongside Task 0, which provides general operational assistance in project management and implementation, 4 tasks focus on specific areas related to the project objectives. Task 1 identifies and assesses the necessary competencies and needs of beneficiary NRAs/TSOs and converts them into T&T objectives and activities that are integrated into a T&T Program. This program consists of a 1-week training held in the EU and 6 specific regions around the world, as well as 1-month tutoring courses held in EU NRAs/TSOs that are all developed by eminent international experts in their respective fields. Task 2 adapts the prepared T&T Program to the actual implementation and coordinates the delivery of the T&T courses. Task 3 provides quality control to ensure the continuous improvement of the course content and delivery methods throughout the implementation of the T&T Program as part of which both the participants' development and their satisfaction are assessed. Task 4 created and operates a T&T Alumni Network in order to foster networking and building long-term partnerships.

Results

The first year of the project focused on the development, testing and validation, and subsequent improvement of the methodologies, approaches and tools to be used for the a) overall project management and work organization, provision of specific support functions such as financial, IT and travel management, b) implementation of the T&T Program, including the organization process of the T&T courses, from the public announcement and application process to the multi-criteria based selection of participants, travel and on-site arrangements, and course delivery; c) evaluation of participant's gained knowledge and satisfaction.

A T&T Topic List was assembled, comprising 20 topics related to nuclear safety, radiation protection and emergency preparedness and response. A T&T Plan with 37 training courses and 23 tutoring courses was developed to be implemented. The courses were complemented with 3 Massive Open Online Courses (MOOCs) to provide the fundamentals and underlying technical knowledge supporting comprehension of the regular courses.

By the end of 2023, 17 training courses and 7 tutoring courses were completed. The training courses were held in 5 regions additional to the EU, spanning across 10 countries, whereas 5 NRAs and TSOs hosted tutoring courses. In total, 284 participants from 43 countries and 69 NRAs/TSOs attended the courses and benefitted from the project. The courses achieved an average participant satisfaction index of 4.64 out of 5.00, reaching 4.25 without exception.

Remaining work

The project is contracted to end in July 2024, by which time all the remaining T&T courses will be held.

This report was produced with the financial support of the European Union. Its contents are the sole responsibility of the authors, the opinions expressed herein do not necessarily reflect the views of the European Union and Commission.

DEVELOPING DOSE MAP CALCULATION METHODS FOR OFF-NORMAL NPP OPERATIONS

Dorottya Jakab, Annamária Pántya, Tamás Pázmándi, Csilla Rudas

Objective

Since the latest comprehensive assessment of the radiation conditions inside the buildings of Paks Nuclear Power Plant (NPP) in 2006, there have been several technological developments and changes (e.g., the introduction of a new fuel type, the extension of fuel cycle from 12 to 15 months) affecting the dose rates in certain locations within the facility, such as in the controlled areas. In recent years, studies have expanded the range of isotopes to be considered in determining the total activity of primary cooling water, with their nuclide-specific activity concentrations also being recalculated. In addition to accounting for changes in the initial source term and input parameter values affected by the technical alterations, it also became timely to review the range of potential off-normal events included in the assessments and to improve the dose calculations for off-normal operation. These conditions necessitated the systematic repetition of the entire series of calculations of the doses from the activities in certain areas within the facility and released into the environment due to the off-normal operations at Paks NPP. This is the primary aim of the project.

Methods

The tasks necessary for the calculation of the off-normal dose map will be carried out in three phases during the two-year duration of the project. The first step involves defining the off-normal operation scenarios to be investigated in the assessments and determining the corresponding source terms. Additionally, the equipment and premises, and areas relevant in terms of activity accumulation and consequent dose rate elevation will be identified for assessment in the defined off-normal events. The second step is to develop the models for dose map assessments and to revise the input data required for these calculations to accurately reflect the conditions expected in the off-normal operation scenarios. The final, third step will be the implementation of the dose map calculations.

Results

In 2023, the previous off-normal dose map assessments and the analyses related to the technical alterations implemented at the NPP in recent years were reviewed, and the main conclusions and lessons learned were summarized. The off-normal operation scenarios to be investigated in the assessments, along with the corresponding source terms, have been determined. Additionally, the equipment and areas relevant in terms of activity accumulation and consequent dose rate elevation to be assessed in these off-normal events have been identified.

It was concluded that there is no reason to consider different off-normal operation scenarios from those stipulated in Paks NPP's current version of the Final Safety Analysis Report. On the other hand, the source terms to be used in the off-normal dose map calculations changed significantly due to the technical alterations, such as the introduction of a new fuel type and the extension of fuel cycle. Consequently, we intend to consider the most recently defined zone inventory and primary cooling water activity concentrations, as well as more recent thermohydraulic reports containing the results of analyses of these conditions, to investigate the off-normal cases.

For the off-normal dose calculations, all premises where radionuclide concentrations in the air may significantly increase as a consequence of an off-normal operation scenario need to be considered. In addition to areas within the hermetic compartments, areas into which radioactive material can be discharged directly or indirectly (by leakage) due to the overpressure in the hermetic compartments are such premises.

Remaining work

In the next phase of the work, the models for dose map assessments will be developed and the input data required for the dose map calculations will be revised so that they reflect the conditions expected in the off-normal operation scenarios as accurately as possible. Accordingly, the dose map calculations will be implemented.

Related publication

- [1] D. Jakab, A. Pántya, T. Pázmándi, Cs. Rudas: *Developing dose map calculation methods for off-normal NPP operations – Part 1*, EK-SVL-2023-722-00-01-00, in Hungarian (2023)

DEVELOPMENT OF SPACE RESEARCH INSTRUMENTS

*János Nagy, László Hevesi, Richárd Kiefer-Szabó, Zoltán Pálos, Gábor Tróznai,
Pál Vizi, Bálint Sódor, Sándor Szalai, Lajos Dinnyés*

Our team participates in ongoing space projects, and is working on new developments in parallel. Ongoing space projects include BepiColombo and Jupiter Icy Moons Explorer (JUICE) projects of the European Space Agency (ESA). For both projects, we have developed space-qualified power supply units and Electrical Ground Support Equipment (EGSE). BepiColombo was launched in October 2018, and JUICE started its eight-year journey to Jupiter on 14 April 2023. Our institute had a Post-delivery support contract for JUICE with the ESA. (PEA: 4000137950 was the contract number in 2023.)

New instruments for space research include the magnetometer and the electron spectrometer from the Hunor project (Hungarian astronaut program). In 2023, we completed the breadboard model of the magnetometer and the block scheme of the electron spectrometer. The magnetometer is a relevant instrument, as the magnetic field vector, as a function of time, is one of the most important parameters to be measured in the space plasma, which is why magnetometers have been installed on board scientific satellites since the very beginning of space research. The Earth's magnetosphere was discovered only by Explorer 1 in 1958.

Electron spectrometer measures the interaction between charged particles arriving on Earth and the Earth's magnetosphere. The sources of charged particles are the solar wind and the cosmic ray. The solar wind contains electrons and ions, mainly H⁺ protons and He²⁺ helium ions, but also a small number of heavier ions. The solar wind contains an equal number of electrons and ionized charges, and is therefore neutral overall. Cosmic rays have significantly less charged particles contents compared to particles from the Sun. The ions in the solar wind come from one direction and can be detected by detectors pointing towards the Sun, while cosmic rays can come from several directions.

Methods

JUICE:



Figure 1: Launch of the JUICE mission onboard the 750-tonne Ariane 5 rocket from the ESA base in Kourou, French Guiana, on 14 April 2023. (ESA Photo)

Spaceprobe will investigate the Jupiter system as an archetype of gas giants, and investigates habitability around gas giants. JUICE was launched on 14 April 2023. It will arrive at Jupiter in 2030, and will spend at least three years making detailed observations of the giant gaseous planet Jupiter and three of its largest moons, Ganymede, Callisto and Europa. It delivers 11 scientific instruments to Jupiter, one of which is the Particle Environment Package (PEP), developed in a broad international cooperation of Swedish, German, Swiss, American, Japanese and Hungarian institutes. Our task was to deliver a power supply unit for the PEP, it is the Direct Current Converter (DCC) that converts the onboard 28 V to voltage ranges required by each instrument with high efficiency. The PEP-Instrument consists of two units PEP-Lo and PEP-Hi with a total of six different sensors. Our DCC ensures the galvanically separated voltages for the four detectors (JEL, NIM, JNA, and JDC) of PEP-Lo unit. PEP will tackle the following research topics: Study and influence of internal and external plasma sources in the Jupiter system; Study of acceleration mechanisms; Characterization of the „magnetodisc“, which interaction processes exist between the rotating Jovian magnetosphere and the complex Ganymede system; Characterization of the moon Callisto as a relict of the evolution history of the Jupiter system; Study of active regions on Europa and Io; Remote sensing of neutral gas tori; Remote sensing of the irregular satellites and the ring system.

Our team supports the processing of the test, calibration and scientific data during the cruise phase. We are developing software that converts PEP telemetry data packets into a readable physical data format, and evaluate service data House Keeping (HK) on the mode and status of the instruments required for DCC operation. These are regularly reported to PEP system developers. A modest amount of data is expected to be received for the evaluation of scientific data. There will be some more data

at the first checkout when the solar wind is observable. Scientific data will be forwarded to physicist colleagues working on the exploration of the Solar System. Our task is to monitor DCC operation with DCC service data, and archive scientific and service data.

Magnetometer development:

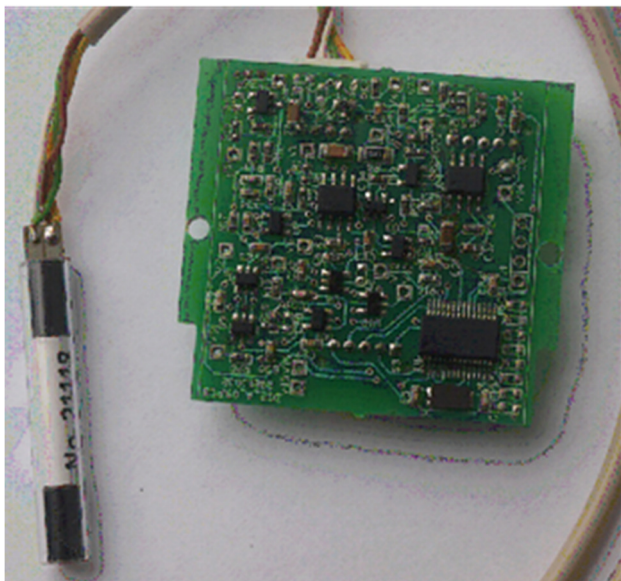


Figure 2: The sensor is the pipe on the left and the signal processing part is the PCB card on the right

The main task of the planned work is to upgrade existing magnetometers for space applications, previously developed exclusively for terrestrial use. The flux-set magnetometer was developed for industrial applications by a company several years ago, now known as Humicin 2000 Ltd., a spin-off from the Central Research Institute for Physics (KFKI). Their magnetometers have successfully been used in Hungary and in other European countries. The core material and the sensors are manufactured by this company. It has the advantage of ultralow weight (a few tens of grams, compared to fluxgate instruments, which usually weigh about 1 kg) and the low power consumption. Flux-set magnetometers are modified versions of fluxgate magnetometers with differences in the core material and signal processing. The main advantage of the flux-set is its very low mass and power consumption of the sensor and electronics.

Electron spectrometer development:

The particles are received through the electron optics. It is divided into 16-32 segments which are controlled by the voltage applied on them. The energy range from which the particles are received is determined by the voltage applied. The electron optics can be designed using dedicated simulation software developed for this purpose, and for test measurements in electron and ion chambers. Particles arriving at the input are fed to a Multi-Channel Plate (MCP) detector with a resistive anode, where the impact location can be calculated from the voltages at the 4 anode corners. The impact location on the MCP determines the segment from where particles came. The Field Programmable Gate Array (FPGA) determines the location of the impact. The processor calculates the distribution and transmits the measurement results. If the number of particles increases, the device and the data transmission switch to a faster mode. The instrument can collect electrons, and if the voltage polarization on the electron optics is reversed, it collects ions.

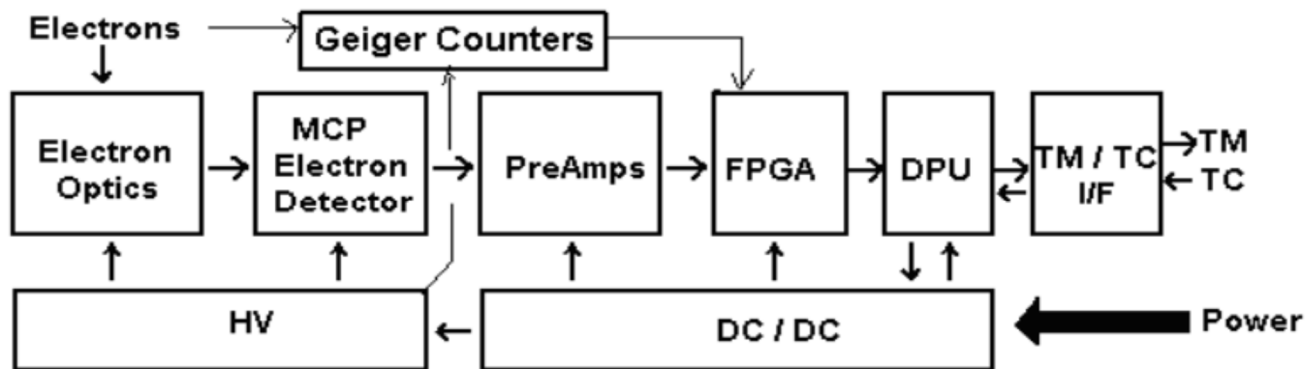


Figure 3: Block scheme of the electron spectrometer

The instrument was only envisioned at the block diagram level, as the cost of the detectors and the front-end electronics was to be approximately a few ten thousand euros, and the design and calibration of the electron optics require significant development capacity.

Results

JUICE:

Since the launch of the Ariane-5, the PEP sensors have been switched as scheduled. The DCC we developed has been working well over the past year. Its temperatures have been in line with the values calculated in simulations, and the DCC efficiency has been between 70% and 80%, depending on the load current.

Magnetometer development:

Calibration and test software is available. The sensors are calibrated and adjusted individually. The attached figure shows the magnetic background value.

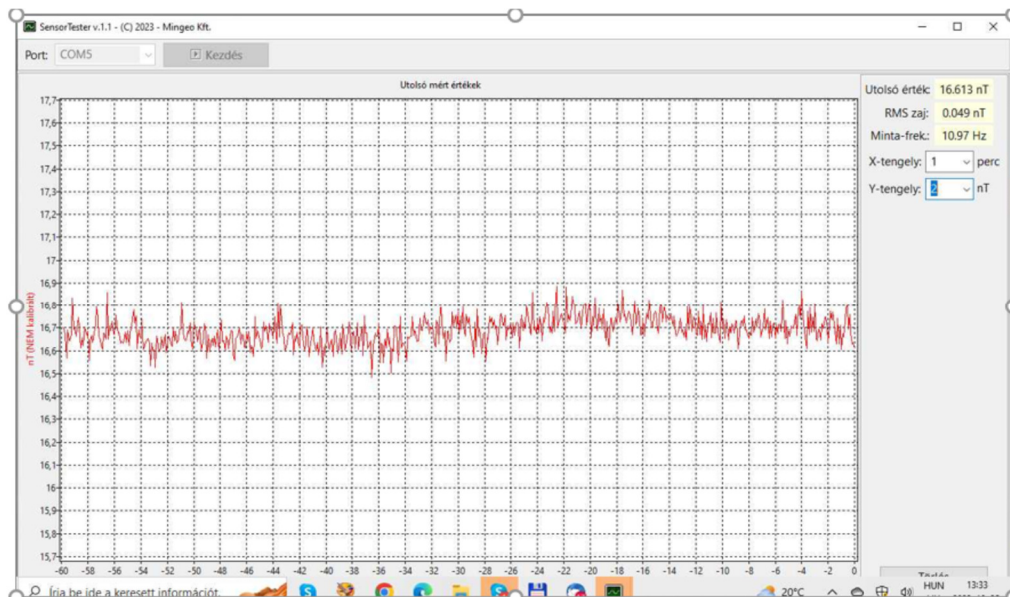


Figure 4: Test of a magnetometer sensor

Electron spectrometer:

We have studied the main design principle of such a particle physics instrument.

Remaining work

JUICE:

Data tracking and installation of a Linux server with available archived HK and scientific data.

Magnetometer:

The model was built from industrial parts; we have also defined the component base for the space-qualified version, but this will require tens of thousands of euros. The space-qualified version has to be built on a space-qualified component base and meet the requirements of the space agency and pass the required tests.

Electron spectrometer:

Further development work will be needed in the mechanical design of the electron optics and support from physicist colleagues.

Related publications

- [1] J. Nagy, L. Szalai at al: *Hungarian Participation in JUICE Project of European Space Agency*, Acta Polytechnica Hungarica **19(9)**, (2022); <https://doi.org/10.12700/APH.19.9.2022.9.2>
- [2] Nagy J., Kerényi M., Frey S.: *Juice a Jupiterhez, Űrszonda magyar közreműködéssel*, Természet Világa **153**, 367-373 (2022)
- [3] Szalai S., Nagy J.: *Fejlesztések naprendszer-kutatási missziókban*, Fizikai Szemle **7-8**, 267-274 (2023)
- [4] Ferencz O., Horváth Á., Szalai S. et. al.: *ELKH Energiatudományi Kutatóközpont: Magyar részvétel az Európai Űrügynökség JUICE küldetésében 2023.04.05.* https://www.galileowebcast.hu/live/live_20230405.html
- [5] Nagy J., Hevesi L., Vizi P. G., Szalai L., Horváth I., Szalai S.: *Magyar részvétel az ESA JUICE projektjében, tápegység fejlesztése a Jupiter jeges holdjai kutatásában*; In: Bacsárdi L., Hirn A. (szerk.) *Magyar Űrkutatási Fórum 2023 - Válogatott közlemények*; Budapest: Magyar Asztronautikai Társaság (2023) 77 p. Paper: MÚF2023-K-06 , 6 p.
- [6] Nagy J. et. al: *Magyar részvétel az Európai Űrügynökség JUICE (Jupiter Icy Moons Explorer), a Jupiter jeges holdjait felfedező küldetésben*, Magyar Űrkutatási Fórum 2023, Poszter
- [7] MANT Űrtábor: Vizi P. G. (ELKH-EK MTSzSz Űrtechnológiai csoport): *Magyar részvétel az ESA JUICE missziójában*, 2023.07.05 10:00 Érdi SZC Kossuth Zsuzsanna Szakképző Iskola és Kollégium 2371 Dabas
- [8] Vizi et al.: 2023/2024 Hazai űrkörkép p. 46-47 printed & <https://www.mant.hu/kiadvanyok/Urkorkep2023.pdf>
- [9] Vizi et al.: 2023/2024 Hungarian Space Kaleidoscope p. 46-47 printed & <https://www.mant.hu/kiadvanyok/HungarianSpaceKaleidoscope2023.pdf>
- [10] H-SPACE 2024, accepted for oral presentation and full paper proceedings ID: 28 Vizi, Nagy et. al.: Hungarian participation in the European Space Agency's JUICE (Jupiter Icy Moons Explorer) mission

RADIATION MONITORING WITH THE RADMAG (RM-S) SPACE WEATHER INSTRUMENT

Balázs Zábori, Attila Hirn, Patrik Pinczés

Objective

Both space-based and ground-based infrastructures and technologies, such as satellite constellations (e.g. telecommunication and navigation systems), power grids and pipelines might be seriously affected by changes in space weather, especially during coronal mass ejections and geomagnetic storms. Earth's cosmic environment is highly influenced by several physical parameters (magnetic field variability, cosmic ray intensity, solar activity, atmosphere, etc.) and, mainly due to the complexity of the magnetosphere, a very good spatial and time resolution is required in space weather monitoring. To achieve this goal, EK initiated the development of a space weather instrument suite, called RadMag. The major goal of the development is to combine tools for radiation and magnetic field measurements into a single payload, which can be utilized aboard different satellite platforms and in different types of orbits. A compact version of RadMag (RM-S) is flying on board the Hungarian RADCUBE CubeSat. For this version, the magnetometer was provided by Imperial College London, and the boom mechanism by Polish company Astronika. The CubeSat platform was provided by the Hungarian company C3S Ltd.

Methods

Ground visualization and on-ground post-processing of data are performed by the RADCUBE/RadMag Science Operation Centre (SOC). LEVEL-0 data (RadMag binaries in .bin and platform auxiliary data in .csv format) were shared with the RadMag consortium by the satellite operator via a dedicated FTP server. LEVEL-0 data in the EK database system were continuously synchronized with the data available on the FTP server. The EK database system used EK's Seafile file server between the 29th of October 2021 and the 4th of January 2022, and EK's NextCloud file server between the 5th of January and the 2nd of May 2022, when nominal operations were finished.

SOC provides auto-interpretation of LEVEL-0 data to provide LEVEL-1A pre-processed data. LEVEL-1A data are distributed to Imperial College London (ICL) (Magnetometer, MAG experiment) and ESA Directorate of Technology, Engineering and Quality (ESA-TEC) (Radiation Hardness Assurance (RHA) experiment). ESA-TEC is also provided with LEVEL-0 data, and ICL with LEVEL-1A HK data according to their requests. RHA and MAG LEVEL-2 data provision is done offline by ESA-TEC and ICL, respectively. RAD LEVEL-2 Data Provision, for the moment, is done manually.

Results

The measured count rates and the calculated absorbed dose rates were plotted on world maps and as function of time. An example of the dose rate maps is shown in Fig. 1. One can see the elevated dose levels in the South Atlantic Anomaly from trapped protons and in the polar regions from precipitating electrons.

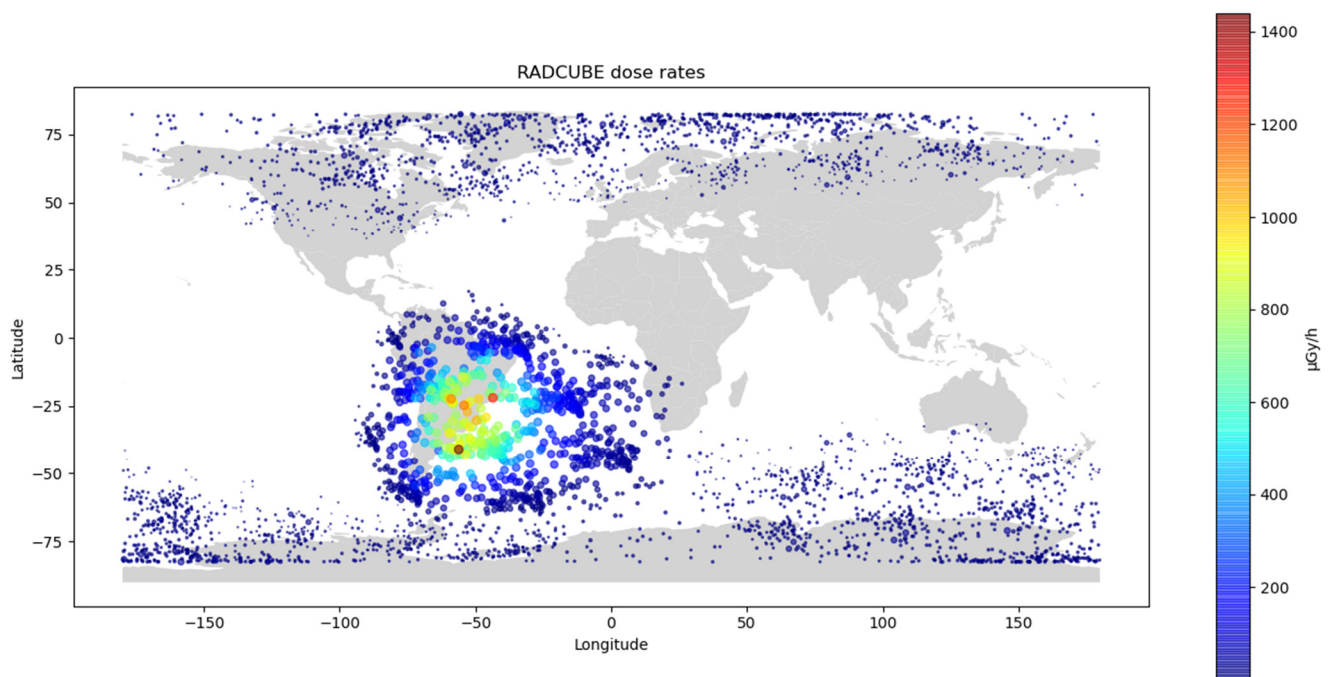


Figure 1: Absorbed dose rates in silicon measured with RadMag on RADCUBE behind approximately 3 mm of aluminium equivalent shielding at 550 km above sea level between the 29th of October 2021 and the 2nd of May 2022

Two solar particle events, one on the 28th of March, and the other on the 2nd of April 2022, were also detected by the RadMag radiation monitor. The corresponding time plot is shown in Fig. 2. One can see the elevated dose rates at higher geomagnetic latitudes. It can also be seen that dose rates did not increase in the South Atlantic Anomaly and at low geomagnetic altitudes during these events.

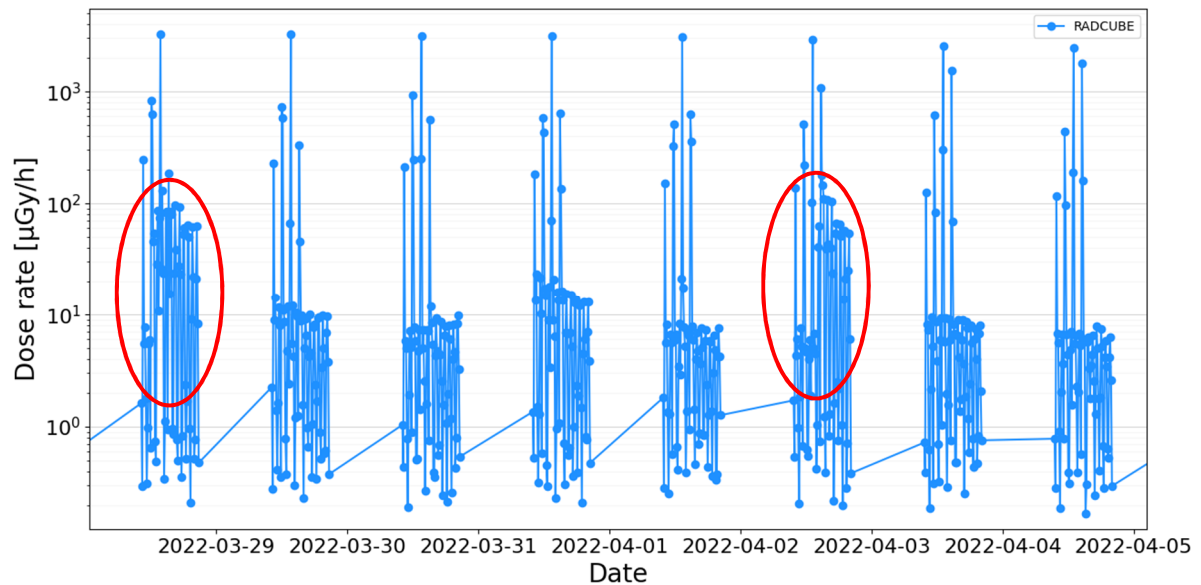


Figure 2: Absorbed dose rates in silicon measured with RadMag on RADCUBE behind approximately 3 mm of aluminium equivalent shielding at 550 km above sea level between the 28th of March and the 5th of April 2022. One can see the elevated dose levels in the South Atlantic Anomaly from trapped protons (peaks), and the effect of two solar particle events on the 28th of March and the 2nd of April 2022 (indicated with red ellipses).

Remaining work

Data provision to the scientific community is planned through ESA's Open Data Interface (ODI). EK will share LEVEL-0, LEVEL-1A and LEVEL-2 RAD data in .csv format. Coordinate transformation will be realized either at SOC or at ODI. Seven days of additional operation of the RadMag radiation monitor is planned in 2024.

Acknowledgement

The work was performed in the frame of the ESA Arrangement No. 4000120860/17/NL/GLC.

DETAILED DESIGN OF THE INTERNAL DOSIMETRY ARRAY FOR GATEWAY, THE SPACE STATION OF THE ARTEMIS PROGRAM

Balázs Zábóri, Attila Hirn

Objective

The Internal Dosimeter Array (IDA) will be the very first European-led internal payload to be hosted within the US Habitation and Logistics (HALO) module for Lunar Gateway. IDA will monitor the internal space dosimetry environment in lunar orbit with the combination of existing and proven instrument technologies in an international collaboration. Dosimetry measurements for exploration mission are of utmost importance as the astronauts will not be protected by the Earth's magnetic field or the atmosphere; hence, they could be exposed to up to 700 times the radiation dose of an average human on Earth from space radiation. The IDA consortium is led by the Centre for Energy Research (EK). In 2023, the main objectives of the IDA project were to release the final design of the IDA payload, verify the design and technical solutions against project and system requirements, confirm compatibility with external interfaces, and do the verification planning and the assembly, integration, and test planning.

Methods

The project is executed following a phased approach defined by the European Cooperation for Space Standardization (ECSS) standards. In year 2023, the project was in phase C (detailed definition). A technical data package comprising management and product assurance documents, requirement documents and databases, detailed design documents, Computer Aided Design (CAD), Final Element- (FEM), and Thermal Mathematical Models (TMM), analysis reports and engineering/verification plans were prepared for Customer's approval for the Critical Design Review.

The instruments integrated in the IDA payload are the European Active Dosimeter (EAD) mobile unit from the German Aerospace Centre (DLR), MediPix from the Czech company ADVACAM s.r.o., the three-dimensional silicon detector telescope TRITEL from EK (subcontractor REMRED Ltd.), and a combined dosimeter package, comprising a Passive Dosimeter for Life science Experiments in Space (PADLES) and an active Dosimeter (D-SPACE) (PDS) from the Japanese Exploration Space Agency (JAXA). The common Electronics Box (E-Box) interfacing with the Gateway subsystems is developed by REMRED Ltd. Structural and thermal design is elaborated by Airbus Defence and Space.

Results

The design of the instrument suite was finalized; engineering models of the instruments and the common electronics box were built (Fig. 1). Planning for assembly, integration verification and testing was accomplished. The first version of the User Manual was issued. The quality of the data package provided by the IDA consortium was found to be very good by ESA. The review objectives have been achieved.



Figure 1: IDA Payload internal structure after front panel opening. The trays from left to right are: TRITEL, Avionics modules (Payload Power Converter Module, Payload Digital Processing Module, Payload Memory Module), PDS, MediPix, and EAD

Remaining work

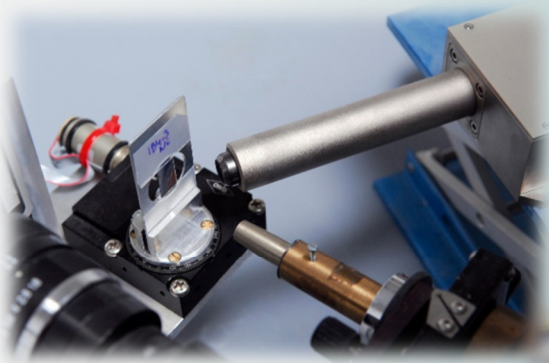
Critical Design Review (CDR) will be completed with the condition of the successful Materials and Processes Control Board (MPCB) and Phase II NASA Safety Review to be conducted in 2024. EM manufacturing, integration and testing will also be performed in 2024. After that, manufacturing and testing of the Proto-Flight Model (PFM) will follow with delivery to NASA in 2025.

Acknowledgment

The implementation of the IDA payload is conducted in the frame of the ESA Contract No. 4000136731/21/NL/AT.



IV. ENERGY SECURITY AND ENVIRONMENTAL STUDIES



NEW (PHOTO)ELECTROCATALYTIC SYSTEMS FOR WATER SPLITTING

Tímea Benkó, Irfan Khan, Dávid Lukács, Sahir M. Al-Zuraiji, Krisztina Frey, Zsolt Kerner, Miklós Németh, Soma Keszei, Antal Koós, Levente Tapasztó, Tamás Ollár, József S. Pap

Objectives

Simple and scalable immobilization of co-catalysts on (photo)electrodes is a viable option to efficiently promote water splitting and thus advance green hydrogen production. Successful combination of co-catalysts with (photo)electrodes can lower the kinetic overpotential need, increase the selectivity and accelerate the overall reaction at a lower energy cost. Currently, only noble metals – Pt at the cathode and IrOx/RuOx at the anode – can meet the practical requirements of over 35,000 h lifetime, high Faraday efficiency (and H₂ purity), current densities above 2 A/cm² and operating cell voltage below 2 V in state-of-the-art Proton Exchange Membrane (PEM) water electrolyzers, overall to reach a larger energy efficiency than 80%. At the same time, photoelectrolysers are lagging much behind in terms of similar, practically relevant values.

For this reason, the group has developed different methods to graft surface co-catalyst candidates on electrodes, in order to promote the complex chemical steps of either the Hydrogen Evolution Reaction (HER) on the cathode or the Oxygen Evolution Reaction (OER) on the anode side. Two strategies are followed: the first one, that utilizes Earth-abundant transition metal compounds as co-catalysts in scalable and soft bottom-up techniques, and another one, that aims to reduce the noble metal load by orders of magnitude, while maintaining performance. The work is financially supported by the NKFIH 132869/2019 and the NKFIH 128841/2018 grants, the RRF-2.3.1-21-2022-00009 and the TKP2021-05 projects.

Methods

Synthesis of the co-catalyst candidates was done according to published procedures. Electrochemical experiments were performed on Bio-Logic SP-150, or VMP-300 potentiogalvanostats. Boron Doped Diamond (BDD), Glassy Carbon (GC), Indium Tin Oxide (ITO), Fluorine-doped Tin Oxide (FTO), BiVO₄/FTO, or α -Fe₂O₃/Ti were used as (photo)anodes. Modifications with co-catalysts to improve the OER was done by simple drop-casting, or electrodeposition. For the HER, 2D-MoS_{2-x}O_x was prepared on Highly Oriented Pyrolytic Graphite (HOPG) support by Chemical Vapour Deposition (CVD) method. Decoration with Pt was done by electrodeposition.

Electrochemical characterization was done by Linear Sweep (LSV), Cyclic (CV) and Square Wave Voltammetry (SWV), Electrochemical Impedance Spectroscopy (EIS) and Controlled Potential Electrolysis (CPE). Photoelectrochemical methods included chopped-light LSV, determination of the Electrochemically Active Surface Area (ECSA), the Incident Photon-to-Current Efficiency (IPCE), and flat-band potential using the Mott-Schottky equation. Quantitative gas analysis of the produced O₂ and H₂ was done using a Shimadzu Tracera 2010 gas chromatograph, or an optical probe (Ocean Optics FOXY). The surface of the electrodes was analyzed by Scanning Tunnelling Microscopy (STM), X-ray Photoelectron Spectroscopy (XPS), Scanning Electron Microscopy (SEM) with Energy Dispersive X-ray (EDX), Raman and Infrared (IR) spectroscopy.

Results

In photoelectrochemical water splitting we applied simple, Fe- and Cu-containing pre-catalysts on nanopyramidal BiVO₄ and α -Fe₂O₃ nanoarray semiconductors (SCs) that were morphologically optimized for efficient light harvesting. In both SCs, surface states lower the charge transfer efficiency that can be improved by co-catalysts. On BiVO₄ the Fe precursor complex *in situ* transformed to α -Fe₂O₃ nanoparticles on V-vacant areas mending their photocurrent-limiting effect. The α -Fe₂O₃ co-catalyst improved the charge transfer efficiency by an order of magnitude, suppressed recombination and reduced the charge transfer resistance. At high potentials, the co-catalyst provided high-valent sites for the OER. The results underlined the metallochaperone-like effect of the bidentate ligand of the precursor complex [1-3].

We developed 'CuO'-modified α -Fe₂O₃ nanoarray photoanodes using a Cu-peptide complex as precursor in electrodeposition [4]. This soft method yielded a conformal ultra-thin layer of amorphous 'CuO' as a co-catalyst over hematite. In pure α -Fe₂O₃, Potentiostatic Electrochemical Impedance Spectroscopy (PEIS) and fast cathodic Cyclic Voltammetry (CV) methods identified two surface states. Introducing 'CuO' co-catalyst enhanced the Photoelectrochemical (PEC) performance, with a potential-dependent function. At lower potentials, 'CuO' acts as a hole reservoir but has limited transferability for OER due to slow formation of higher-valent oxidation states of Cu. At higher potentials, 'CuO' suppresses surface recombination and serves as a catalytic centre. Ti doping eliminates the lower-energy surface state improving PEC efficiency compared to pure α -Fe₂O₃. However, 'CuO' deposition does not further enhance the PEC performance in Ti-doped hematite. Ti-doping functions as hole storage, allowing hole transfer from active Ti-sites to 'CuO', which acts as a hole trap, leading to the conclusion that the 'CuO' co-catalyst enhances the PEC performance of hematite in case of available lower-energy surface states [5,6].

We also developed an efficient hematite-based tertiary photoanode system. Briefly, hematite nanorods were surface-modified with boron doped g-C₃N₄ (B-C₃N₄), then with carbon nanotubes economically obtained from methane pyrolysis and used as pyrolytic Carbon Nanotubes (p-CNTs), via a facile two-step dip-coating followed by a post-heat treatment process. The formed α -Fe₂O₃/B-C₃N₄/p-CNTs heterojunction rationally modulated the interface charge property and boosted the spatial

charge separation of the anode. A remarkable enhancement was observed in PEC water splitting performance with photocurrent density reaching 3.3 mA cm^{-2} at 1.23 V versus Reversible Hydrogen Electrode (RHE), a value ~ 3.2 times that of the pristine hematite under visible light irradiation [7].

Concerning the HER, Pt is the best and most widely studied electrocatalyst. We explored a metal-semiconductor transition in small Pt clusters realized through enhanced interaction with 2D MoS_2 support, yielding novel, two atoms thick Pt structures with sizeable bandgaps ($\sim 0.3 \text{ eV}$). The semiconducting Pt clusters displayed exceptionally high HER activity ($\sim 1400 \text{ s}^{-1}$ @ 100 mV), reaching that of commercial Pt/C catalysts at orders of magnitude lower Pt loadings of ~ 10 nanograms/ cm^2 , utilizing Pt a hundred times more efficiently than Pt single atom catalysts [8].

Non-noble metal alternatives, i.e., Fe(II) complexes containing bidentate ligands (L) were also studied in more detail to understand how the predominant solution equilibrium species affect the redox stabilization of the reduced complex forms, and thus promote HER. In the applied ligand series, a heterocyclic donor group by the 2-pyridyl function was systematically changed that was expected to define the predominant species and affect the redox stabilization of the reduced complex. In fact, the differences in the redox behaviour of the compounds in acetonitrile correlated with the basicity of the ligands. Addition of trifluoroacetic acid as proton source suggests that the complexes act as homogeneous catalysts with activities from $k_{\text{obs}} (\text{s}^{-1}) = 0.03, 1.1$ and 10.8 s^{-1} at overpotentials of 0.81, 0.76 and 0.79 V, respectively. The activity can be associated with the $[\text{Fe}(\text{L})_2(\text{S})_2]^{2+}$ form, where S stands for a monodentate solvent or substrate ligand. Kinetic studies and controlled potential electrolysis were used to explore the structure-activity relationships for the complexes. In contrast, the low spin $[\text{Fe}(\text{L})_3]^{2+}$ acts as a bystander species in the reaction mixture [9-10].

Related publications

- [1] T. Benkó, S. Shen, M. Németh, J. Su, Á. Szamosvölgyi, Z. Kovács, G. Sáfrán, S. M. Al-Zurairi, A. Sápi, Z. Kónya, J. S. Pap: *BiVO₄ charge transfer control by a water-insoluble iron complex for solar water oxidation*, Appl. Cat. A - Gen. **2023**, 652, 119035 <https://doi.org/10.1016/j.apcata.2023.119035>
- [2] J. S. Pap, T. Benkó, S. Shen, L. Vayssieres: *Exploiting immobilization, re-dissolution and degradation resulting from ancillary ligands of molecular complexes in water oxidation catalysis*, E-MRS Fall Meeting, Symposium B - Advanced catalytic materials for (photo)electrochemical energy conversion, September 18-21, **2023**, Warsaw, Poland, oral presentation
- [3] J. S. Pap, T. Benkó, M. Li, S. Shen, L. Vayssieres: *Hydrophobic, redox-active, precursory - ancillary ligand choices for electrode surface immobilization of molecular water splitting electrocatalysts*, 4th International Workshop on Graphene and C₃N₄-Based Photocatalysts and Others (IWGCP4), October 13-16, **2023**, Xi'an, China, invited oral presentation
- [4] Lukács D.: *Molekuláris és heterogén vízóxidációs katalízis réz-peptid komplexekkel*, PhD dolgozat, Pannon Egyetem, Kémiai és Környezettudományi Doktori Iskola, (2023) <https://doi.org/10.18136/PE.2023.849>
- [5] T. Benkó, S. Shen, M. Németh, D. Lukács, J. S. Pap: *$\alpha\text{-Fe}_2\text{O}_3$ -'CuO' nano-heterostructure for efficient photoelectrocatalytic water oxidation using a Cu-complex*, EuropaCat 2023, session Photo-driven processes for fuel and organic synthesis, August 27-September 1, **2023**, Prague, Czech Republic, poster presentation
- [6] T. Benkó, S. Shen, M. Németh, D. Lukács, Zs. Czigány, J. S. Pap: *Soft electrodeposition of 'CuO' on $\alpha\text{-Fe}_2\text{O}_3$ nanoarrays using Cu-peptides for photoelectrocatalytic water oxidation*, 4th International Workshop on Graphene and C₃N₄-Based Photocatalysts and Others (IWGCP4), October 13-16, **2023**, Xi'an, China, poster presentation
- [7] I. Khan, T. Benkó, A. Nagyné Horváth, S. Shen, J. Su, M. Németh, Endre Z. Horváth, J. S. Pap: *Economically viable carbon nanotubes on visible-light driven semiconductor for practically efficient water oxidation*, 4th International Workshop on Graphene and C₃N₄-Based Photocatalysts and Others (IWGCP4), October 13-16, **2023**, Xi'an, China, oral presentation
- [8] T. Ollár, P. Vancsó, P. Kun, A. A. Koós, E. V. Sukhanova, Z. I. Popov, M. Németh, K. Frey, B. Pécz, P. Nemes-Incze, C. Hwang, J. S. Pap, and L. Tapasztó: *Semiconducting Pt clusters stabilized on 2D MoS₂ for ultrafast hydrogen evolution*, Nature Energy, under review
- [9] S. Keszei, T. Ollár, M. Németh, K. Frey, L. Tapasztó, J. S. Pap: *Electrocatalytic hydrogen evolution by iron(II) complexes with bidentate aromatic N-donor ligand*, manuscript under revision
- [10] J. S. Pap, S. Keszei, T. Ollár, L. Tapasztó: *The role of ligand heteroatoms in electrocatalytic hydrogen evolution by iron(II) N-heterocyclic complexes*, EuropaCat 2023, session Electrocatalysis, including fuel cells, August 27-September 1, **2023**, Prague, Czech Republic, oral presentation

HYDROGEN OR SYNGAS BY CATALYTIC METHANE CONVERSION

Andrea Beck, Miklós Németh, Tamás Korányi, Anita Horváth

Objective

Our catalytic studies of two methane conversion processes yielding H₂ gas without CO₂ formation were continued. The methane dry reforming reaction (DRM: CH₄+CO₂⇌2CO+2H₂) was investigated over CeO₂-Al₂O₃ supported Ni and NiIn catalysts using equimolar and biogas composition as reactant gas mixtures or extremely long time on stream. The methane pyrolysis in an inert atmosphere to get pure H₂ gas and solid carbon (CH₄⇌C+2H₂) was investigated over NiMo/MgO catalysts after a reactor upscaling step and under different gas compositions as well. The pyrolytic carbon product was tested in photoelectrocatalytic water splitting as anode modifier and produced in larger amounts for lithium-sulphur batteries as a composite electrode material.

Methods

Catalyst characterizations by XRD, TPR, XPS, TEM and DRIFTS (in the presence of CO/CO₂/CH₄+CO₂) were completed on NiIn/CeO₂-Al₂O₃ catalysts previously prepared. Extremely long, 4-day DRM tests were carried out in the Slovenian partner's lab with a stoichiometric, 1:1 reactant ratio at 675 °C, while the effect of temperature enhancement and application of biogas composition (CH₄:CO₂=70:30) was studied in our further DRM measurements. The NiMo/MgO catalyst series prepared and characterized earlier were applied for methane pyrolysis in a horizontal quartz reactor in 50% CH₄/Ar and also in 10%H₂+50%CH₄/Ar flow at 800 °C after in situ reduction by H₂ at the same temperature. The used catalysts with carbon products were studied in more detail by HRTEM and STEM-EDS.

Results

As for the DRM studies, the catalytic and structural changes due to the presence of 0.25 wt% indium on the 3 wt% Ni/CeO₂-Al₂O₃ catalyst prepared by the impregnation method were completed and published. In the 6-hour-catalytic methane dry reforming tests at 650 °C with an equimolar reactant mixture, both samples were stable and produced essentially no carbon, but indium lowered the activity. In the 4 day-longevity tests at 675 °C performed in another reactor setup in Ljubljana, stable activity was achieved by the In-promoted catalyst in contrast with the continuous deactivation of the unpromoted Ni sample due to coking and sintering. Indium, partially alloyed with nickel, could better keep nickel in the metallic state, and the increased CO₂ activation ability, the intimate Ni(In)-CeO₂ interface inside the support pores resulted in practically no coking. In our 6 hour-DRM tests at 690 °C, some deactivation was observed as the higher reaction temperature enhanced the CH₄ cracking step with the simultaneous increase of the H₂/CO ratio. DRM tests in 70% CH₄ - 30% CO₂ mixture (biogas composition) revealed controversial results that must be related to the different surface sites required to activate the reactants depending on the metal surface composition. Namely, on NiIn sample the methane conversion rate decreased, while on pure Ni sample it increased in the high excess of methane, and this catalyst slightly deactivated, but the bimetallic one was stable. In a repeated reaction after a regeneration (oxidation/reduction) step, the CH₄ conversion increased on the bimetallic catalyst suggesting irreversible partial dealloying of the original NiIn surface, while decreased on the monometallic catalyst likely due to sintering.

As for methane pyrolysis studies, the meticulous (HR)TEM and STEM-EDS analysis of the spent highly active NiMo/MgO catalysts revealed the optimal stability of the Ni/Mo=0.9 alloy and the detrimental segregation of the alloys with nickel excess. A catalytic test with the concomitant addition of 10% H₂ to the 50%CH₄ in Ar stream was also realized. The results showed the improvement of the catalytic properties: 25 mg carbon nanotubes were obtained with modified morphology on a least effective NiMo/MgO sample in contrast to the 15 mg carbon in the absence of hydrogen. The catalytic reactor was further equipped with a larger volume quartz tube to accommodate more carbon and so minimize the chance of reactor plug-in at higher reaction times. The same type of activity profile was obtained in this wider quartz tube as in the case of the original thin tube, validating the applicability of the new setup.

As for the transfer of pyrolytic carbon product into new, value-added application routes, the development of an efficient photoanode system for photoelectrochemical (PEC) water oxidation was linked in, where a remarkable enhancement was achieved by the addition of our catalyst containing carbon nanotubes to the boron-doped g-C₃N₄ promoted hematite nanorods containing anode. As a further important step, we transferred our pyrolytic carbon product to apply as nanocarbon/sulfur composite electrode material in lithium-sulphur batteries in the HUN-REN Research Centre for Natural Sciences.

Related publications

- [1] A. Horváth, M. Németh, A. Beck, G. Sáfrán, V. La Parola, L. F. Liotta, G. Žerjav, M. Roškarič, A. Pintar: *Longevity increase of an impregnated Ni/CeO₂-Al₂O₃ dry reforming catalyst by indium*, Applied Catalysis A, General **669**, 119495 (2024) <https://doi.org/10.1016/j.apcata.2023.119495>
- [2] A. Horváth, Final report of the bilateral Slovenian-Hungarian Tét project (# 2019-2.1.11-TÉT-2020-00188) entitled "Methane-CO₂ dry reforming over bimetallic Ni supported on nanoshaped or promoted CeO₂: in-situ/operando investigation of their working states", (2023)
- [3] I. Khan, T. Benkó, A. Horváth, S. Shen, J. Su, M. Németh, Zs. Horváth, J. Pap: *Economically viable carbon nanotubes on visible-light driven semiconductor for practically efficient water oxidation*, oral presentation, The 4th International Workshop on Graphene and C₃N₄-Based Photocatalysts and Others, 13-16 October 2023, Xi'an, China

EXAMINATION OF THE RECYCLABILITY OF ELECTRONIC WASTE USING NUCLEAR ANALYTICAL AND IMAGING METHODS

Noémi Anna Buczkó, Boglárka Maróti, László Szentmiklósi

Objective

Our research aims to develop an analytical methodology suitable for the comprehensive elemental analysis of various Waste Electrical and Electronic Equipment (WEEE) by using neutron and X-ray-based methods. During the research, we focus on valuable and hazardous elements, as well as on elements that are of high importance and at the same time a high supply risk for the European economy (critical elements).

Methods

- Prompt Gamma Activation Analysis (PGAA), Instrumental Neutron Activation Analysis (INAA), In-beam Neutron Activation Analysis (in-beam NAA), and Portable X-ray Fluorescence Spectroscopy (pXRF) to determine the elemental compositions of WEEE,
- Neutron and X-ray radiography and tomography to obtain 2D and 3D structural information on the samples.

Results

In previous years, the in-beam NAA method became applicable to measure the absolute concentrations of relevant elements in the WEEE. This required the correction of the effect of neutron self-shielding and neutron scattering occurring during the irradiation of the sample in the neutron beam. It was successfully achieved in 2023, with the combined interpretation of Monte Carlo simulations and measurements.

In 2023, one of our main research directions was the elemental composition determination of LED light sources. For this purpose, commercial LED light sources were disassembled, and the LED chips, in which part the valuable and critical elements are presumably concentrated, were separated from the light bulb. They were measured with INAA, PGAA, and in-beam NAA, and the advantages and limitations of each method were identified. It was found that a combination of the methods is required for a comprehensive analysis of LED chips. With INAA, many valuable or critical elements were identified such as Ga, Ag, Au, Cu, Ce, Eu, and Lu. However, yttrium, which is a presumed main component of LED chips and an important critical element, could not be measured with INAA, and quite high detection limit was achieved with this method. However, the yttrium content of LED chips was successfully measured with PGAA. Among the most important critical and valuable elements, Ag and Cu were measurable in all samples with PGAA, and the Au and Ga contents of some LEDs were also measurable. By applying in-beam NAA following PGAA measurements, the detection limits of Ga and Au were improved, and these elements were measurable in all samples. In addition, low detection limits were achieved for most hazardous elements using the combination of different methods. Significant differences were found between the raw concentrations and elemental ratios measured by different methods. The reasons for the discrepancies, such as neutron self-shielding were successfully identified. The results are currently being corrected.

The applicability of the PGAA and in-beam NAA methods was also investigated to analyse intact LED light sources without disassembly, in a completely non-destructive way. However, the detection limits were found to be too high for the detection of the most important valuable, critical, and hazardous elements in the case of non-destructive measurements. Further, the separated LED chips were also measured with a pXRF spectrometer to test the applicability of such a cheap, quick, and easily accessible method for the characterization of such waste. For the portable XRF device, a factory calibration mode suitable for testing LED chips is currently not available. Thus, the quantitative analysis could not be performed yet, but the qualitative analysis was made by the analysis of measured spectra. Based on the XRF spectra, among the most important valuable/critical elements, Ga, Ag, Cu, and Y were detectable in all samples, and the Au, Ce, Eu, and Lu content of some samples was also measurable. Based on the results of the neutron-based methods, an own, matrix-matched calibration is being established for the portable XRF device which can enable quantitative analysis. It is planned to investigate whether the detection limit of each element can be improved.

Other types of WEEE were also investigated. The applicability of the non-destructive PGAA method for measuring the lithium content of Li batteries was tested. It was found that in the case of the cobalt-containing Li battery types, the Co content strongly interferes with the analytical lines of lithium. Thus, the determination of the Li content was only possible with a high uncertainty. The element composition of solar cells was also determined using a combination of PGAA, in-beam NAA, and INAA. In the case of solar cells, the indium content of the samples was successfully detected, which is an assumed component of solar cells and an important critical element. The tungsten content of traditional light bulbs was also successfully detected using a combination of PGAA and in-beam NAA.

The results were presented as an oral presentation at the 3rd International Conference on Radioanalytical and Nuclear Chemistry (RANC-2023, May 7–12, 2023, Budapest, Hungary), and as a poster at the 'MKE 4. Nemzeti Vegyészkonferencia' (National Chemistry Conference, July 10–12, 2023, Eger, Hungary). The results were also presented as an extended abstract and an oral presentation at 'Őszi Radiokémiai Napok' (Autumn Radiochemistry Days) in October 2023, in the section devoted to the 'Vértes Attila young scientists' competition'.

Related publications

- [1] N. A. Buczkó, B. Maróti, Z. Kis, L. Szentmiklósi: *Elemental composition analysis of different electronic waste with neutron-based techniques*, In: I. Józai, (szerk.) *Őszi Radokémiai Napok Budapest, Magyarország: Magyar Kémikusok Egyesülete* (2023) pp. 24-29., 6 p.
- [2] N. A. Buczkó, B. Maróti, K. Gméling, L. Szentmiklósi: *Neutron-based elemental composition analysis of electronic waste items*, oral presentation, RANC-2023 conference, May 2023
- [3] N. A. Buczkó, B. Maróti, K. Gméling, L. Szentmiklósi: *Elektronikus hulladékok elemösszetételének vizsgálata nukleáris analitikai módszerekkel (Examination of the elemental composition of electronic waste using nuclear analytical methods)*, poster presentation, 'MKE 4. Nemzeti Vegyészkonferencia', July 2023

EFFECT OF THE ENERGY-EFFICIENT HIGH ENERGY IONIZING RADIATION TREATMENT ON DEGRADATION OF METOPROLOL AND OXACILLIN FOCUSING ON THE REMOVAL RATE AND ANTIMICROBIAL ACTIVITY

Renáta Homlok, Krisztina Kovács

Introduction

In the last two decades, radiation chemical research has shifted towards the degradation of highly stable toxic molecules in wastewater. This research specifically involves the application of gamma or electron beam radiation from a ^{60}Co source or a linear electron accelerator of the Radiation Chemistry Department.

Recently, the department's primary mission has been to ascertain the requisite absorbed dose (energy deposited by irradiation in unit mass) for the degradation of harmful organic contaminants in wastewater. These contaminants can be various antibiotics and other drug molecules, such as β -blockers, which are resistant to conventional biological treatment methods for sewage water. The importance of this research is growing by the ever-increasing interest in the chemical characterization of the products resulting from the radiation induced degradation of molecules, but also in the evaluation of the biological effects of these products using microbiological techniques and appropriate bacteria, at different absorbed doses.

Methods

γ -radiolysis and pulse radiolysis experiments were performed to investigate the effect on degradation of Metoprolol and Oxacillin. The transient intermediates of degradation reactions for Metoprolol were studied by pulse radiolysis technique using 4 MeV accelerated electrons with a pulse length of 800 ns and an optical system with a 1 cm path length cell utilizing kinetic spectrophotometric detection. Radical scavenging experiments were used to identify and quantify the participating free radicals. The starting molecules and their degradation products were characterized by sum parameters applied in wastewater analysis like UV-Vis spectrophotometry, Chemical Oxygen Demand (COD), Total Organic Carbon (TOC) content, Biochemical Oxygen Demand (BOD) and toxicity measurements.

In the biochemical type investigations, two types of *Staphylococcus aureus* strains of bacteria (sensitive and resistant) were used to study their behaviour in suspensions under the effect of ionizing radiation in the presence and absence of Oxacillin. 0.5 McFarland density suspensions from 24 hours old Tryptone Soya Agar (TSA) cultures of *S. aureus* B.02174 (resistant) and B.01755 (sensitive) were prepared in purified water. Growth was tested in Tryptone Soya Broth (TSB) with different Oxacillin concentrations. For sensitive strains 0.0625, 0.125, 0.25, 0.5 and 1 g ml⁻¹, while for resistant strains 1, 2, 4, 8, 16, 32, 64, 128, 256 and 512 g ml⁻¹ Oxacillin concentrations were applied. Measurements were done in triplicate. Growth was followed during 24 hours by absorbance measurement (at 595 nm) every 30 minutes at 37 °C using a MultiSkan Ascent equipment (Thermo Electron Corporation). Oxacillin solutions at concentrations of 1 g dm⁻³ (2.5 mmol dm⁻³) and 0.042 g dm⁻³ (0.1 mmol dm⁻³) were irradiated with absorbed doses ranging from 0 to 10 kGy. The effects of the irradiated antibiotic solutions on the growth of the sensitive strain were then evaluated at an Oxacillin concentration of 1 mg dm⁻³ (2.5 $\mu\text{mol dm}^{-3}$) using the MultiSkan Ascent equipment, as previously described.

Results

The results related to radiolytic degradation of Metoprolol showed that it takes place through the hydroxyl radical ($\cdot\text{OH}$) intermediates of water disintegration and occurs on the aromatic ring through the formation of hydroxycyclohexadienyl type radicals, resembling the patterns observed in the case of other β -blockers such as Propranolol, Atenolol, and Nadolol. The effect of pH was investigated at pH 7 and 12 in $\cdot\text{OH}$ reactions. In protonated form (at low doses) Metoprolol showed higher reactivity towards $\cdot\text{OH}$. The rate constant in $\cdot\text{OH} + \text{Metoprolol}$ reaction is found to be $4.8 \pm 0.3 \times 10^9 \text{ mol}^{-1} \text{ dm}^3 \text{ s}^{-1}$. The oxidative reactions with $\cdot\text{OH}$ were proven to be effective in the degradation of Metoprolol which can be verified based on UV-Vis spectra. At 2.5 kGy the aromatic peak at 225 nm disappeared showing degradation of the ring and the termination of the aromatic conjugation. Oxidation and mineralization processes took place parallel. Their rates were measured to be: 17 mg dm⁻³ O₂ kGy⁻¹ (COD) and 1.7 mg dm⁻³ C kGy⁻¹ (TOC), respectively. Among the beta-blockers investigated the rate of oxidation and mineralization was the highest for Metoprolol. BOD measurements confirmed that Metoprolol is a non-biodegradable compound. However, using 2.5 kGy absorbed dose the forming degradation products became biodegradable. Based on the toxicity tests, the forming degradation products were more poisonous at low doses compared to the starting molecule. At higher absorbed doses this increased toxicity disappeared. Removal of Metoprolol can effectively be achieved using appropriate doses *via* radiolytic reactions.

In addition to simply removing various types of pharmaceuticals, attention must be drawn to the critical issue of antibiotic resistance in the presence of antibiotics in wastewater. Antibiotic resistance refers to the ability of bacteria to withstand the effects of antibiotics, rendering these medications less effective or entirely ineffective. This phenomenon poses a significant threat to public health, as it can lead to persistent infections, increased healthcare costs, and a higher risk of spreading

infections that are resistant to treatment. The Minimum Inhibitory Concentration (MIC) represents the minimal concentration at which bacterial growth is still observed despite the inhibitory effect of the antibiotic. Monitoring the development of resistance and regularly assessing MIC values are crucial for maintaining the proper and effective use of antibiotics.

In the experiments two *S. aureus* bacterium strains were used: the Oxacillin-resistant B.02174 strain and the Oxacillin-sensitive B.01755 strain. For the B.01755 strain, the MIC was found to be below 1 mg cm⁻³, while for *S. aureus* B.02174, the MIC was 128 mg cm⁻³. During the tests two Oxacillin solutions with concentrations 2 – 3 orders of magnitude higher than the MIC of the sensitive strain were irradiated with 2 – 10 kGy absorbed doses. Two series of experiments were performed with concentrations of 1 g dm⁻³ (2.5 mmol dm⁻³) and 0.042 g dm⁻³ (0.1 mmol dm⁻³), respectively. In the case of 1 g dm⁻³ concentration solution, at low doses, complete growth inhibition of the sensitive *S. aureus* strain was observed, which showed that Oxacillin was not inactivated, and exerted its inhibitory effect. At higher doses, the antibiotic was partially inactivated, so the sensitive strain multiplied, but to a lesser extent than in the control antibiotic-free sample. This was observed even in the case of the antibiotic treated with the highest, 10 kGy dose. In an irradiated solution with a lower concentration (0.042 g dm⁻³), Oxacillin lost its ability to retard the multiplication of sensitive *S. aureus* even at 2 kGy, the lowest dose used.

Our results emphasize a dose-dependent effect on the inhibitory properties of the antibiotic, showing complete growth inhibition at lower doses for the sensitive *S. aureus* strain. Nevertheless, at higher doses, Oxacillin exhibited partial inactivation, allowing for some multiplication of the sensitive strain, even at the highest absorbed dose tested. Furthermore, at a lower concentration of Oxacillin (0.042 g dm⁻³), losing the inhibitory effect at the lowest absorbed dose (2 kGy), suggests a potential threshold for maintaining antibacterial activity under irradiation conditions.

Conclusion

This year, the degradation of Metoprolol (β -blocker) and Oxacillin (antibiotics molecule) were in the focus. A key finding of this investigation is that an absorbed dose of 1 to 2 kGy proves sufficient to transform these potentially harmful molecules into less toxic forms. Furthermore, this dose has been observed to effectively deactivate bacteria responsible for the spread of antibiotic resistance. It is important to note, however, that the effectiveness of irradiation treatment may vary on an individual basis and should be assessed accordingly.

Remaining work

In our earlier investigations, we acquired a comprehensive understanding of the radiolytic degradation processes of various β -blockers. Our intention is to extend this research by exploring potential relationships between degradation efficiency and the chemical structure of beta-blockers. Additionally, we aim to conduct a detailed examination of the influence of the water matrix on degradation processes. Furthermore, we would like to extend our research scope to include an examination of the impact of irradiation on eDNA (external DNA) degradation.

Related publications

- [1] K. Kovács, Á. Simon, T. Tóth, L. Wojnárovits: *Free radical chemistry of atenolol and propranolol investigated by pulse and gamma radiolysis*, Radiation Physics and Chemistry **196**, 110141 (2022) <https://doi.org/10.1016/j.radphyschem.2022.110141>
- [2] K. Kovács, T. Tóth, L. Wojnárovits: *Evaluation of Advanced Oxidation Processes for β -blockers degradation: a review*, Water Science and Technology **85** (2), 685 (2022) <https://doi.org/10.2166/wst.2021.631>
- [3] K. Kovács, A. Tegze, A., Bezsenyi, L. Wojnárovits: *Hydroxyl radical induced degradation of the β -blocker Nadolol and comparison with Propranolol*, Journal of Environmental Chemical Engineering **11:4**, 110330 (2023) <https://doi.org/10.1016/j.jece.2023.110330>
- [4] E. Takács, J. Wang, L. Chu, T. Tóth, K. Kovács, A. Bezsenyi, L. Szabó, R. Homlok, L. Wojnárovits: *Elimination of oxacillin, its toxicity and antibacterial activity by using ionizing radiation*, Chemosphere **286**, 131467 (2022) <http://dx.doi.org/10.1016/j.chemosphere.2021.131467>
- [5] L. Wojnárovits, J. Wang, L. Chu, T. Tóth, K. Kovács, A. Bezsenyi, L. Szabó, R. Homlok, E. Takács: *Matrix effect in the hydroxyl radical induced degradation of β -lactam and tetracycline type antibiotics*, Radiation Physics and Chemistry: The Journal for Radiation Physics Radiation Chemistry and Radiation Processing **193**, 109980 (2022) <https://doi.org/10.1016/j.radphyschem.2022.109980>
- [6] M. Kovács, L. Wojnárovits, R. Homlok, A. Tegze, Cs. Mohácsi-Farkas, E. Takács, Á. Belák: *Changes in the behaviour of Staphylococcus aureus strains in the presence of oxacillin under the effect of gamma radiation*, Environmental Pollution **340**, 122843 (2024) <https://doi.org/10.1016/j.envpol.2023.122843>

EXAMINATION OF ELECTROCHEMICAL REDUCTION PROCESSES (HYDROGEN DEVELOPMENT AND CO₂ REDUCTION)

Tamás Ollár, Krisztina Frey

Objectives

During the development of catalysts for Hydrogen-Evolution Reaction (HER), we produced catalysts that can also be used in other electrocatalytic reactions. The general feature of the mentioned catalysts is that metal clusters are separated on a 2D MoS₂ support, which are 2-3 nm wide and 2-4 Å high, and the electron conduction properties also differ from the properties of bulk metals. We are doing pioneering work in the development of these catalysts, and this type of cluster is not yet widely used, which is why we've planned to use these catalysts in other electroreduction processes. We plan to implement the electrochemical reduction of CO₂. In this connection, we contacted Dr. Csaba Janáky, professor at the University of Szeged, whose research group has successfully been working on the development of CO₂ reduction processes for years. He offered his help to develop our system, but as a first step, we will test the catalysts we have developed in their system. In the framework of the Sunergy collaboration, I've contacted Alessandro Senocrate, an employee of the Swiss EMPA (Swiss Federal Laboratories for Materials Science and Technology), who deals with CO₂ reduction and invited him to our institute for a discussion and presentation. The visit took place in November and the title of his presentation was "The Importance of Substrate Control and Standardized Analytics in Electrochemical CO₂ Reduction".

Methods

For the catalysts, 2D-MoS_{2-x}O_x was prepared on Highly Oriented Pyrolytic Graphite (HOPG) supported by Chemical Vapour Deposition (CVD) method. Decoration with Pt (and with other metals as Au, Pd) was done by electrodeposition. Electrochemical characterization of the catalysts was done by Linear Sweep Voltammetry (LSV), Cyclic Voltammetry (CV) and Electrochemical Impedance Spectroscopy (EIS). Electrochemical experiments were performed on Bio-Logic SP-150. The surface of the electrodes was analyzed by Scanning Tunnelling Microscopy (STM), X-ray Photoelectron Spectroscopy (XPS) and Scanning Electron Microscopy (SEM).

Results

Catalysts are produced using a method developed by ourselves. Metal clusters were deposited on a 2D-MoS_{2-x}O_x surface grown on HOPG. These catalysts are primarily designed to increase the efficiency of the hydrogen-producing half-reaction of water splitting. Examination of the prepared catalysts showed that the metal clusters have semiconducting properties. The semiconducting Pt clusters displayed exceptionally high HER activity (~1400 s⁻¹ @ 100 mV), reaching that of commercial Pt/C catalysts at orders of magnitude lower Pt loadings of ~10 nanograms/cm², utilizing Pt a hundred times more efficiently than Pt single-atom catalysts. We produced several types of metal-containing catalysts. This year, we worked out the exact reproducibility of the catalysts produced. In the second half of the year, we made catalysts that we can take to the research group of Dr. Csaba Janáky, where we will examine their behaviour in the process of electrochemical CO₂ reduction.

Acknowledgement of cooperation

We thank our colleagues for their cooperation, which is essential for our work. We thank József Pap for his help with the electrochemical measurements and Miklós Németh for the XPS measurements, to the colleagues working at the MFA, Levente Tapasztó and his group (Antal Koós, Péter Nemes-Incze, Gergely Dobrik, Péter Vancsó, Péter Kun) for the STM measurements, for Tunnelling Spectroscopy, MoS₂ innovation for DFT calculations and Levente Illés for the SEM measurements.

Related publications

- [1] T. Ollár, P. Vancsó, P. Kun, A. A. Koós, E. V. Sukhanova, Z. I. Popov, M. Németh, K. Frey, B. Pécz, P. Nemes-Incze, C. Hwang, J. S. Pap, and L. Tapasztó: *Semiconducting Pt clusters stabilized on 2D MoS₂ for ultrafast hydrogen evolution*, Nature Energy, under review
- [2] T. Ollár, A. A. Koós, P. Vancsó, P. Kun, P. Nemes-Incze, J. S. Pap, K. Frey and L. Tapasztó: *Pt nanoparticles, clusters and single atom sites on MoS₂ sheets for electrocatalytic water splitting*, EuropaCat 2023, August 27-September 1, 2023, Prague, Czech Republic, oral presentation
- [3] T. Ollár, A. A. Koós, P. Vancsó, P. Kun, P. Nemes-Incze, J. S. Pap, K. Frey and L. Tapasztó: *Enhancing the electrocatalytic activity of Pt in hydrogen evolution reaction through 2D MoS₂ interaction and size control*, E-MRS Fall Meeting, September 18-21, 2023, Warsaw, Poland, oral presentation
- [4] K. Frey, J. S. Pap, D. Lukács, Z. Lábadi, D. Mukherjee, N. Szász, M. Németh, P. Petrik: *Tracking surface processes on water oxidizing anodes using high-sensitivity operando ellipsometry*, EuropaCat 2023, August 27-September 1, 2023, Prague, Czech Republic, oral presentation

POWER PRODUCTION FROM LOW-TEMPERATURE HEAT SOURCES

Attila R. Imre

Objective

For a sustainable community, one needs to utilize existing, preferably renewable heat sources to produce electricity. One of these sources – a renewable one – is the geothermal heat, and another one – a non-renewable – is the industrial waste heat. Usually, these heat sources are low-temperature ones, therefore, traditional steam Rankine-Clausius cycles cannot be used to turn their heat to power. Therefore, another solution, the Organic Rankine Cycle (ORC) should be used. One of the biggest problems for the ORC technology is the relatively high cost caused by the low heat-to-power efficiency, the internal losses and the relative complexity of the device, causing high installation and maintenance costs. The negative influence of some of these factors can be reduced by the proper choice of the organic working fluid fitted to the temperatures of the heat source and the heat sink (usually the air).

Methods

Thermodynamic data were taken from RefProp database and NIST Webbook for efficiency calculations. Calculations were done by our own codes.

Results

Existing and previously not properly utilized heat sources might provide us with new possibilities for a low-emission, sustainable way of power production. Most of these sources have low heat flux as well as low temperature, causing low heat-to-power efficiency and net power production. Still, considering that they already exist, without the use of any fuel, they might be a cost-effective solution for the production of electricity, assuming low installation and maintenance costs, for example, by simplifying the devices used for power production. For ORCs-based power cycles, this means that the omission of superheaters or recuperative heat exchangers and the use of simple expanders and small heat exchangers would lead to the simplest set-up, but for that, special steps should be taken upon the selection of working fluids with a fitting expander. The criteria for favourability is to have a nonideal expansion process starting and ending in (or very near) saturated vapour states to avoid problems related to wetness/dryness between the given maximal and minimal expansion temperatures. The design can be simplified under the simultaneous working fluid and expander selection method presented in this study, regardless of the type and isentropic efficiency of the expander. The proposed approach is illustrated in Figure 1. [1]

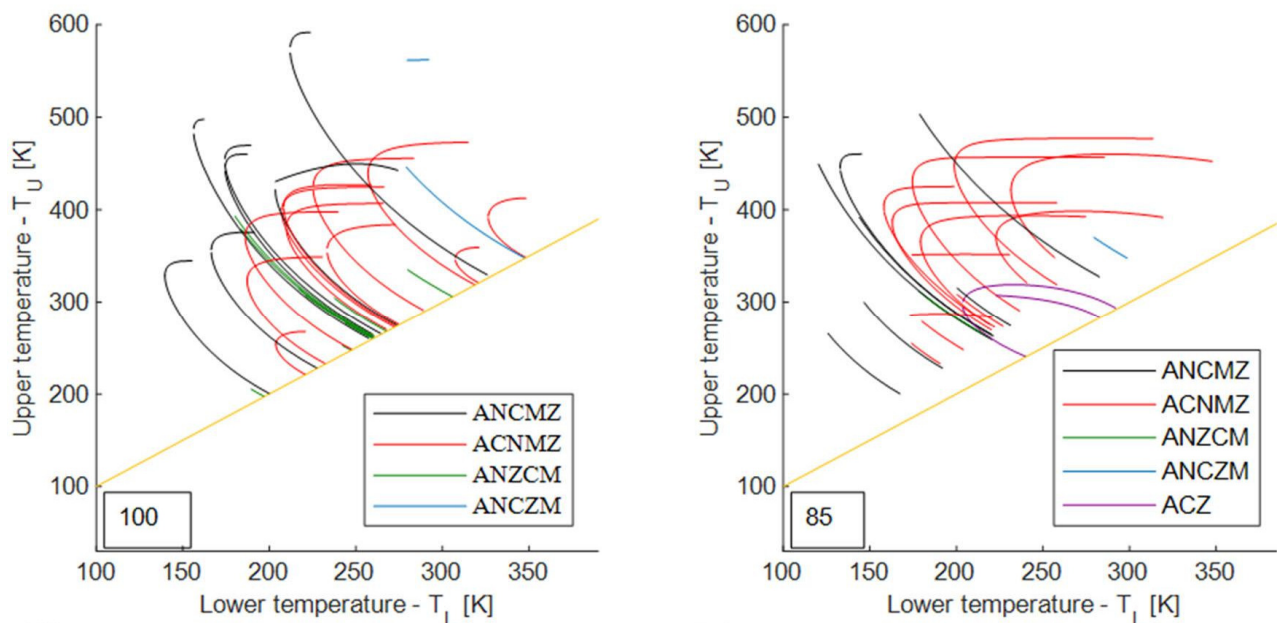


Figure 1: Selection of proper working fluid for a given heat source represented by the turbine inlet (T_U) and outlet (T_L) temperatures with a perfect expander (internal efficiency: 100%) and a more realistic one (85%). Each curve represents a different working fluid. [1]

For the selection of potential working fluid, several thumb rules are used. One of them states that for ORC and other similar applications, fluids with higher liquid-vapour critical temperatures are better, i.e. they can have higher cycle efficiency as well as net-work output at the same heat source/heat sink temperature. Studies establishing this statement usually consider only 3-6 randomly picked fluids. In our study, 13 alkanes and 10 halogenated alkanes were investigated with two different kinds of subcritical cycles, namely the ORC and the Trilateral Flash Cycle (TFC). Pure and mixed (with various compositions)

working fluids were used. It has been shown that although the critical temperature is an important factor, it can be correlated with output parameters only by using chemically similar working fluids. [2]

Following this line, mixtures were studied. Four different thermodynamic models were used; they differed by the definition of the maximal and minimal cycle temperatures. Three different scenarios were investigated in all models by picking components from different working fluid classes (defined by their expansion properties as wet or dry fluids) to prepare zeotropic mixtures. The main focus of our study was on the investigation of the effect of the critical temperature (T_{cr}) of the mixture and the class of the components (wet/wet, wet/dry, and dry/dry) on thermal efficiency (η_{th}) and net-work output (W_{net}). Results indicate that occasionally, but not always, the zeotropic mixtures with higher critical temperatures (but not always) outperform other mixtures under given conditions. Therefore, it cannot be asserted that the higher thermal efficiency and net-work output are monopolized by the highest critical temperature of all mixed working fluids. [3]

In the fourth part, the ORC system combined with Thermal Energy Storage (TES) was studied by utilizing low- and medium-temperature heat sources. Several approaches were reviewed using TES and subcritical ORCs with two-phase expanders. Various possible control systems were compared, and possible directions for future developments of design and control systems were discussed. This study aimed to provide researchers and engineers with an insight into the challenges involved in this process, making the industrialization of ORC technology more extensive, particularly when combined with TES and a two-phase expansion system. [4]

Related publications

- [1] A. Groniewsky, R. Kustán and A. R. Imre: *Simultaneous working fluid and expander selection method for reaching low-threshold technology Organic Rankine Cycle (ORC) design*, Energy Science & Engineering, **11**, 2330–2350 (2023) <http://doi.org/10.1002/ese3.1457>
- [2] A. M. Ahmed, A. R. Imre: *Effect of the working fluids critical temperature on thermal performance for trilateral flash cycle and organic Rankine cycle*, International Journal of Thermofluids, **20**, 100417 (2023) <https://doi.org/10.1016/j.ijft.2023.100417>
- [3] A. M. Ahmed, A. R. Imre: *Effect of critical temperature and category of zeotropic mixture working fluids on the thermal performance in subcritical ORC*, International Journal of Thermofluids, **20**, 100400 (2023) <https://doi.org/10.1016/j.ijft.2023.100400>
- [4] A. R. Imre, S. Daniarta, P. Błasiak, P. Kolasieński: *Design, Integration, and Control of Organic Rankine Cycles with Thermal Energy Storage and Two-Phase Expansion System Utilizing Intermittent and Fluctuating Heat Sources – A Review*, Energies **16**, 5948 (2023) <https://doi.org/10.3390/en16165948>

ENERGY STRATEGY AND ENVIRONMENTAL EFFECTS

Bálint Hartmann, Lilla Barancsik, Endre Börcsök, Veronika Oláhne Groma, Dalma Günther, Bálint Sinkovics, Tamás Soha, Milán Sőrés, Viktória Sugár

Power system security ^{[1][2][3]}

The focus area was part of the two-year research project ELKH SA-44/2021 “Renewable based power system stability”.

Power grids can be described by the second-order Kuramoto model, which possesses inertia. We found that the European HV power grid has a graph dimension $d_g = 2.6(1)$, but the spectral dimensions seem to be below $d_s = 2$. Still, the occurrence of chimera-like patterns can be observed via order parameters and confirmed by a community-level synchronization study. We demonstrated the level of local synchronization by showing the local Kuramoto order parameter, but similar results have been found by calculating the local frequency spreads. We performed an extensive numerical study of the synchronization transition of the second-order Kuramoto model in 2D and 3D. We provided numerical evidence that, while the phase-order parameter exhibits crossover transition, which diverges with the system size in a power-law manner, the frequency-spread-order parameter exhibits real phase transition in 3D. In the latter case, the finite size dependence of the critical point is negligible on the system sizes we investigated, and the transition point for an infinite system, estimated through extrapolation, is also very close to those measured in finite systems except for a logarithmic correction in 2D. However, the transitions of both order parameters exhibit hysteresis behaviour, with steady-state values, which depend on the initial conditions.

We revisited the topic of the size distribution of forced outages in power systems to formulate possible theoretical explanations of the uniformness of these distributions. To address a shortcoming of previous studies, long-term outage data of various power systems were collected and analyzed. First, exponents of power-law fits were extracted to cross-check the results with related literature; then this step was repeated after setting a threshold, speculating that the understanding of the manifested power law for the unavailable duration constitutes a crucial ingredient for the understanding of general power-law behaviour in outage distributions. Based on the numerical results, potential explanations were presented, and a power spectral analysis was performed to demonstrate that the studied outage data are composed of many random events as well as some correlated events characterized by the $1/f$ noise. This hints that SOC (Self-Organized Critical) processes could take place in outage events. Therefore, for outage events, we consider the system under study as the combination of spontaneous isotropic percolation and a branching process, implying directed percolation criticality. Although a SOC explanation based on the directed percolation criticality for the heavy tails in outage duration distributions is tempting, given that the majority of the outage events occurred out of random causes, the manifested power laws in outage duration cannot be attributed to the responses to SOC cascading failures alone. The power spectra of the outage duration time series further indicate a lack of $1/f$ noise, leading us to conjecture an extended HOT (Highly Optimized Tolerance) explanation for the heavy tails in outage duration distributions. This can be quite sensible, as on the one hand, power-grid infrastructures are built more or less in a self-organized manner to meet customers’ demands, so they are more rigid to give rise to SOC processes, despite some measures being introduced to confine the spread of outages. On the other hand, the needed maintenance resources in responses to outage events can be more fluidly distributed and allocated, permitting a greater extent of optimization for economic efficiency.

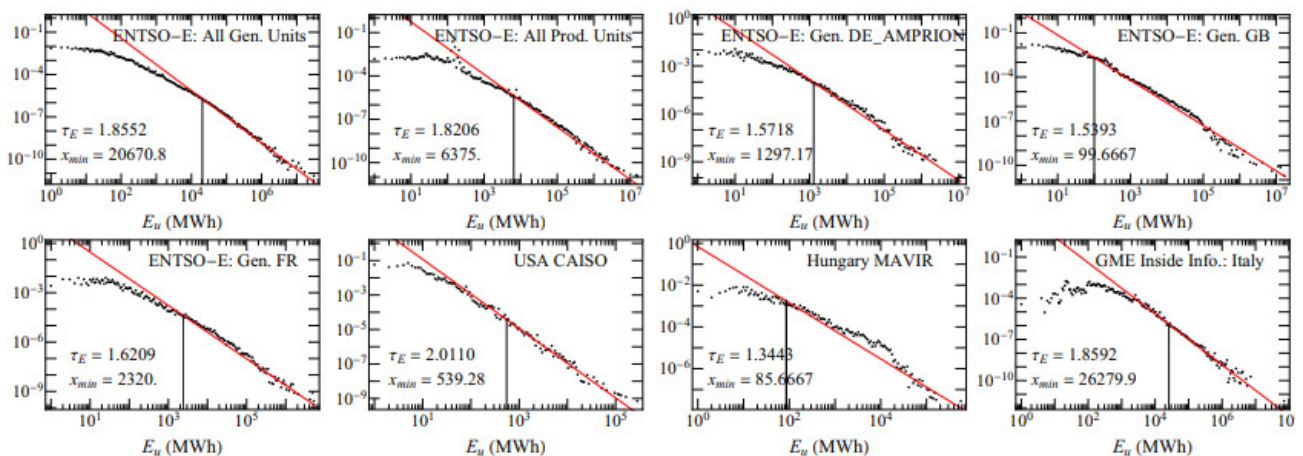


Figure 1: Probability distributions (black dots) of generation outages measured in terms of the unavailable duration. For the ENTSO-E data, we show the generation outage data for the control areas “DE_AMPRION,” “GB,” and “FR,” as well as the generation and production outage data from all control areas. The fitted power laws and their corresponding x_{min} values are marked by solid red lines and vertical black lines, respectively.

The similarities in the graph topological electrical measures between the power-grids of Europe and North America, especially the cable length distributions, suggest a universality hypothesis, which breaks down as we go towards the lower level sub-

systems or as the consequence of under-sampling, like subsets of real data. The latter can very well be observed for the obviously incomplete EU22 power-grid case, which provides results, resembling to smaller regions, like for the USHW, corresponding to the North-West states of the US. In general, universality is expected to occur in the infinite system size limit, according to statistical physics and the behaviour in smaller systems can deviate from it. Our extensive, continent sized analysis provides an opportunity to observe it. We have also shown a frequency fluctuation analysis of Hungarian data that can be described by similar super-statistics and q exponent, as the ones published for the Nordic grid region recently.

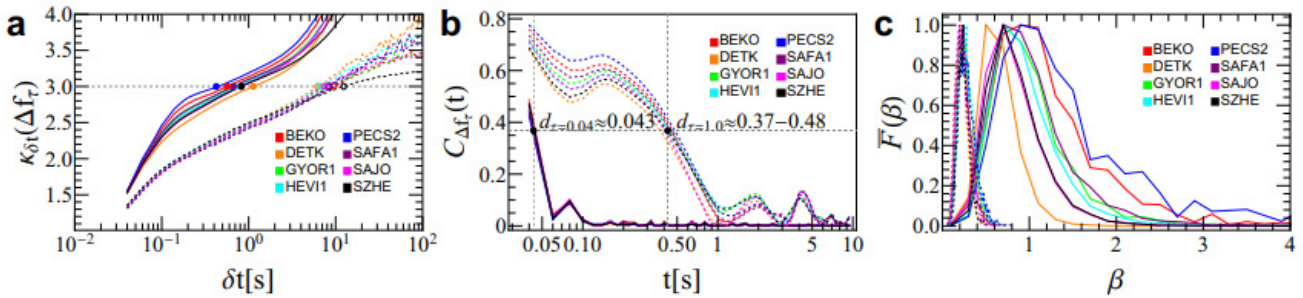


Figure 2: (a) Snippet kurtosis, (b) connected auto-correlation functions, and (c) spectra of frequency increments of different Hungarian substations at time lags $\tau = 0.04$ seconds (solid curves) and $\tau = 1$ second (dashed curves)

Electric power systems ^[4]

The focus area was part of the research and development project 2021-2.1.1-EK-2021-00002 ‘‘Tesseract Energy Storage’’, in which the first NaS battery of Hungary will be installed on the premises of the Centre for Energy Research. In the first half of the year, the public procurement procedure for the battery and converter unit was concluded. A contract was signed with DC-Therm Kft. for the order of the NaS battery from the Japanese NGK Ltd. and the converter unit from the Swiss company IndriveTec AG. Both units were delivered to the Csilleb erc site at the end of January 2024. The technical specification of the site’s electrical connection planning has been prepared. The network connection request has been submitted to EON, and authorization of the inverter is also in progress. We finalized the MATLAB/Simulink parameters of the site and the battery model and examined the operation of the battery in different scenarios, for example, peak shaving, weekdays and weekends.

By the end of 2023, the total installed solar Photovoltaic (PV) capacity in Hungary was planned to exceed 5,500 MWp, of which almost half, roughly 2,200 MWp was to be connected to the low voltage (LV) distribution grid. Considering the proliferation of distributed photovoltaic entities our study aimed to present a method to quantify the renewable hosting capacity of the Hungarian LV networks. Due to the low observability and large extent of the LV grid, there is no local field measurement on most of the topology. For this reason, the Distribution System Operator faces an enormous investment need (i.e.: smart meter, power analyzer acquisition) to reveal and quantify the local grid attributes and assess the remaining hosting capacity level of every LV transformer area. Nevertheless, the effect of locally connected residential energy producers on the network are affected by multiple factors as follows: length and diameter of the cables, distribution of the plants, load pattern of the residents (incl.: the penetration of Electric Vehicles (EVs) and heat pumps) and many other factors. For this reason, every LV transformer area is a unique combination of these variables. To tackle the mentioned challenges, the research work was characterized by the following objectives:

- Use large amounts of real network topology data to guarantee representativeness;
- Create LV test bus systems that can be used to model different network topologies that appear nationally;
- Identify the main factors that influence the local impact of local energy production;
- Develop a model that can quantify the local network effect of distributed energy production.

As an initial hypothesis, we implemented a Monte Carlo sampling procedure based on the evaluation of power flow equations for various operational conditions of the LV network. The procedure is evaluated across representative LV test topologies. The advantage of the Monte Carlo simulation is that it allows to explore the local state (e.g., voltage) of the power grid on a statistical basis without the need for extensive measurements of generation and consumption. Thus, for an electrical parameter of the network (e.g., node voltage), the probability density function of the value at each time instant is determined instead of modelling one single realization of the time series. The following descriptive factors were considered: length of LV lines, PV capacity, and number of households.

Initially, the simulation was run on nine different topologies to investigate the importance of the descriptive variables influencing the renewable hosting capacity. The results showed that line length has a priority over the other factors and should be treated as a primary network descriptor for high PV penetration. The lower figure denotes an illustrative sample of the spatial distribution of voltage limit violation at nodal level. In the meantime, the temporal probability of limit violation is illustrated by the upper graph revealing the influential factor of PV penetration.

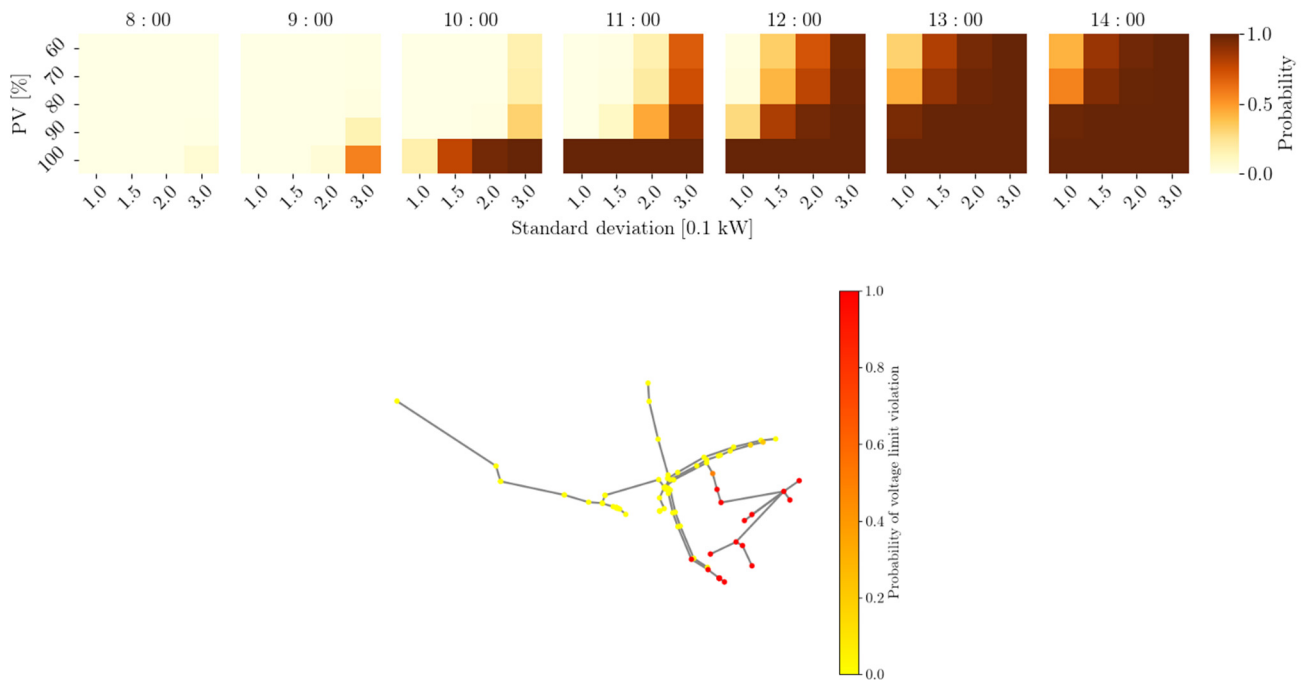


Figure 3: The probability of voltage limit violation in the 8:00-14:00 period of day (top); the location of voltage limit violations on an LV network topology (bottom)

Energy meteorology and climatology [5]

In recent years, with the growing proliferation of Photovoltaics (PV), accurate nowcasting of PV power has emerged as a challenge. Global Horizontal Irradiance (GHI), which is a key factor influencing PV power, is known to be highly variable as it is determined by short-term meteorological phenomena, notably cloud movement. Deep learning and computer vision techniques applied to all-sky imagery are demonstrated to be highly accurate nowcasting methods, as they encode crucial information about the sky's state. While these methods utilize deep neural network models, such as Convolutional Neural Networks (CNN) and attain high levels of accuracy, the training of image-based deep learning models demands significant computational resources. This necessitates the development of resource-efficient methodologies that, in addition to allowing the integration of various data sources, ensure adequate estimation accuracy. To tackle the mentioned challenges, the research work was characterized by the following objectives:

- Use a computationally economic forecasting technique based on a deep learning model;
- Utilize both all-sky imagery and meteorological data for maximum accuracy;
- To decrease the amount of input data, introduce all-sky image features instead of utilizing the images themselves;
- Investigate the forecast accuracy concerning different combinations of meteorological parameters;

We propose a forecasting technique, based on a fully connected Artificial Neural Network (ANN). We utilize both all-sky imagery and meteorological data, however, information on the sky's state is encoded as a feature vector extracted using traditional image processing methods. We introduce multiple all-sky image features (namely cloud cover, cloud inhomogeneity, cloud count and cloud periodicity), decreasing the amount of input data and model complexity. We investigate the forecast accuracy by different combinations of meteorological parameters (scenarios), in particular temperature, pressure, relative humidity, and wind speed. The model is evaluated using two years of measurements from an on-site all-sky camera and an adjacent meteorological station. Our findings demonstrate that the model provides comparable accuracy to CNN-based methods, yet at a significantly lower computational cost.

The ANN models were optimized regarding their hyperparameters and compared in terms of accuracy and resource requirements. The results show that while the composition of meteorological data does not significantly affect accuracy, networks using fewer meteorological data but with more complexity can recognize intricate weather patterns. Overall, it can be concluded that there is no significant impact on the accuracy of estimation, whether the neural network receives sky images or parameter vectors extracted from images as input data. However, there is a substantial difference in the resources required for training the network.

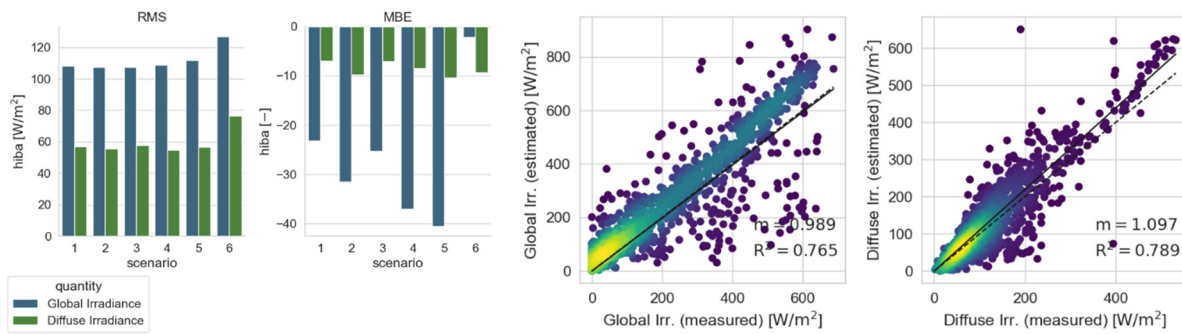


Figure 4: Overall accuracy of the model across the entire dataset (left), Regression plot of scenario 2, the scenarios with the highest accuracy containing all meteorological parameters (right)

Energy statistics [6][7]

In the context of the future of electricity supply, it holds significant importance to determine the appropriate ratios. Specifically, finding the most cost-effective way to reduce the carbon dioxide emissions in the electricity sector using current technologies is crucial. Our team has successfully been developing a modelling tool for many years. This tool enables the optimization of energy systems for regions or countries according to various objective functions. This framework aiming to model the source composition of domestic electricity and heat production has now successfully been expanded to a European scale.

During the modelling process, we selected hourly data on consumption and electricity generation alternatives from the ENTSO-E database, based on which we conducted multi-objective optimization for 36 European countries. A general characteristic of the data used for developing long-term scenarios is the high level of uncertainty, which we addressed through a comprehensive sensitivity analysis. A robust optimization with Monte Carlo simulation was implemented for this analysis. However, the computational requirements of the simulation became manageable only with simplifications, so our calculations were performed on a country-by-country basis. In our calculations, we considered 20 electricity generation alternatives, including pumped storage. In the multi-objective optimization, we implemented individual weighting for each country based on five criteria. This was necessary because, beyond carbon dioxide emissions, it is crucial that energy is not only cost-effective but also reliably accessible, and sourced from environmentally benign origins. In recent times, the security of energy supply has taken precedence over economic and environmental considerations. Nevertheless, during our model calculations, we took into account five factors (economy, air pollution, carbon index, risk of accident and geopolitical factor), each assigned weighting reflecting their significance in the calculations.

Beyond determining the criteria weights for each European country, we conducted the most complex analyses for Hungary. Therefore, we primarily illustrate the opportunities provided by the developed methodology. Our study focuses on the Carbon Intensity indicator, which serves as the primary measure of carbon neutrality established in the European Green Deal. Thus, in the following, we present the results of the Hungarian pilot study based on carbon intensity calculations. Simulation results are shown in Figure 5.

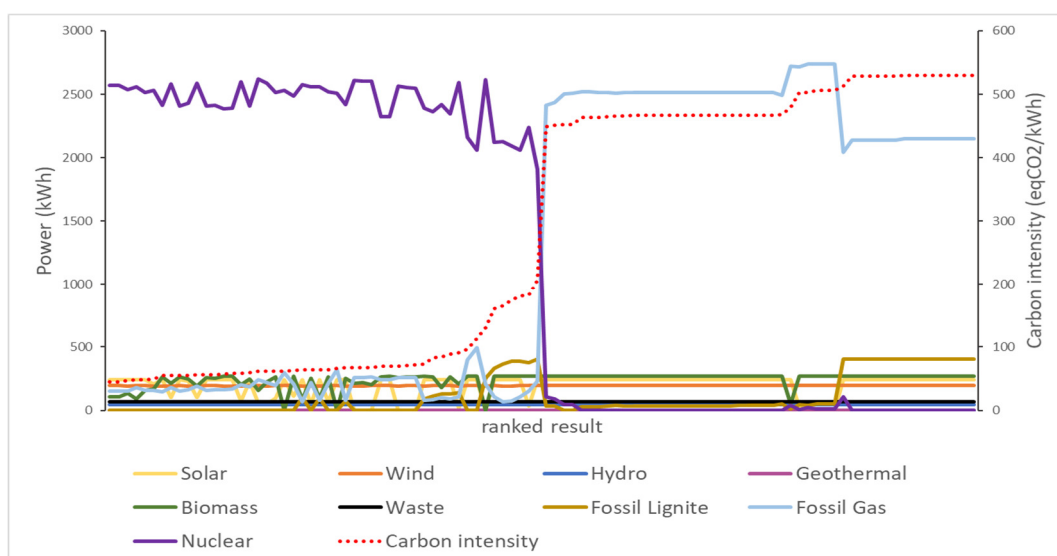


Figure 5: Simulation results ranking the composition of the energy mix in Hungary based on carbon intensity

Findings indicate that nuclear energy is an essential component of Hungary's energy supply, and the existing four units along with the new power plant can seamlessly be integrated into the domestic power infrastructure. This integration can lead to a

reduction in the current carbon intensity from 72.9 gCO_{2eq}/MJ to 12.4 gCO_{2eq}/MJ. If the nuclear capacity remains at its current level, any additional capacity needs may be met, in part, by an increased reliance on natural gas. Under the best-case scenario, this approach can achieve a carbon intensity of 50.6 CO_{2eq}/MJ. However, nuclear energy's exclusion from the energy mix, brought about by highlighting the risk of accidents, leads to a carbon intensity of 129.3 gCO_{2eq}/MJ.

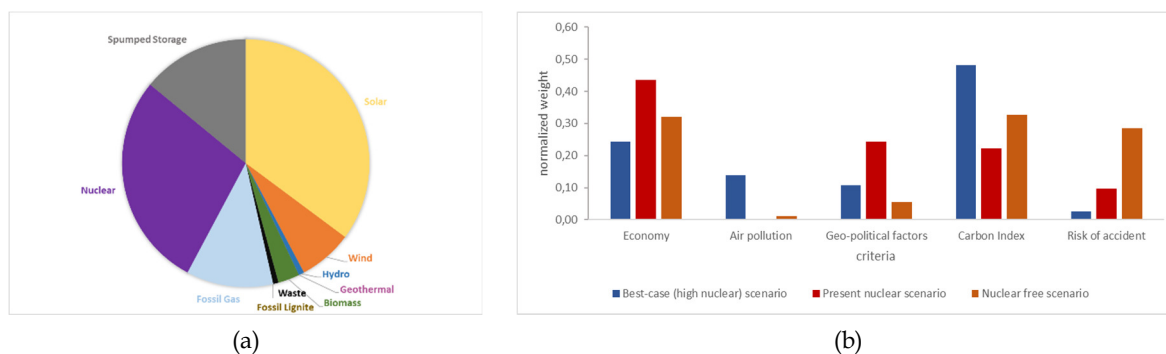


Figure 6: (a) Criteria weights for different scenarios; (b) installed capacity of Hungary for the best-case scenario

In cases where solutions yield the most favourable carbon intensity (Figure 6 (a)), it is unsurprising that the climate impact plays a dominant role, while economic factors take a secondary position (Figure 6 (b)). The current level of nuclear energy coupled with increased natural gas usage becomes prominent when the climate effect's significance diminishes, particularly when considering investment costs and geopolitical risks.

The future reduction of carbon dioxide intensity heavily relies on the advancement of energy storage technologies. This is because relying solely on consumers connected to the "smart electricity grid" for regulation is insufficient. Simultaneously, nuclear energy, as a fundamental power source, cannot easily be replaced. It's vital to emphasize that nuclear energy doesn't compete directly with intermittent renewable sources like solar or wind energy. Instead, it plays a distinct role in ensuring a secure energy supply, much like natural gas (and hydrogen) power plants, which offer flexibility.

PhD studies

Endre Börcsök obtained his PhD this year. The central focus of his PhD research was the utilization of Multi-Criteria Decision Analysis (MCDA) support methodologies within the energy sector. In the initial stages, the MCDA-AHP (Analytic Hierarchy Process) method was applied to assess energy production alternatives, considering 15 different aspects. However, a simple comparison of alternatives falls short of providing sufficient information for making an investment decision. To accurately ascertain the required installed capacity, it is imperative to undertake a comprehensive evaluation of the potential, production, and consumption datasets. To delve deeper into this field, Hungarian and European models were developed. These models utilize hourly demand and production data to identify optimal energy production scenarios, treating it as a distribution problem and taking various criteria into account. This developed multi-objective optimization framework allows for iterative analysis, making it suitable for global sensitivity analysis. In multi-objective optimization, the most critical task is ranking and evaluating the importance of the considered criteria. To determine the criteria weights, a representative survey was implemented with the HUN-REN Centre for Social Sciences, where the energy preferences of Hungarian society were gauged using the MCDA-ANP method. Recently, the energy statistics group has devised a novel approach to define decision preferences. The energy statistics research group assessed the importance of energy decision criteria for European countries by examining historical data series and previous decisions. Combining our modelling tools with expertise in social sciences, the energy statistics research group is currently actively participating in the EUROfusion SES project.

Milán Sörös conducted a successful department defence of his PhD thesis in 2023 and his public defence in January 2024. He developed a simulation framework that considers empirical ageing parameters without a detailed list of electrochemical parameters, and is able to find the optimum according to the user's preference between profit and impact on lifespan during the electricity market operation of the battery system. The presented simulation framework can support investment decision preparation processes by estimating for a longer period of time. During income maximization process the simulation framework takes into account the empirical aging data from literature. In addition, it is capable of supporting the management of daily market decisions when implemented for shorter periods. This version provides the opportunity to manage continuous (even from hour to hour) energy price changes. Based on these, it is demonstrated that the practical utilization of the two methods is different. The first is suitable for supporting longer-term, strategic decisions, while the second supports shorter operating decisions. He also developed a measurement procedure to estimate battery capacity loss based on the measured voltage. It is important to take the first third of the life into account, because the capacity loss of the cells is greater than in the middle part of the life.

Tamás Soha submitted his PhD thesis in 2023. The doctoral thesis consists of two major parts: one about biogas utilization while the other is dealing with power-to-gas technology. The constantly growing fossil fuel dependence from mostly Russian imports poses a threat in these times, when the global energy crisis affects supply safety and results in high energy carrier costs for Hungary. In order to decrease the dependency on natural gas, which is a key factor in the energy transition, carbon-free gaseous substitutes are required in the mid-term. Regarding the biogas part of the thesis, a regional agricultural biomass potential calculation was carried out, using statistical and geodata. Substrate scenarios were created considering different

animal manure and plant biomass rates. Based on their resource needs, spatial distribution, and logistic possibilities, a GIS-based methodology has been developed to define the potential biogas plant locations and their capacities and performances. Results show that the share of plant biomass in the substrate highly affects all the aforementioned indicators, as higher rates are preferred. Concerning the Power-to-Gas (PtG) part, a complex site suitability analysis was carried out in the same study area, considering several spatial factors. These include terrain, protected natural areas, settlements, land use, and infrastructure (power lines, gas grid, water network, district heating systems and roads). The factors were weighted by a multi-criteria decision-making tool, namely AHP, and then the whole area was rated by its suitability for PtG plants. Potential biogas plants from the first part and their attributes were also included, as the necessary CO₂ was assumed to have originated from biogas. The Geographical Information System (GIS) analysis then selected the best sites for PtG development, considering capital investment costs and performance.

Bálint Sinkovics continued his research to model the impact of the generation of small residential-scale PV plants with no metering device on the aggregated (national) load curve. The initial hypothesis of the research was that a new local minimum in the load curve would develop gradually between 10 and 16 hours as the solar penetration increases. To validate this, load data for the years 2019-2022 with very different solar penetration levels were used. Based on the data, two types of clustering were applied: (i) clustering of daily load time series, which gives the typical load curve characteristics, (ii) clustering of load data taking into account mean temperature, the gradient of load reduction after the morning peak load and solar panel penetration.

Lilla Barancsuk conducted research to investigate a solar irradiation estimation method based on an ANN, combining image processing methods and data-driven approaches. The input of the network are meteorological data and sky image features, which characterize the state of the sky, such as cloud cover and average pixel intensity. The ANN model is a multilayer perceptron network comprising highly regularized units of a feed-forward layer, a dropout layer, and a batch normalization layer. Multiples of these units are connected forming a fully connected architecture. The number of units, the number of neurons in the fully connected layers, the learning rate, the dropout rate, and the activation function are determined by hyperparameter optimization. The ANN approach is comprehensively evaluated using multiple meteorological data combinations. For each input combination, the hyperparameters of the ANN are optimized, and the resulting architectures are compared in terms of network complexity and accuracy. The findings indicate that the composition of weather data has no substantial effect on accuracy; however, models operating with reduced meteorological data lead to the development of more complex networks. These intricate networks demonstrate an ability to recognize detailed weather correlations.

Related publications

- [1] B. Hartmann, S. Deng, G. Ódor, J. Kelling: *Revisiting and Modelling Power-Law Distributions in Empirical Outage Data of Power Systems*, PRX Energy **2**, 033007 (2023) <https://doi.org/10.1103/PRXEnergy.2.033007>
- [2] B. Hartmann, I. Papp, K. Benedek, S. Deng, G. Ódor, J. Kelling: *Dynamical Heterogeneity and Universality of Power-grids*, arXiv:2308.15326, submitted
- [3] G. Ódor, I. Papp, K. Benedek, B. Hartmann: *Improving Power-grid Systems via Topological Changes, or How Self-organized Criticality Can Help Stability*, arXiv:2310.09042, submitted
- [4] G. Ballai, M.A. Sörös, L. Vásárhelyi, I. Szenti, R. Kun, B. Hartmann, D. Sebők, F. Farkas, A. Zahoor, G. Mao: *Exploration of Li-ion Batteries during a Long-Term Heat Endurance Test Using 3D Temporal Microcomputed Tomography Investigation*, Energy Technology **11**, 2300207 (2023) <http://dx.doi.org/10.1002/ente.202300207>
- [5] D. M. Günter, L. Barancsuk, V.O. Groma, B. Sinkovics: *Az égboltkamerák szerepe a fotovillamos termelés rövidtávú előrejelzésében*, Elektrotechnika **5-6**, 116 (2023)
- [6] E. Börcsök, V.O. Groma, Á. Gerse, J. Osán: *Determination of Country-Specific Criteria Weights for Long-Term Energy Planning in Europe*, Energies **16**, 4920 (2023) <http://dx.doi.org/10.3390/en16134920>
- [7] T. Soha, V. Sugár, B. Hartmann: *Analysis of PV Potential and Visibility in Heritage Environment Using GIS and LiDAR*, submitted

CHEMICAL EVOLUTION AND RADIONUCLIDE RETENTION STUDIES FOR HIGH-LEVEL RADIOACTIVE WASTE DISPOSAL

Margit Fábrián, János Osán, István Tolnai, Ottó Czömpöly, Barbara Somfai

Objective

The aim of our work was to study the chemical evolution of a steel/concrete and a glass/copper/bentonite system held under conditions like those that could be predicted for a deep geological waste repository. Long-term exposure to repository conditions could result in significant alterations to the Engineered Barrier System (EBS) materials during the service life. The host media can be a source of oxygen, reactive ions and other species that can cause significant alterations to the system during its operation. The effects of radiation, temperature, and mechanical stress must also be considered when various forms of degradation are calculated.

Scale model systems were assembled in such a way that close to real conditions were established. Our model EBS comprises carbon-steel and copper modelling the canister; and concrete and bentonite, modelling the low permeability buffer surroundings. The main goal was to understand the characteristics, applicability, and stability of the whole system, from the structural properties of the canister to the concrete/bentonite response in the repository.

Quantifying the long-term entrapment of radionuclides (RN) in the solid phases of the host rock around the radioactive waste repository is a crucial step toward understanding diffusion and transport mechanisms. Hence, in a separate subproject, sorption and diffusion characteristics of a cation representing a key RN (Ni^{2+}) were studied on clay-rich rock sections of the Boda Claystone Formation (BCF). Irreversibly formed Ni-containing phases in the natural BCF rock sample were investigated on the nanoscale using transmission electron microscopy coupled with energy-dispersive X-ray spectrometry on suspension samples through the identification of individual mineral phases and their composition. The sorption reversibility was also studied in equilibrium conditions using isotope exchange involving inactive Ni^{2+} ions and radiotracer (^{63}Ni). Competitive sorption of Ni^{2+} and Co^{2+} ions on crushed BCF rock samples (and petrographic thin sections) studies aimed at the distribution of competing ions at sorption sites.

Methods

To get information on the effect of long-term exposure, a scaled-down model system was assembled with close to realistically expected disposal conditions to understand the chemical evolution of the contacting material surfaces and the stability of the system, all the way from the structural and dissolution properties of the modelled container system to the buffer response in the repository. Both of our experiments were carried out with three identical model setups containing steel-concrete and copper-bentonite. To provide the necessary physical conditions, each prepared model setup was embedded into an external and an internal Teflon container. During the experiments, all the three steel/concrete setups were fully saturated by conditioned MQ-water (Ultrapure Grade 1 water) and the three glass/copper/bentonite systems were saturated by synthetic BCF-groundwater.

The steel/concrete experimental setup was prepared in triplicate, for each cell two Teflon containers were built to enable water saturation of the test samples during the experiments. The concrete was poured into the Teflon moulds placing the C-steel container in the centre. The core of the cell was composed of a steel container with a height of 45 mm and a diameter of 20.64 mm. The internal Teflon container had a height of 100 mm and a diameter of 50 mm. The internal Teflon container surface area was about 140 cm² and 5 holes with 0.7 mm diameter were randomly drilled through it to ensure saturation. The external Teflon container had a height of 160 mm, a diameter of 90 mm, and was used as a container for soaking water, which was made by mixing 77 g of crushed concrete with 700 ml of MQ-water for three days. Each experimental setup was weighted monthly to exclude leakage. All three cells were sealed to maintain anoxic conditions. A constant temperature of 80 ± 2 °C was imposed during the whole experiment. The corrosion potential was monitored using a Pt reference electrode. One of the experimental setups was opened for post-mortem characterization after 3, 7 and 12 months (hereafter referred to as SC-3M, SC-7M, SC-12M with SC for Steel/Concrete). After disassembling the experimental setup, the C-steel containers were covered with adherent concrete, making direct characterization of the steel surface difficult. The corrosion interfaces were thus investigated in cross-section by Scanning Electron Microscopy - Energy Dispersive X-ray Spectrometry (SEM/EDX) and micro-Raman methods. The solutions were analyzed by Inductively Coupled Plasma Optical Emission Spectroscopy (ICP-OES) and Ion Chromatography (IC).

The glass/copper/bentonite experimental setup was prepared in triplicate, for each cell two Teflon containers were built to enable water saturation of the test samples during the experiments. The internal vessel contained a mixture of bulk glass (borosilicate), copper pieces (rod, tape, sliver) and B75-type bentonite (crushed, <100 µm fraction). The environmental conditioning of the model setup due to the BCF groundwater was carried out at room temperature. The external vessel contained the enclosed internal vessel as well as 75 ml of groundwater. To ensure the continuous saturation of the system, holes with 0.7 mm diameter were randomly drilled through the walls of the internal vessels. All the containers were filled with the same glass/copper/bentonite mixture and kept in an incubator at 80 °C. After periods of 3, 6 and 9 months one container was opened for post-mortem characterization and named as GCuB-3M, GCuB-6M and GCuB-9M, respectively. A portion of the initial glass/copper/bentonite mixture was preserved and kept dry for reference, and an initial sample of the groundwater mixture used was also preserved for similar purposes. Post-mortem characterizations of the solid phase were performed using Scanning Electron Microscopy (SEM), Energy Dispersive X-ray spectroscopy (EDX) and X-ray Photoelectron

Spectroscopy (XPS). With the Inductively Coupled Plasma Optical Emission Spectroscopy (ICP-OES) and Ion Chromatography (IC) analyses of the liquid phase we predict the chemical durability of the system, thanks to the obtained leachates at each stage of the experiments.

Sorption and diffusion characteristics of the BCF host rock for Ni^{2+} were also studied. Sorption of Ni^{2+} was investigated both alone and in the presence of Co^{2+} on both crushed rock samples and petrographic thin sections using conditioned synthetic BCF groundwater for the solutions holding the Co and Ni cations. Sorption isotherms (sorbed amount as a function of the equilibrium concentration, $C_{\text{eq}}(\text{M})$, in the liquid phase) were recorded through batch experiments in the 10^{-6} - 10^{-2} M equilibrium concentration regime using non-radioactive ions of interest. Equilibrium concentrations in the liquid phase were determined using ICP-OES. To investigate the reversibility of sorption, radiotracer $^{63}\text{Ni}^{2+}$ was added to the suspensions, which were already in equilibrium with inactive Ni^{2+} . After 30 days, liquid scintillation counting was performed on the liquid phases of both the initial suspensions and those equilibrated with $^{63}\text{Ni}^{2+}$. The adsorbed fractions were calculated for both the inactive and active Ni and compared to determine the reversibly adsorbed part of Ni.

Diffusion cells accommodating 4-6 mm thick slices of full diameter (62 mm) core sections were used. To monitor the diffusion in the rock, the changes in concentration of Ni and Co during the experiment lasting several months were measured in the liquid phase using ICP-OES. Initial Ni/Co concentrations in the range of 10^{-3} - 10^{-2} M were applied.

In order to identify newly formed nickel-rich phases, particles were transferred from suspensions of crushed rock treated with inactive Ni^{2+} at the high concentration regime (10^{-3} - 10^{-2} M) onto copper mesh grids coated with lacey carbon support film. Cross-sectional transmission electron microscopy (XTEM) technique was used to study the particles in BCF. This measurement was carried out using a FEI-Themis (Scanning) Transmission Electron Microscope (STEM) equipped with a Cs corrected objective lens in High Resolution Transmission Electron Microscope (HRTEM) mode, which provides a point resolution of approximately 0.07 nm. The microscope was operated at 200 kV.

Results

Connected to the 431

Fig. 1 gives the relationship of corrosion potential with months of exposure. The evolution of the corrosion potential measured on the three steel/concrete setups (3M, 7M, 12M) follows the same characteristics at all stages of experiments. The strongly negative values during the first two months are linked to the corrosion of the C-steel. Afterwards, the potentials decrease to reach small constant positive values that are assumed to be driven by the formation of a passivation layer. Film passivation in less than 50 days is notable for all three setups.

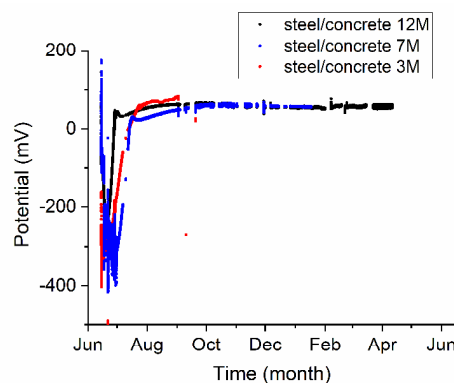


Figure 1: Evolution with time of the measured corrosion potentials on the standard hydrogen scale for the three cells at 80 °C

Fig. 2 a, b, c present SEM images of the steel/concrete interfaces after 3, 7, 12 months of experimental time. There is no indication of voidage or free space in between the concrete and the steel. The pouring of the concrete had led to tight interfaces since the beginning of the experiment. On each of the three samples the formation of 20-60 μm long Fe-oxide ingrowths were detected. These SEM results show that micro-cracks appeared even in a short term (3 months) and could have initiated changes of the carbon steel surface (Fig. 2 a). However, these ingrowths remained relatively short and did not exceed 100 μm in length after 7 and 12 months (Fig. 2 b, c).

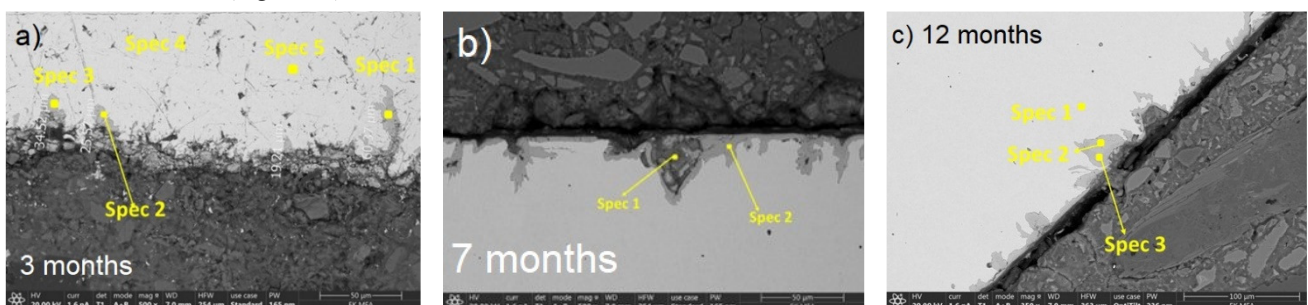


Figure 2: SEM micrograph of the steel-concrete interface after 3 (a), 7 (b) and 12 (c) months

Table 1 gives the results of the SEM-EDX analyses for minerals at the corrosion interfaces after 3, 7 and 12 months based on the points marked in Fig. 2. Corrosion products after 3 months consisting of Fe - O can be distinguished from the C-steel, which is primarily composed of Fe. The EDX analyses after 7 months with again a Fe - O signature typical of iron oxide corrosion products (Spectrum 2), but there is also a mixed signal composed of Ca - Al - Si - S and Fe oxide.

Table 1: SEM/EDX elemental composition at selected positions after 3-7-12 months (wt. %)

Spectra	O	Mg	Al	Si	Ca	S	K	Mn	Fe	Cl/Ti
3 months										
Spec 1 corr prod	47.09	-	-	1.67	0.16	-	-	0.36	50.72	-
Spec 2 corr prod	44.01	-	-	0.18	0.18	-	-	0.28	55.38	-
Spec 3 corr prod	47.64	-	-	0.47	0.11	-	-	0.21	51.57	-
Spec 4 C-steel	-	-	-	0.65	-	-	-	0.59	98.76	-
Spec 5 C-steel	-	-	-	0.97	-	-	-	0.61	98.42	-
7 months										
Spec 1 conc/corr prod	56.45	3.43	2.41	12.10	3.59	0.51	0.08	0.15	21.13	0.05/0.06
Spec 2 corr prod	46.84	-	-	0.34	0.14	-	-	0.37	52.31	--
12 months										
Spec 1 C-steel	-	-	-	0.46	-	-	-	-	99.54	-
Spec 2 corr prod	51.46	-	-	-	0.08	-	-	-	48.46	-
Spec 3 corr prod	58.26	-	-	-	0.12	-	-	-	41.62	-

According to the results of the SEM-EDX, the corrosion process had an impact on the steel-concrete interfaces. With micro-Raman investigations mainly magnetite (Fe_3O_4) and hematite ($\alpha\text{-Fe}_2\text{O}_3$) could be identified as corrosion products after 3 months (Fig. 3a) and 7 months (Fig. 3b). The corrosion protrusion is formed of magnetite, no other corrosion products could be identified by micro-Raman. After 12 months of experiments, no substantial change in the Raman spectra was observed (Fig. 3c). Mainly magnetite and hematite were still detected. For all the exposure periods tested, magnetite was identified as the main corrosion product. No iron-carbonates or iron-sulphides were identified.

The liquid phase (soaking water) was sampled from the external Teflon container after 3, 7 and 12 months. Ca, K, Mg, Na and Si concentrations were determined using ICP-OES, while IC was used for Cl^- and SO_4^{2-} (Table 2). The Na and Ca concentrations progressively, but moderately increased with time. The concentration of K and Si did not change significantly. Higher Mg concentration was measured after 12 months. The evolution of chloride and sulphate concentrations was less smooth, but the increase after 12 months was near 25% for chloride and 50% for sulphate.

Table 2: Evolution of the chemistry of the aqueous solution sampled in the external Teflon container

Concentration [mg/L]	Ca	K	Mg	Na	Si	Fe	Al	Cl^-	SO_4^{2-}
Soaking water	97	24	2	219	43	0.4	0.8	505	100
3 months	-	-	-	-	-	-	-	449	157
7 months	117	19	1	238	44	<DL*	<DL	505	115
12 months	135	26	18	299	47	<DL	<DL	618	145

* DL stands for detection limit.

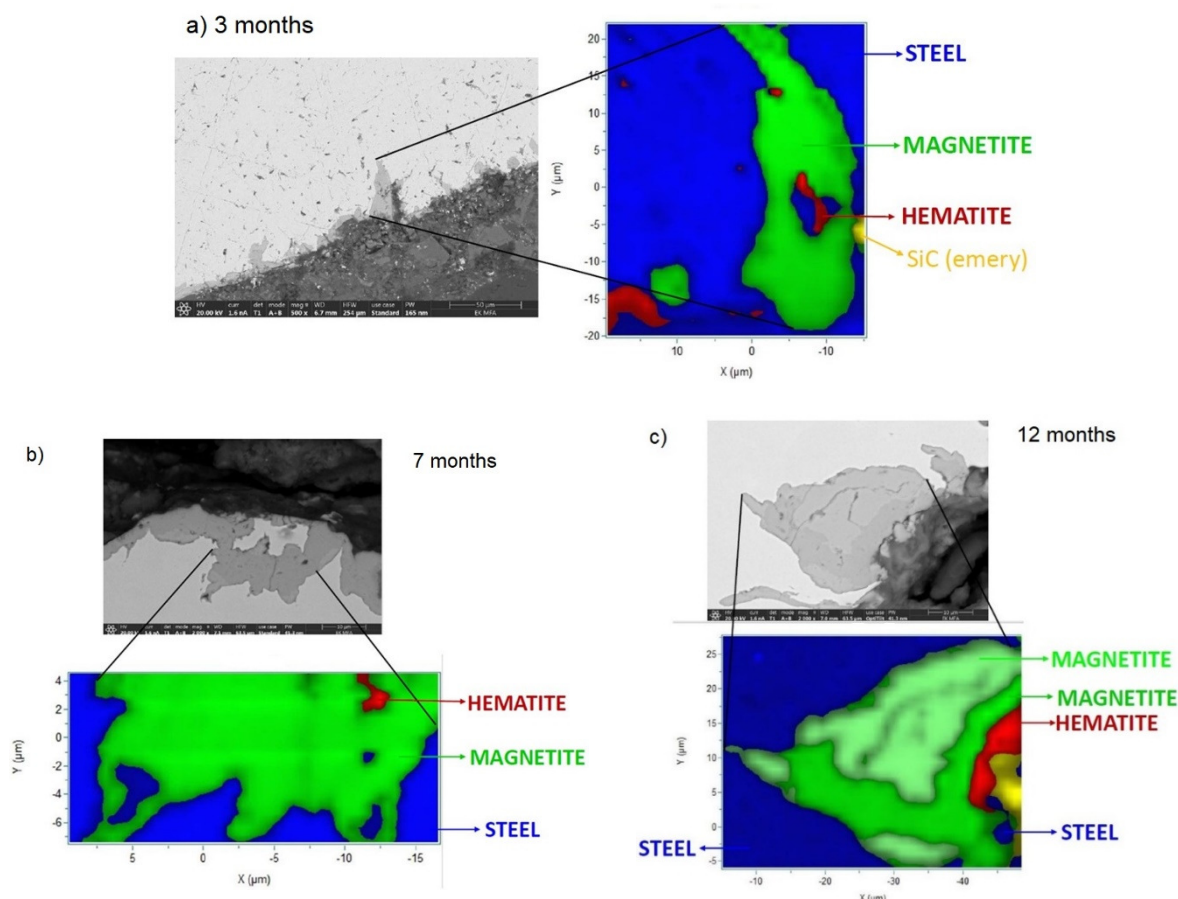


Figure 3: Micro-Raman mapping obtained after 3 months (a), 7 months (b) and 12 months (c)

The current experimental setup examined the combined chemical evolution of two major components, namely the waste canister and the concrete buffer, used in deep geologic disposal at a temperature of 80 °C. The materials chosen for analysis, S235JR carbon steel and CEM II/B based concrete, are commonly used as reference materials in the Hungarian disposal concepts. However, the findings are applicable to other disposal systems and engineering barriers as well. During the experiments, it was observed that a uniform corrosion process occurred, resulting in the rapid passivation of the C-steel cylinders. Throughout the entire 12-month duration of the experiment, magnetite was identified as the primary corrosion product, even after only 3 months of exposure. The results show that the passivation of the containers under the tested conditions is promising for further investigations. [More details in the Ref. 1]

Connected to the 130

After 3- and 6-month exposure to the groundwater, the setups were opened for post-mortem characterization. The last setup, signed with 9 months, is still in progress. During the 3- and 6 months experiments, the corrosion potential was continuously monitored (Cu vs. Pt electrode in bentonite). The corrosion potential measured in the first month (both cases) shows an increasing trend, then changes to a constant value, and a plateau is formed, which indicates the formation of a passive layer. The positive values indicate the presence of oxidic conditions in the test system.

With SEM/EDX investigations we focused on the composition and nature of alteration products formed on the glass/copper and within the bentonite. Slight corrosion behaviour appears on the Cu-rod but no S species are detected in the corrosion product layer.

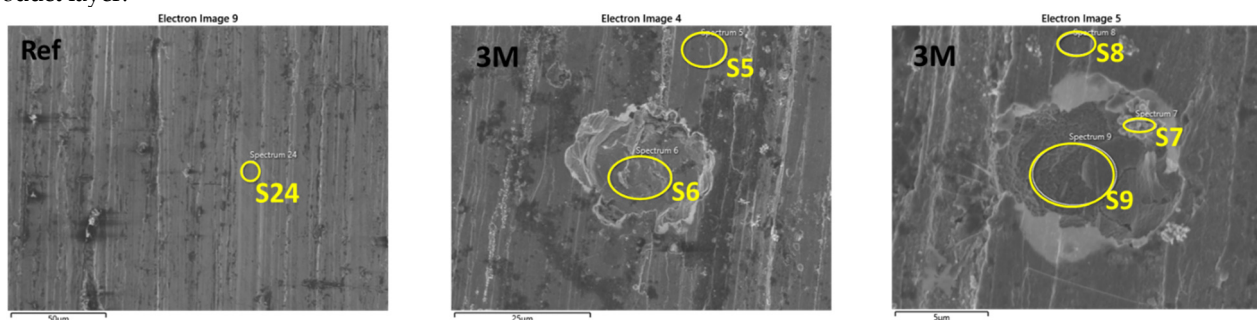


Figure 4: SEM micrograph of the copper-rod interface after 3 months

Table 3: SEM/EDX elemental composition at selected positions after 3 months (wt. %)

Element	Reference (Spec 24)	Spec 5	Spec 6	Spec 7	Spec 8	Spec 9
C	3.23	5.93	4.01	12.01	3.78	3.4
N	-	1.37	-	-	-	-
O	0.58	4.85	6.32	4.44	6.07	-
Si	-	0.36	0.97	1.72	0.46	-
S	-	5.39	2.36	16.22	3.74	6.05
Ti	-	-	-	-	12.18	-
Cu	96.19	82.11	86.35	65.62	73.77	90.56
Total	100.0	100	100	100	100	100

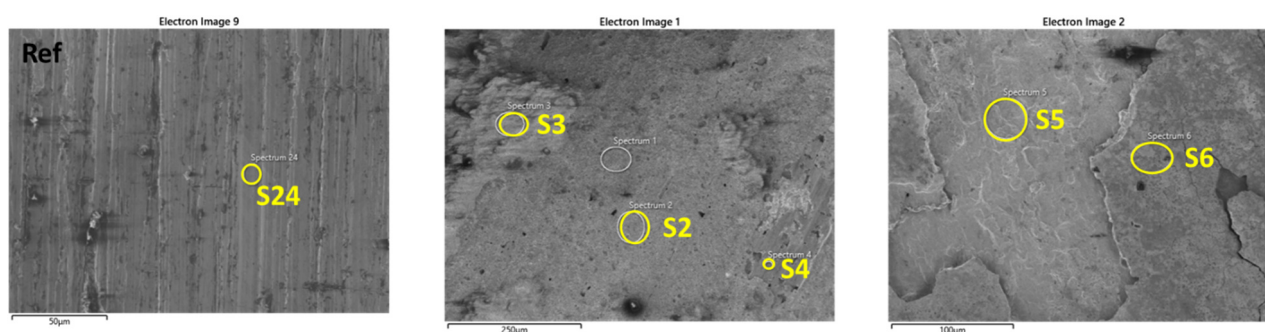


Figure 5: SEM micrograph of the copper-rod interface after 6 months.

Table 4: SEM/EDX elemental composition at selected positions after 6 months (wt. %)

Element	Reference (Spec 24)	Spec 2	Spec 3	Spec 5	Spec 5	Spec 6
C	3.23	2.25	2.73	1.67	3.31	8.07
O	0.58	18.65	38.34	9.8	12.52	21.14
Na	-	-	0.62	-	-	-
Mg	-	0.87	2.67	-	-	-
Al	-	2.51	6.86	-	-	0.4
Si	-	6.43	22.79	-	0.25	1.43
S	-	-	-	-	-	-
K	-	1.16	2.79	-	-	-
Fe	-	2.42	4.69	-	-	-
Cu	96.19	65.71	18.51	88.53	83.82	68.96
Total	100	100	100	100	100	100

After the completion of the 3- and 6-month experiments the groundwater solution was analyzed by ICP-OES/IC. The measured K and Na concentrations increased, while the Ca, Mg and Si concentrations decreased. Concentrations of Cl⁻ and SO₄²⁻ ions as determined by ion chromatography in the final pore water show an increasing tendency from the initial soaking water and in function of time.

Table 5: Evolution of the chemistry of the aqueous solution sampled in the internal Teflon container

Concentration [mg/L]	Ca	K	Mg	Na	Si	Cu	B	Cl ⁻	SO ₄ ²⁻	pH	Cond. (µS/cm)
Soaking water	124±5	7±0.3	58.3±2	391±15	5±0.3	NA	NA	872±43	192±9	8.03	3389
3 months	39.8±2	28±1	32.8±1	970±39	5.2±0.2	LOD	1.1±0.1	954±48	309±15	7.05	3354.2
6 months	28.3±2	27.7±3	25.6±3	844.8±27	2.9±3	LOD	1.1±0.2	1003±13	355±11	7.87	3353.9

Supplementary surface analysis was carried out for the glassy samples after 3 and 6 months with XPS directly on the 55mol%SiO₂-10mol%B₂O₃-25mol%Na₂O-5mol%BaO-5mol%ZrO₂ matrix glass to observe changes and possibly formation of secondary phases. Measured spectra were evaluated by determining the peak intensities. Detected peaks: Si 2p (92eV), O 1s (532 eV), B 1s (186eV), Ca 2p (350eV), Ba 3d (780eV), Zr 3d (182eV) as well as 3p (336eV), K 2p (292eV), Mg KL2(310eV), Na 1s (1072eV), C 1s (284 eV), 3 independent positions/samples measured. Decomposition of complex peak shapes with peak fitting algorithm was applied where necessary: - B: B1s interferes with Zr 3d doublet and Mg KL4 peak and Ba 4p 1/2;

- Ca 2p: interferes with Zr 3p doublets. Component concentration was calculated with sensitivity factors from ALTHERMO1 library by assuming a homogeneous target.

Table 6: The calculated composition (atomic %) from the results of XPS measurements. The error is <1%.

	Si2p	Zr3d	O1s	Ba3d5	Na1s	Ca2p3	K2p	MgKL1	B1s	Sum
Reference	20.5	1.68	60.80	1.5	11.73	0.8	0.47	1.37	2.0	100
3 months	17.63	7.77	67.86	0.30	2.87	1.87	0.50	0.77	0.50	100
6 months	14.96	9.34	69.60	0.21	2.17	0.46	0.46	1.1	0	100

We investigated the effect of bentonite on the chemical behaviour of copper and borosilicate glass in repository concepts (saturated media, constant 80°C). Early corrosion behaviour appears after 15 days, this layer may initially partially passivate the Cu, which is unstable in the presence of dissolved O₂ and is at least partially converted to a layer of Cu₂O. After 75 days of exposure, the corrosion potential doesn't change. Based on SEM/EDX the surface layer is built-up by Cu₂O, Cu₂S and CuCO₃[Cu₂CO₃(OH)₂ (malachite), cupric chloride (CuCl₂·3Cu(OH)₂-atacamite]. We continued the experiments, which ended at the end of November. [3]

Connected to the 432

The sorption isotherms of Ni(II) and Co(II) were found to be similar if only Ni(II) or Co(II) ions were added to the synthetic pore water in batch experiments (Fig. 6, left). In the high concentration region (10⁻²–10⁻⁴ M) where adsorption mainly occurs via ion exchange and formation of a new phase is dominant, Ni has higher K_d values, meanwhile in the 10⁻⁶–10⁻⁴ M region (where adsorption takes place at the weak sites) the K_d values of cobalt are higher and get closer (half order of magnitude lower) to the ones collected without competitive conditions [4,5].

Ni(II) sorption reversibility was studied by adding ⁶³Ni radiotracer while keeping the equilibrium conditions. The isotope exchangeable fraction is determined by both the availability of strong sorption sites and the formation of new phases. The maximum reversibility was found as 0.7 that can be explained by the contribution of strong sorption sites (Fig. 6, right). As the strong sites reach saturation at around 10⁻⁷ M equivalent concentration for illite, the sorption reversibility is expected to increase with increasing concentrations. However, the formation of a new phase causes a decrease of reversibility reaching as low as 0.3 for the highest concentration studied $C_{eq} = 5 \times 10^{-4}$ M [4, 5].

Diffusion experiments and modelling of Ni(II) and Co(II) through-diffusion in BCF rock samples revealed a higher apparent diffusion coefficient (D_a) and a lower rock capacity factor (a) for Ni(II) than Co(II), both separately and in competitive conditions, applying the same initial concentration. Smaller a and higher D_a values were obtained for higher initial concentrations. D_a was found to be in the range of 10⁻¹³ m²/s, similarly to selenium at high concentrations [6, 7]. From the rock capacity factor, K_d values were calculated. Compared to the adsorption isotherm data they tend to be lower, however, the results of transferability from compacted to diluted systems should be taken into consideration (in a compacted system K_d is lower at the same concentration).

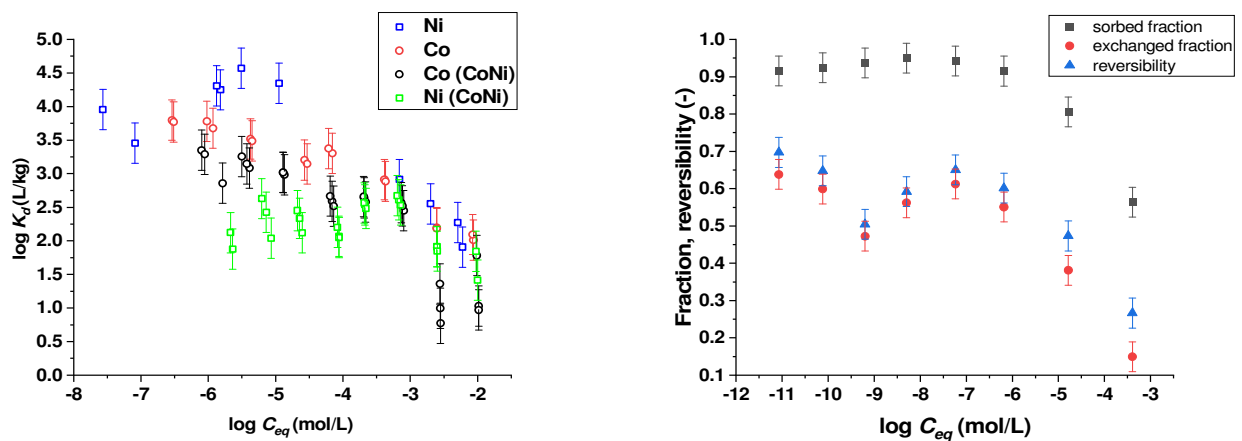


Figure 6: (left) Distribution coefficient (K_d) versus equilibrium concentration (C_{eq}) obtained at pH=8. Co and Ni mean the radionuclides were separately present, while Co (CoNi) and Ni (CoNi) show the data obtained for Co and Ni in competitive conditions, respectively. (right) Sorbed, exchanged fraction and reversibility as a result of isotope exchange experiments with inactive Ni and ⁶³Ni radiotracer.

Connected to the 125

Batch sorption data of Ni(II) on Boda Claystone were underpredicted with the 2-site protolysis of non electrostatic surface complexation and cation exchange sorption model for illite at the high-concentration range above 10⁻⁶ M. It was confirmed by Extended X-ray Absorption Fine Structure (EXAFS) studies that surface-induced precipitation of Ni solids occurs in addition to sorption via surface complexation and ion exchange phenomena. Neoformed Ni phyllosilicate particles were identified on montmorillonite treated with high Ni concentrations by TEM suggesting that the irreversibly formed Ni phases can be

identified on the nanoscale in natural argillaceous rocks as well. TEM and EDS investigations were performed on individual particles. In accordance with the presumptions, no adsorbed Ni on rutile, albite and hematite was identified. Ni was found to be connected to crystallites of clay minerals characteristic for BCF (illite and chlorite), which were identified based on the layer distances of $R=10 \text{ \AA}$ (illite) and $R=14 \text{ \AA}$ for chlorite (Fig. 6). Ni was enriched on the edges of particulates with a double concentration of Fe (Fig. 7, Table 7). The formation of a new Ni-containing phase was confirmed at the nanoscale but its unambiguous identification needs further investigation [4, 5].

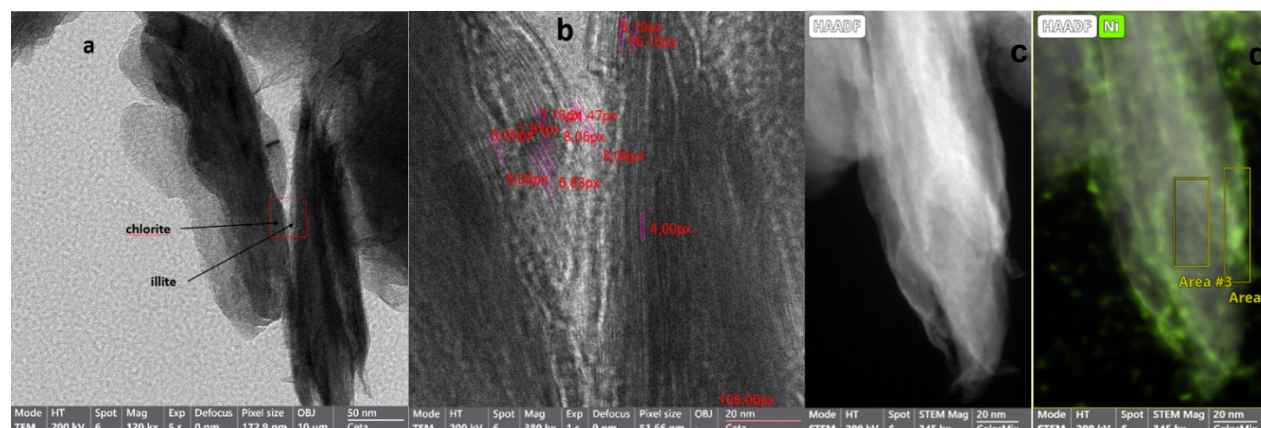


Figure 7: TEM image of the overlapping particles (a), high-resolution image of the overlay with visible lattice spacing (b), annular dark-field image (c) and nickel elemental map (d) of the investigated area around the illite particle. Particles could be classified based on lateral distances: chlorite (lattice spacing of $8.06 \text{ px} \approx 14 \text{ \AA}$) and illite (lattice spacing of $5.2 \text{ px} \approx 10 \text{ \AA}$). Enrichment of nickel was identified and the composition of main elements (Si, Mg, Al) of the nickel-rich phase altered from illite (Table 7).

Table 7: Elemental composition of the studied area presented in Figure 6 c-d. Area 1 (full) gives the composition of the whole map, Area 2 corresponds to the nickel-rich phase around the illite particle and Area 3 gives the average composition of the illite particles treated with Ni ($C_i = 10^{-3} \text{ M}$).

Element	at%	+/-	at%	+/-	at%	+/-
	Area 1 (full)		Area 2		Area 3	
O	57.92	2.07	56.4	1.96	55.69	2.11
Na			1.35	0.36	1.17	0.27
Mg	6.57	1.25	4.36	0.88	9.31	1.72
Al	9.19	1.68	7.87	1.47	9.7	1.77
Si	13.07	2.21	11.18	1.95	12.16	2.09
Cl	0.36	0.07	0.62	0.19	0.21	0.09
K	1.04	0.18	1.1	0.26	0.69	0.15
Ca	0.24	0.03	0.41	0.12	0.23	0.06
Fe	5.52	0.72	5.16	0.7	6.93	0.9
Ni	6.09	0.87	11.55	1.56	3.92	0.58

Connected to the 128

The most feasible and accepted way for storage of high-level radioactive waste is the vitrification process, where the active elements are melted into a glass form, and then deposited in a deep geological formation. A new borosilicate glass formula containing mixed lanthanides and uranium with different concentrations was developed, with the highest waste/glass ratio known to date. A combination of neutron- and X-ray based techniques is needed to determine their structure, due to the complementary scattering character of neutrons and X-rays. The local environment of U, Ce, Nd, Eu ions was studied, which serves the immobilization of high-level wastes. Amorphous samples were investigated using X-ray Absorption Near-Edge Structure (XANES) and Extended X-ray Absorption Fine Structure (EXAFS) in transmission mode at Diamond Light Source B18. The composition of the samples are: $(100-x)\text{wt\%Matrix}+x\text{wt\%UO}_3$, $x = 10, 20, 30, 40$. (The Matrix composition: $[55\text{mol\%SiO}_2-10\text{\%B}_2\text{O}_3-25\text{\%Na}_2\text{O}-5\text{\%BaO}-5\text{\%ZrO}_2]$, with sign of M1, M2, M3, M4, respectively.) The EXAFS evaluation of the samples containing uranium revealed that the U in the glass structure differs from the initial UO_3 form used during the synthesis and based on the fitting model around 48-66 wt% of uranium remains in the U(VI) form as uranyl with linear arrangement with 2 O atoms ($\text{O}=\text{U}=\text{O}$) and 6 oxygen atoms in an equatorial plane and U(V) in tetrahedral, octahedral and 8-fold coordination based on the fitting model. The mixed valance of U as U(V) and U(VI) was verified by XANES.

Table 8: Best EXAFS fit results of U local environment.

	% U ⁶⁺	R (Å)	DW (x10 ⁻³ Å ²)	R (Å) (±0.02)	DW (x10 ⁻³ Å ²)
M1	48 ± 6	1.83 ± 0.01	1.7	2.13	6.5
		2.27 ± 0.03	4.3		
M2	46 ± 8	1.83 ± 0.01	1.2	2.12	6.2
		2.27 ± 0.03	3.8		
M3	59 ± 5	1.85 ± 0.01	3.2	2.10	3.1
		2.27 ± 0.03	1.6		
M4	46 ± 3	1.84 ± 0.01	1.3	2.11	7.9
		2.26 ± 0.03	3.6		

Based on the initial findings, the samples containing cerium exhibited a distinguishable transformation from Ce(IV) to Ce(III). Despite the addition of cerium in the form of CeO₂ during the glass preparation, the Ce component was exclusively observed in its trivalent state within the final samples. The analysis indicated that the oxidation state of Eu and Nd remained unchanged throughout, with both elements observed predominantly in the form of Eu(III) and Nd(III). Preliminary evaluation of the XANES/EXAFS spectra revealed that no formation of Eu(III) or Nd(III) clusters were detected in the glass structure. During the EXAFS evaluation of the Matrix-UCeNdEu sample, a noticeable distinction in the R-space becomes apparent, in the second neighbours of U an additional broad peak distribution appears within the range of 2.5-3.5 Å.

This work was supported by the H-2020 European Joint Program on Radioactive Waste Management (EURAD) – 847593. Research is part of the PhD work of O. Czömpöly (125) and I. Tolnai (128). Both PhD students have successfully completed the complex exam and are preparing the related publications.

Remaining work

This was the last year of a five-year EURAD-847593 project.

Related publications

- [1] M. Fabian, O. Czömpöly, I. Tolnai, L. De Windt: *Interactions between C-steel and blended cement in concrete under radwaste repository conditions at 80°C*, Scientific Reports **13**: 15372 (2023), DOI: 10.1038/s41598-023-42645-6 <http://dx.doi.org/10.1038/s41598-023-42645-6>
- [2] I. Tolnai, J. Osan, O. Czömpöly, A. Sulyok, M. Fabian: *Glass/steel/clay interactions in a simulated radioactive waste geological disposal system*, Scientific Reports **13**: 20381 (2023), <http://dx.doi.org/10.1038/s41598-023-47578-8>
- [3] M. Fabian, O. Czömpöly, B. Somfai, I. Tolnai: *Characteristics of a glass/copper/bentonite model system under repository conditions*, lecture at the EUROCLAY2023, 23-27 July, 2023, Bari, Italy.
- [4] O. Czömpöly, F. Szabo, T. Kolonits, Z. Fogarassy, J. Osan: *Migration properties of nickel in Boda Claystone Formation*, lecture at the EUROCLAY2023, 23-27 July, 2023, Bari, Italy
- [5] O. Czömpöly, F. Szabo, T. Kolonits, Z. Fogarassy, D. Zambo, L. Van Laer, M. Aertsens and J. Osan: *Migration properties of nickel and cobalt in Boda Claystone Formation*. Manuscript in preparation
- [6] O. Czömpöly, M. Fábíán, T. Korányi, G. Nagy, Z.E. Horváth, S. Pollastri, I. Zizak, M. Aertsens and J. Osán: *Adsorption and diffusion of selenite on Boda Claystone Formation*, Applied Clay Science **241**, 106997 (2023) <https://doi.org/10.1016/j.clay.2023.106997>
- [7] J. Osan, O. Czömpöly, T. Korányi, S. Pollastri, I. Zizak: *Retention of selenite on the host rock of a potential high-level radioactive waste repository*, lecture at the EUROCLAY2023, 23-27 July, 2023, Bari, Italy

METHODOLOGY DEVELOPMENT FOR THE INVESTIGATION OF THE ELEMENTAL AND ORGANIC CARBON CONTENT OF SIZE-FRACTIONATED ENVIRONMENTAL AEROSOL SAMPLES

Szilvia Kugler, Veronika Groma, Endre Börcsök, János Osán

Objective

Carbonaceous aerosols containing Organic Carbon (OC) and Elemental Carbon (EC) are important components of the atmospheric aerosol mass up to 20-50%. Their proportion in the total mass in fine ($d < 2.5 \mu\text{m}$) and ultrafine ($d < 100 \text{ nm}$) size range can be even more significant. Numerous analytical procedures and monitoring equipment are available to determine the EC and OC content of the aerosols using thermo-optical methods, but they are destructive and not suitable for low mass size fractionated samples. It is known from the literature that certain parameters obtained by Raman spectroscopy and the five-band curve fitting (G, D1-D4) can be suitable for the determination of the chemical structure of graphene and other carbonaceous materials, but the methodology for evaluating environmental samples is not well developed.

The goal of our study is to develop a methodology that is suitable for determining the elemental and organic carbon content of size fractionated aerosol samples collected during a short measurement time of up to a maximum of four hours. The methodology is based on the combination of cascade impactor sampling and Raman spectroscopy. Due to the non-destructivity of the chosen analytical method, the collected samples are readily available for complementary microscopy and spectroscopy for elemental and morphological analysis of aerosol particles.

Principal Component Analysis (PCA) is a widely used statistical technique that facilitates the reduction of data dimensionality, which could be used for the evaluation of Raman spectral data. Our objective was to demonstrate that the estimation of EC and OC content in each aerosol sample could be achieved based on appropriately selected principal components.

Methods

The environmental samples were collected during an intensive measurement campaign, which was performed during the middle to the end of January 2020 close to the centre and main traffic routes in Budapest. The samples were collected using an in-house developed 9-stage extension of the May type impactor. The May-impactor has aerodynamic cut-off diameters of 17.9, 8.9, 4.5, 2.25, 1.13, 0.57, 0.29, 0.18, and 0.07 μm , for stages 1–9, respectively, at a flow rate of 16.7 L/min. Samples were collected on $20 \times 20 \text{ mm}^2$ Si wafers for 4 h periods four times a day (00–04 a.m., 06–10 a.m., 11 a.m.–03 p.m., 04–08 p.m.) [1]. Si substrates were found to be appropriate for subsequent analysis with Raman spectroscopy. A laboratory sample containing 100% EC was also collected with the same impactor and used as a reference for the data analysis.

The Raman measurements were performed on a Renishaw InVia Raman spectrometer attached to a Leica DM2700 microscope with 633 nm excitation. In total, the size range of 70 – 180 nm of 38 samples (37 environmental and 1 laboratory) was investigated at five different positions. Furthermore, for selected samples, we performed an examination of additional stages up to 9 μm to study the size distribution of EC and OC.

For an independent determination of EC and OC content of the ambient aerosol, a real-time total carbon aerosol analyzer (Model TCA-08, Aerosol Magee Scientific, Ljubljana, Slovenia) was operated simultaneously with the impactor, which measured the EC and the Total Carbon (TC) concentration at a time resolution of one hour.

PCA was conducted on the total dataset of Raman spectra, using the “PCA for spectroscopy” application within MicroCal Origin.

Results

A distinct part of the Raman spectra containing the carbon-related peaks was selected ($1000\text{--}1700 \text{ cm}^{-1}$), which was background corrected and normalized to the selected area. In the next step, we performed a five-band curve fitting available from the literature across all recorded spectra as shown in Figure 1 (4 Lorentzian and 1 Gaussian curve). The G band centred at $\sim 1580 \text{ cm}^{-1}$ identifies the graphitic content in soot nanoparticles. There are four other bands D1, D2, D3 and D4 typical for disordered carbon structure at $\sim 1360 \text{ cm}^{-1}$, $\sim 1620 \text{ cm}^{-1}$, $\sim 1530 \text{ cm}^{-1}$ and $\sim 1180 \text{ cm}^{-1}$, respectively.

Each spectrum was cross-referenced with the mean of the hourly EC, OC and TC concentrations monitored in parallel using TCA equipment for the sampling period. It was found that the parameters of the fitted distribution functions were highly sensitive to background correction. Consequently, the assessment conducted through the limited methodologies existing in the literature—specifically, considering the parameters of the fitted distributions and their combination to estimate EC and OC content in the aerosol sample—failed to yield robust results for these samples.

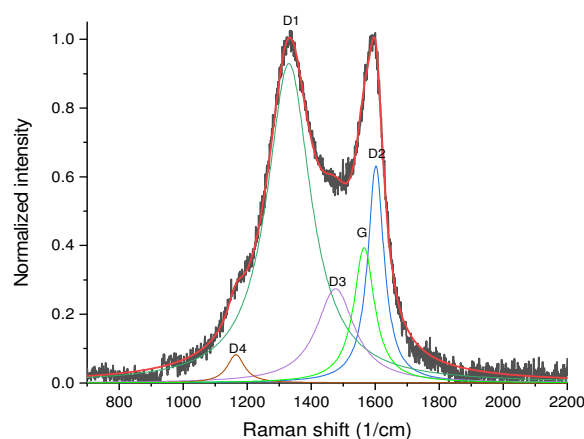


Figure 1: Five-peak fitting results from Raman spectra of aerosol particles from 70-180 nm size fraction of an environmental sample collected in Budapest

Data dimensionality reduction of the measured Raman spectra was performed using the PCA method, where the evaluation of components was scrutinized on the subset of stage 9 from all samples collected. This examination involved assessing all spectra recorded for each sample individually, as well as considering the average of spectra belonging to a given sample. The selection of the smallest size range was deliberate, as literature suggests that in urban environment, the proportion of EC in aerosol mass is the most significant in the size range below $0.5\ \mu\text{m}$. Results of PCA showed that the first two components already describe nearly 90% of variance in the dataset. The best results were found when all individual spectra were considered, for which the obtained scores are shown in Figure 2.

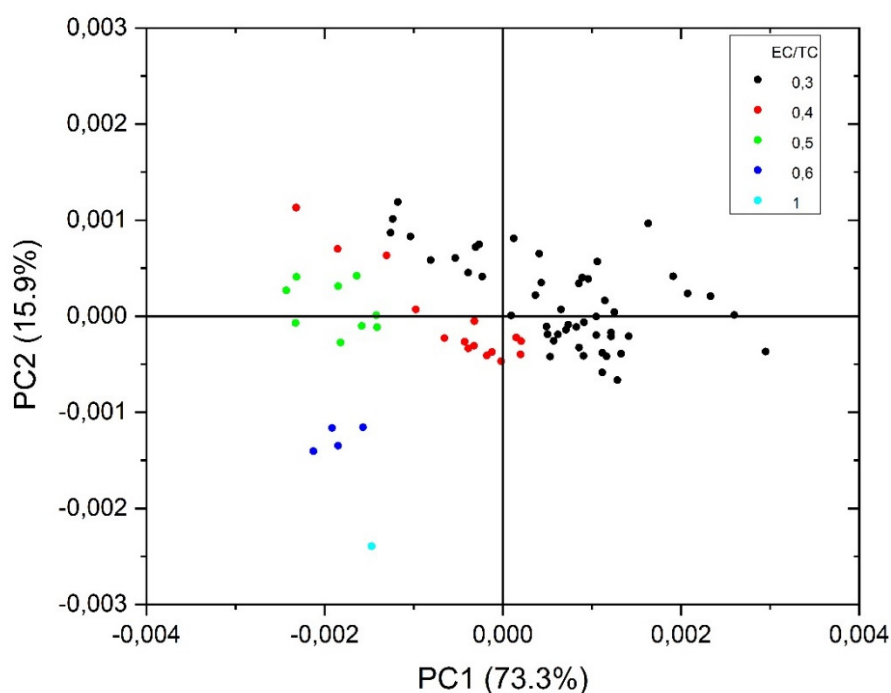


Figure 2: PCA score plot for the Raman spectral dataset of 38 measured samples

Upon assessing the spectra obtained from all measurement points, it became evident that the EC and OC fractions along the sampled strip exhibit inhomogeneity, highlighting the influence of the sampling duration. Remarkably, the sampling and evaluation method demonstrated a reliable performance even with the sample of the smallest mass. This suggests its applicability to samples collected over shorter periods. However, given the noteworthy temporal fluctuations in atmospheric EC and OC concentrations, refining the methodology is crucial. This involves analysis of reference samples across the entire concentration range, a task that is a part of our future plans.

The EC and OC content in samples of unknown composition can be computed using the principal components derived from the entire sample set. We utilized these components to evaluate the size distribution of EC/TC in certain samples collected during the winter campaign. The outcomes for one of the selected samples are depicted in Figure 3. Notably, we observed that the Raman spectra measured were not suitable for evaluation in size ranges larger than $2.5\ \mu\text{m}$. In alignment with our initial expectations, the concentration of elemental and organic carbon in this size range was found to be negligible.

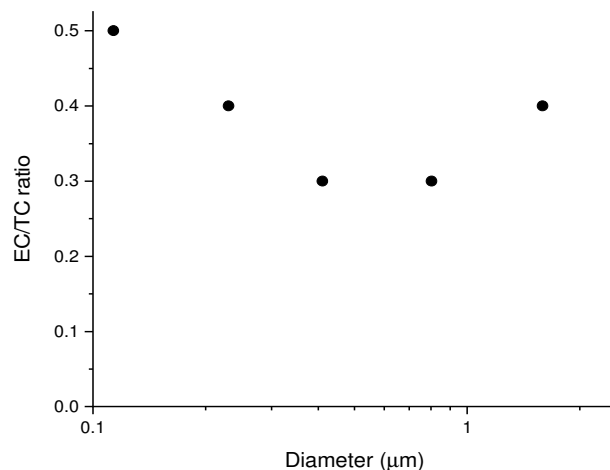


Figure 3: Results of size-fractionated sample measured during winter

Remaining work

We plan to continue with the clarification of PCA method using reference samples for EC/TC concentration ratio and to study the lower limit of the presented method as a function of the sample quantity in the case of environmental samples.

Related publications

- [1] V. Groma, B. Alföldy, E. Börcsök, O. Czömpöly, P. Furi, A. Horváthné Kéri, G. Kovács, S. Török, J. Osán: *Sources and health effects of fine and ultrafine aerosol particles in an urban environment*, *Atmos. Pollut. Res.* **13**:(2), 101302 (2022) <https://doi.org/10.1016/j.apr.2021.101302>
- [2] J. Osán, O. Czömpöly, V. Groma, E. Börcsök, Sz. Török: *Városi aeroszolok forrásazonosítása méretfrakcionált mintavétel és röntgenspektrometriai módszerek kombinációjával*, Előadás a XV. Magyar Aeroszol Konferencián, Hévíz (2022)
- [3] Sz. Kugler, V. Groma, B. Alföldy, E. Börcsök, R. Holomb, M. Veres, J. Osán: *The application of Raman spectroscopy for the investigation of the elemental and organic carbon content of size-fractionated environmental aerosol samples*, (In preparation)

INTEGRATED METHODOLOGY FOR DISTRIBUTED GEOTHERMAL CO-HEAT AND -POWER PRODUCTION

Eszter Békési¹, Kristóf Porkoláb¹, Tamás Soha², Bálint Hartmann², Réka Zsebők³, János Gianone³, Martin Mayer³, Attila R. Imre^{2,3}

1. Institute of Earth Physics and Space Science; 2. Centre for Energy Research; 3. Budapest University of Technology and Economics

Objective

In the present geopolitical situation, geothermal energy utilization has gained increasing importance. In Hungary, available geothermal heat sources are mostly in the 40-120 °C temperature range, utilized mainly in the form of direct heat for agricultural applications, district heating and balneology. Geothermal resources – to some limited extent – can also be suitable for power production by binary geothermal plants [1]. Among these possibilities, various heating applications (where natural gas is substituted) and power production (due to the general applicability and easy transportability of electricity) are among the most desired ones. Also, one has to keep in mind that, unlike other renewable sources, geothermal heat and power production are well-predictable and available permanently, showing only minor seasonal changes (in the case of power production).

In the framework of this project, we investigated scenarios to extend the current geothermal operations for (1) geothermal power generation and/or (2) further geothermal heat production. To achieve that, we developed a methodology to integrate subsurface (geological) with surface conditions, and parameters to pinpoint potential locations for new geothermal wells. The geographical features of the surface determine the limiting factors for any construction, including those which are mainly connected to sub-surface operations, i.e. geothermal energy utilization in this case. Surface conditions can be categorized into three main classes: environmental, social and technical. Besides the limiting factors, surface features include also the potential consumers, which can be characterized by their location, energy demand and other technical attributes. Thus, it is important to consider local geography for medium and large-scale planning processes. Considering the heat demand of Bóly and neighbouring settlements, we further refined the site selection procedure and provided predictions for long-term geothermal production. A further location (Szarvas-Csabacsüd) has been analyzed to extend the project.

Determination of geothermal potentials

The Bóly geothermal area is located in southwest Hungary, with a single operating geothermal doublet of 2.5 MWth installed capacity [2]. The geothermal production and injection wells are drilled east of Bóly, and have been in operation since 2002, providing heat supply for various public institutions. The geothermal wells target a fractured Jurassic limestone reservoir, with a flow rate of 17 l/s and production temperature of 76 °C from ~1.6 km depth.

The study area constitutes a 10 km radius circle around the centre of Bóly. The workflow started with the geological investigation of the area based on various available datasets. We collected information about the currently operating well doublet system from the Geothermal Information Platform [2]. Lithologies from all available boreholes of the study area as well as seismic sections, were collected from the database of the Geological, Geophysical and Mining Data Store [3]. Additionally, structural geological maps of [4] and [5] were utilized to constrain the geometry of the geothermal reservoir (fractured Jurassic limestone) in the study area. Based on this information, we produced maps of the depth, thickness, and temperature of the geothermal reservoir.

The reservoir geometry and temperature maps served as input for evaluating geological risks associated with geothermal development. In the evaluation, we created so-called Common Risk Segment (CRS) maps [e.g. 6,7] for three main components: (1) temperature, (2) hydrogeology (~permeability and presence of geothermal fluids), (3) geochemistry (~fluid composition). The CRS maps quantify the geological probability (Chance of Success - CoS) of a geothermal project in terms of the different factors. Therefore, a target temperature, flow rate, and chemical composition must be defined to produce the maps. We chose the parameters of the operating geothermal doublet (production temperature of 76 °C, flow rate of 17 l/s and relatively low gas content) as target values. The resulting CRS maps are presented in Fig. 1, indicating higher CoS in an E-W oriented band, constrained by two so-called fault structures in the north and southwest outlined in Figure 1a. Along these faults, the reservoir is basically “cut” and elevated to a near-surface position in the northern and southern part of the study area, resulting in very low predicted reservoir temperatures that are not sufficient for utilization (Figure 1a, red colour).

Based on the three component CRS maps, we produced a Composite Common Risk Segment (CCRS) map representing the overall geological CoS for geothermal reservoir development (Figure 2). The CCRS map is created by multiplying the three components. The CCRS map indicates the highest CoS in the vicinity of the operating geothermal doublet. This results in having information from this location, while further away, the factor of increased uncertainty is mirrored in the decreasing values. Still, the greenish to light yellow areas could be considered for potential development. The CCRS map was further integrated with various surface factors to narrow the areas that can be considered for development.

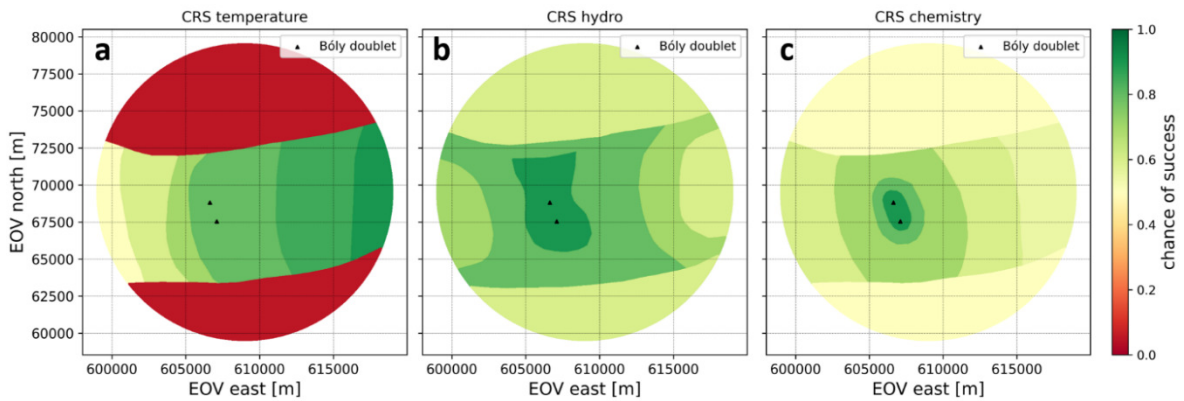


Figure 1: Common Risk Segment (CRS) maps for the three main geological risk components of geothermal development (a: temperature, b: hydrogeology, c: geochemistry)

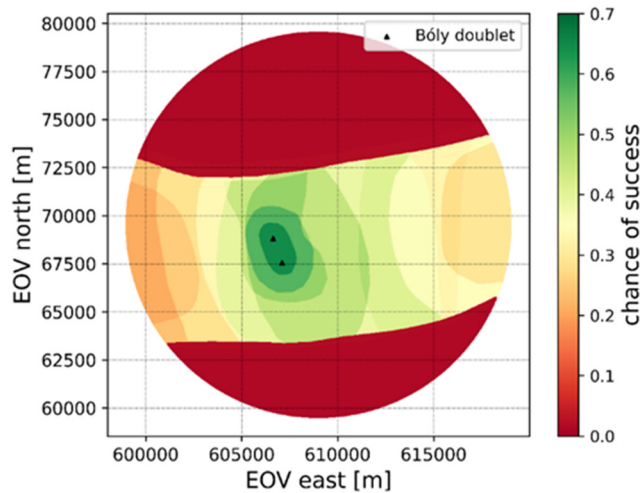


Figure 2: Composite Common Risk Segment (CCRS) map representing the integrated geological risks. Greenish values show a higher chance of success, indicating suitable areas for geothermal development.

Data collection regarding the geographical factors was done using official EU and Hungarian databases (National Regional Development and Spatial Planning Information System, Corine Land Cover) for spatial and technical attributes, completed by open-source data (OpenStreetMap (OSM) and satellite images from Google). The road network of the OSM was extended by manual satellite image interpretation, considering dirty roads and other lower-level roads. Since official data regarding the annual heat demand of the Hungarian settlements does not exist, the pan-European HotMaps database was used. Each settlement was associated with the values of the heat demand raster covered by their extent. The spatial data were processed and implemented into a GIS (Geoinformatics System) environment using ArcMap 10.4 software. Population, the number of households and energy consumption data were collected from the Hungarian Central Statistical Office for each settlement included in the study area.

Each geographical feature was considered as a site suitability factor for finding the most favourable locations of geothermal wells. The criteria were categorized by their properties and were associated with value scores. The process was done empirically except for the Chance of Success layer. For most of the criteria, exclusion categories were considered as areas forbidden for construction of any geothermal facility, including the 800 m impact zone of the operating geothermal wells to the west of Bóly (Figure 3). Each vector layer was converted to a raster to fill the raster cells by their value scores. If any of the cells received 0 value score on a criterion layer, the location of that cell was considered as prohibited area regardless of its values by other suitability criteria. The suitability value scores were weighted according to their importance during the final suitability evaluation. The extreme importance of the geological conditions was highlighted by multiplying its values by 0.5, while land use, nature reserve and residential areas received a 0.1 weight. The power grid accessibility criterion was multiplied by 0.05 and road network proximity by 0.15. Considering the criteria and their weightings, the final site suitability map was created (Fig. 3). Environmental, geological, and social aspects were integrated in this way into a single layer.

Based on this integrated site suitability map, we highlighted potential subsurface (i.e. reservoir level) and surface positions of well doublets (Fig. 3). We concentrated on locating a maximum number of potential geothermal doublets in the study area, similar to the methodology described in [8]. For the positioning of the wells, we considered the orientation and relative magnitude of the present-day stress field in the area and the geometry of pre-existing geological structures in the reservoir. These factors are essential to minimize drilling risks and maximize well productivity, while further on-site geophysical measurements would be necessary to verify the suggested orientations.

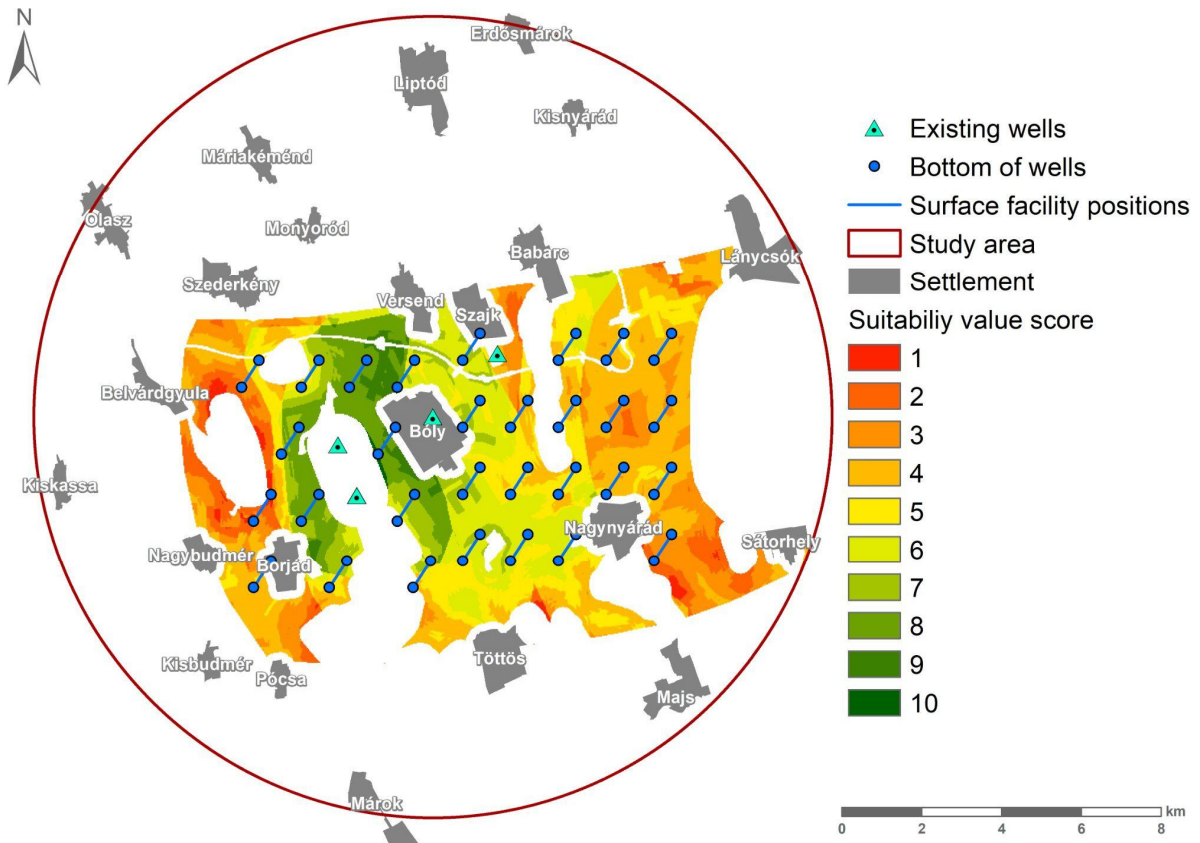


Figure 3: Geothermal facility site suitability of the rated area and the well doublet location alternatives. Void areas are prohibited for geothermal development. Straight lines between the well bottom points represent the possible location of the surface geothermal facility.

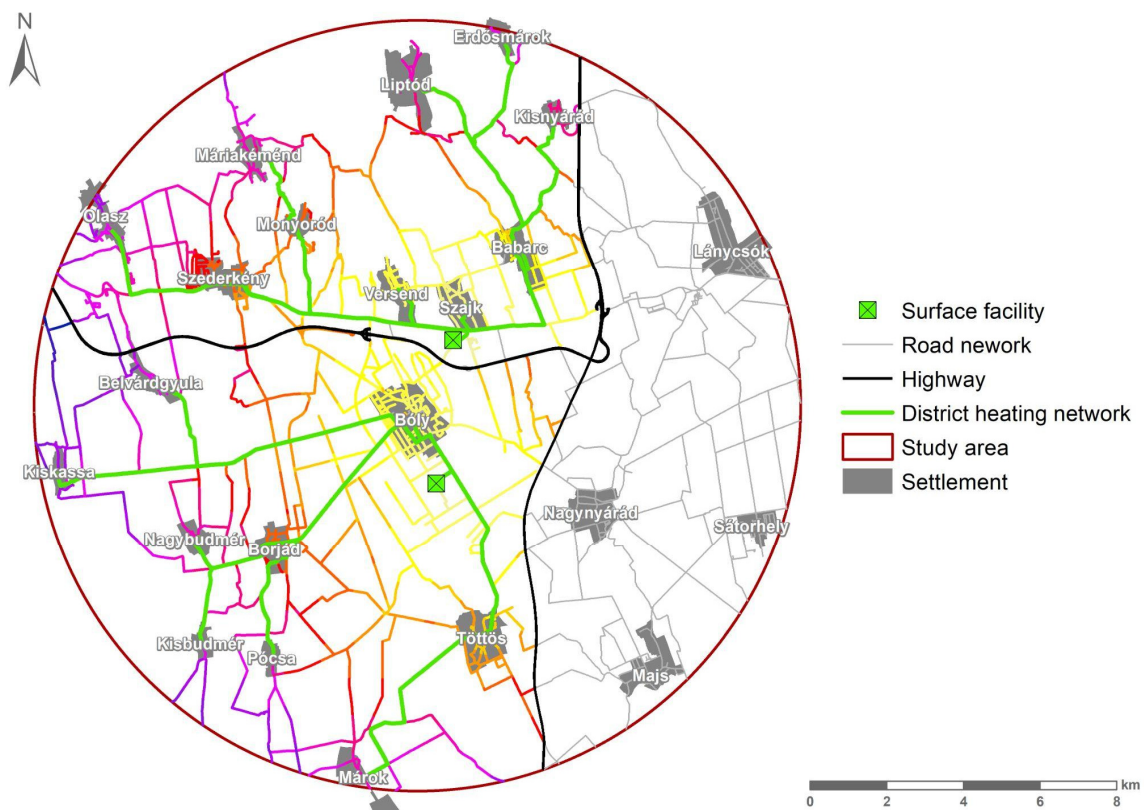


Figure 4: Suggested district heating pipeline network layout connecting the new geothermal facilities with the consumers

The total rated area (value score > 0) is 74.4 km², 23.7% of the total study area. Areas characterized by value scores 6-10 were identified as potential sites for geothermal well drilling and its surface facility. Their extent is 13,3 km², only 4.2% of the total study area. Location alternatives for the well doublets are also presented in Fig. 2. Two doublets were selected, one of each side of the highway which crosses the study area. The highway was considered as a barrier for geothermal district heating pipelines. The pipeline layouts from the geothermal surface facilities to the consumers, i.e. the point features representing the centroid of the settlements, were designed based on the local road network by using the Network Analyst tool in ArcMap. The main criterion is to find the shortest route from the heat source to the demand points, regardless of their distance. The local highways were identified as barriers that pipelines could not cross. Distances on the road network from the heat sources are presented as a heatmap, along with the suggested district heating pipeline layouts in Fig. 4. Out of the 19 settlements, 9 are connected to the southern facility (near Bóly), and 10 can be connected to the northern one (near Szajk). The mean pipeline length is 8,405 m, while the longest route is 12,450 m, connecting Kiskassa to the southern facility.

With the help of a 2D numerical simulator [9], we modelled the performance of the two selected doublets near Bóly and Szajk (Figs. 4, 5a) for a period of 200 years. For the modelling, we chose a constant reinjection temperature of 35 °C for simplicity and a constant flow rate of 20 l/s (Fig. 5b). Temperatures in the reservoir start to drop near the injection wells as the cold water propagates through the fractures/pores of the reservoir rock (Fig. 5a). The theoretical capacity of both doublets is around 4.2 MWth for ~75 years (Fig. 5c), followed by a significant drop due to the decrease of production temperature associated with the cooling of the reservoir due to reinjection (the cold water front emerges towards the production wells). It is important to keep in mind that production temperatures and doublet capacity may drop earlier in case of higher flow rates. Additionally, in the case of electricity generation, the capacity of the system depends on the efficiency of the binary power plant, determined by, e.g., the type of working fluid and production temperatures.

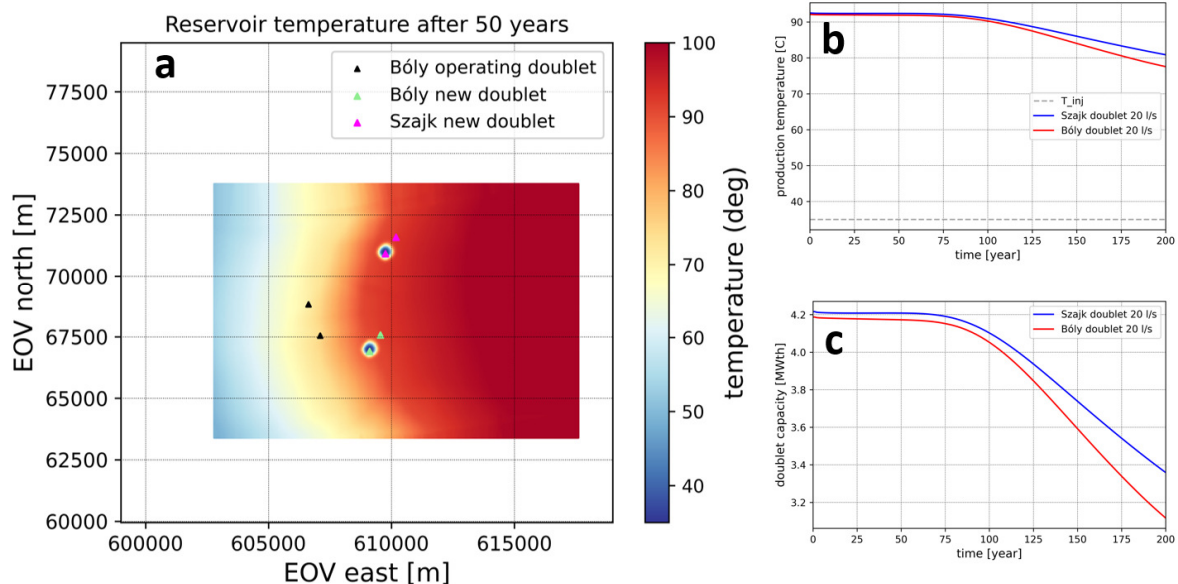


Figure 5: (a) Modelled temperature in the reservoir after 50 years of geothermal operation of the Szajk and Bóly new doublets (b) Evolution of production and injection temperatures, and (c) theoretic doublet capacity for the period of 200 years

Utilization of geothermal heat for heating and power production

The temporal distribution of the heating demand is determined by the outdoor temperature, for which data are taken from a TMY (Typical Meteorological Year) database describing an average year in hourly increments. The annual heating demand was divided into hourly heat demands in proportion to the difference between the assumed indoor temperature of 20 °C and the ambient temperature at the current hour. The nominal supply and return temperature of the heating system was assumed to be 70/50 °C, but this temperature is required only at the nominal outdoor temperature of -11 °C for Bóly. As the heat transfer surface of the heaters is constant, the heaters can transfer the required heat to the air of the room at lower temperatures if the heat demand is lower than the nominal one. The heating water temperature affects the return temperature of the geothermal fluid, thus the heat output that can be extracted from it. At high ambient temperatures, the geothermal heat can supply the entire demand, whereas, below a certain temperature, an additional peak heat source is required, as shown in Figure 6.

For geothermal fluid temperatures below 100 °C, power generation is possible with an Organic Rankine-Cycle (ORC). The efficiency of power generation depends on the temperature of heat input and heat removal, as well as on the design and working fluid of the cycle. Since the latter is not known at the preliminary design stage, the efficiency of the ORC cycle was assumed to be 40% of that of the Carnot cycle at the same temperature limits, based on empirical examples. The vaporization temperature was 10 °C lower than the well-head temperature, and the condensation temperature, assuming air condensers, was 15 °C higher than the ambient temperature. The model thus constructed takes into account the seasonal variation of efficiency, and hence of electrical output, through the ambient temperature.

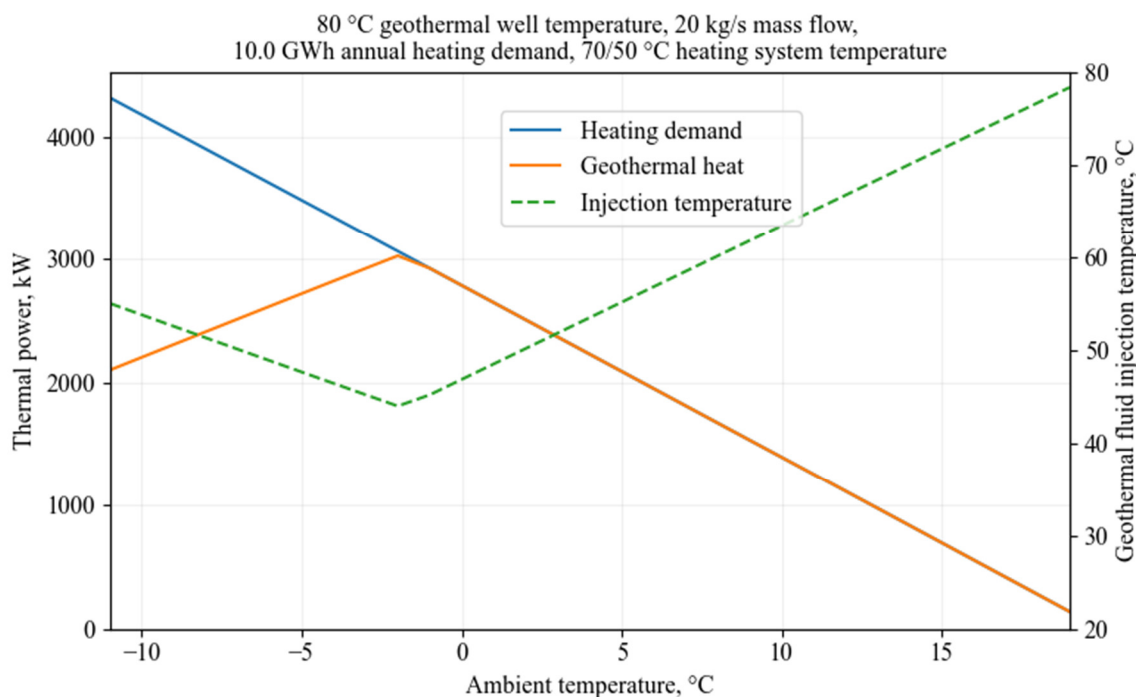


Figure 6: Heating demand and geothermal fluid reinjection temperature as a function of ambient temperature in a given outlet temperature

For the on-surface installation, a combined system was assumed to be used for heating and power generation, with a priority on satisfying heating demands first, with the remaining mass flow going to the ORC system. In this way, both the geothermal share in the heat supply can be maximized, and the summer use of geothermal heat could be solved. The drawbacks are the relatively high investment cost and the lower utilization of the ORC system compared to a fully power-producing geothermal power plant, increasing the production costs for power. In such a case, however, the economics can only be understood for the two systems together, and the revenue from the heat supply may offset the higher costs.

Bóly, total annual heating + DHW heat demand 25.62 GWh

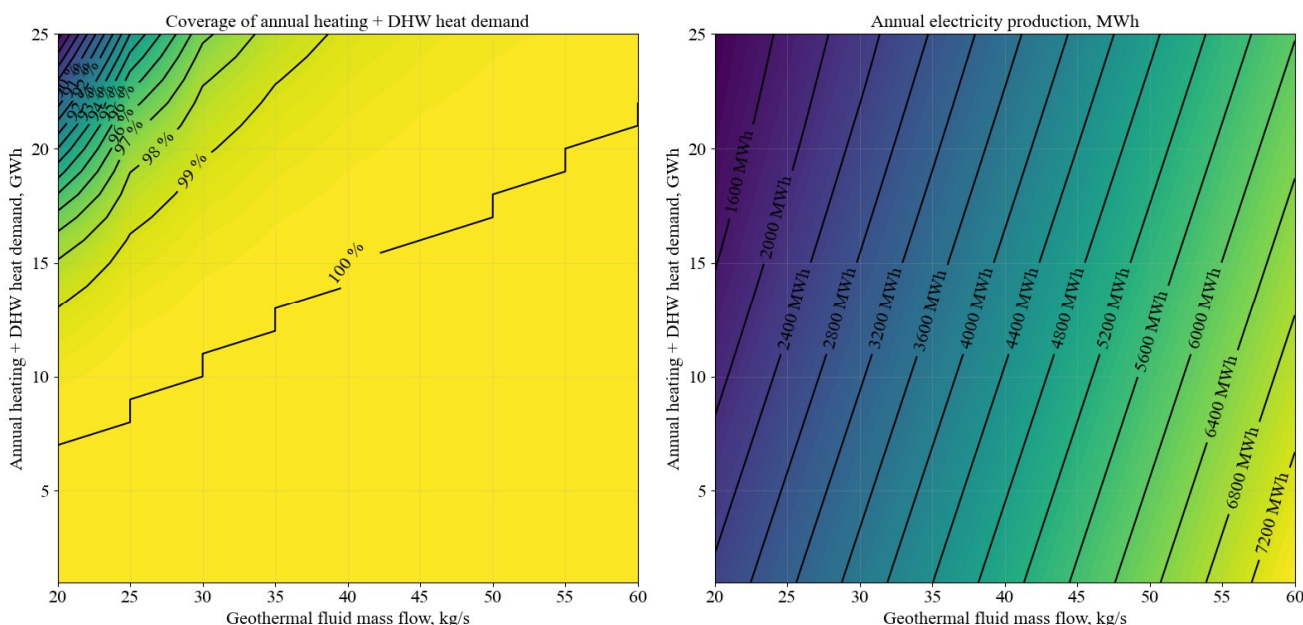


Figure 7: Percentage of heat demand and the amount of additional power that can be produced as a function of the geothermal well mass flow and the annual heat demand

For district heating, the key question is how much of the annual connected demand can be met by geothermal heat, while for power generation, the annually produced amount is the key issue. The parameters that determine these quantities are the well-head temperature, the fluid mass flow rate and the annual heat demand of the consumers connected to the geothermal

district heating system. The well-head temperature of the selected well pair near Bóly – for this application – is taken as 91 °C, and the heat demand is considered to be 75% heating and 25% for Domestic Hot Water (DHW). The vertical axis in Figure 7 shows how much of Bóly's 25.63 GWh annual heating heat demand can be connected to the newly developed geothermal district heating system, while the horizontal axis shows the fluid mass flow. If we could connect consumers providing half of the total heat demand to the district heating system, we would need a mass flow of about 35 kg/s to cover all of this heat demand. In this case, the system would be able to produce about 3600 MWh of electricity per year.

One of the uses of these power&heat systems is the possibility to construct a power-network independent local heating system, where the ORC device can generate power sufficient to support all systems needed to keep the heating alive during local or general power failure, even when the power grid is totally collapsing. When the amount of net power is sufficiently high, even part of the local critical infrastructure can be powered from this local, day-and-night source.

Utilization of the geothermal heat for stand-alone power production

If the heat cannot be used locally (due to the lack of proper local demands), it can be fully used to generate power by ORC [10]. The design, efficiency and performance of the equipment of these power plants depend on the input parameters, which are, in practice, the water yield, well-head temperature and the ambient temperature (when air is used for cooling in the condenser). However, different working fluids can be chosen for these input parameters based on the optimum power and thermal efficiency [11]. Since the aim is to install several small geothermal units, a uniform methodology has been created to quickly determine the optimal working fluid and calculate the expected performance. Asimptote's FluidProp [12] and Cycle-Tempo [13] programs were used for these calculations.

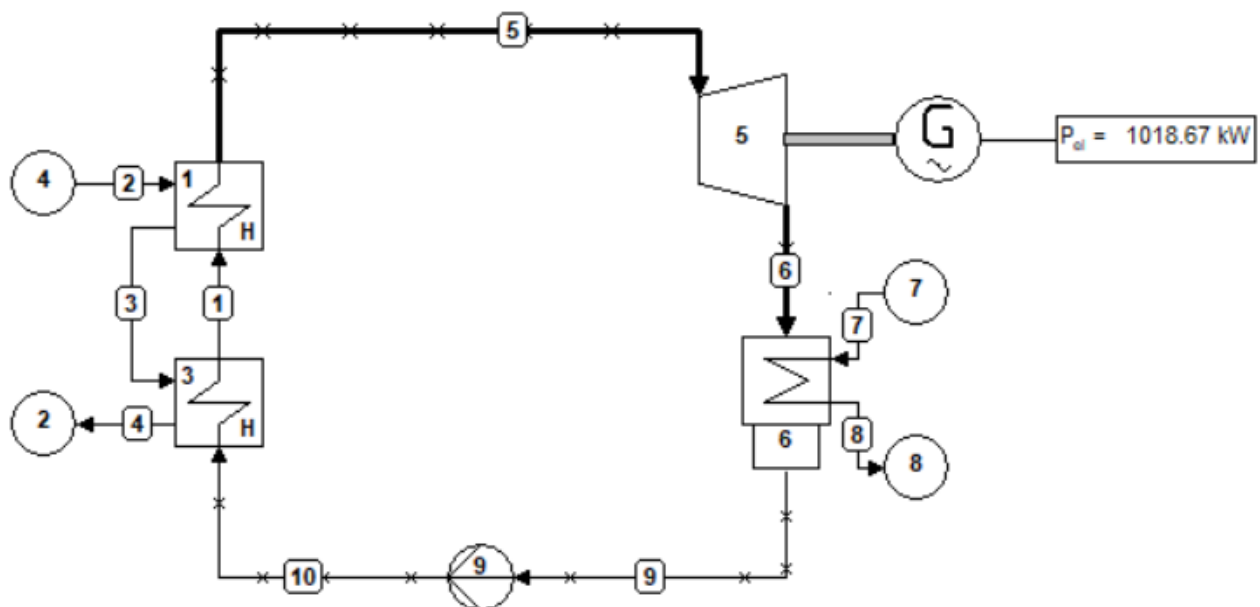


Figure 8: Layout of an ORC system, utilizing geothermal heat source (4) as a heat source (maximal temperature 91 °C, volume flow of geothermal water: 40 l/s). The self-consumption of the pump is not deducted.

A small unit can produce 1.01 MW of electricity from a geothermal well water yield of 40 l/s, subject to variable parameters (Figure 8). Although these small geothermal units seem incomparable with nuclear plants for production, one should keep in mind that several hundreds of existing wells are already available, not to mention the location of potentially productive drilling. In this way, one can construct a loose network of geothermal power plants with total power production close to a smaller nuclear one; according to present estimates, Hungary can easily reach 1000 MW_e of power production based on geothermal heat in a relatively short time.

There are several locations in Hungary where existing geothermal wells could provide heat and electricity at a rate depending on the actual demand of heat and electricity prices. A preliminary study has been conducted for the Szarvas K-110 well, located close to Csabacsüd (where the potential injection well is located), a medium village where several potential users of the geothermal heat could be identified. Additionally, the distance of Szarvas (a medium-sized town with an existing district heating network) is also not significant. Presently, the district heating system of Szarvas needs 500 GJ/year, but the company is willing to extend the covered area; therefore, additional heat sources would easily be utilized.

The capacity of the Szarvas K-110 well would easily satisfy the heating demand, and the remaining heat could be used to generate electric power. The system could provide 700 kW of thermal and 540 kW of electric power according to the estimated heat demands. Concerning the self-consumption of the geothermal co-heat and power system, it is negligible for heat but remarkable for power; therefore, the total annual production would be only 3730 MWh_{el}. For the financial calculations, the

Day Ahead Market data of the AFRY has been used [14]. Although the total power production seems to be small, but concerning the fact that the system would be installed on existing geothermal wells, the Return on Investment (ROI) time would be less than 7 years, making a project financially viable.

Conclusions

We designed a methodology integrating subsurface and surface parameters for geothermal field development. In the subsurface (geological) analysis, we produced CRS maps for various components and gathered them into a CCRS map to quantify the chance of success of geothermal development. Based on the integrated site assessment, we chose two new doublet locations and modelled doublet performance. Results show that the two new doublets could provide the region a long-term continuous heat supply. Considering that this study is theoretical and often based on sparse datasets, a detailed geological-geophysical site survey would be necessary to reduce pre-drilling geological risks.

It was shown that local heating and or power demands can be satisfied using these sources. Concerning power production, each small geothermal power plant could provide power for a few neighbouring towns or villages. In this way, one can easily construct a decentralized energy system where components can operate autonomously, but together, they can improve grid resilience and help mitigate grid disturbances.

An additional location in Békés County was investigated. A geothermal system could provide heat for potential new users in Csabacsúd or the expansion of the existing district heating network of Szarvas. Using the remaining heat to produce electricity proved technically and economically viable.

Related publications

- [1] B. Lindal: *Industrial and other applications of geothermal energy*. In: Armstead, H.C.H., ed., *Geothermal Energy*, UNESCO, Paris. (1973)
- [2] OGRE - Geothermal Information Platform, Mining and Geological Survey of Hungary, https://map.mbfisz.gov.hu/ogre_en/, last access: 01 November 2022
- [3] Mining and Geological survey of Hungary, <https://mbfisz.gov.hu>, last access: 01 November 2022
- [4] B. Koroknai, G. Wórum, T. Tóth, Z. Koroknai, V. Fekete-Németh and G. Kovács.: *Geological deformations in the Pannonian Basin during the neotectonic phase: New insights from the latest regional mapping in Hungary*. *Earth-Science Reviews*, 211, 103411 (2020)
- [5] Haas J., Budai T., Csontos L., Fodor L., Konrád Gy.: *Magyarország pre-kainozoos földtani térképe 1: 500 000 (Pre-Cenozoic geological map of Hungary, 1:500,000)*. Magyar Állami Földtani Intézet (2010) - in Hungarian
- [6] S. Grant, N. Milton and M. Thompson: *Play fairway analysis and risk mapping: an example using the Middle Jurassic Brent Group in the northern North Sea*. In *Norwegian Petroleum Society Special Publications* (Vol. 6, pp. 167-181). Elsevier (1996)
- [7] J. Maury, V. Hamm, A. Loschetter and T. Le Guenan.: *Development of a risk assessment tool for deep geothermal projects: example of application in the Paris Basin and Upper Rhine graben*. *Geothermal Energy*, 10, 1-23 (2020) <https://doi.org/10.1186/s40517-022-00238-y>
- [8] C.J.L. Willems and H.M. Nick: *Towards optimization of geothermal heat recovery: An example from the West Netherlands Basin*. *Applied Energy*, 247, 582-593 (2019) <http://dx.doi.org/10.1016/j.apenergy.2019.04.083>
- [9] DoubletCalc2D Software - <https://www.nlog.nl/en/tools>, last access: 01 November, 2022
- [10] FluidProp Software, <https://asimptote.com/fluidprop/>
- [11] Cycle-Tempo Software, <https://asimptote.com/cycle-tempo/>
- [12] E. Macchi and M. Astolfi: *Organic Rankine Cycle (ORC) Power Systems: Technologies and Applications*; Elsevier-Woodhead Publishing: Duxford, UK (2016)
- [13] A.M. Ahmed, L. Kondor and A.R. Imre: *Thermodynamic Efficiency Maximum of Simple Organic Rankine Cycles*, *Energies* 14, 307 (2021) <http://dx.doi.org/10.3390/en14020307>
- [14] Day Ahead Market prices from AFRY, <https://afry.com/>, last access 01 November 2023.

CATALYTIC METHANE PYROLYSIS COMBINED WITH MICROCOMBINATORIAL TEM STUDIES

Anita Horváth, Miklós Németh, Andrea Beck, Tamás Korányi, György Sáfrán, Zsolt Horváth, István Rigó, Miklós Veres

Objective

The non-oxidative decomposition of methane, viz. methane pyrolysis ($\text{CH}_4 \rightleftharpoons \text{C} + 2\text{H}_2$) yields extremely clean hydrogen gas and only solid carbon, without the production of any CO_2 , but the process is not industrialized yet. Application of proper catalysts can decrease the temperature requirement of the reaction and produce valuable nanostructured carbon besides hydrogen. This new research field was initiated via the development and study of bimetallic NiMo-based supported catalysts and complemented with the novel one-sample concept microcombinatorial Transmission Electron Microscopy (TEM) method. Both approaches are completely new in Hungary. Moreover, the microcombinatorial TEM method for catalytic purposes was never done in the world. The literature suggested that the addition of Mo to Ni can induce a synergetic catalytic effect in methane pyrolysis, but the reasons for the optimal Ni-Mo cooperation at the nanosize level were not known. Our aim was to ascertain the existence and reveal the reasons and structural background of the synergetic interaction between nickel and molybdenum. First, supported NiMo/MgO ("real") catalysts were produced with two different Mo loadings and investigated by sophisticated surface sensitive techniques before and after the CH_4 decomposition reaction. In order to investigate a complete range of Ni/Mo atomic ratios, the microcombinatorial TEM method was applied to produce a NiMo thin layer of linearly varying composition and then, via high temperature reduction, NiMo alloy particles over the surface of a tiny 3 mm TEM grid. These bimetallic alloyed islands/particles were to be studied to reveal any change in alloy composition due to the reduction pretreatment and then to the catalytic reaction carried out over the same TEM grid and to spot any carbon deposition after the CH_4 decomposition test by TEM, X-ray Photoelectron Spectroscopy (XPS) and Raman techniques. The applicability of this novel microcombinatorial TEM method for catalytic studies was evaluated based on our test reactions and structural results obtained over the "real" catalyst samples, and the next steps of upcoming development were determined.

Methods

For the preparation of the supported catalyst samples, chemical deposition of metal precursor ions was done over the MgO support at 80 °C (MoNi1.2 and MoNi0.4) or at room temperature (MoNi0.4_RT). The bimetallic catalysts beside 7 wt% Ni contained 13 wt% or 4 wt% Mo (Mo/Ni=1.2 or 0.4). Reference 13% Mo/MgO and 7% Ni/MgO catalysts were prepared at 80 °C via the same adsorption-precipitation method. The samples were calcined at 550 °C in air and reduced in hydrogen at 800 °C. Structural characterization by TEM and scanning TEM coupled with Energy Dispersive Spectroscopy (STEM-EDS), X-ray Diffraction (XRD) and XPS were performed. The catalytic properties were investigated in 50% CH_4 /Ar flow at 800 °C for 3 hours or until deactivation of the catalyst. The amount of coke was determined after pyrolysis and its structure was analysed by Raman Spectroscopy (I_G/I_D) and High-Resolution TEM.

The microcombinatorial Ni-Mo samples were fabricated by DC magnetron sputtering of the two metals. Fluences from the regulated-power Ni and Mo sputtering sources were exposed to the TEM grid (after probing several ones, on a commercial Au grid covered by SiO_2 thin film) through a slot moving in sync to produce a strip along an axis of the grid with linearly increasing Mo/Ni atomic ratio. The samples were measured by TEM and EDS, plus by XPS in as prepared state, and STEM-EDS and High Resolution Transmission Electron Microscopy (HRTEM) after reduction treatment in 10% H_2 /Ar at 800 °C for 30 min, then after a subsequent treatment in 50% CH_4 /Ar flow at 800 °C for 30 min. The latter case was investigated by Raman spectroscopy, too.

Results

The supported bimetallic catalysts had an average metal particle size between 5-8 nm after the reduction treatment and nice and homogeneous distribution over the support as shown in Fig. 1a. The STEM-EDS analysis showed that the larger bimetallic alloy particles mostly seen in samples with bulk Mo/Ni=0.4 atomic ratio were all extremely Ni-rich, while in the smaller ones the Mo/Ni ratio was much higher. This was in perfect agreement with the Ni (200) peak fitting of the XRD curves. The catalyst with Mo/Ni=1.2 ratio contained XRD-silent smaller nanoparticles, but according to the STEM-EDS analysis (see Fig. 1b), they were alloyed with a maximum of 1/1 Mo/Ni ratio. Moreover, some separated Mo entities in the MgO support were detected in MoNi1.2 sample and also in MoNi0.4_RT.

In methane pyrolysis tests at 800 °C, after the initial high methane conversion values, all samples showed deactivation tendency, but it was the lowest for MoNi1.2 being still active after 3 hours of reaction (Fig. 1c). The bimetallic catalysts produced moderately irregular graphitic multiwalled carbon nanotubes with different yields: the highest amount of carbon nanotubes was formed over MoNi1.2 sample (3.2 mg C/mg_{cat}). The monometallic Ni and Mo references deactivated quickly during the catalytic test after forming only several layers of well-ordered graphene around Ni, and highly defective carbon shells around Mo particles (basically encapsulating type carbons).

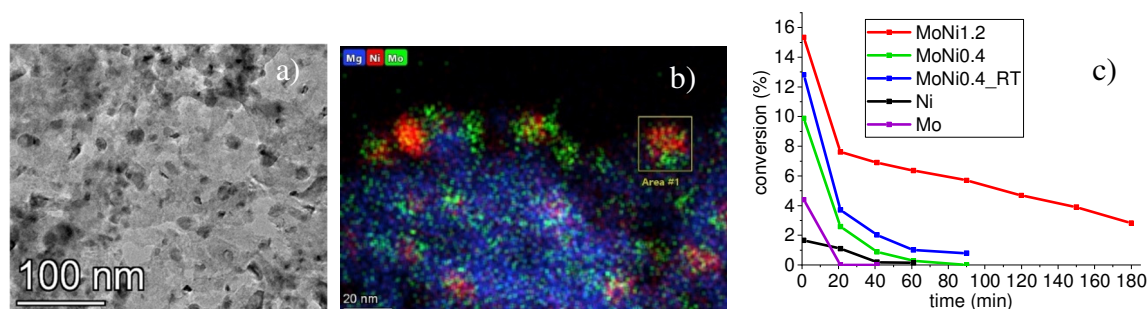


Figure 1: TEM image of the best bimetallic MoNi/MgO sample, MoNi1.2 after reduction (a); STEM-EDS map of Mg, Ni and Mo over the same catalyst (b); CH₄ conversion versus time during the pyrolysis tests at 800 °C on the MgO supported samples (c)

The superiority of the catalyst with Mo/Ni=1.2 ratio in terms of activity, stability and carbon yield was explained by meticulous HRTEM and STEM-EDS analysis of all the spent samples. These revealed that the equimolar alloyed NiMo particles did not seem to segregate during the carbon nanotube growth process unlike the ones in the other catalysts with Mo/Ni=0.4 ratio that contained less Mo and more Ni within every single nanoparticles. Fig. 2 depicts the different morphology of the spent samples with the low and the high Mo-loadings. It is easy to detect that the dark metallic phases are strongly segregated into Mo-rich elongated particles and Ni-rich separated parts with pear or other, irregular shapes. This segregation was hardly observed in MoNi1.2 according to the last column of Fig. 2.

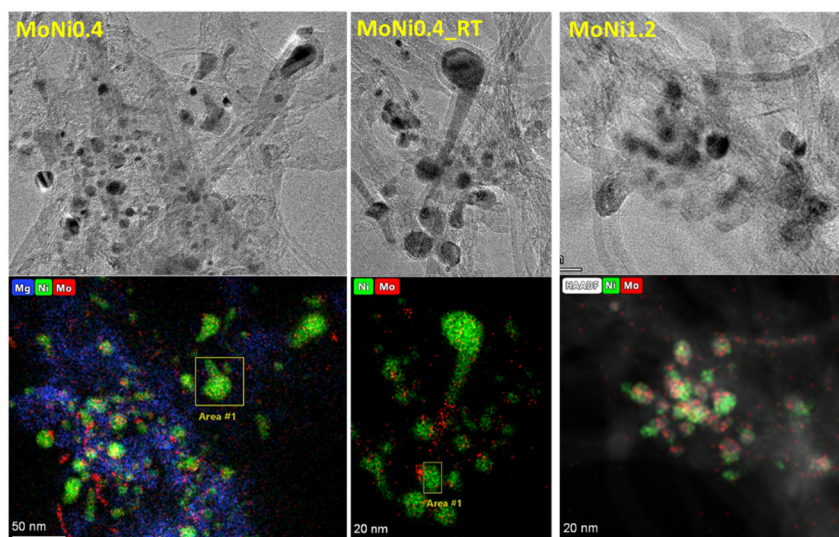


Figure 2: TEM images (upper row) and STEM-EDS maps of Ni and Mo (lower row) of the bimetallic supported catalysts after the methane pyrolysis showing a strong segregation tendency for samples with Mo/Ni=0.4 ratio

The presented results underscore the importance of bimetallic NiMo/MgO catalysts in augmenting the efficacy of methane pyrolysis for the generation of hydrogen and the synthesis of carbon nanotubes. Additionally, this study elucidated the fundamental mechanisms that govern the catalytic behaviour of these materials. The most prominent novelty of our work is the disclosure of the nanoscale segregation of bimetallic particles during the carbon deposition process depending on the Mo/Ni atomic ratio, affecting the catalyst lifetime.

The microcombinatorial TEM preparation method patented in the MFA is able to produce thin layers of two components with linearly changing composition in a computer-controlled way using magnetron sputtering of the two metal sources. However, for catalytic purposes, to mimic the supported catalyst morphology, where nanometre sized metal particles are dispersed on a supporting oxide, the thin films must be broken up into particles or small islands. Reduction treatment of this thin layer at high temperature was expected to result in NiMo alloy particles in our case. The peculiarity of this method is that the same TEM grid can be studied by TEM after any type of treatment and so the distribution of the 2 metals can directly be investigated. Moreover, our eventual plan was to carry out CH₄ decomposition over the very same TEM grid containing the NiMo particles of different composition and size, and to see if the coke formation is also influenced by the alloy composition as in the case of the “real” catalyst samples. As this idea is extremely novel and we had no experience of using TEM grids at such high temperatures, we faced several problems and complications that were not foreseen. The screening search for a proper grid and the grid covering membrane (that is needed to accommodate the nanoparticles) that is stable after the high temperature treatments took very long time. The carbon membrane used generally in TEM grids must have been expelled in our case, as carbon formation and analysis after the CH₄ decomposition was our purpose. The Cu grid covered by a home-made SiO₂ layer was not stable enough and finally, a commercial Au grid covered by a SiO₂ membrane was purchased and used. This withstood the high temperature treatments applied in our investigations. However, it turned out that Sn contamination on

one side of the pristine grid/membrane was detrimental to further studies, and so we had to pay attention to where to do sputtering next.

Fig. 3a-c show the scheme of the grid and two TEM images of the thin layer formed between the Mo end on the left and the Ni end on the right. It is easy to see that an increase of Ni concentration along the axis of the sputtered layer makes the film less homogeneous. XPS was applied to measure the elemental composition of the same layer and the linescan with a step of 150 μm shown in Fig. 3d proved that the planned combination of the two metals was achieved (linear decrease of Mo concentration was accompanied by the increase of Ni in the layer.)

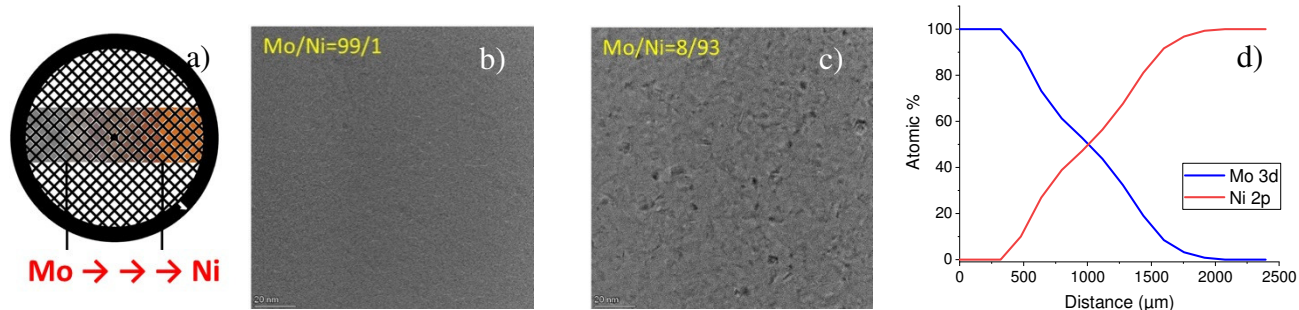


Figure 3: Scheme of the bimetallic layer over the TEM grid of 3 mm in diameter (a); TEM image of the layer at the Mo end (b); TEM image of the layer close to the Ni end (c); the change of Mo and Ni surface concentration (linescan) along the axis of the sputtered area as measured by XPS (d)

After a treatment in hydrogen at 800 $^{\circ}\text{C}$, the NiMo layer broke up into irregular or spherical particles depending on the location along the axis of the grid. Fig. 4 shows the various different morphologies detected. Fortunately, there were areas corresponding approximately to the bimetallic composition of our supported samples. However, at those places (at Mo/Ni=0.5 and 1.1) the STEM-EDS mapping revealed that large particles were mostly composed of nickel and the smaller ones were richer in Mo (Fig. 5a), just as in the real supported samples. This means, TEM-EDS on larger areas and STEM-EDS maps on smaller territories do not necessarily agree, showing inhomogeneity in the alloy composition. Interestingly, where Mo was in high excess (TEM-EDS Mo/Ni=3.3), we could find two types of particles: extremely Mo-rich together with the equimolarly alloyed ones, which were detected in our most active supported MoNi1.2 sample as well (see Fig. 5b).

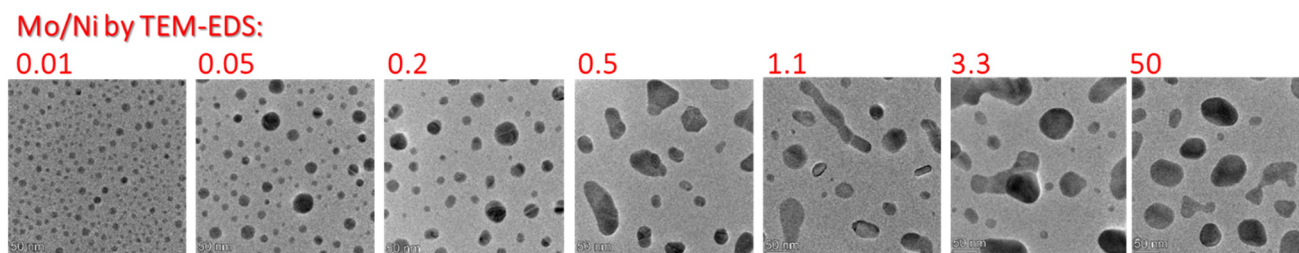


Figure 4: TEM images after the high temperature reduction treatment at different Mo/Ni concentrations

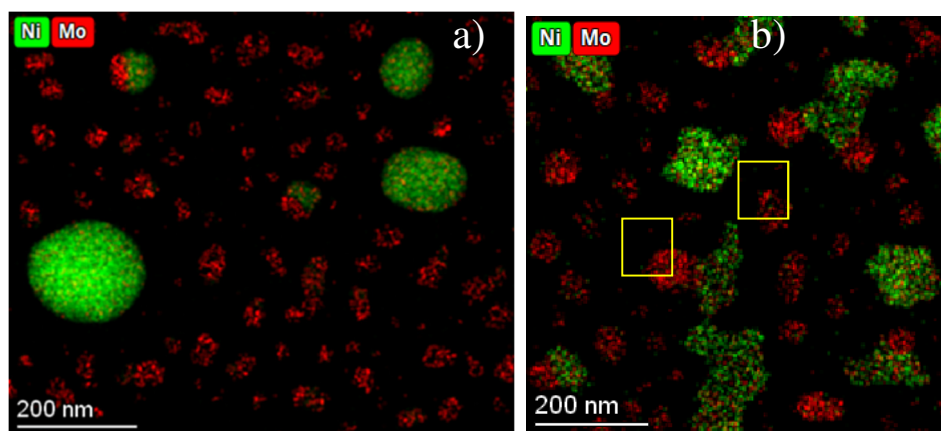


Figure 5: Ni and Mo STEM-EDS maps at places where the TEM-EDS determined Mo/Ni=1.1 (a); and where Mo/Ni=3.1 was determined, with the close to equimolar alloys (some of them framed) (b)

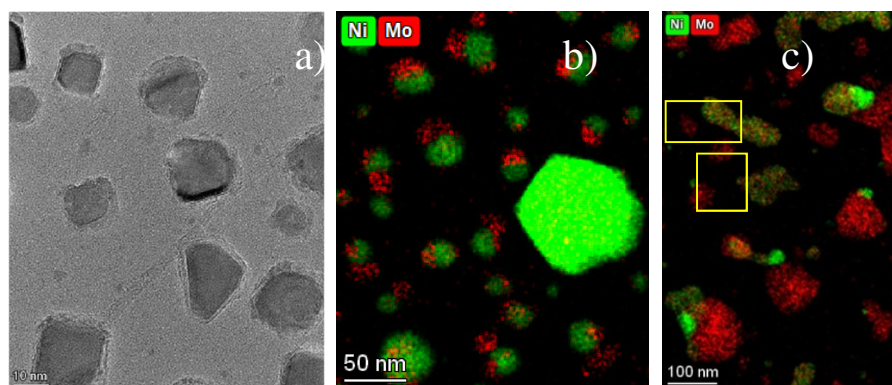


Figure 6: Carbon nanotube and coverage at the Ni end of the grid after pyrolysis step (a); alloy segregation at a place of the grid where Ni is in high excess, Mo/Ni=0.2 (b); stable alloy with Mo/Ni=1.2 detected after pyrolysis at the Mo-rich place of the grid (c)

The next step during our research was to carry out CH₄ decomposition at 800 °C on the bimetallic particles formed on the grid. After this imitated pyrolysis, carbon deposition could be detected only at the Ni end of the grid. Fig. 6 shows the 2 nm thin carbon nanotubes and the same-sized carbon coverage formed around the Ni particles. However, as the Mo content increased along the grid axis, these carbon structures disappeared in contrast to what we expected based on the results of the real supported catalysts (bimetallic samples produced more carbon nanotubes). Thus, we could not detect distinct carbon morphologies at the bimetallic range of the grid, and the quantification of amorphous or dissolved carbon by TEM is not possible yet, because we need a proper reference over the grid. As for the segregation phenomena caused by the CH₄ contact, we can declare the followings. At places where Mo/Ni=0.2 was determined by TEM-EDS, the small particles of about 20 nm were partially segregated into a Mo-rich and a Ni-rich part, while the large ones were made of mostly nickel (Fig. 6b). Whereas, at the same location as in Fig. 5b (at Mo/Ni=3.1), the unsegregated alloy composition with about Mo/Ni=1.2 ratio (framed in the figure) was found beside the other segregated ones with different composition (Fig. 6c). This is in nice accordance with the supported catalysts.

The very same grid after CH₄ contact could be analyzed by Raman spectroscopy as shown in Fig. 7a-c. The graphitic nature of the carbon suggesting nanotube or graphene layer morphology was detected at the Ni end of the grid, but other places were free of this kind of carbon, as Fig. 7c shows. The complete agreement of Raman and TEM results about the carbon structure are very promising as we can exactly allocate the places on the grid in μm size range and thus the same place can be measured by TEM and Raman as well. Raman spectroscopy is a surface sensitive technique, while TEM works in transmission mode, and all components of the thin sample are measured. This is why additional (and different) results could be obtained by Raman in the future, when, hopefully, a stronger carbon deposition will be achieved.

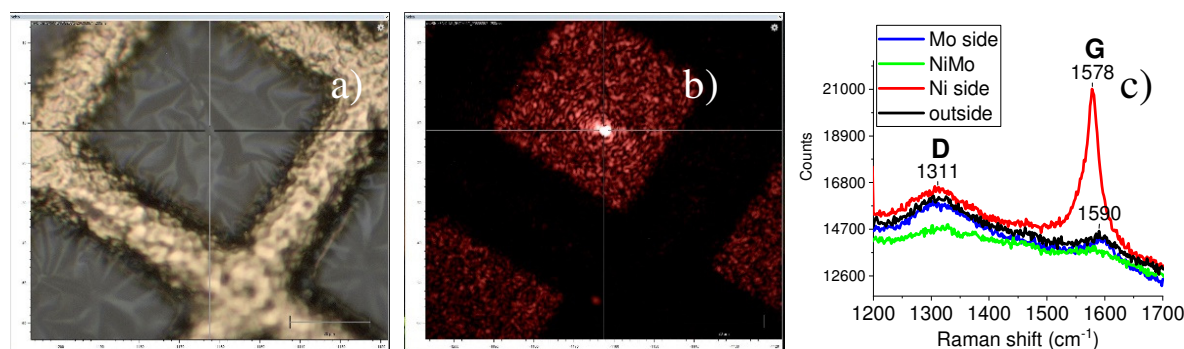


Figure 7: TEM grid after the pyrolysis under the Raman microscope (a); the same place under laser beam during Raman measurement (b); Raman spectra taken at the Ni and Mo end of the grid and in the middle (NiMo), finally, outside of the deposited layer (c)

The anomaly of the carbon formation (absence of abundant carbon nanotubes) over the grid sample can be explained by several reasons. The strongest argument is the unfortunate germanium impurity detected at the very end of the EDS spectra analysis. The germanium component was alloyed with nickel and originated probably from the grid sample holder. Germanium is very mobile under reducing atmospheres and could penetrate the metallic nickel during CH₄ decomposition, as we used a different sample holder for this step accidentally. The other reason could be the absence of MgO supporting oxide layer, as here, SiO₂ was the commercial grid membrane that ensures a much weaker interaction with the NiMo particles. The third reason is the disagreement of metal particle size on the grid and in the supported catalysts, being much smaller, under 10 nm, in the latter case. As catalytic reaction greatly depends on the presence of alloys and their impurity, the metal-support interaction and the dispersion of the metal components, these 3 must be well-controlled and kept in the focus of our future developments. All in all, this brand new microcombinatorial TEM sample preparation and investigation method of alloys for methane pyrolysis producing pure H₂ and carbon, is a very promising, perspective and exciting tool, and deserves continuation. The work will be useful for the scientific or industrial community dealing with methane utilization to produce

hydrogen and precious carbon structures (as fibres, nanotubes) without CO_x formation, as a bridge in the transition from fossil to the renewable energy-based economy.

Remaining work

Preparation of new microcombinatorial samples without contaminations is to be performed with different metal particle sizes on MgO thin film covered Au grid, to produce carbon nanotubes in large amount. Additionally, the quantification of carbon formed is to be worked out. Finally, the results of the research need to be published. For completing the planned research work, a new project proposal for one more year will be submitted.

Related publications

- [1] A. Horváth, M. Németh, A. Beck, Gy. Sáfrán, Zs.E. Horváth, I. Rigó, Z. May and T.I. Korányi: *Methane pyrolysis on NiMo/MgO catalysts: change of bimetallic composition as a governing factor of catalytic performance*, ACS Applied Nano Materials, under review (2023)
- [2] A. Horváth, M. Németh, T.I. Korányi, A. Beck, Gy. Sáfrán, Zs.E. Horváth and I. Rigó: *Methane Pyrolysis on NiMo/MgO: Details of the Synergetic Effect*, poster, 15th European Congress on Catalysis, 27 August 2023 - 01 September 2023, Prague, Czech Republic
- [3] T.I. Korányi, M. Németh, A. Beck and A. Horváth: *Catalytic Decomposition of Methane for Producing Hydrogen Gas and Carbon Nanotubes*, oral presentation, 9th Conference of the Federation of the European Zeolite Associations, 2-6 July 2023, Portorož-Portorose, Slovenia
- [4] A. Beck, M. Németh, T.I. Korányi, Gy. Sáfrán, L. Borkó, Zs.E. Horváth, I. Rigó and A. Horváth: *Structural background of the synergetic bimetallic effect of NiMo/MgO catalysts in methane pyrolysis*, online oral presentation, International Conference on "Current Problems in Catalysis", 25-29 September 2023, Kyiv, Ukraine
- [5] Horváth A., Beck A., Németh M., Sáfrán Gy., Olasz D., Szász N. és Horváth Zs.: *Metánbontás Ni-Mo katalizátorokon: a mikrokombinatorikus TEM módszer bevezetése a kétfémes rendszer vizsgálatára*, előadás, Anyagtudományi Szimpózium, 2023. október 4-6., Mátraháza, Magyarország
- [6] Horváth A., Beck A., Németh M., Sáfrán Gy., Olasz D. és Horváth Zs.: *Metán pirolízis NiMo/MgO katalizátorokon: a szinergikus hatás részletei*, előadás, az ELFT Vákuumfizikai, -technológiai és Alkalmazásai Szakcsoport, az MTA Felületkémi és Nanoszerkezeti Munkabizottság, a Magyar Vákuumtársaság és az MTA Elektronikus Eszközök és Technológiák Tudományos Bizottság közös szeminárium, 2023. október 24., EK MFA, Budapest, Magyarország

TRACKING SURFACE PROCESSES ON WATER OXIDIZING ANODES USING HIGH-SENSITIVITY OPERANDO ELLIPSOMETRY

József Sándor Pap, Zoltán Lábadi, Dávid. Lukács, Miklós Németh, Noémi Szász, Debashis Mukherjee, Krisztina Frey, Péter Petrik

Objective

In electrochemistry, the redox transformations take place within a thin diffusion layer. The use of non-invasive *operando* optical probing methods, such as the optical waveguide lightmode spectroscopy and the ellipsometry, can provide more sophisticated insight into the electrode processes. Ellipsometry probes a sub-nanometre thickness underneath the electrode surface, with quantitative spectroscopic capabilities and a time resolution of a few seconds. Optical models are applicable for the quantitative determination of layer thicknesses and intra-layer spectroscopic dispersions.

The electrolysis of water to H₂ and O₂ is an appreciated technology to chemically store renewable energy. For this purpose, efficient electrocatalysts are highly desired in this field. Novel catalytic systems often utilize 1st-row transition metals, including molecular catalysts. The latter substances especially tend to change during the initial phase of catalysis, where ellipsometry could be a very useful tool. We realized that several oxygen-producing molecular Cu-peptide anode pre-catalysts undergo substantial changes during use, as demonstrated *via* electrochemical characteristics, solution spectroscopy and *ex situ* surface analysis. However, the nature of the rapid initial processes and consequences on the long-term operation of the resulting catalysts remained so far unexplored. Especially, the optimized decomposition of a precursor may result in very active surface layers, exhibiting remarkable stability. We attempted to determine the optimal thickness and morphology of the catalyst layer by following the degradation timedynamics of a Cu-based pre-catalyst using *operando* ellipsometry, and subsequently, additional *ex situ* experiments were made to characterize the long-term catalytic performance and morphology.

Methods

Ellipsometry is an optical technique for the investigation of the thickness and dielectric properties (complex refractive index or dielectric function) of thin films. It measures the change of polarization upon reflection or transmission, and compares it to an optical model. It can be used to characterize the composition, roughness, thickness (depth), crystalline nature, doping concentration, electrical conductivity and other material properties. The measured signal is the change in polarization as the incident radiation interacts with the material structure of interest. The polarization change is quantified by the amplitude ratio (Ψ), and the phase difference (Δ). As the signal depends on the thickness, as well as on the other above-mentioned material properties, ellipsometry can be considered as a universal tool for contactless determination of thickness and optical constants of material layers.

We have prepared two sets of catalyst samples, under identical experimental conditions. The first set was used for the ellipsometry and electrochemistry experiments, while the second set was prepared to verify the repeatability of the sample preparation and monitor the stability of the catalysts in 20-24 hour long water splitting experiments.

Cyclic voltammetry (CV), Chronoamperometry (CA), or Chronopotentiometry (CP) was carried out using a BioLogic SP-150 potentiostat. The Indium Tin Oxide (ITO) or Fluorine-doped Tin Oxide (FTO) electrode was set as the working electrode in a three-electrode setup (Pt aux. and Ag/AgCl reference). CV (-0.5 V to +1.2 V), CA (1.08V) and CP (150 μ A) experiments were done in CuGGG (0.19 mM) / borate (0.1 M, pH = 9.29) buffer. Ellipsometry measurements were performed at the angle of incidence of 70°, with a data acquisition time of 2 s for whole Ψ and Δ spectra, where Ψ and Δ denote the amplitude ratio and the phase, respectively, between the reflection coefficients of light polarized parallel and perpendicular to the plane of incidence. The spectral range has been limited to the optically transparent region of the cell.

The optical model consisted of a glass slide, an indium-tin-oxide layer with a nominal thickness of 100 nm, and a top layer created by the electrochemical process. The glass slide and the ITO layers were described by the Cauchy and Lorentz oscillator dispersions, respectively. The top layer was modelled using the B-Spline approach, which describes the spectral dependence of the dielectric function using attached polynomials. Besides ITO, we also started to investigate the FTO glass as a support for deposition of copper layer by electrochemical method concurrently with the ellipsometry. The thickness of FTO layer has been 600 nm and its roughness was specified to 34.8 nm, which means it is much rougher than the ITO is. Even though its higher roughness, the build-up of the layer could successfully be monitored in real time by this technique.

After depositing the copper layer, the surface morphology of the samples was characterized by Scanning Electron Microscope (SEM/EDX), and the oxidation states of the copper oxide were measured by X-ray Photoelectron Spectroscopy (Thermo Fisher Escalab Xi+ XPS).

Results

We investigated the deposition of the copper layer using Cyclic Voltammetry (CV). The deposition process was terminated at different predefined voltages (-0.42 V, 0.9 V, 1.02 V, 1.2 V) between -0.5 V and 1.2 V, and the variation of the layer thicknesses was simultaneously followed by the ellipsometry measurements. The layer-building process was also followed as a function of electrochemical cycles (n=1, 1.5, 2, 2.5, 6.5, 8.5, 137). For illustration, a 2.5 cycle-long deposition process is plotted in Figure 1, where the current peaks directly correspond to the thickening of the layer.

CA and CP measurements were also performed, where the time evolution of the layer thickness has been determined at a constant voltage and current level of 1.08 V and 150 μ A, respectively. The electrochemical and ellipsometric signals show a good time correlation for all three sample preparation methods and allow the coherent interpretation of the electrochemical deposition process.

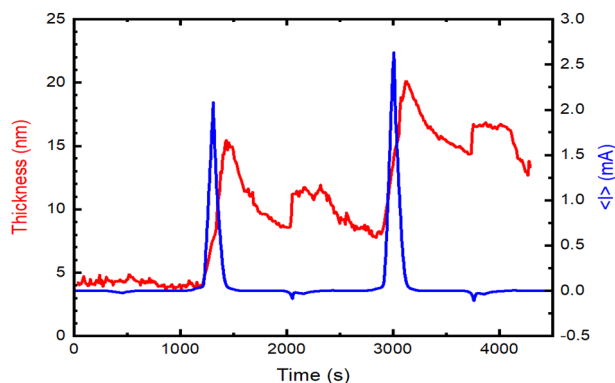


Figure 1: Time-dependent current and layer thicknesses during cyclic voltammetry experiment

The conclusions were supported by XPS and SEM/EDX measurements, the most commonly used techniques to characterize the deposited layers. Cu(II)-oxide particles of 50-100 nm diameters were observed. The XPS and the SEM data (Fig. 2) of the sample shown in Figure 1 depict the different oxidation states and morphology of the Cu on the surface.

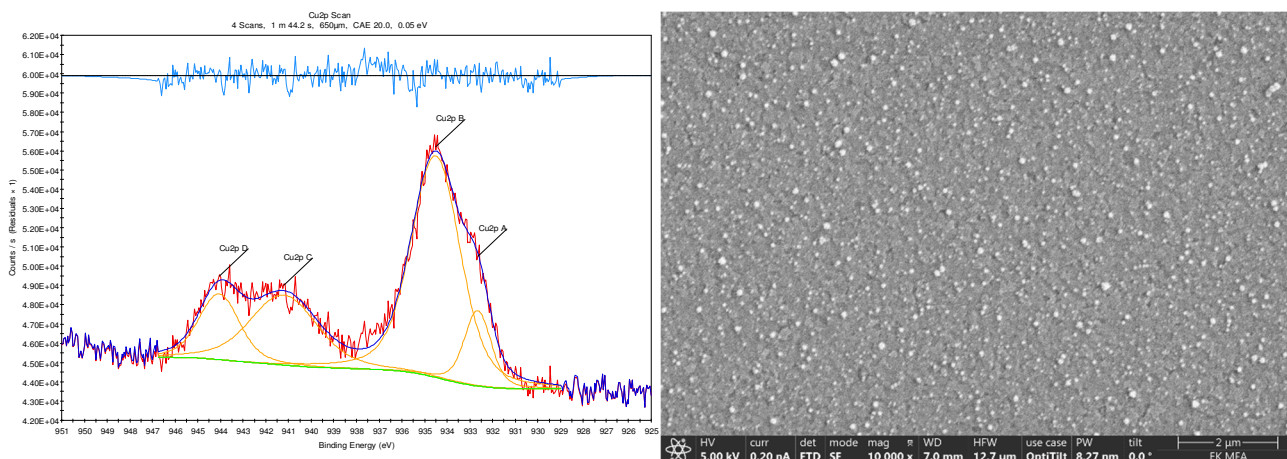


Figure 2: Cu 2p_{3/2} spectra of Cu-oxide layer deposited by CV (2.5 cycles) (left) and SEM image of this surface (right)

The thickness of the produced Cu layer, or the Cu particle size, differed depending on the experimental conditions. The amount of Cu detectable on the surface by XPS varied between 3-24 atom%. We observed that X-rays could reduce some of the Cu(II) into Cu(I) during the XPS measurements if the Cu-content of the surface is less than 5 atom%. This phenomenon was not detected at higher concentrations (Fig. 3).

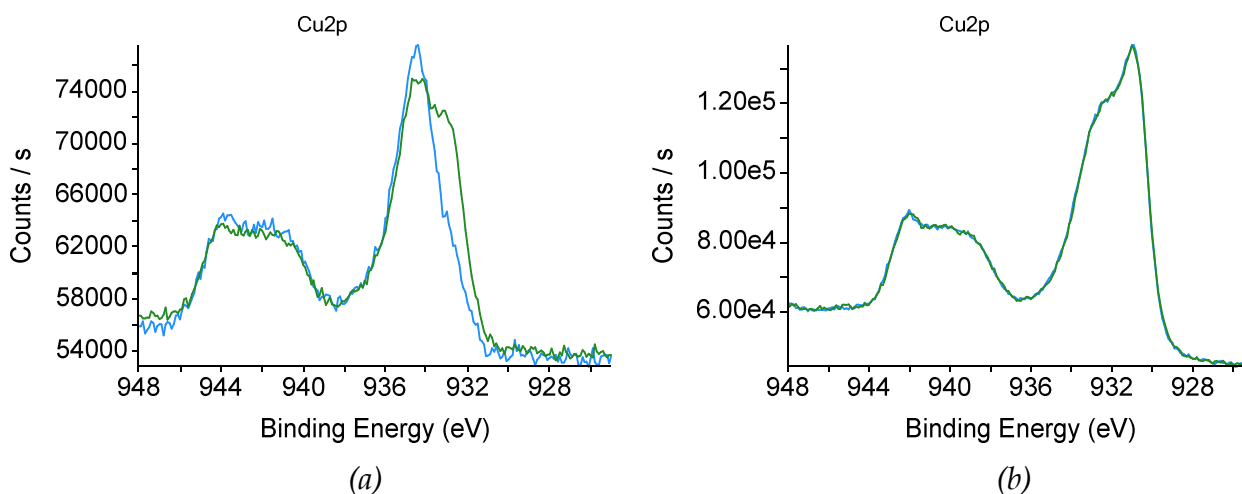


Figure 3: Cu 2p_{3/2} spectra of Cu-oxide layer deposited by CA (1.08 V, 30 min) and CP (150 μ A, 65 min). The blue line shows the first measurement, while the green the repeated XPS measurement of the same sample.

The largest amount of Cu could be deposited onto ITO surface using the CP preparation method (150 μ A, 65 min). The Cu content at the surface was measured to be 22.79 atom% by XPS (a), while much less, maximum 3.5 atom% of Cu was detected by EDX (b) on the same sample. Such differences of the reported Cu contents are due to the different probing depths of the two techniques. In this case, Cu particles were not observable on the surface by SEM (Fig. 4). A possible explanation is that the sizes of the particles are smaller than the spatial resolution of the instrument.

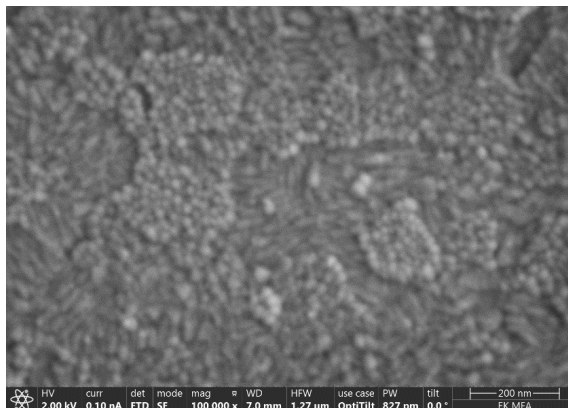


Figure 4: SEM image of a sample prepared via CP at 150 μ A, 65 min

During an *in situ* sample preparation in the ellipsometric cell, a significant re-deposition process (Fig. 5) was observed if the sample was not removed immediately after the end of the electrochemical deposition. If the sample was left in place, the signal of the ellipsometer stabilized only slowly and approached a constant level.

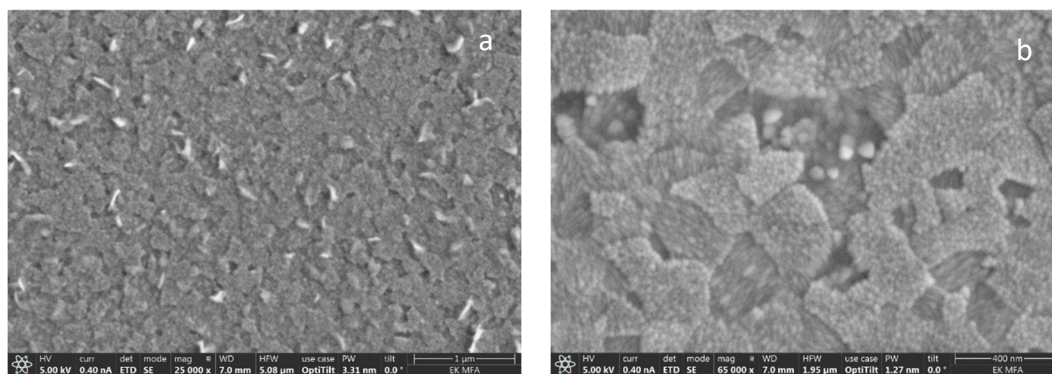


Figure 5: SEM images to visualize the re-deposition after a chronoamperometric sample preparation at 1,08V 30 min. a) The sample was removed immediately from the ellipsometric cell and b) after the stabilization of the ellipsometer signal.

The prepared samples have been tested for stability in water-splitting experiments. It was found that thicker Cu layers exhibit higher catalytic activities and show better time stability.

We concluded that the goal of the research was achieved, as we have proven the fitness of ellipsometry for the *operando* observation of electrochemical processes. Although individual measurements are evaluated, the synthesis of the various results, including SEM and XPS, is still in progress. We presented the results at numerous conferences and expect to publish them in two D1 category journals. This innovative methodology can be used in future surface-catalysis research to thoroughly understand the near-surface processes, and thereby preparing more efficient and durable catalysts for industrially relevant processes.

Related publications

- [1] K. Frey, J.S. Pap, D. Lukács, M. Németh, Z. Lábadi, D. Mukherjee, P. Petrik: *Tracking surface processes on water oxidizing anodes using high-sensitivity operando ellipsometry*, 15th Pannonian International Symposium on Catalysis, Jastrzębia Góra, Poland, 4-8.09.2022.
- [2] Z. Lábadi, J.S. Pap, K. Frey, P. Petrik: *Application of ellipsometry for in-situ monitoring of electrochemical processes*, TCM-TOEO 16-21 October 2022, Knossos Greece.
- [3] J. Pap, D. Lukács, S. M. Al-Zurajji, M. Németh, K. Frey, S. Shen, L. Vayssieres: *Studying water oxidation catalysts on transparent conductive oxides*, TCM-TOEO 16-21 October 2022, Knossos Greece.
- [4] K. Frey, J. S. Pap, D. Lukács, Z. Lábadi, D. Mukherjee, N. Szász, M. Németh, P. Petrik: *Tracking surface processes on water oxidizing anodes using high-sensitivity operando ellipsometry*, 15th European Congress on Catalysis, Prague, Czech Republic, Augustus 27 – September 1.

- [5] K. Frey, Z. Lábadi, D. Lukács, D. Mukherjee, N. Szász, P. Petrik, J.S. Pap: *Operando ellipsometry, a highly-sensitive and integrated tool to observe and optimize the electrochemical anodic catalyst formation for water splitting applications*, D1 paper in preparation.
- [6] Z. Lábadi, K. Frey, D. Lukács, D. Mukherjee, N. Szász, J.S. Pap, P. Petrik: *In situ study of elemental electrochemical processes and Faradaic efficiencies by ellipsometry*, D1 paper in preparation.

MODELLING THE AIRBORNE TRANSMISSION OF SARS-CoV-2 IN A HOSPITAL WARD DURING NURSING CARE ACTIVITIES

Szilvia Kugler, Péter Fűri, Árpád Farkas, Veronika Groma, János Osán, Balázs Madas

Objective

To monitor airborne transmission of SARS-CoV-2 from one patient to another in a hospital ward during the COVID-19 pandemic was an important challenge to solve, since the scientific community already emphasized the predominance of this mode of transmission of the virus [1]. However, the factors that influence the concentration of respiratory droplets and aerosol particles that potentially contribute to hospital-associated transmission of SARS-CoV-2 are not fully explored yet. The goal of our work was to determine the change of aerosol load during different nursing care activities in a hospital ward. It was also an aim to use the measured data to simulate the deposition rates (deposited particle number or mass/unit time) and deposition density rates (deposited particle number or mass/unit time/unit surface of airways) of the inhaled particles in different regions of the airways (extrathoracic, bronchial and acinar).

Methods

Aerosol number and mass concentration measurements were performed in a closed patient room with one PCR positive COVID-19 patient (Department of Pulmonology, Semmelweis University, Budapest, Hungary) over a 24-hour period with Optical Particle Counters (Grimm Aerosoltechnik, Portable Aerosol Spectrometer, model 1.109). Several different activities were recorded, and six representative ones were selected for the simulations with the Stochastic Lung Model (SLM), including patient's activities (coughing, movements, etc.), diagnostic and therapeutic interventions (e.g., diagnostic tests and drug administration), as well as nursing patient care (e.g., bedding and hygiene). The increase in particle concentration of all sizes was sensitive to the type of activity in the room. Table 1 shows the type of activity in the room, where the classified categories are: A) physician and/or nurse visit for medical diagnostic examinations and/or therapy administration; B) nursing care; C) patient's activity. The highest increase in the number concentration of the submicron range ($< 1 \mu\text{m}$) particles was found during activities nr. 2 and 3. In the supermicron range ($> 1 \mu\text{m}$) an intensive increase in particle concentration was found during activities nr. 3 and 6.

Table 1: Description of the selected activities. A) physician and/or nurse visit; B) nursing care; C) patient's activity.

Activity number	Type of activity	Number of personnel	Activity duration (min)
1	C	0	6
2	A	1	16
3	B	2	30
4	A	2	15
5	A	3	28
6	A and B	3	25

To determine the particle airway deposition distribution the SLM was applied. The respiratory volume was set to 500 cm^3 , the functional residual capacity was 2100 cm^3 , the inhalation time was 1.9 seconds, the breath hold between inhalation and exhalation was 0.1 seconds, and the exhalation time was 2 seconds. All simulations assumed nasal breathing.

Results

The deposition rates were obtained by multiplying the number or mass of particles inhaled in a minute with the fraction of deposited particles. The number of particles inhaled per unit time depends on the breathing pattern (inhaled volume, respiratory frequency) and the particle concentration in the air. The highest number concentrations were measured during activities nr. 2 and 3. Since the deposition rates are essentially dependent on the particle concentration in the air, the highest deposition rates were obtained for activity nr. 3 where the highest aerosol number concentration was measured (see Figure 1). Regarding the number deposition rates, acinar deposition dominates for all six activities as Figure 1A demonstrates it. The vast majority of the inhaled mass was in the supermicron size range that is why the mass deposition rates were the highest in the extrathoracic region. For this size range, the upper airways (nose, pharynx, larynx) are a very good filter as shown in Figure 1B.

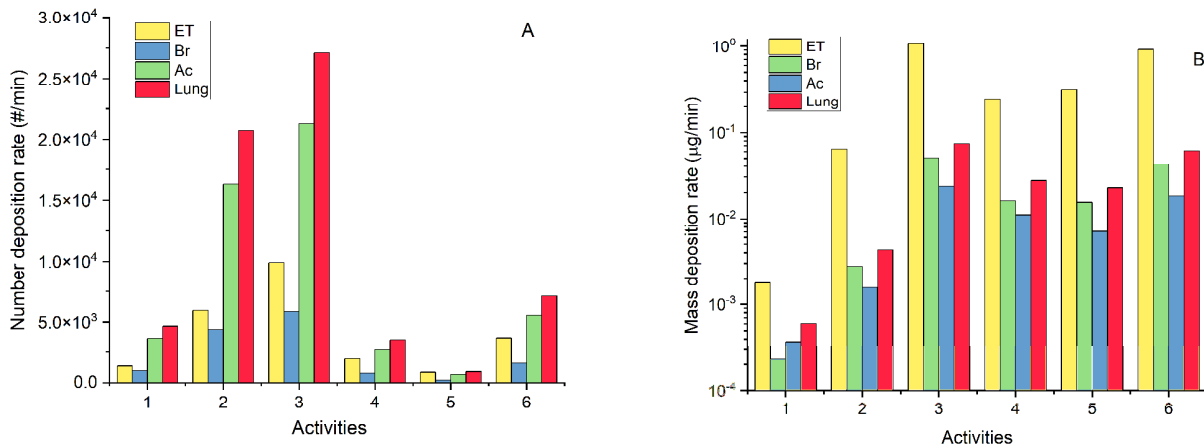


Figure 1: Extrathoracic (ET), bronchial (Br), acinar (Ac) and lung deposition rates of the number (A) and mass (B) of inhaled aerosol particles in the studied patient room

The number of particles deposited per unit surface (1 cm²) of airway epithelium per minute (deposition density rate) was obtained by dividing the deposition rate by the surface area of the airways. It is important to highlight that various parts of the human airways have very different surface areas. The upper airways are very small, with a surface area of only about 470 cm². The bronchial region of the lung is larger, with a surface area of 2700 cm². The acinar region of the lung has a huge surface area of about 148 m². Large number of particles must deposit in the acinar region to obtain high deposition density rates in this part of the lung.

Figure 2 shows the number and mass of particles deposited per unit surface area of the airways per unit time for all six activities. The deposition density rate is at least five or even six orders of magnitude higher in the upper airways than in the bronchial or acinar regions of the lung in both cases.

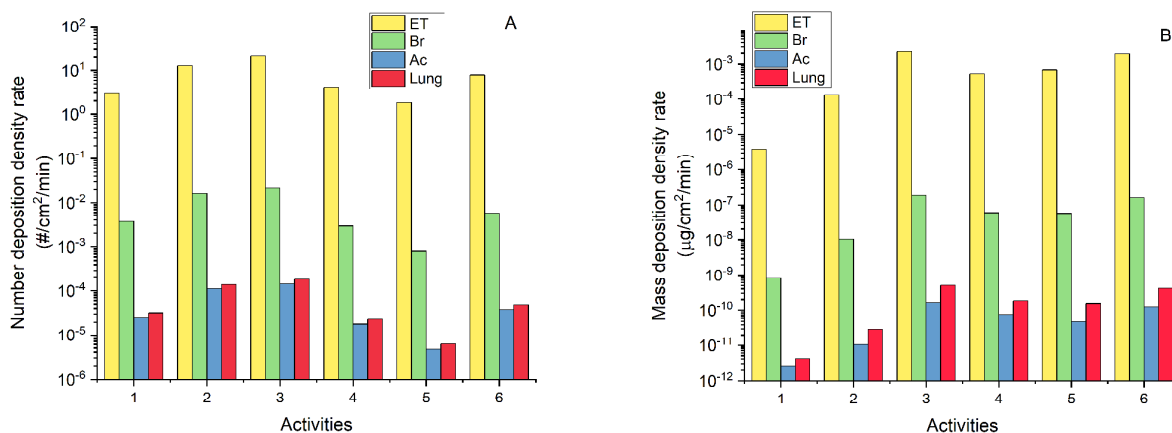


Figure 2: Extrathoracic (ET), bronchial (Br), acinar (Ac) and lung deposition density rates of the number (A) and mass (B) of inhaled aerosol particles in the studied patient room

Our results demonstrated that the number of particles deposited in unit time was the highest in the acinar region, while in terms of particles mass the extrathoracic region had the highest burden. Meanwhile, the deposition density rate was several orders of magnitude higher in the upper airways than in the lung. It means that even short periods of health care professional-patient interaction and minimal patient activity in a hospital ward may significantly increase the concentration of submicron particles, which mainly deposit in the acinar regions, while mainly nursing activities increase the concentration of supermicron particles depositing in the extrathoracic airways. Our data emphasize the need for effective interventions to limit hospital-associated transmission of SARS-CoV-2.

Related publication

- [1] V. Groma, Sz. Kugler, Á. Farkas, P. Fűri, B. Madas, A. Nagy, T. Erdélyi, A. Horváth, V. Müller, R. Szántó-Egész, A. Micsinai, G. Gálffy and J. Osán: *Size distribution and relationship of airborne SARS-CoV-2 RNA to indoor aerosol in hospital ward environments*, Scientific Reports **13**, 3566 (2023) <https://doi.org/10.1038/s41598-023-30702-z>

INCREASING THE STABILITY OF POWER SYSTEMS WITH HIGH RENEWABLE ENERGY SHARE BY THE USE OF COUPLED OSCILLATORS

Bálint Hartmann, Géza Ódor, Shengfeng Deng, István Papp, Kristóf Benedek

Objective

Power-grids are among the largest man-made complex systems, staying in the synchronization state of billions of nodes. Formerly, power-law-tailed cascade size distributions have been found by outage statistics and DC (Direct Current) models. The spread of renewable resources poses unprecedented pressure on system stability. Our aim is to show how this can be modelled by Kuramoto-like synchronization models, which describe the real power flow in AC (Alternating Current) systems.

Methods

We revisited the topic of the size distribution of forced outages in power systems to formulate possible theoretical explanations of the uniformness of these distributions. To address a shortcoming of previous studies, long-term outage data of various power systems were collected and analyzed. First, exponents of power-law fits were extracted to cross-check the results with related literature; then this step was repeated after setting a threshold, speculating that the understanding of the manifested power-law for the unavailable duration constitutes a crucial ingredient for the understanding of general power-law behaviour in outage distributions.

Results

Based on the numerical results, potential explanations were presented, and a power spectral analysis was performed to demonstrate that the studied outage data are composed of many random events as well as some correlated events characterized by the $1/f$ noise. This hints that SOC (Self-Organized Critical) processes could take place in outage events. Therefore, for outage events, we consider the system under study as the combination of spontaneous isotropic percolation and a branching process, implying Manna universality class criticality. Although the heavy tails in outage duration distributions are tempting, given that the majority of the outage events occurred out of random causes, the manifested power-laws in outage duration cannot be attributed only to correlated events of repair mechanisms. The power spectra of the outage duration time series further indicate a lack of $1/f$ noise for small f , leading us to conjecture an extended HOT (Highly Optimized Tolerance) explanation for the heavy tails in outage duration distributions for outages with small frequencies.

The similarities in the graph topological and electrical measures between the power grids of Europe and North America, especially the cable length distributions, suggest a universality hypothesis, which breaks down as we go towards the lower level sub-systems or as the consequence of under-sampling, like subsets of real data. The latter can very well be observed for the obviously incomplete EU22 power-grid case, which provides results, resembling to smaller regions, like for the USHW (U.S. Health Works Medical Group) corresponding to the North-West states of the US. In general, universality is expected to occur in the infinite system size limit, according to statistical physics and the behaviour in smaller systems can deviate from it. Our extensive, continent-sized analysis provides an opportunity to observe it. We have also shown a frequency fluctuation analysis of Hungarian data that can be described by similar super-statistics and q exponent, as the ones published for the Nordic grid region recently.

Related publications

- [1] [B. Hartmann](#), S. Deng, G. Ódor, J. Kelling: *Revisiting and Modelling Power-Law Distributions in Empirical Outage Data of Power Systems*, PRX Energy **2**, 033007 (2023) <https://doi.org/10.1103/PRXEnergy.2.033007>
- [2] G. Ódor, S. Deng: *Synchronization transition of the second-order Kuramoto model on lattices*, Entropy **25**, 164 (2023) <http://dx.doi.org/10.3390/e25010164>
- [3] G. Ódor, I. Papp, K. Benedek, [B. Hartmann](#): *Improving power-grid systems via topological changes, or how self-organized criticality can help stability*, Physical Review E **6**, 013194 (2024) <https://doi.org/10.1103/PhysRevResearch.6.013194>
- [4] S. Deng, G. Ódor: *Chimera-like states in neural networks and power systems*, Chaos **34**, 033135 (2024) <https://doi.org/10.1063/5.0154581>
- [5] [B. Hartmann](#), I. Papp, K. Benedek, S. Deng, G. Ódor, J. Kelling: *Dynamical heterogeneity and universality of power-grids*, arXiv:2308.15326, under review in Sustainable Energy, Grids and Networks



V. NUCLEAR ANALYSIS AND CHEMISTRY



THE RENEWED COLD NEUTRON IMAGING FACILITY, NORMA

Zoltán Kis

Objective

The Budapest Neutron Centre (BNC) operates the cold neutron beam imaging station, NORMA, for non-destructive testing. For the NORMA station there have been increasing requests to reach higher spatial resolution and the ability to follow time-dependent processes. Among these needs, some of the most important problems are related to energy production and storage. In this field, higher spatial resolution (some tens of microns or better) together with variable exposure times (from tenths of a second up to a few times in tens of seconds) need to probe the structure and operational characteristics of fuel cells and electric batteries. Therefore, the system used successfully so far was completely redesigned and installed for a variety of tasks.

Methods

Both our own and international experiences have shown that the requirements cannot be well met by one type of system, and therefore a system optimized for two sets of tasks was designed at the conceptual design level. The new system is based on the principle of three independent modules allowing for highly configurable settings. It is to operate finding the right balance between the necessary spatial resolution, the sufficiently shorter or longer temporal resolution and a large enough field of view. The systematic study of the setups clearly shows parameters' effects helping the right choice for the measurement tasks. Among the rarely investigated parameters, we studied both the effect of the pixel binning and the change of lens f-stop value on the spatial resolution.

Results

The results of spatial resolution and exposure time measurements using the three cameras and two scintillation screens are shown in Table 1 and in the panels of Fig.1. It can be seen that the inherent blur of the scintillation screens masks and overrides the different values got from theoretical calculations. Gadox screen has the best resolution, and the LiF/ZnS screen is inferior to it from this viewpoint, however, Li-based screen needs lower exposure time. There are ways to shorten the exposure times of the Gd-based screens while keeping the wide dynamic range of 16-bit images. The currently installed tandem setup considerably increases the light collection effectiveness resulting in a gain factor of 3. Moreover, the use of Charge Coupled Device (CCD) and scientific-grade Complementary Metal-Oxide Semiconductor (sCMOS) cameras offers the freedom of choosing the right detector system, too. The range of native pixel and chip sizes provides well-tailored effective pixel size, i.e., spatial resolution and exposure times in the adaptable field of view. According to the recent camera developments, one of the available sCMOS type cameras can provide both exceptionally long exposure time and large well depth in small pixels, so providing both high dynamic range and good spatial resolution in 16-bit mode.

Table 1: Spatial resolution (theoretical and measured) and exposure time values of the various configurations

Configuration	Camera	Lens	Theo. (μm)	Li100 (μm)	Exp. (s)	Gd10 (μm)	Exp. (s)
Medium-resolution	iKon-M	Milvus 2/100M	52	149	12 (16bit)	77	232 (16bit)
	Neo 5.5		26	126	30 (16bit)	47	38 (12bit)
	QHY600M		15	110	2.5 (16bit)	43	60 (16bit)
High resolution	Neo 5.5		16.3	-	-	34	12 (16bit)
	QHY600M		9.4	-	-	33	20 (16bit)

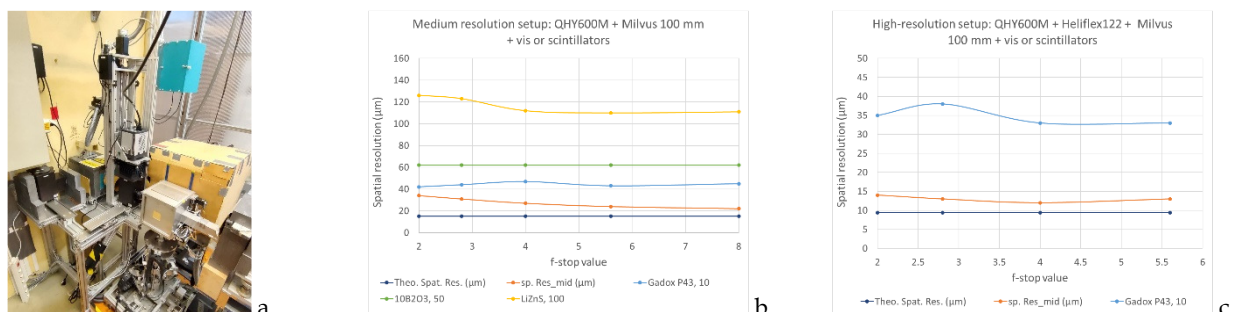


Figure 1: The renewed NORMA system, and its theoretical and measured spatial resolution values from different optical setups

Remaining work

The project continues in the framework of National Laboratory for Renewable Energy with measuring fuel cells in operando.

Related publication

- [1] Z. Kis: *The redesigned neutron imaging facility, NORMA at BNC, Budapest*, Review of Scientific Instruments **95**(7), (2024) <http://dx.doi.org/10.1063/5.0208844>

PERFORMANCE TESTING OF LOW-DIMENSIONAL COLD NEUTRON MODERATORS AT THE BUDAPEST RESEARCH REACTOR

Laura Draskovits, Peter Konik, Márton Markó, Viktor Mészáros, László Rosta

Objective

A major milestone in cold neutron moderator developments has been the invention of low-dimensional geometries, such as the so-called “butterfly moderator” at the European Spallation Source. Monte-Carlo simulations have shown that if liquid para-hydrogen is used as moderator material, these novel devices can increase significantly the neutron source brightness desired by most types of neutron instruments. Various designs were extensively studied by Monte Carlo simulations, while few experiments are available to validate them. The dedicated Cold Moderator Test Facility (CMTF) installed as an out-of-pile equipment at the 10 MW Budapest Research Reactor (BRR) aims to overcome difficulties in experimental investigation of moderator properties.

Methods

A radial channel beamline is looking directly on the reactor core; thus an unusually hard neutron spectrum is available. The beam hits a Be plate installed in a Pb reflector placed close to the channel exit. Neutrons scattered by this Be are slowed down in the cryogenic moderator cell tested, which is also installed in the Pb block. Cold neutrons leaving the moderator assembly (e.g. a tube-type vessel filled with liquid p-hydrogen) through a collimator are measured by a Camera Obscura system with a time-of-flight option using a chopper system. This device enables to measure the spatial and spectral distribution of neutrons emerging from the moderator, thus its various features are characterized.

Results

This work has been a part of a project supported by the HUN-REN Proof of Concept program (2021) as well as a H2020 project (EURIZON). We have created a unique measuring station for testing the concept and validating the model calculations for the innovative solution to enhance neutron moderator performances. We have modelled and built two versions of a Low-Dimensional Neutron Moderator cell (LDM) operating with liquid para-hydrogen and tested them with a neutron beam [1]. This has taken the LDM technology from TRL-3 to three levels higher (TRL-6).

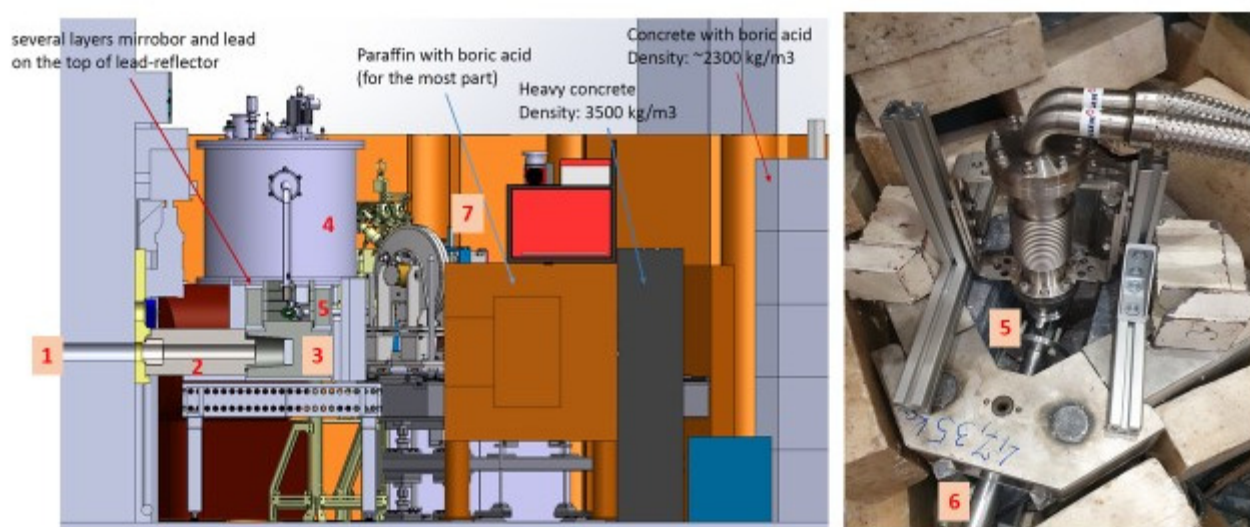


Figure 1: The schematic engineering design of the cold moderator test facility at the BRR (left) and the liquid hydrogen moderator vessel in the reflector with the pipelines from the cryostat (right). 1 – Reactor channel, 2 – thermal beam collimator, 3 – Be-Pb reflector block, 4 – cryostat with closed cycle refrigerator, 5 – liquid hydrogen moderator vessel, 6 – cold neutron optical line, 7 – spectrum analyser.

Remaining work

With the deployment of the CMTF and its development for user application, and the significant international collaboration potential in this area, the achievement of TRL-7 is also very close. The commercial service potential has also been demonstrated. This technology is ready to apply for the construction of a new high performance cold source at BRR.

Related publication

- [1] V. Santoro, L. Rosta et al.: *The HighNESS Project at the European Spallation Source: Current Status and Future Perspectives*, In Nuclear Science and Engineering **198(1)**, 31-63 (2023) <https://doi.org/10.1080/00295639.2023.2204184>

RESULTS OF THE HUN-REN EK ELECTRON CYCLOTRON RESONANCE PROTON ION SOURCE

Gábor Anda, Sándor Bató, Balázs Leskó

Objective

Due to the diminishing availability of traditional neutron sources, there has been a surge in the development of accelerator-based alternatives worldwide over the past two decades. Our developments began in 2021 at HUN-REN EK, focusing on the creation of an Electron Cyclotron Resonance (ECR) proton ion source utilizing permanent magnets. The primary objective of this project was to achieve a 20mA beam at 35keV beam energy, while ensuring a normalized emittance below 1π mm mrad.

Significant progress was made approximately a year ago, with the attainment of about 5mA using 250W of Microwave Power (MP) and an aperture diameter of 4mm. However, continuous measurement was restricted by the elevated temperature of the Faraday Cup (FC). To address this limitation, a novel water-cooled FC design was devised, allowing the FC to be moved in and out of the beam axis as needed. This innovation not only mitigated temperature-related measurement constraints but also contributed to beam stability, particularly during long pulses.

Water-cooled Faraday cup

The FC is situated within the 6-armed diagnostic chamber immediately following the ion optic, as depicted in Figure 1. In this setup, plasma is generated within the cavity, and ions are subsequently extracted via the Pierce electrode. The ion optic facilitates the formation of the beam, which then impacts the base plate of the FC for measurement purposes. To be able to measure beam current at the base plate, the secondary electrons must be prevented to leave it. This is done by biasing the housing of the FC to -500V. The design of the FC housing allows for easy observation of the base plate, with the top (or bottom, as shown in Figure 1) being open. Since excited protons do not emit visible light, an infrared camera is utilized to capture and visualize the beam shape.

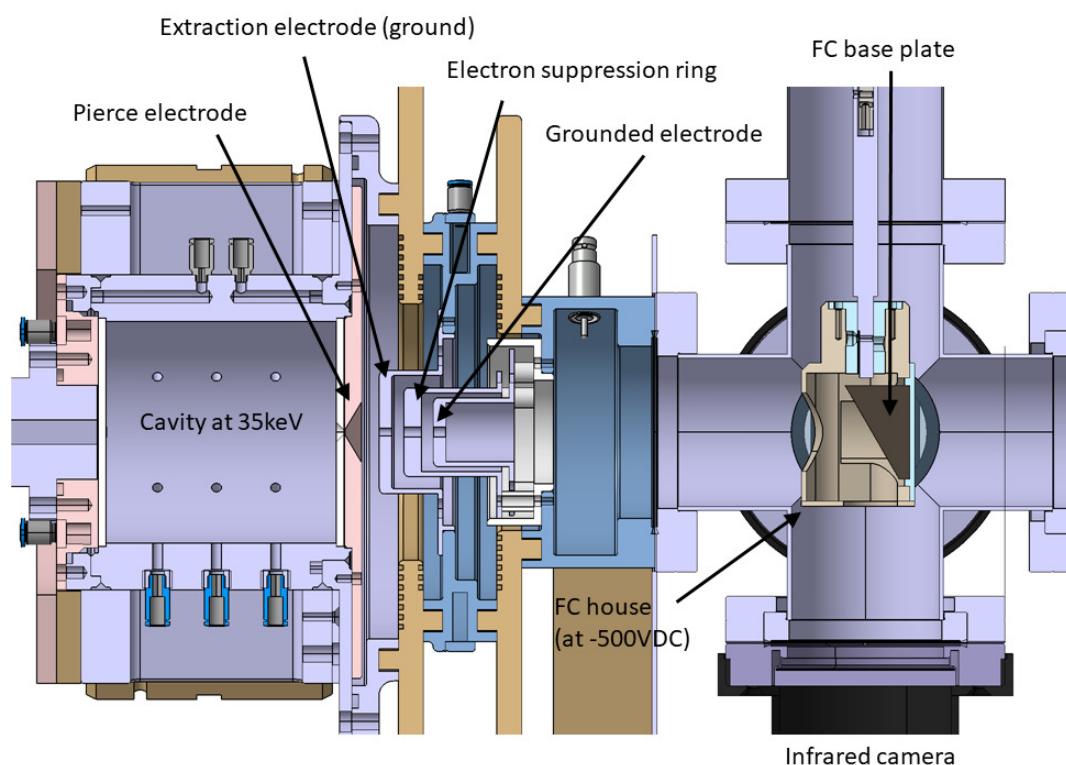


Figure 1: Layout of the proton ion source: cavity, ion optic and FC

To maintain optimal operating conditions and prevent current flow along the cooling lines, the FC is cooled using deionized water. Cooling pipes are brazed to the base plate, as illustrated in Figure 2, with green indicating the cooling channels. To ensure the structural integrity of the system and to prevent overheating, thorough thermomechanical calculations were conducted using Finite Element Analysis (FEA) methods. These calculations were essential in confirming that the temperature of the base plate remains well below its melting point, as demonstrated in Figure 2.

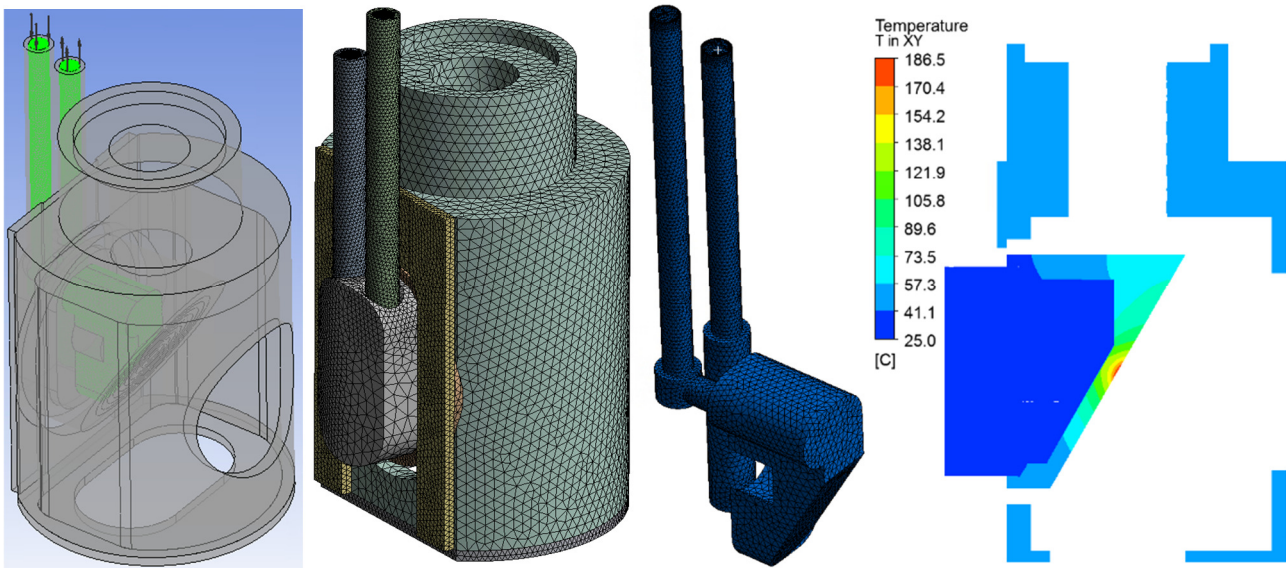


Figure 2: Layout of the water-cooled FC (from left to right): model, used mesh quality, cooling parts, simulation results

Measurements

To optimize the beam current within the FC, adjustments were made by varying the hydrogen flow while maintaining a constant microwave power (250W). The resulting measured beam is illustrated in Figure 3, featuring parameters of 35kV, 5mA, and approximately a 15mm diameter. Continuous beam measurements were conducted over a duration of approximately 5 hours, at intervals of 30 to 60 minutes. Notably, the instability of the beam current remained below 0.1%, meeting the requirements set forth for the Radio Frequency Quadrupole (RFQ).

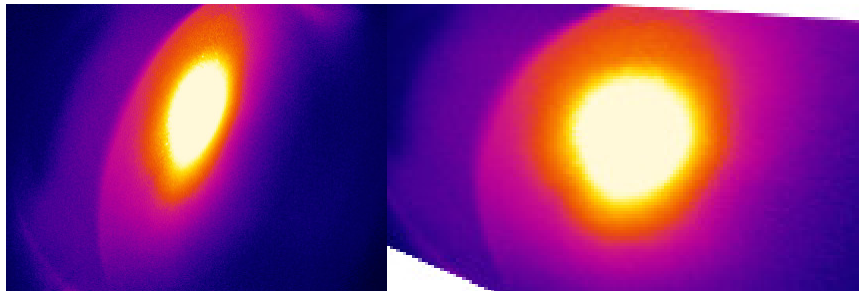


Figure 3: Proton beam in the FC measured by the infrared camera. Left: distorted picture. Right: corrected picture.

Remaining work

To prepare the proton source for its final configuration, we need to focus the beam before it enters the RFQ. To achieve this, we're currently developing a water-cooled solenoid. Additionally, we must assess the beam's emittance parameter, which describes its spatial and momentum spread. This measurement is crucial for ensuring that the beam aligns with the RFQ's requirements. By fine-tuning the beam's characteristics to match those needed by the RFQ, its performance can be maximized within the accelerator setup.

HYBRID PHOTONIC NANOARCHITECTURES BASED ON BUTTERFLY WINGS AND IN SITU GROWN METALLIC NANOPARTICLES

Krisztián Kertész, Andrea Vargáné Beck, László Péter Biró, Zsófia Baji, Endre Zsolt Horváth, Gábor Piszter, Gergely Nagy, Anita Nagyné Horváth, Zsolt Bálint

Objective

The interaction between nanostructures and electromagnetic radiation has extensively been investigated. In parallel, there is a dynamically evolving multidisciplinary field focusing on the examination and design of biological and bioinspired materials. Our primary focus lies in the modification of butterfly wings with structural colours to enhance their optical and surface properties. By combining biological photonic nanostructures with nanometre-sized metal particles, several potential applications become visible. Our plan involves conducting in situ preparation of metal nanoparticles within the intricate chitinous 3D nanoarchitecture using a light-induced reduction method, starting from precursor solutions. As the liquid completely permeates the structure, we anticipate a uniform deposition of plasmonic nanoparticles. This not only results in an increased surface area for interaction but also leads to the modification of the photonic crystal throughout the entire volume. This process yields a complex organic-inorganic hybrid nanoarchitecture with finely tuneable optical properties.

Methods

The materials used for nanoparticle preparation were ultrapure water, reagent-grade sodium citrate, HAuCl_4 and AgNO_3 precursors. The reactions were conducted in a glass cuvette placed on a temperature controlled magnetic stirrer. Nanoparticles (NPs) were formed while illuminating the cuvette using a small area solar simulator ORIEL LCS-100. As templates, we used the blue wings of the male *Polyommatus icarus*, *Morpho rhetenor helena*, *Hypochrysops polycletus* butterfly species. The wings were detached from the body of the butterfly and mounted on microscope glass slides using (Poly)methyl methacrylate (PMMA) photoresist as an adhesive. Such prepared samples were cleaned by soaking in absolute ethanol overnight followed by washing with ethanol and drying. The samples were placed in a 5 cm × 5 cm × 1 cm glass cuvette with the ingredients necessary for nanoparticle preparation. We also prepared butterfly wings coated with Au using physical vapour deposition as control samples. For this, wing pieces were mounted onto glass slides, and a gold wire of 99.99% was evaporated using a resistively heated tungsten boat source controlling the thickness by a vibrating quartz balance. To add a conformal coating onto the wing nanoarchitecture, Atomic Layer Deposition (ALD) of ZnO was performed. Reflectance spectroscopy measurements were conducted using an Avantes modular fibre-optic system consisting of a spectrophotometer, a stabilized deuterium-halogen light source, an integrating sphere, and a white diffuse tile as a reference. The extinction of the prepared sols was measured in a 1 cm light path quartz cuvette using the same spectrophotometer. For scanning electron microscopy, small pieces of butterfly wings were cut and mounted on Scanning Electron Microscope (SEM) stubs with conductive tape, and images were taken at the cut surface using Thermo Fisher Scientific Scios 2 DualBeam apparatus. A few drops of sols from the in situ growth were dried on carbon coated copper grids and inspected with a Thermo Fisher Scientific THEMIS 200 Transmission Electron Microscope (TEM). X-ray Diffraction (XRD) measurements were carried out with a D8 Discover X-ray diffractometer on a few mm spot.

Results

First, we performed the optimization of the growth process without using butterfly wing samples. In a glass cuvette, the optimal parameters (total solution volume, concentrations, time, temperature, illumination) for gold nanoparticle synthesis were investigated. As a result, we obtained the following protocol with the best outcome: 6 ml of ultrapure water was kept at a constant temperature (50 °C) while 698 µl of 10 mM sodium citrate and 269 µl of 5.2 mM HAuCl_4 precursors were added. During continuous stirring, the cuvette was illuminated with the maximum light power of 100 W for 15 min. First, gold seed nucleation occurs followed by growth, and this process can be observed with naked eye: the solution turns from pale yellow to light red. The formation of the nanoparticles was followed by spectral analysis of the solution's absorbance; the characteristic peak of the precursor decreases, and at the same time, the peak of the plasmonic resonance of the spherical nanoparticles appears at around 580-590 nm (Fig. 1A).

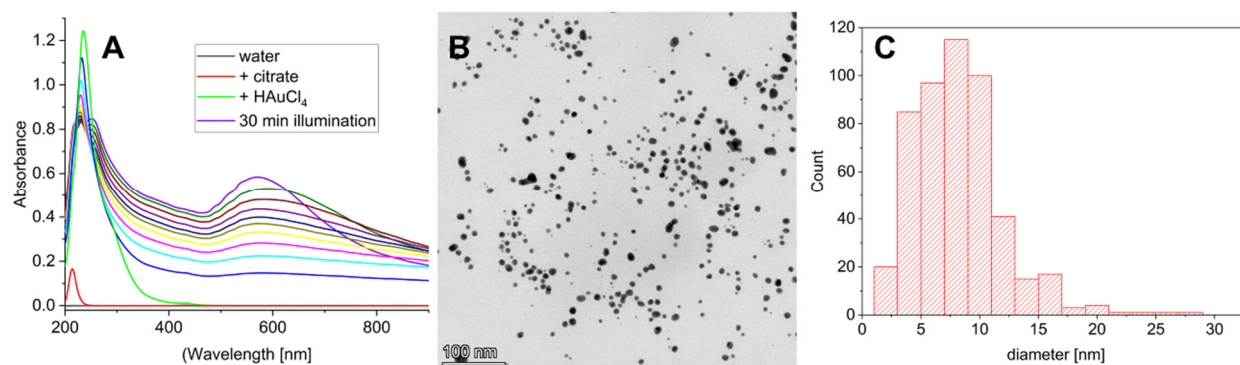


Figure 1: (A) Absorbance spectra of the sol, (B) TEM, and (C) size histogram of prepared Au nanoparticles

Using this protocol, we obtained spherical Au nanoparticles (Fig. 1B) with size distribution shown in Fig. 1C. While keeping all parameters the same, at the end of the 15-min illumination a next dose of 269 μl HAuCl₄ precursor can be added, followed by a repeated 15-min illumination. Through this process, an increase of nanoparticle number and size can be achieved and can be repeated further, as desired. However, due to the initial citrate concentration, the size of the Au nanoparticles is locked in the 10–20 nm diameter range.

Next, using the method described above, we prepared samples using butterfly wings of different species as substrates. The general workflow we developed is the following: butterfly wings attached to glass slides were cleaned and their surface wax layer was removed by ethanol treatment; this was followed by one or more cycles of gold nanoparticle deposition; soaking in distilled water to eliminate excess citrate and NaCl crystals from the substrate; SEM investigation of the dried wing cross-sections to obtain information on nanoparticle formation and penetration. To follow the change of the optical properties, reflectance spectra measurements were performed at certain stages of this workflow. In this way, a series of experiments were carried out using species with different wing scale nanostructures but with generally blue or violet wing surfaces.

Put in a wider context, regarding the structural and optical properties of the resulting hybrid bio-nanocomposites, three types of Au deposition methods were compared: (i) growth of Au particles inside the nanopores of butterfly wing scales by light-induced in situ chemical reduction, (ii) drop-drying of the aqueous Au sol formed during the procedure (i) in the bulk liquid phase, and (iii) physical vapour deposition of Au thin film onto the butterfly wing. By the first method, the Au nanoparticles integrated inside the photonic nanoarchitecture of the butterfly wing and kept their nanosized dispersion after drying (Fig. 2A), while by the second method, a large number of Au nanoparticles deposited on the outer surface of the wing scales aggregated in non-uniform clusters (Fig. 2B). For the wing coated with 15 nm Au by physical vapour deposition, the close to conformal coating of the top surface can be observed (Fig. 2C).

From optical point of view, it was found that when Au nanoparticles are grown inside the nanopores of the wing scales or are deposited by drop-drying Au sol on the wing, the original optical properties of the biological photonic nanoarchitecture are tuned by the integration of the Au nanoparticles. As shown by the spectra in Figures 2D and 2E, the spectral properties are borrowed both from the pristine chitin photonic nanoarchitecture and the Au nanoparticles as modificatory components. Opposite to this, when the wing is coated by physical vapour deposition by 5 nm or 15 nm Au, no shift is seen in the spectral position of the reflectance maxima (Fig. 2F) for any of the two gold thicknesses used. The reduction in the amplitude of the reflectance maximum is associated with the reduced transmittance of the Au layers; the effect is that of a filter placed into the light path between the illuminating source – wing, wing – detector system. In all cases, the magnitude of the observed effect scales with the amount of the Au used to alter the properties of the butterfly wing. When comparing the in situ growth with the drop-drying of Au sol, the former is more advantageous for the production of samples with uniform and deep penetration of the Au nanoparticles into the original biological photonic nanoarchitecture than the drop-drying method. We faced the problem of crystalline NaCl and sodium citrate residue appearance as a result of the reduction reaction which can be eliminated with a 70-hour-long water soaking as we demonstrated using XRD measurement. During the water soaking, the nanoparticles were not removed from the surface of the nanoarchitecture.

The increased amount of Au nanoparticles incorporated in the hybrid photonic nanoarchitecture increased the magnitude of the spectral shift, but at the same time reduced the amplitude of the reflectance maximum associated with the starting biological photonic nanoarchitecture. Therefore, one has to balance these two effects. Fortunately, nature has developed a very large “library” of precisely tuned photonic nanoarchitectures in butterfly wings, which can be produced in a cheap and environmentally friendly process. Thus, by selecting wings with suitable physical colour, the desired spectral modifications can easily be achieved.

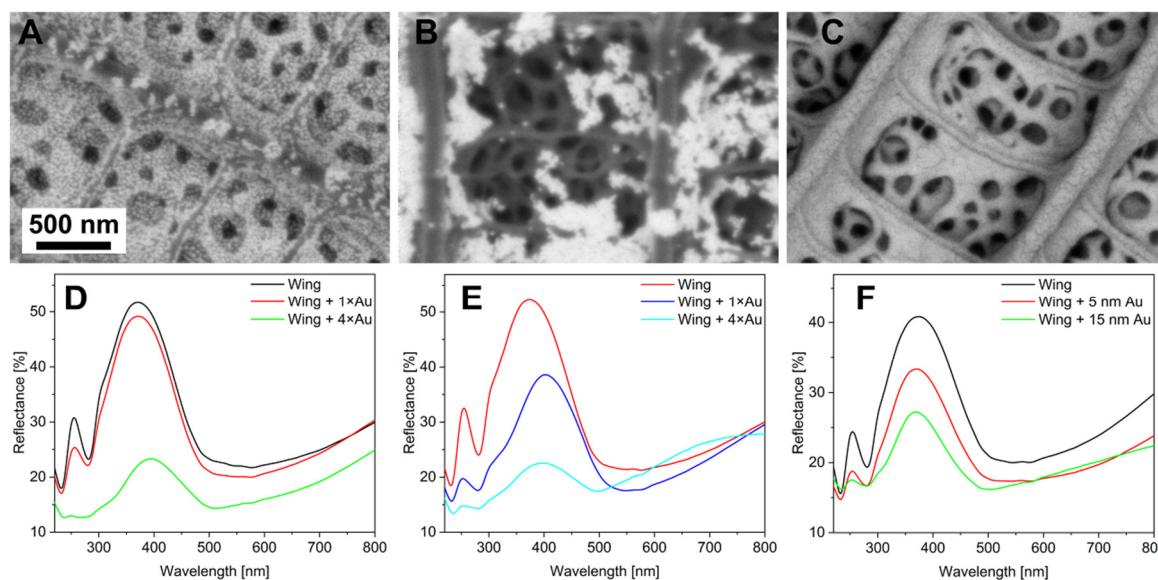


Figure 2: Top view SEM images of the *Polyommatus icarus* wing scales decorated with Au nanoparticles using (A) in situ growth, (B) drop-drying and (C) physical vapour deposition methods. Reflectance spectra of the ethanol pretreated wings before and after (D) in situ growing using 1 and 4 doses of Au precursor, (E) drop drying of sols prepared in (D) and (F) physical vapour deposition of 5 and 15 nm of Au.

To start a route to more complex structures, we performed in situ gold deposition on butterfly wings with conformal ZnO layer of different thicknesses. Earlier, we demonstrated how an additional ZnO layer deposited to the complex 3D nanoarchitecture can shift the reflectance peak to higher wavelengths and the shift is increasing with the deposited layer thickness. Here, 5 and 15 nm ZnO were deposited on several wing samples, and then we followed the newly developed protocol of nanoparticle growth. As an example, we present the pristine *Morpho rhetenor helena* species with its characteristic photonic crystal structure (Fig. 3A), and that after 15 nm of ZnO conformal layer and growth of duplicated quantity of Au nanoparticles (Fig. 3B). Although the nanoparticles are in a large number, they are well separated in the full volume of the scale, which is promising for applications. The optical reflectance is on Fig. 3C, where the blue peak edge is shifted to the higher wavelengths.

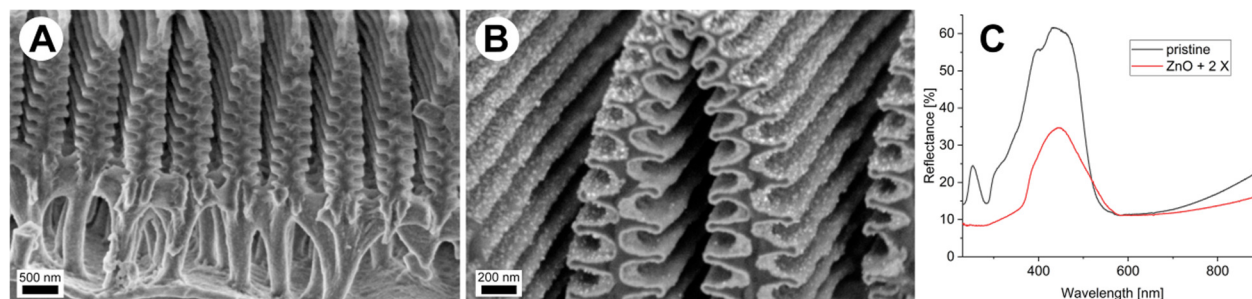


Figure 3: SEM images of *Morpho rhetenor helena* wing scale (A) in pristine state, (B) after ALD of ZnO followed by in situ growth of Au NPs, and (C) and their reflectance spectra

Another surface modification we investigated earlier is the oxygen plasma etching of the butterfly wing nanostructures producing a conformal decrease of chitin thickness, and consequently the shift of the reflectance peak towards the shorter wavelengths. This also turned the inherently superhydrophobic wings into hydrophilic, which is beneficial considering that the native bare wing cannot be submerged in water. One case presented is *Hypochrysops polycletus* with a well-ordered 3D structure (Fig. 4A). A 20 s plasma treatment was applied, then 4 times in situ gold growth was conducted. Fig. 4B shows the state after the second round. The optical reflectance spectra are presented for the initial pristine wing and all performed growth repetitions (Fig. 4C).

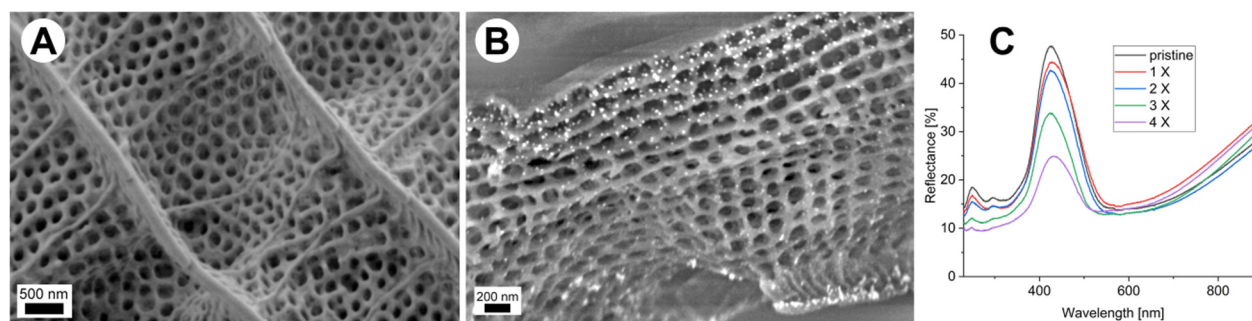


Figure 4: SEM images of *Hypochrysops polycletus* wing scale (A) in a pristine state, (B) after oxygen plasma etching and after the second round of Au nanoparticle growth, and (C) their reflectance spectra

Summarizing the most important achievements of the one-year-long research program: we have successfully introduced plasmonic Au nanoparticles into the photonic nanoarchitectures of butterfly wing scales resulting in modification of their original optical properties. The newly developed in situ growth of Au NPs by light induced reduction of the preparation solution filled into the wing scale pores and provided nicely distributed single particles, while by drop-drying of Au sol led rather to aggregated Au NPs on the outer surface of the wing scales. The in situ growth method worked well also on wing scales covered by ALD prepared ZnO semiconductor thin film or etched by oxygen plasma. The hybrid photonic nanoarchitecture produced this way seems to be more advantageous for possible applications, such as photocatalysis.

The results of this work were presented at the 2023 Fall Meeting of the European Materials Research Society.

Remaining work

We will continue the collaboration of the two groups and the Hungarian Natural History Museum (HNHM) to prepare new samples based on the accumulated knowledge during this year. We plan to extend the growth method toward bimetal or metal-semiconductor particles and more complex photonic structures with atomic layer deposition before and after the nanoparticle deposition. There is a near future plan to reveal the basis of possible applications for photocatalysis and surface enhanced Raman spectroscopy, where a certain improvement is expected compared to the bare biological structure or the metallic nanoparticle surfaces in themselves.

Related publication

- [1] K. Kertész, G. Piszter, A. Beck, A. Horváth, G. Nagy, Gy. Molnár, Gy. Z. Radnóci, Zs. E. Horváth, L. Illés and L. P. Biró: *Hybrid Bio-Nanocomposites by Integrating Nanoscale Au in Butterfly Scales Coloured by Photonic Nanoarchitectures*, *Photonics* **10**, 1275 (2023) <https://doi.org/10.3390/photonics10111275>

MATERIALS SCIENCE APPLICATIONS OF NEUTRON SCATTERING

László Almásy, Indu Dhiman, Zoltán Dudás, Ihor Gapon, Adél Len,
Márton Markó, Dániel Merkel, Tamás Veres

Objective

Small Angle Neutron Scattering (SANS) has been applied to characterize the nanostructure of Zr-based metal-organic frameworks, uni- and multilamellar vesicles, multiwall carbon nanotube/graphite/polyester ternary composites, TEMPO (2,2,6,6-tetramethylpiperidine-1-oxyl) - oxidized cellulose fibres; neutron reflectometry was used to study multi-layer Ti/NixMoy heterostructures; and neutron diffraction was used to assess questions related to lithium-ion batteries.

Results

Enhanced *in vitro* drug delivery using Zr-based metal-organic frameworks (Zr-MOFs)

Three Zr-MOF systems were developed and characterized as carriers for water-soluble and reduced water-soluble drugs, resulting in improved dissolution rates and controlled drug release. With a high drug loading capacity of 99.78%, these materials are suggested for application as drug adsorbents in polluted waters. The drug release from Zr-MOFs depended on pore size and environmental pH, offering a customizable pore network for tailored usage in biomedical applications, ensuring efficient drug encapsulation and controlled release. [1]

Protein-induced transformation of unilamellar to multilamellar vesicles triggered by a polysaccharide

Morphological transitions of Didodecyldimethylammonium Bromide (DDAB) cationic vesicles and hybrid DDAB/Hyaluronic Acid (HA) vesicles were studied upon addition of Bovine Serum Albumin (BSA) at pH 7, where BSA was overall negatively charged (Figure 1a). SANS (Figure 1b) was used to extract the size distributions of the nanovesicles, the thickness of the DDAB bilayers and their lamellarity. Characteristic peaks in the SANS patterns indicate the presence of multilamellar interfaces, while the formation of multilamellar vesicles induced by BSA depends on the amount of added HA. Consequently, higher lamellarities were observed at higher BSA contents. The work demonstrates a simple methodology to tune the encapsulation of globular proteins in vesicular nanoassemblies by affecting their lamellarity and has direct implications on the application of vesicles and liposomes in protein delivery. Apart from shedding light on the structural transition caused by the protein and tuned by the polysaccharide, this work presents a system that may have great potential for controllable and enhanced encapsulation of globular proteins for nanodelivery applications. [2]

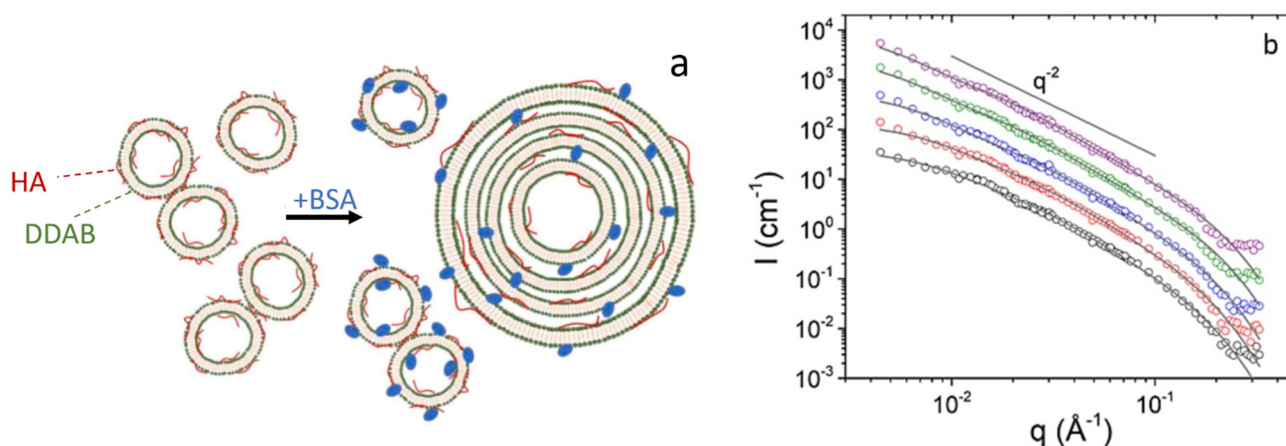


Figure 1: Schematic diagram of the interaction of HA and BSA with the DDAB vesicles (a). SANS data from DDAB and HA-decorated DDAB vesicles. Dots represent the SANS intensities and lines represent the SANS intensities fitted by the unilamellar vesicles model.

Study of Multi-walled Carbon Nanotube (MWCNT)/graphite/polyester ternary composites

The study employed SANS, infrared, and Raman spectroscopy for structural characterization of the MWCNT/graphite/polyester ternary composites. Electrical measurements were carried out across a frequency range of 100 Hz to 1 MHz and a temperature range of 200–380 K. The Alternating Current (AC) conductivity exhibited a frequency dependence following Jonscher's power law. The temperature-dependent behaviour of the AC conductivity suggested that the electrical conduction within the material was a thermally activated process.

The temperature dependence of the Direct Current (DC) conductivity indicated a pronounced positive and negative temperature coefficient of resistivity below and above the critical temperature, respectively. In comparison to MWCNT/polyester or Gr/polyester composites, the percolation threshold of the MWCNT/Gr/polyester composite is much lower. Applying the Arrhenius equation to analyze the temperature dependence of DC conductivity revealed that the inclusion of MWCNT and Gr in the polyester matrix resulted in a decrease in activation energy. [3]

TEMPO-oxidized cellulose hydrogels

Investigation of hydrogels formed by 2,2,6,6-tetramethylpiperidine-1-oxyl (TEMPO)-oxidized cellulose fibres and polyvalent cations by SANS and Raman spectroscopy. Using different experimental methods, the sol-gel transitions between the gel and liquid phases were determined as a function of the type, concentration, and pH of cations in aqueous suspensions of TEMPO cellulose fibres. We have shown that at the supramolecular level, the stiffness and flexibility of the fibrils depend on and can be controlled by the pH value of the suspension. [4]

Multi-layer Ti/NixMoy heterostructures

Low-periodic (<100 nm) multi-layer Ti/NixMoy heterostructures synthesized by magnetron sputtering for use in neutron reflectometry experiments were studied. The quasi-homogeneous approach, adjusting the effective scattering length density, enhances sensitivity. Analysis of specular reflectivity curves supports the homogeneous approximation. Magnetron sputtering produces ~1.5 nm low-period structures, enabling a quasi-homogeneous approach. The Ti/NixMoy structures, with varied sublayer thicknesses, facilitate tuning the effective scattering length in neutron reflectometry experiments. The practical accuracy of approximating the specular-reflection curve by the homogeneous layer model is valid up to $qz \sim 0.08 \text{ \AA}^{-1}$, suitable for in situ neutron reflectometry experiments. [5]

Cu/Ti supermirrors for extremely low-spin-flip applications

The avoiding of neutron beam depolarization is crucial in the "PERC" experiment (measurements of angular correlation coefficients in decay of free polarized neutrons). Cu/Ti neutron supermirror was developed and optimized for high overall reflectivity and low spin-flip. After characterization of the samples by X-ray diffraction, reflectometry and Superconducting Quantum Interference Device (SQUID) magnetometry, polarized neutron reflectivities were measured at GINA. Based on the results and theoretical considerations an upper limit of $< 1.8 \times 10^{-5}$ is given for the spin-flip ratio which makes these neutron mirrors suitable for extremely low-spin-flip applications. [6]

Li-ion battery related studies by neutron diffraction

With total scattering neutron powder diffraction measurements on spinel-structured High Entropy Oxides (HEOs), suitable candidate materials for lithium-ion batteries have been performed at the Material test (MTEST) diffractometer. We expected that Bragg scattering part contributes to the better determination of the oxygen sites and the cation occupancies in the lattice, while the diffuse scattering contribution gives information about the degree of order between the atomic sites. Total scattering powder diffraction pattern is obtained. Further structural investigation is underway by the Reverse Monte Carlo method, together with the measured X-ray diffraction patterns.

Neutron powder diffraction experiment was carried out at the MTEST diffractometer at low temperature (150K) on commercially available Lithium-ion batteries of type INR18650HG2 by LG with a nominal capacity of 3000 mAh. The experiment was performed on fatigued cells with stabilized state-of-health of 80% (corresponding to a capacity of 2400 mAh) prepared with different cycling protocols and on a "fresh" reference cell with a nominal state-of-health of 100%. In total 8 cells were measured, revealing information about the structure of electrodes, cell housing, current collectors, and most importantly, the frozen electrolyte. Depending on the previous cycling/aging of the cells, the amount of electrolyte was found to vary, pointing to different liquid electrolyte loss in the cells. This behaviour can be correlated with the amount of LiC_6 and LiC_{12} observed in the structure of the cells, showing also a specific degree of fatigue depending on the different electrochemical cycling protocols in the cell.

The macromolecular diffractometer (NMX) at the European Spallation Source (ESS) in Lund requires three $51.2 \times 51.2 \text{ cm}^2$ detectors with reasonable detection efficiency, sub-mm spatial resolution, a narrow Point-Spread Function (PSF), and good time resolution. We tested the improved version of the NMX detector prototype consisting of a Triple-GEM (Gas Electron Multiplier) detector with a natural Gd converter and a low material budget readout. The detector was successfully tested at the neutron reactor of the Budapest Neutron Centre (BNC) and the D16 instrument at the Institute Laue-Langevin (ILL) in Grenoble. The measurements with Cadmium and Gadolinium masks in Budapest demonstrate that the point-spread function of the detector lacks long tails that could impede the measurement of diffraction spot intensities. On the D16 instrument at ILL, diffraction spots from Triose phosphate isomerase w/2-phosphoglycolate (PGA) inhibitor were measured both in the MILAND Helium-3 detector and the Gd-GEM. The comparison between the two detectors shows a similar point-spread function in both detectors, and the expected efficiency ratio compared to the Helium-3 detector. Both measurements together thus give good indications that the Gd-GEM detector fits the requirements for the NMX instrument at ESS. [7]

Related publications

- [1] C. Cretu, R. Nicola, S. A. Marinescu, E. M. Piciorus, M. Suba, C. Duda-Seiman, A. Len, L. Illés, Zs.E. Horváth, A. M. Putz: *Performance of Zr-Based Metal–Organic Framework Materials as In Vitro Systems for the Oral Delivery of Captopril and Ibuprofen*, Int. J. Mol. Sci. **24**, 13887 (2023) <https://doi.org/10.3390/ijms241813887>
- [2] A. Papagiannopoulos, A. Sklapani, A. Len, A. Radulescu, E. Pavlova, M. Slouf: *Protein-induced transformation of unilamellar to multilamellar vesicles triggered by a polysaccharide*, Carbohydrate Polymers **303**, 120478 (2023) <https://doi.org/10.1016/j.carbpol.2022.120478>
- [3] R. Belhimria, Z. Samir, S. Boukheir, S. Soreto Teixeira, A. Len, A. Szakál, M. E. Achour, A. Anson-Casaos, M. El Hasnaoui, L. C. Costa: *Effect of structural properties in the electrical impedance spectrum of multi-walled carbon nanotube/graphite/polyester ternary composites*, J. Phys. D: Appl. Phys. **56**, 465104 (2023) <https://doi.org/10.1088/1361-6463/acf0cc>

- [4] A. Rossetti, A. Paciaroni, B. Rossi, C. Bottari, L. Comez, S. Corezzi, L. Melone, L. Almásy, C. Punta, A. Fiorati: *TEMPO-oxidized cellulose nanofibril/polyvalent cations hydrogels: a multifaceted view of network interactions and inner structure*, *Cellulose* **30**, 2951-2967 (2023) <https://doi.org/10.1007/s10570-023-05058-2>
- [5] M. V. Avdeev, I. V. Gapon, D. Merkel, M. S. Yerdauletov, D. M. Djanseitov, T. V. Tropin: *Low-Period Multilayer Ti/NixMoy Films with Variable Quasi-Homogeneous Structure for Neutron Reflectometry*, *Journal of Surface Investigation: X-Ray Synchrotron and Neutron Techniques* **17**, 886-891 (2023) <https://doi.org/10.1134/S1027451023040225>
- [6] J. M- Gómez-Guzmán, M. Opel, T. Veres, P. Link, L. Bottyán: *Structural, electrical and magnetic properties of reactively DC sputtered Cu and Ti thin films. Application to Cu/Ti neutron supermirrors for low spin flip applications*, *Nuclear Instruments and Methods in Physics Research A* **1059**, 169005 (2024) <https://doi.org/10.1016/j.nima.2023.169005>
- [7] D. Pfeiffer, F. Brunbauer, V. Cristiglio, R. Hall-Wilton, M. Lupberger, M. Markó, H. Muller, E. Oksanen, E. Oliveri, L. Ropelewski, A. Rusu, J. Samarati, L. Scharenberg, M. van Stenis, P. Thuiner, R. Veenhof: *Demonstration of Gd-GEM detector design for neutron macromolecular crystallography applications*, *Journal of Instrumentation* **V18, 04**, P04023 (2023) <https://doi.org/10.1088/1748-0221/18/04/P04023>

FUNCTIONAL SILICA MATERIALS FOR ENVIRONMENTAL AND MEDICAL APPLICATIONS

László Almásy, Zoltán Balogh, Çok Selay Sert, Indu Dhiman, Zoltán Dudás, Adél Len, Dániel Pércsi

Objective

With a wide spectrum of diverse studies and scientific investigations, this comprehensive report delves into several key areas of materials science and characterization techniques. The report explores the selective recovery of aqueous silver ions using thiol-functionalized mesoporous silica sorbents, and delves into the synthesis and characterization. Additionally, it investigates methyl-functionalized superhydrophobic silica monolith and optimized synthesis methods for hybrid borosilicate aerogels with potential applications in bone regeneration.

Results

Selective and high-capacity recovery of aqueous Ag(I) by thiol functionalized mesoporous silica sorbent

The high concentration of silver compounds in surface waters can have toxic effects on the human body; moreover, silver is a valuable industrial raw material. Therefore, for the selective recovery of Ag(I) ions from aqueous solutions using the sol-gel method, mesoporous, mercaptopropyl-functionalized silicon dioxide xerogels have been tested. The material was characterized using low voltage Scanning Electron Microscopy (SEM), N₂ sorption porosimetry, Small-Angle Neutron Scattering (SANS), energy-dispersive X-ray analysis and X-ray Photoelectron Spectroscopy (XPS). The zeta potential in the aqueous phase was investigated as a function of pH. The xerogel exhibited excellent selectivity for Ag(I) binding at pH=5.0, with a very high sorption capacity of 238 mg/g. The sorption equilibrium was reached rapidly, within 15 minutes, providing a significant advantage in terms of practical functionality of the present xerogel sorbents. Quantitative recovery of Ag(I) and regeneration of the sorbent were achievable with a 10.0 mM Na₂S₂O₃ solution. The binding mechanism was explained by the formation of Ag(I) clusters on the surface, a common occurrence for silver ions in the presence of thiol groups. This accounts for the outstanding selectivity of the sorbent for silver ions. [1]

Methyl functionalized superhydrophobic silica monoliths synthesis and characterization

Silica xerogels possessing high specific surface area, retain their monolithic form through gradual functionalization with methyl groups, which can be utilized in the adsorption of metals, organic solvents, and drug delivery. Superhydrophobicity was achieved in these materials through post-synthetic surface treatment by our group. Structural characterization of the monoliths was conducted both before and after surface treatment, including analysis of chemical structure (Fourier-Transform Infrared Spectroscopy (FT-IR), solid-state Nuclear Magnetic Resonance (NMR)), morphology (SEM, N₂ porosimetry, SANS), and hydrophobic-hydrophilic profile (contact angle measurements). [3]

Optimized synthesis and physicochemical characterization of hybrid borosilicate aerogels

The optimized synthesis and comprehensive physicochemical characterization of hybrid borosilicate aerogels represent a promising avenue in addressing the ongoing demand for viable alternatives to autografts for treating bone defects. Despite the enduring use of autografts as the primary treatment method, their limited availability and associated surgical complications have spurred a growing need for synthetic bone substitutes that facilitate bone regeneration. Substantial research corroborates the beneficial biological effects of boron-containing bioglasses, particularly when utilized as bone scaffolds and hybridized with biocompatible, biodegradable polymers like Polyvinyl Alcohol (PVA). Employing the sol-gel method akin to bioglass production, the fabrication of aerogels involves supercritical drying, preserving their inherent porous structure. This characteristic not only facilitates fluid permeability but also underscores their mesoporous nature, conducive to cell adhesion. The integration of borosilicate aerogels with varying molar masses of PVA and diverse sources of Ca(II) (CaCl₂, β-Ca₃(PO₄)₂, and hydroxyapatite) into the gel backbone underwent meticulous scrutiny encompassing detailed analyses of their chemical structure (FT-IR, solid-phase NMR), morphology (SEM, N₂ porosimetry, SANS), and nanoscale hybrid systems through contrast variation SANS measurements. Moreover, the examination of the quantity (Inductively Coupled Plasma Optical Emission Spectrometry (ICP-OES)), crystal structure (X-ray diffraction), size (Transmission Electron Microscopy (TEM)), and contrast variation (SANS) of the integrated Ca(II) sources provided invaluable insights into their integration within the gel backbone. In vitro biological assessments validated the non-cytotoxic nature of the produced aerogels, showcasing favourable outcomes in terms of cell adhesion. These compelling findings underscore the potential utilization of aerogel microparticles in suspension as a promising avenue in the realm of bone regeneration. Presented in the form of a manuscript, these results are undergoing submission, while ongoing efforts to enhance the mechanical and biological properties entail the synthesis of borosilicate aerogels hybridized with alternative polymers like pectin and alginate, with ongoing testing to optimize their characteristics. [5]

Related publications

- [1] P. Herman, D. Pércsi, T. Fodor, L. Juhász, Z. Dudás, Zs.E. Horváth, V. Ryukhtin, A.M. Putz, J. Kalmár, L. Almásy: *Selective and high capacity recovery of aqueous Ag(I) by thiol functionalized mesoporous silica sorbent*, *Journal of Molecular Liquids* **387**, 122598, 11 (2023) <http://dx.doi.org/10.1016/j.molliq.2023.122598>
- [2] S.S. Çok F. Koç, Z. Dudás N. Gizli: *The Methyl Functionality of Monolithic Silica Xerogels Synthesized via the Co-Gelation Approach Combined with Surface Silylation*, *Gels* **9**, 33 (2023) <http://dx.doi.org/10.3390/gels9010033>
- [3] Z. Balogh, A. Len, V. Baksa, A. Krajnc, P. Herman, G. Szemán-Nagy, Zs. Czigány, I. Fábíán, Z. Dudás: *Structural characteristics and in vitro bioactivity of borosilicate – polyvinyl alcohol (PVA) hybrid aerogels for bone regeneration* *ACS Applied Nano Materials* **7**:(4), 4092 (2024)

HERITAGE SCIENCE APPLICATIONS OF NUCLEAR ANALYTICAL AND STRUCTURAL STUDIES

Zsolt Kasztovszky, Zoltán Kis, John Gait, Zoltán Kovács, Veronika Szilágyi, Katalin Bajnok, Boglárka Maróti, Adél Len, László Szentmiklósi, László Rosta, Katalin Gméling

Objective

Various objects of our Cultural Heritage made of different kinds of materials (such as rocks and minerals, metals, ceramics, and glass) have been investigated with the available, mostly non-destructive methods, to obtain information on their provenance, production technology, current condition, or authenticity.

Methods

The applied methods utilize the non-destructive and partly destructive neutron-based instruments of the Budapest Neutron Centre (BNC), such as Prompt-gamma Activation Analysis (PGAA), Neutron-Induced Prompt Gamma-ray Spectroscopy - Neutron Optics and Radiography for Material Analysis (NIPS-NORMA), RAD, or Neutron Activation Analysis (NAA), as well as complementary Scanning Electron Microscopy with Energy Dispersive Spectroscopy (SEM-EDS), portable X-Ray Fluorescence (pXRF), portable Near InfraRed (NIR)- and Raman Spectroscopy.

Results

Several particular multi-technique studies have been conducted to investigate objects made of rocks, metals, ceramics, and glass, with the Hungarian National Museum, the Museum of Fine Arts, the Museum of Ethnography, the Eötvös University and the Institute for Nuclear Research (Atomki). Through the IPERION HS projects, European partners have joined some interesting projects.

- Analysis of ancient ceramics with SANS and μ -CT

The analysis of ancient pottery technology progressed during 2023 through the HUN-REN PoC project "Developing non-destructive X-ray and neutron analytical techniques for the investigation of ancient pottery forming techniques". In particular, advances have been made in increasing the speed and efficiency of X-ray micro-Computed Tomography (μ -CT) and Small Angle Neutron Scattering (SANS) data processing, analysis, and interpretation, thereby reducing previous bottlenecks in the analysis workflows, and making the analysis of larger, archaeologically significant datasets practically feasible. In parallel with these methodological developments, the PoC project has transitioned from the measurement of experimental control samples to archaeological case studies analyzing ancient pottery with μ -CT and SANS. Two domestic projects have begun in collaboration with the Hungarian National Museum, the HUN-REN Research Centre for the Humanities, and the University of Szeged, examining Neolithic and Late Roman/Early Medieval pottery from Jász-Nagykun-Szolnok County and the southern Lake Balaton region, with, to date, a combined total of 83 SANS measurements and 49 μ -CT measurements. In addition, three multinational projects have begun, run in collaboration with the University of Innsbruck, the University of Vienna, and the Czech Academy of Sciences, aiming to identify pottery technology in Iron Age Sicilian, Roman Age Austrian, and Late Medieval pottery from the Netherlands. A further project, in collaboration with the Technical University of Munich, examining ancient Egyptian and Nubian pottery from northern Sudan is scheduled for early 2024.

- The provenance of ancient Egyptian figurines (in cooperation with the Museum of Fine Arts)

In cooperation with the Egyptian Antiquities Collection of the Museum of Fine Arts, a further 10 figurines supposed to be made of lapis lazuli have been studied with PGAA. The aim was to check if they were made of lapis lazuli and to identify their raw material source. Although based on the elemental composition some figurines were found to be non-lapis lazuli without doubt, the provenance identification of the lapis lazuli was partly inconclusive. Various statistical methods are being applied to reveal similarities and differences between the objects and the raw material reference samples. An MSc student from ELTE is currently working on statistical evaluation of the experimental results [1-2].

- Paria project

The initial step of the Paria project has been implemented. According to the plans, different artifacts of an Inka administrative centre, Paria (in Bolivia), are going to be investigated to understand such important processes as the procurement system of raw materials and consumer goods, handicraft activities, or division of labour. This year, PGAA investigations on stone beads decorating clothes were done. The chemical analysis proved the variable utilization of colourful mineral materials, like sodalite, azurite, malachite, and crysocola.

- Study of Folk Pottery

Continuing our previous research on white folk pottery from the collection of the Museum of Ethnography, chemical characterization by PGAA was fulfilled. Further chemical studies by NAA are planned on a subset of samples. Products from one group of the observed pottery districts (Gömör) were investigated in detail [3] and compared to medieval Árpáadian Age archaeological white pottery [4]. According to our first results, it is possible to differentiate the medieval white earthenware products based on their relation to the raw materials of Modern Age pottery districts.

- Non-destructive study of Bronze Age defensive and offensive weapons (in cooperation with the Hungarian National Museum, OTKA project, Gábor Tarbay, NKFIH PD 134910)

Within the Community Archaeological Program, two new hoards were excavated by the Hungarian National Museum in the Budakeszi-Őzölgy-tető site in 2017. The hoards contain more than 100 metal objects, therefore, an effective non-destructive methodology was established to gain preliminary alloy composition data to set up a further measurement strategy. The XRF results showed that the objects are either Cu-Sn alloys or Cu-Pb-Sb ingots. Several high Zn- and Fe-containing objects were also identified, which can be dated to the Medieval, Early Modern Period, or World War II eras [5]. Within the same project, three swords with leaded hilts [6] and a disc-butted axe [7] were examined in more detail to conclude their production technology.

- Provenance of obsidian archaeological objects

With the help of PGAA and handheld XRF, the provenance of various obsidian archaeological objects has been determined. The raw material of a 4400 B.C. obsidian blade that was excavated at Csongrád, Hungary, proved to originate from Anatolia, which represents an extremely long-distance transport of the object or the raw material. The raw materials of other obsidian objects found in Olád (Western Hungary) and Targowisko (South Poland) have been identified as good quality Carpathian 1 (C1) from Tokaj Mts. [8-9].

- Large facility analytical studies of polished and ground stone artifacts for the reconstruction of Prehistoric trans-regional trade routes in the Carpathian Basin (OTKA project, Zsolt Kasztovszky, NKFIH K 131814)

In the 4th project year, cca. 50 raw material samples for archaeological stone have been analyzed by SEM-EDX and PGAA to identify the possible outcrops to associate with the previously analyzed stone tools. The geological reference samples, mostly consisting of amphibolite, basalt, and gabbro, have been collected on field trips to the Little Carpathians, Mecsek, and Börzsöny. Further 50 raw materials and stone tools from Moravia have been analyzed by PGAA, within the Transnational Access (TNA) of the IPERION HS project. [10].

Within the IPERION HS project, a set of Roman and Late Antique glass fragments have been analyzed by PGAA. The objects were discovered in several archaeological sites on the western shore of the Black Sea. The study aimed to reveal the vivid commercial and cultural connections throughout the Roman Empire during the 1st-6th century AD. The results are currently under evaluation [11].

Related publications

- [1] S. Szende: *Statistical analysis of modern elemental analytical measurements data for the provenance study of archaeological findings*, MSc Thesis, ELTE TTK, in prep.
- [2] J. Zöldföldi, Zs. Kasztovszky, Sz. Sándor, F. Kevély: *Lapis Lazuli in Ancient Egypt*, SR2A – 10th International Conference on Synchrotron Radiation and Neutrons in Art and Archaeology, Nov 21 – 24, 2023, Munich, Germany
- [3] V. Szilágyi, G. Vida: *Characterization of the Gemer whiteware (Slovakia): first steps for the implication of a traceable folk pottery material type to the archaeological data*, EMAC 2023 Pisa – 16th European Meeting on Ancient Ceramics, June 21 – 24, 2023, Pisa, Italy
- [4] V. Szilágyi, E. Simonyi, G. Tomka, M. Wolf, Z. Kovács, P. Kónya, K. Gméling, A. Kreite: *Medieval to early Modern Age (12th – 18th c.) whiteware on the Hungarian Plain (Alföld, E Hungary): a foreign material group in the pottery record*, EMAC 2023 Pisa – 16th European Meeting on Ancient Ceramics, June 21 – 24, 2023, Pisa, Italy
- [5] J.G. Tarbay, B. Maróti: *Preliminary handheld XRF analysis of Late Bronze Age metal finds from the Budakeszi-Őzölgy-tető site (Pest county, Hungary)*, *Archeometriai Műhely* **20**, 23-35 (2023)
- [6] J.G. Tarbay, B. Maróti: *Late Bronze Age Swords with Leaded Hilts from Hungary*, *Communicationes Archaeologicae Hungariae* **2022**, 83–96 (2023) <http://dx.doi.org/10.54640/CAH.2022.83>
- [7] K. Nowak, J.G. Tarbay, B. Maróti, Z. Kis, Gy. Káli: *Czekan z tarczowatym obuchem z Ciska. Śmiercionośna broń czy oznaka prestiżu? [A disc-butted axe from Cisek. A deadly weapon or a sign of prestige?]* (in Polish with English summary), *Rocznik Muzeum Górnośląskiego w Bytomiu Przyroda* **23**, 85-110 (2023)
- [8] Zs. Kasztovszky, A. Markó, Sz. T. Sándor, K. Biró: *Egy újabb példa a prompt-gamma aktivációs analízis alkalmazására obszidián régészeti leletek eredetmeghatározásában: Egy különleges csongrádi penge* (in Hungarian), *Őszi Radiokémiai Napok*, Oct. 16-18, Balatonszárszó.
- [9] Zs. Kasztovszky, A. Markó, Sz. T. Sándor, K. Biró: *The applicability of prompt-gamma activation analysis to obsidian provenance studies. The case of a strange find: a blade from Csongrád (South-East Hungary)*, SR2A – 10th International Conference on Synchrotron Radiation and Neutrons in Art and Archaeology, Nov 21 – 24, 2023, Munich, Germany
- [10] V. Szilágyi, Zs. Kasztovszky, E. Kereskényi, B. Péterdi, T. Sági, K. T. Szilágyi, K. Biró, Gy. Szakmány: *Raw material characterization or provenance identification? Different levels in the research of polished stone tools by PGAA*, SR2A – 10th International Conference on Synchrotron Radiation and Neutrons in Art and Archaeology, Nov 21 – 24, 2023, Munich, Germany
- [11] R. Bugoi, A. Tarlea, V. Szilágyi, L. Cliante, Zs. Kasztovszky: *Transparency at its best: neutrons used to probe archaeological glass finds from Romania*, SR2A – 10th International Conference on Synchrotron Radiation and Neutrons in Art and Archaeology, Nov 21 – 24, 2023, Munich, Germany

APPLICATIONS OF NUCLEAR AND X-RAY ANALYTICAL TECHNIQUES TO CHEMISTRY, MATERIAL AND NUCLEAR SCIENCES

Boglárka Maróti, László Szentmiklósi, Katalin Gméling, Noémi Anna Buczkó

Objective

We determined the elemental compositions of various kinds of samples using PGAA, PGAI, NAA, and portable XRF methods. The data obtained were useful in catalysis, material, and heritage science. Our other task was the dissemination of these state-of-the-art methods to students of numerous universities.

Methods

- Prompt Gamma Activation Analysis (PGAA) and Neutron Activation Analysis (NAA) to determine the bulk elemental composition, portable X-ray Fluorescence (pXRF) to determine the elemental composition of near-surface regions,
- Education of university students, conducting lab exercises.

Results

The analysis workflow of prompt gamma activation analysis at the BNC's PGAA and Neutron-Induced Prompt Gamma-ray Spectroscopy - Neutron Optics and Radiography for Material Analysis (NIPS-NORMA) facilities relied so far on the use of the Hypermet-PC gamma spectrometry software and the ProSpeRo concentration calculation Excel macro. This evaluation procedure was established in the late nineties and became technically obsolete and unproductive. To overcome this limitation, computer-controlled sample changers and neutron collimators were installed, and new, state-of-the-art ORTEC DSPEC 502A digital gamma spectrometers were put in place. The much-improved data acquisition had to be matched with a capable and more automated spectrum evaluation procedure. For this purpose, the 2022.2 version of the Hyperlab software package was developed, tested, validated, and deployed. Finally, the ProSpeRo concentration calculation utility was made compatible with Hyperlab's efficiency and peak list format. The novel analysis workflow was proven to be backward-compatible and delivers the results more efficiently [1]. An invited lecture has been presented about this topic at the RANC-2023 conference and the FRM-II user meeting.

There is a need in the neutron activation analytical community for radiation-resistant, disposable sample holders, which are easy to prepare and cost-effective. 3D printing, also known as additive manufacturing, could offer an obvious solution if radiation-resistant, acid-proof, and heat-resistant filament materials can be identified. PEEK, PEKK, PEI, and other ultra-high temperature plastics were irradiated in the vertical channels of the reactor. The Stratasys ULTEM 1010 filament was found to contain the lowest level of impurities, all detectable elements are below mg/kg level, and only a few mg/kg of Cl, Fe, and Mg were found. This, however, shows visual signs of degradation, by changing its colour due to neutron exposure [2]. Therefore, the search for an appropriate raw material shall be continued.

The League of advanced European Neutron Sources (LENS, <https://lens-initiative.org/>), a collaboration comprising nine European-level neutron research facilities, supports the international scientific community by providing access to beamline instruments and/or offering related expertise. The European neutron ecosystem is experiencing a period of significant change and has been destabilized following the closure, prolonged maintenance downtime periods, COVID-19 pandemic-related issues, or underutilization of several facilities. Within this collaboration, BNC called for "BNC LENS beam time" proposals to ease the unprecedented shortage of neutrons in several neutron sources. The action targeted neutron users whose experiment(s) have allocated beam time at any LENS facility's user program but not yet scheduled for any reason, provided that - at least an essential part of - the experiment is technically feasible to accomplish on BNC instruments. Several of these experiments were completed in 2023, while the related data processing activities are still in progress.

As a follow-up of the V4-Korea RADCON project, the activation-calculation methodology for bulky samples irradiated inside the reactor core has been published. We managed to achieve 10-20% agreement with the experimentally measured activity values [3]. As the culmination of several years of efforts, the results of a systematic geochemical study on the micro- and trace contaminants of Hungarian gravel mines were published [4]. We have reported a novel elemental composition analysis procedure for non-homogeneous samples, by combining local PGAA with tomography and state-of-the-art Monte Carlo calculations [5]. In combination with Small Angle Neutron Scattering (SANS) experiments, PGAA has been used to characterize deuterated syndiotactic-polystyrene model systems that can be used as proton-exchange membranes [6].

We contributed to two chapters in the handbook of Non-Destructive Material Characterization Methods. One described the general properties of neutrons relevant for material analysis [7], while the other was dedicated to the technical description of prompt gamma activation analysis and instrument neutron activation analysis [8].

We disseminated our activities to the general public in the YouTube stream of a popular video blogger, Csaba Magyarósi, reaching a remarkably broad audience, 112k viewers [9].

Related publications

- [1] L. Szentmiklósi, Zs. Révay, J. Östör, B. Maróti: Improved analytical workflow for prompt-gamma activation analysis, *J. Radioanal. Nucl. Chem.*, <http://dx.doi.org/10.1007/s10967-023-09071-4>
- [2] K. Gméling, Z. Schneider, D. Pesti, G. Benyács, S. Janik: *Qualifying the raw materials of additive manufacturing for use in Neutron Activation Analysis*, poster presented at the RANC-2023 conference, May 2023
- [3] I. Harsányi, A. Horváth, Z. Kis, K. Gméling, D. Jozwiak-Niedzwiedzka, M. A. Glinicki, L. Szentmiklósi: *Assessment of neutron-induced activation of irradiated samples in a research reactor*, *Nuclear Engineering and Technology* **55(3)**, 1036-1044 (2023) <http://doi.org/10.1016/j.net.2022.11.004> (impact factor: 2.7)
- [4] K. Gméling, V. Szilágyi, I. Harsányi, L. Szentmiklósi: *Hungarian fine-to-coarse aggregate, a possible constituent of near-vessel structural concrete of nuclear power plants*, *Materials (Advances in Sustainable Civil Engineering Materials Special Issue)* **16(9)**, 3520 (2023) <http://doi.org/10.3390/ma16093520> (impact factor: 3.4)
- [5] L. Szentmiklósi, B. Maróti, Z. Kis: *Quantitative, non-destructive elemental composition analysis of 3D-structured samples*, *Journal of Analytical Atomic Spectrometry* **38**, 333-341 (2023) <http://doi.org/10.1039/D2JA00316C> (impact factor: 3.4)
- [6] M. M. Schiavone, D. H. Lamparelli, C. Daniel, M. Golla, Y. Zhao, H. Iwase, H. Arima-Osonoi, S. Takata, L. Szentmiklósi, B. Maróti, J. Allgaier and A. Radulescu: *Extended Q-range small-angle neutron scattering to understand the morphology of proton-exchange membranes: the case of the functionalized syndiotactic-polystyrene model system*, *Journal of Applied Crystallography* **56(4)**, 947-960 (2023) <http://doi.org/10.1107/S1600576723005496> (impact factor: 6.1)
- [7] C. Stieghorst, L. Szentmiklósi, B. Maróti, K. Gméling, E. Lehmann: *Neutrons – characteristics and sources*, in *Non-Destructive Material Characterization Methods*, Editors: A. Otsuki, S. Jose, M. Mohan, S. Thomas, 1st Edition (2023) Elsevier, p. 189-204, ISBN 978-0-323-91150-4, <http://doi.org/10.1016/B978-0-323-91150-4.00005-7>
<https://shop.elsevier.com/books/non-destructive-material-characterization-methods/otsuki/978-0-323-91150-4>
- [8] L. Szentmiklósi, C. Stieghorst, K. Gméling, B. Maróti: *Chemical analysis with neutrons*, in *Non-Destructive Material Characterization Methods*, Editors: A. Otsuki, S. Jose, M. Mohan, S. Thomas: 1st Edition (2023) Elsevier, p. 621-682 ISBN 978-0-323-91150-4, <http://doi.org/10.1016/B978-0-323-91150-4.00010-0>
<https://shop.elsevier.com/books/non-destructive-material-characterization-methods/otsuki/978-0-323-91150-4>

STRUCTURAL ASPECTS OF IRON-, TIN- AND GOLD-BASED MATERIAL SYSTEMS STUDIED BY MÖSSBAUER SPECTROSCOPY AND OTHER METHODS

Zoltán Klencsár, Sándor Stichleutner, Maria Gracheva, Károly Lázár

Objective

We aim to gain insights into the structure, composition, and relevant properties of diverse iron-, tin- and gold-based materials of interest, such as catalysts, iron citrate solutions, hematite suspension, and an iron(II)-azido compound.

Methods

Besides ^{57}Fe and ^{119}Sn Mössbauer Spectroscopies (MS), we also have utilized X-band electron paramagnetic resonance spectroscopy and other complementary methods to perform non-destructive analysis of the investigated samples.

Results

Despite the crucial role of iron(III) citrate systems in iron metabolism, the coordination chemistry of ferric citrate in aqueous solutions remains a matter of debate, especially for the physiological pH values. By applying ^{57}Fe Mössbauer and X-band electron paramagnetic resonance spectroscopies, we performed a detailed analysis of the environments of iron in solutions prepared with various iron-to-citrate ratios and pH values [1,2]. The formation of both polynuclear and mono-nuclear species was observed in the presence of citrate excess at physiological pH. At the same time, when iron and citrate were present at equimolar concentration, the ratio of iron incorporated into the monomeric species was negligible. Comparative evaluation of both X-band Electron Paramagnetic Resonance (EPR) and ^{57}Fe Mössbauer spectra revealed the presence of several mononuclear species with different structures in the solutions.

^{57}Fe Mössbauer spectroscopy has been applied to reveal the oxidation state and siting of iron species in coal fly ash zeolite with increased iron oxide content, prepared by double-stage alkaline conversion of high iron separate of lignite coal ash [3]. It was found that iron is present in various forms in the catalysts. It could be detected as a separate, finely dispersed spinel-type iron oxide or ferrite phase but also as a constituent of a Na-X-type zeolite lattice. Iron was found to occupy lattice positions as an isolated cation as well.

^{119}Sn Mössbauer measurements of AuSn-supported catalysts, obtained by simple impregnation on a reducible (TiO_2) and a non-reducible (Al_2O_3) metal-oxide, revealed the presence of SnO_2 , which was recognized to favour the electrons' exchange to form radicals, interacting with oxygen [4]. Such interaction, in particular, could be favoured by the co-presence of Au. Moreover, the same metal composition on the catalyst's surface resulted in a different catalytic behaviour depending on the support.

Materials with mesoporous structures can be beneficial for both catalysis and gas detection due to the large surface area and interconnected cavity network formed by the pores. Based on the ^{119}Sn Mössbauer spectroscopy analysis of mesoporous SnO_2 samples decorated with platinum at different (0, 1, 3, 5, 10, 15 mol%) Pt concentrations by the use of microwave-assisted hydrothermal synthesis, it was established that tin is present in the samples exclusively in the Sn^{4+} oxidation state. The ^{119}Sn Mössbauer spectra did not indicate the presence of a tin phase other than cassiterite (SnO_2). However, a correlation was found between the Pt concentration and the room temperature ^{119}Sn isomer shift in Pt-containing samples, suggesting that submicron-sized Pt particles adhering to the surface of SnO_2 particle agglomerates can influence the electron structure of SnO_2 [5].

The iron(II)-azido compound $[\text{Fe}(\text{4-epy})_2(\text{N}_3)_2]_n$ (FEN) with a spin integer ($S = 2$) dimerized honeycomb lattice exhibits reentrant spin glass behaviour below ~ 28 K owing to competing ferro- and antiferromagnetic exchange-coupling interactions. We have worked out a new analysis methodology of the ^{57}Fe Mössbauer spectra of FEN recorded in the temperature interval of 14-60K [6]. For $T \geq 35$ K the main component of the spectra is a quadrupole doublet characterized by isomer shift of $\delta \approx 1.2$ mm s^{-1} and quadrupole splitting of $\Delta \approx 2.7$ mm s^{-1} , originating clearly from high-spin Fe^{2+} ions. With decreasing temperature the doublet component gradually transforms to magnetic components due to the slowing down of spin fluctuations as temperature approaches the glass transition temperature from above, reflecting the presence of a range of Fe^{2+} spin fluctuation frequencies. Based on the decomposition of spectra measured at $T \leq 20$ K, the electronic and magnetic state of Fe^{2+} ions can be associated mainly with two different iron microenvironments, which differ in the apparent magnitude and local orientation of the hyperfine magnetic field sensed by the ^{57}Fe nucleus. The new analysis methodology enabled the consistent description of the ^{57}Fe Mössbauer spectra of FEN in the applied range of temperatures, and with decreasing temperature (for $T \leq 30$ K) it revealed a gradual decrease in the concentration of Fe^{2+} ions exhibiting the paramagnetic behaviour characteristic of the sample at higher ($T \geq 35$ K) temperatures.

Hematite nanoparticle suspension, with a colloid size of 10-20 nm, was characterized among others by ^{57}Fe Mössbauer spectroscopy and was subjected to Fe utilization by the flavin-secreting model plant cucumber [7]. While biological utilization of Fe resulted in a suppression of Fe deficiency responses, alterations in the structure and distribution of the hematite

nanoparticles were revealed by ^{57}Fe Mössbauer spectroscopy, High Resolution Transmission Electron Microscopy (HRTEM), and Energy Dispersive X-ray Spectroscopy (EDS) element mapping. The nanoparticles were stacked in the middle lamella of the apoplast, where Fe mobilization was evidenced by the reduction in the particle size, suggesting that Fe release from nanoparticles does not require contact with the plasma membrane.

An overview of the application of Mössbauer spectroscopy in the field of catalysts was also presented [8].

Related publications

- [1] M. Gracheva, Z. Homonnay, Z. Klencsár, K. Kovács: *Iron(III) citrate complexes at physiological pH*, 3rd International Conference on Radioanalytical and Nuclear Chemistry, 7-12 May 2023, Budapest, Hungary, Book of abstracts (Akadémiai Kiadó) p. 156.
- [2] M. Gracheva, Z. Klencsár, Z. Homonnay, Á. Solti, K. Kovács: *Iron citrate complexes at biologically relevant conditions*, XXXVII International Conference on the Application of the Mössbauer Effect, September 3-8, 2023, Cartagena de Indias, Colombia, Book of abstracts (eds.: K. Edilma, G. Téllez, C. Augusto, B. Meneses) p. 30.
- [3] S. Boycheva, Á. Szegedi, K. Lázár, C. Popov, M. Popova: *Advanced high-iron coal fly ash zeolites for low-carbon emission catalytic combustion of VOCs*, *Catalysis Today* **418**, 114109 (2023) <https://doi.org/10.1016/j.cattod.2023.114109>
- [4] M. Stucchi, A. Vomero, S. Stichleutner, K. Lázár, E. Pitzalis, C. Evangelisti, L. Prati: *Exploring the Effect of Sn Addition to Supported Au Nanoparticles on Reducible/Non-Reducible Metal Oxides Supports for Alkane Oxidation*, *Chemistry* **5**, 1560-1576 (2023) <http://dx.doi.org/10.3390/chemistry5030107>
- [5] I. Đurasović, G. Štefanić, G. Dražić, R. Peter, Z. Klencsár, M. Marciuš, T. Jurkin, M. Ivanda, S. Stichleutner, M. Gotić: *Microwave-Assisted Synthesis of Pt/SnO₂ for the Catalytic Reduction of 4-Nitrophenol to 4-Aminophenol*, *Nanomaterials* **13**, 2481 (2023) <http://dx.doi.org/10.3390/nano13172481>
- [6] Y.Q. Zhai, Y.F. Deng, Z. Fu, E. Feng, Y. Su, T. Shiga, H. Oshio, Z. Klencsár, J. Wang, Y.Z. Zheng: *Correction to "Reentrant Spin Glass and Large Coercive Field Observed in a Spin Integer Dimerized Honeycomb Lattice"*, *Advanced Functional Materials* **33**, 2111468 (2023) <http://dx.doi.org/10.1002/adfm.202111468>
- [7] A. Singh, M. Gracheva, V. K. Kis, Á. Keresztes, M. Sági-Kazár, B. Müller, F. Pankaczi, W. Ahmad, K. Kovács, Z. May, Gy. Tolnai, Z. Homonnay, F. Fodor, Z. Klencsár, Á. Solti: *Apoplast utilisation of nanohaematite initiates parallel suppression of RIBA1 and FRO1&3 in Cucumis sativus*, *Nanoimpact* **29**, 100444 (2023) <https://doi.org/10.1016/j.impact.2022.100444>
- [8] K. Lázár: *Mössbauer Spectroscopy of Catalysts*, In: Y. Garcia, J.H. Wang, T. Zhang (eds.): *Mössbauer Spectroscopy: Applications in Chemistry and Materials Science*, Weinheim, Germany: Wiley-VCH Verlag (2023) pp. 113-143.
- [9] K. A. Béres, Z. Homonnay, B. Barta Holló, M. Gracheva, V. M. Petruševski, A. Farkas, Zs. Dürvanger, L. Kótai: *Synthesis, structure, and Mössbauer spectroscopic studies on the heat-induced solid-phase redox reactions of hexakis (urea-O) iron (III) peroxodisulfate*, *Journal of Materials Research* **38**(4), 1102-1118 (2023)
- [10] M. Gracheva, Z. Klencsár, V. K. Kis, K. A. Béres, Z. May, V. Halasy,... & K. Kovács: *Iron nanoparticles for plant nutrition: Synthesis, transformation, and utilization by the roots of Cucumis sativus*, *Journal of Materials Research* **38**(4), 1035-1047 (2023) <http://dx.doi.org/10.1557/s43578-022-00686-z>
- [11] E. Kuzmann, K. Nomura, S. Stichleutner, A. Nakanishi, J. Pechousek, L. Machala, Z. Homonnay, R. Vondrasek, V.A. Skuratov, L. Krupa, O. Malina, T. Ingr, S. Kubuki: *Swift heavy ion irradiation-induced amorphous iron and Fe-Si oxide phases in metallic ^{57}Fe layer vacuum deposited on surface of SiO₂/Si*, *Journal of Materials Research* **38**, 1061-1073 (2023) <http://dx.doi.org/10.1557/s43578-022-00767-z>
- [12] D. G. Merkel, G. Hegedűs, M. Gracheva, A. Deák, L. Illés, A. Németh, F. Maccari, I. Radulov, M. Major, A.I. Chumakov, D. Bessas, D. L. Nagy, Z. Zolnai, S. Graning, K. Sájerman, E. Szilágyi, A. Lengyel: *Ion-induced nanopattern formation in FeRh thin films*, *ESRF Highlights* **2022**, 28 (2023)
- [13] D. G. Merkel, K. Sájerman, T. Váczi, S. Lenk, G. Hegedűs, S. Sajti, A. Németh, M. A. Gracheva, P. Petrik, D. Mukherjee, Z. E. Horváth, D. L. Nagy, A. Lengyel: *Laser irradiation effects in FeRh thin film*. *Materials Research Express* **10**(7), 076101 (2023) https://ui.adsabs.harvard.edu/link_gateway/2023MRE....10g6101M/doi:10.1088/2053-1591/ace4a3
- [14] A. K. Potluri, M. Sági-Kazár, M. Gracheva, K. Solymosi, L. Colucho Hurarte, H. Castillo Michel, Á. Solti: *Nitric oxide is a potential negative regulator of the plastidial iron uptake and incorporation*, In: K. Hagymási, T. Janda, M. Pál, P. Poór, G. Szalai: *Programme & Abstracts - 12th Congress of the Hungarian Free Radical Society*, 52 (2023)
- [15] M. Sági-Kazár, M. Gracheva, E. Enkhbileg, V. Bonanni, M. Žižić, K. Vogel-Mikuš, K. Solymosi, A. Gianoncelli, Á. Solti: *Transient and local iron accumulation in chloroplasts under senescence*, In: K. Hagymási, T. Janda, M. Pál, P. Poór, G. Szalai: *Programme & Abstracts - 12th Congress of the Hungarian Free Radical Society*, 53 (2023)
- [16] S. Zhao, R. Ge, Z. Klencsár, Y. Li, A.I. Rykov, W. Zhou, D. Liu, T. Zhang, J. Wang: *^{57}Fe Mössbauer spectroscopic study of lunar soil samples returned by the Chang'e-5 mission*, XXXVII International Conference on the Application of the Mössbauer Effect, September 3-8, 2023, Cartagena de Indias, Colombia, Book of abstracts (eds.: K. Edilma, G. Téllez, C. Augusto, B. Meneses) p. 32.

NEUTRON AND X-RAY RADIOGRAPHY AND TOMOGRAPHY AT THE BUDAPEST NEUTRON CENTRE

Zoltán Kis, László Horváth, László Szentmiklósi

Objective:

We develop and use imaging instrumentation and methodology at the Budapest Neutron Centre (BNC).

Methods

Energy-filtered neutron and X-ray imaging in 2D and 3D, real-time imaging in 2D, volume rendering

Results

The installation of the fully renewed imaging system at NORMA station (*Fig.1 a*) is finished in the framework of the Renewable Energies National Laboratory project. The main results are the significantly improved spatial resolution (some tens of microns) and light collection (*Fig.1 b*). The station became a more versatile system, which is now capable of real-time monitoring of the fuel cells in operation, and to fulfil other general and specialized neutron imaging tasks.

In cooperation with FRM2 (Forschungsreaktor München, Germany), the development of new borated screens produced with an improved milling process continued at NORMA. For screens using boron as neutron sensitive material, a new preparation method was introduced. An example is shown for a $\text{Na}_{10}\text{B}_5\text{O}_8(1:1)$ ZnS:Cu screen in *Fig.1 c*, where the inner ring corresponds to 50 μm spatial resolution. Results show that their resolution seems rather independent of screen thickness, and screen thickness can be increased for larger detection efficiency without significantly losing spatial resolution. The light output of the borated screens is up to more than two times as high as for the 10 μm thick Gadox screen.

In an OTKA project, we took part in the investigation of luminescence processes in microstructured semiconductors. A promising B-containing neutron absorber material is boron carbide, B_4C . The relative light yield of the newly developed B_4C -based scintillation materials was measured at the NORMA facility to provide a more comprehensive analysis of the neutron-photon conversion in the neutron detection process. The ^{10}B isotope enriched boron carbide layers were tested for their neutron capture and conversion efficiency through the $^{10}\text{B}(n,\alpha)^7\text{Li}$ reaction (*Fig.1 d*).

In the quality control of manufacturing, dimensional metrology is crucial. It is not well known, how neutron tomography can be used for dimensional metrology. Investigations at the RAD station provided information on selecting a gauge that can evaluate and compare X-ray and neutron tomography. It can be concluded that the Ti6Al4V alloy and ZrO_2 spheres with Y_2O_3 are potential candidates for a comparison measurement between neutron and X-ray tomography.

As a pilot study, we aimed to contribute to the understanding of plants' survival in a drought environment. The Haberlea rhodopensis is a unique resurrection plant (*Fig. 1 e*), but the contribution of root and leaf tissues to uptake is not fully understood. Real-time Neutron Radiography (NR) provided invaluable information about the process's dynamics using AI-based segmentation techniques.

We continued the successful cooperation in the field of cultural heritage science (museums, ELKH proof-of-concept))

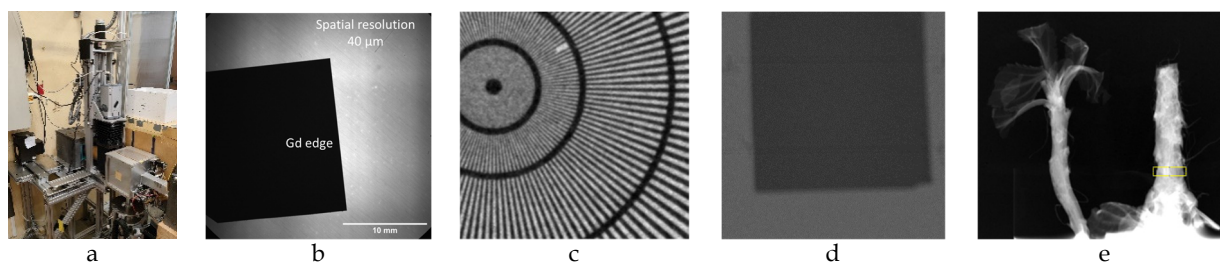


Figure 1: Neutron imaging results: see text for further information

Related publications

- [1] B. Schillinger, W. Chuirazzi, S. Cool, A. Craft, Z. Kis, L. Szentmiklósi, & A. Tengattini: *New Measurements on Borated Neutron Imaging Screens at Budapest Neutron Centre (BNC)*. Journal of Physics: Conference Series **2605(1)**, 12009 (2023) <https://doi.org/10.1088/1742-6596/2605/1/012009>
- [2] A. Marczis, Z. Kis, Á. Drégelyi-Kiss: *On the material selection of gauge for the comparison of X-ray and neutron tomography*, Springer book series Lecture Notes in Mechanical Engineering. Industrial Engineering in the Industry 4.0 Era. ISPR2023, October 5-7, 2023, Antalya (2023).
- [3] M. Venczel, Á. Veress, L. Szentmiklósi, & Z. Kis: *Dynamic Thermal Neutron Radiography for Filling Process Analysis and CFD Model Validation of Visco-Dampers*, Machines, **11(4)**. (2023) <https://doi.org/10.3390/machines11040485>

- [4] B. Bozzini, S. Cazzanti, R. Hippoliti, Z. Kis, L. Rovatti, F. Tavola: *Non-destructive analysis of Pb-acid battery positive plates, based on neutron tomography*, Journal of Physics: Energy (2023) <https://doi.org/10.1088/2515-7655/ad0b89>
- [5] J. G. Tarbay, B. Maróti, Z. Kis, G. Káli, & B. Soós: *Re-evaluation of the Late Bronze Age "warrior equipment" from the collection of the Ministry of Defence, Military History Institute and Museum, Hungary*, Journal of Archaeological Science: Reports **51**, 104115 (2023) <https://doi.org/https://doi.org/10.1016/j.jasrep.2023.104115>

PREPARATION AND CHARACTERIZATION OF GLASSES IN THE ZnO - B₂O₃ - Bi₂O₃ - WO₃ SYSTEM

Margit Fábíán, Margarita Milanova¹, Reni Iordanova¹

¹ Institute of General and Inorganic Chemistry, Bulgarian Academy of Sciences

Objective

Among many potential host glass materials, binary ZnO-B₂O₃ glasses have been attracting continuous scientific interest as a host for luminescence applications. Homogeneous binary zinc-borate glasses are formed in a very narrow range of compositions between 50-70 mol% ZnO because of the existence of a very large region of immiscibility of two liquids in ZnO-B₂O₃ system. It has been reported that the addition of other components as Bi₂O₃ and WO₃ to ZnO-B₂O₃ glasses induces the expansion of the glass-forming region. In this work we investigate the glass formation tendency of the compositions 50ZnO:(40-x)B₂O₃:xBi₂O₃:yWO₃, x = 1, 5, 10; y = 10, 15 (mol%) by applying the melt quenching method. The aim is to gain structural information and to check the possibility of obtaining bulk glass from these complex glass compositions that could be interesting for optical applications.

Methods

The glass formation ability of the compositions 50ZnO:(40-x)B₂O₃:xBi₂O₃:yWO₃, x = 1, 5, 10; y = 10, 15 (mol%) is investigated by applying the melt quenching method, using reagent grade ZnO, WO₃, H₃BO₃ and Bi₂O₃ as raw materials. The homogenized batches were melted at 1200°C for 20 min in a platinum crucible in air. The melts were cast into a graphite mould. The glass samples produced were annealed at the glass transition temperature for 2 hours to release the inner stress produced in the casting process. The obtained samples were investigated by: X-Ray Diffraction analysis (XRD) (Bruker D8 Advance diffractometer, Cu K α radiation); Differential Scanning Calorimetry (DSC) (DSC 404 F3 Pegasus Netzsch), Infrared spectroscopy (IR) (Nicolet-320 FTIR spectrometer) and optical microscopy (Optical microscopy ZEISS Primostar). Physical properties of glasses were investigated by measuring the densities of glass samples and by calculating the molar volume, oxygen molar volume, and oxygen packing density values.

Results

X-ray amorphous sample was obtained from the composition 50ZnO:39B₂O₃:1Bi₂O₃:10WO₃. Visually and by optical microscopy observation, it was found that this glass sample is characterized by good transmittance and homogeneity. Phase separation and surface crystallization of ZnWO₄ were established by optical microscopy and X-ray diffraction measurements (Figure 1) of quenched samples with nominal compositions of 50ZnO:30B₂O₃:5Bi₂O₃:15WO₃ and 50ZnO:25B₂O₃:10Bi₂O₃:15WO₃.

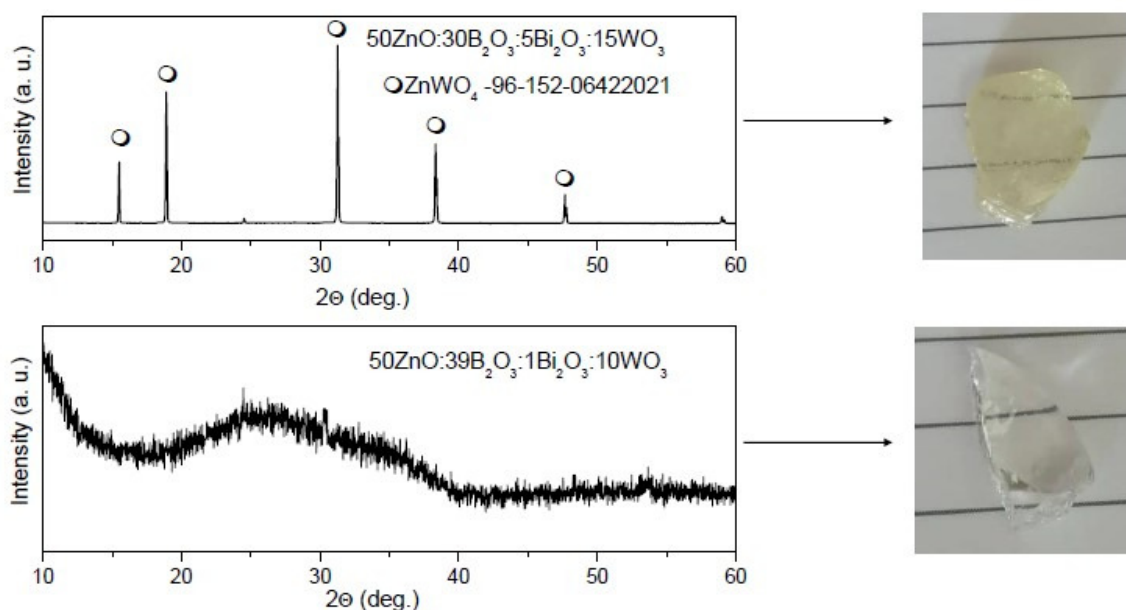


Figure 1: XRD analysis and photograph of the quenched samples

Based on the obtained IR spectral data it was established that the glass structure consists of BiO₆, BO₃, BO₄, WO₄ and WO₆ structural units (see Figure 2).

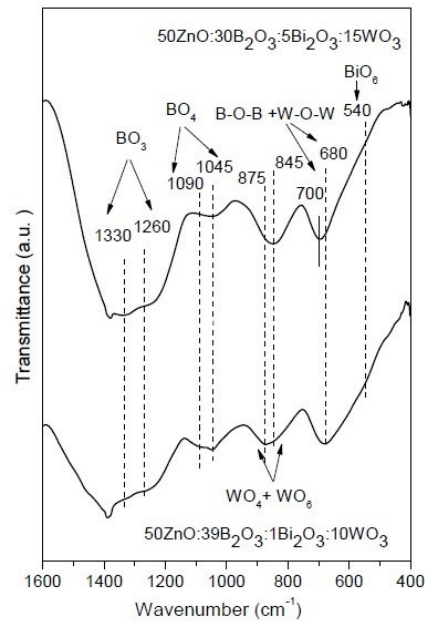


Figure 2: IR analysis of the sample: 50ZnO:30B₂O₃:5Bi₂O₃:15WO₃

The obtained glass 50ZnO:39B₂O₃:1Bi₂O₃:10WO₃ is characterized by high density ($\rho=4,102$ g/cm³) (Table 1) and good thermal stability $\Delta T = T_x - T_g$ that make this glass composition interesting for further investigations as glass matrix for hosting of active Eu³⁺ ions.

Table 1: Nominal compositions (mol%), density ρ (g/cm³), molar volume V_m (cm³/mol), oxygen molar volume V_o (cm³/mol), Oxygen Packing Density OPD (mol/L) of glass 50ZnO:39B₂O₃:1Bi₂O₃:10WO₃

ZnO	B ₂ O ₃	WO ₃	Bi ₂ O ₃	ρ_g	V_m	V_o	OPD
50	39	10	1	4.102±0.003	23.32	11.66	85.76

The doping effect of WO₃ on the structure and luminescent properties of ZnO-B₂O₃-Bi₂O₃ glass was investigated. The synthesized amorphous networks are built up of metaborate, [BO₂O], pyroborate, [B₂O₅]⁺, orthoborate triangular units, [BO₃]³⁻ and octahedral [WO₄O₂]²⁻ species with four bridging and two non-bridging oxygens. Bismuth atoms participate as BiO₆ groups. WO₃ modify the borate network, causing BO₄→BO₃ transformation and, as a result, formation of high number of BO₃ units with non-bridging oxygens.

Remaining work

The work has been completed.

Related publications

- [1] D. Aleksandrov, M. Milanova, R. Iordanova and M. Fabian: *Preparation and characterization glasses in the ZnO-B₂O₃-Bi₂O₃-WO₃ system*, poster, INFRAMAT-2022 United Research Infrastructure in Support of Industry, Culture and Technology Conference, Plovdiv, Bulgaria, 12-14 September 2022
- [2] L. Aleksandrov, A. Yordanova, M. Milanova, R. Iordanova and M. Fabian: *Doping effect of WO₃ on the structure and luminescent properties of ZnO-B₂O₃-Bi₂O₃: Eu³⁺ glass*, Journal of Chemical Technology and Metallurgy **58**(4), 707-715 (2023) <http://dx.doi.org/10.59957/jctm.v58i4.104>

PREPARATION AND CHARACTERIZATION OF GLASSES IN THE ZnO - B₂O₃ - Bi₂O₃ - WO₃:Eu₂O₃ SYSTEM

Margit Fábíán, Margarita Milanova¹, Reni Jordanova¹

¹ Institute of General and Inorganic Chemistry, Bulgarian Academy of Sciences

Objective

The design of new glass compositions remains a very active field of research due to their exciting application possibilities and the ability to fabricate them in a larger scale with lower production cost. Glasses are key materials for the development of lasers and optoelectronic devices. In particular, glasses doped with trivalent europium ions are commonly used as red emitting materials for field emission technology and LEDs, because of the intense red Eu³⁺ emission at 612 nm. As the luminescent properties of Eu³⁺ ions strongly depend on the chemical composition and structure of the host glass matrix, searching for a suitable Eu³⁺ glass matrix is of paramount importance for achieving high-intensity fluorescence and high brightness. In this work we investigate the glass formation, structure, thermal stability, and optical properties of ZnO:B₂O₃:Bi₂O₃:WO₃ glass doped with 0.5 mol % Eu₂O₃. The aim is to gain structural information and to check the possibility to obtain a bulk glass from these complex glass compositions that could be interesting for optical applications.

Methods

The glass formation ability of the compositions in mol% of 50ZnO:(49-x)B₂O₃:1Bi₂O₃:xWO₃:0.5Eu₂O₃, x=1, 5, 10 were investigated by applying the melt quenching method, using reagent grade ZnO, WO₃, B₂O₃ and Eu₂O₃ as raw materials. The homogenized batches were melted at 1200°C for 20 min in a platinum crucible in air. The obtained samples were investigated by: X-ray diffraction analysis (XRD; Bruker D8 Advance diffractometer, CuKα radiation), Differential Scanning Calorimetry (DSC; NETZSCH DSC 404F3), Infrared (IR; Nicolet-320 FTIR) and Photoluminescence spectroscopy (Ocean Insight HR 2000+). Neutron Diffraction (ND) data have been obtained on the two-axis 'PSD' diffractometer (Neutron Diffractometer with a Position Sensitive Detector system) at the 10 MW Budapest research reactor (λ₀=1.068 Å). Physical properties of glasses were investigated by measuring the densities of glass samples and by calculating the molar volume, oxygen molar volume, and oxygen packing density values.

Results

IR spectroscopy confirmed the presence of trigonal BØ₃ units connecting superstructural groups, [BØ₂O] metaborate groups, tetrahedral BØ₄ units in tetraborate groups (Ø=bridging oxygen atom), borate triangles with non-bridging oxygen atoms, [WO₄]²⁻ tetrahedral, and octahedral [WØ₄O₂]²⁻ species (Figure 1).

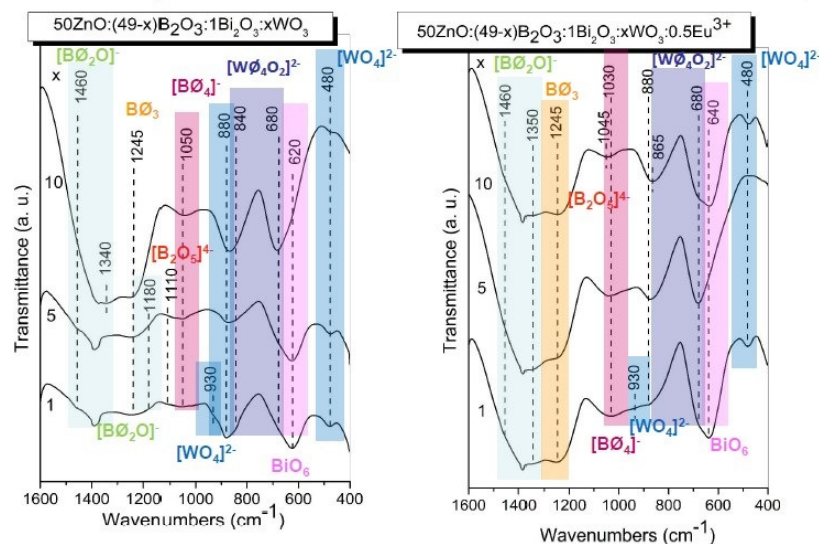


Figure 1: IR spectra of 50ZnO:(49-x)B₂O₃:1Bi₂O₃:xWO₃ and 50ZnO:(49-x)B₂O₃:1Bi₂O₃:xWO₃:0.5Eu₂O₃ (mol%) samples

Neutron diffraction experimental data were simulated by Reverse Monte Carlo (RMC) modelling (Figure 2). From the RMC simulation partial atomic pair-correlation functions ($g_{ij}(r)$), and average coordination number distributions (CN_{ij}) have been revealed with good stability and statistics. In the function of $g_{ij}(r)$ we specify a range in r over which atoms are counted as neighbours. This can be understood as defining coordination shells. Introducing a min point (position of minimum values on the lower) and max point (the upper side of the corresponding peak), are presented in Table 1, where we present the average coordination numbers.

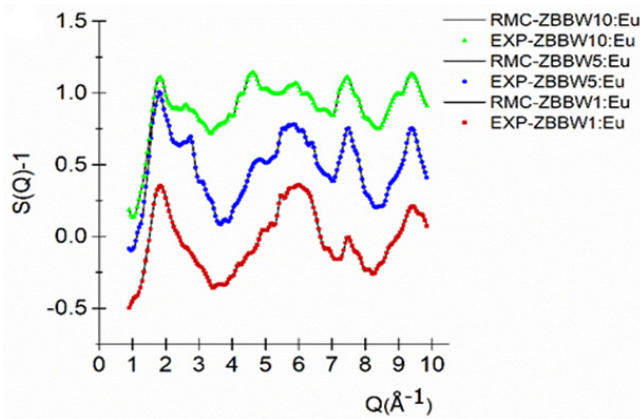


Figure 2: Experimental (colour sign) and RMC (black line) simulated neutron scattering structure factors for $50\text{ZnO}:(49-x)\text{B}_2\text{O}_3:1\text{Bi}_2\text{O}_3:x\text{WO}_3:0.5\text{Eu}_2\text{O}_3$, $x = 1, 5$ and 10 mol% glasses

From the obtained structural parameters, we have concluded that the glassy network is formed mainly by trigonal BO_3 (a few tetrahedral BO_4 were also identified) and tetrahedral ZnO_4 groups.

Table 1: Average coordination numbers (CN_{ij}) calculated from RMC simulation. In brackets, the interval is indicated, where the actual coordination number was calculated.

Sample	CN_{ij} (Zn-O)	CN_{ij} (B-O)	CN_{ij} (W-O)	CN_{ij} (O-O)
ZBBW1:Eu	4.01 ± 0.05 (min: 1.80-max: 2.20)	3.90 ± 0.05 (min: 1.20-max: 1.65)	6.20 ± 0.1 (min: 1.65-max: 2.23)	5.63 ± 0.1 (min: 2.20-max: 2.60)
ZBBW5:Eu	3.99 ± 0.05 (min: 1.80-max: 2.20)	3.52 ± 0.05 (min: 1.20-max: 1.65)	6.42 ± 0.1 (min: 1.60-max: 2.25)	5.32 ± 0.1 (min: 2.20-max: 2.60)
ZBBW10:Eu	3.97 ± 0.05 (min: 1.80-max: 2.20)	3.48 ± 0.05 (min: 1.20-max: 1.65)	6.73 ± 0.1 (min: 1.60-max: 2.25)	5.54 ± 0.1 (min: 2.20-max: 2.60)

Figure 3 shows the photoluminescent excitation spectra of Eu^{3+} doped $50\text{ZnO}:(49-x)\text{B}_2\text{O}_3:1\text{Bi}_2\text{O}_3:x\text{WO}_3$ ($x = 1, 5$ and 10 mol%) glasses monitoring the $5\text{D}_0 \rightarrow 7\text{F}_2$ red emission of Eu^{3+} at 612 nm. The glasses obtained presented strong 612 nm red luminescence with excitation at 394 nm. The positive effect of WO_3 on the luminescence intensity of the Eu^{3+} doped zinc bismuth borate glass was established.

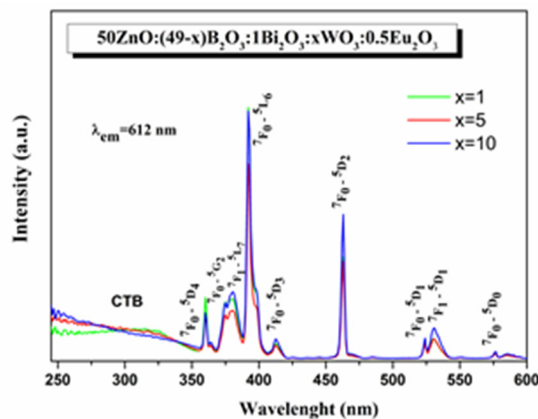


Figure 3: Excitation spectra of $50\text{ZnO}:(49-x)\text{B}_2\text{O}_3:1\text{Bi}_2\text{O}_3:x\text{WO}_3:0.5\text{Eu}_2\text{O}_3$ ($x = 1, 5$ and 10 mol%) glasses

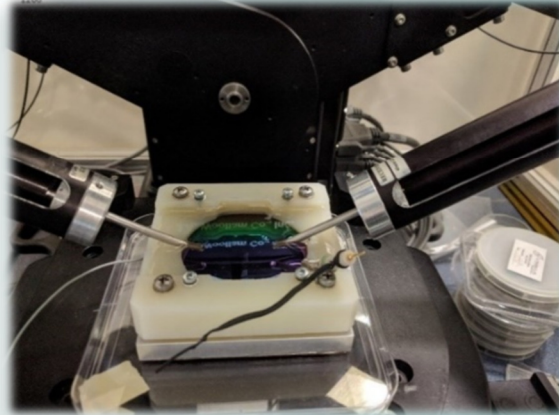
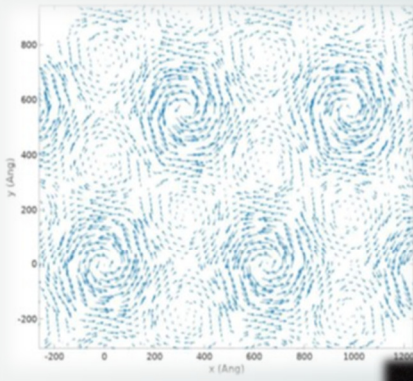
The results of this investigation show that the zinc borate glass matrix with the simultaneous presence of both Bi_2O_3 and WO_3 is very suitable for implementing the active Eu^{3+} as it possesses reticulated and rigid glass structure, ensuring a more asymmetrical local structure around Eu^{3+} sites, yielding accordingly a higher luminescence of the incorporated Eu^{3+} ions. On the other hand, both bismuth and tungsten oxides have a synthesizer effect by transferring the emission energy non-radiatively to the activator Eu^{3+} which additionally improves its luminescence properties. This suggests that the obtained glasses are potential candidates for red light-emitting phosphors.

Remaining work

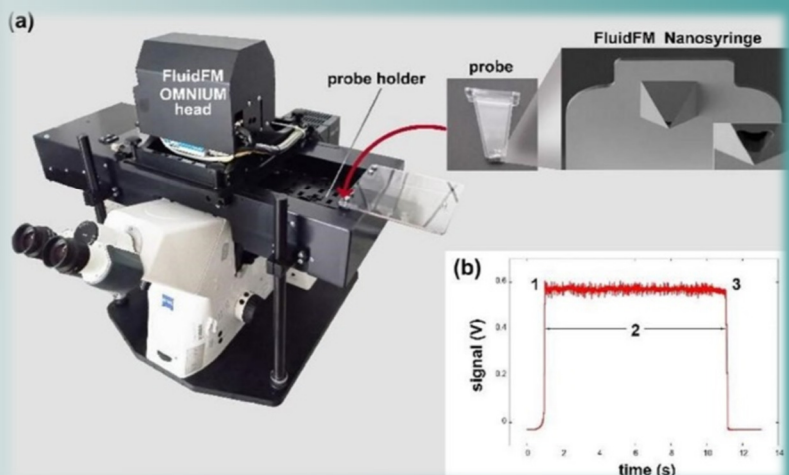
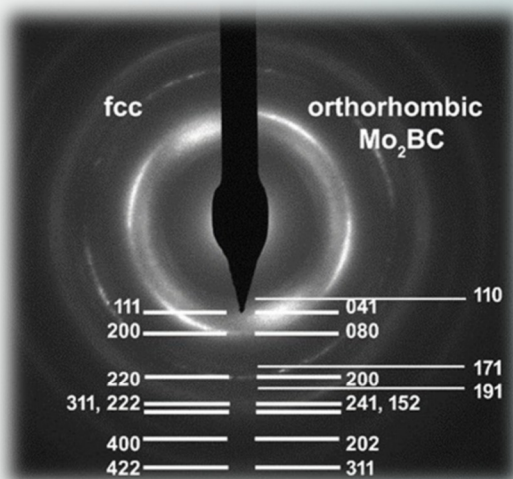
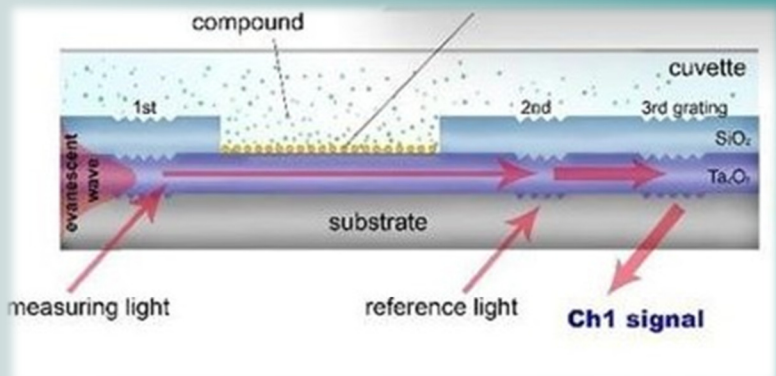
The work has been completed.

Related publications

- [1] A. Yordanova, M. Milanova, R. Iordanova, M. Fabian, L. Aleksandrov and P. Petrova: *Network structure and luminescent properties of $\text{ZnO-B}_2\text{O}_3\text{-Bi}_2\text{O}_3\text{-WO}_3: \text{Eu}^{3+}$ glasses*, *Materials* **16**, 6779 (2023) <http://dx.doi.org/10.3390/ma16206779>
- [2] M. Milanova, L. Aleksandrov, A. Yordanova, R. Iordanova, M. Fabian and P. Petrova: *Network structure of $\text{ZnO-B}_2\text{O}_3\text{-Bi}_2\text{O}_3\text{-WO}_3:\text{Eu}^{3+}$ glasses*, poster, SizeMat4 Fourth Workshop on Size-Dependent Effect in Materials for Environmental Protection and Energy Application Conference, Pomorie, Bulgaria, 10-14 May 2023



VI. RESEARCH AND DEVELOPMENT IN INSTITUTE OF TECHNICAL PHYSICS AND MATERIAL SCIENCES



IDENTIFICATION OF GRAPHITE WITH PERFECT RHOMBOHEDRAL STACKING BY ELECTRONIC RAMAN SCATTERING

OTKA KKP 138144, TKP2021-NKTA-05, OTKA K 146156, OTKA PD 146479, OTKA K 134258, OTKA K 132869, OTKA FK 142985, 2022-1.2.5-TÉT-IPARI-KR-2022-00006

A. Pálinkás, K. Máriy, K. Kandrai, Z. Tajkov, M. Gmitra (CLTP SAS, SK), P. Vancsó, L. Tapasztó, and P. Nemes-Incze

There are two energetically favourable configurations for stacking graphene layers in graphite: the stable and most common hexagonal (or AB), and the naturally rare, metastable rhombohedral (or ABC) stackings (Fig. 1.a). While the hexagonal phase has well-known properties, the latter is now receiving significant interest. That is because Rhombohedral Graphite (RG) is one of the simplest systems that can host a multitude of emergent, strongly correlated electronic phenomena. In recent years, state-of-the-art measurements have demonstrated, for example, unconventional superconductivity in 3-layer, correlated insulators in 4-layer, and fractionalization of the Hall resistance in 5-layer RG. The strength of electronic interactions, which drive these phenomena, increases with the addition of more rhombohedrally stacked graphene layers. However, until now, there were no reliable methods to identify thicker, perfect (defect-free) rhombohedral graphite layers. We have shown that perfect RG with 3 to 12 layers has a unique fingerprint owing to the Electronic Raman Scattering (ERS) process, which can be harnessed to overcome the identification challenge.

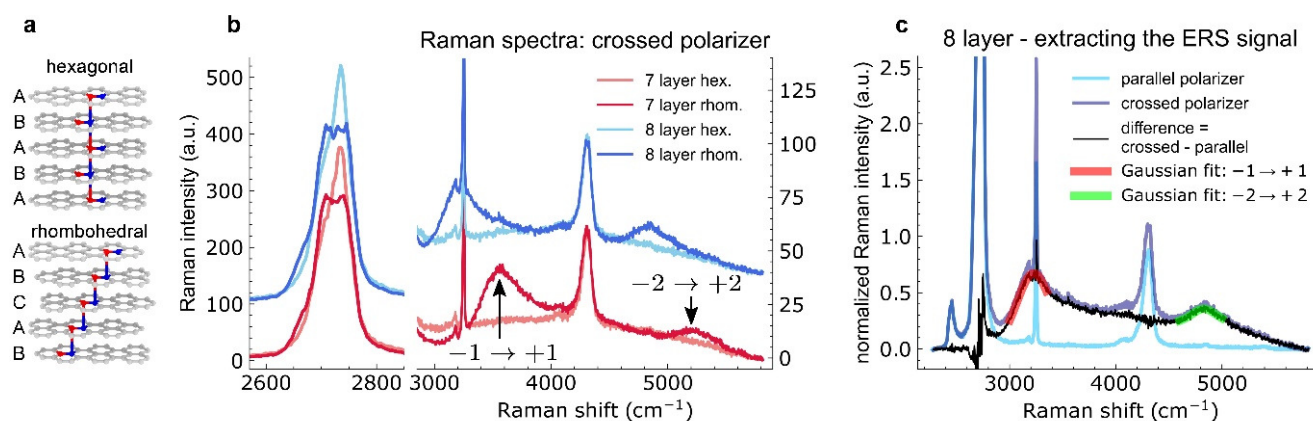


Figure 1: a) Schematic representation of the hexagonal and rhombohedral stackings of graphite layers. b) Raman spectra of the 7 and 8 layer regions of hexagonal or rhombohedral stackings, measured using crossed polarization. Arrows mark the ERS signal. c) Extracting the ERS signal. This is achieved by subtracting the spectrum measured with parallel polarization from the one measured, using the crossed polarizer configuration.

Fig. 1.b displays the phonon-originated 2D peak in the Raman spectrum alongside a broad ERS response for a 7- and 8-layer thick graphite sample, having perfectly stacked rhombohedral and hexagonal regions. Note, a polarizer is positioned in the path of the scattered light, oriented perpendicularly to the polarization of the incoming excitation laser. This "crossed polarizer" setup amplifies the visibility of the ERS signal, which otherwise is only ~1% of the 2D peak intensity, therefore cannot be detected in most measurements. Thanks to this "crossed polarizer" arrangement it becomes ~10% of the 2D peak intensity, as shown in Fig. 2.b. The polarization dependence of the scattered light also confirms that the broad peaks stem from ERS. If the polarizer in the path of the scattered light is in the parallel configuration, the broad peaks are absent, whereas they are clearly present in the crossed polarizer setup (Fig. 1.c). This comparison can also be used to separate the ERS peaks from phonon peaks of graphite. Subtracting the parallel polarized spectra, leaves us with the ERS signal. We fit the resulting ERS peaks by Gaussians to determine the Raman shift of the peaks. The result of this procedure is shown in Fig. 1.c.

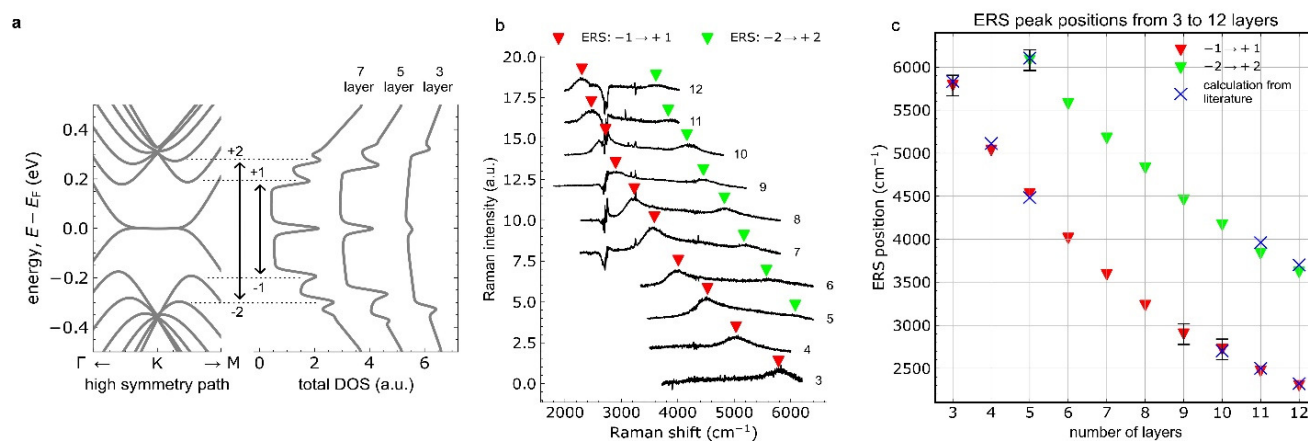


Figure 2: (a) Left: Band structure around the K point of a 7-layer RG slab. Energy is with respect to the Fermi level (E_F). Right: Density Of States (DOS) at selected RG thicknesses. The transitions between the DOS peaks, which result in the ERS signal, are shown by arrows. (b) Difference of crossed/parallel spectra for perfect RG with graphene layer numbers between 3 and 12. Positions of the ERS peaks are shown by red and green triangles. (c) ERS peak positions for the first and second transitions are showing a clear trend on layer number. Blue crosses show the previously calculated ERS peak positions from the literature [1 and 2].

This procedure is applied to defect-free RG samples with thicknesses varying from 3 to 12 graphene layers (Fig. 2.b). Each sample undergoes meticulous examination using Atomic Force Microscopy (AFM) to ensure accurate layer count. A clear trend can be observed in Fig. 2.c: with increasing layer number the $-1 \rightarrow +1$ and $-2 \rightarrow +2$ peaks continuously shift to lower energy (lower Raman shift). The ERS measurements directly reveal the energy of the electron-hole excitations related to the DOS peak separations ($-1 \rightarrow +1$ and $-2 \rightarrow +2$) of the bulk band edges (Fig. 1.2.a).

The introduction of ERS as a fast and accessible optical characterization method to identify rhombohedral graphite without stacking faults, breaks down a major hurdle in exploring the properties of RG. ERS characterization of RG samples is expected to enable a consistent comparison of results from different samples and research groups, which is essential for the development of the field. These findings enable the identifications and the further examinations of perfect, thick RG, represent a great step forward over the state-of-the-art, and thus would play a role in exploring the myriad of strongly-correlated electronic phenomena.

Related publications

- [1] A. García-Ruiz, S. Slizovskiy, M. Mucha-Kruczyński*, and V.I. Fal'ko: *Spectroscopic Signatures of Electronic Excitations in Raman Scattering in Thin Films of Rhombohedral Graphite*, Nano Lett. **19**, 6152–6156 (2019) <https://doi.org/10.1021/acs.nanolett.9b02196>
- [2] A. McEllistim, A. Garcia-Ruiz, Z.A.H. Goodwin, and V.I. Fal'ko: *Spectroscopic signatures of tetralayer graphene polytypes*, Phys. Rev. B **107**, 155147 (2023) <http://dx.doi.org/10.48550/arXiv.2302.07374>

STABILIZING GIANT MOIRÉ SUPERLATTICES IN TWISTED BILAYER GRAPHENE

OTKA KKP 138144, TKP2021-NKTA-05, OTKA K 132869, OTKA FK 142985, 2022-1.2.5-TÉT-IPARI-KR-2022-00006

G. Dobrik, P. Kun, M. Szendrő, P. Vancsó, R. Csanádi, P. Nemes-Incze, and L. Tapasztó

Realizing moiré superlattices with small twist angles in bilayer graphene, corresponding to large moiré wavelengths (> 10 nm) is required for engineering a flat band, which in turn can give rise to various correlated electronic states at low temperatures. This has been demonstrated in the so-called magic angle graphene with a twist angle of about 1.1° , and moiré wavelength of about 13 nm. Moreover, theory predicts that four more magic angles are expected at lower twist angles, hence larger moiré wavelengths. However, the experimental realization of twisted bilayer graphene samples with twist angles smaller than 1° turned out highly challenging, due to the strong structural reconstruction emerging at such small twist angles.

Unfortunately, these reconstructions destroy the flat band, and hence no correlated electronic states are expected for reconstructed moiré superlattices. In fact, it has been shown that even at the first magic angle, structural reconstructions are already present, and they are increasing the dispersion of the flat band; however, their effect is not strong enough to fully destroy the flatness of the band. This is not the case for twist angles around 0.5 degrees, corresponding to the second predicted magic angle, hence the experimental realization and investigation of lower magic angles remained elusive. This is even more regrettable, as it has been predicted that the correlation effects become stronger at lower magic angles. Therefore, stabilizing moiré superlattices against structural reconstructions is highly desirable, as it can further increase the correlation effects at the first magic angle, and it can also enable the realization and study of the predicted lower magic angles in Twisted Bilayer Graphene (TBG).

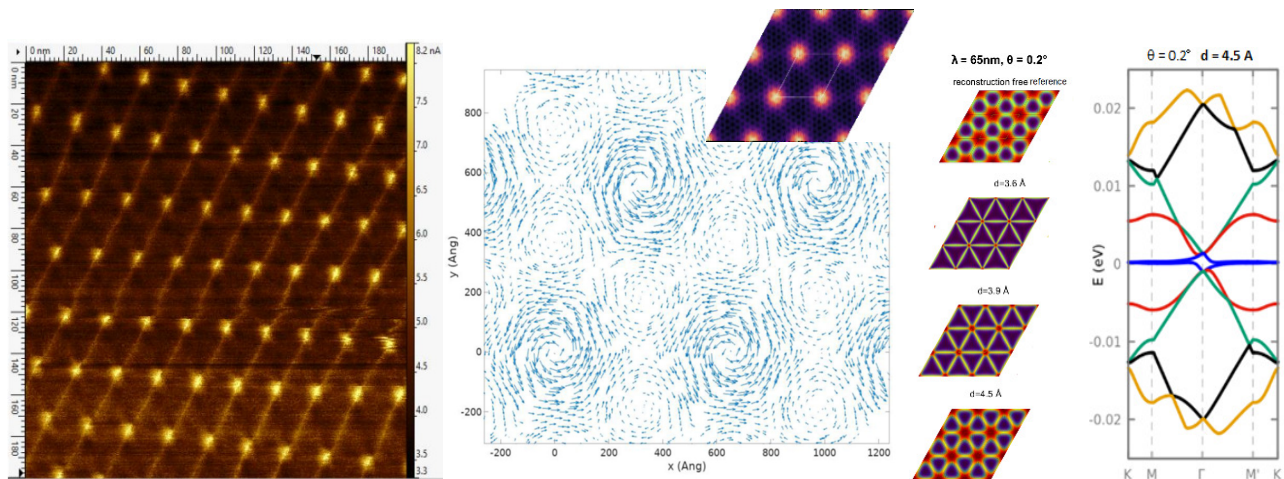


Figure 1: a) Strongly reconstructed moiré superlattice in a twisted bilayer graphene (TBG) with a twist angle of 0.5° , measured by conductive AFM. b) Molecular dynamics simulations of structural reconstructions in TBG for a twist angle of 0.2° . c) Simulated lattice structures of TBG for different interlayer distances revealing the weakening of the structural reconstructions with increasing interlayer gap. The electronic structure of a 0.2° rotated TBG at an increased interlayer distance preserving the flat band

After accidentally realizing an unreconstructed moiré superlattice with 65 nm wavelength, corresponding to a twist angle of 0.2 degrees, we have been systematically investigated by simulations, which effects could be responsible for stabilizing such small twist angle superlattices, against structural reconstructions. We have investigated various factors such as heterostrain, or substrate pinning, but found that only increasing the interlayer distance will enable avoiding the reconstructions and preserving the flat band at lower (magic) twist angles. Indeed, we were able to measure an increased interlayer distance in our sample displaying reconstruction-free moiré superlattice corresponding to 0.2° twist angle. Next, we have investigated by systematic simulations, what can cause an increased interlayer distance. We have investigated the effect of corrugation both induced by the SiO_2 support, as well as induced into the bottom graphene sheet (by cyclic thermal annealing); however, none of these factors could assure an increased interlayer separation. Intercalating atoms in between the two graphene layers would obviously increase the interlayer distance. However, there are two problems with this approach: (1) unless the intercalation is done by a fully continuous and ordered atomic intercalant layer, the interlayer separation would not be homogeneous, resulting in samples of poor quality, and (2) intercalating even a single atom (eg. Ar), will separate the layers further apart than needed, in order to avoid mechanical coupling, but preserve the electronic coupling between various stacking configurations. We observed experimentally an interlayer separation of about 0.7 Å, by AFM measurements, yet still the (unreconstructed) moiré superlattice has been observed in topographic STM images, due to electronic effects, as well as a flat band has been observed in tunnelling spectroscopy measurements.

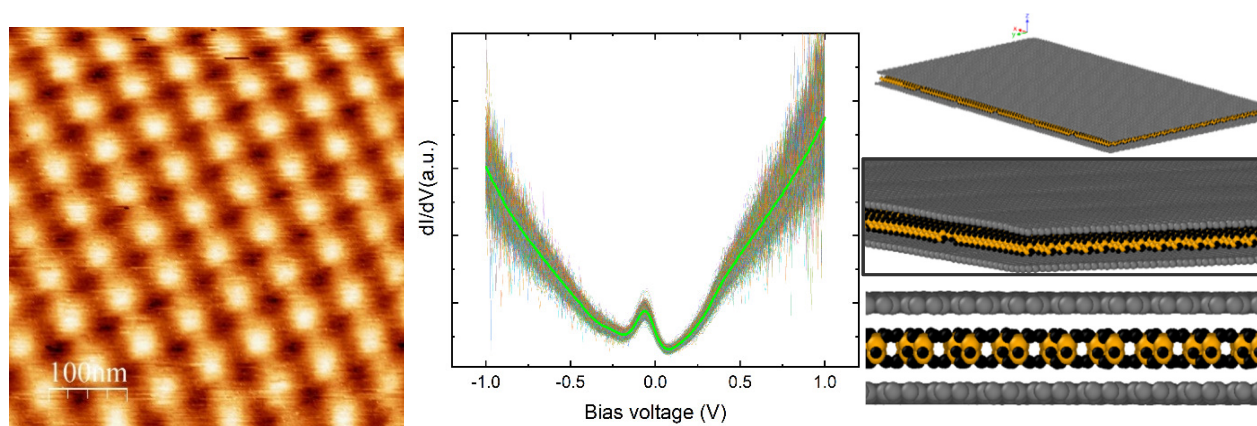


Figure 2: a) STM image of a reconstruction-free TBG superlattice with a periodicity of 65 nm, corresponding to a twist angle of 0.2 degrees. b) Tunnelling spectra revealing the presence of flat band in the form of a peak in the local density of states, near the Fermi level. c) Structural model from molecular dynamics simulations of a TBG with a spacer layer of self-organized alkane molecules intercalated between the graphene layers.

What is a suitable spacer molecule that is capable to form a continuous self-organized molecular layer in between the two graphene layers? Recently we have shown that such continuous, self-organized layers can indeed spontaneously form on top of graphene under ambient exposure, consisting of simple alkanes. We have run the simulations to see if such a self-organized alkane layer would indeed be suitable to act a spacer layer, and decouple mechanically the two graphene layers. Our Molecular Dynamics (MD) simulations show that this is indeed the case, since the interlayer separation is increased to about 0.8 Å in good quantitative agreement with the measurements. The important question remaining is, how can the two layers be still electronically coupled at such large separations. Our detailed calculations revealed that the p_z graphene orbitals decay much slower in the van der Waals (vdW) gap when the alkane layer is present in the vdW gap, corresponding to an effective distance of about 0.4 Å in vacuum, which indeed nicely reproduces the formation of the flat bands without structural reconstructions. The next step is to develop a sample preparation method when such TBG samples with a self-organized alkane spacer layer can be fabricated with a good yield in order to enable the systematic study of lower magic angles and stronger correlations in twisted bilayer graphene samples.

2D MoS₂ CRYSTALS CAN STABILIZE SEMICONDUCTING Pt STRUCTURES

OTKA KKP 138144, OTKA K 132869, TKP2021-NKTA-05, GrapheneCore3 Flagship

T. Ollár, P. Kun, P. Vancsó, A. Koós, P. Nemes-Incze, J.S. Pap, L. Tapasztó

Decreasing the size of the metal nanoparticles is a viable route to improve the noble metal utilization efficiency in catalysts. As the metal particle size is reduced, besides increasing the fraction of accessible surface atoms, an energy gap is also expected to open, below a critical size, due to quantum confinement effects. However, experimentally realizing and studying an energy gap in metal nanoparticles, turned out highly challenging. An energy gap has been observed in small Au nanocrystals, particularly, when their thickness has been reduced to one or two atomic layer. The observation of an energy gap in Pt nanostructures turned out even more challenging. Recent studies report the opening of an energy gap of about 0.2 eV in thiol capped, small (< 2.5 nm) Pt nanoparticles, based on NMR studies. However, the catalytic properties of nonmetallic Pt nanocrystals remained largely unexplored. We emphasize that here we focus on unoxidized, elemental Pt nanoparticles, as opposed to oxidized Pt structures that have been studied before, and are often also referred to as nonmetallic Pt.

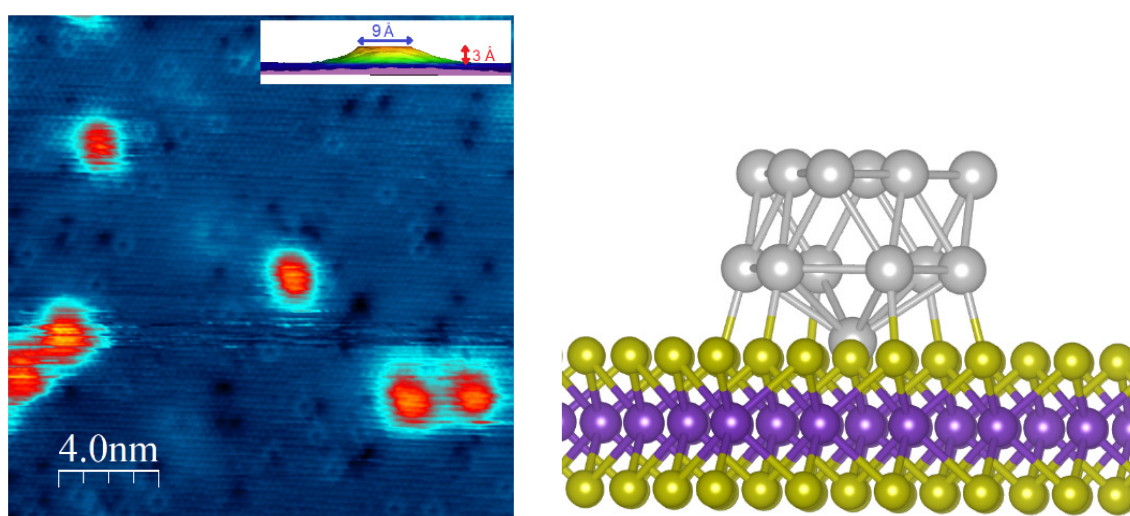


Figure 1: a) STM image of Pt nanoclusters of about 1 nm diameter and 0.3 Å height electrochemically deposited on 2D MoS₂ crystals. The flattened geometry corresponding to two Pt atom thickness, indicates a strong metal-support interaction. The smaller bright and dark features in the STM image correspond to S atom vacancy defects of the 2D MoS₂ support that can act as anchors for stabilizing ultra-fine Pt clusters. b) Simulated (Density Functional Theory (DFT)) structure of a Pt₁₃ cluster anchored to a S atom vacancy of the 2D MoS₂ crystal, reproducing the experimentally observed bilayer Pt structure.

Metal-support interaction is a powerful tool for engineering the atomic and electronic structure of metal nanoparticles. While MoS₂ is regarded as a rather weakly interacting support, the chemical affinity between Pt and S holds the potential for a strong interaction.

However, unleashing the full strength of Pt-MoS₂ interactions for Pt nanocrystals is hindered by their large (> 10%) lattice mismatch with MoS₂. A better interface matching can be achieved for small (< 1 nm) Pt clusters, due to their higher plasticity. However, we show that under proper kinetic deposition conditions, a strongly enhanced adhesion can be realized between small (~1 nm) Pt clusters and 2D MoS₂ crystals.

Gaining information on the electronic structure of Pt nanoparticles is of key importance for understanding and optimizing their catalytic performance. This, is of particular importance in our case, since both the flattened morphology (quantum size effects), and the enhanced metal-support interaction are expected to have a strong influence on the electronic structure. While tunnelling spectroscopy measurements can directly probe the electronic structure of metal nanostructures, the available data on catalyst nanoparticles is very scarce. This is mainly due to charging effects, owing to the weak electronic coupling to the support. Due to the enhanced coupling emerging from the stronger Pt/MoS₂ interaction, we were able to resolve the fine details of the Local Density Of States (LDOS) of small Pt clusters by tunnelling spectroscopy, within the energy window (-1.8 eV to + 0.3 eV), opened by the band gap of the 2D MoS₂ support. The most striking feature, is a sizeable energy gap of about 0.3 eV, with fully suppressed Pt LDOS near the Fermi energy (0 V), evidencing the semiconducting nature of bilayer Pt clusters (Fig. 2.a).

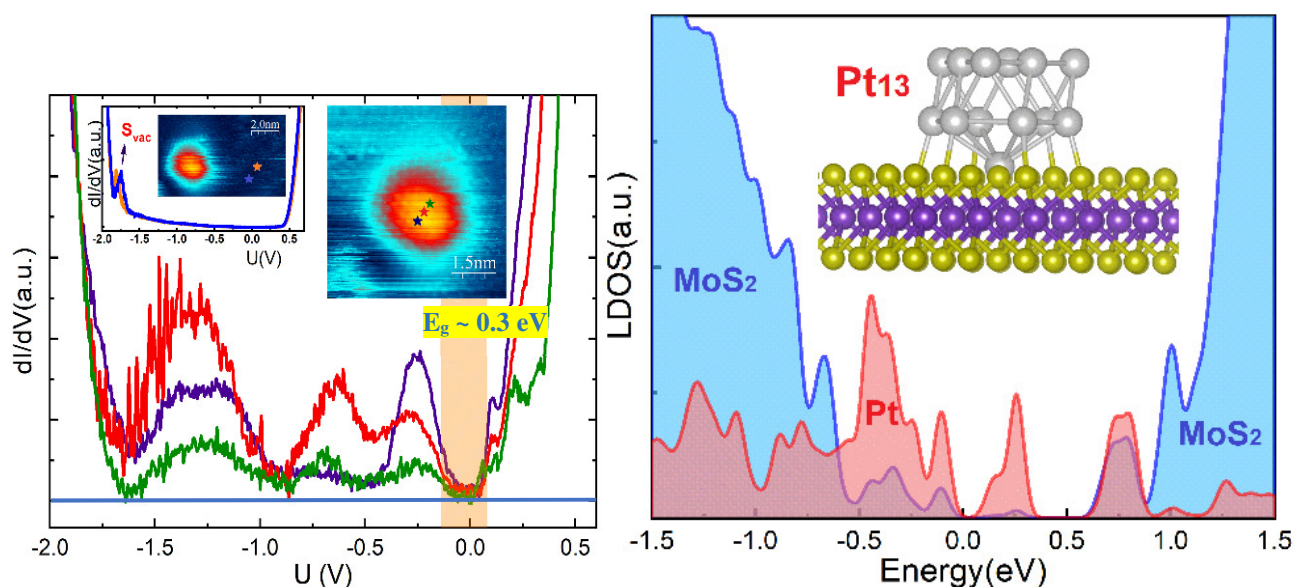


Figure 2: a) Tunnelling spectra recorded on a Pt cluster at the positions marked in the right inset, revealing a bandgap of ~ 300 meV. Left inset shows the tunnelling spectra on MoS_2 away from Pt clusters, with a single peak characteristic to sulphur vacancies. b) Calculated (DFT) local density of states (LDOS) of a Pt_{13} cluster, anchored by an S_{vac} to the 2D MoS_2 support. Red and blue areas represent contributions from the Pt cluster and the MoS_2 support, respectively.

To compare with the measured STM data, we have calculated the topographic STM images of the simulated bilayer Pt cluster structures, and found their heights to be about $3\text{-}4$ Å, in good quantitative agreement with the experimentally measured cluster heights. To directly compare with our tunnelling spectroscopy measurements, we have calculated by DFT the LDOS of such bilayer Pt clusters adsorbed on 2D MoS_2 , comprising 10, 13 and 27 Pt atoms. We found that all the investigated bilayer Pt clusters are characterized by a sizeable energy gap at the Fermi level, in good agreement with the experimental findings. The calculated LDOS of the Pt_{13} clusters (Fig. 2.b) displays the best agreement with tunnelling spectroscopy measurements (Fig. 2.a), which also matches the size of the measured clusters most closely.

HYBRID BIO-NANOCOMPOSITES BY INTEGRATING NANOSCALE AU IN BUTTERFLY SCALES COLOURED BY PHOTONIC NANOARCHITECTURES

K. Kertész, G. Piszter, A. Beck, A. Horváth, G. Nagy, Gy. Molnár, Gy. Z. Radnóczy, Zs. E. Horváth, L. Illés and L. P. Biró

Plasmonic metallic nanoparticles, like Au, can be used to tune the optical properties of photonic nanoarchitectures occurring in butterfly wing scales possessing structural colour. The effect of the nanoscale Au depends on the location and the amount deposited in the chitin-based photonic nanoarchitecture. The following three types of Au introduction methods were compared regarding the structural and optical properties of the resulting hybrid bio-nanocomposites: (i) growth of Au nanoparticles inside the nanopores of butterfly wing scales by a light-induced in situ chemical reduction of HAuCl_4 in aqueous solution containing sodium citrate, as a new procedure we have developed, (ii) drop-drying onto the wing of the aqueous Au sol formed during procedure (i) in the bulk liquid phase, and (iii) physical vapour deposition of Au thin film onto the butterfly wing. We investigated all three methods at two different Au concentrations on the wings of laboratory-bred, blue-coloured male *Polyommatus icarus* butterflies and characterized the optical properties of the resulting hybrid bio-nanocomposites.

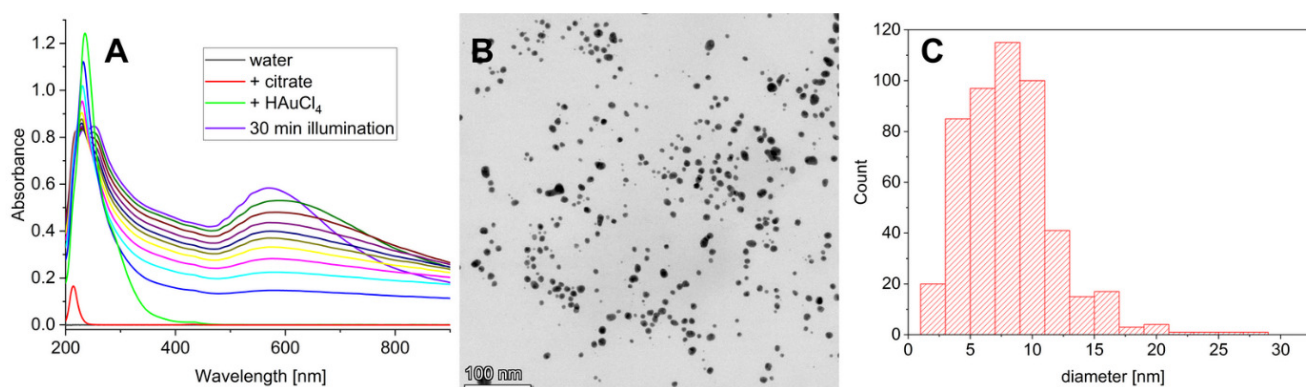


Figure 1: a) Evolution of the absorbance spectra of the reaction medium on the addition of the reactants and during 30-min of illumination, b) TEM image, and c) size histogram of prepared Au nanoparticles

Starting with ultrapure water, sodium citrate and HAuCl_4 precursors in a cuvette with white light illumination first, gold seed nucleation occurs followed by growth, and this process can be observed with naked eye: the solution turns from pale yellow to light red. The formation of the nanoparticles was followed by spectral analysis of the solution's absorbance; the characteristic peak of the precursor decreases, and at the same time, the peak of the plasmonic resonance of the spherical nanoparticles appears at around 580-590 nm (Fig. 1.a). Using this protocol, we obtained spherical Au nanoparticles (Fig. 1.b) with size distribution shown in Fig. 1.c.

When Au nanoparticles are grown inside the nanopores of the wing scales (by placing as a piece of wing in the cuvette under illumination) or are deposited by drop-drying Au sol on the wing, the original optical properties of the biological photonic nanoarchitecture are tuned by the integration of the Au nanoparticles into the photonic nanoarchitecture. As shown by the spectra in Fig. 2.d and 2.e, the spectral properties are borrowed both from the pristine chitin photonic nanoarchitecture and the Au nanoparticles as modificatory components. Opposite to this, when the wing is coated by physical vapour deposition by 5 nm or 15 nm Au, no shift is seen in the spectral position of the reflectance maxima (Fig. 2.f) for any of the two gold thicknesses used.

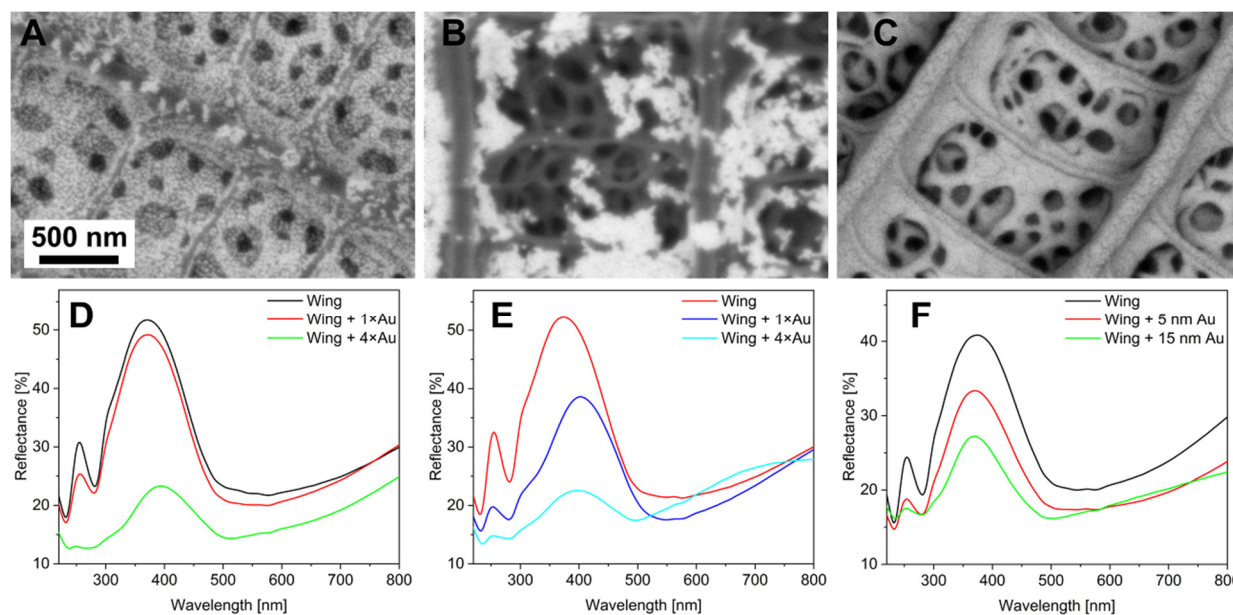


Figure 2: Top view SEM images of the *Polyommatus icarus* wing scales decorated with Au nanoparticles using a) in situ growth, b) drop-drying and c) physical vapour deposition methods. Reflectance spectra of the ethanol pretreated wings before and after d) in situ growing using 1 and 4 doses of Au precursor, e) drop drying of sols prepared in d), and d) physical vapour deposition of 5 and 15 nm of Au.

The reduction in the amplitude of the reflectance maximum is associated with the reduced transmittance of the Au layers; the effect is that of a filter placed into the light path between the illuminating source – wing, wing – detector system. In all cases, the magnitude of the observed effect scales with the amount of the Au used to alter the properties of the butterfly wing. When comparing the in situ growth with the drop-drying of Au sol, the former is more advantageous for the production of samples with uniform and deep penetration of the Au nanoparticles into the original biological photonic nanoarchitecture than the drop-drying method.

The increased amount of Au nanoparticles incorporated in the hybrid photonic nanoarchitecture increased the magnitude of the spectral shift, but at the same time reduced the amplitude of the reflectance maximum associated with the initial biological photonic nanoarchitecture. Therefore, one has to balance these two effects. Fortunately, nature has developed a very large “library” of precisely tuned photonic nanoarchitectures in butterfly wings, which can be produced in a cheap and environmentally friendly process. Thus, by selecting wings with suitable physical colour, the desired spectral modifications can be easily achieved.

PHOTOCATALYTIC DYE DEGRADATION WITH BIOTEMPLATED ZNO PHOTONIC NANOARCHITECTURES BASED ON MORPHO BUTTERFLY WINGS

OTKA PD 143037, TKP2021-NKTA-05

G. Piszter, G. Nagy, K. Kertész, Zs. Baji, K. Kovács, Zs. Bálint, Zs. E. Horváth, J. S. Pap, and L. P. Biró

Photonic nanoarchitectures of butterfly wings can serve as biotemplates to prepare semiconductor thin films by atomic layer deposition. The resulting biotemplated nanoarchitecture preserves the structural and optical properties of the natural system, while it also has the features of the deposited functional material. When photocatalytic thin films are applied, such as ZnO or TiO₂, the coated wings can be used directly in heterogeneous photocatalysis to decompose pollutants dissolved in water upon visible light illumination.

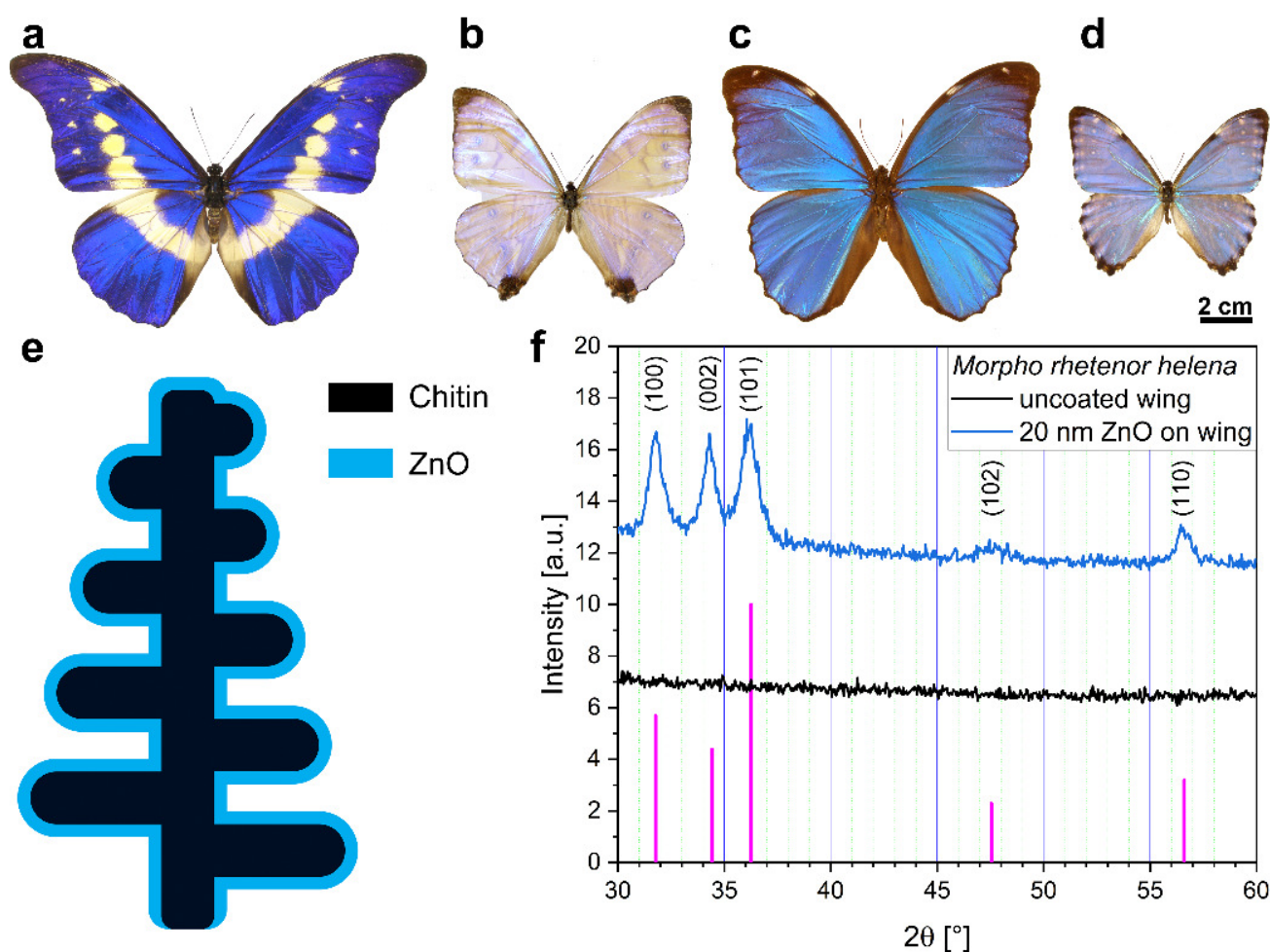


Figure 1: Photographs of male *Morpho* specimens in dorsal view. a) *M. rhetenor helena*, b) *M. sulkowskyi*, c) *M. menelaus*, d) *M. portis* are shown. e) Schematics of a *Morpho*-type nanostructure cross-section with the as-deposited ZnO thin film. f) X-ray diffractogram shows a nanocrystalline, wurtzite-type structure of 20 nm ZnO deposited on the *Morpho* wing.

In the present work, we utilized photonic nanoarchitectures of *Morpho* butterflies as biotemplates for ZnO thin films. According to our previous studies, the *Morpho*-based templates were the most effective photocatalysts. Therefore, we extended our investigations to four species representing this butterfly genus, with similar photonic nanoarchitectures in their wing scales, but with different structural colours (Fig. 1.a-d, from deep blue to greenish blue). To our best knowledge, it is for the first time that biotemplates with similar nanostructures, but with different optical properties are used within the same experimental setup to test the relation of the different optical properties with the photocatalytic performance.

ZnO is one of the semiconductors that can be grown on the surface of the biological photonic nanoarchitectures using low-temperature atomic layer deposition. This way, the micro- and nanoscale features of the chitinous cover scales are well preserved by the thin films without the need for a post-annealing process which would damage the biological material. X-ray diffraction measurements showed that the as-deposited ZnO had a nanocrystalline, wurtzite-type structure on the butterfly wings (Fig. 1.f).

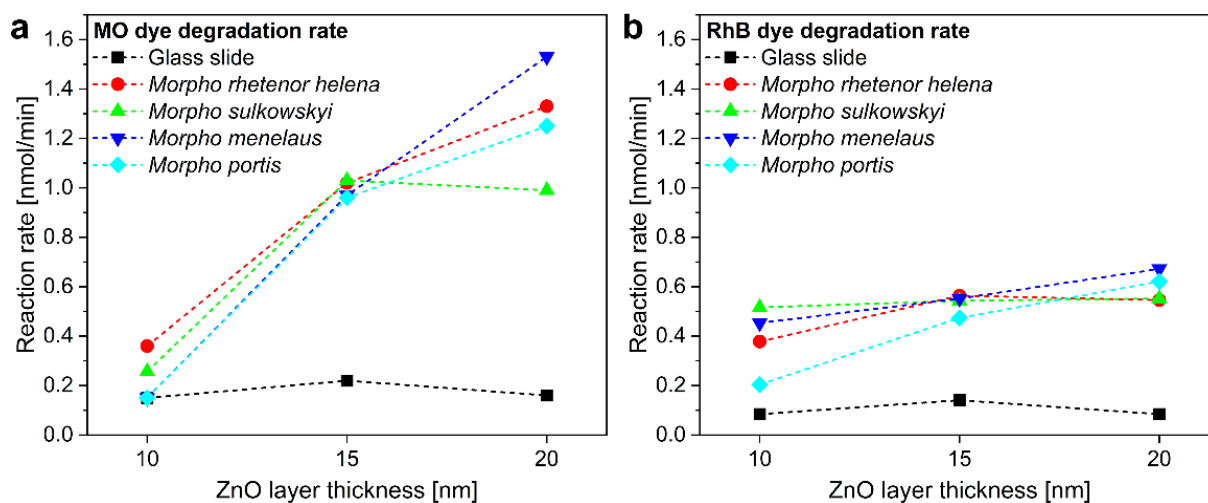


Figure 2: Reaction rate versus ZnO layer thickness for glass slide substrates and *Morpho* butterfly wings when a) methyl orange or b) rhodamine B test dyes were decomposed upon visible light illumination

We examined how the decomposition rate of Methyl Orange (MO) and rhodamine B (RhB) dyes depends on the structural colour of the biotemplates and the thickness of the applied ZnO coating upon visible light illumination. Using methyl orange, we measured a ten-fold increase in photodegradation rate when the 20 nm ZnO-coated wings were compared to similarly coated glass substrates (Fig. 2.a). Using rhodamine B, a saturating relationship was found between the degradation rate and the thickness of the deposited ZnO on butterfly wings (Fig. 2.b). We concluded that the enhancement of the catalytic efficiency can be attributed to the slow light effect due to a spectral overlap between the ZnO-coated *Morpho* butterfly wings' reflectance with the absorption band of dyes, thus the photocatalytic performance could be changed by the tuning of the structural colour of the butterfly biotemplates.

Our findings may facilitate the application of biotemplated semiconductor photonic nanoarchitectures as a bioinspired testing platform of photocatalysts, where evolutionary adjustments in the structural colour can tune the activity of the surface to achieve a selective catalytic degradation of different pollutants.

CONTACT ANGLE DETERMINATION BY THE CAPILLARY BRIDGE PROBE AND SESSILE DROP METHOD ON PTFE SURFACES

OTKA FK 128901

N. Nagy

The developed indirect Capillary Bridge Probe method combines the accuracy of the Wilhelmy method and the general usability of the sessile drop method without their limitations. The method is based on the use of a liquid bridge as a probe: the capillary bridge of the test liquid is stretched between the base of a cylinder and the investigated surface under equilibrium conditions. The advancing contact angle on the sample can be measured during the stepwise or slow (quasi-static) decrease of the bridge length. The receding contact angle is determined during the retraction of the cylinder (Fig. 1).

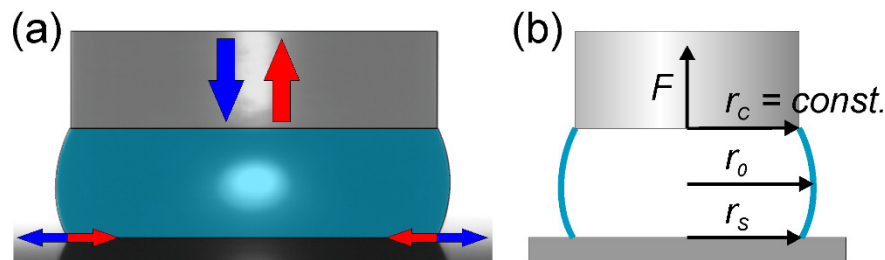


Figure 1: a) Recorded image (coloured) of a water capillary bridge on a polytetrafluoroethylene (PTFE) surface. The blue and red arrows indicate the advancing and receding phase. b) Schematics of an $r-\theta$ type liquid bridge with all parameters necessary for the analytical evaluation: capillary force (F), neck/haunch radius (r_0), and surface radius (r_s). The radius of the upper contact line is constant ($r_c = 1 \text{ mm}$) due to the contact line pinning on the cylinder's rim.

The contact angle is calculated from Delaunay's analytical solution, while the three necessary parameters are the measured capillary force (F_c), the radius of neck or haunch (r_0), and the radius of the contact line (r_s) on the investigated surface. The latter two parameters are obtained from the automated analysis of the captured image of the liquid bridge. The radius of the upper contact line (r_c) is constant since it pins on the rim of the cylinder.

Fig. 2.a shows the measured capillary force as a function of the bridge length recorded on a PTFE surface. The bridge volume was $1.7 \mu\text{L}$. The graph shows hysteresis. After the snap-in, the capillary force increases with the decreasing bridge length. It changes its sign during the cycle: there is an $F=0 \mu\text{N}$ transition in the approaching phase and in the retraction phase, after the turn. The negative (attractive) force has a minimum value in the retraction phase. After this point, the magnitude of the capillary force decreases until the pull-of. The insets show typical bridge shapes during the measurement cycle.

In Fig. 2.b, the lower drawings show the idea to find identical complete bridge shapes corresponding to the different classes. The determined contact angle as a function of the contact radius (r_s) are plotted in Fig. 3.a Plotting contact angles vs. contact radius is a useful representation because the change of the radius indicates that the angle actually corresponds to advancing or receding state of the contact line. The contact angles in Fig. 3.a were calculated based on the measured data of Fig. 2.a. The insets show characteristic evaluated profiles for different classes. It can be seen that the captured profiles are in remarkable agreement with the calculated ones. Contact angle hysteresis can be observed during the approach-retraction cycle.

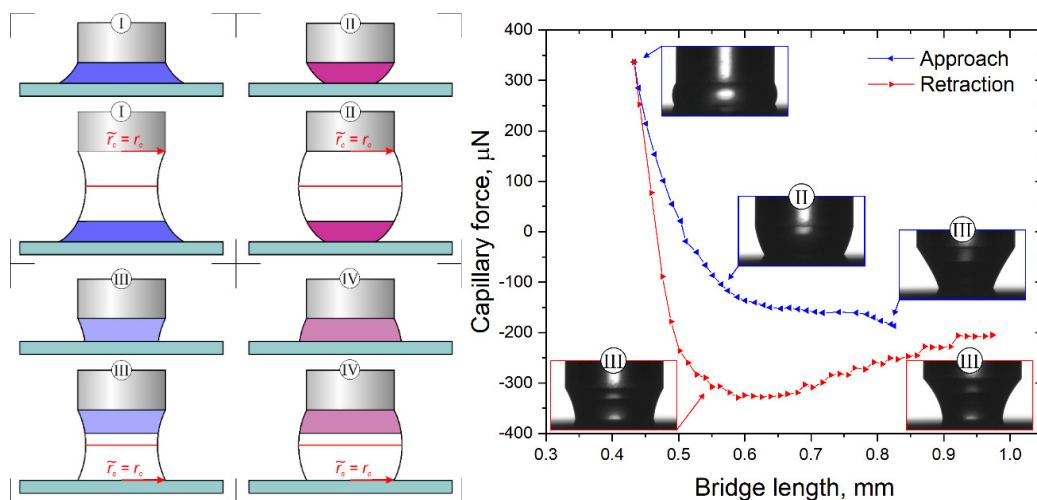


Figure 2: a) Capillary force as a function of the bridge length measured on a PTFE surface. The insets show typical equilibrium states of water capillary bridges during the measurements. The Roman numbers refer to the class of the incomplete form b) Schematics of the classification of incomplete capillary bridges.

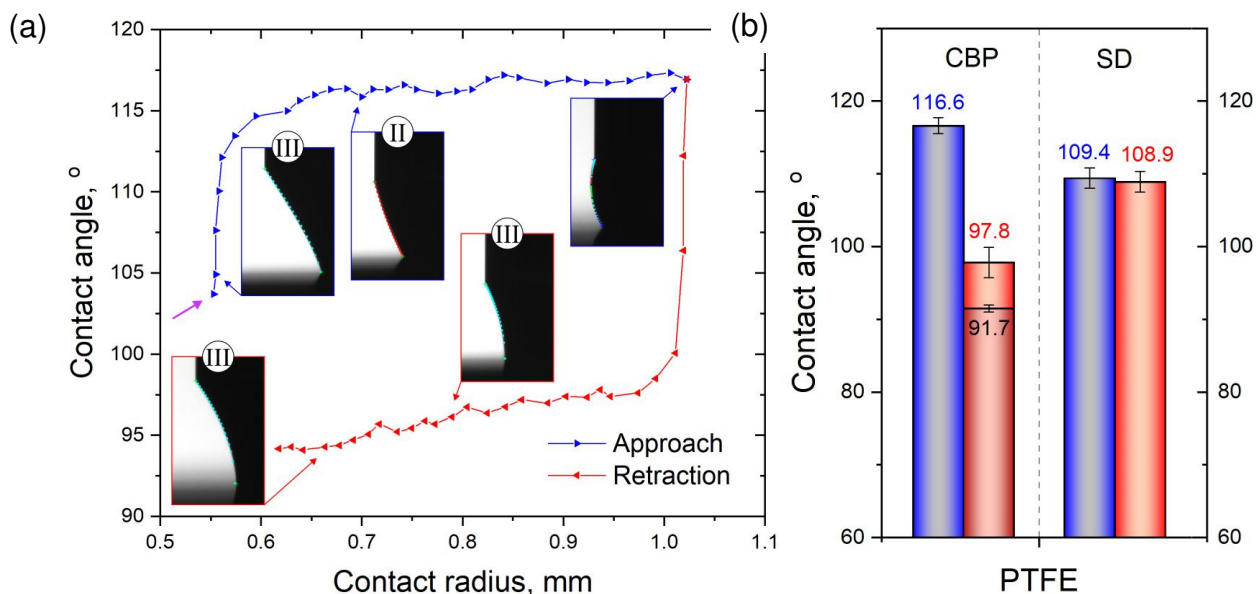


Figure 3: a) Contact angle as a function of the contact radius determined on a PTFE surface. The insets show the evaluated profiles of the capillary bridges. b) Advancing and receding contact angles determined by the Capillary Bridge Probe (CBP) and the Sessile Drop (SD) methods.

Sessile drop measurements were carried out on the same PTFE surfaces for comparison. The advancing and receding contact angles were determined applying the drop build-up technique in the range of 6–20 μL at five different measuring position. The comparison chart is shown in Fig. 3.b. The results of the sessile drop method practically do not show any contact angle hysteresis, while the magnitude of the standard deviation refers to the presence of surface imperfections. However, according to the capillary bridge probe method the hysteresis is considerable ($>18^\circ$). The shorter length of the contact line can explain the higher sensitivity of this method on surface imperfections. Furthermore, the AFM analysis revealed micrometre size granular regions between large smooth plateaus. These deeper imperfections are not wetted during the sessile drop measurements, but a Cassie-Wenzel wetting transition was occurred due to high capillary pressures during the capillary bridge probe measurements [1, 2].

Related publications

- [1] N. Nagy: *Contact Angle Determination on Hydrophilic and Superhydrophilic Surfaces by Using r - θ -Type Capillary Bridges*, *Langmuir* **35**(15), 5202-5212 (2019) <https://doi.org/10.1021/acs.langmuir.9b00442>
- [2] N. Nagy: *Capillary Bridges on Hydrophobic Surfaces: Analytical Contact Angle Determination*, *Langmuir* **38**(19), 6201-6208 (2022) <https://doi.org/10.1021/acs.langmuir.2c00674>

SURFACE SODIFICATION AND SELF-ASSEMBLY OF GOLD NANOPRISMS

OTKA FK FK128327

D. Zámbo, D. Kovács, G. Südi, Z. Zolnai, A. Deák*

Nanosized gold nanoparticles are of interest in many research fields as they have a large optical extinction cross-section at specific wavelength due to the excitation of localized surface plasmons. At the wavelength (photon energy) of these sharp resonant peaks the optical spectrum is determined primarily by the shape and size of the particles, allowing the design of nanoparticles for a specific application in sensorics, photothermal or energy harvesting applications. For every application, however, the surface ligand layer of the particles is of crucial importance, as its presence is always necessary to ensure processability and functionality of the particles.

Our recent research focused on the latter aspect of this field, namely the formation of a composite ligand layer on the surface of gold nanoprisms [1]. The importance of composite ligand layers lies in their ability to combine different molecular functionalities at the same time, e.g. particle stability and specific functional groups. In our study we relied on the subtle changes in the plasmon resonance peak of the nanoprisms upon exposing them to a combination of different thiolated molecules. When these molecules bind to the particles' surface, their impact is twofold. First, they will influence the resonant energy as it depends on the dielectric properties of the particles' optical near field. Second, the surface-bound molecules induce image dipoles at the surface that leads to an enhanced scattering of the electrons. This additional plasmon decay channel leads to broadening of the plasmon peak and is referred to as chemical interface damping. Detailed analysis of the simultaneous change of the plasmon energy (energy shift) and damping change (peak broadening) can help to clarify the build-up and structure of mixed ligand layers. To access these values, however, the optical changes have to be monitored in-situ in the liquid environment and the level of individual particles, otherwise inhomogeneous peak broadening inherently present in an ensemble measurements does not allow to extract the necessary information.

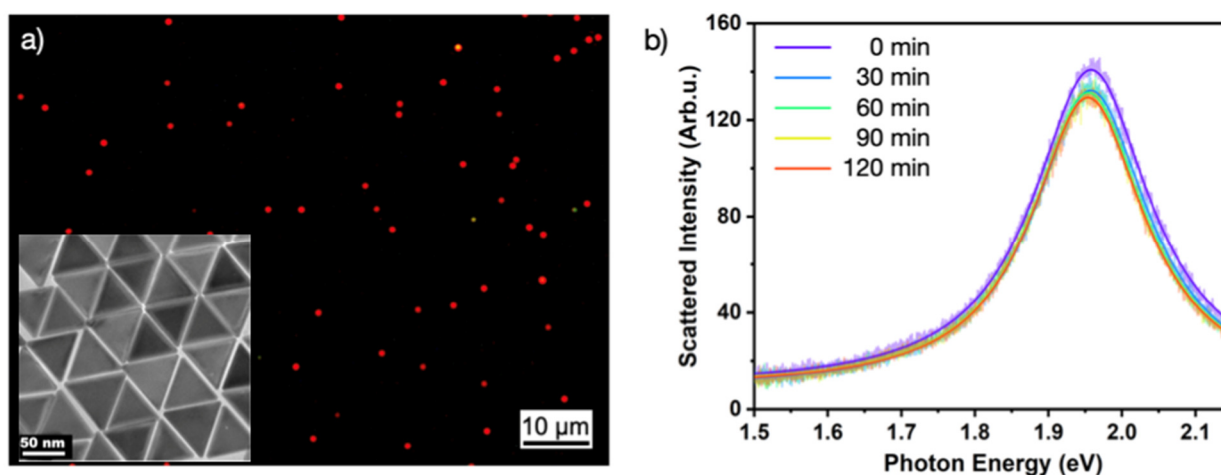


Figure 1: Typical optical dark-field microscopy image of a nanoprism sample for single-particle spectroscopy

a) The inset shows the TEM image of the particles.

In b) the time-dependent scattering spectra of a single nanoprism is shown upon exposing it to 100 μM aqueous mPEG-SH solution. The spectra are evaluated with by fitting an intraband-transition corrected damped oscillator model (solid lines) to obtain resonance energy (ΔE_{res}) and damping ($\Delta \Gamma$) changes

For this purpose, we performed our measurements on individual gold nanoprisms in a liquid flow cell combined with a laboratory-developed microspectroscopy setup that allows to investigate the scattering spectra of individual nanoparticle with high confidence and accuracy (see. Fig. 1). The thiol molecules used for the mixed ligand shell preparation were Mercaptolhexadecyl trimethylammonium bromide (MTAB), a positively charged thiol which is the thiolated analogue of the original capping ligand of the prisms, and a 5000 Da large neutral polymer (thiolated Polyethylene Glycol (PEG) - mPEG-SH).

Fig. 2 shows the changes of the resonance energy and plasmon damping as a function of time upon thiol addition. When the two thiols are introduced sequentially into the flow cell (Fig. 2.a and Fig. 2.b), the resonance energy change for the MTAB/PEG sequence (Fig. 2.a) indicates that PEG can bind to the surface even when MTAB is already present: there is an additional significant red-shift (ΔE_{res} decrease) upon introducing PEG after 30 minutes which cannot be observed for opposite order of addition. This also means that already surface bound neutral polymer (PEG) might block the adsorption of the second, charged thiol (MTAB). Interestingly, when the two molecule types are applied simultaneously (Fig. 2.c), both the damping and resonance energy changes are significantly larger. This means a ligand layer that is more dense than in the previous two cases.

This can be interpreted as the formation of a composite ligand layer, where the MTAB molecules occupy the surface area between the PEG anchoring points, the latter being inherently further away from each other due to the steric repulsion between the polymer chains.

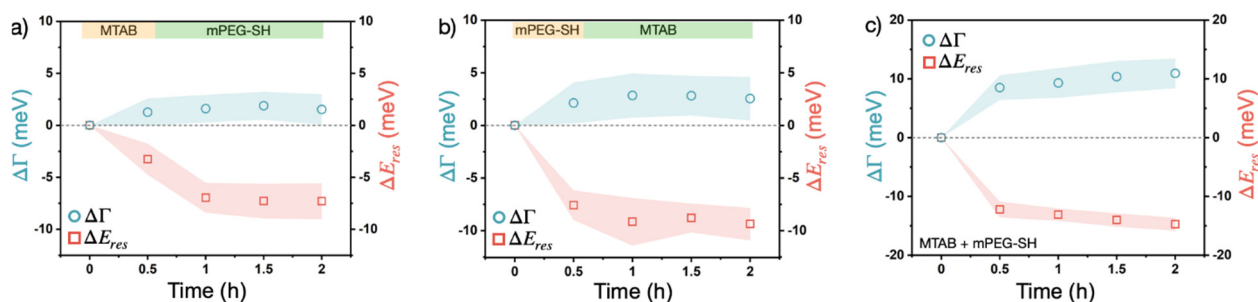


Figure 2: Resonance energy (ΔE_{res}) and damping ($\Delta\Gamma$) changes for individual nanoparticle when exposed to two thiol molecules of different types. For a) and b) the two thiols are applied sequentially as indicated by the colour-bar in the top of the figures. For c) the mixture of the two molecules is applied. For all cases the concentration is $10\ \mu\text{M}$ MTAB, $100\ \mu\text{M}$ mPEG-SH.

Besides the fundamental character of the results of this study, their practical implication are that when two molecules of different size are to be used for surface modification in order to dress the particles with different functionalities, the following should be considered: sequential adsorption with the smaller sized thiol added first is to be used when accessibility of this surface modified particle surface region is of importance but the simultaneous addition of the molecules should be preferred when the goal is to achieve highest molecular loading.

Related publication

- [1] D. Zámbo, D. Kovács, G. Südi, Z. Zolnai, A. Deák: *Composite Ligand Shells on Gold Nanoprisms – an Ensemble and Single Particle Study*, RSC Adv. **13**:(44), 30696–30703 (2023) <https://doi.org/10.1039/D3RA05548E>

MULTICOMPONENT HETERONANOPARTICLES FOR PHOTOCATALYTIC APPLICATION

TKP2021-NKTA-05, OTKA FK 142148

D. Kovács, A. Deák, Gy. Z. Radnóczy, Zs. E. Horváth, A. Sulyok, R. Schiller, D. Zámbo*
 *Corresponding author: zambod@inf.elte.hu

Multicomponent nanoparticles are in the spotlight of the nanoscience owing to the synergistic properties emerging between components at the nanoscale. Especially in semiconductor-metal heteronanosystems, the combination of the nanoparticle building blocks enables the utilization of novel photophysical processes. Exciting the charge carriers in the semiconductor component generates electrons and holes being relevant in photo-driven applications such as photocatalysis. Nevertheless, metal nanoparticles or domains being in direct contact with the semiconductor acts as an efficient electron reservoir due to the larger work function of most of the metals compared to that of the transition metal-chalcogenide semiconductors. This is not only advantageous in the separation of the photogenerated charge carriers, but also expands the lifetime of the electrons, thus, they can be utilized in a wider timescale in reduction reactions.

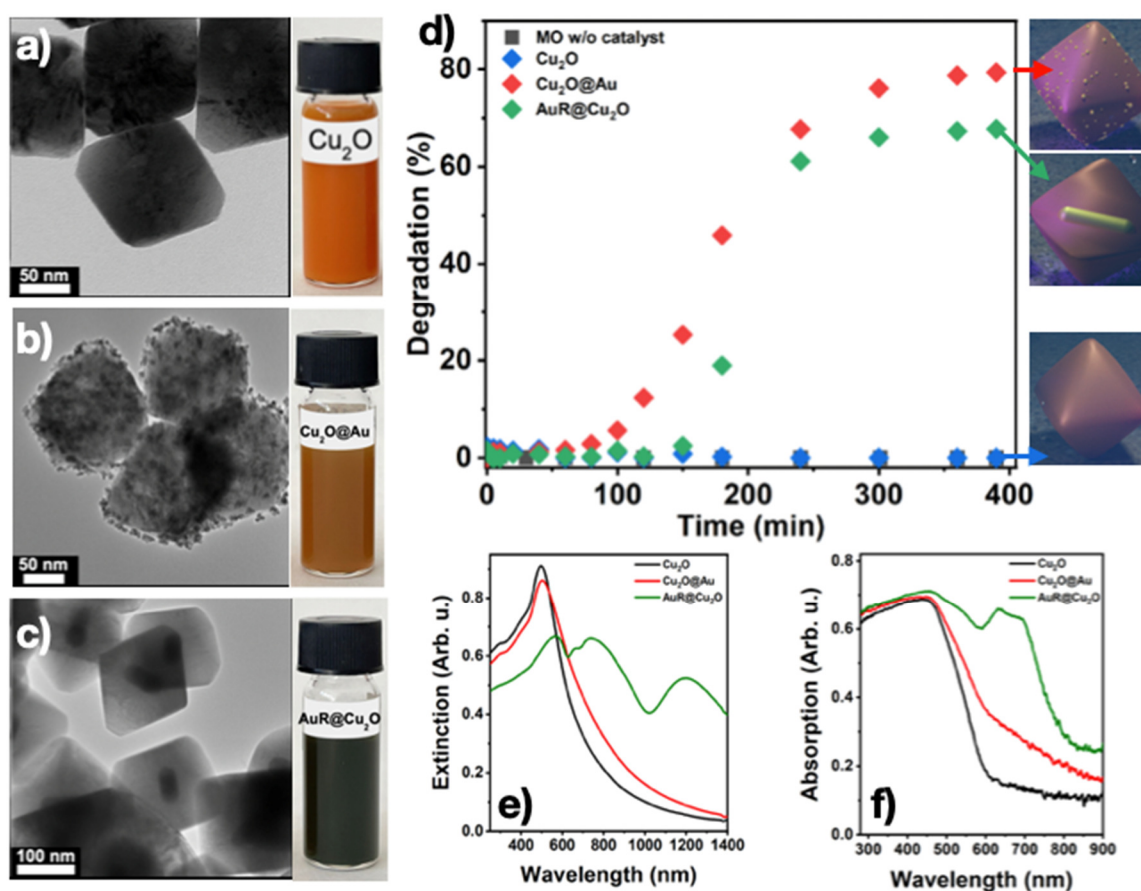
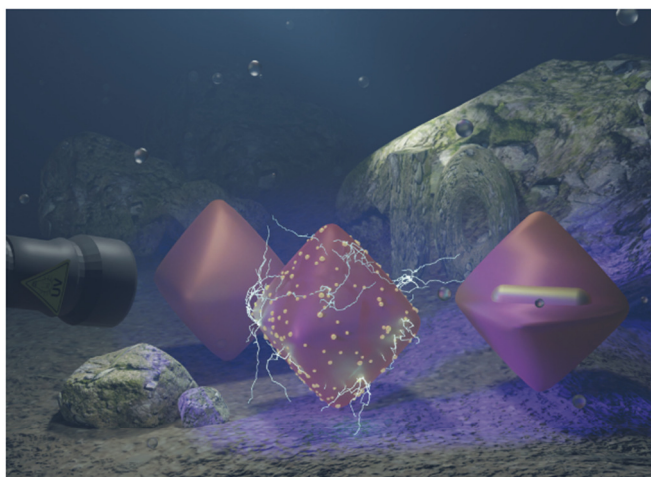


Figure 1: TEM images and the corresponding photographs of the pristine Cu₂O (a), Cu₂O@Au (b) and AuR@Cu₂O (c) nanoparticles. Photocatalytic degradation of methyl orange by using the different heteronanoparticles as catalyst (d). Extinction (e) and absorption spectra of the heteroparticles' aqueous solutions at identical Cu₂O concentrations. [1]

Copper(I)-oxide is an abundant, eco-friendly, and easy-to-synthesize p-type semiconductor, which – in a form of a nanoparticle – shows tuneable optical and electronic properties depending on its morphology. Although it had been demonstrated recently that Cu₂O nanoparticles are promising photocatalysts, its potential is significantly limited due to the intraparticle photophysical properties. Despite the high carrier density, the low mobility, short diffusion length of the minority carrier and the often-existing defects in the crystal structure restrict the utilization of the generated carriers upon illumination. Our aim was to circumvent this limitation *via* combining the Cu₂O with gold nanoparticles.



Showing research from the group of Dr Dániel Zámbo at Centre for Energy Research, Institute of Technical Physics and Materials Science, Hungary.

Position of gold dictates the photophysical and photocatalytic properties of Cu_2O in $\text{Cu}_2\text{O}/\text{Au}$ multicomponent nanoparticles

Boosting the colloidal stability and photocatalytic activity of copper(II)-oxide nanooctahedra via synthesising $\text{Cu}_2\text{O}/\text{Au}$ multicomponent nanoparticles in outstanding shape, size, and compositional uniformity. The form and position of gold in the heterooctahedra essentially govern the photophysical properties of copper(II)-oxide, enabling the separation of the photoexcited carriers. Revealing the optical properties, energy landscape as well as photocatalytic activity of the particles synthesized under powerful control over the parameters is demonstrated.

As featured in:



See Dániel Zámbo et al., *J. Mater. Chem. C*, 2023, 11, 8796.



rsc.li/materials-c

Registered charity number: 207890

Figure 2: Published cover artwork for our article in *The Journal of Materials Chemistry* [2]

While gold had already demonstrated the capability of enhancing the photocatalytic properties of Cu_2O , it was still unclear how the form and the location of the gold governs the underlying processes. Thus, we designed model systems, in which the morphology, concentration and the composition of the Cu_2O and Au were kept identical while the form of the gold was varied. We compared the optical, photophysical and photocatalytic properties of pristine Cu_2O octahedra with that of $\text{Cu}_2\text{O}/\text{Au}$ heteronanoparticles, where the gold was introduced in two different ways: gold nanorods were embedded into octahedral Cu_2O particles ($\text{AuR@Cu}_2\text{O}$) or small Au nanograins were deposited onto the surface of the octahedra ($\text{Cu}_2\text{O@Au}$). It was an important aspect of the work to demonstrate that the photophysical properties of Cu_2O can be improved upon low-power UV illumination being off-resonant with the plasmon modes of the gold components, thus, we were able to investigate the processes from the semiconductor point of view instead of utilizing any plasmon-generated processes such as hot-electron injection or plasmon-assisted charge transfer.

We showed that the radiative recombination of the photogenerated excitons are suppressed in the heteronanoparticles, however, this does not directly imply their better spatial separation. Therefore, the energy landscape of the particles was revealed by single-point Kelvin probe and a major difference in the Schottky-barriers was identified: in the $\text{AuR@Cu}_2\text{O}$ particles, only the photogenerated electrons could reach the particles outer surface, while in its $\text{Cu}_2\text{O@Au}$ counterpart, both generated carriers can be available for chemical reactions. This also manifested in the photocatalytic activity of the particles, namely the pristine Cu_2O was found to be inactive in the degradation of a model pollutant (methyl orange), however, the $\text{Cu}_2\text{O}/\text{Au}$ systems showed enhanced activity [1]. It is important to note that $\text{AuR@Cu}_2\text{O}$ particles can suffer from significant photocorrosion, while $\text{Cu}_2\text{O@Au}$ particles preserved their morphology and showed even higher activity (80% of dye degradation). The work has been published in *The Journal of Materials Chemistry C* [1] and we also provided a cover artwork for the issue (Fig. 2) [2]. The work underlined the role of the position and form of the gold in the multicomponent $\text{Cu}_2\text{O}/\text{Au}$ heteronanoparticles and paved the way towards the preparation of novel photocatalysts.

Related publications

- [1] D. Kovács, A. Deák, G. Z. Radnóczy, Z. E. Horváth, A. Sulyok, R. Schiller, O. Czömpöly, D. Zámbo: *Position of Gold Dictates the Photophysical and Photocatalytic Properties of Cu_2O in $\text{Cu}_2\text{O}/\text{Au}$ Multicomponent Nanoparticles*, *J. Mater. Chem. C* **11**:(26), 8796–8807 (2023) <https://doi.org/10.1039/D3TC01213A>.
- [2] Back Cover. *J. Mater. Chem. C* **11**:(26), 9038–9038 (2023) <https://doi.org/10.1039/D3TC90154H>

3-COLOUR ELLIPSOMETRIC MAPPING TOOL WITHOUT MOVING COMPONENTS

VOC-DETECT M-era-Net project, OTKA NNE 131269

B. Nugusse^{1,2}, Gy. Juhász¹, Cs. Major¹, P. Petrik^{1,4}, S. Kálvin¹, Z. Gy. Horváth³, M. Fried^{1,2*}

¹Institute of Technical Physics and Materials Science, Centre for Energy Research, ²Institute of Microelectronics and Technology, Obuda University, ³Institute for Solid State Physics & Optics, Wigner Research Centre for Physics, ⁴Department of Electrical Engineering, University of Debrecen

Non-destructive techniques are important methods to use during all stages of the thin film processes. Spectroscopic Ellipsometry (SE) is one of such methods. SE is a non-destructive, noninvasive and non-intrusive optical technique. It is a technique that measures the change in polarization state of the measurement beam induced by reflection from or transmission through the sample. Ellipsometry measures the amplitude ratio ($\tan \psi$) and phase difference (Δ) between the parallel (p) and normal (s) polarizations. During data analysis, information about the system under the study is obtained by fitting measured ellipsometric spectra to optical and structural models, as ellipsometry does not give a direct information of the sample in consideration.

Generally, the aim of this research is to make a prototype optical mapping tool for materials using only cheap parts such as a tablet, monitor, big screen TV (LCD or LED) and a pinhole camera [1, 2, 3] with CMOS Sensor with Integrated 4-Directional Wire Grid Polarizer Array (Sony's IMX250MYR CMOS), shown in Fig.1. Our arrangement shows similarity to the solution of Bakker et al [4], using a computer screen as a light source and a webcam as a detector in an imaging off-null ellipsometer. The new concept of the non-collimated beam ellipsometer prototype is set up as shown in Fig. 1.

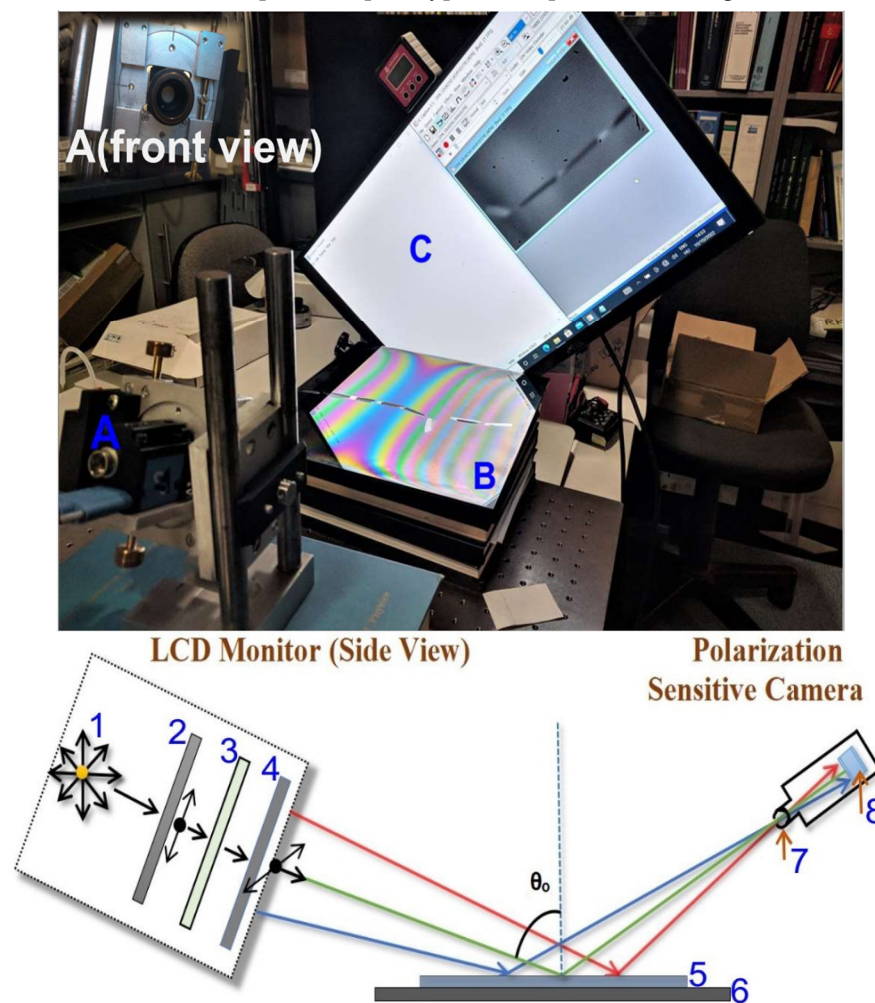


Figure 1: (a) Experimental set-up: A) Polarization sensitive camera B) Sample + Sample holder C) LCD monitor rotated into 45° position – Upper-left: the pinhole in front of the camera (b) Schematics of the non-collimated beam ellipsometer: 1) Light source 2) Vertical polarizer 3) Liquid crystal cell 4) Horizontal polarizer - (C) 5) Sample - (B) 6) Sample holder 7) Pinhole (sub-mm size) 8) Camera sensor (A)

A LED-LCD monitor (or a TV), see Fig. 2.a (C) serves the polarized RGB coloured light (see the built-in polarizer sheet, number 4 in Fig. 1.b) and a polarization sensitive camera behind a pinhole (7&8) together. The LCD monitor (Dell UltraSharp™ U2412M, GB-LED) is used in a 45-degree rotated position, measured by a digital angle gauge with 0.1 deg precision. In straight-through position, we can detect the extinction of the polarization sensitive camera better than 10^{-2} . The polarization sensitive camera sensor (The Imaging Source Company's DYK 33UX250 USB 3.0 Polarsens camera), see in Fig. 1.a (A) and in Fig. 2 serves the polarization state data, from 0, 45, 90, 135-degree rotation positions (plus 3 RGB colours in each position). This arrangement is equal to a conventional static photometric rotating analyzer ellipsometer. The sample is illuminated by a non-collimated light through a fixed polarizer at an azimuth of 45 degrees to the plane of incidence. The reflected light passes through a virtual "rotating analyzer" and the intensity is captured by a two-dimensional position sensitive photodetector system at four different angular positions of the analyzer. Minimum 3 different analyzer positions are required. These four polarization states (intensity) data (at 0, 45, 90, 135-degree rotation positions) are enough (the fourth date is good to reduce the error) to determine the ellipsometric angles: ψ and Δ . Our camera serves the data for 3 colours, so we have 3×2 measured ψ and Δ . Schematic structure of a 2/3-inch Sony CMOS Pregius Polarsens sensor (IMX250MZR) is shown in Fig. 2.b and Fig. 2.c. The main advantage of the assembly is that *there are no moving parts in the system!*

We used a Woollam M-2000DI Rotating Compensator Spectroscopic Ellipsometer as a control measuring device. The M2000 SE system with the CompleteEASE software is used to serve the optical properties, layer thicknesses and other related parameters of the sample. In principle, as the angle of incidence varies along the surface, a point-by-point angle of incidence calibration (see Fig. 1.b) is needed using a well-known silicon-dioxide-silicon (SiO_2/Si) sample. Each pixel gets a calibrated angle value. The procedure is similar to a conventional ellipsometric measurement. The refractive indices are known, only the angle of incidence and the thickness of the SiO_2 layer are the unknown parameters, where they can be calculated from the measured ellipsometric parameters.

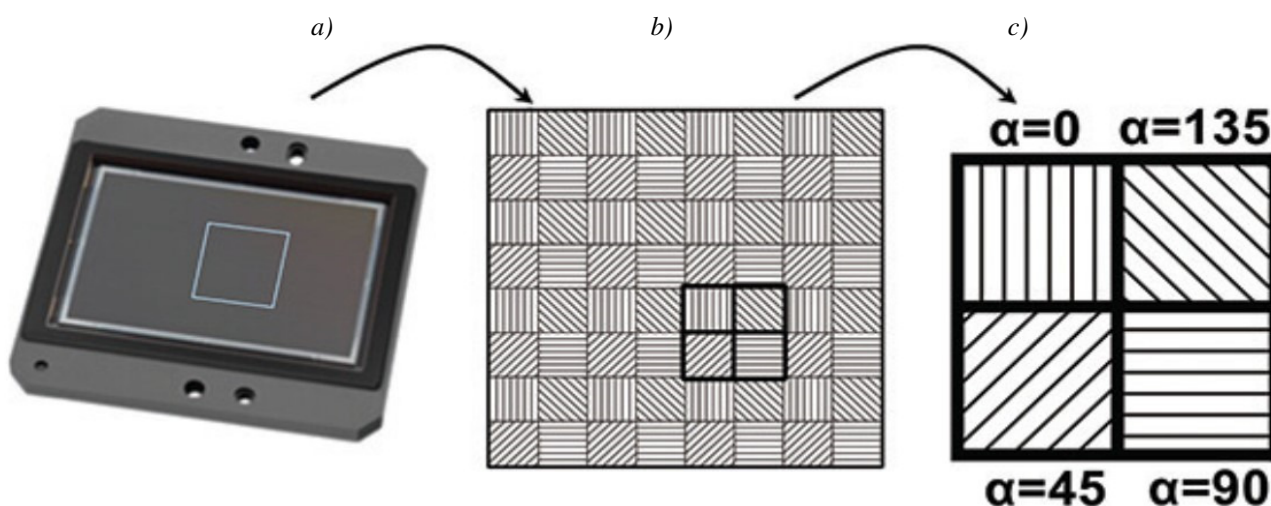


Figure 2: Schematic structure of a 2/3 inch Sony CMOS Pregius Polarsens sensor (IMX250MZR) a). Camera sensor b). Polarizer array matched to detector pixels c). Unit cell (Super pixel)

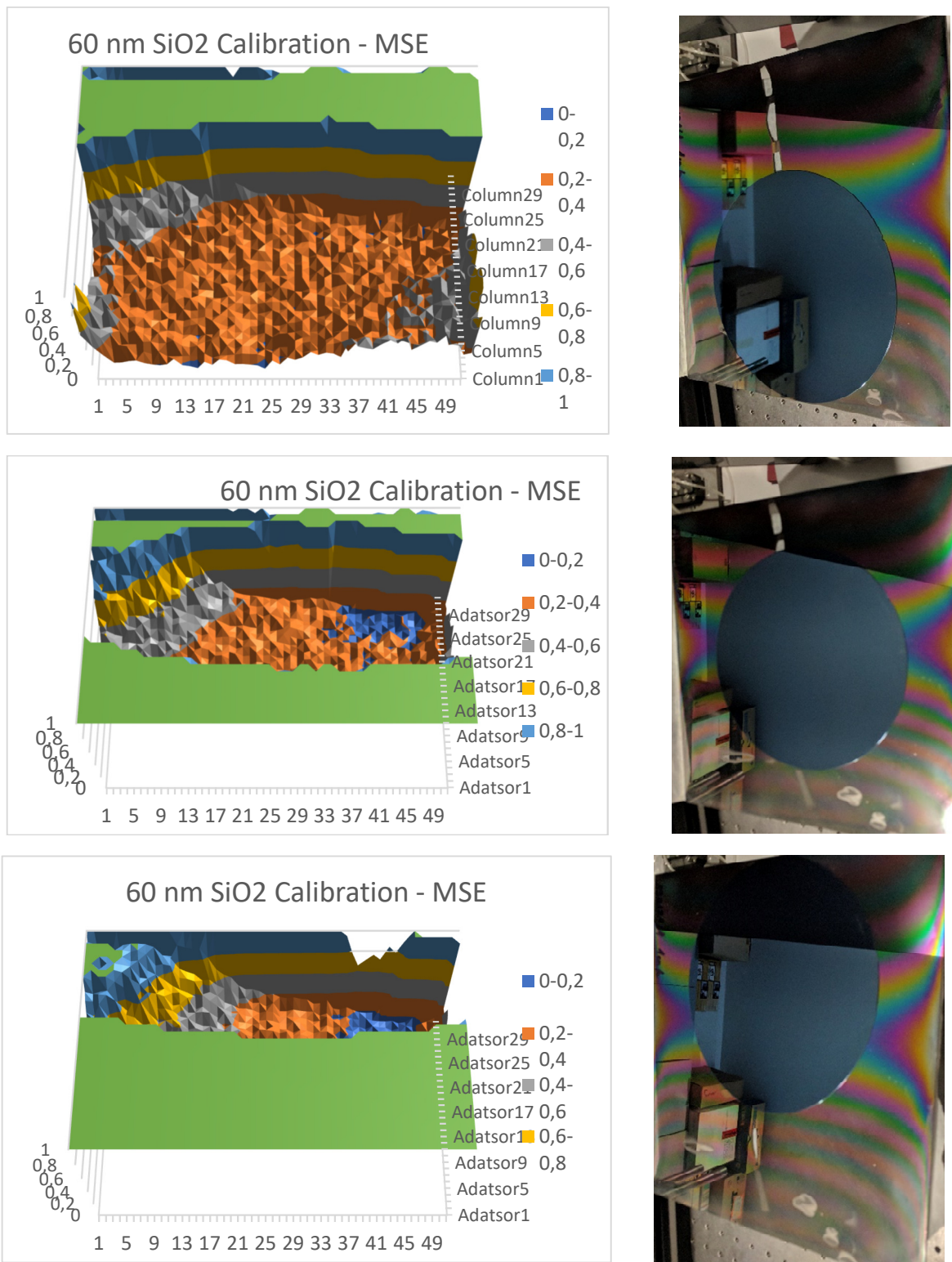


Figure 3: The Mean Squared Error (MSE) maps of the 20 cm diameter SiO₂ samples in the case of different positions. The higher MSE values show the areas, where no sample.

A 20 cm diameter, nominally 60 nm thick SiO₂/Si sample was used to determine the angle of incidence point-by-point. We put the sample different positions (see the photos in Fig. 3) and one can see “good” areas from the Mean Squared Error (MSE) maps. The second step was choosing the points of lowest MSE values from the experimental results of these three different positions and developing corresponding single map calibration of the MSE and actual angle of incidence calibration for each coordinates. The results are shown in Fig. 4 below.

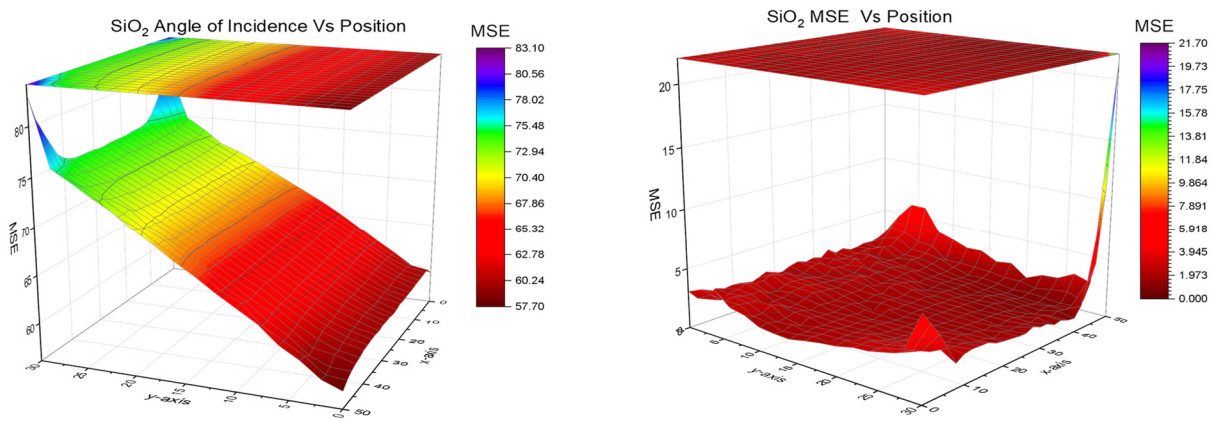


Figure 4: MSE and corresponding angle of incidence calibration for each coordinates, respectively

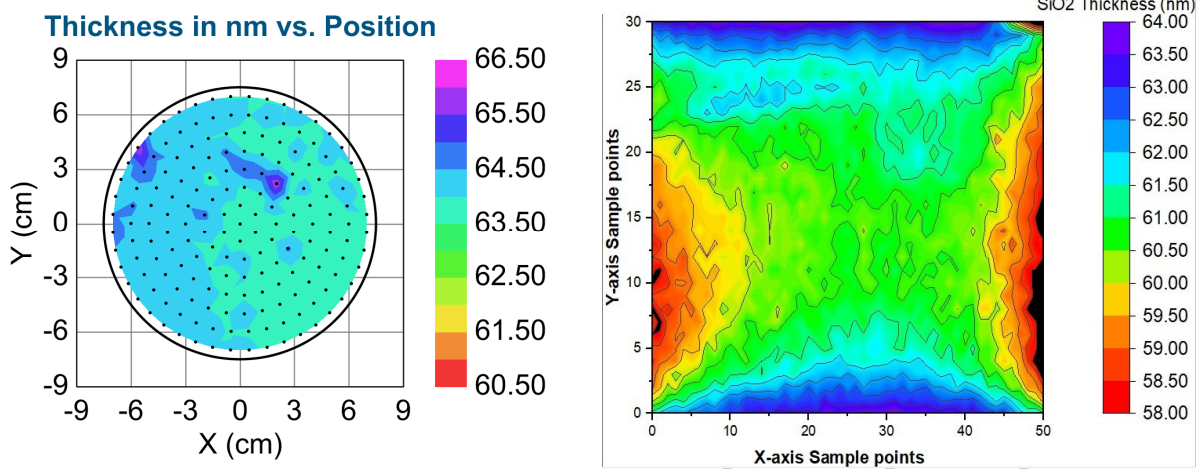


Figure 5: Determined thickness maps from M2000 ellipsometer (left) and the corresponding measurements from the “Cheap” imaging tool assembly (right). The two scale are shifted by 2.5 nm.

Our M2000 ellipsometer can map only 15 cm diameter area in one cycle, while the “Cheap” imaging tool assembly maps bigger area than the actual size of the measured Si-wafer, see Fig. 3. The more interesting part is only the central part of the map, a region that shows the thickness of the sample, about 60-61 nm, which is close to the other (to the left) map from the conventional M2000 ellipsometer. The two scales are shifted by 2.5 nm. Determined thickness differences between “Cheap” imaging tool and M2000 measurements are about 2 nm, see Fig. 5.

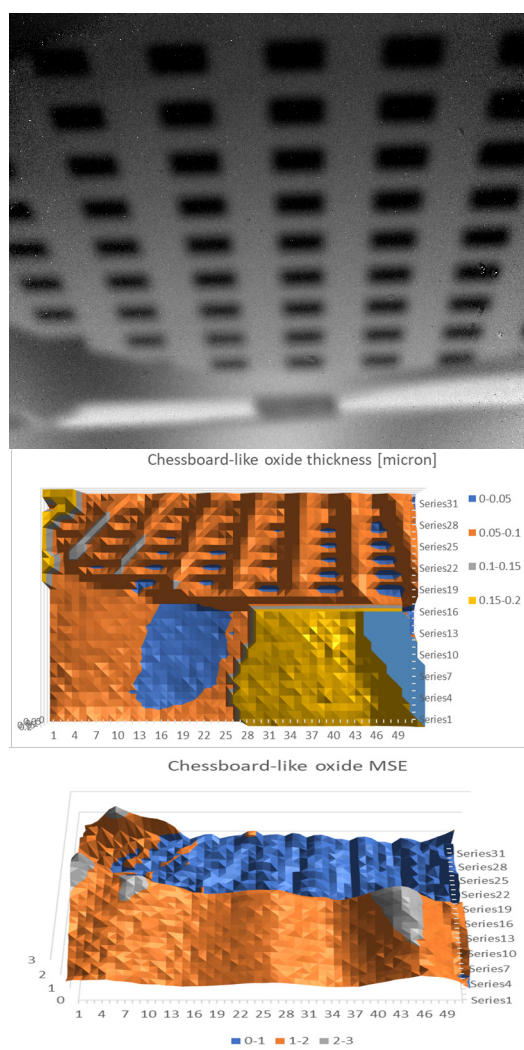


Figure 6: Illustration of the resolution, which is better than 5 mm. This is a silicon dioxide-covered silicon wafer “delta-contrast” picture (top). The bright parts are the original (nominally 100 nm thick) oxide layer, which is shown in the thickness-map, too (centre). The dark squares are the 4x4 mm sized etched native oxide covered silicon surface.

The pinhole camera couple the sample points directly to the pixels of the sensor matrix one-by-one. This detection system is almost without background. The measured area is determined by the size of the monitor and the sensor-pinhole, pinhole-sample and sample monitor distance-ratios. The lateral resolution is also determined by the distance ratios and the pinhole diameter. The pinhole diameter (presently 0.2 mm) is a compromise between the detected intensity (measuring time, presently 1-4 seconds) and the lateral resolution. One can see the illustration of the resolution (presently better than 5 mm) on Fig. 6, where a chessboard-like etched silicon dioxide-covered silicon wafer “delta-contrast” picture can be seen. The bright parts are the original (nominally 100 nm thick) oxide layers, the dark squares are the 4x4 mm sized etched native oxide covered silicon surfaces. The MSE map shows where the sample is (low MSE, blue part) and one can see the squares in the thickness-map, too, see Fig. 6 centre [5].

Related publications

- [1] C. Major, G. Juhász, Z. Lábadi, M. Fried: *High speed spectroscopic ellipsometry technique for on-line monitoring in large area thin layer production*, 2015 IEEE 42nd Photovoltaic Specialist Conference (PVSC), 2015, pp. 1-6, <https://doi.org/10.1109/PVSC.2015.7355640>
- [2] G. Juhász, Z. Horváth, C. Major, P. Petrik, O. Polgár, M. Fried: *Non-collimated beam ellipsometry*, *Physica Status Solidi C* **5**:(5), 1081-1084 (2008) <https://doi.org/10.1002/pssc.200777862>
- [3] Z. Gy. Horváth, G. Juhász, M. Fried, C. Major, P. Petrik: *Imaging optical inspection device with a pinhole camera*; EP2160591B1, Submission Number: PCT/HU2008/000058, NSZO: G01N21/8422, Country of patent: Europe
- [4] J. W. P. Bakker, H. Arwin, I. Lundström, and D. Filippini: *Computer screen photoassisted off-null ellipsometry*, *Applied Optics* **45**:(30), 7795-7799 (2006) <https://doi.org/10.1364/AO.45.007795>
- [5] B. Nugusse, Gy. Juhász, Cs. Major, P. Petrik, S. Kálvin, Z. Gy. Horváth, M. Fried: *Multi-colour ellipsometric mapping tool from cheap parts*, *SPIE Proceedings* **12428**, Photonic Instrumentation Engineering X; 124280H (2023) <https://doi.org/10.1117/12.2649926>

NANOSCALE MONITORING OF WATER CONDENSATION IN ELECTROCHEMICAL MIGRATION-INDUCED PRINTED CIRCUIT BOARD (PCB) FAILURE

TKP2021-EGA-04, OTKA K 131515

A. Romanenko, A. Gharaibeh, B. Medgyes, P. Petrik

Electrochemical Migration (ECM), triggered by humidity in conductor-dielectric-conductor systems, poses a reliability challenge in miniature electronic systems. This study focused on the inadequacy of existing methods to monitor nanoscale water build up during ECM. The experiments utilized an FR-4 board with Sn electrodes, subjected to controlled cooling by a Peltier module. Dual-spot in-situ ellipsometry, electrical measurements, and optical imaging were employed (Fig 1). The ellipsometry setup, provided high sensitivity to nanoscale changes in the adsorbed water layer. The experiment involved shifting the light spot between the Sn film and the solder mask surface, ensuring comparability under the same environmental conditions. The initial adsorption phase, not visible by optical microscopy, was revealed, and the growth of droplets was tracked. Ellipsometry spectra were analyzed to separate the water layer thickness and volume fraction, providing nanoscale insights into water condensation.

The results showed differences in water condensation behaviour between the solder mask and Sn surface, influencing the ECM process. This research highlights the unique capabilities of ellipsometry in characterizing nanoscale films during ECM. The study identifies the quasi-static limit as a critical factor influencing ellipsometry measurements during droplet formation. Differences in droplet size and density between the solder mask and Sn surface were observed, shedding light on the water condensation dynamics at a molecular level.

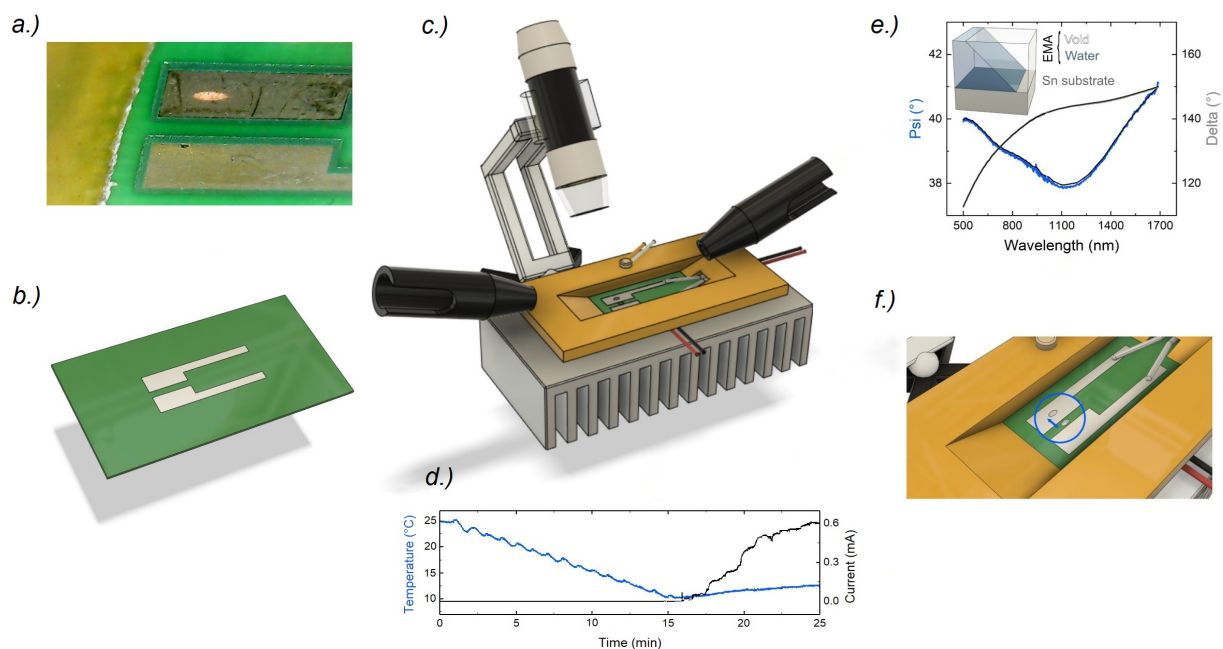


Figure 1: a) Top-down image of the sample and the condensed water layer. b) Schematic image of the sample layout. c) The measurement setup. d) The shortcut current. e) Typical measured (solid lines) and fitted (dashed lines) ellipsometry spectra on the Sn film of the sample at 7 minutes. f) Demonstration of the two-channel simultaneous in-situ measurement by moving the focused light spot back and forth between the Sn film and the FR-4 board.

INVESTIGATION OF ELECTROCHROMIC, COMBINATORIAL TiO_2 - SnO_2 MIXED LAYERS

OTKA NN 131269, OTKA K 128319, OTKA K 131515

N. T. Ismaeel, Z. Lábadi, P. Petrik, M. Fried

Electrochromic films have been used as smart windows for preservation of buildings from extra heating materials and also applied in energy-effective glassing, automobile sunroofs, smart windows and mirrors. Metal oxides are widely studied with respect to their electrochromic behaviour and properties for the applications as display devices and smart windows. Transition metal oxides such as titanium, tungsten, nickel, vanadium and molybdenum oxides have been considered as promising electrochromic materials [1]. The coloured state of pure TiO_2 coatings is grey and this oxide was not used alone in electrochromic devices because its coloration is not very strong. Chronoamperometric experiments associated with transmittance spectra in LiClO_4 -propylene carbonate solutions were carried out and compared with the optical properties of titanium oxide films with different stoichiometries. While TiO_2 was investigated as electrochromic material, SnO_2 or TiO_2 - SnO_2 mixtures were studied only as photocatalytic material. During this work, reactive magnetron sputtering (in Ar- O_2 plasma) have been used to produce all combinations of TiO_2 - SnO_2 mixed layers on silicon wafers. The object of this study was to investigate the properties of TiO_2 - SnO_2 mixed layers as electrochromic materials, to compare the 'goodness' of the diverse Spectroscopic Ellipsometry optical models, and to find the optimal composition of mixed metal oxides deposited by reactive sputtering.

TiO_2 - SnO_2 mixed layers were deposited in a reactive (Ar + O_2) gas mixture at $\sim 10^{-3}$ mbar process pressure. 30 sccm/s Ar and 30 sccm/s O_2 volumetric flow rates have been applied inside the chamber. The substrates were 4-inch diameter IC-grade and 3-inch diameter highly conductive (0.001 Ωcm) Si-wafers. The linear walking speed was 5 cm/s (back and forth) at the geometry which can be seen in Fig. 1. 50-50 % composition can be expected in the middle of the specimen. The Si-wafers and control Si-strips were placed on a 30 cm \times 30 cm glass, see Fig. 1. The power of the plasma was in the range of 0.75-1.5 kW for the two targets autonomously. 300 walking cycles were applied. Fig. 1 presents that the sputtering targets have been placed at 35 cm from each other. According to the measurements, the two 'material streams' have been overlapped around the centre of the substrate glass. The Metal/Oxygen atomic ratio of the layers was 1:2 at the applied oxygen partial pressure according to the SEM-EDS measurements.

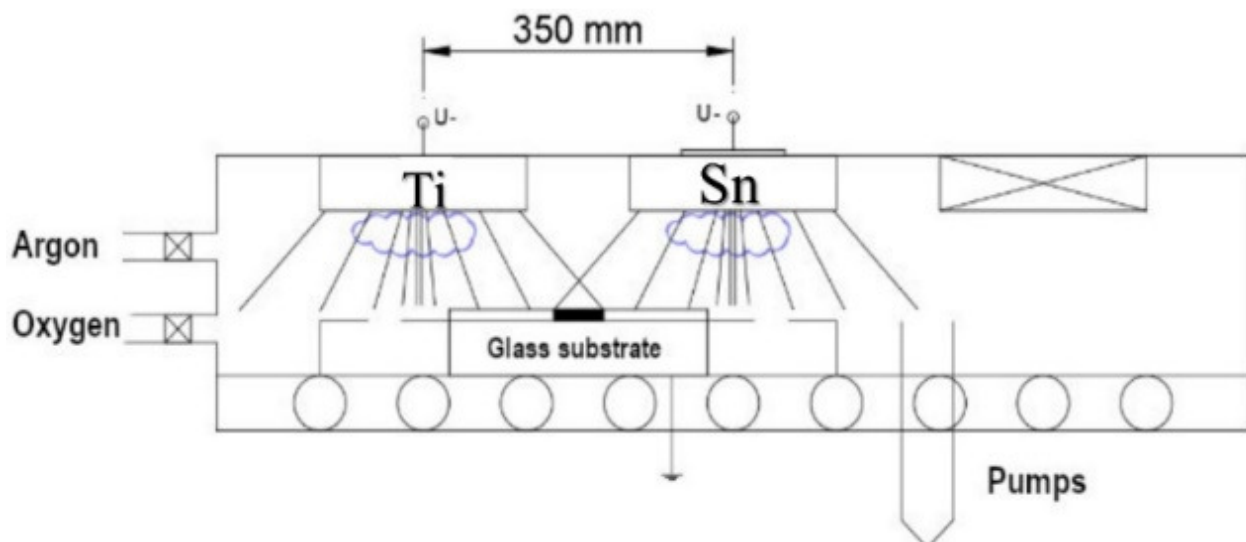


Figure 1: Arrangements of the two targets in closer position (35 cm from each other)

Optical mapping was performed by a Woollam M2000 SE equipment; the measurements were evaluated with the CompleteEASE software. To obtain the mapping parameters, oscillator functions and compact optical models have been used. The „goodness” of the optical model is depending on the value of the Mean Squared Error (MSE), so the lower MSE refers to the better fit because of the difference between curves. The silicon wafers and Si-strips (Fig. 2.a) have been used for Scanning Electron Microscopy (SEM, Dual-beam SEM+FIB Thermo Scientific Scios2) with Energy Dispersive Spectroscopy (EDS) measurements.

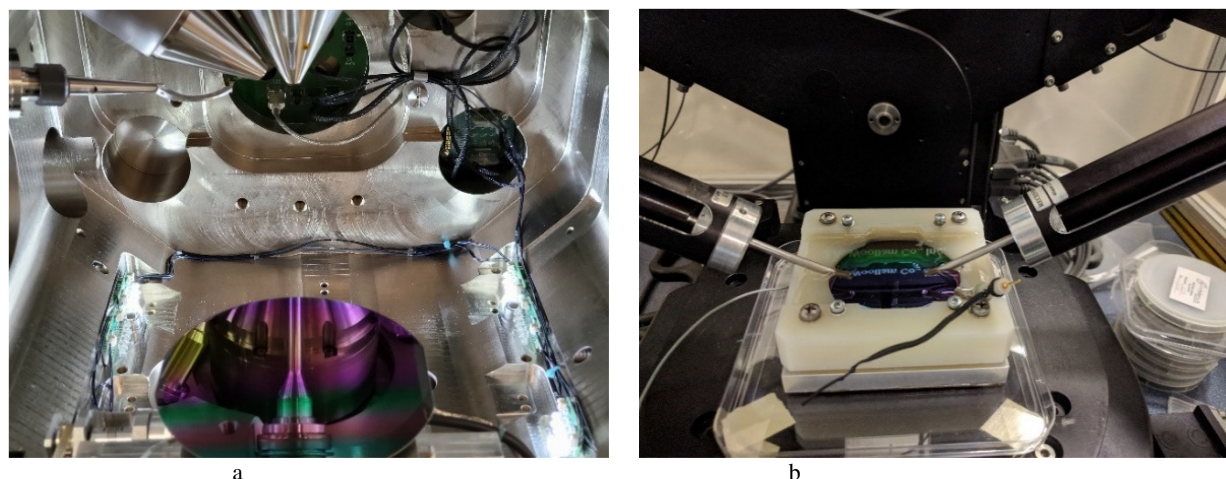


Figure 2: a) Combinatorial $\text{TiO}_2\text{-SnO}_2$ layer on a 4-inch Si-wafer in the SEM-chamber b) Electrochemical fluid cell for in-situ, real-time SE measurements.

In order to characterize the coloration process electrochemical Li injection was carried out on layers deposited onto the 3-inch diameter highly conductive ($0.001 \Omega\text{cm}$) Si-wafers. The electrochemical measurements were performed in a liquid cell filled with 1 M lithium perchlorate (LiClO_4) / propylene carbonate electrolyte, and a Pt wire counter electrode was placed into the electrolyte alongside with a reference electrode, see Fig. 2.b. Controlled potential was applied through the cell during a 4 min coloration. After the coloration process, the whole sample (in dry state) was mapped by Spectroscopic Ellipsometry (SE). In order to evaluate the SE spectra we applied a multilayer optical model (Si-substrate/interface-layer/T-L(TiO_2)+T-L(SnO_2)-mixed layer/surface-roughness-layer), and compared two dispersion relations: a., the Bruggeman Effective Medium Approximation (EMA) calculation, and b., The Tauc-Lorentz (T-L) oscillator model. Details of the calculation can be found in [2]. Both models give good results, however, the MSE is significantly lower for the 2-T-L model especially around the 50-50 % composition. After the coloration process, we could map the colorized layer using a simple one-layer Cauchy dispersion optical model. We see a maximum value (maximum light absorption) around 0.5 cm. Comparing this results with the composition curve, we can state that the optimal composition is 30-70 % for $\text{TiO}_2\text{-SnO}_2$.

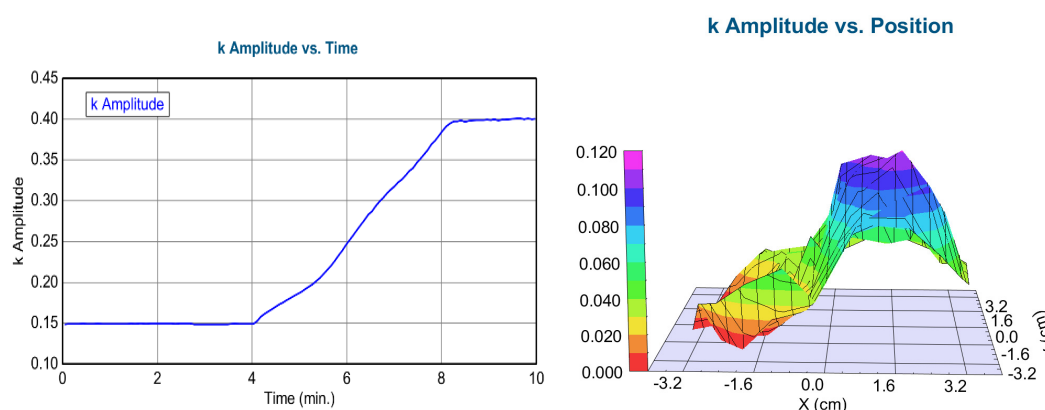


Figure 3: Imaginary part of the refractive index (k Amplitude) as a function of time for highly-conductive-Si in liquid-cell during coloration (time-scan, simple Cauchy-model) - left. Here we can mention that from 0-4 minute's there is low absorption but from 4-8 minute's there is a growing absorption. Map of the k parameter after coloration (simple Cauchy-model) - right

Related publications

- [1] C. G. Granqvist: *Handbook of Inorganic Electrochromic Materials*, Elsevier: Amsterdam, The Netherlands (1995)
- [2] N. T. Ismaeel, Z. Lábadí, P. Petrik, M. Fried: *Investigation of Electrochromic, Combinatorial $\text{TiO}_2\text{-SnO}_2$ Mixed Layers by Spectroscopic Ellipsometry using Different Optical Models*, *Materials* **16**(12), 4204 (2023) <https://www.mdpi.com/journal/materials>

REACTIVE SPUTTER DEPOSITION OF Ga_2O_3 THIN FILMS USING LIQUID GA TARGET

TKP2021-NKTA-05

M. Gajdics, M. Serényi, T. Kolonits, A. Sulyok, Zs. E. Horváth and B. Pécz

Ga_2O_3 , as an ultrawide bandgap semiconductor has numerous potential applications in the field of optoelectronics, high-power electronics and gas sensing. Gallium oxide thin films can be grown by a variety of methods, among them, sputtering is a commonly used technique. In most cases, a ceramic Ga_2O_3 target is used for sputtering of Ga_2O_3 . In our work, we demonstrate an alternative method, i.e. reactive sputtering of a liquid Ga target. Modelling of this reactive sputtering process was performed based on the Berg model [1].

Liquid gallium was placed in a circular crucible fabricated from a 0.2 mm Ni plate. The diameter of the container was 75 mm and the height of its side wall was about 3 mm. This target was reactively sputtered in a radio frequency sputtering device. Different samples were prepared by varying the oxygen flow and the DC target potential. The composition of the samples was analyzed by energy dispersive spectroscopy and X-ray photoelectron spectroscopy, respectively. The optical parameters and the thickness of the films were determined by spectroscopic ellipsometry.

It was shown that using high enough oxygen flow rate (32 sccm – standard cubic centimetre per minute), it is possible to achieve higher oxygen atomic ratios than for a film sputtered non-reactively using a ceramic Ga_2O_3 target. Although, the DC target potential has only a minor effect on the average oxygen atomic ratio of the layers, using higher potentials can be detrimental to the surface quality of the films as little Ga-rich droplets can form on the surface. Ellipsometry measurements have shown that the extinction coefficient of the films prepared at higher oxygen flow rates becomes zero in the UV wavelength range (Fig. 1.a), thus they have the potential for solar-blind optoelectronic applications. It was also found that the refractive index (at 632.8 nm) of the layers tend to decrease as the oxygen atomic ratio increases (Fig 1.b).

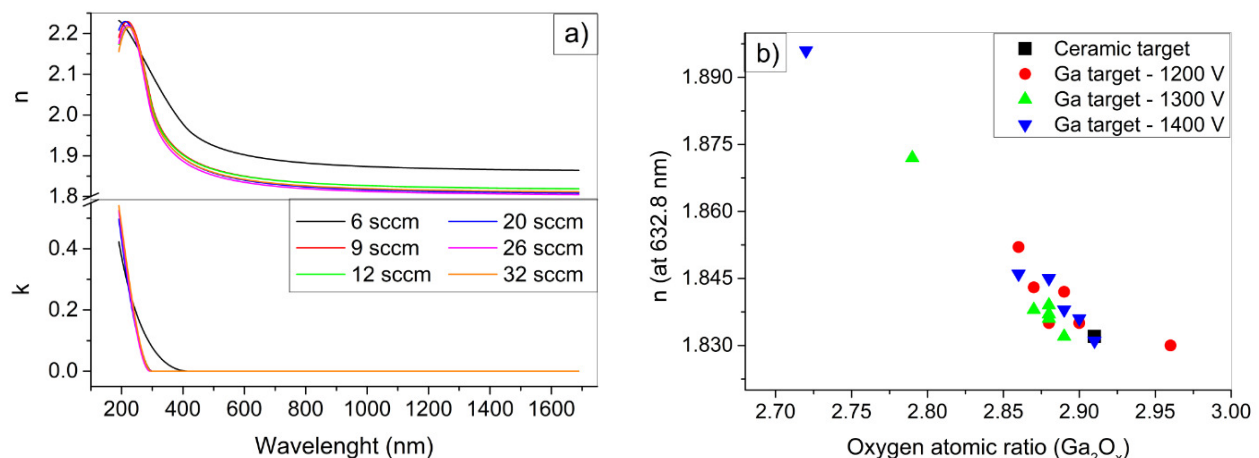


Figure 1: a) The refractive indices (n) and extinction coefficients (k) as a function of the wavelength for the samples sputtered at a 1400 V DC target potential. b) The refractive indices (at 632.8 nm) of the gallium oxide films as a function of the oxygen atomic ratio.

The thickness of the films was also determined by ellipsometry (see Fig. 2). Significantly higher deposition rates were found for the samples prepared using the liquid target compared to the ceramic one. For example, 9.4 nm/min growth rate was achieved at 20 sccm oxygen flow rate (0.113 Pa O_2 pressure) for the liquid target, while only 5.3 nm/min for the ceramic one (using 1400 V DC target potential in both cases). The upgraded Berg model was used to model the reactive sputtering process and the thickness data were fitted based on this model (Fig. 2, solid lines). As a result, different sputtering parameters such as the sputtering yields and the sticking coefficient were determined. The fitted parameters suggest that the preferential sputtering of Ga becomes more significant as the DC target potential increases.

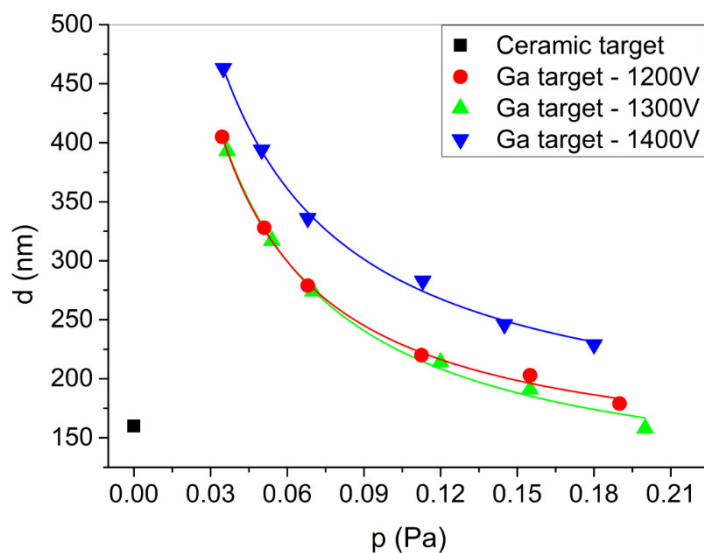


Figure 2: The film thickness at different oxygen partial pressures and DC target potentials, as measured by ellipsometry, and the fit to the data points (solid lines) using the Berg model

Related publication

- [1] S. Berg, E. Särhammar, T. Nyberg: *Upgrading the "Berg-Model" for Reactive Sputtering Processes*, Thin Solid Films **565**, 186–192 (2014) <http://dx.doi.org/10.1016/j.tsf.2014.02.063>

RESONANCE-BASED KRETSCHMANN-RAETHER ELLIPSOMETRY UTILIZING PLASMONIC AND PERIODIC NANOSTRUCTURES AT SOLID-LIQUID INTERFACES

TKP2021-EGA-04, EMPIR POLight 20FUN02, OTKA K 146181

D. Mukherjee, B. Kalas, S. Burger, Gy. Sáfrán, M. Serényi, M. Fried, P. Petrik

Because of their beneficial and adaptable characteristics, nanostructures have been the subject of extensive investigation for a long time. One of the many avenues of scientific and medical inquiry that nanostructures have opened up is plasmonic nanostructures. Research and technology in the subject of plasmonics, in general, rely on the collective oscillation of free electrons in metallic thin films or other metallic nanostructures in response to electromagnetic radiation [1]. Plasmonic nanostructures are those that have the ability to produce and regulate light at the nanoscale. These nanoscale devices' small size and form allow them to manipulate light waves in a variety of ways. The interaction of plasmons with light causes Surface Plasmon Polariton (SPP) resonance to be seen at the interface of metal layers and dielectrics (such as air or liquids). This is the result of an intensely restricted surface wave that spreads over the interface and decays exponentially in the dielectric ambient and the metal layer. To subtly customize the ideal wavelength range for SPP, several metals are alloyed together to change the plasmonic material's chemical makeup [2]. It works well for adjusting metallic nanostructures and thin films' optical response. Noble metals like Ag, Au, and Pt have been favored for SPP applications because of their abundance of free electrons, despite the well-known optical losses caused by interband optical transitions. Ag is the most readily available material in the Vis-NIR range and has the finest properties for plasmonic applications. Moreover, metal alloys and intermetallics are interesting possibilities for alternative plasmonic materials due to their high free electron densities [3].

In SPR spectroscopy, a thin Au film is commonly used as the sensing layer. When surface plasmons are present, incoming light can couple with them to produce a dip in the reflectance spectrum. The precise wavelength (λ) value of this dip is determined in large part by the thickness (d) and optical properties of the Au layer, the angle of incidence (θ) of the light beam, the optical properties of the configuration, and - most importantly - the optical properties of the investigated ambient close to the Au surface. Developing original layer designs can also help to boost sensitivity. Using one or more 2D layers (such as graphene or molybdenum disulfide) on top of the Au film in addition to the naked Au layer might result in improved sensing performance.

The Kretschmann-Raether configuration [4], which enables the study of the optical characteristics of materials, is based on the concepts of ellipsometry, in which light is reflected at an interface between a solid and a liquid. The use of nanostructures to in-situ surface-enhanced Kretschmann-Raether (KR) ellipsometry has proven successful. Using this kind of optofluidics technology, ellipsometric measurements may be performed by non-invasively transducing evanescent fields to surface plasmon polariton. Using a Woollam M-2000DI rotating compensator spectroscopic ellipsometer in the $\lambda = 190\text{-}1700$ nm wavelength range and adjustment using the KR geometry, the θ was allowed to be extended up to 75° for focus extension. For the KR Spectroscopic Ellipsometry (KRSE) configuration, an enhanced hemisphere has been utilized to provide an ideal signal-to-noise ratio in the critical spectral band below 300 nm.

Micro combinatory was used to deposit a combinatorial film at room temperature on a thin UV-grade Fused Silica (FS) substrate measuring 25 mm by 10 mm (length by width) and 150 ± 25 μm . A layer with a gradient composition of $\text{Ag}_x\text{Al}_{1-x}$, spanning from $0 < x < 1$, was generated by the deposition. On the 25 mm long substrate, a gradient track of 20 mm is bounded by 2.5 mm long lead-in portions of one target's flux. The setup moves a shutter with a 1 mm by 10 mm slot above the substrate in tiny increments, and the power of the two magnetrons is controlled in time with the slot movement. As the slot passes over the substrate, the Ag fluence progressively drops from 100 to 0 and the Al fluence gradually increases from 0 to 100 resulting in the required composition gradient. The variable thickness, which may be used to modify the wavelength of maximum sensitivity, was made possible by the exact control of the slot movement (Fig. 1).

Principal advantages of the combinatorial deposition method are:

- When the deposited layer is created in a single process step, all sample preparation parameters and substrate properties are guaranteed to be the same, with the exception of the modulated parameter (the composition and/or thickness).
- They are also easier to use and more efficient since the optical measurement and assessment may be automatically carried out by a lateral scan. The evaluation approach also supports an interpretation based on a single process. This method allows for the characterization of more substantial modulations and unanticipated fluctuations of the qualities, without assuming any lateral dependency.

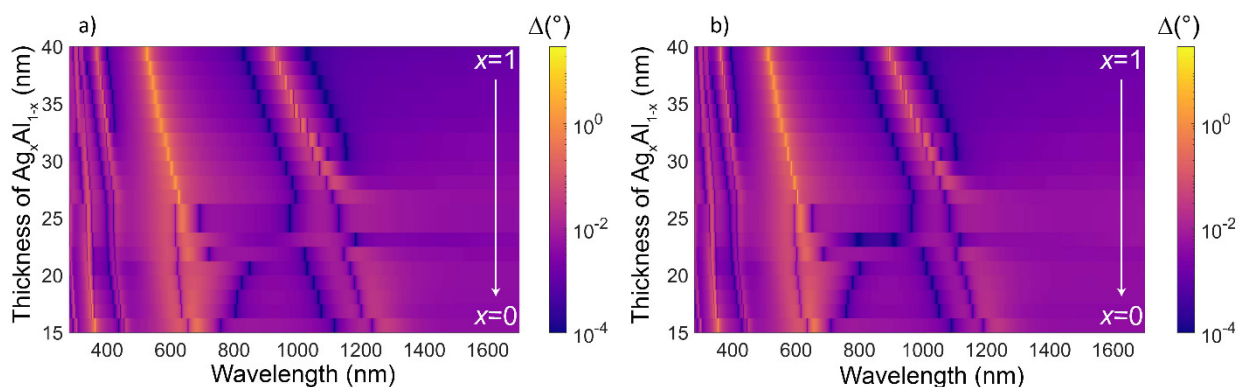


Figure 1: Variation of the ellipsometric phase shift ($\Delta = \arg(r_p/r_s)$) as a function of the thickness of the $\text{Ag}_x\text{Al}_{1-x}$ layer and the wavelength for angles of incidence (AOI) of 71° (a) and 73° (b).

The generated sensor structure's compositions with $x = 0$ (pure Al) and $x = 1$ (pure Ag) had optimal thicknesses because the optical properties of these pure phases were believed to be more reliable than those of mixed phase references. This one-sample combinatorial device is now tuned only for linearly graded compositions and thicknesses, but it would be feasible to tweak the lateral thickness profile after finding the optical properties for all values. To examine the change in Δ for $\Delta n_{\text{water}} = 10^{-4}$, Transfer Matrix Method (TMM) computations were performed. These statistics clearly show that the lower AOI value (71°), which is the closest to the comparable value of the total internal reflection angle, is where the highest sensitivity may be attained.

It was demonstrated that the phase information obtained from ellipsometry, in conjunction with variable resonant features, can be applied to periodic Au grating structures (Fig. 2) as well as combinatorial $\text{Ag}_x\text{Al}_{1-x}$ structures made by sputtering on glass plates connected to a hemi-cylinder in the KR geometry. $\Delta = \arg(r_s/r_p)$ is the phase measurement formula, where r_p and r_s are the polarized light reflection coefficients parallel and perpendicular to the plane of incidence, respectively.

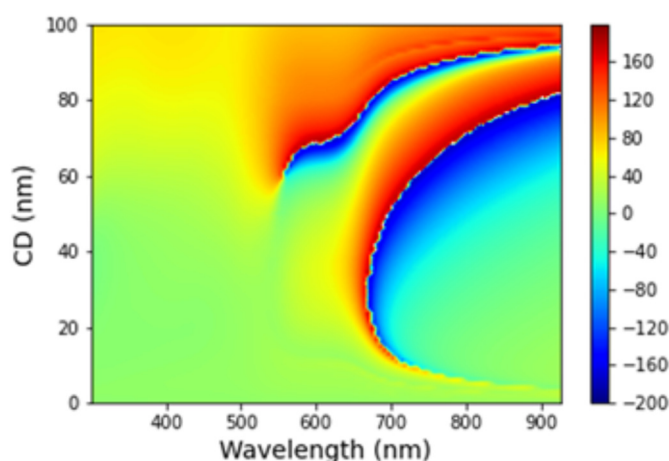


Figure 2: Δ ellipsometric angle calculated for different Critical Dimension (CD) and wavelength values in the KR configuration for a gold layer on glass with a thickness and period of 200 nm and 100 nm, respectively.

The ellipsometer resolution in space (focused spot) and time is generally 0.3 mm by 0.9 mm and 1 s, respectively. Sensitivities of 10^{-6} and $10 \text{ pg}/\text{mm}^2$ in refractive index and surface mass density units, respectively, may be reached at an ideal plasmonic setup. Au gratings were designed and modelled utilizing transfer matrix and finite element (JCMwave) methods in order to build phase retrieval and sample parameter reconstruction method. They are mostly significant for determining which grating settings in experimental studies show the greatest promise.

Related publications

- [1] E. Wijaya, C. Lenaerts, S. Maricot, J. Hastanin, S. Habraken, J.-P. Vilcot, R. Boukherroub and S. Szunerits: *Surface plasmon resonance-based biosensors: From the development of different spr structures to novel surface functionalization strategies*, *Current Opinion in Solid State and Materials Science* **15**(5), 208–224 (2011)
- [2] C. Gong and M. S. Leite: *Noble metal alloys for plasmonics*, *ACS Photonics* **3**(4), 507–513 (2016) <https://doi.org/10.1021/acsp Photonics.5b00586>
- [3] P. West, S. Ishii, G. Naik, N. Emani, V. Shalaev and A. Boltasseva: *Searching for better plasmonic materials*, *Laser & Photonics Reviews* **4**(6), 795–808 (2010) <https://doi.org/10.1002/lpor.200900055>
- [4] E. Kretschmann and H. Raether: *Notizen: Zur plasmaresonanzemission im festen körper*, *Zeitschrift für Naturforschung A* **23**(4), 615–617 (1968) <https://doi.org/10.1515/zna-1968-0424>

MAKYOH IMAGING AND TOPOGRAPHY

F. Riesz

Makyoh imaging, named after the Japanese ‘magic mirror’, denotes an optical imaging mechanism, where a plane (or, more generally, a spherical) wave is reflected from a flat, or slightly convex mirror having small height deviations, causing intensity variations in a far-field screen image because of the local ray deflections. The intensity distribution reflects somehow the mirror height map. The first application of this principle was probably the Oriental magic mirror; a modern application is Makyoh topography, used mostly for the visualisation of surface defects or texture of semiconductor wafers.

The main result of the past year is the proposal of a novel approach for the imaging of the ancient mirror: the *visual image* of the back relief pattern, rather than its height topography is compared to the reflected Makyoh image (Fig. 1) [1]. The visual image depends on the environmental illumination conditions (light directionality and scattering degree) and surface reflection properties in a complex way, but it can be stated the both images are essentially emphasise edges (gradient changes) of the back relief, thus their correspondence can be established. Fig. 1 shows intensity profile calculations of the Makyoh and the visual back images for three characteristic back patterns: a narrow and a wide mound and a ridge for diffuse and directional (oblique) back illumination; back reflection is assumed mixed (diffuse with wide specular component). Convolution with a Gaussian was used for pattern transfer modelling to obtain the front surface profiles. For diffuse illumination, the correspondence of the two images is striking; the specular component can relate to the main reflection peak for the narrow mound.

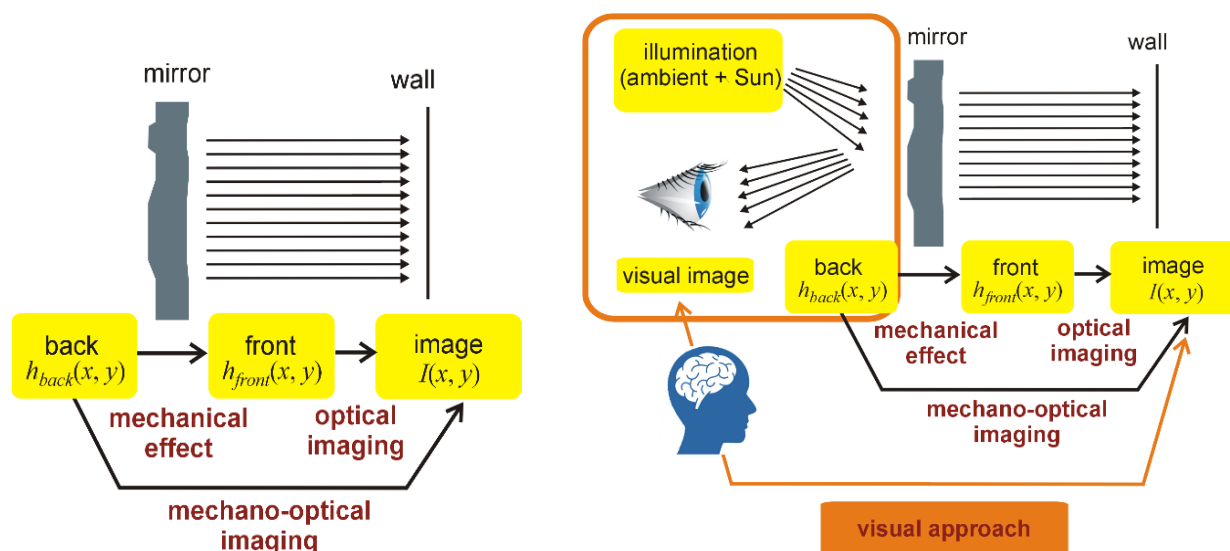


Figure 1: Scheme of the traditional mechano-optical (left) and the proposed visual (right) approaches of Makyoh imaging

Related to this, the various approximations of the Makyoh imaging were analysed and compared. The most popular is the Laplacian approximation introduced by Berry. We hypothesised that a certain class of ancient mirrors (namely, Japanese mirrors) operate in the post-Laplacian regime, where stronger focusing of the concave arcs occur, leading narrower and higher-intensity image regions (Fig. 3). This imaging is characteristic to globally flat or less curved mirrors. These results have relevance to the modern application of Makyoh as well, since the studied samples (mostly, semiconductor wafers) are usually also globally flat.

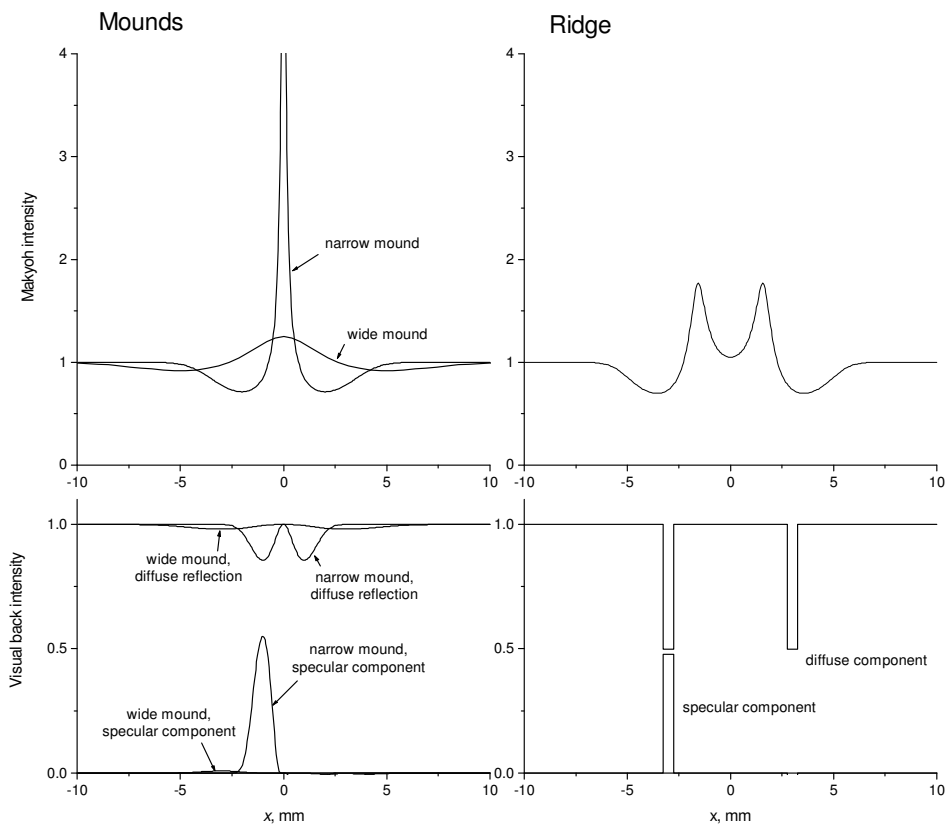


Figure 2: Calculated intensity profiles of the Makyoh and the reflection visual back images for three characteristic back relief patterns

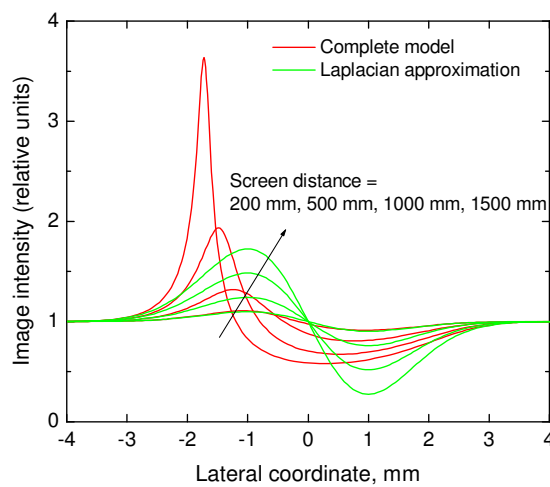


Figure 3: Makyoh image intensity profiles produced by a one-dimensional abrupt back surface step (after convolution with a Gaussian with $d = 1$ mm, resulting $1\text{-}\mu\text{m}$ height in the front face) at various screen distances, calculated using the Laplacian approximation and the complete model

Related publication

[1] F. Riesz: *Visual Approach to the Imaging of Magic Mirrors (Makyohs)*, Results in Optics **12**, 100477 (2023) <https://doi.org/10.1016/j.rjo.2023.100477>

TEM OF INNOVATIVELY USED OF PtSi CONTACT MATERIAL

2019 2.1.7-ERA-NET-2022-00032, *QuantERA II SIQUOS*

J. Lábár, B. Pécz, Y. Yao¹, D. F. Fernandes¹, T. Košutová¹, T. Kubart¹, Z. Zhang¹,
F. Lefloch², F. Gustavo², A. Leblanc², S.-L. Zhang¹

¹ Division of Solid-State Electronics, Department of Electrical Engineering, Uppsala University, Sweden,

² Université Grenoble Alpes, CEA, Grenoble, France

PtSi has long been used as contact material in microelectronics. It is usually formed by the self-aligned-silicide (SALICIDE) process. Novel application of PtSi in cryogenic temperatures as superconducting material of source and drain in silicon-based Josephson field-effect transistors (JoFETs) requires that the thickness of the PtSi layer is reduced considerably. Our SIQUOS project aims at manufacturing such JoFETs as part of Qubits. This reduction in thickness brought up new technological challenges that did not exist in conventional microelectronics.

Current SALICIDE process involves thermal oxidation at 600°C to protect the formed PtSi from being etched off during the subsequent chemical etching in aqua regia aiming to selectively remove unreacted Pt present on the surrounding oxide layers. However, sub-10 nm PtSi films tend to agglomerate and even break into discrete PtSi islands upon thermal treatments above 500°C. To mitigate this technical issue, an innovative ambient-temperature chemical oxidation step was introduced. The results below prove that this change in technology was successful. While 5 nm thick layers manufactured with the conventional technology broke into islands (Fig.1), the new process flow resulted in homogeneous PtSi layers (Fig. 2) of the same thickness. All technology steps except the new oxidation were identical, including subsequent etching in aqua regia.

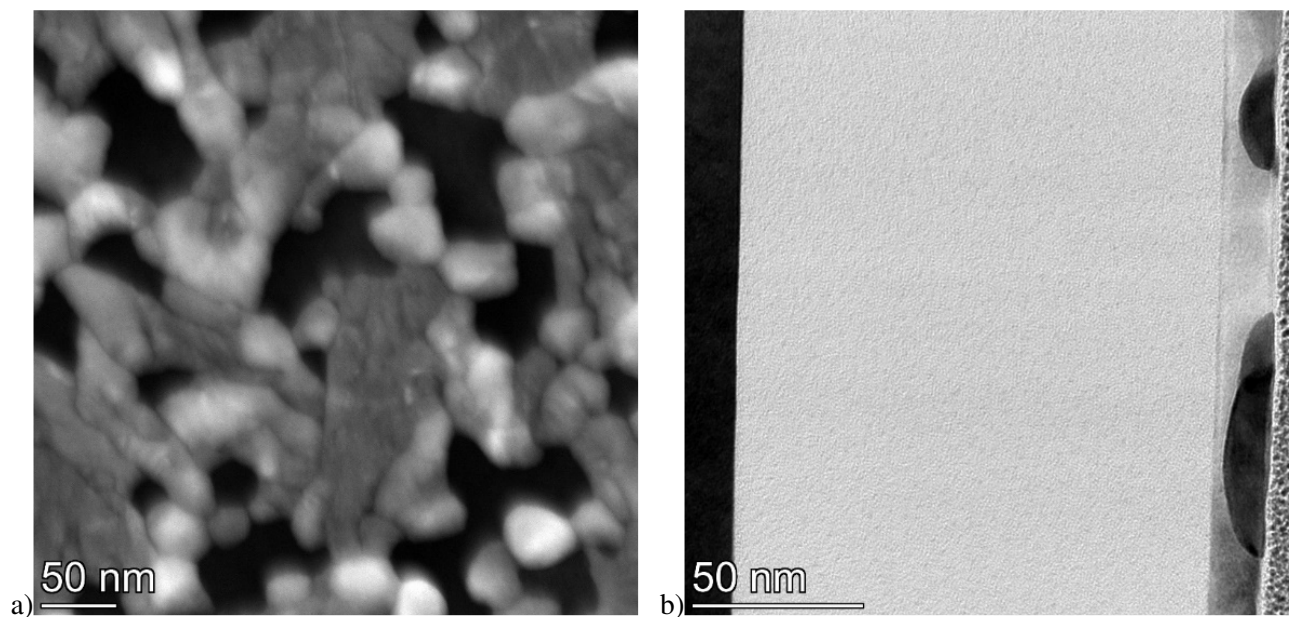


Figure 1: a). Plan-view High-angle Annular Dark-field (HAADF) image of 5 nm thick PtSi layer. Thermal oxidation and subsequent etching in aqua regia. The layer is full of holes. b) Cross-section Bright Field (BF) image of 5 nm thick PtSi layer. Thermal oxidation and subsequent etching in aqua regia. The layer broke into islands.

In contrast to the conventional Pt-SALICIDE process involving thermal oxidation, the new process flow with chemical oxidation produces continuous, uniform protecting oxide on top of PtSi, which protects the ≤5nm thick PtSi from being etched away (when remaining Pt is removed). Superconductivity of the layers is measured and slight dependence on both layer thickness and annealing temperature is determined [1].

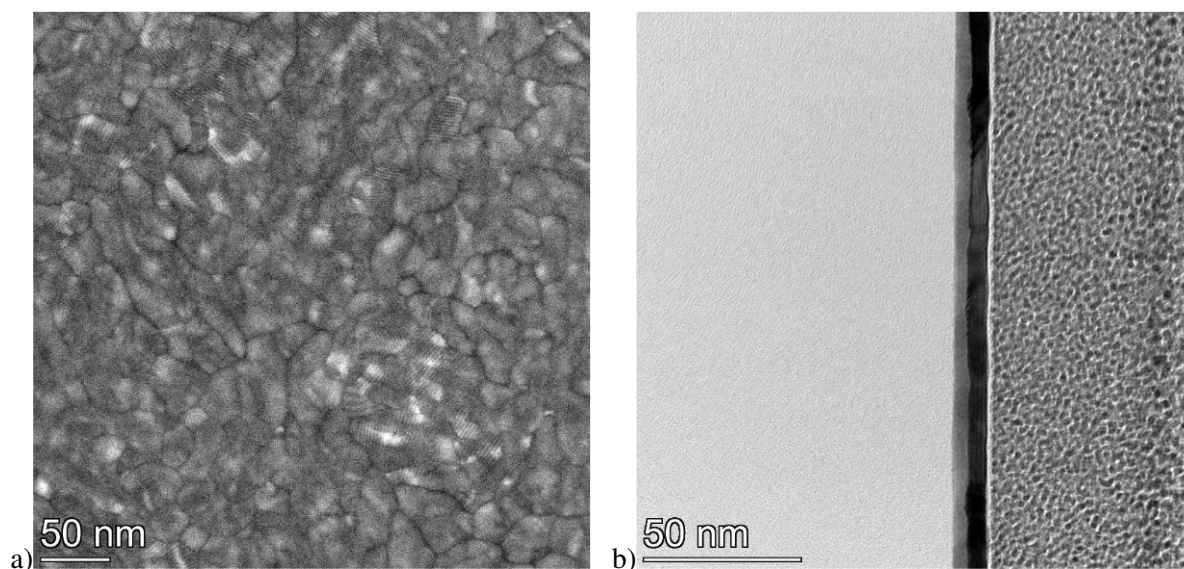


Figure 2: a) Plan-view HAADF image of 5 nm thick PtSi layer. New, ambient temperature, chemical oxidation and subsequent etching in aqua regia. The layer is continuous, even pin holes cannot be observed in it. b) Cross-section BF image of 5 nm thick PtSi layer. New, ambient temperature, chemical oxidation and subsequent etching in aqua regia. The layer is continuous.

Related publication

- [1] Y. Yao, D. F. Fernandes, T. Košutová, T. Kubart, Z. Zhang, F. Lefloch, F. Gustavo, A. Leblanc, J. L. Lábár, B. Pécz, Shi-Li Zhang; *Self-aligned formation of superconducting sub-5 nm PtSi films*, APL Quantum 1 June **1(2)**: 026112 (2024) <https://doi.org/10.1063/5.0205444>

REACTIVE SPUTTER DEPOSITION OF Ga_2O_3 THIN FILMS USING LIQUID GA TARGET

TKP2021-NKTA-05

M. Gajdics, M. Serényi, T. Kolonits, A. Sulyok, Zs. E. Horváth and B. Pécz

Ga_2O_3 , as an ultrawide bandgap semiconductor has numerous potential applications in the field of optoelectronics, high-power electronics and gas sensing. Gallium oxide thin films can be grown by a variety of methods, among them, sputtering is a commonly used technique. In most cases, a ceramic Ga_2O_3 target is used for sputtering of Ga_2O_3 . In our work, we demonstrate an alternative method, i.e. reactive sputtering of a liquid Ga target. Modelling of this reactive sputtering process was performed based on the Berg model [1].

Liquid gallium was placed in a circular crucible fabricated from a 0.2 mm Ni plate. The diameter of the container was 75 mm and the height of its side wall was about 3 mm. This target was reactively sputtered in a radio frequency sputtering device. Different samples were prepared by varying the oxygen flow and the DC target potential. The composition of the samples was analyzed by energy dispersive spectroscopy and X-ray photoelectron spectroscopy, respectively. The optical parameters and the thickness of the films were determined by spectroscopic ellipsometry.

It was shown that using high enough oxygen flow rate (32 sccm – standard cubic centimetre per minute), it is possible to achieve higher oxygen atomic ratios than for a film sputtered non-reactively using a ceramic Ga_2O_3 target. Although, the DC target potential has only a minor effect on the average oxygen atomic ratio of the layers, using higher potentials can be detrimental to the surface quality of the films as little Ga-rich droplets can form on the surface. Ellipsometry measurements have shown that the extinction coefficient of the films prepared at higher oxygen flow rates becomes zero in the UV wavelength range (Fig. 1.a), thus they have the potential for solar-blind optoelectronic applications. It was also found that the refractive index (at 632.8 nm) of the layers tend to decrease as the oxygen atomic ratio increases (Fig 1.b).

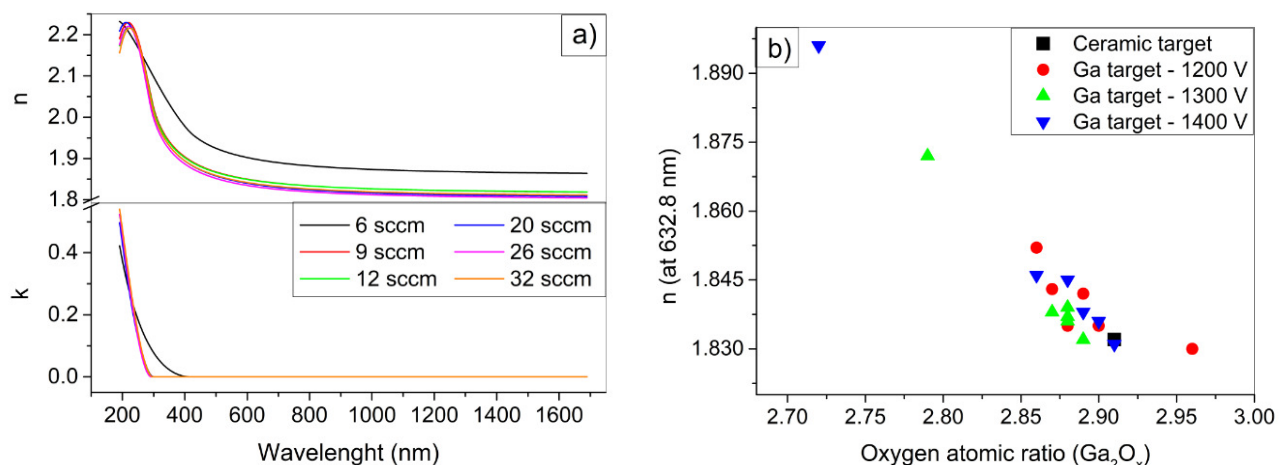


Figure 1: The refractive indices (n) and extinction coefficients (k) as a function of the wavelength for the samples sputtered at a 1400 V DC target potential a). The refractive indices (at 632.8 nm) of the gallium oxide films as a function of the oxygen atomic ratio b).

The thickness of the films was also determined by ellipsometry (see Fig. 2). Significantly higher deposition rates were found for the samples prepared using the liquid target compared to the ceramic one. For example, 9.4 nm/min growth rate was achieved at 20 sccm oxygen flow rate (0.113 Pa O_2 pressure) for the liquid target, while only 5.3 nm/min for the ceramic one (using 1400 V DC target potential in both cases).

The upgraded Berg model was used to model the reactive sputtering process and the thickness data were fitted based on this model (Fig. 2, solid lines). As a result, different sputtering parameters such as the sputtering yields and the sticking coefficient were determined. The fitted parameters suggest that the preferential sputtering of Ga becomes more significant as the DC target potential increases.

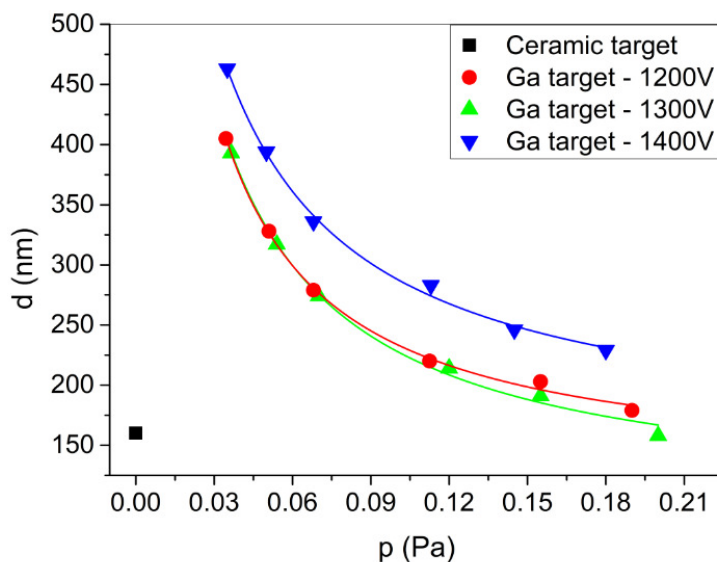


Figure 2: The film thickness at different oxygen partial pressures and DC target potentials, as measured by ellipsometry, and the fit to the data points (solid lines) using the Berg model

Related publication

- [1] S. Berg, E. Särhammar, T. Nyberg: *Upgrading the "Berg-Model" for Reactive Sputtering Processes*, Thin Solid Films **565**, 186-192 (2014) <http://dx.doi.org/10.1016/j.tsf.2014.02.063>

INDUSTRIALLY DEPOSITED HARD AND DAMAGE RESISTANT W-B-C COATINGS

VEKOP-2.3.3-15-2016-00002, VEKOP-2.3.2-16-2016-00011

Zs. Czigány, K. Balázs, M. Krokker¹, P. Souček¹, P. Vasina¹

¹ Department of Physical Electronics, Masaryk University, Brno, Czech Republic

The study investigates the properties of deposited W-B-C coatings, examining the influence of chemical composition and deposition regimes on mechanical properties of sputter-deposited coatings composed of tungsten, boron and carbon [1]. The research employs an industrial batch-coater equipped with a segmented target, examining the coatings under both laboratory-like and industrial preparation conditions through stationary and single-axis rotation depositions. The coatings are systematically studied across a range of chemical compositions, revealing predominantly amorphous structures (Fig. 1).

Intriguingly, specific compositions exhibit the formation of short-range ordered tungsten borides or nanocrystalline cubic tungsten carbide structures. Morphological differences are observed, with stationary coatings generally more compact and smoother, while rotation induces columnar growth. Surface roughness varies across compositions and regimes, with high-boron coatings exhibiting rugged surfaces. Despite inherent multilayer formation during industrial preparation with substrate rotation, the impact on structure and composition is found to be minimal. The W₂BC composition, in particular, displays a fully amorphous structure and impressive mechanical properties despite the lack of internal stress. Mechanical properties, including hardness and effective elastic modulus, range from 10 GPa to 29 GPa and 130 GPa to 440 GPa, respectively. Higher boron content correlates with increased hardness and modulus. Residual stress analysis reveals that nanocrystalline coatings exhibit higher internal compressive stress. Damage resistance assessment based on elastic modulus reduction under indentation is generally used to rank coatings. W₂BC demonstrates superior damage resistance compared to nitrides (TiN, AlCrN). No severe cracking or chipping was caused by the load applied to the cube-corner indenter and the imprints exhibited a pile-up of material. The study extends comparisons with Mo-B-C coatings, highlighting similarities in mechanical properties despite structural differences. W-B-C emerges as a unique amorphous material with good damage resistance and mechanical performance, offering potential applications in protective coatings.

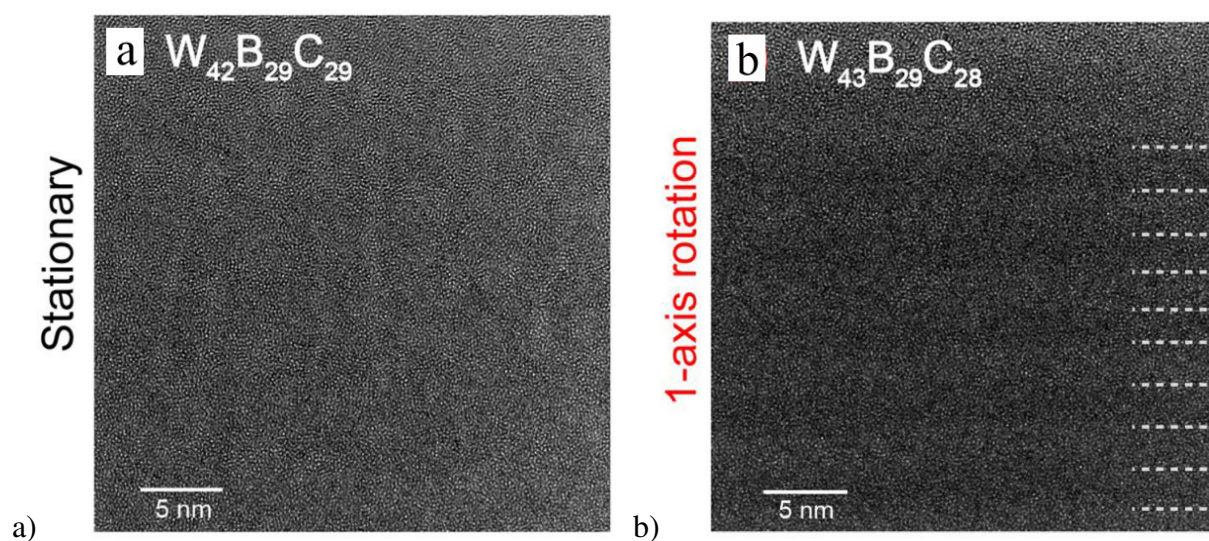


Figure 1: a) HRTEM images of WBC coatings deposited on stationary and b) rotating substrate. In figure b) the film shows a slight multilayer character due to substrate rotation.

Related publication

- [1] M. Krokker, P. Souček, L. Zábranský, V. Buršíková, Zs. Czigány, V. Sochora, K. Balázs, M. Jílek, P. Vašina: *Industrially deposited hard and damage resistant W-B-C coatings*, *Surface & Coatings Technology* **454**, 129150 (2023) <https://doi.org/10.1016/j.surfcoat.2022.129150>

EFFECT OF Nb INCORPORATION IN Mo₂BC COATINGS ON STRUCTURAL AND MECHANICAL PROPERTIES - AB INITIO MODELLING AND EXPERIMENT

VEKOP-2.3.3-15-2016-00002, VEKOP-2.3.2-16-2016-00011

Zs. Czigány, K. Balázsi, J. Ženíšek¹, P. Soucek¹, P. Vasina¹

¹ Department of Physical Electronics, Masaryk University, Brno, Czech Republic

This study [1] investigates the structural and mechanical implications of niobium (Nb) incorporation into magnetron-sputtered Mo₂BC coatings, employing both theoretical ab initio modelling and experimental approaches. The aim was to explore the stability of the orthorhombic (Mo_{1-x}Nb_x)₂BC phase as molybdenum is gradually replaced by niobium.

Theoretical calculations, based on substituting Mo atoms in the orthorhombic Mo₂BC cell, predicted the stability of the (Mo_{1-x}Nb_x)₂BC solid solution up to 37.5% Nb substitution. At this point, the elastic and shear moduli were maximized, and the enthalpy of formation suggested increased stability compared to common coatings like AlTiN. However, experimental results unveiled the formation of an unexpected fcc NbC-like structure at high Nb contents, challenging the theoretical predictions. All coatings exhibited a columnar structure with nanometre-sized grains and amorphous regions, impacting the stability of the orthorhombic Mo₂BC-like phase compared to theoretical calculations. At the stability limit, coating hardness increased by 25%, and the elastic modulus rose by 60%, attributed to lattice strain generated by Nb substitution. The study concludes with an exploration of the mechanical properties of (Mo_{1-x}Nb_x)₂BC solid solutions. Theoretical predictions showcased a non-linear relationship with Nb content, explained by microstrain within the nanolaminated structure and crosslinking of boron chains. Theoretical stability predictions aligned with experimental trends up to 37.5% Nb substitution, beyond which structural changes led to decreased stability.

Selected Area Electron Diffraction (SAED) investigation provides insights into the challenges of distinguishing between cubic and orthorhombic structures, especially for small grain sizes. Diffraction analysis of Mo₂BC shed light on the similarities of the two structures. Strong reflections in the SAED pattern of Mo₂BC also can be indexed as an fcc phase which has a (111) preferred orientation. However if we want to interpret all the reflections of Mo₂BC, the structure of orthorhombic Mo₂BC seems a proper choice. Mo₂BC can be better indexed as orthorhombic Mo₂BC, however, its strong reflections coincide with allowed reflections of fcc structure, and weak reflections coincide with cubic reflections forbidden in fcc system (Fig. 1).

Therefore, the orthorhombic cell can be interpreted as a supercell generated from the fcc cell. The orthorhombic phase contains alternating planes containing stiff carbidic and boridic bonds with a high degree of ionicity and weaker metallic planes. Within the orthorhombic unit cell, the arrangement of heavy metal atoms (Mo, Nb) preserve a cubic (fcc) arrangement characteristic for cubic transition metal carbides.

In summary, this research contributes to the detailed understanding of Nb incorporation in Mo₂BC coatings, emphasizing the need for a holistic approach encompassing theoretical modelling and experimental validation for informed coating design and development.

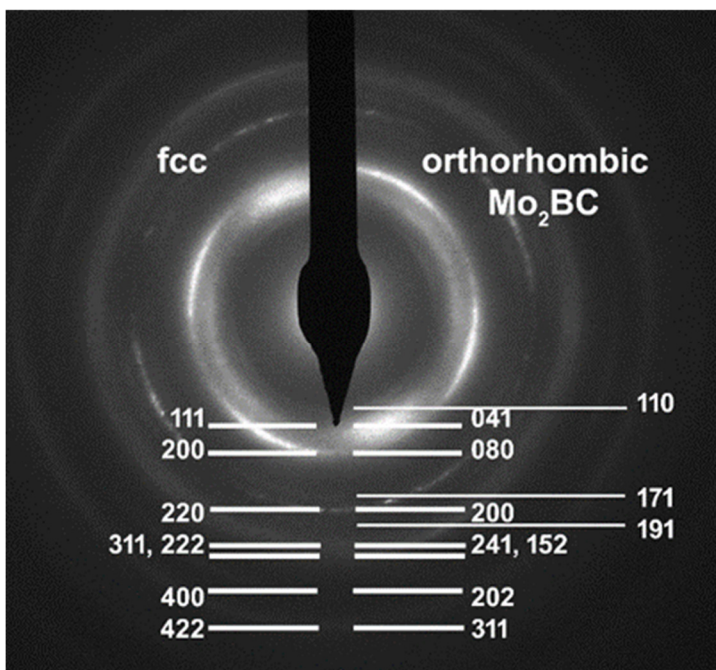


Figure 1: Electron diffraction pattern of Mo₂BC. Strong reflections can be indexed as an fcc phase which has a (111) preferred orientation. The strong reflections of orthorhombic structure coincide with allowed reflections of fcc, however weak reflections of orthorhombic structure coincide with cubic reflections forbidden in fcc system. Therefore, the orthorhombic cell can be interpreted as a supercell generated from the fcc cell.

Related publication

- [1] J. Ženíšek, P. Souček, P. Ondračka, Zs. Czigány, V. Buršíková, D. Holec, K. Balázs, P. Vašina: *Effect of Nb incorporation in Mo₂BC coatings on structural and mechanical properties – ab initio modelling and experiment*, *Acta Materialia* **268(3)**, 119741 (2024) <http://dx.doi.org/10.1016/j.actamat.2024.119741>

COMPOSITION DEPENDENT STRUCTURE, MORPHOLOGY AND MECHANICAL PROPERTIES OF THE $Al_{1-x}Cu_x$ THIN FILM SYSTEM

VEKOP-2.3.3-15-2016-00002, VEKOP-2.3.2-16-2016-00011

D. Olasz, G. Sáfrán, N. Szász, T. Kolonits, N.Q.Chinh

We continued the nanoindentation measurements on the AlCu thin film system (Fig. 1) with a comprehensive Transmission Electron Microscopy (TEM) study to explore the correlations between mechanical, morphological and structural properties. Focus Ion Beam (FIB) cross-sectional lamellae were prepared from 15 layers of $\sim 1.7 \mu\text{m}$ thickness of different compositions formed by DC sputtering representing the full $Al_{1-x}Cu_x$ composition range ($0 \leq x \leq 1$), of which 12 have already been TEM examined [1].

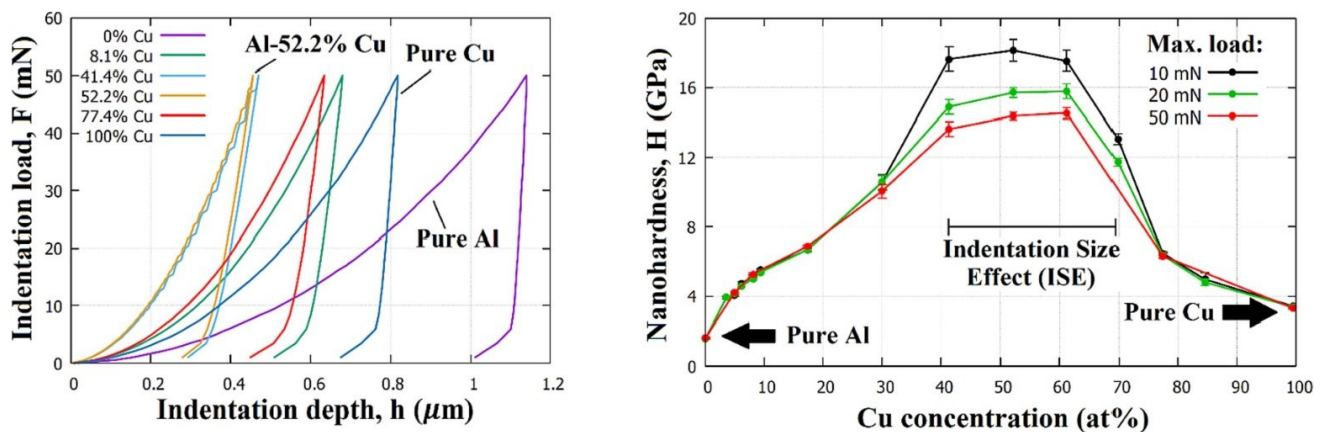


Figure 1: a) Indentation curves and b) hardness of AlCu thin films as a function of Cu alloying concentration

In Fig. 2, bright field TEM images show the morphological evolution of the layers at the indicated copper concentrations x ($Al_{1-x}Cu_x$) with increasing alloying concentration. A drastic reduction in grain size can be observed even with small amounts of Cu alloying. Using Selected Area Electron Diffraction (SAED) techniques, we have shown that in the range $x = 3.6 - 17.4 \%$ Cu, the θ - Al_2Cu phase appears in addition to the α -Al phase, which is in agreement with the predictions of the equilibrium phase diagram [2]. Both the grain size decrease and the appearance of the θ phase [3], lead to a significant increase in the strength and hardness of the layer, which can be clearly observed in Fig. 1. The layer containing 52.2 at% Cu shows a γ - Al_4Cu_9 phase composition, which is no longer consistent with the equilibrium phase diagram - and this indicates the non-equilibrium nature of the sputtered thin film. The γ phase is a high strength phase of $\sim 15 \text{ GPa}$ [3], which is in good agreement with our measured hardness of $\sim 16 \text{ GPa}$.

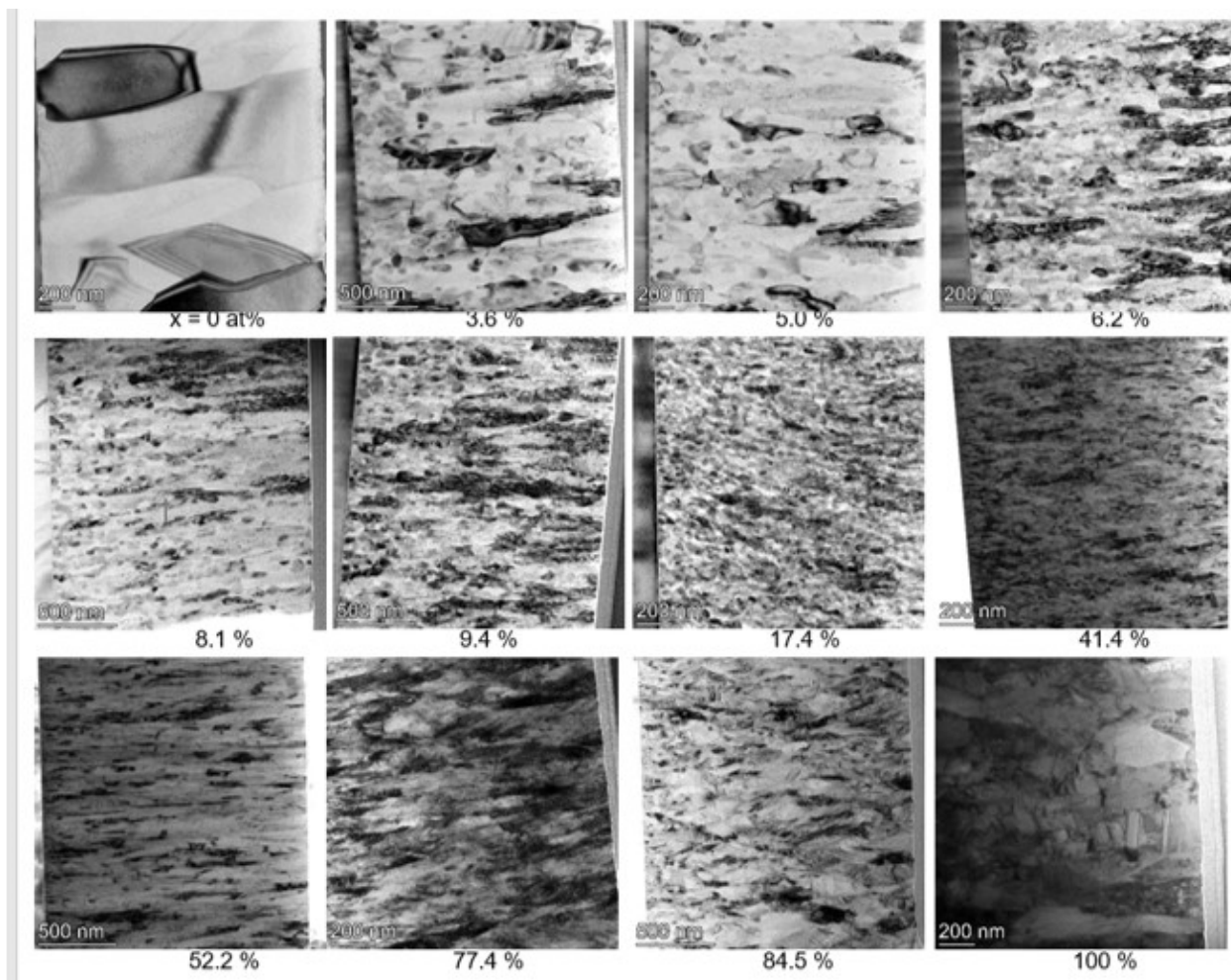


Figure 2: Bright Field (BF) TEM cross-section series showing the morphological evolution of AlCu layers as a function of Cu(x) alloying concentrations representing the full compositional range

Related publications

- [1] G. Sáfrán, P. Petrik, N. Szász, D. Olasz, NQ. Chinh, M. Serényi: *Review on High-Throughput Micro-Combinatorial Characterization of Binary and Ternary Layers towards Databases*, *Materials* **16(8)**: 3005 (2023) <https://doi.org/10.3390/ma16083005>
- [2] L. J Murray: *The aluminium-copper system*, *International Metals Reviews* **30**, 211 – 234 (1985)
- [3] W. Bedjaoui, Z. Boumerzoug, F. Delaunois: *Solid-State Diffusion Welding of Commercial Aluminium Alloy with Pure Copper*, *Int. J. Automot. Mech. Eng.* **19(2)**, 9734-9746 (2022) <http://dx.doi.org/10.15282/ijame.19.2.2022.09.0751>

COMBINATORIAL CHARACTERISATION OF THE COMPLETE Y-TI-O THIN LAYER SYSTEM; ISSUES OF DC AND HIPIMS SPUTTERING PROCESSES

Ministry of Culture and Innovation KDP-2021 C1792954, OTKA K 143216

D. Olasz, M. Serényi, M. Gajdics, V.K. Kis, I. Cora, M. Németh, G. Sáfrán

The Y-Ti-O family of materials, which has several promising phases from a technological point of view, offers an excellent opportunity for a comprehensive microstructural characterisation by microcombinatorial fabrication and testing techniques. The results [1] of the microstructural investigation of the reactive DC magnetron sputtered variable composition coatings are summarized in the phase map shown in Fig. 1, which covers the whole Y-Ti composition range up to 800 °C. A very important result is that the pyrochlore-structured $Y_2Ti_2O_7$ phase could be produced under favourable conditions at a significantly lower temperature, as low as 700 °C, compared to other methods.

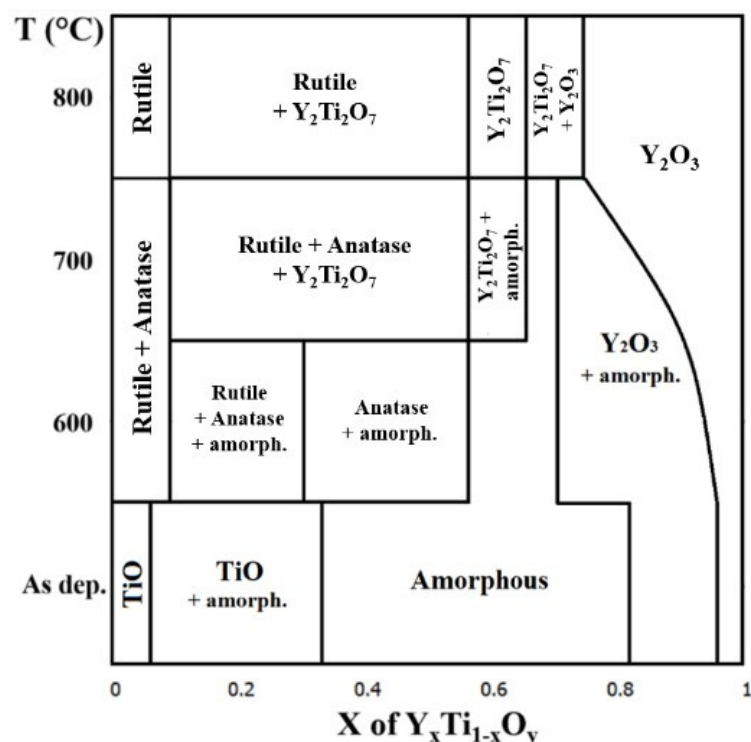


Figure 1: Phase map of the $Y_xTi_{1-x}O_y$ thin film system prepared by microcombinatorial DC magnetron sputtering over the entire $0 \leq x \leq 1$ composition range up to 800 °C

High Power Impulse Magnetron Sputtering (HIPIMS) is a more stable and controllable growth technique than DC, which offers an excellent opportunity to produce the desired perovskite lattice ($YTiO_3$) phase with the right experimental parameters. When reactively sputtering two targets with very different sputtering properties -Y and Ti - together, finding the right settings is a very difficult task, which is not well discussed in the literature. The method used for combinatorial characterization via DC sputtering - varying the power - cannot be applied in reactive sputtering due to its non-linear behaviour (Fig. 2).

In the experiments carried out in the last year, we have determined the fundamental parameters: frequency and pulse length, optimal pulsation parameters of the reactive gas, optimal bias voltage of the sample holder etc. The variation of the layer composition we made possible by using the "burst" mode: by varying the number of bursts (N) separately for each target, it is possible to vary the composition of the sputtered layer along the length of the combinatorial sample (Table 1).

Table 1: Effect of the number of Y and Ti bursts (N_Y ; N_{Ti}) on the composition of the layer

N_Y	N_{Ti}	x; $Y_xTi_{1-x}O_y$ (SEM EDS)
10	10	0.49
10	3	0.60
3	10	0.24

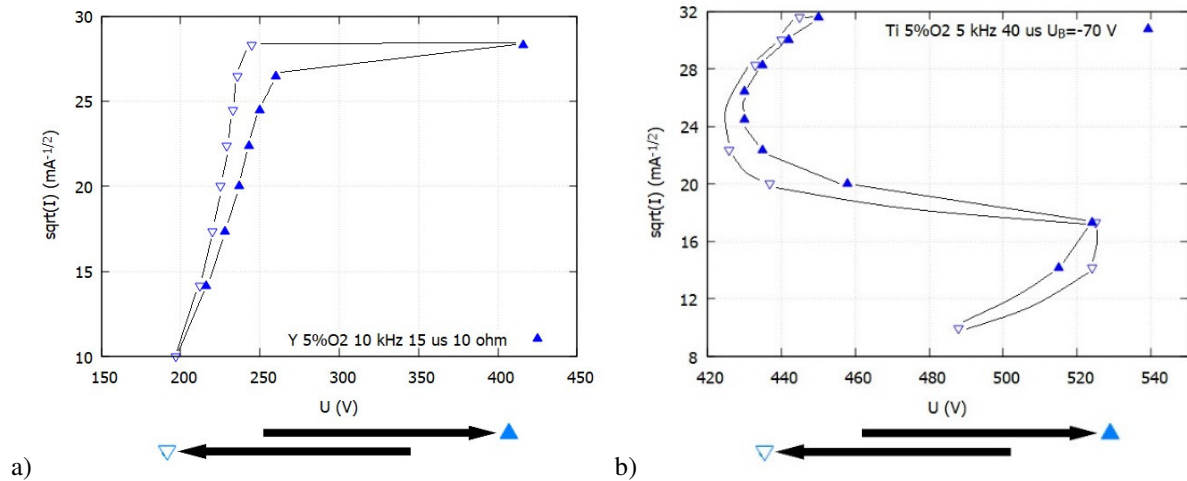


Figure 2: Features of U-I hysteresis during reactive sputtering in 5 % O_2 gas for (a) Y target (b) %Ti target

Fig 3.a shows the chamber during HIPIMS sputtering of a Y-Ti-O layer in burst mode, and Fig. 3.b shows a combinatorial Y-Ti-O layer of varying composition deposited along a Si substrate. Understanding the further effects of the sputtering parameters, we plan to deposit combinatorial layers for TEM analysis onto TEM grids so that comprehensive structural analysis can be efficiently performed.

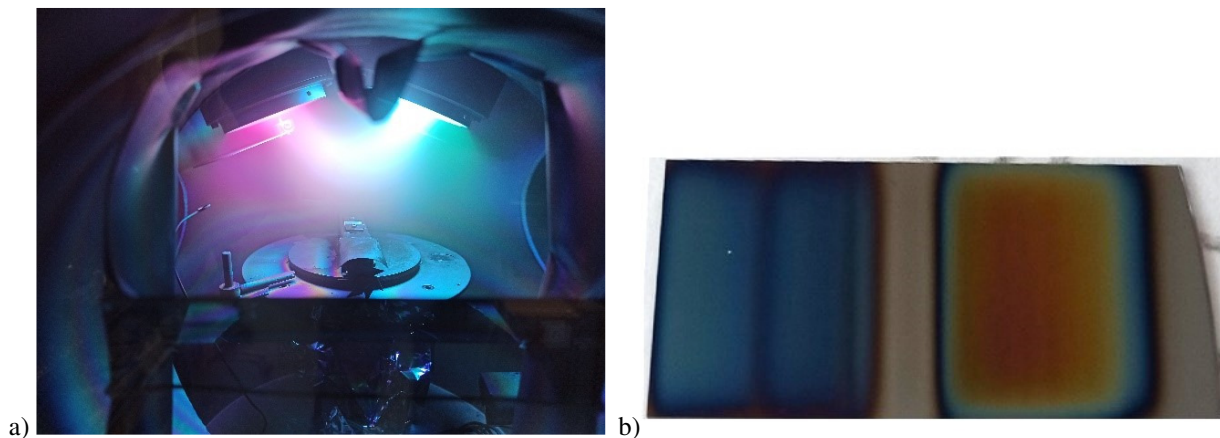


Figure 3: a) Y-Ti-O layer growth in burst-HIPIMS sputtering mode b) Combinatorial Y-Ti-O thin film

Related publication

- [1] D. Olasz, V. Kis, I. Cora, M. Németh, G. Sáfrán: *High-Throughput Micro-Combinatorial TEM Phase Mapping of the DC Magnetron Sputtered $Y_xTi_{1-x}O_y$ Thin Layer System*, *Nanomaterials* **14**, 925 (2024) <https://doi.org/10.3390/nano14110925>

CATALYTIC METHANE PYROLYSIS COMBINED WITH MICROCOMBINATORIAL TEM STUDIES

OTKA K 143216, OTKA K 146032

Horváth, M. Németh, A. Beck, Zs. Horváth, D. Olasz, M. Serényi, Gy. Sáfrán

Methane pyrolysis ($\text{CH}_4 \rightleftharpoons \text{C} + 2\text{H}_2$) yields extremely clean hydrogen gas and only solid carbon, without the production of any CO_2 , but the process is not industrialized yet. Application of proper catalysts can decrease the temperature requirement of the reaction and produce valuable nanostructured carbon beside hydrogen [1]. Sample preparation was done by i) chemical deposition of Ni and Mo metal precursor ions over the MgO support or ii) microcombinatorial TEM method [2] using DC magnetron sputtering over a TEM grid.

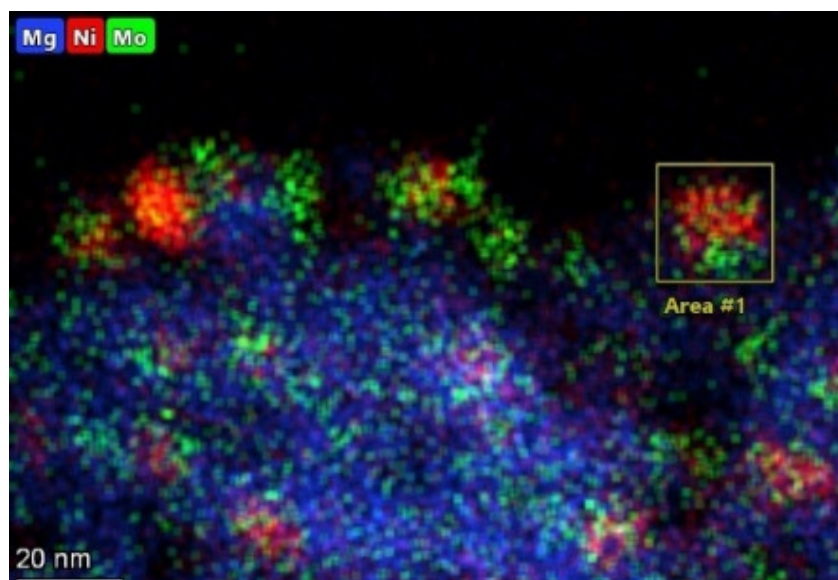
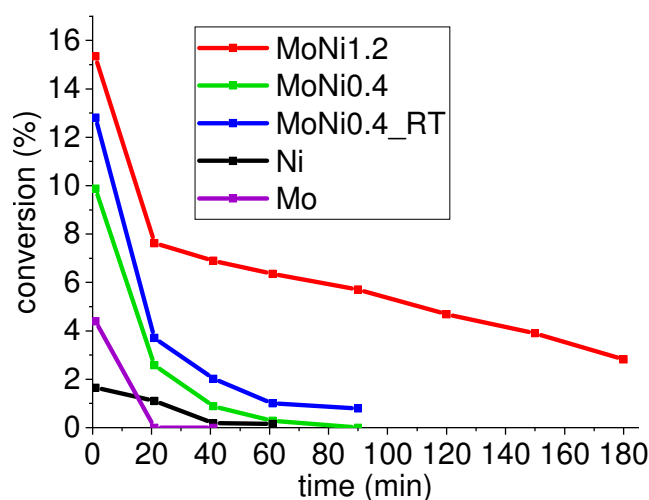


Figure 1: CH_4 conversion during the pyrolysis tests at 800 °C on the MgO supported samples (top); elemental maps of the reduced MoNi1.2 sample (bottom)

This latter method is able to produce thin layers of two components with linearly changing composition across a TEM grid, and these layers upon high temperature reduction transform into metallic particles or islands. NiMo/MgO catalyst samples (7 wt% Ni and 4% or 12% Mo loading designated by MoNi0.4 and MoNi1.2 atomic ratios, respectively) were reacted in 50% CH_4/Ar stream using a horizontal reactor at 800 °C. The supported catalysts were investigated by XRD, Temperature Programmed Reduction (TPR), XPS, HRTEM and STEM-EDS prior to and after the CH_4 pyrolysis [3]. The microcombinatorial Ni-Mo samples were investigated by XPS, TEM and STEM-EDS before and after a reduction treatment and carbonization in a methane stream.

The bimetallic NiMo/MgO samples produced carbon nanotubes with 50-320% yield, while monometallic Ni/MgO or Mo/MgO deactivated fast. The superiority of the MoNi_{1.2} catalyst in terms of activity, stability and carbon yield was explained by the presence of the equimolar alloyed NiMo particles (Fig. 1). The novel microcombinatorial TEM method (TEM grid shown in Fig. 2.a) resulted NiMo alloy particles with different compositions (Fig 2.b). It was ascertained that the Ni/Mo~1 alloy composition (framed with yellow in Fig. 2.b) did not seem to segregate during the carbonization process. The existence, the reasons and structural background of the synergetic interaction between nickel and molybdenum were revealed.

The microcombinatorial TEM method was first applied for catalytic purposes. The most prominent novelty of our work was the disclosure of the nanoscale segregation of bimetallic MoNi particles during carbon deposition process depending on the Mo/Ni atomic ratio and affecting the catalyst lifetime.

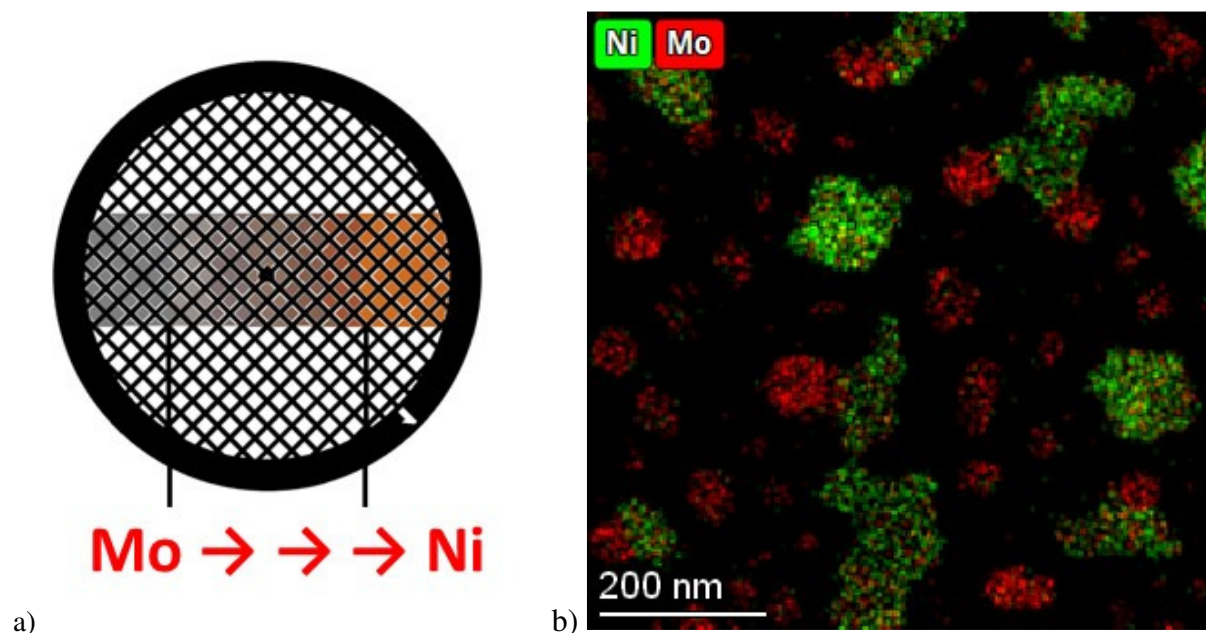


Figure 2: a) Scheme of TEM grid with Ni and Mo deposited in linearly changing atomic ratio. b) STEM-EDS elemental maps of a representative area of the grid after reduction at 800 °C with some equimolar alloys framed

Related publications

- [1] T.I. Korányi, M. Németh, A. Beck, A. Horváth: *Recent Advances in Methane Pyrolysis: Turquoise Hydrogen with Solid Carbon Production*, *Energies* **15**, 6342 (2022) <https://doi.org/10.3390/en15176342>
- [2] G. Sáfrán, P. Petrik, N. Szász, D. Olasz, NQ. Chinh, M. Serényi: *Review on High-Throughput Micro-Combinatorial Characterization of Binary and Ternary Layers towards Databases*, *Materials* **16(8)**: 3005 (2023) <https://doi.org/10.3390/ma16083005>
- [3] A. Horváth, M. Németh, A. Beck, G. Sáfrán, Z.E. Horváth, I. Rigó, Z. May, T.I. Korányi: *Methane pyrolysis on NiMo/MgO catalysts: the significance of equimolar NiMo alloy resisting nanosize segregation during the reaction*, *Applied Catalysis A: General* **676**, 119651 (2024) <https://doi.org/10.1016/j.apcata.2024.119651>

REDUCTIVE TREATMENT OF $\text{Ti}_{0.8}\text{Sn}_{0.2}\text{O}_2\text{-C}$ COMPOSITE SUPPORTED PT

OTKA K 143216

E. Dódony, C. Silva^{1,2}, K. Salmanzade¹, I. Borbáth², D. Olasz, Gy. Sáfrán, A. Kuncser³,
E. Pászti-Gere⁴, A. Tompos¹, Z. Pászti¹

¹Institute of Materials and Environmental Chemistry, Research Centre for Natural Sciences, Hungary, ²Department of Physical Chemistry and Materials Science, Faculty of Chemical Technology and Biotechnology, Budapest University of Technology and Economics, Hungary, ³National Institute of Materials Physics, Magurele, Romania, ⁴Department of Pharmacology and Toxicology, University of Veterinary Medicine, Hungary

Transition metal-doped titania and carbon composites have emerged as highly effective supports for platinum (Pt) electrocatalysts in Proton Exchange Membrane (PEM) fuel cells. These advanced supports utilize the oxide component to stabilize Pt particles, while the dopants serve a co-catalytic role. Among various dopants, tin (Sn) stands out as a particularly valuable addition. A notable feature of TiO_2 -supported Pt catalysts is the Strong Metal-Support Interaction (SMSI), which involves the migration of partially reduced oxide species from the support to the Pt surface during reductive treatment. To assess how SMSI affects the stability and performance of Pt/ $\text{Ti}_{0.8}\text{Sn}_{0.2}\text{O}_2\text{-C}$ catalysts, the structural and catalytic properties of freshly prepared samples were analyzed using X-Ray Diffraction (XRD), Transmission Electron Microscopy (TEM), X-ray Photoelectron Spectroscopy (XPS), and electrochemical tests, and compared with those of catalysts reduced in hydrogen at high temperatures.

Results indicated that the uniform oxide coverage on the carbon substrate promoted the formation of high-density Pt-oxide-C triple junctions. The electrocatalytic behaviour of the as prepared catalysts was determined by the atomic closeness of Sn to Pt, while even a low temperature reductive treatment resulted in Sn-Pt alloying. The segregation of tin oxide on the surface of the alloy particles, a characteristic material transport process in Sn-Pt alloys after oxygen exposure, contributed to a better stability of the reduced catalysts.

As part of our laboratory collaboration, we conducted investigations on the structure, morphology, and elemental composition of the catalysts using the THEMIS TEM of the Thin Films Department. This involved obtaining and analyzing high-resolution and low-resolution images, as well as element mapping with transmission electron microscopy [1].

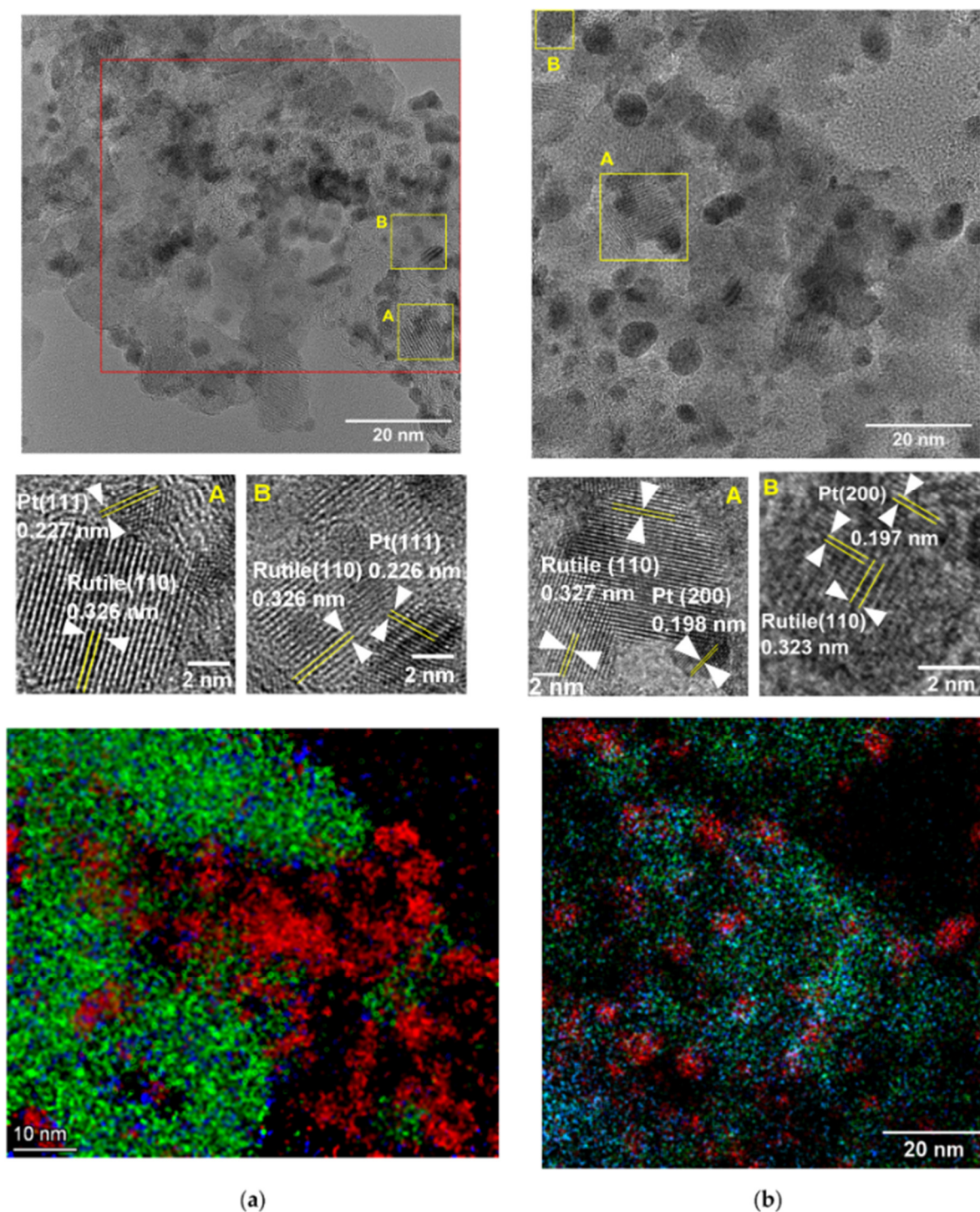


Figure 1: TEM micrographs and elemental maps for (a) the as prepared $\text{Pt}/\text{Ti}_{0.8}\text{Sn}_{0.2}\text{O}_2\text{-C}$ electrocatalyst and (b) the $\text{Pt}/\text{Ti}_{0.8}\text{Sn}_{0.2}\text{O}_2\text{-C}$ electrocatalyst reduced at 200 °C. The locations of the details A and B are indicated by yellow rectangles in the micrographs. The STEM/EDS elemental maps correspond to the area of the red rectangle in (a) and to the entire image area in (b). Colour code: red: Pt, green: Ti, blue: Sn.

Related publication

- [1] C. Silva, K. Salmanzade, I. Borbáth, E. Dódy, D. Olasz, Gy. Sáfrán, A. Kuncser, E. Pászti-Gere, A. Tompos, Z. Pászti: Reductive Treatment of Pt Supported on $\text{Ti}_{0.8}\text{Sn}_{0.2}\text{O}_2\text{-C}$ Composite: A Route for Modulating the Sn–Pt Interactions, *Nanomaterials* **13**(15), 2245 (2023) <http://dx.doi.org/10.3390/nano13152245>

MICROSTRUCTURE AND GROWTH OF α -Mn(Cu) SOLID SOLUTION FILMS

OTKA K 143216

K. Hajagos-Nagy, Zs. Czigány, Gy. Radnóczy

Bulk Mn-Cu alloys are well-known magnetic and shape-memory alloys, which are created from γ -Mn(Cu) solid solution by martensitic (fcc \rightarrow fct) transformation. The stable form of Mn at room temperature, α -Mn, is considered problematic due to its brittleness; even though the α -Mn structure contains many promising properties, such as para-, antiferro- and weakly ferromagnetic behaviour, anomalous Hall Effect and high pressure (220 GPa) stability. The reason behind these properties is the crystal structure of α -Mn, which is considered unique among the elements. It is analogous to the χ phase found in intermetallic systems. The stability of Mn atoms in 3 different electron configurations is almost the same; therefore, Mn is able to create an elementary cell in which atoms of different valence/size are present in different crystallographic positions.

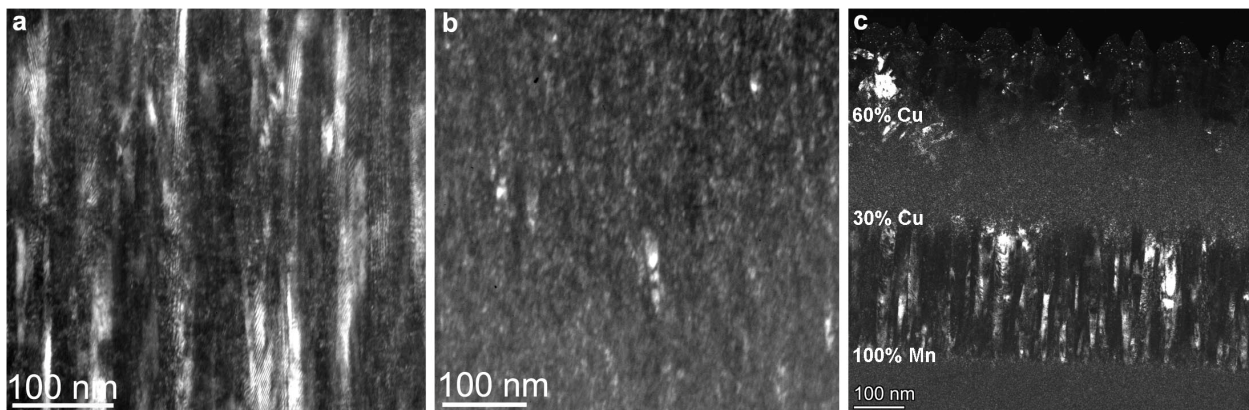


Figure 1: Microstructure of Mn-Cu films with Cu content of 10 at% (a), 20 at% (b) and 0-60 at% (c) on dark field TEM images.

A possible way of minimizing the brittleness of bulk α -Mn is to use thin film deposition techniques and alloying. In our previous work, we mapped the Cu-Mn thin film system from the point of view of its use in very-large-scale integrated circuits. We discovered that, contrary to our expectations, α -Mn could dissolve at least 10 at% Cu content and the α -Mn(Cu) solid solution was present up to 30 at% Cu. In the current work, we investigated the microstructure and growth of the α -Mn(Cu) layers.

We investigated the non-equilibrium solubility of Cu in α -Mn on a 50 nm thick combinatorial sample grown by DC magnetron sputtering, where the composition varied linearly between pure Mn and 50 at% Cu content. The films contain a crystalline phase up to 30 at% Cu content; the grain size varies between 2-10 nm. Electron diffraction intensity distributions showed that α -Mn can dissolve 30 at% Cu. We examined film growth on 0.5-1 μ m thick films, comparing discrete and variable composition (gradient) layers. At 10 at% Cu content a single-phase α -Mn(Cu) solid solution layer grows with a columnar structure (Fig. 1.a). As the Cu content increases, an amorphous minority phase appears and hinders the growth of the α -Mn(Cu) grains (Fig. 1.b). Examination of gradient films showed that the columnar structure characteristic of single-phase growth can be maintained until the crystalline phase ceases (Fig. 1.c). This can be beneficial in many applications where minimization of grain boundaries is required.

MULTIFUNCTIONAL BIOMINERALIZED CALCIUM PHOSPHATE-LOADED BIOPOLYMER COMPOSITES AS BIODEGRADABLE COATINGS ON IMPLANTS

OTKA FK 146141

M. Furkó

Bioactive ceramics and scaffolds are extremely important in many biomedical or orthopedic applications owing to their positive interactions with human tissues. There are enormous efforts to develop bioceramic particles that meet the high-quality standard in a cost-effective way. Among the numerous bioceramics, calcium phosphates are the most suitable since the main inorganic compound in human bones is the hydroxyapatite which is a specific phase of the Calcium Phosphates (CaPs) or apatites. The CaPs can be applied as bone substitutes, types of cement, drug carriers, implants, or coatings. In addition, bioresorbable bioceramics have great potential in tissue engineering since they are usually used as scaffolds that can advance the healing process of bones during the normal tissue repair mechanism. The newest advancement in the CaPs is when they are incorporated with active biomolecules such as Mg, Zn, Sr, and so on. The chemical composition, crystallinity, size, and morphology of the CaP particles and their aggregates play a critical role in determining their properties and potential applications.

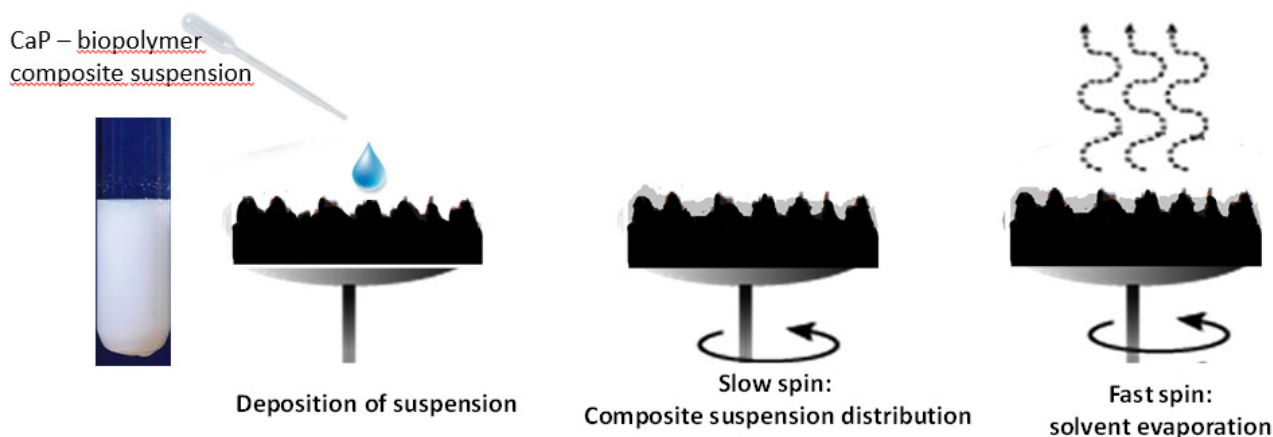


Figure 1: Schematic illustration of spin coating method.

In our work, amorphous or nanocrystalline calcium phosphates (ACPs) and their combination with biopolymers are prepared as coatings or scaffold matrices. The innovative types of resorbable coatings for load bearing implants that can promote the integration of metallic implants into human bodies. Owing to the bioactive mineral additions (Mg, Zn, Sr) in optimized concentrations, the base CP particles became more similar to the mineral phase in human bones (dicalcium phosphate (dCP)). The coatings were prepared by spin coating technique (Fig. 1).

We investigated and compared the surface roughness of the substrate and the coated substrate and the result showed that the polymer composite decreased the roughness values. The SEM-FIB cross sectional cut revealed a very thin, around 1-5 μm layer. The thickness of the layer was uneven due to the substrate's rough surface. The CP-biopolymer composite can be produced as fibres via electrospinning method (Fig. 3). In this case, the resulting composites consist of spider web-like entangled fibres with unevenly incorporated calcium phosphate particles. The CaP particles are embedded between the fibres.

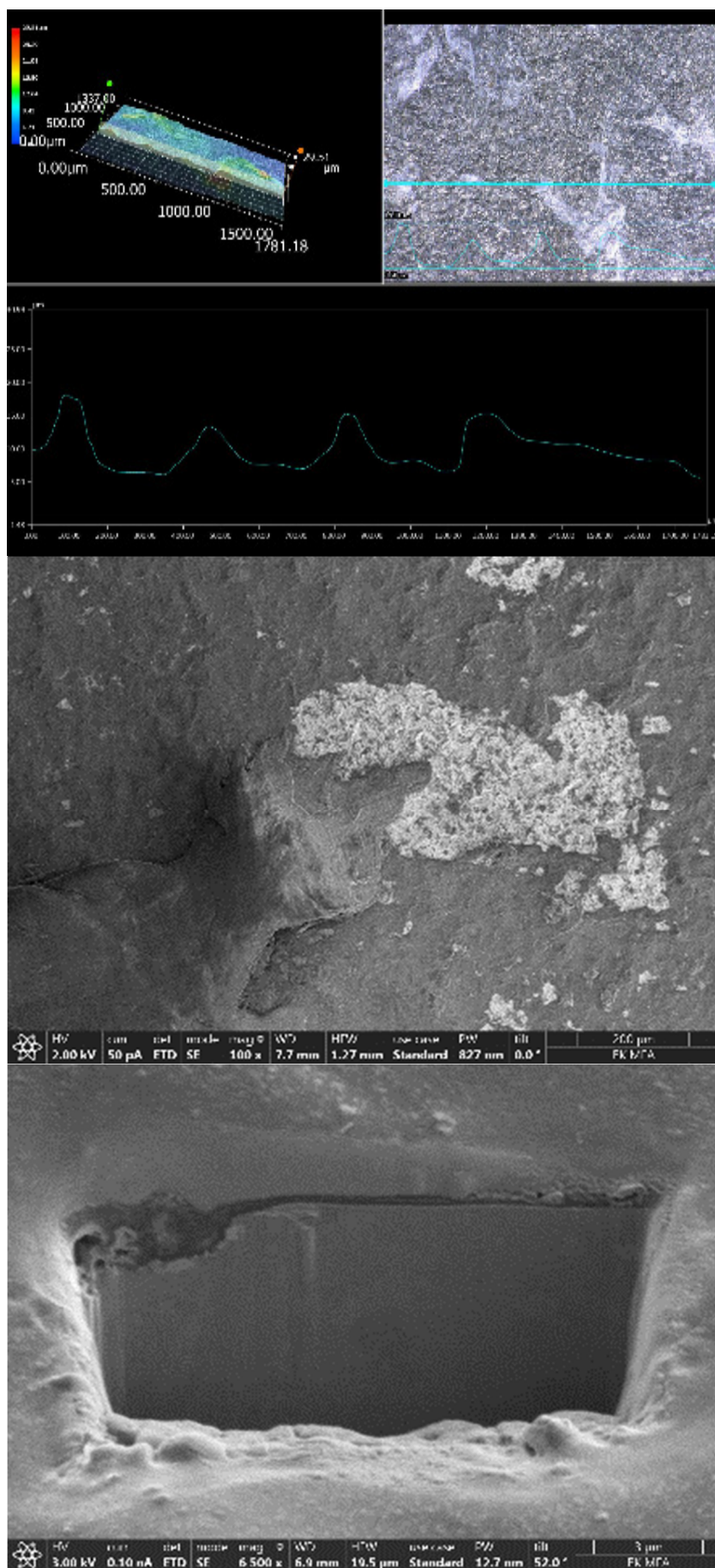


Figure 2: Optical microscope and SEM images of calcium phosphate-PCL thin layer, as well as cross sectional FIB cut for thickness measurement

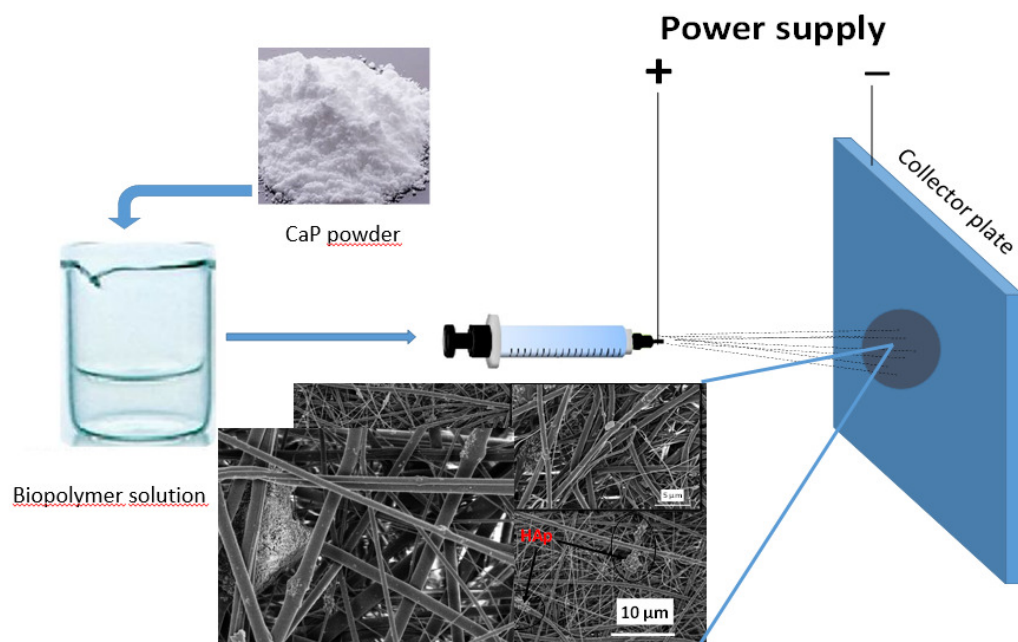


Figure 3: Schematic illustration of electrospinning technique

Related publications

- [1] A. García-Ruiz, S. Slizovskiy, M. Mucha-Kruczyński*, and V.I. Fal'ko: *Spectroscopic Signatures of Electronic Excitations in Raman Scattering in Thin Films of Rhombohedral Graphite*, *Nano Lett.* **19**, 6152–6156 (2019) <https://doi.org/10.1021/acs.nanolett.9b02196>
- [2] A. McEllistrim, A. Garcia-Ruiz, Z.A.H. Goodwin, and V.I. Fal'ko: *Spectroscopic signatures of tetralayer graphene polytypes*, *Phys. Rev. B* **107**, 155147 (2023) <https://doi.org/10.1103/PhysRevB.107.155147>

R+D+I DEVELOPMENT AND UTILIZATION OF HIGH-PERFORMANCE ELECTRONIC CHIPS "CHIPCER" PHASE 1

GFM - ÁFF/96/1/2023.

*K. Balázs, Cs. Balázs, T. Kolonits, K. Hajagos-Nagy, E. Dódony, A. Jakab Fenyvesiné,
B. Erki, V. Varga, A. Kovács*

The Hungarian government has accepted the Ministry of Economic Development's proposal to launch an R+D+I project for chip-carrying ceramic wafers, so Hungary is also starting to enter the semiconductor manufacturing market. The project, whose partners are the Bay Zoltán Nonprofit Ltd. (PI), Neumann Ltd., Budapest Technical University (BME) and the Thin Film Physics Laboratory of HUN-REN EK MFA, started from 2024 January 1st.

Our task is to develop thin (several hundred micrometres) ceramics as a chip substrate used in the automotive industry and high-performance electronics and to facilitate their production on an industrial scale. In the first year of the project, we determined the ceramic to be tested, the silicon nitride, an important parameter of which is that European suppliers provide the raw materials, thereby making the production process independent of various external influences.

All novel results are confidential.

DIGITALIZATION OF POWER ELECTRONIC APPLICATIONS WITHIN KEY TECHNOLOGY VALUE CHAINS

Horizon Europe 101096387 PowerizeD

*K. Balázsi, C. Balázsi, T. Kolonits, M. Furkó, K. Hajagos-Nagy, E. Dódonny,
A. Fenyvesiné Jakab, V. Osváth, V. Varga, A. Kovács, B. Erki*

PowerizeD is an innovative EU funded project aiming to develop breakthrough technologies of digitized and intelligent power electronics to enable sustainable and resilient energy generation, transmission and applications. The project is supported by the Chips Joint Undertaking and its members, including the top-up funding by the national Authorities of Germany, Belgium, Spain, Sweden, Netherlands, Austria, Italy, Greece, Latvia, Finland, Hungary, Romania and Switzerland, under grant agreement number 101096387. Co-funded by European Union.

The project focuses on improving the way energy is produced and transmitted through the use of digitized and intelligent electronic energy, which will greatly contribute to the decarbonisation of European society and the protection of our climate.

The research results so far are not yet public, professional publications can only be published after the permission of the project leader, Infineon.

QUANTIFICATION OF PIEZORESPONSE FORCE MICROSCOPY FOR THIN $\text{Al}_{(1-x)}\text{Sc}_x\text{N}$ FILM

TKP2021-NVA-03

N. Q. Khánh, L. Pósa, and J. Volk

The most common methods used to study the piezoelectric properties of thin nitride films are those that give the average value of the piezoelectric constant d_{33} , such as the direct piezoelectric Berlincourt piezometer or the inverse piezoelectric vibrometer. As the dimension of the device shrink, there is an increasing need to determine the distribution of d_{33} at the nanometer scale. Piezoresponse Force Microscopy (PFM) in principle can fulfill this demand, however, using sharp tip probe, different non-piezoelectric interfering phenomena, for example electrostatic force, flexoelectricity, substrate clamping effect, unexcited matrix material restraining effect etc., make the quantification of PFM difficult.

To overcome the aforementioned problems we have applied high spring constant (nominally 42 N/m) probe and top electrode for PFM measurement, as well as substrate clamping correction to the d_{33f} measured on $\text{Al}_{(1-x)}\text{Sc}_x\text{N}$ films prepared by pulse DC reactive ion sputtering system (VAKSIS – MiDAS). Fig. 1 shows the average effective d_{33f} determined from $1\mu\text{m}^2$ scans with and without Pd top electrode on AlN films having different Sc content. The use of a top electrode results in higher d_{33f} for each film, since the restraining effect of the unexcited volume around tip/sample contact is decreasing rapidly with increasing top electrode diameter, i.e. the contact perimeter to its area ratio decreases.

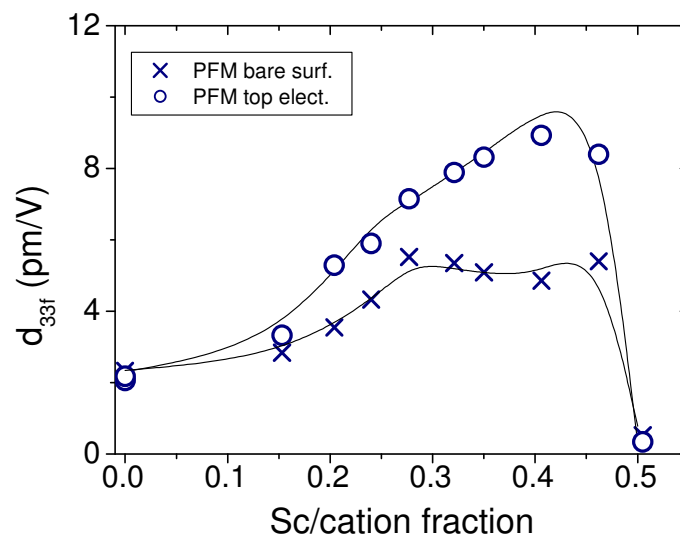


Figure 1: Effective piezoelectric coefficient d_{33f} measured by PFM on bare surface and with top electrode as a function of Sc fractions in $\text{Al}_{(1-x)}\text{Sc}_x\text{N}$ film. Lines are to guide the eyes.

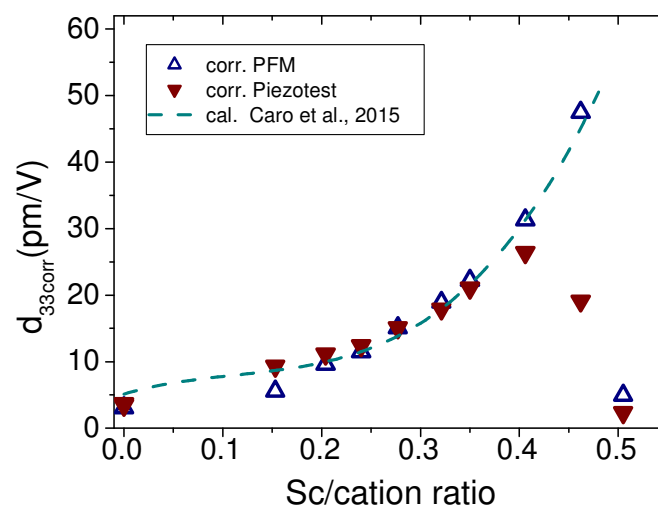


Figure 2: Corrected d_{33corr} values of d_{33f} determined by PFM and Piezotest using top electrode as a function of Sc fraction in nitride film deposited at 1.5 mTorr with 60% N_2 gas ratio. The DFT calculated d_{33} is also shown.

To obtain a more correct result (d_{33corr}), we have taken into account the effect of substrate for converse piezoelectric (cp) measurement,

$$d_{33corr_cp} = \frac{d_{33f_cp}(s_{11} + s_{12})}{(s_{11} + s_{12} + s_{13})} \quad (1)$$

where S_{ij} are the elastic compliance constants of nitride film, and $S_{13} \sim S_{33}/2$.

We used the values of the elastic compliance constants S_{ij} calculated using Density Functional Theory (DFT) reported in literature for substrate effect correction of the d_{33f} measured with top electrode. Fig. 2 shows the so corrected piezoelectric coefficients (opened triangle) determined using top electrode for films deposited at 1.5 mTorr with 60% N_2 gas ratio. The corrected d_{33corr} values are in good agreement with those obtained from the Berlincourt piezometer (closed triangle) and from the reported DFT calculation (dashed line) in the range of Sc fraction (x) up to ca. 0.35. At higher x , they differ significantly from each other. The difference may be due to the fact that pure wurtzite crystal cell was used for DFT calculation, while the piezoelectric and elastic properties of the deposited $Al_{(1-x)}Sc_xN$ films are effected by a number of factors at high x , such as crystal softening, formation of multi-phase etc.

For inhomogeneous sample, the corrected d_{33corr} is lower, as being an average, but using top electrode for local calibration, one can obtain d_{33corr} image from d_{33f} measured by PFM on bare film, where the correction factor is

$$d_{33corr} = \frac{d_{33fta}}{d_{33fba}} \times \frac{(s_{11} + s_{12})}{(s_{11} + s_{12} + s_{13})} \times d_{33fb}, \quad (2)$$

where d_{33fta} is the averaged effective piezoelectric coefficient measured with top electrode, d_{33fba} and d_{33fb} are the average and individual values measured on bare nitride, respectively. The first component is the matrix effect correction, and the second one is the clamp effect correction. Fig. 3 shows d_{33corr} image of samples having Sc fraction of about 0.24, but deposited under different conditions, namely 2 mTorr, 30% N_2 and 1.5 mTorr, 60% N_2 . One can see that 30% N_2 and 2 mTorr together result in only few areas ($\sim 20\%$ of whole map) with d_{33corr} values higher than 10.5 pm/V, compared to 50% areal ratio of such high d_{33corr} in other case. Furthermore, the fluctuation of d_{33corr} is much stronger for higher working pressure, and lower N_2 gas ratio (see the line-cut in Fig. 3). [1]

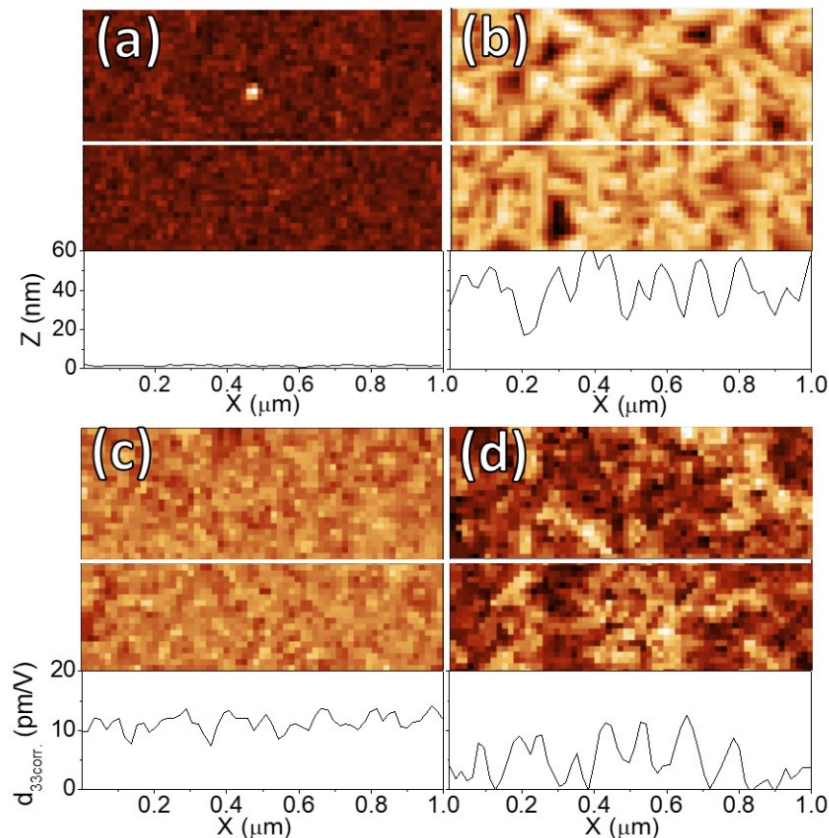


Figure 3: Morphology and d_{33corr} maps of nitride film deposited at 1.5mTorr, 60% N_2 (a,c) and 2 mTorr, 30% N_2 (b, d). White lines indicate the line-cuts

Related publication

- [1] N. Q. Khánh, Z. E. Horváth, Z. Zolnai, P. Petrik, L. Pósa, and J. Volk: *Effect of process parameters on co-sputtered $Al_{(1-x)}Sc_xN$ layer's properties: Morphology, crystal structure, strain, band gap, and piezoelectricity*, Materials Science in Semiconductor Processing, **169**, 107902 (2024) <http://dx.doi.org/10.1016/j.mssp.2023.107902>

A RUTHERFORD BACKSCATTERING/CHANNELLING AND SPECTROSCOPIC ELLIPSOMETRY STUDY OF ϵ - Ga_2O_3

2019-2.1.11-TÉT-2019-00066

Z. Zolnai, P. Petrik, A. Németh, J. Volk, M. Bosi, L. Seravalli, and R. Fornari

Nowadays, gallium oxide (Ga_2O_3) has become a promising candidate for a number of applications, e.g. power electronics and solar-blind UV-C detectors due to its unique intrinsic properties, such as extra-wide bandgap ($E_g > 4.5$ eV) and high critical breakdown field, estimated to be higher than that of SiC and GaN [1]. Most scientific works to date focused on monoclinic β - Ga_2O_3 , the thermodynamically stable polymorph. Nevertheless, there is an increasing interest about other polymorphs, the less explored α , γ , δ , κ , and ϵ phases, as they generally possess a crystallographic structure with higher symmetry and lower anisotropy compared to the β -phase. Therefore, characterization of various polymorphs and transitions between them upon thermal annealing achieved extensive scientific interest.

In this work the structure of thin Ga_2O_3 layers grown by Metal-Organic Vapour Phase Epitaxy (MOVPE) at temperature of 650°C on α - Al_2O_3 substrate has been analyzed by Rutherford Backscattering Spectrometry in combination with channelling (RBS/C) and Spectroscopic Ellipsometry (SE). For the as-grown Ga_2O_3 layer RBS/C angular scan curves were performed (Fig. 1) around the major crystallographic axis oriented nearly perpendicular to the sample surface. The measured widths ($\Psi_{1/2}$) and minimum yields (χ_{\min}) of the angular scans were determined separately for the Ga and O component and were compared to calculations based on the continuum steering potential model for axial channelling.

The distinct $\Psi_{1/2}$ values of $\sim 0.63^\circ$ and $\sim 0.38^\circ$ measured for Ga and O are related to differences in average atomic numbers and average interatomic distances of the atomic rows containing Ga and O atoms along the $\langle 0001 \rangle$ axial channel of Ga_2O_3 . In addition, the relatively high χ_{\min} for oxygen (Fig. 1 right) can be explained by a cross-steering effect between different atomic rows with larger and smaller $\Psi_{1/2}$ values. Similar behaviour of χ_{\min} has been reported for NbC and SiC crystals. The measured $\Psi_{1/2}$ and χ_{\min} of the Ga and O sublattice can be correlated with a crystal structure which contains O atoms arranged in a 4H Hexagonal Closely Packed (HCP) lattice and Ga atoms which preferentially occupy octahedral interstitial sites in the 4H cell (with estimated values of $\Psi_{1/2} \sim 0.59^\circ$ for Ga and $\sim 0.34^\circ$ for O). This structure is closely related to the ϵ -phase of Ga_2O_3 [2]. Note, significantly different $\Psi_{1/2}$ values than the measured ones can be expected for tetrahedral site occupancy of Ga in a 4H oxygen lattice and also for $\langle -201 \rangle$ -oriented β - Ga_2O_3 . The low channelling RBS yield for Ga (Fig. 1) reveals good crystalline quality of the Ga_2O_3 epilayer, however, a thin interface region is also detected (the peak in the red line around channel 450) with somewhat different crystallographic orientation and defect/strain content compared to the epilayer on top. Nevertheless, the Al angular scan curve (Fig. 1) reveals good matching between the c-axis of the α - Al_2O_3 substrate and of the ϵ - Ga_2O_3 layer, verifying high quality epitaxial growth.

After annealing at 1000°C , remarkable structural transformation occurs perpendicular to the sample surface as it is detected by significant changes in the RBS/C spectra (Fig. 2). Such effect primarily can be attributed to transition from the ϵ - to the β -phase in the Ga_2O_3 film [3]. As SE measurements show, annealing also leads to noticeable changes in the dielectric function of the Ga_2O_3 layer, especially around the absorption edge (4.5-5 eV photon energy range in Fig. 2). In this case, 6h annealing with high cooling rate results in downshift of the optical absorption edge on the photon energy scale as compared to 2h annealing with low cooling rate. The observed SE trends may be related to variation of the preferred crystallographic orientation of the β -phase with respect to the Al_2O_3 substrate after annealing, and differences in residual strain and defect structure determined by the annealing conditions [3].

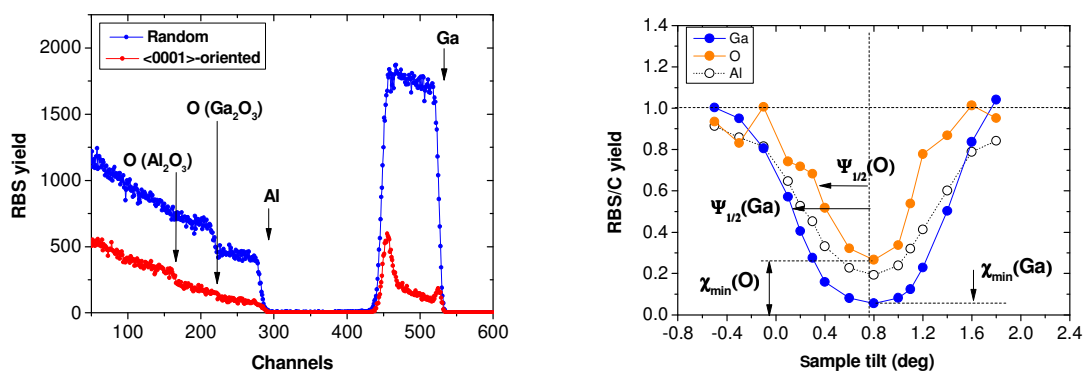


Figure 1: (Left) Random and channelling 2 MeV He^+ RBS/C spectra of a $\langle 0001 \rangle$ -oriented ϵ - Ga_2O_3 layer epitaxially grown on Al_2O_3 substrate. Spectrum edges for different elements in the thin layer and in the underlying substrate are indicated. (Right) 2 MeV He^+ RBS/C angular scan curve for the Ga and O components of $\langle 0001 \rangle$ -oriented ϵ - Ga_2O_3 . Critical angles for channelling, $\Psi_{1/2}$ and minimum yields, χ_{\min} , are indicated. Angular yield for Al in the α - Al_2O_3 substrate is also shown for comparison.

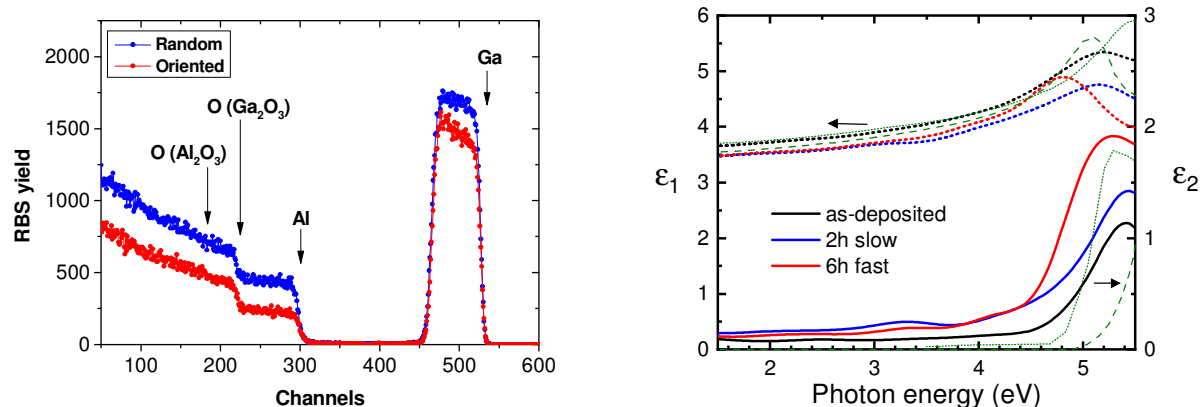


Figure 2: (Left) Random and oriented 2 MeV He⁺ RBS/C spectra of a Ga₂O₃ layer epitaxially grown on Al₂O₃ substrate and annealed at 1000 °C for 2h. Spectrum edges for different elements in the thin layer and in the underlying substrate are indicated. (Right) Real (ϵ_1) and imaginary (ϵ_2) parts of the dielectric functions for as-grown and post-annealed Ga₂O₃ layers measured by SE. Annealing was performed for 2h with slow and for 6h with fast cooling. Ordinary and extraordinary (short- and long-dashed green lines) dielectric functions of single-crystalline β -Ga₂O₃ from [4] are also plotted for comparison.

Our concept, based on RBS/C and SE analysis, gives the opportunity to ascertain correlations between crystal symmetry (polymorph structure), crystalline quality, interface features, and optical properties of as-grown and annealed Ga₂O₃ layers, as a function of depth on the nanoscale.

Related publications

- [1] Gallium Oxide: Technology, Devices and Application, ed. S. Pearton, F. Ren and M. Mastro, Elsevier, 2018, ISBN: 9780128145210 (e-book), ISBN: 9780128145227 (Imprint)
- [2] I. Cora, F. Mezzadri, F. Boschi, M. Bosi, M. Čaplovičová, B. Pécz: *The real structure of ϵ -Ga₂O₃ and its relation to κ -phase*, Cryst. Eng. Comm. **19**, 1509 (2017) <http://dx.doi.org/10.1039/C7CE00123A>
- [3] R. Fornari, M. Pavesi, V. Montedoro, D. Klimm, F. Mezzadri, I. Cora, B. Pécz, F. Boschi, A. Parisini, A. Baraldi, C. Ferrari, E. Gombia, M. Bosi: *Thermal stability of ϵ -Ga₂O₃ polymorph*. Acta Materialia. **140**, 411-416 (2017) <https://doi.org/10.1016/j.actamat.2017.08.062>
- [4] C. Sturm, J. Furthmüller, F. Bechstedt, R. Schmidt-Grund, M. Grundmann: *Dielectric tensor of monoclinic Ga₂O₃ single crystals in the spectral range 0.5–8.5 eV*, APL Materials. **3**(10), 106106 (2015) <http://dx.doi.org/10.1063/1.4934705>

He⁺ ION BEAM-INDUCED LUMINESCENCE FROM DEFECT CENTRES IN α -Al₂O₃

OTKA K 143263, TKP2021-NVA-03

Z. Zolnai, M. K. Pal*, E. Kótai*, and E. Szilágyi*

*Institute for Particle and Nuclear Physics, HUN-REN Wigner Research Centre for Physics, Budapest, Hungary

Al₂O₃ is a promising scintillator material for energetic charged particle detection due to its luminescence in the near UV-visible spectral range emitted by optically active centres related to impurities or structural defects introduced into the wide bandgap material [1]. To study and optimize scintillator-based particle detector structures, ion beam-induced luminescence (IL) is a sensitive and effective analytical method. In this work, the IL light emission of α -Al₂O₃ was induced by a 1.5-MeV He⁺ ion beam and measured as a function of irradiation time (ion fluence) in the wavelength range of 200 nm - 1100 nm. We used He⁺ projectiles to simulate the effect of the daughter product in the ¹⁰B(n, α)⁷Li reaction, when thermal neutrons are detected via their conversion to 1.47-MeV α and 0.84-MeV Li⁺ projectiles which then generate light emission in a scintillator through electronic stopping. Two prominent IL emission bands were found and recognized as the well-known F and F⁺ centres [2, 3] related to oxygen vacancy defects with two electrons and one electron captured, respectively.

For a scintillator, sufficient sensitivity and proportionality between the number of α -particles (α -flux) and the intensity of the α -induced IL emission can be achieved if the response of the scintillator is fairly intense and stable in time. In order to see the effect of initial concentration of F and F⁺ centres on the IL response of Al₂O₃, both unimplanted and pre-implanted sapphire samples were measured by the IL technique. Pre-implantation was performed with 2.8-MeV energy N⁺ ions in the fluence range of 5 \times 10¹³ - 5 \times 10¹⁴ N⁺/cm², resulting in relatively high defect densities in the top 2 μ m region of the α -Al₂O₃ crystal. He⁺-IL experiments and N⁺ ion irradiation (pre-implantation) were performed by the EG-2R Van de Graaff accelerator at the HUN-REN Wigner Research Centre for Physics in Budapest.

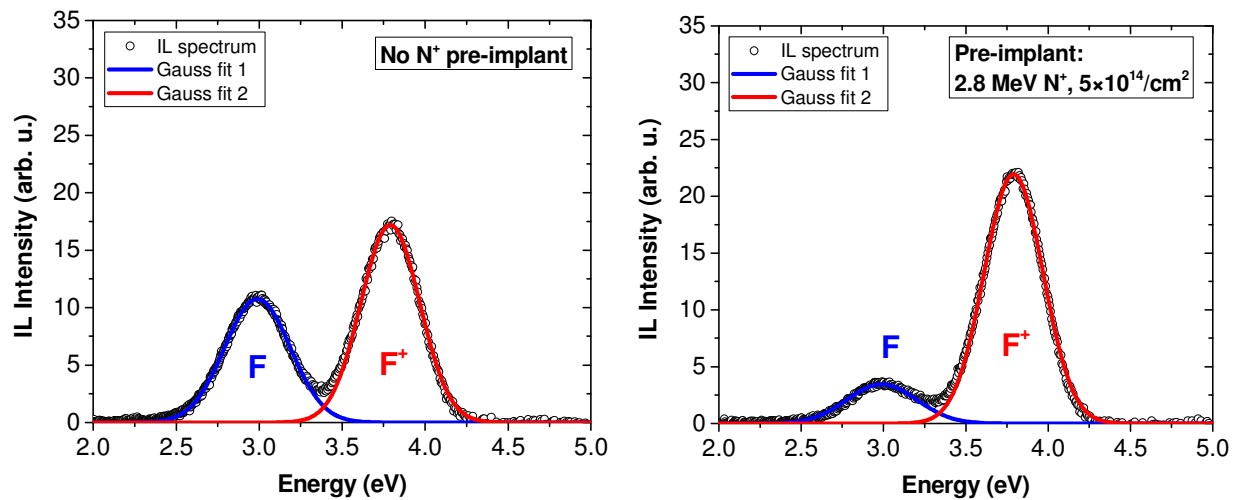


Figure 1: 1.5-MeV He⁺ ion beam-induced luminescence (IL) spectra of the F and F⁺ centres at a fluence of 1.2 \times 10¹⁶ He⁺/cm² for (left) unimplanted Al₂O₃, and for (right) Al₂O₃ pre-implanted with 2.8-MeV N⁺ ions to a fluence of 5 \times 10¹⁴ N⁺/cm² before the IL measurement. Blue and red lines show Gaussian fits for the emission bands related to the F and F⁺ centres.

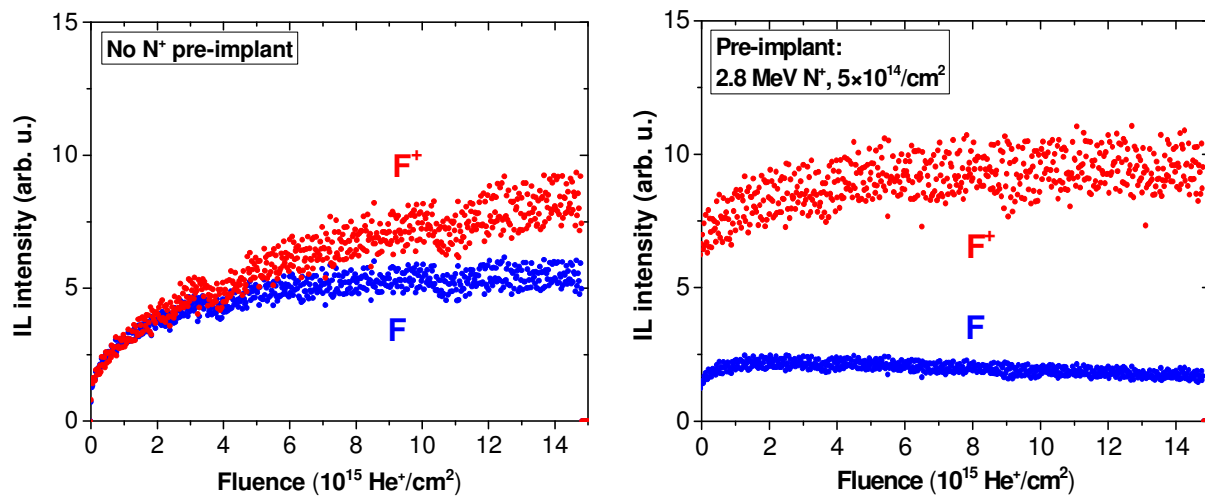


Figure 2: Evolution of 1.5-MeV He^+ ion beam-induced luminescence (IL) intensity of the F and F^+ centres vs. the He^+ irradiation fluence for (left) unimplanted Al_2O_3 and for (right) Al_2O_3 pre-implanted with 2.8-MeV N^+ ions to a fluence of $5 \times 10^{14} \text{ N}^+/\text{cm}^2$ before the IL measurement

Fig. 1 shows IL spectra of $\alpha\text{-Al}_2\text{O}_3$ after $1.2 \times 10^{16} \text{ He}^+/\text{cm}^2$ irradiation, both without and with N^+ pre-implantation. Spectra are shown after appropriate background subtraction and intensity normalization, taking into account the instrument function along the optical detection path and the quantum efficiency of the Charge Coupled Device (CCD) detector. Gaussian fits of the two prominent IL bands give peak positions of 2.99 eV and 3.79 eV, and Full Widths at Half Maximums (FWHM) of 0.42 eV and 0.35 eV, for the F and F^+ centres, respectively. These values agree well with previously reported ones [2, 3]. Strikingly lower F-centre related peak appears for the N^+ pre-implanted sample compared to the unimplanted one.

In Fig. 2, for $\alpha\text{-Al}_2\text{O}_3$ without N^+ pre-implantation, the emergence of the IL peaks starts after the He^+ ion beam was switched on. At higher He^+ fluences, a sublinear increase of the F and F^+ centre related IL intensity occurs. Nevertheless, for the F^+ centre a monotonous intensity increase can be seen, while for the F centre the IL yield saturates at a fluence of about $5 \times 10^{15} \text{ He}^+/\text{cm}^2$. The increasing IL yield trends are due to He^+ ion beam-induced defects, i.e., newly generated F and F^+ centres of which concentration increases with the He^+ fluence. On the other hand, for N^+ pre-implanted Al_2O_3 , relatively high F^+ -centre related IL appears right at the beginning of the IL experiment and the IL yield saturates already at a fluence of $4 \times 10^{15} \text{ He}^+/\text{cm}^2$. No significant change, yet slight decrease for the F-centre related IL can be observed. A striking difference is the more pronounced split between the IL yields of the two centres for the N^+ pre-implanted sample as compared to the unimplanted one.

In conclusion, significantly higher F^+ centre related IL can be detected in the low fluence range of He^+ ion irradiation for a sapphire sample with higher defect, i.e. F^+ centre concentration introduced by N^+ pre-implantation. Both for the F and F^+ centre, the IL intensity vs. He^+ fluence is more stable for higher initial defect concentrations. Differences in the F^+ to F centre related IL yield ratios can be due to different defect concentrations and compositions and related changes in the He^+ ion beam-induced excitation and subsequent de-excitation processes. These results can be utilized to optimize the structural properties of Al_2O_3 for charged particle detection via IL emission.

Related publications

- [1] G. Akselrod, M. S. Akselrod E. R. Benton, and N. Yasuda: *A novel Al_2O_3 fluorescent nuclear track detector for heavy charged particles and neutrons*, Nucl. Instr. Meth. B: **247**:(2) 295-306 (2006) <https://doi.org/10.1016/j.nimb.2006.01.056>
- [2] J. D. Brewer, B. T. Jeffries, and G. P. Summers: *Low-temperature fluorescence in sapphire*, Phys. Rev. B: **22**, 4900-4906 (1980) <https://doi.org/10.1103/physrevb.22.4900>
- [3] B. D. Evans and M. Stapelbroek: *Optical properties of the F^+ center in crystalline Al_2O_3* , Phys. Rev. B: **18**, 7089 (1978) <https://doi.org/10.1103/PhysRevB.18.7089>

ENHANCING THE NUCLEATION IN ATOMIC LAYER DEPOSITION: A STUDY ON VANADIUM SULPHIDE AND OXIDE LAYERS

OTKA FK 139075

Zs. Baji, Cs. Dücső, A. Sulyok, Zs. Fogarassy, O. Hakkel

Atomic Layer Deposition (ALD) consists of the consecutive chemisorption and reaction of different precursor materials on a substrate surface. According to theory, in ALD, when one precursor material is introduced into the reaction chamber, it chemisorbs on the heated substrate surface and connects to the reactive surface species on it. When all the available connection sites are taken, the surface is saturated, and the remaining unreacted precursor material is cleared out of the reaction space with an inert gas, and the next precursor is lead into the chamber. Once again, this precursor only reacts with the species of the first one, which are chemically bonded to the surface, after which, another purging follows with an inert gas. Thus, the result of each ALD cycle is exactly one monolayer of the composite material, in theory. However, there are limiting factors in the ALD growth as well. Supposing, that the basic conditions are satisfied, that is, the precursor is stable at the given temperature, the surface temperature is sufficiently high to activate the required chemical reactions, and the dosing of the precursor material is enough to saturate the surface, there are still limiting factors. The saturation density of a given surface depends on the number of reactive sites for the precursor adhesion, as well as the steric hindrance of the precursor molecules. As the ALD precursors are rather large molecules, therefore, when one binds to the surface, it covers more than one connection sites, although it only connects to one. This results in a lower than one monolayer per cycle growth in a usual practical ALD deposition process.

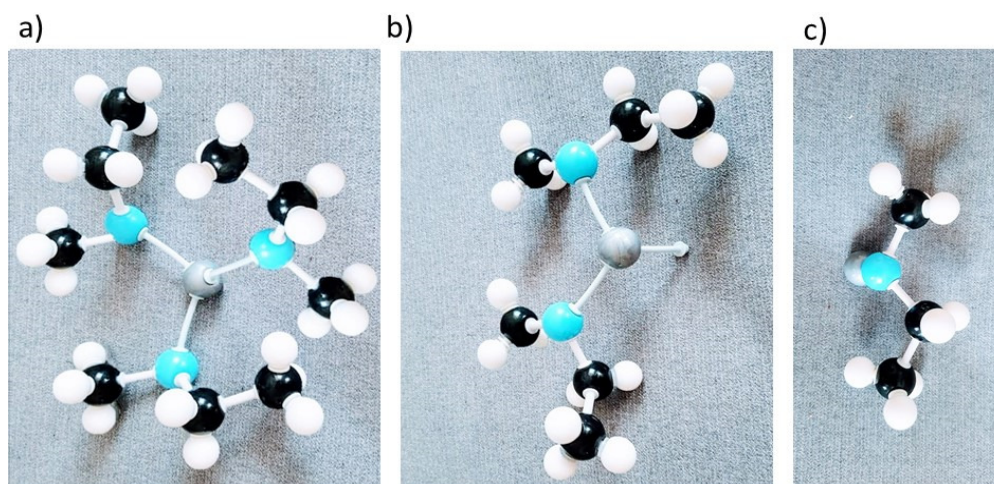


Figure 1: The different connection types of the TEMAV precursor to the Si surface: single bond with 3 remaining ligands (a), double bond with two remaining ligands (b), and one remaining ligands (c) covering more than one available sites

The other crucial hindering factor is the number of connecting sites on the surface. In a well-established layer growth, this barrier is not present, however, in the initial stages of nucleation it may cause difficulties. In most ALD processes, especially in the case of Si or sapphire substrates, the growth starts by the connection of the precursor molecule to the surface OH species. These can then act as nucleation centres for the following growth cycles.

One way to enhance the nucleation of ALD layers is to use longer precursor exposures in the first growth cycle to help the adsorption of precursor molecules to all available connection sites in the initial phase (first ALD cycle) of the growth. The other possible approach is to specially pre-treat the substrate surface in order to increase the density of the chemically active groups. In the case of oxide ALD, this means the hydroxylation of the surface. This may involve plasma or acidic pre-treatment followed by dipping the sample in water to fill the broken bonds with hydroxyl groups. In the case of sulphide layers, however, the situation is more complex.

The growth of sulphide films with atomic layer deposition also starts by the chemisorption of the metallic precursor to the hydroxyl groups on the surface followed by the sulphur containing precursor pulse, which is most commonly H_2S . This means that the first monolayer of the sulphide material consists of a metallic monolayer connected on one side to oxygen, and on the other side to sulphur, and in the further growth steps, more metal-sulphide monolayers follow.

The control of the nucleation of ALD growth is crucial, on the one hand, for the purpose of research aiming at the deposition of few atomic layer thick continuous layers. In the present research the initial growth of vanadium-oxide and vanadium-sulphide was studied on different surfaces. It was found that the growth of vanadium-sulphide always starts with an island-like growth, while vanadium-oxide exhibits a layer-by layer growth on sapphire, which is a lattice matched substrate, while an island-like growth is typical on silicon. The merging of the islands can be enhanced in both cases with an extra long initial ALD cycle to leave enough time for the precursors to fill all the connection sites on the surface.

The other approach is to increase the number of available and active surface sites with chemical pre-treatments of the surface. The number of surface OH groups can be increased with oxygen plasma treatment or a piranha etching prior to ALD growth. This improved the nucleation of both materials. However, the ligand exchange processes in the case of the vanadium-sulphide growth further hinders the nucleation process. This means that the as the V-S bonds are energetically more favourable than the connection of the metal to the OH groups on the surface, the chemisorbed V atoms agglomerate into islands where they share the already connected S atoms and form V-S bonds converted from the V-O bonds. While the surface OH groups resurface, the deposition must continue in a next cycle. Therefore, it proved to be a more favourable approach to increase the OH coverage of the silicon surface, and then exchange these to surface thiol groups to initiate the growth of vanadium-sulphide. With the thiolisation of the surface and 10 long pulses the continuous coverage shown in Fig. 2.c and 2.d could be achieved, as compared to the scattered islands shown in Fig. 2.a and 2.b.

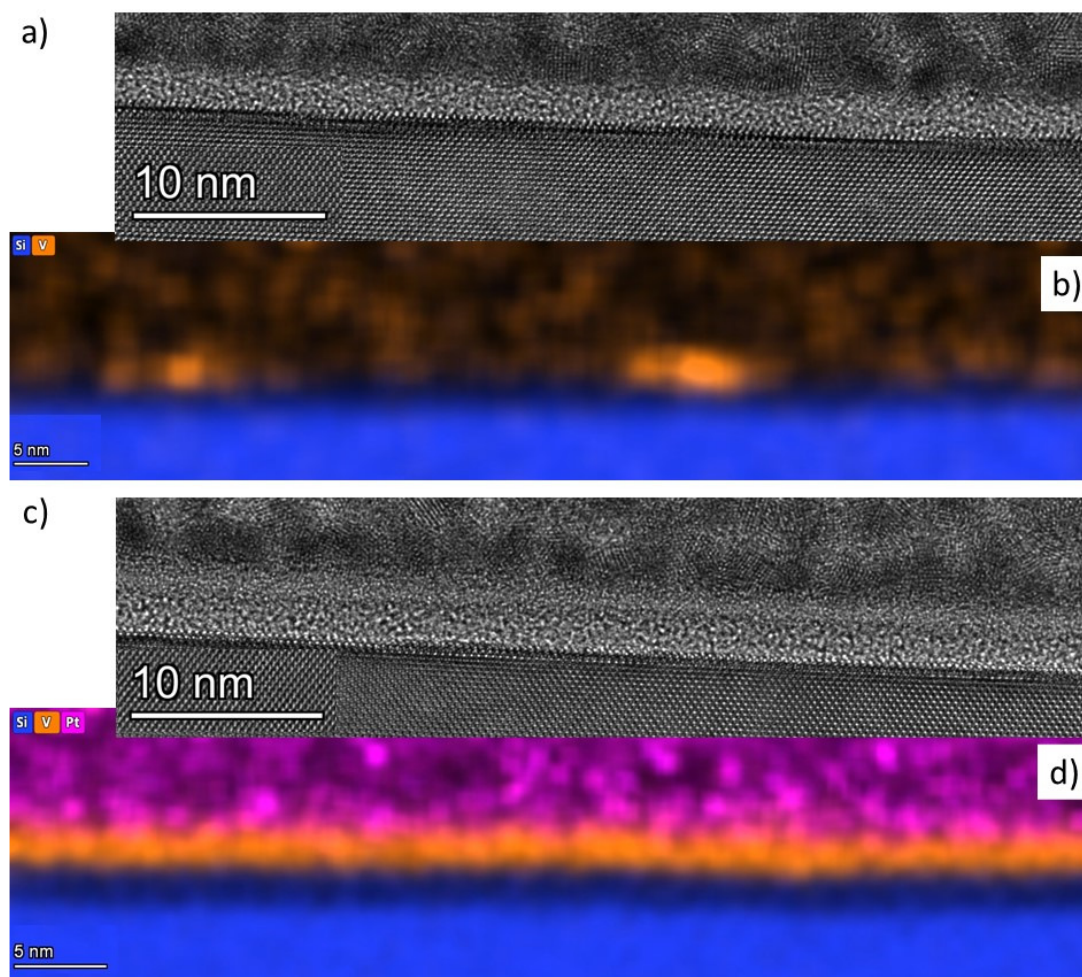


Figure 2: Island like vanadium-sulphide after 5 ALD cycles (a and b), and a continuous vanadium-sulphide layer on a thiolised Si surface after 10 long cycles (c and d)

RESISTOR NETWORK SIMULATION OF VO₂ NANOGAPS

OTKA K143282, János Bolyai Research Scholarship,
 ÚNKP Postdoctoral Scholarship

L. Pósa, Sebastian Werner Schmid¹, Tímea Török, Miklós Csontos²

¹Department of Physics, BME, Budapest, Hungary, ²EMPA, Dübendorf, Suisse

We employed two-dimensional resistor network model to simulate the dynamic behaviour of our nanosized VO₂ device. In this concept, the active region is modelled as an array of cells arranged in a square lattice (Fig. 1.a). Each cell corresponds to a small, nanosized part of the VO₂ layer, in such a way that its electronic state is still well defined, which can be either insulating (I-VO₂, blue) or metallic (M-VO₂, red). To obtain more accurate results, we applied realistic contact geometry by using gold cells (Gold, yellow) in the simulation area arranged in rectangular and triangular shapes. The 20 nm large electrode separation in the real device is converted into 2 cells in the simulation, accordingly, the cell size in our model is 10x10 nm, whereas the thickness of the layer is 40 nm. Each cell consists of four identical resistors, and initially all VO₂ cells are in the insulating OFF state. In analogy to the experimental setup, a load resistor (R_L) is connected in series with the resistor network and the waveform generator.

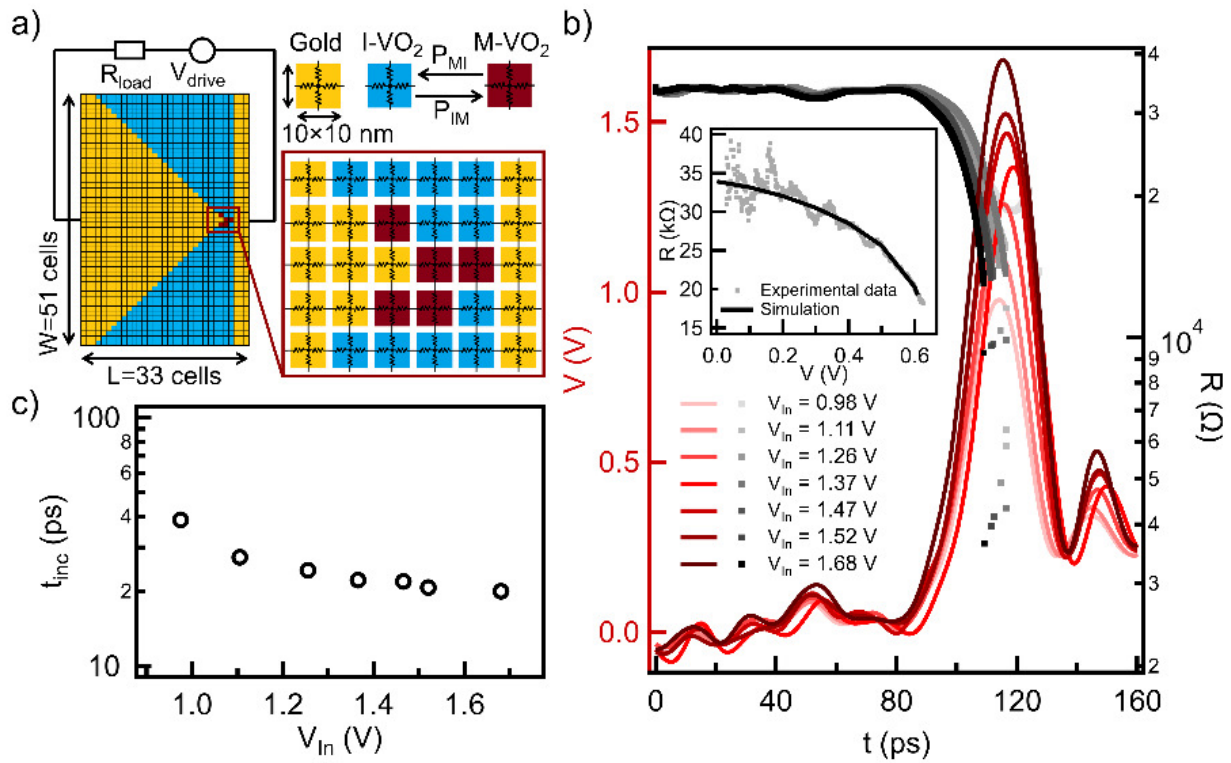


Figure 1: (a) Schematic diagram of the resistor network model and the electrical circuit. The cells in yellow correspond to the gold electrodes with very low resistivity. Cells in blue and red represent the 40 nm thick VO₂ layer, which is in thermal contact with an electrically perfectly insulating substrate. These cells can be either in the insulating (blue) or metallic (red) phases, the dynamics of the transformation between the two states is determined by the transition probability of P_{IM} and P_{MI} . (b) The experimentally applied waveforms (red curves) and the resistance answer of the resistor network (grey dots). At the moment of the set transition the resistance suddenly jumps several orders of magnitude. The different shades of red and grey corresponds to the different voltage amplitudes. The inset shows the experimentally captured $R(V)$ curve of the device in the high resistance state (grey dots) and its fit by the simulation (black curve). (c) The simulated incubation time versus driving voltage amplitude, showing good agreement with the experimental data.

The electrothermal model of the resistor network simulation is based on our previous finite element simulation in COMSOL Multiphysics [1], applied to the high resistance state of a similar VO₂ phase change memory device. The resistance of a single resistor of an I-VO₂ cell depends on both the local temperature and the local electric field, whereas in the ON state, we assumed temperature and electric field independent resistance. However, the device operation was only modelled until the moment of the set transition, therefore the electrical and thermal parameters of the ON state do not affect the outcome of the simulation.

In our model, the phase transition is a thermally activated process, in which the transition probabilities of the cells (P_{IM} and P_{MI}) depend exponentially on the temperature. The local temperature is determined from the heat equation considering the

positive contribution of Joule-heating and the negative contribution of the heat conduction to the neighbouring cell and to the substrate. Furthermore, a boundary thermal resistance was considered between the VO₂ and the gold cells.

The electrical and thermal material properties of the VO₂ layer were determined by fitting the experimental R(V) trace of the device by the simulation, see inset of Fig. 1.b. After setting the device-specific parameters, the experimentally realized voltage signals (red curves in Fig. 1.b) could be applied to the resistor network. The model was solved by using 0.1 ps long time steps. The grey curves in Fig. 1.b show the evolution of device resistance in time. In all cases, the phase transition can be captured by the sudden jump of the device resistance, and, in agreement with the experiment, it occurs earlier as the voltage amplitude is increased. To study this trend quantitatively, we determined the incubation time using the same method as for the experimental data, calculated from the moment when the incoming pulse reaches 10% of its maximum until the resistance jump. The simulated incubation times (Fig. 1.c) fall to the same 10-50 ps regime as our experimental observation with a similar decreasing tendency with the pulse amplitude [2].

Related publications

- [1] L. Pósa et al.: *Interplay of thermal and electronic effects in the mott transition of nanosized VO₂ phase change memory devices*, ACS Applied Nano Materials **6**, 9137–9147 (2023) <https://doi.org/10.1021/acsnm.3c00150>
- [2] S. W. Schmid et al.: *Picosecond Femtojoule Resistive Switching in Nanoscale VO₂ Memristors*, ACS Nano **18**, 21966–21974 (2024) <https://doi.org/10.1021/acsnano.4c03840>

ALGaN/GaN HETEROSTRUCTURE BASED FREQUENCY SELECTIVE VIBRATION SENSOR

TKP2021-NVA-03

P.L. Neumann, Á.J. Vándorffy, J. Ferencz, J. Volk

GaN, as a piezoelectric, piezoresistive, and pyroelectric wide-bandgap semiconductor, can be a key material for the new generation of power electronics and micro- and nanoelectromechanical systems (MEMS, NEMS). While commercial Si-based sensors show limited applicability in the field of human bioimplants due to their low interaction rate with the body, GaN shows excellent biocompatibility [1]. Beyond its outstanding behaviour, epitaxial thin compound-alloy layers are already commercially available on Si carrier wafers, which are technologically compatible with standard Si MEMS processes. However, in contrast to conventional Si piezoresistive devices here, the mechanical strain influences the density of the 2-dimensional electron-gas (2DEG) at the AlGaN/GaN interface by changing the magnitude of polarisation vector discontinuity [2]. Here, we present a novel AlGaN/GaN heterostructure-based resonant cantilevers for frequency-selective vibration analysis, which can offer a new solution for fully implantable cochlear implants. The external mechanical vibrations generated, e.g., by the middle ear's eardrum, can be converted into electrical signals. Hence, the magnitude and the frequency of the vibration can be determined.

The 2DEG sensor elements were fabricated on a commercial High-Electron-Mobility Transistor (HEMT) epilayer stack (GaN/AlGaN/GaN) grown onto a 4" Si wafer (NTT-AT). Meander-shaped MESA structures were formed at the eigenfrequency-related locations (antinodes) and at the anchoring position of the beam, where the strain in the thin beam layer is the highest. The desired locations were determined by finite element analysis using Comsol Multiphysics (Fig. 1.a). The carrier Si layer was etched back by a deep reactive etching step, while the final cantilever tailoring was done by focused ion beam (Fig. 1.b). The metal electrodes were prepared by e-beam evaporation and a subsequent Rapid Thermal Annealing (RTA) step for Ohmic contacts. The significant built-in stress causes the cantilever to bend after release.

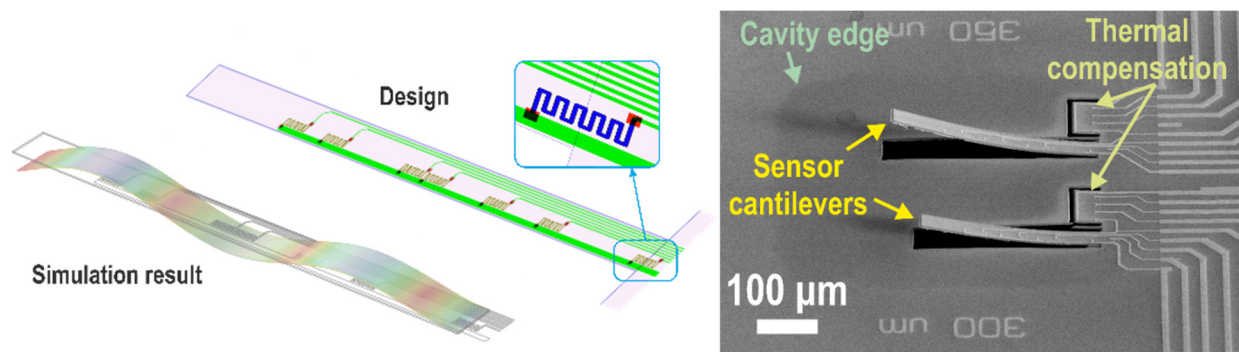


Figure 1: Schematic (top) and dynamic simulation (below) of the AlGaN/GaN beam (450 μm long) with the MESA meander sensor elements in the antinode positions (a-left). SEM image of the 350 μm and 300 μm long compound semiconductor beams with the resistive meanders (b-right) Thermal compensation beams were fabricated using the same meander elements.

During the previous study as a force sensor experiment, a continuous base signal moving was observed on sensor elements. Analysis of the problem at IV curves of sensor elements on membrane and on bulk show different behaviour because the membrane sensor meander increased the resistance instead of above bulk, which was linear. It can be ascribed to thermal effect: though the thermal resistivity is almost the same for Si and for GaN, heat channel is significantly shallower for the cantilever (1.2 vs. 400 μm). To eliminate the self-heating problem, thermal compensation was applied using a subsidiary beam. All sensor elements and the equivalent value reference resistors set the exact temperature dependence behaviour for the sensor device.

The vibration modes of the cantilevers were analysed using a scanning vibrometer (SmarAct PicoScale) confirming the frequency selectivity of the fabricated cantilevers. The obtained resonances agreed well with the FEA results (Fig. 2.a). As expected, the resistance changes due to externally induced static stress in the layer showed linear dependence. This was followed by electrical tests using a Source-Measure-Unit (SMU) to study the self-heating effect and the effect of thermal compensation. Finally, dynamic electromechanical tests were performed on the wire-bonded dies (Fig. 2.b) to study the sensitivity and frequency-tunability of the sensor. Besides the results of dynamic electromechanical tests, the role of the composition of the $\text{Al}_x\text{Ga}_{1-x}\text{N}$ barrier layer, the length and position of the sensitive channel, as well as the thermal stability of the heterostructure sensor will also be addressed.

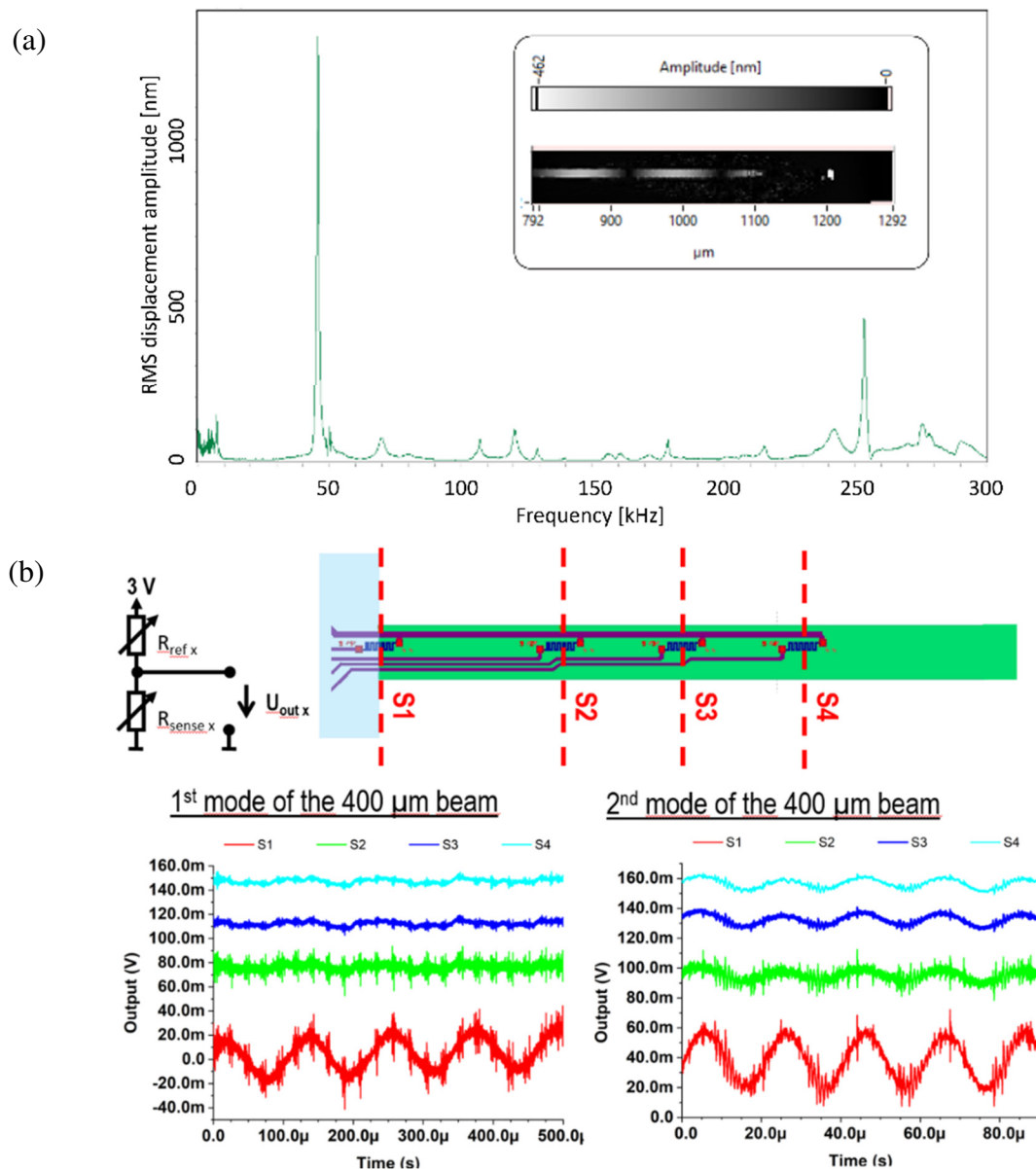


Figure 2: Frequency analysis of a 450 μm beam by scanning vibrometer (a-top). The inset shows the amplitude response for external excitation at one resonance frequency. The output voltages are of the voltage dividers during shaking at the resonance frequencies (b-bottoms). The output voltage characteristics reflects well the position of the meanders on the cantilever.

Related publications

- [1] S.A. Jewett, M.S. Makowski, et al.: Gallium nitride is biocompatible and non-toxic before and after functionalisation with peptides, *Acta Biomaterialia* **8**:(2), 728-7333 (2012) <https://doi.org/10.1016/j.actbio.2011.09.038>
- [2] J. Jiang, Q. Wang, B. Wang, et al.: Direct lift-off and the piezo-phototronic study of InGaN/GaN heterostructure membrane, *Nano Energy* **59**, 545-552 (2019) <https://doi.org/10.1016/j.nanoen.2019.02.066>

SMART SCALPEL – A NOVEL FORCE-SENSOR-BASED SURGERY HAND TOOL

TKP2021-NVA-03

J.M. Bozorádi, A. Nagy, F. Braun, L. Illés, P. Révész, J. Volk*

**Department of Otorhinolaryngology-Head and Neck Surgery, University of Pécs, Hungary*

In 2022 we carried out experiments on various ex-vivo samples at the Clinic of the University of Pécs. Our goal was to determine the rupture force necessary to cut the chorda tympani, also known as the taste sensing nerve. This small part of the human ear is very easily damaged during surgeries related to otosclerosis and other illnesses. Development of equipment used in this area could greatly benefit from the results. During the earlier tests we suspected that neither micro manipulation, nor traditional tissue testing methods (such as axial and indentation testing) will be suitable for this particular tissue. In early 2023 we carried out an in-situ measurement technique utilizing handheld electronics developed according to the needs of medical professionals. A new UV hardened polymer covering was also developed for the 3 dimensionally sensitive force sensor placed in the scalpels' tip. Last year we reported that the estimated force necessary to cut the chorda tympani could be as high as 1.77 N. Our recent findings from in situ measurements on human cadavers elaborate on this. (Tissue tests were conducted under ethical authorization 8733 – PTE 2023.)



Figure 1: "Smart scalpel" surgical force measurement tool: head and electronics with covering

The electronics and its coverings were specified with the ergonomics for the surgeon and its application during actual surgical procedures in mind. The tip itself was also designed for easy handling during surgical conditions. The Bluetooth Low Energy circuit ran from a fast chargeable super capacitor which provided about an hour of continuous use. Calibration of the sensor heads were done via reference force gauge both during sensor development and on-site by the surgeon's movements. Readout and data acquisition still run on a laptop using a LabView VI, however we have started the development of an Android based version. Sample preparation consisted of the normal surgical procedure done by the surgeon. After lifting the eardrum to make the inner ear and the chorda tympani accessible, a total number of 10 measurements were performed with varying results. In five cases we measured similar tear characteristics to the in vitro samples. The surgeon concluded that these cuts were not characteristic of the rupture phenomena that occurs during surgery. However, he confirmed that even this – with a load of 300-500mN – is sufficient to damage the structure of the chorda tympani. On the other hand, cuts were deemed appropriate by the surgeon are uncertain as to the value of the tensile force. The measured values are magnitudes higher than what the sensor could theoretically withstand. The two possible explanations are either measurement error, or that the needle tip was hit to the wall of the inner ear. However, if we look at the force characteristics right before the spikes, we see a similar magnitude as with previous measurements, which further proves that a force as low as a few hundred millinewtons are enough to rupture such sensitive tissue of the human body.

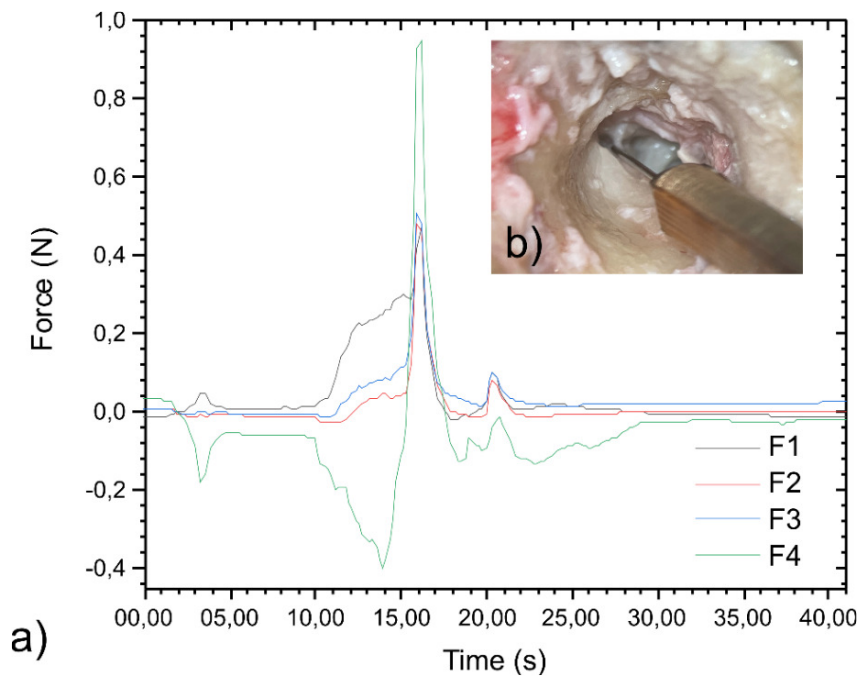


Figure 2: Force sensor signals recorded during a chorda tympani rupture test (a).
Photo of the smart scalpel in operation (b).

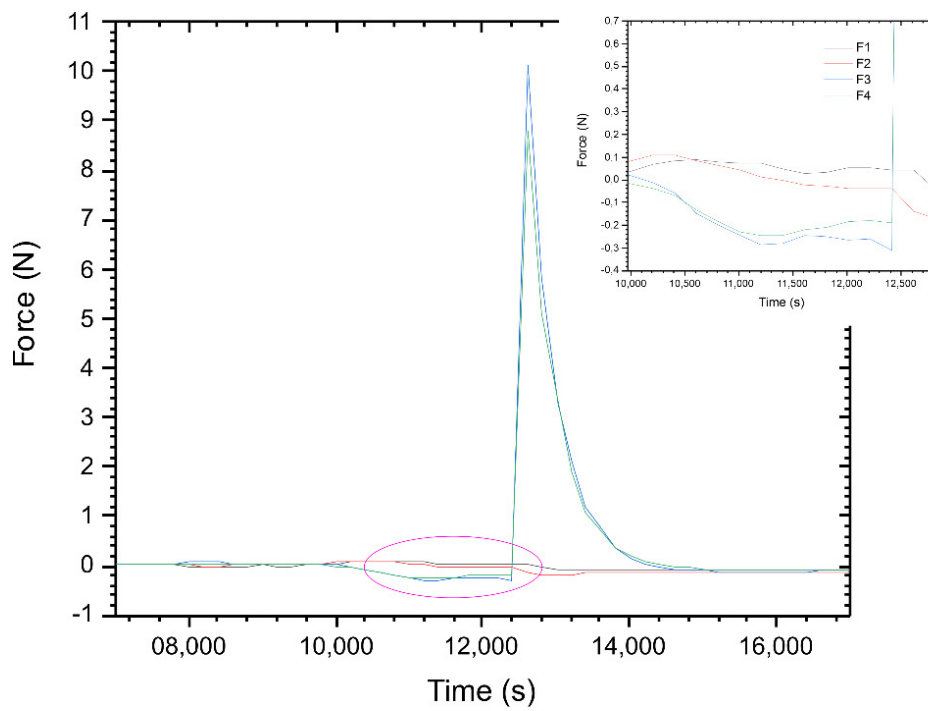


Figure 3: Pulsed rupture characteristics of the so called "perfect cut"

FIRST STEPS TOWARD KITAEV TRANSMON GENERATION

Quantum bits with Kitaev Transmons (QuKIT) HORIZON-EIC-2022-PATHFINDERCHALLENGES-01-06-101115315

M. Sütő*, Z. Kovács, P. Makk*, Sz. Csonka*

*in collaboration with the Department of Physics, BME, Budapest, Hungary

While quantum computing promises algorithms that are orders of magnitude faster than what is achievable by normal computers, the physical realization of such systems is highly challenging. One of the most dominant obstacles is their sensitivity to noise, which strongly limits their current viability. Joining the QuKIT international collaboration, we aim to create a system capable of accommodating a fault tolerant quantum bits by combining the well-established and controllable transmon qubit with a Kitaev chain. It introduces topological protection (Fig. 1.a) to significantly enhance their tolerance to external noise. While creating a transmon qubit is a well-established process requiring a high quality superconducting thin film, the challenge of the proposal coming from the other two parts: the realization of the Kitaev chain, and the coupling of the two systems. Our part in the collaboration is related to both challenges.

To realize topological superconductivity required for the Kitaev chain, we use an InAs based near surface (7 nm below surface) two-dimensional electron gas (2DEG), which is contacted by an epitaxially grown aluminium layer. This introduces proximity superconductivity into the semiconductor through their high-quality interfaces. The heterostructure is shown in Fig 1.b. Our primary goal is to realize a minimal Kitaev chain, for which the first step would be a simple quantum dot, that later can be expanded to create Andreev molecules (two dots coupled by a superconducting lead), then the Kitaev chain itself. The fabrication of the devices has already started (Fig. 1.c). Here the Al layer is removed from the surface, which is then covered by AlO_x thin film. Afterwards we created two sets of gate electrodes, to form the qdot, which electrodes are shown in the SEM image. While in its current form it is only capable of hosting a single quantum dot, the design is highly scalable, and the fabrication steps are basically unchanged. Our aim is to measure a quantum dot this spring, and in the meantime optimize the aluminium's chemical etching, to create a qdot-SC-qdot device, achieving half of a minimal Kitaev chain.

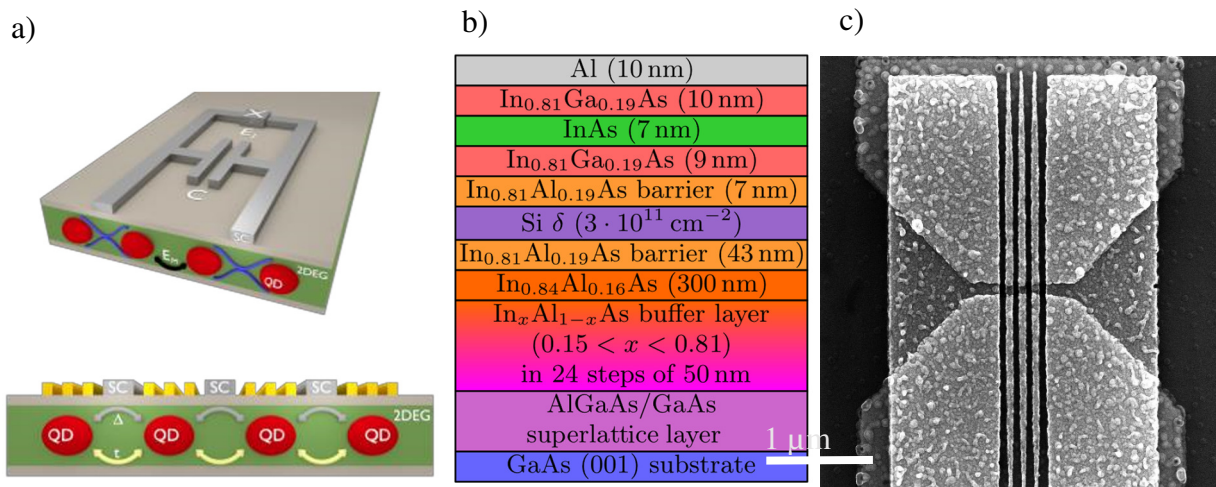


Figure 1: Schematics of the novel Andreev qubit formed by coupling a traditional transmon to a minimal Kitaev chain (a) (source: QUKIT Proposal Part B). A great candidate for the realization of the Kitaev qubit: near surface InAs 2DEG contacted by an epitaxial Al layer (b). One of our early attempts to fabricate gate electrodes necessary for a simple quantum dot that is scalable to create Andreev molecules and eventually a minimal Kitaev chain (c).

WEARABLE GAS SENSORS FOR EMERGENCY AND EXTREME CONDITIONS

Thematic Excellence Program TKP2021-NVA-03

F. Bíró, I. Bársony, Z. Szabó, Cs. Dücső

Gas sensor applications for wearable devices

In the „Chemical gas sensors” workpackage of the Thematic Excellence Programme TKP2021-NVA-03 „Environmental monitoring sensors for emergency and extreme conditions” project we plan to develop wearable and mobile gas sensors (on drones and controlled robots) for detection dangerous gases carry high risk during natural or industrial disaster management (time frame: April 1. 2022 – March 31. 2026). The primary goal is the recognition of methane leakage; however, detection of other risky gases will also be investigated. Our goal is to reach the TRL4 (in demo devices) and TRL6 for prototypes with dedicated readout and communication electronics, or commercial demo kit.

Two families of gas sensors are considered:

low cost solid-state catalytic and chemoresistive sensors for demo applications

target gases: H₂S, HCN, NH₃, N₂O, Cl₂ or HCl (1-10-100ppm - Threshold Limit Value (TLV) level or above) – upon the interest of the corresponding partner of supervising authority

moderate cost optical sensor for more accurate concentration measurements

target gases: CH₄, LPG, PB 1–5 %v/v (possibly CH₄ ~ 100 ppm)

Test platform for chemoresistive gas detectors

Regardless the operation principle, the calorimetric or chemoresistive sensors operate at elevated temperatures between 100 – 500°C. The basis of our calorimetric sensors is a newly developed small diameter (150µm) microhotplate exhibiting ±1% temperature uniformity on the heated area below 550°C. The stability of the heater is 5000 hours at least at the operation temperature of 530°C, thereby in pulsed mode operation ca. 5 years operation can be achieved. The power dissipation at 500°C is 27mW/1.5V, so the chip can be utilized in portable or wearable devices for personal safety. A utility model protection was given for the microhotplate design in 2021 (*Microheater with uniform surface temperature*, U 20 001150, registration number 5279). Accordingly, we exploit our previously developed microhotplate structure as the carrier of the gas sensitive material.

In a parallel device development, we have started to elaborate a dedicated tool for functional testing the chemoresistive materials. Our goal to provide easy-to-use platform for the laboratories intended to develop gas sensing materials for testing the performance of their locally deposited sensing layers. Our kit will contain an easy-handle hotplate chip with read-out electrodes and a masking element to enable the selective deposition of the sensitive layer. With this kit many research group can easily enter in the device development as they do not need the complex technology to fabricate the carrier chip.



Figure 1: Microheaters with different electrodes for performance testing the sensitive materials

Optical gas sensing

We have been investigating the construction and capability of methane detection by non-dispersive operation principle in the mid infrared region. The goal is to develop a complete setup consists of MEMS elements, such as microheaters and reflectors for IR source, optical channels and detectors. Test setup was built from commercial components, whereas the electronics was constructed in modular form for **driving the IR source** and the **appropriate read-out**. The preliminary results show that the construction is capable to detect methane in the 500 – 50000 ppm concentration range with the accuracy of 1-10%. We continued the work with the construction of a **dedicated and optimized electronics** to minimize the device size and investigate its long term performance. In frame of the TKP 2021-NVA-03 Grant 2nd workpackage design and fabrication of novel prototypes of Non-Dispersive Infrared (NDIR) optical gas detector had been carried out. Based on preliminary experimental

results the compact analogue and also the digital version of the NDIR methane detector have been designed and fabricated. Calibration procedure, sensitivity and stability tests were performed indoor. According to test results we may say that **digital NDIR sensors are capable to response in 7-8 seconds to 1 or 2 %v/v methane exposure as it is recommended by the industrial standard.** Meanwhile, the detector consumes 120-150mA current which is still below the maximum permissible 200mA current consumption. Fig. 2 illustrates the constructed devices and some experimental results.

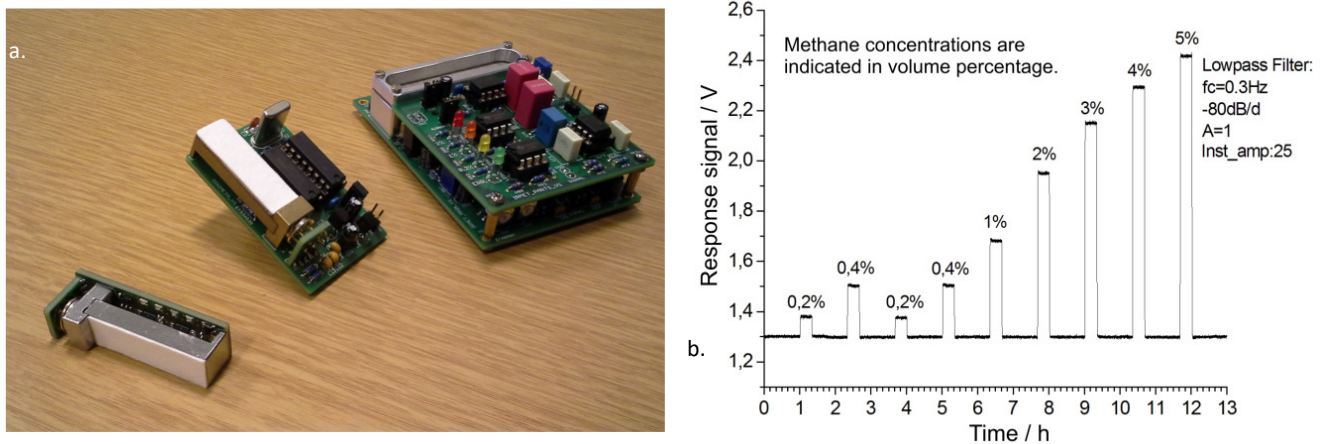


Figure 2: Illustration of the NDIR detector prototypes and their response signals. a) The analogue (right) and the two versions of the digital NDIR methane detectors equipped with dust filters. Device at left was designed for the portable gas sensing systems. b) Typical response signal of the analogue detector.

Microcalorimeters

Having in hand the **stable heaters** we now also focus on other applications. In cooperation with the University Debrecen we develop a **micro-calorimetric measuring method** to investigate thermally indicated physical-chemical phenomena in thin films. [1] [2]

Related publications

- [1] F. Bíró, A. Deák, Cs. Dücső, Z. Hajnal: *Microheater with uniform surface temperature*, Utility model: U 20 001150, registration number 5279
- [2] L. Harasztosi, I. A. Szabó, F. Bíró, R. Gy. Kiss, G. Battistig: *Temperature Calibration of Twin Micro-heater Based Microcalorimeter*, *Sensors&Transducers* **260**:(1), 7-13 (2023)
http://www.sensorsportal.com/HTML/DIGEST/P_3288.htm

3D MEMS FORCE SENSOR FOR TISSUE RECOGNITION

H2020-ECSEL-2017-2-783132 POSITION-II, 2018-2.1.6-NEMZ-ECSEL-2018-00001

J. M. Bozorádi, Zs. Bérces, P. Földesy, G. Pap (Uzsoki Hospital), Cs. Dücső, P. Fürjes

Laparoscopic devices have been widely used in the past decades during surgical procedures. Currently they are the golden standard in minimal invasive surgery. Furthermore combining these devices with robotic platforms is more and more common. Minimally Invasive (robotic) Surgery (MIS) offers several advantages for the patients, although the lack of sensory feedback for the surgeon is also a barrier in its progress. Gathering immediate multi-parametric information about the physical and anatomic conditions of tissues is crucial for the operator to precisely control the robotic actions or support the tissue recognition and pathologic characterization. Smart devices with integrated MEMS force sensors can provide such feedback and improve the safety of these interventions or help in on-site pathologic decisions. *A growing interest was recognised in these compact systems to be able to provide information regarding tissue thickness, stiffness, composition and the effect of the surgeon's current action.*

Accordingly our goal was to develop a novel device with integrated micromachined 3D force sensors to provide tactile information about the different organs and tissues touched. Piezoresistive force sensory units were integrated with dedicated readout electronics and precisely controlled linear motors solving the accurate tissue deformation to provide more information about the mechanical (elastic) parameters of the analysed materials. We demonstrated the complex, automatized measurement system – as well as hardware and software solutions – which is capable of implementing in vitro mechanical tissue characterization and thus provides elastomeric and pathological data. On the basis of the preliminary results both a compact measurement setup and a prototype electronics were adapted in a more compact test stage applicable for on-site in vitro human tissue measurements (see Fig. 1). This version was outfitted with a more robust precision stepper motor which had a DC servo controller integrated for component reduction. Without any reference force gauge, it relies only on the sensor and electronics developed at Microsystems Laboratory. Disposable sensor PCB-s were used for sterility reasons, each calibrated before distributing them in a 3D printed carrybox to the hospital. The whole measurement can be controlled through a LabView based Windows application.

The setup and the LabView based software package were optimized for the easy use of medical professionals. The human tissue measurements were initialized in the Uzsoki Hospital, after receiving ethical permissions – as presented in Fig. 1. More than 40 samples were tested with various results which involved a section of the large intestine in most cases. Numerical analysis of the force-displacement curves shows that an integrated version of the system can be used to determine tissue thickness and the modulus of elasticity. However, to provide relevant feedback to medical personnel we need a more complex and statistically larger dataset with more information. [1]

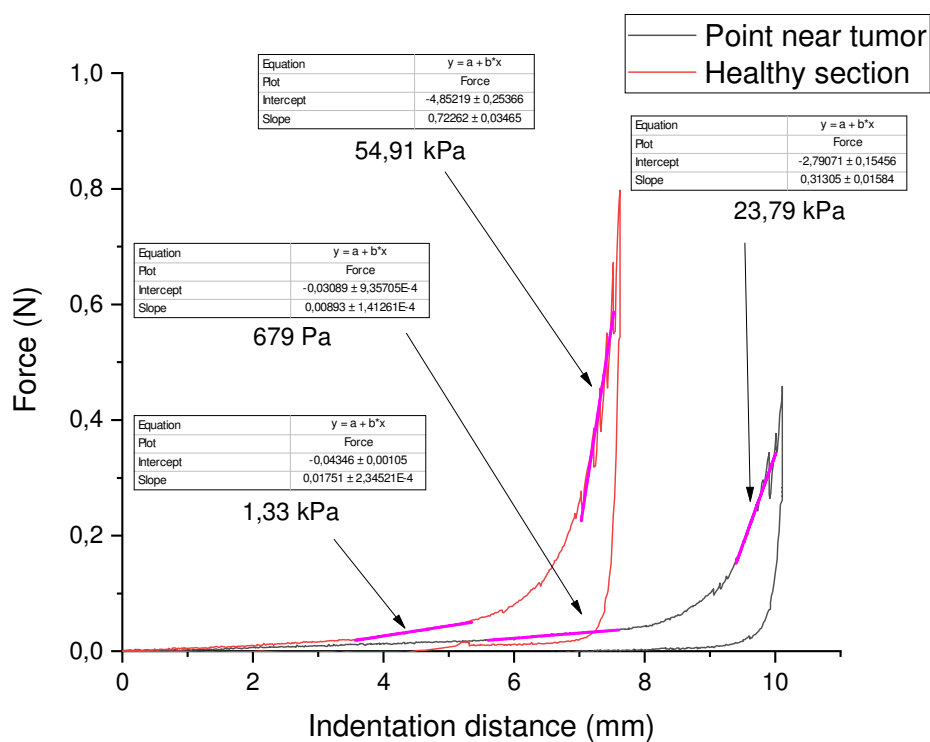
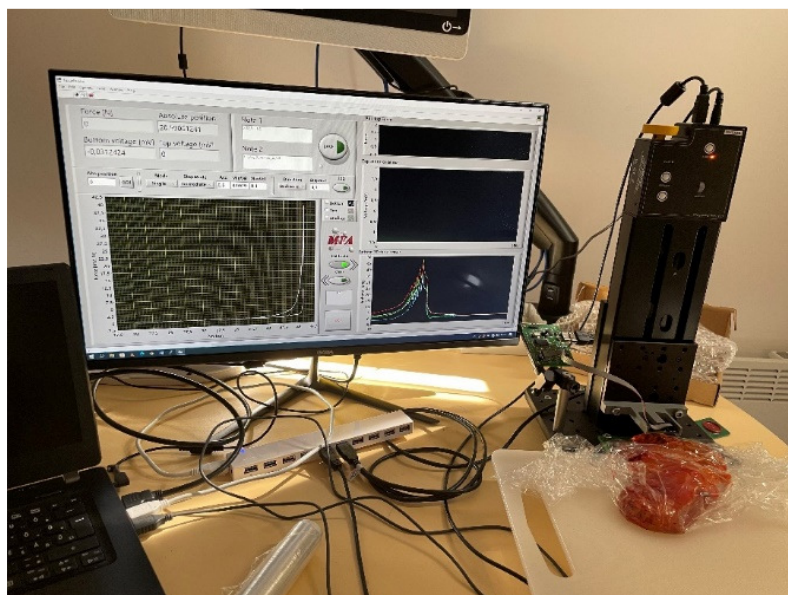


Figure 1: Compact automated tissue elasticity measurement setup in the Uzsoki Hospital (top), and the comparison of the mechanical characteristics (force vs. deformation function) of the healthy and cancerous gastric tissues (bottom)

Related publication

- [1] Bozorádi J. M.: 3D MEMS erőmérő szenzorok alkalmazása biomechanikai vizsgálatokra, 36. OTDK Műszaki Tudományi Szekció, Egészségtudomány 1 Tagozat, II. HELYEZÉS – témavezető: Fürjes Péter

MICROFLUIDIC METHODS FOR PARTICLE AND CELL MANIPULATION AND ANALYSIS

Thematic Excellence Program TKP2021-EGA-04

A. Bányai, L. Bató, Zs. Szomor, E. Leelőssyné Tóth, M. Varga (77Elektronika Ltd.), P. Fürjes

In the field of microfluidics, the development of medical Point-of-Care (POC) diagnostic platforms, which can be used at the patient's bedside, ambulances or medical offices, has received great emphasis in recent decades. The applied integrated Lab-on-a-Chip cartridges must include transport and filtration of the liquid sample, positioning of cells and bacteria in the detection chamber over the sensing layer, and high sensitive detectors also.

Lateral focusing model particles and real cell samples

Related to the development of the Rapid Urine Bacteria Analyser (RUBA) by 77 Elektronika Kft., the need arose for a consumable, which is suitable for appropriate sample transport, sample preparation, target separation, enrichment, and lateral positioning in the sensor zone. In urine elements with various size can be found from the squamous cells with a typical diameter of 60 μm , through various shapes and sizes (crystals, fungi, hematopoiesis), even bacteria with a size of 1- 4 μm . The advantage of the label-free cell separation methods is that these can be performed by utilising the variety of the physical parameters of the cells - size, shape, density, flexibility, polarizability. Hydrodynamic principle based **microfluidic filters and lateral concentrating structures** were developed and evaluated by their filtration efficiency for different particle sizes. The particle size, the channel geometry, its cross-section and the flow Reynolds number also influence the focal points of the particles' position in the cross-section of a microfluidic channel. Counter-rotating Dean vortices in the channel cross-section also can help the degree of focusing. Particles of different sizes occupy different equilibrium positions in the flow. The method can be used to filter cancer cells, to separate haematopoiesis or bacteria, also in the case of samples that behave as non-Newtonian fluids (milk, undiluted blood).

The possibilities of lateral concentration and positioning of cells and particles were investigated in a microfluidic channel with a periodically changing cross-section and geometry with asymmetrical bends. In this case the focusing positions of the particles in the channel are affected by the appropriate ratio of the occurring hydrodynamic forces: the radial migration is more dominant as the ratio of the particle size to the channel size and the Reynolds number of the flow increase, in addition, the secondary Dean flow occurring in the tortuous channel. The position of focused beads were tested at different flow rates. As expected, the larger beads were focused in the middle of the channel with a shorter path, but the concentration of the smaller beads could only be achieved by significantly narrowing the critical cross-section of the fluidics or by significantly increasing the period number. The experimental measurements were compared to the results of the numerical simulation of finite element models, examining the effect of the channel cross-section and the flow velocity on the behaviour of the emerging Dean vortices. The simulation results were in good agreement and supported the experimental data (Fig. 1). Accordingly, the applicability of the applied model was convincing in case of predicting the behaviour of the microfluidic systems.

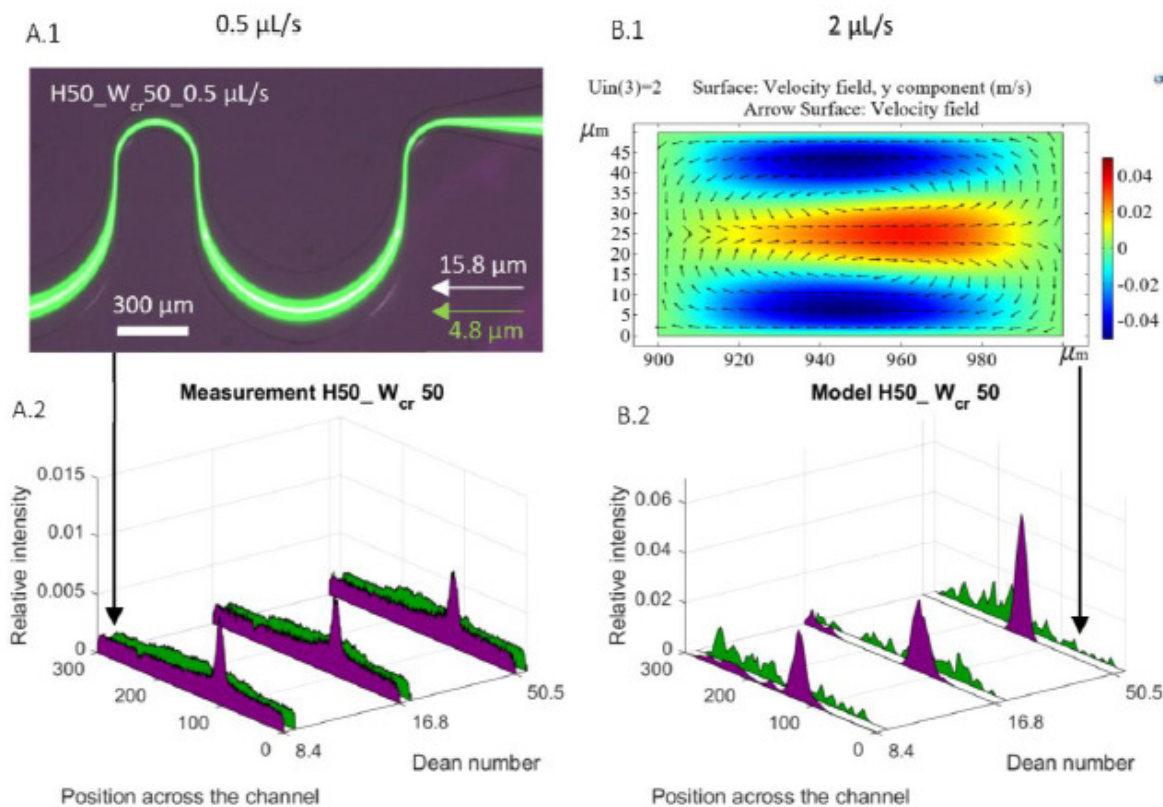


Figure 1: Illustration of the behaviour of rigid polystyrene beads (\varnothing 4.8 and 15.8 μm) in $H50_{W_{cr}50}$ fluidic channels with different critical cross-sections at flow rates of 0.5 – 1 – 2 $\mu\text{L/s}$ (Dean numbers calculated from it). Experimental results: detection of the bead positions taken at the output based on fluorescence intensity (A.1 – A.2). The results of the numerical simulations illustrate the distribution of the velocity field in the x - y plane in the smaller bend of the channel ($W_{cr} + 50 \mu\text{m}$) at a flow rate of 2 $\mu\text{L/s}$ (B.1), as well as the lateral distribution of the beads (on the y axis) after 23 bends (B.2).

Spherical polystyrene particles are well suited for modelling the behaviour of cells in microfluidic systems, where the degree of deformation of the cells or their form of movement in the flow does not affect their equilibrium positions. Model bead position map was recorded for reproducing the behaviour of the chosen biological cells in our microfluidic system: *E. coli* [0.5-2 μm ; stick], red blood cell [2.5; 6-8 μm ; disc-shaped biconcave], yeast *Saccharomyces cerevisiae* [5-10 μm ; round or oval] and HeLa cell line [16-29 μm ; diverse, inhomogeneous, spherical in suspension], which differ not only in size but also in shape. To set up a position map (Fig. 2), the following bead sizes were used: $\varnothing = 0.5 - 1.1 - 1.97 - 2.9 - 4.8 - 5.4 - 6.08 - 10.2 - 15.8 - 16.5 \mu\text{m}$. The experiments took place in the chosen $H=25_{W_{cr}=50}$ structure. The equivalent bead size used for modelling the biological sample was determined by overlapping the lateral focusing positions.

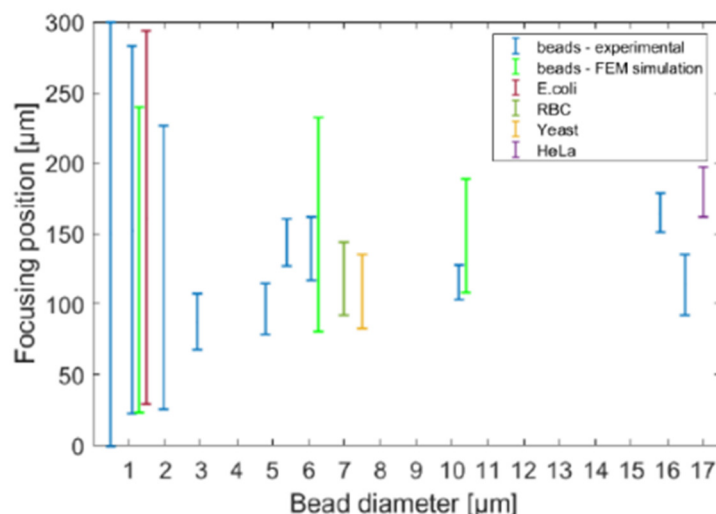


Figure 2: Lateral focusing of biological cells and polystyrene beads in the $H25_{W_{cr}50}$ channel (at 1 $\mu\text{L/s}$). The lateral focusing was examined by fluorescent or dark field microscope at the last bend of the microfluidic channel. The represented focusing position map is valid for rigid polystyrene beads of different sizes and biological target cells; the FEM calculated lateral position of some particle dimensions is also demonstrated.

Microfluidic environment for analysis single cells and cell populations

In vitro testing of cell populations or individual cells in artificial systems that model their real environment is highly prospective from a biomedical and environmental point of view. Specially designed microfluidic systems allow the development of such a controllable chemical environment that is comparable to the size of cells. The application of such Organ-on-Chip devices, which integrate sensing functions, can be a significant step in the research of pharmaceutical agents, but also in facilitating the spread of personalized medicine. Cell trapping and in-vitro analysis are powerful tools that enable the investigation of cell viability and proliferation in microfluidic structures.

Diffusion coefficients of dedicated molecules were measured in the free-diffusion based obstacle free microfluidic device using fluorescent microscopy. The simple design of the device and ease of application enables fast measurements and easy fabrication. Diffusion coefficient of fluorescently labelled Bovine Serum Albumin (BSA), immunoglobulin G and rhodamine B were determined using fluorescent microscopy. To acquire the intensity profiles along the channels time-lapse images were taken. A developed Python evaluation code was applied to fit complementary error functions to the measured profiles and calculate the diffusion coefficient. The measured diffusion coefficients were in nice accordance with the values found in literature and estimated by the Stokes-Einstein-equation.

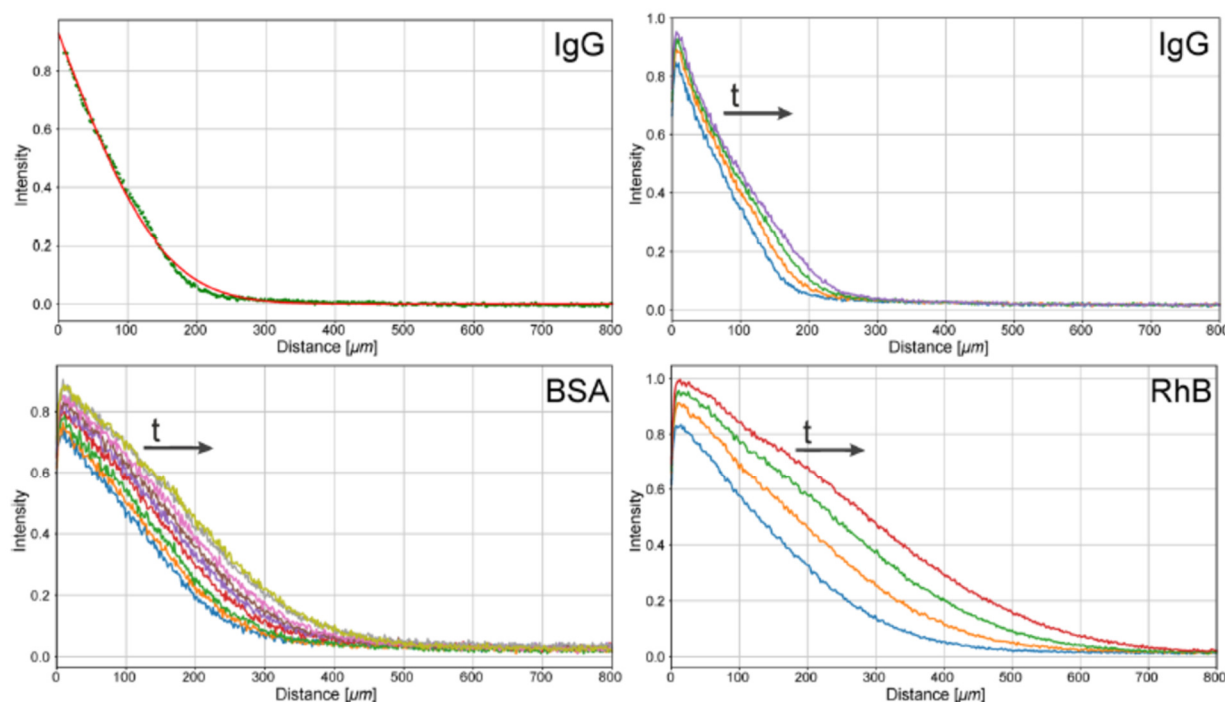


Figure 3: The first image is raw data of an IgG profile (green) and the fitted error function (red) serving as an example of the fitting with error below 1%. Time evolution of the diffusion profiles of the measured proteins IgG, BSA and rhodamine B along the 800 μm wide main channel. The time difference between the profiles is 30 s.

Two-phase microfluidic systems for cell analytical applications

In the last two decades, the utilization of microengineered systems has revolutionized the manner in the fields of chemical and biological sciences in which high-throughput experimentation is conducted. The capacity to construct intricate microfluidic architectures has empowered researchers to devise novel experimental formats for processing extremely small analytical volumes within short timeframes and with remarkable efficiency. By reducing the reaction volumes, heat transfer is enhanced, leading to significant reductions in overall reaction times when conducted on a chip. These artificial microscopic containers enable accelerated mixing of chemical agents, prevent contamination and non-specific molecular binding on channel walls, and support highly parallelized processes with the opportunity of single cell or molecule analysis. In this work high performance Finite Element Modelling (FEM) were applied for comprehensive analysis and description of fluid and heat transfer phenomena in two-phase microfluidic system to be able to predict reliably the thermal environment of proposed chemical reactions in the droplet size containers.

A novel Computational Fluid Dynamics-based multi-modal optimization approach is introduced and employed to investigate the impact of geometry, materials, and flow parameters of the two-phase microfluidic system on the evolving temperature distribution in a multi-zone thermal flow model. Finite element modelling code - COMSOL Multiphysics - was applied to analyse the droplet formation process in 3D two-phase models to achieve more accurate comprehension of the flow characteristics and heat transfer by comparison the single and two-phase fluid flow systems. The analysis is based on the numerical solution of the governing Navier-Stokes, continuity equations and coupled heat transfer model. For handling multiphase fluids in 3D models a robust Level Set calculation method was applied. During the study, the temperature distribution alongside the channel has been investigated at different volume flows, considering the inhomogeneous thermal

capacity, heat conductivity and convection within and between the fluidic environment and the generated droplets as the system reaching the equilibrium state. Fig. 4 represents the evolving flow characteristics and temperature distribution in the time dependent single and two-phase model at the initial time period when the heater surface has reached the 90°C temperature and droplet formation has been starting. The temperature distribution was analysed at different heights in the fluidic channel by comparison single phase to two-phase flows in order to reveal the effects of material inhomogeneity using similar flow rates. Higher although localised fluid temperatures were estimated in the two-phase flow according to the higher thermal conductivity of the oil phase. The periodic character of the temperature distribution in the two-phase flow demonstrates the inhomogeneous local heat capacity and the significantly decreased convective heat transfer through the boundary surface of a droplet. [1-6]

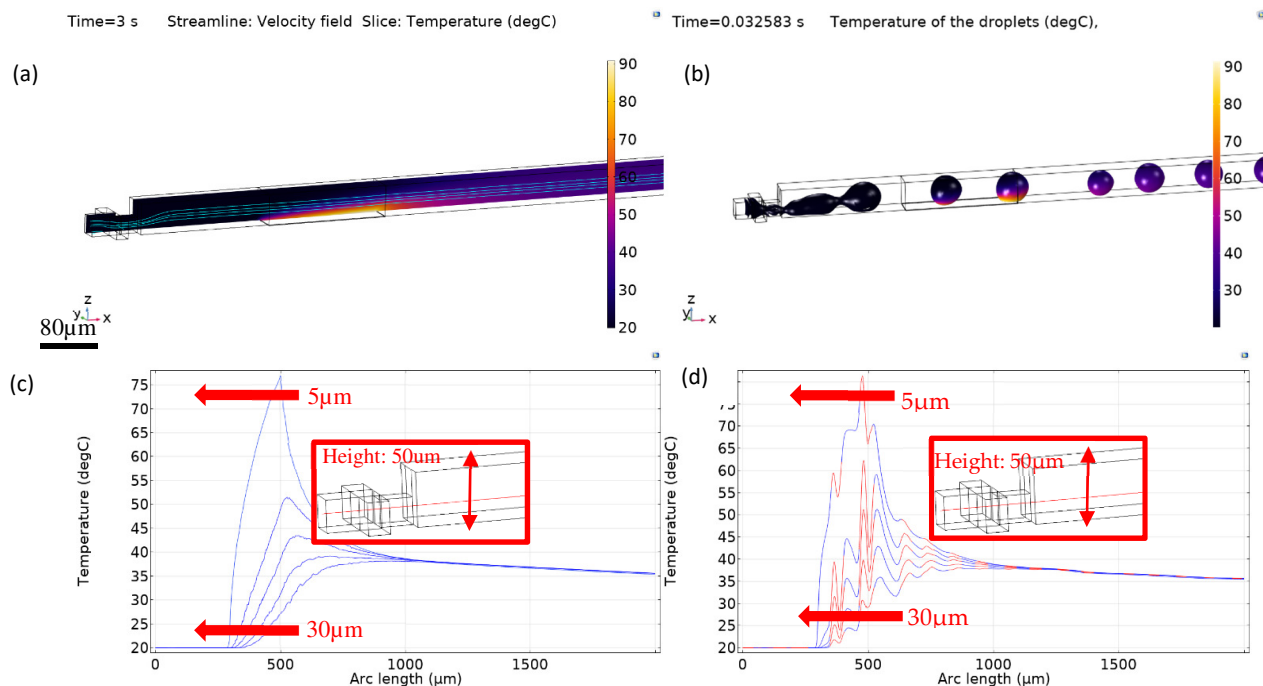


Figure 4: Simulated temperature distribution longwise the channel in case single phase flow (a) and within the generated droplets (b). Cut lines (c, d) also represent the temperature distribution longwise the channel, while the red segments indicate the location of the droplets. The flow rate was 0.295 µl/s.

Related publications

- [1] A. Bányai, E. Farkas, H. Jankovics, I. Székács, E. L. Tóth, F. Vonderviszt, R. Horváth, M. Varga, P. Fürjes: *Dean-Flow Affected Lateral Focusing and Separation of Particles and Cells in Periodically Inhomogeneous Microfluidic Channels*, *Sensors* **23**(2), 800, (2023) <http://dx.doi.org/10.3390/s23020800>
- [2] Bányai A., Bató L., Leelőssyné Tóth E., Varga M., Fürjes P., Áramlástani jelenségek mikroszkopikus mérettartományban – mikrofluidikai rendszerek és alkalmazásai, *Fizikai Szemle LXXIII* 383-389 (2023)
- [3] L. Bató, P. Fürjes: *An obstacle-free microfluidic system for monitoring protein diffusion*, XXIX. Congress of the Hungarian Association of Biophysics, Budapest, Hungary, 2023
- [4] L. Bató, P. Fürjes: *Microfluidic System With Integrated Electrode Array for High-Throughput EIS Analysis of Localised Cells*, *Proceedings of EuroSensors 2023 Conference*, Lecce, Italy, 2023 (MDPI Proceedings, oral presentation)
- [5] Zs. Szomor, E. L. Tóth, P. Fürjes: *Finite Element Modelling and Analysis of Fluid Dynamic Phenomena in Two-phase Droplet Based Microfluidic Systems*, XXIX. Congress of the Hungarian Association of Biophysics, Budapest, Hungary, 2023
- [6] Zs. Szomor, E. L. Tóth, P. Fürjes: *3D Finite Element Modelling of Heat Transfer in Continuous Flow Two-phase Droplet Microfluidic Systems Using On-chip Thermal Control*, *Therminic 2023 - 29th International Workshop for Thermal Investigations of ICs and Systems*, Budapest, Hungary, 2023, <https://doi.org/10.1109/THERMINIC60375.2023.10325685>

SMALL SCALE PRODUCTION AND DEVELOPMENT OF NEAR INFRARED LEDs FOR SPECTROSCOPIC APPLICATIONS

ECSEL-2019-1-IA -876190Moore4Medical, 2019-2.1.3-NEMZ_ECSEL-2020-00005

B. Beiler, J. M. Bozorádi, Cs. Dücső, F. Bíró, P. Fürjes, Z. Szabó

Infrared spectroscopy is a very popular measurement technique especially in food industry, pharmaceutical industry and agriculture for the detection and measurement of organic materials. The 1st-3rd harmonic absorption bands of valence-bond vibrations in the -OH, -NH and -CH functional groups are located in the range of the Near Infrared (NIR), where smaller signals can be measured effectively in practice. NIR LEDs have narrow wavelength; therefore, they are suitable for measurements at given wavelength. Further advantages of LEDs compared to incandescent lamps are their small dimensions, high efficiency, and low power consumption, which is critical in small handheld devices.

GaInAsP/InP is an ideal material system for the fabrication of double heterostructure devices as the emission wavelength is easily tuneable between 950-1650 nm. As InP has higher bandgap than the lattice-matched GaInAsP active layer the absorption losses inside the device structure can be minimized. In order to tune the emission wavelength of the LED, the composition of the semiconductor light-emitting layer has to be properly set. Our high quality single peak LED chips (1220nm) have a stable market.

Wide emission-spectrum NIR LEDs

Specific InGaAsP/InP layer structures were grown by Liquid Phase Epitaxy (LPE) to fabricate wide emission-spectrum near-infrared LEDs. The final multilayer structure could be achieved in two consecutive LPE growth steps: by growing 2 InGaAsP photoluminescent layers with the emission peaks of about 1300 nm and 1450 nm first, and by growing other photoluminescent (1650 nm) and active (1200 nm) layers in the second step. Samples were fabricated and characterized by optical transmittance measurements, by photo-luminescent measurements using various excitation sources in the NIR range, and by scanning electron microscopy to measure layer thicknesses and verify epitaxial crystal formation. The results were continuously fed back to refine the growth parameters.

LED chips were characterized electrically and optically (Fig. 1) after dicing. The 500x500 μm^2 LED chips were driven with continuous I_{FW} . A NIR spectrophotometer was used to examine the emission spectrum at a 30° angle to the normal of the chip. The emitted optical power was estimated using a small area InGaP photodiode at a 45° to the normal of the chip in a well-defined geometry. The shape of the spectra is quite stable, only slightly distorts with the increasing current due to the saturation in the thinner layers. The angle distribution of the radiation shows the expected Lambertian (cosine) pattern and the spectrum is independent of the angle.

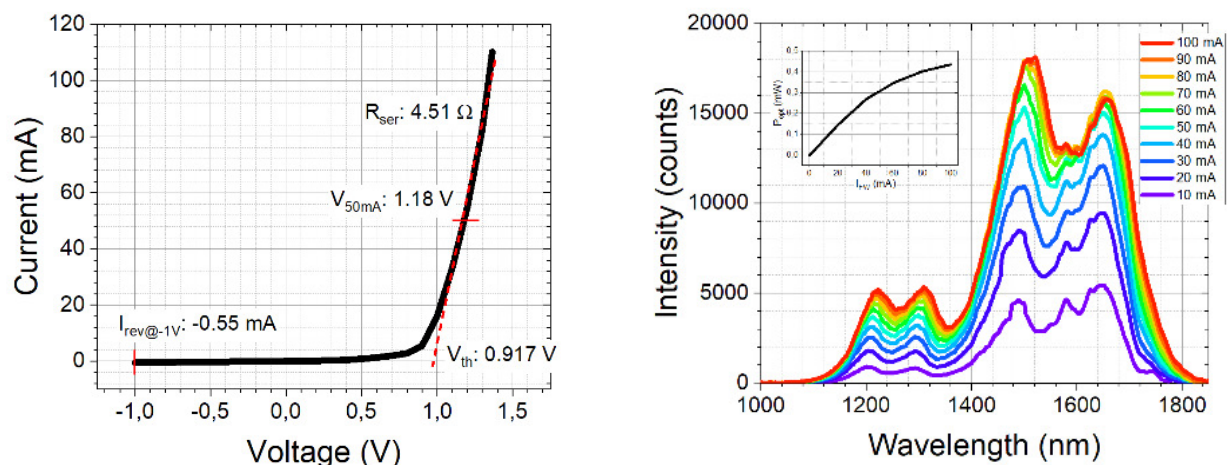


Figure 1: I-V characteristic of the LED chip (left) and the emission spectra of the 4-wavelength LED chip at I_{fw} 10-100 mA and the total optical power vs. I_{fw} in the inset (right)

The total emitted optical power of the wide spectrum LED was compared to the emission of a standard LED with a similar wavelength as the active layer. The power of the primarily emitted wavelength distributes on a wide wavelength range, which is the reason for the lower intensities. The emitted optical power, however, shows only 3x lower power compared to the reference LED, which is mainly originates from the natural conversion loss of the photon energy.

CELL CULTURE MEDIA ANALYSIS IN ORGAN-ON-CHIP APPLICATIONS

ECSEL-2019-1-IA -876190Moore4Medical, 2019-2.1.3-NEMZ_ECSEL-2020-00005

B. Beiler, Zs. Baji, L. Bató, K. Pankász, Zs. Szomor, J. M. Bozorádi, Z. Szabó, P. Fürjes

Optical Spectroscopy in microfluidic environment

The concentration of molecular markers – such as relevant amino-acids, carbohydrates and drugs – is an important signal of the metabolic or chemical processes unfolding in Organ-on-Chip (OoC) applications. In recent years the advanced and miniaturized sources, detectors and spectrometers has proven the applicability of optical spectroscopy to be an excellent tool for the analysis of different sample compositions or chemical reactions. UV-Vis or infrared spectroscopy combined with microfluidic sample transport and preparation can be a powerful, in-situ analysis method for continuous monitoring of complex cell culture media and revealing the molecular fingerprints of the relevant molecular contents.

Polymeric microfluidic cuvettes were fabricated by CNC milling and also by hot embossing techniques using microstructured molds. The optical measurements were carried out in the wavelength range of 950 - 1690 nm using Avantes spectrophotometer combined with optical fibre waveguide for excitation and detection. The **sample volume effect** was characterized by comparison the spectral transmittances of benchmark aqueous solutions (ethanol-water, lactate-water) measured in a standard macroscopic cuvette and in microfluidics. In case of the microfluidic cuvettes transmittance and transreflectance mode spectral analysis were also elaborated. The IR absorbance of water over 1400 nm wavelength causes significant deterioration of the signal-to-noise ratio and this effect could be eliminated by using radically shorter pathways of the microfluidic cuvettes as highlighted in Fig. 1.

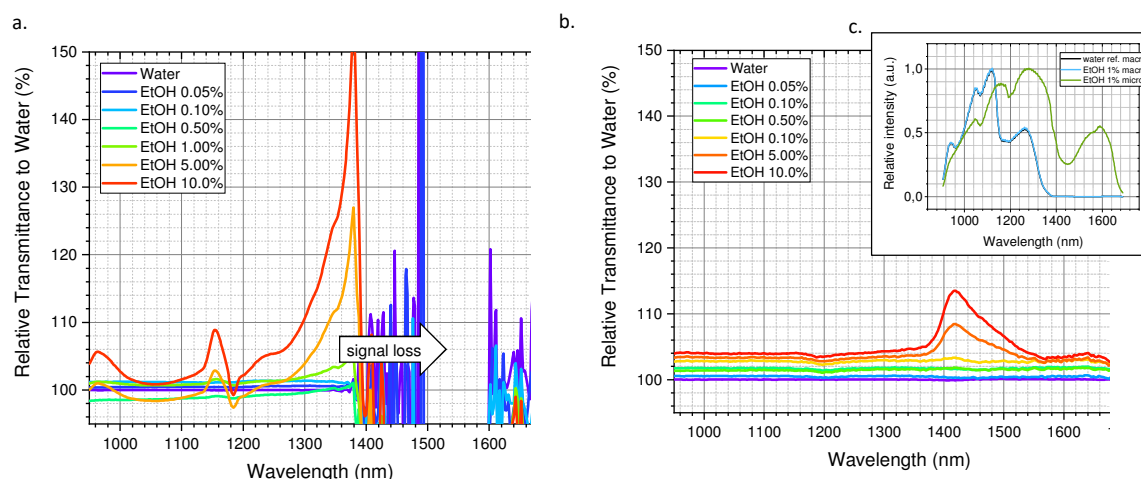


Figure 1: Concentration-dependent near-IR transmittance spectra for ethanol solutions (0.05, 0.1, 0.5, 1.0, 5.0, 10 % v/v) compared to water as reference in macroscopic (a.) and microfluidic (b. HE, 100 μ m, transmittance) cuvettes. Relative intensities (c.) demonstrates the signal loss over 1400 nm wavelength.

OoC-compatible microfluidic cuvettes were designed and manufactured for transreflectance mode optical measurements with adequate material properties, excellent surface quality and suitable architecture. By decreasing the optical path, the aspecific absorbance of water could be decreased, resulting in an increase of the signal-to-noise ratio. The optical measurement setup was characterised in case of fluorescent analysis, too.

The first electronic board for optical transmittance and photoluminescence measurement was tested with cuvette and transistor outline-packaged LEDs and photodiodes. The board features an LED driver, a 4-channel photodiode input, and lock-in detection. Based on our comprehensive tests, the compact LED and detector driver electronics were designed and manufactured to be tested and integrated with the optical measurement head.

Electrochemical analysis of cell culture media

Besides different marker molecules – such as relevant amino-acids, carbohydrates, etc. and drugs as antibiotics – pH is another important parameter to characterize the metabolic parameters of cell cultures and tissues in Organ-on-Chip applications. Miniaturized and robust pH detectors based on potentiometric, conductometric methods or Ion-Selective Field Effect Transistors (ISFET) and Extended Gate Field Effect Transistors (EGFET) have been demonstrated utilising various ion sensitive metal-oxide (MO_x) materials such as RuO_2 , IrO_2 , TiO_2 , SnO_2 , Ta_2O_5 , WO_3 , ZnO , etc. In case of the ISFET and EGFET pH sensors the source-drain current of the transistor is controlled by the electrostatic field generated by the gate covered by

ion-sensitive material. The pH sensitivity of the gate materials can be explained by the surface charging of the metal-oxides mainly due to specific adsorption of H^+ / OH^- ions, protonation and deprotonation reactions at surface sites. The MO_x sensing layer can be fabricated by screen printing, vacuum sputtering, sol-gel or electrodeposition methods and characterized mainly by potentiometry, Cyclic Voltammetry (CV) and Electrochemical Impedance Spectroscopy (EIS) to define their sensing performance. The electrochemical method implemented in integrable architecture was proved to be applicable for pH measurement in various culture media. [1-3]

Electrochemical electrodes including integrated Pt reference / counter electrodes and metal-oxide working electrodes with comb-like Pt or Au contacts were manufactured on Borofloat™ glass substrate (Fig. 2.c.). Titanium-oxide layers were deposited by vacuum sputtering and Atomic Layer Deposition (ALD) at 300°C and 100° as sensitive materials. The MO_x functionalized electrochemical electrodes were connected as extended gate in the proposed EGFET based circuit represented in Fig. 2.a-b and the performance of the system was tested. The pH sensitivity of the EGFET based circuit containing different MO_x materials were characterized using pH calibration solutions. The TiO_2 layers deposited by sputtering and ALD prepared at 300°C showed moderated pH sensitivity according to their perfectly stoichiometric, inert structure. The TiO_x layer deposited by ALD at 100°C proved to be perfectly applicable for pH sensing applications having close to Nernstian 59.12 mV/pH response (Fig. 2.d). The difference of the pH sensitivities of various titanium-oxides can be explained by the material structures and compositions.

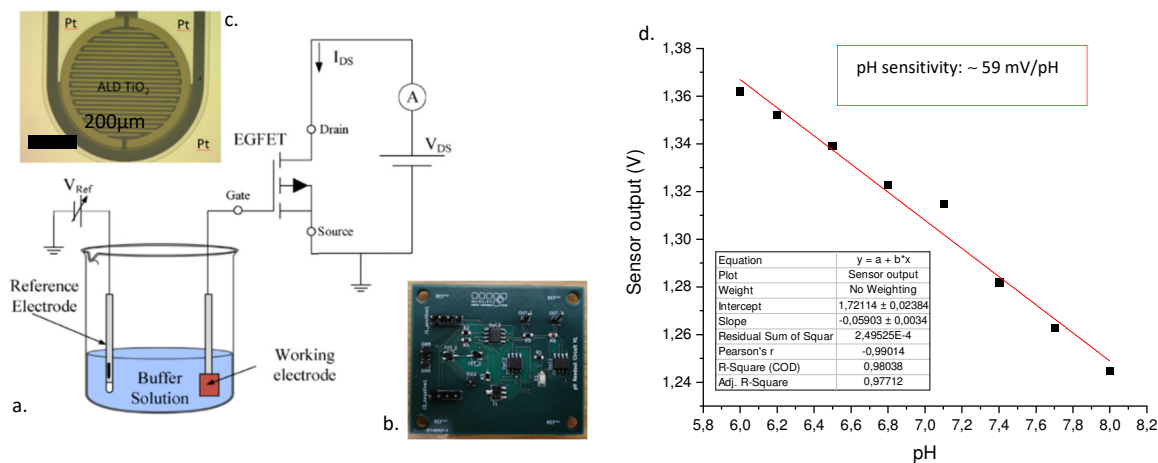


Figure 2: Schematic measurement setup (a.) representing the electronic architecture of EGFET based pH sensor, the manufactured read-out electronics (b.) and the MO_x functionalized working electrode (c.). The pH sensitivity of the non-stoichiometric TiO_x layer was close to the Nernstian response.

Related publications

- [1] Fűrjes P., Szabó Z.: Új hazai fejlesztés is hozzájárulhat a gyógyszerhatóanyag-vizsgálatok felgyorsításához, Innotéka 2023/09
- [2] Z. Szabó, K. Pankász, J. M. Bozorádi, O. Hakkel, Sz. Bella, B. Fabinyi, S. Meucci, P. Fűrjes: Microfluidic Cuvette for Near Infrared Spectroscopy, Proceedings of Eurosensors 2023 Conference, Lecce, Italy, 2023 (MDPI Proceedings, oral presentation)
- [3] Zs. Szomor, L. Bató, Cs. Dücső, Zs. Baji, P. Fűrjes: Non-Stoichiometric Titanium-Oxide Gate Electrodes for EGFET Based pH Sensors, Proceedings of Eurosensors 2023 Conference, Lecce, Italy, 2023 (MDPI Proceedings, oral presentation)

DEAN-FLOW AFFECTED LATERAL FOCUSING AND SEPARATION OF PARTICLES AND CELLS IN PERIODICALLY INHOMOGENEOUS MICROFLUIDIC CHANNELS

LP2012-26/2012 Lendület, OTKA ERC_HU 117755, TKP2021-EGA-04, OTKA KKP 129936

A. Bányai, E. Farkas, H. Jankovics, I. Székács, E. Leelőssyné Tóth, F. Vonderviszt, R. Horváth, M. Varga (77E), P. Fürjes

The purpose of the recent work is to give a better explanation of how Dean vortices affect lateral focusing and to understand how cell morphology can alter the focusing position compared to spherical particles. The position and extent of the focused region were investigated using polystyrene fluorescent beads with different bead diameters ($\varnothing = 0.5, 1.1, 1.97, 2.9, 4.8, 5.4, 6.08, 10.2, 15.8, 16.5 \mu\text{m}$) at different flow rates (0.5, 1, 2 $\mu\text{L/s}$). Size-dependent focusing generated a precise map of the equilibrium positions of the spherical beads at the end of the periodically altering channels, which gave a good benchmark for focusing multi-dimensional particles and cells. The biological samples used for experiments were rod-shaped *Escherichia coli* (*E. coli*), discoid biconcave-shaped Red Blood Cells (RBC), round or ovoid-shaped yeast, *Saccharomyces cerevisiae*, and soft-irregular-shaped HeLa cancer-cell-line cells to understand how the shape of the cells affects the focusing position at the end of the channel (Fig. 1) [1].

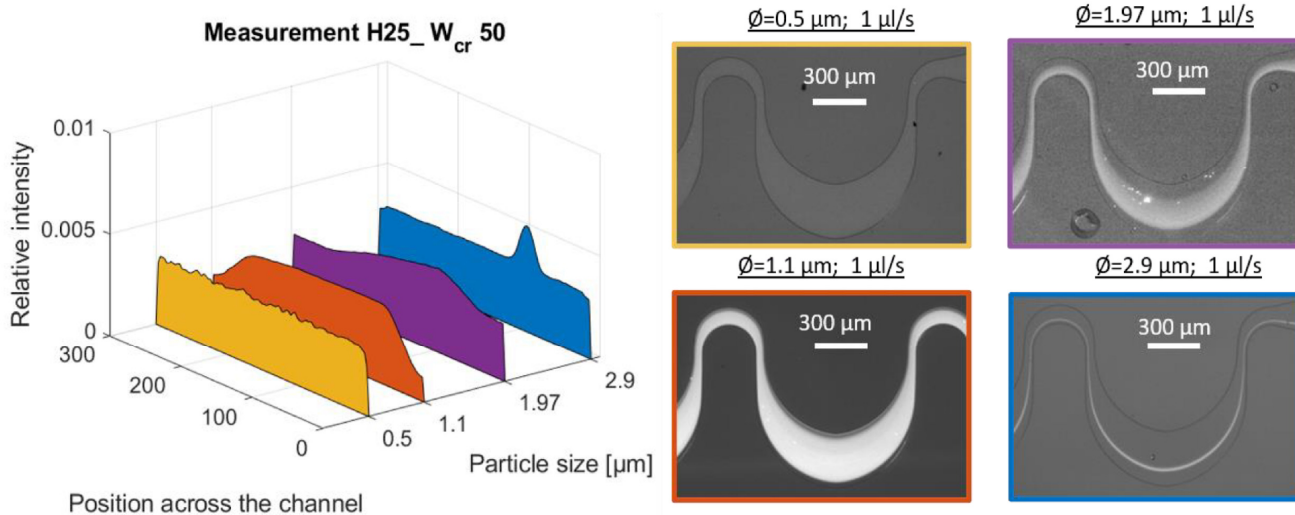


Figure 1: The size limit of lateral focusing in channel H25_Wcr50 at 1 $\mu\text{L/s}$. The applied bead sizes are $\varnothing = 0.5, 1.1, 1.97$ and 2.9 μm .

Related publication

- [1] A. Bányai, E. Farkas, H. Jankovics, I. Székács, E. Leelőssyné Tóth, F. Vonderviszt, R. Horváth, M. Varga (77E), P. Fürjes: *Dean-flow affected lateral focusing and separation of particles and cells in periodically inhomogeneous microfluidic channels*, *Sensors* **23**(2): 800 (2023) <http://dx.doi.org/10.3390/s23020800>

LABEL-FREE BIOSENSING OF LIGNANS FOR THERAPEUTICS USING ENGINEERED MODEL SURFACES

LP2012-26/2012 Lendület, OTKA ERC_HU 117755, TKP2021-EGA-04, OTKA KKP 129936, OTKA PD 131543, OTKA PD 134195

B. Péter, B. Majoros, S. Kurunczi, A. V. Ács, I. Székács, Sz. Bősze (ELTE), G. M. Kovács (ELTE), I. Boldizsár (ELTE), R. Horváth

The label-free interaction analysis of macromolecules and small molecules has increasing importance nowadays, both in diagnostics and therapeutics. In the blood vascular system, Human Serum Albumin (HSA) is a vital globular transport protein with potential multiple ligand binding sites. Characterizing the binding affinity of compounds to HSA is essential in pharmaceuticals and in developing new compounds for clinical application. Aryltetralin lignans from the roots of *Anthriscus sylvestris* are potential antitumor therapeutic candidates, but their molecular scale interactions with specific biomolecules are unrevealed. Here, we applied the label-free Grating-Coupled Interferometry (GCI) biosensing method with a polycarboxylate-based hydrogel layer with immobilized HSA on top of it. With this engineered model surface, we could determine the binding parameters of two novel aryltetralin lignans, deoxypodophyllotoxin (DPT), and angeloyl podophyllotoxin (APT) to HSA (Fig. 1).

Exploiting the multi-channel referencing ability, the unique surface sensitivity, and the throughput of GCI, we first revealed the specific biomolecular interactions. Traditional label-free kinetic measurements were also compared with a novel, fast way of measuring affinity kinetics using less sample material (Repeated Analyte Pulses of Increasing Duration (RAPID)). Experiments with well-characterized molecular interactions (furosemide to carbonic-anhydrase (CAII) and warfarin, norfloxacin to HSA) were performed to prove the reliability of the RAPID method. In all investigated cases, the RAPID and traditional measurement gave similar affinity values. These results could also be adapted to other biomolecules and applications where sample consumption and the rapidity of the measurements are critical [1].

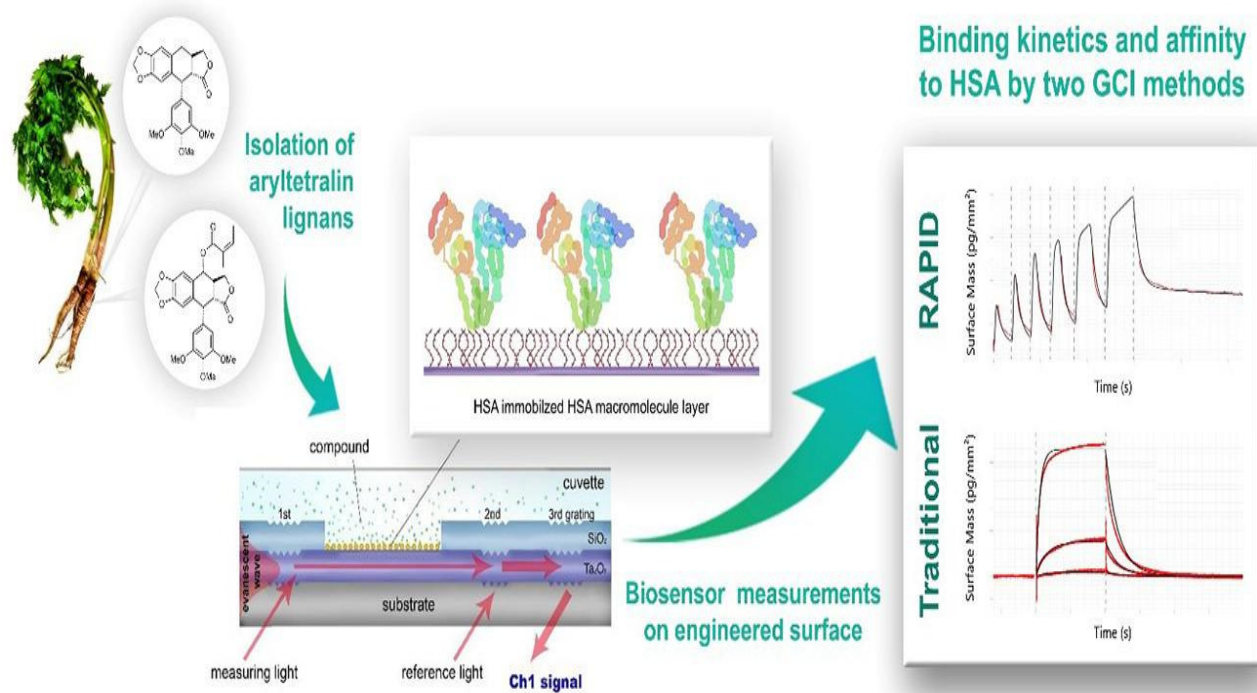


Figure 1: Schematic illustration of the applied methodology

Related publication

- [1] B. Péter, B. Majoros, S. Kurunczi, A. V. Ács, I. Szekacs, Sz. Bősze, G. M. Kovács, I. Boldizsár, R. Horvath: *Label-free biosensing of lignans for therapeutics using engineered model surfaces*, International Journal of Biological Macromolecules **233**, 123528 (2023) <https://doi.org/10.1016/j.ijbiomac.2023.123528>

DESIGN, FABRICATION, AND CHARACTERIZATION OF PICOWELL ARRAYS ON CYCLIC OLEFIN COPOLYMER SURFACES GENERATED WITH A 10.5 MeV N⁴⁺ ION MICROBEAM

LP2012-26/2012 Lendület, OTKA ERC_HU 117755, TKP2021-EGA-04,
OTKA KKP 129936

I. Bányász (Wigner), I. Rajta (ATOMKI), V. Havránek (NPI, Prague), A. Mackova (NPI, Prague), A. J. Laki (Pázmány University), M. S. Z. Kellermayer (SE), Z. Szittner, S. Kurunczi, Sz. Novák, I. Székács, R. Horváth, M. Fried, G. U. L. Nagy (Óbuda University)

Handling of picoliter-to-nanoliter-scale volumes and objects has increasing importance in life sciences. This is the volume scale of cell extractions and individual living cells. Here, we introduce a method of generating a picoliter-scale device by direct writing of picowell arrays on a ZEONOR™ copolymer surface with high-energy medium-mass ion microbeam. Arrays of various microstructures were written in the sample using a microbeam of 10.5 MeV N⁴⁺ ions at various implanted ion fluences. The best array was obtained by implantation of annuli of 10 and 11 μm of inner and outer diameters with a fluence of 7.8×10^{12} ions/cm² (Fig. 1) [1].

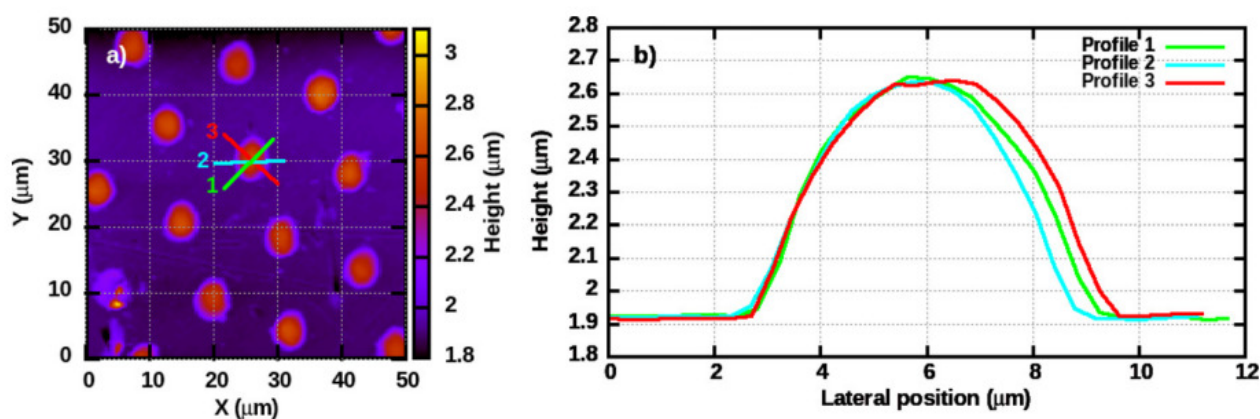


Figure 1: Height-contrast AFM image (a) of part of array D, and topographical height profiles along the indicated sections of a user-defined single element (b) in it.

Related publication

- [1] I. Bányász, I. Rajta, V. Havránek, A. Mackova, A. J. Laki, M. S. Z. Kellermayer, Z. Szittner, S. Kurunczi, Sz. Novák, I. Székács, R. Horváth, M. Fried, G. U. L. Nagy: *Design, fabrication, and characterization of picowell arrays on cyclic olefin copolymer surfaces generated with a 10.5 MeV N⁴⁺ ion microbeam*, Applied Physics Letters **123**(5), 053701 (2023) <https://doi.org/10.1063/5.0155681>

NANOINJECTION OF EXTRACELLULAR VESICLES TO SINGLE LIVE CELLS BY ROBOTIC FLUIDIC FORCE MICROSCOPY

LP2012-26/2012 Lendület, OTKA ERC_HU 117755, TKP2021-EGA-04, OTKA KKP 129936, Bolyai Scholarship, OTKA PD 131543, OTKA PD 134195

K. D. Kovács, T. Visnovitz (SE), T. Gerecsei, B. Peter, S. Kurunczi, A. Koncz (SE), K. Németh (SE), D. Lenzinger (SE), K. V. Vukman (SE), A. Balogh, I. Rajmon, P. Lőrincz (SE), I. Székács, E. I. Buzás, R. Horváth

In the past decade, Extracellular Vesicles (EVs) have attracted substantial interest in biomedicine. With progress in the field, we have an increasing understanding of cellular responses to EVs. In this Technical Report, we describe the direct nanoinjection of EVs into the cytoplasm of single cells of different cell lines. By using robotic fluidic force microscopy (robotic FluidFM), nanoinjection of Green Fluorescent Protein (GFP) positive EVs and EV-like particles into single live HeLa, H9c2, MDA-MB-231 and LCLC-103H cells proved to be feasible. This injection platform offered the advantage of high cell selectivity and efficiency. The nanoinjected EVs were initially localized in concentrated spot-like regions within the cytoplasm (Fig. 1). Later, they were transported towards the periphery of the cells. Based on our proof-of-principle data, robotic Fluidic Force Microscopy (FluidFM) is suitable for targeting single living cells by EVs and may lead to information about intracellular EV cargo delivery at a single-cell level [1].

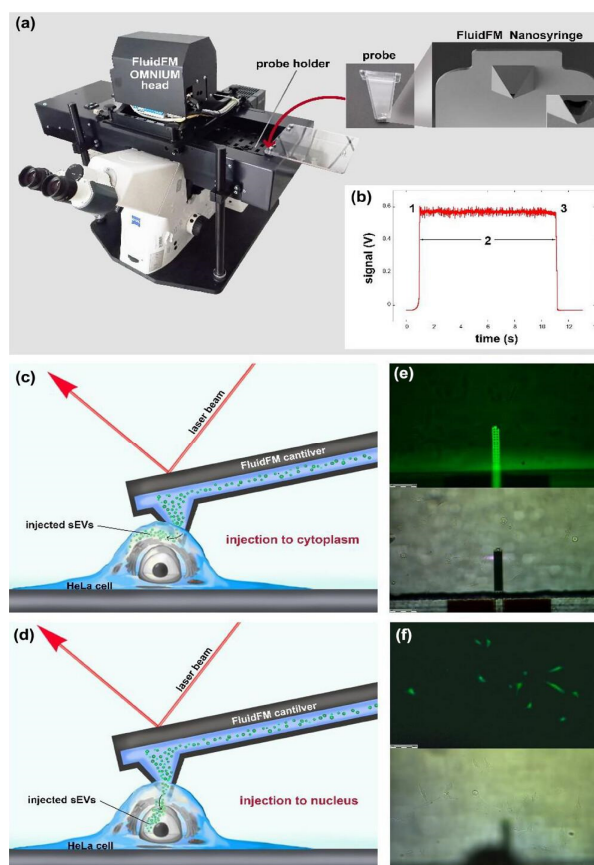


Figure 1: Summary of the FluidFM measurements. (a) Photo of the FluidFM appliance, probe and the FluidFM Nanosyringe. (b) Change of the voltage signal during injection of a live cell. (c) Schematic illustration of the injection of small Extracellular Vesicles (sEVs) to the cytoplasm by FluidFM. (d) Schematic illustration of the injection of sEVs to the nucleus by FluidFM. (e) Microscopic image of the FluidFM cantilever in fluorescent mode (upper part) and bright field mode (bottom part). (f) Microscopic image of the cells in fluorescent mode (upper part) and bright field mode (bottom part).

Related publication

- [1] K. D. Kovács, T. Visnovitz, T. Gerecsei, B. Peter, S. Kurunczi, A. Koncz, K. Németh, D. Lenzinger, K. V. Vukman, A. Balogh, I. Rajmon, P. Lőrincz, I. Székács, E. I. Buzás, R. Horváth: *Nanoinjection of extracellular vesicles to single live cells by robotic fluidic force microscopy*, Journal of Extracellular Vesicles **12(12)**: 12388 (2023) <https://doi.org/10.1002/jev2.12388>

POLYSACCHARIDE-BASED NANO-ENGINEERED MULTILAYERS FOR CONTROLLED CELLULAR ADHESION IN LABEL-FREE BIOSENSORS

LP2012-26/2012 Lendület, OTKA ERC_HU 117755, TKP2021-EGA-04,
OTKA KKP 129936, OTKA PD 131543, OTKA PD 134195

M. Wasilewska (Poland), A. Michna (Poland), A. Pomorska (Poland), K. Wolski (Poland),
S. Zapotoczny (Poland), E. Farkas, Z. Szittner, I. Szekacs, R. Horvath

Controlling cellular adhesion is a critical step in the development of biomaterials, and in cell-based biosensing assays. Usually, the adhesivity of cells is tuned by an appropriate biocompatible layer. Here, synthetic poly(diallyldimethylammonium chloride) (PDADMAC), natural chitosan, and heparin (existing in an extracellular matrix) were selected to assemble PDADMAC/heparin and chitosan/heparin films. The physicochemical properties of macroion multilayers were determined by Streaming Potential Measurements (SPM), Quartz Crystal Microbalance (QCM-D), and Optical Waveguide Lightmode Spectroscopy (OWLS). The topography of the wet films was imaged using Atomic Force Microscopy (AFM). Polysaccharide-based multilayers can be considered versatile systems for medical applications. One can postulate that the presented results are relevant not only for modelling studies but also for applied research (Fig. 1) [1].

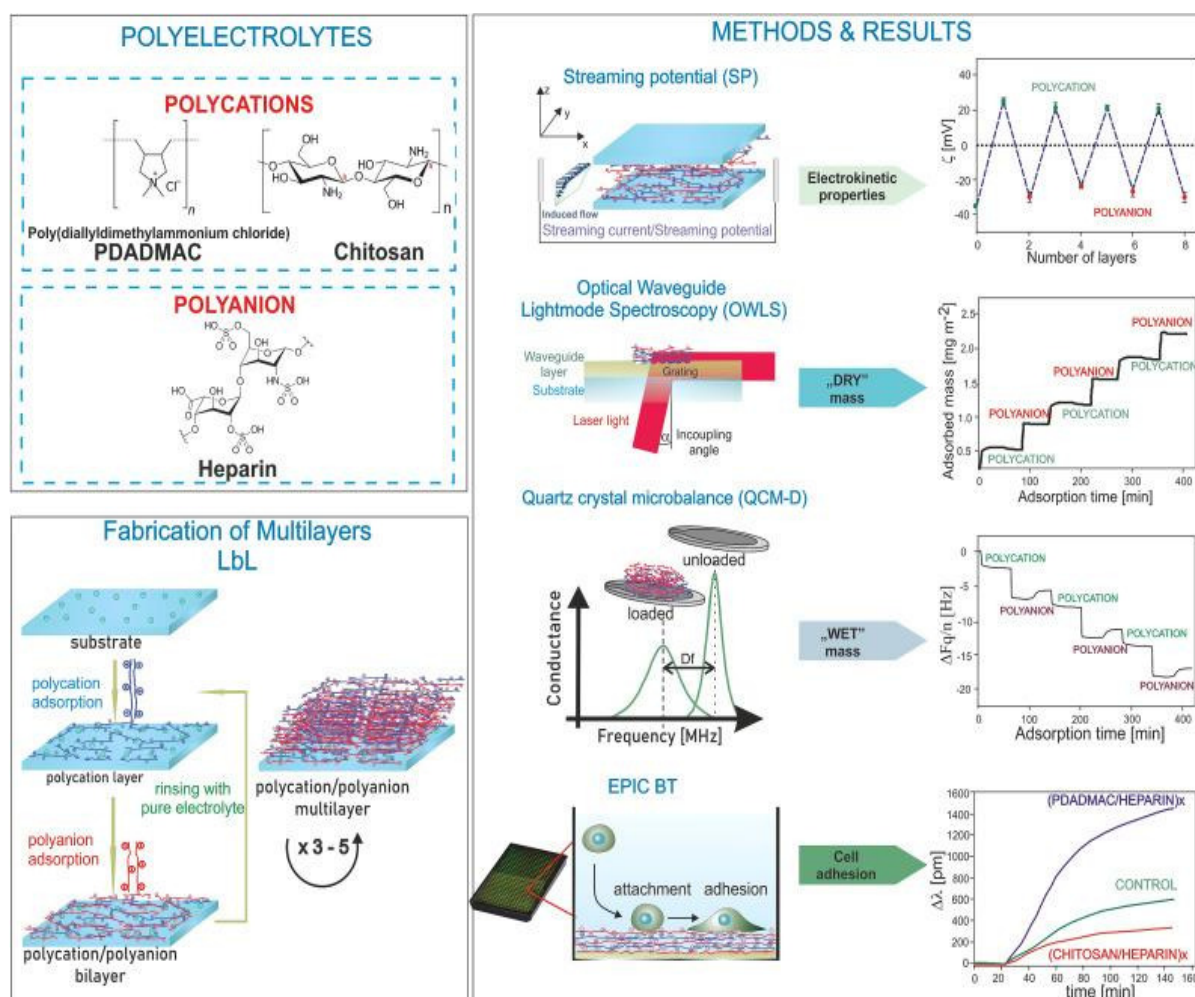


Figure 1: Scheme representing the procedures used to prepare/investigate PDADMAC (or chitosan)/ heparin films

Related publication

- [1] M. Wasilewska, A. Michna, A. Pomorska, K. Wolski, S. Zapotoczny, E. Farkas, Z. Szittner, I. Szekacs, R. Horvath: Polysaccharide-based nano-engineered multilayers for controlled cellular adhesion in label-free biosensors, International Journal of Biological Macromolecules **247**, 125701 (2023) <https://doi.org/10.1016/j.ijbiomac.2023.125701>

THE COMPETITION OF ALLIANCES WITH INNER BLOCKING MECHANISM

OTKA K 128989

A. Szolnoki and X. Chen

Competitors in an intransitive loop of dominance can form a defensive alliance against an external species. The vitality of this superstructure, however, is jeopardized if we modify the original rock-scissors-paper-like rule and allow that the vicinity of a predator blocks stochastically the invasion success of its neighbouring prey towards a third actor. To explore the potential consequences of this multipoint interaction we introduce a minimal model where two three-member alliances are fighting but one of them suffers from this inner blocking mechanism. We demonstrate that this weakness can be compensated by a faster inner rotation which is in agreement with previous findings. This broadly valid principle, however, is not always true here because the increase of rotation speed could be harmful and results in a series of reentrant phase transitions on the parameter plane.

In our model two three-member loops compete. One of them still represents the traditional rock-scissors-paper-like interaction where during a potential invasion only the state of involved pair counts. In the alternative triplet, however, we introduce a blocking mechanism. More precisely, staying at the rock-scissors-paper example, a rock will only beat scissors with a limited probability if there is a paper in the nearest neighbourhood of the actor representing rock state. Further details are explained in Fig. 1.

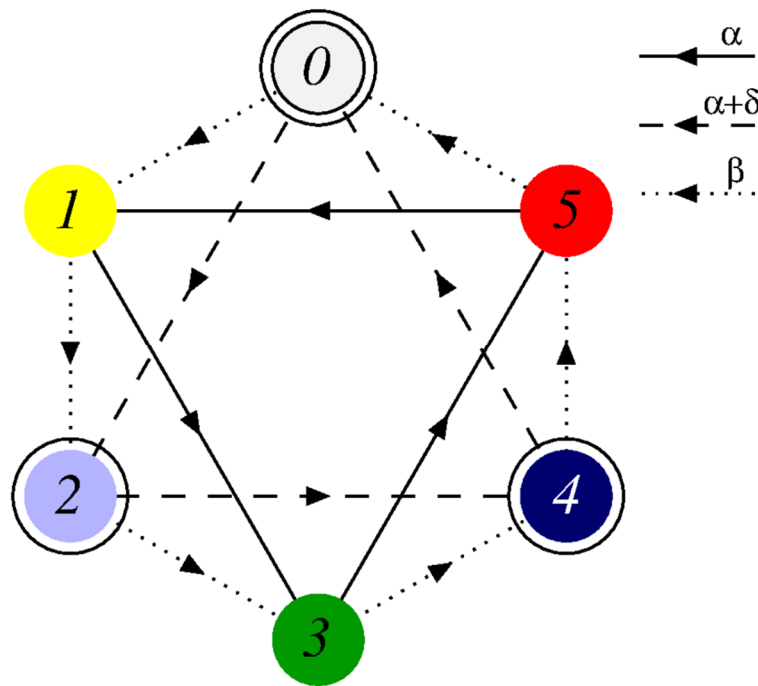


Figure 1: Food-web characterizing the microscopic dynamics in our six-member ecological system. Arrows indicate the direction of invasion between species. Two triplets form defending alliances, whose members are in a rock-scissors-paper-like relation. While the inner invasion probability in the $1 \rightarrow 3 \rightarrow 5 \rightarrow 1$ loop is α , the same probability in the $0 \rightarrow 2 \rightarrow 4 \rightarrow 0$ circle is $\alpha + \delta$. Importantly, the members of the latter triplet can block each other with probability γ . If, for instance, there is a species 4 in the neighbourhood of species 0 then the $0 \rightarrow 2$ or the $0 \rightarrow 1$ invasion is blocked with probability γ . The invasion probability between the members of competing triplets is β .

Fig. 2 shows some representative phase diagrams, when the inner invasion of odd-labelled triplet is fast, moderate, or very weak. When the inner rotation is fast, displayed in panel (a), the system behaviour is similar to those we observed for large β . Namely, $(1+3+5)$ species can form a solid winning alliance almost everywhere, the only exception is the low γ - large δ corner where the faster rotation in the even-labelled triplet can compensate the shortage of blocking. When the invasion strength in the sound triplet is weaker, shown in panel (b), we can observe that there is a parameter region where neither $(0+2+4)$ nor $(1+3+5)$ alliance is strong enough to beat the rival group hence all six species survive. If we fix γ , for instance, and only increase the value of δ then we can detect some non-monotonous behaviour: starting from $(1+3+5)$ phase we can enter to "all," after $(0+2+4)$, followed by "all" again, and finally arriving back to $(1+3+5)$ phase again.

The top-left panel of Fig. 3 illustrates quantitatively the above mentioned curious re-entering phenomenon. In all three cases the evolution starts from a prepared initial state where triplets are separated by domains containing neutral species. The common starting state is shown in panel (a) where we indicate those species who are present in a specific stripe. In Case I the sound $(1+3+5)$ triplet beat both $(0+3)$ and $(1+4)$ duplets. In Case II both triplets can grow on the expense of domains formed

by duplets. When triplets meet and the superiority of even-labelled triplet over odd-labelled triplet becomes evident. In Case III the inner rotation in the blocked triplet is almost maximal and duplet of neutral pairs becomes stronger again. While too fast rotation could be harmful for blocked triplet, the sound triplet still dominates the two-member domains, hence odd-labelled group will be the final victor, no matter they would be weaker against the even-labelled group in a direct interaction.

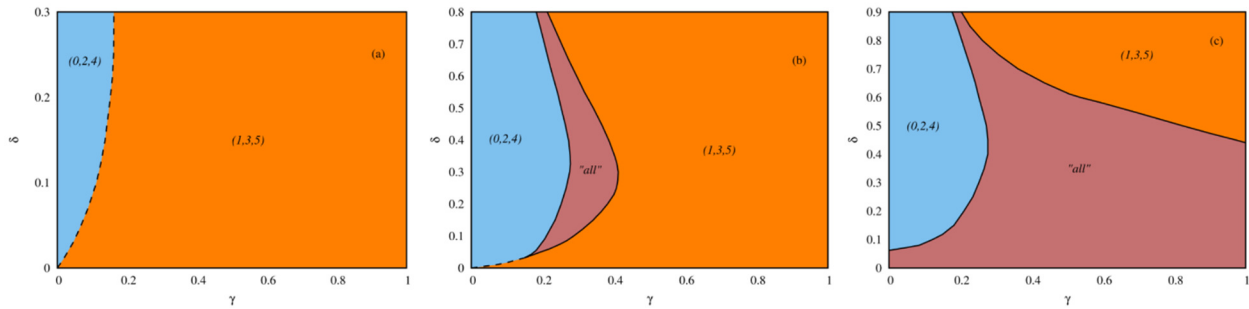


Figure 2: Phase diagrams when interaction between rival triplets is intermediate ($\beta = 0.5$). Horizontal axis shows the γ blocking strength while vertical axis denotes the δ extra value of inner invasion in the even group. (a) to (c) respectively show cases when the inner invasion strength in the odd-labelled group is strong ($a = 0.7$), moderate ($a = 0.2$), or very weak ($a = 0.1$). Light blue (orange) marks the parameter area where even (odd) species prevail, while pink shows the area where all six species coexist. Dashed (solid) lines denote the position of discontinuous (continuous) phase transition points.

Our system provides a nice example that the consequences of dynamical rules determining the vitality of a solution are more subtle than we might expect based purely on the microscopic dynamical rules. As we show, when two triplets compete their frontier serves as a birthplace of alternative solutions. Namely, there is always a chance that a two-member solution of neutral species emerges. If the rotation speed is too high in the blocked triplet then such two-member solution, formed by a triplet member and an external species, can be more effective: while the invasion of external party is not blocked, it can meet more easily with its internal predator who cannot beat it due to blocking. As a consequence, the two-member formations invade the blocked triplet, leaving only the alternative triplet alive. Importantly, the defensive mechanism still working in the sound triplets, hence they eventually prevail. No matter they would be weaker in a direct comparison against the blocked triplet. [1]

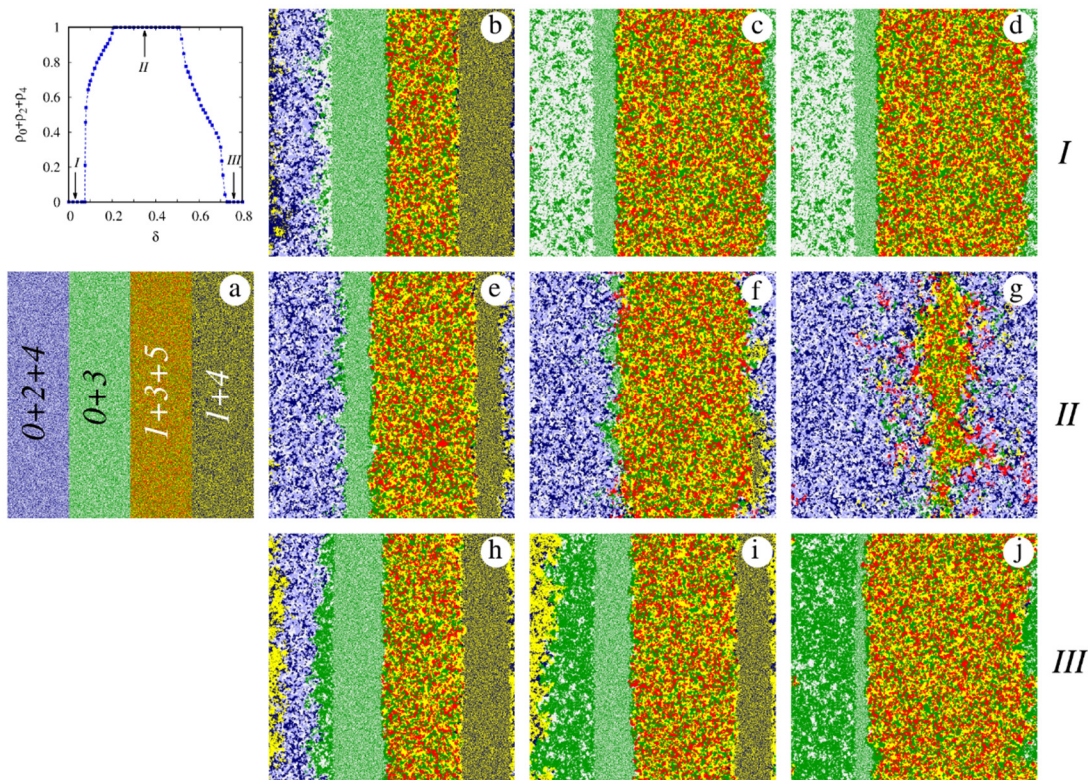


Figure 3: Reentrant phase transitions when rotation intensity is changed in the blocked triplet. Panel in the top-left corner shows the order parameter in dependence of δ at $\beta = 0.5$, $a = 0.2$, and $\gamma = 0.25$. Arrows show the positions of the δ values where we launched the evolution from a specific initial state shown in (a). The diverse evolution of patterns in cases I, II, and III are shown in the rows. Final destinations, which are (1+3+5), (0+2+4), and (1+3+5) phase again, are not shown. The colour code of species is identical those used in Fig 1. The applied linear system size is $L = 800$.

Related publication

[1] A. Szolnoki, X. Chen: When faster rotation is harmful: The competition of alliances with inner blocking mechanism, Physical Review Research 6, 023087 (2024) <https://doi.org/10.1103/PhysRevResearch.6.023087>

REVISITING AND MODELLING POWER-LAW DISTRIBUTIONS IN EMPIRICAL OUTAGE DATA OF POWER SYSTEMS

*B. Hartmann, S. Deng, G. Ódor, and J. Kelling**

**HZDR Dresden-Rossendorf*

The size distributions of planned and forced outages and their restoration times in power systems have been studied for almost two decades and have drawn great interest as they display heavy tails. Understanding heavy tails has been provided by various threshold models, which are self-tuned at their critical points, but as many papers pointed out, explanations are intuitive, and more empirical data are needed to support hypotheses. In this paper, we analyze outage data collected from various public sources to calculate the outage energy (Fig. 1) and outage duration exponents of possible power-law fits. Temporal thresholds are applied to identify crossovers from initial short-time behaviour to power-law tails. We revisit and add to the possible explanations of the uniformness of these exponents. By performing power spectral analyses on the outage event time series and the outage duration time series (Fig. 2), we find that, on the one hand, while being overwhelmed by white noise, outage events show traits of self-organized criticality, which may be modelled by a crossover from random percolation to a directed percolation branching process with dissipation, coupled to a conserved density. On the other hand, in response to outages, the heavy tails in outage duration distributions could be a consequence of the highly optimized tolerance mechanism, based on the optimized allocation of maintenance resources. [1]

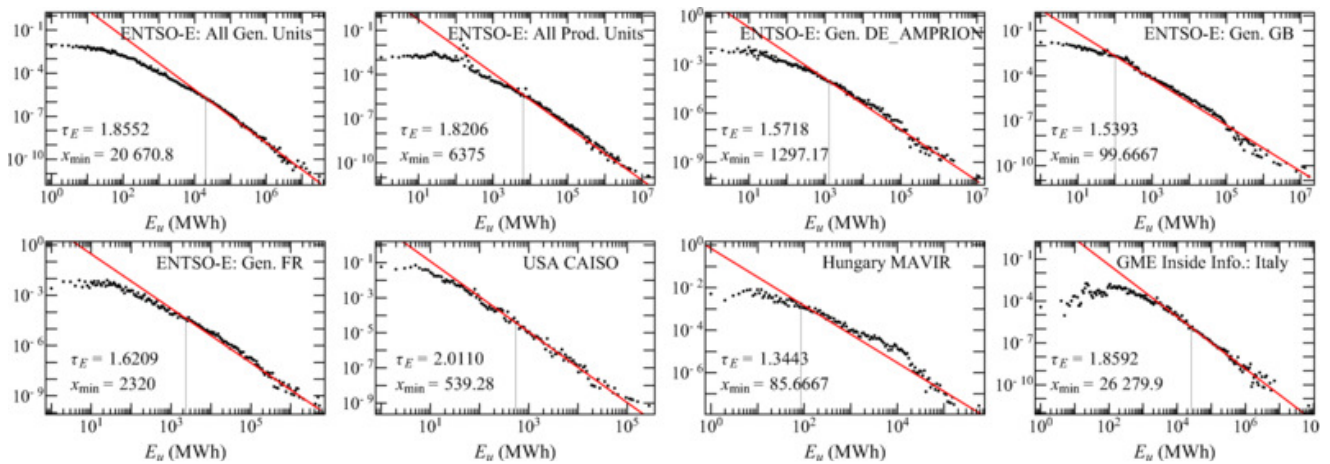


Figure 1: Probability distributions (black dots) of generation outages measured in terms of the unavailable energy. For the ENTSO-E data, we show the generation outage data for the control areas "DE_AMPRION," "GB," and "FR," as well as the generation and production outage data from all control areas. The fitted power laws and their corresponding E_{min} values are marked by solid red lines and vertical black lines, respectively.

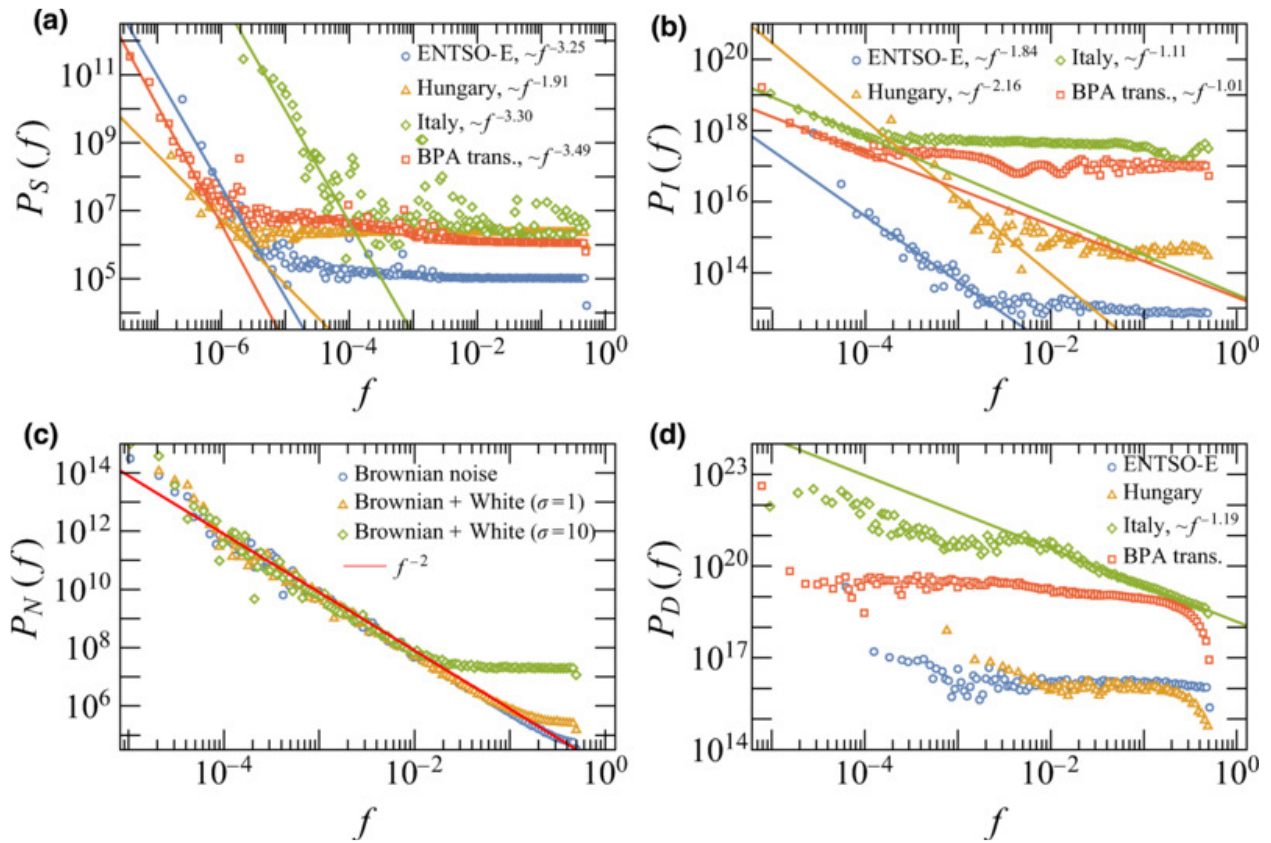


Figure 2: Power spectra of the time series of (a) the number of outage events $S(t)$, (b) the intervals between successive outage events $I(t)$, (c) the Brownian noise $N(t)$, with and without the presence of a white noise background, and (d) the outage duration $D(t)$. In panels (a), (b), and (d), we show the respective power spectra for the ENTSO-E generation outage data from all control areas, the Hungarian MAVIR generation outage data, the GME Italian generation outage data, and the BPA transmission outage data.

Related publication

[1] B. Hartmann, S. Deng, G. Ódor, and J. Kelling: *Revisiting and Modelling Power-Law Distributions in Empirical Outage Data of Power Systems*, PRX Energy **2**, 033007 (2023) <https://doi.org/10.1103/PRXEnergy.2.033007>

SCALING LAWS OF FAILURE DYNAMICS ON COMPLEX NETWORKS

G. Pál¹, Zs. Danku¹, A. Batool¹, V. Kádár¹, N. Yoshioka², N. Ito², G. Ódor, F. Kun³

¹ Department of Theoretical Physics, Faculty of Science and Technology, University of Debrecen, Hungary. ² RIKEN Centre for Computational Science, Kobe, Japan, ³ Institute for Nuclear Research (Atomki), Hungary.

The topology of the network of load transmitting connections plays an essential role in the cascading failure dynamics of complex systems driven by the redistribution of load after local breakdown events. In particular, as the network structure is gradually tuned from regular to completely random a transition occurs from the localized to mean field behaviour of failure spreading. Based on finite size scaling in the fibre bundle model of failure phenomena, here we demonstrate that outside the localized regime, the load bearing capacity and damage tolerance on the macro-scale, and the statistics of clusters of failed nodes on the micro-scale obey scaling laws with exponents which depend on the topology of the load transmission network and on the degree of disorder of the strength of nodes.

Most notably, we show that the spatial structure of damage governs the emergence of the localized to mean field transition: as the network gets gradually randomized failed clusters formed on locally regular patches merge through long range links generating a percolation like transition which reduces the load concentration on the network. The results may help to design network structures with an improved robustness against cascading failure. [1]

Related publication

- [1] G. Pál, Zs. Danku, A. Batool, V. Kádár, N. Yoshioka, N. Ito, G. Ódor, F. Kun: *Scaling laws of failure dynamics on complex networks*, Scientific Reports **13**, 19733 (2023) <https://doi.org/10.1038/s41598-023-47152-2>

SPONTANEOUS SYMMETRY-BREAKING IN SPATIAL EVOLUTIONARY GAMES

C. Hauert* and G. Szabó

*Department of Mathematics, University of British Columbia, Vancouver, BC, Canada

Spontaneous symmetry-breaking occurs in a wide scale of models describing order-disorder phase transitions when the temperature is increased. The best-known examples are the ferromagnetic-paramagnetic phase transitions or similar ordering in the atomic arrangements (e.g., solid electrolytes, metal-hydrogen systems, electro-chromatic materials, atomic depositions on a single crystal, etc.) described by lattice gas models. In these systems one of the two or more equivalent states is stabilized at low temperatures.

In spatial evolutionary games players with different strategies are located on the sites of a lattice or graph. These players can represent species in biological systems or human individuals with some possible strategies in economic models. The pair interactions between the neighbouring players are described by simple matrix games and the evolution of strategy distribution is controlled by consecutive random strategy updates. Spontaneous symmetry-breaking was previously reported in social and biological systems where game theoretical interactions enforced the appearance of critical (continuous) phase transitions with spontaneous symmetry-breaking belonging to the Ising- or Potts-type universality class.

Christoph Hauert suggested a model where similar symmetry-breaking phase transitions are caused by the separation of interaction and imitation neighbourhoods. In this model the players are located on the sites of a two-layer square lattice. The players get incomes from games with five nearest neighbours located on the opposite layer while they can adopt strategy from one of their four nearest neighbours in the same layer. The interaction is described by a two-strategy donation game when the cooperative player provides a benefit b to their partner at a cost c ($b > c > 0$). The defective player declines to pay the cost that yields zero income for the partner. In this social dilemma the selfishness dictates to choose defection for both players who receive nothing. On the contrary, the players receive higher income ($b-c$) for mutual cooperation. The macroscopic behaviour is quantified by the average frequency of cooperation and their fluctuations on both layers with using Monte Carlo simulations for different cost-to-benefit (c/b) ratio at a fixed noise level in the imitation process as illustrated in Fig. 1.

The results show several curiosities. On both layers the cooperation becomes extinct simultaneously if b/c goes to a threshold value ($r_1 \sim 0.0228$) (from below) dependent on the noise level. This extinction process belongs to the directed percolation universality class and accompanied with a power law divergence in the fluctuation. There exists a range of b/c where cooperation occurs with the same frequency on both layers. Spontaneous symmetry-breaking can be observed in the cooperation frequencies if $r_2 < c/b < r_1$ ($r_2 \sim 0.002166$). For this state the players in one of the layers exploit the others. The corresponding critical phase transition possesses the general features observed for the two-dimensional Ising model. Notice that this type of exploitation occurs when the average frequency of cooperation is sufficiently large (> 0.5) and it reaches a maximum when c/b is decreased. For further decrease in c/b results in rarer and larger avalanches (bursts) in the time-dependence of cooperation frequencies as it is indicated by the huge increase of fluctuations.

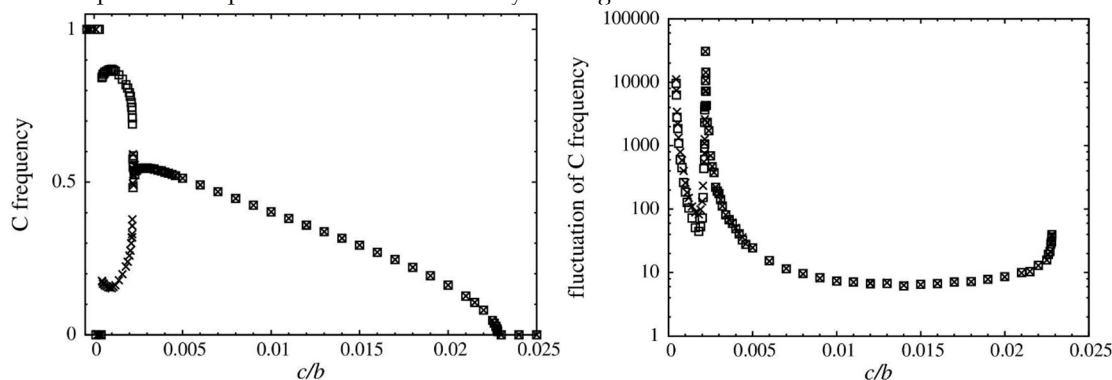


Figure 1: Strategy frequencies in the upper and lower square lattice (left) and their fluctuations (right) vs. c/b at low noises in the imitations. Boxes and crosses denote Monte Carlo data in the upper and lower layers.

Due to this phenomenon the finite system can evolve into one of the states where strategy distributions are homogeneous in both layers. The final state depends on the initial state, size, and stochastic events. Finally, we emphasize the absence of spiteful behaviour for negative cost ($c < 0$) when the solitary defector benefits from the high loss she caused for her co-players in several spatial evolutionary games. The present model can explain some phenomena reported in biological systems.

Preliminary results indicate similar phenomena in other models and raise the clarification of other mechanisms yielding spontaneous symmetry breaking or polarizations in many biological or social systems. [1]

Related publication

- [1] C. Hauert and G. Szabó: Spontaneous symmetry breaking of cooperation between species, *PNAS Nexus* **3(9)**, 326 (2024) <https://doi.org/10.1093/pnasnexus/pgae326>

AN INVESTIGATION OF EVOLUTIONARY POTENTIAL GAMES USING THE TENSOR RENORMALIZATION GROUP METHOD

OTKA PD 138571

B. Király

Some of the structurally simplest many-player models of game theory become equivalent to classical spin models when the strategy choices of the players follow the so-called logit strategy update rule, a close relative of Glauber dynamics. Consequently, the properties of these game-theoretic models can be directly studied using concepts and methods developed in the field of statistical physics. This project fits into this interdisciplinary approach.

The emergence of coordination has always interested game theorists. Recent research has shown that general coordination-type symmetric pair interaction games consist of linear combinations of voluntary games that describe coordination between strategy pairs: In such an elementary coordination game, the two interacting players receive equal rewards when they choose the same coordinated strategy; similarly, they are both punished when they choose opposing coordinated strategies; and neither of them receives any payoff when either one of them chooses any other strategy. As basic building blocks, these elementary coordination games have a key role in determining outcomes in general games. In an effort to learn more about their interplay with each other and the remaining (self-dependent, cross-dependent, and cyclic dominance) elementary game types, the Tensor Renormalization Group (TRG) method introduced by Michael Levin and Cody P. Nave was applied to a couple of games defined by simple combinations involving elementary coordination components. The players were located at the sites of square lattice and followed the logit strategy update rule.

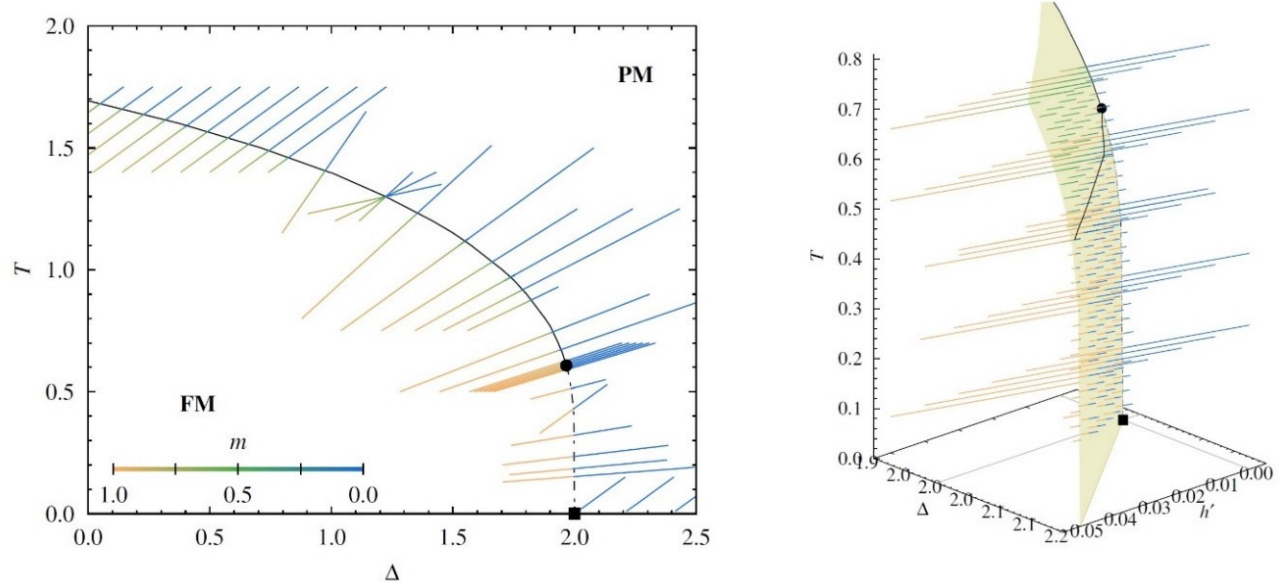


Figure 1: Heat maps of the TRG magnetization along elementary coordination game cross sections of the Blume-Capel model in the absence and presence of an external magnetic field. The data used to draw the zero-field phase boundary were taken from Zierenberg et al.: *Eur. Phys. J. Special Topics* 226 (2017) 789.

The first game combines an elementary coordination with self-dependent games (games, in which a player's payoffs are independent of their opponent's strategy choice) that respect and break the symmetry of its two coordinated strategies. This game model is equivalent to an unusual parametrization of the Blume–Capel model of statistical physics: The presence of the neutral, non-coordinated strategies acts as an effective temperature-dependent crystal field and thus defines oblique cross sections of the phase diagram of the Blume–Capel model. (see Fig. 1)

The second, five-strategy game models the interplay between different elementary coordination components. It consists of two competing coordination-type subgames, one involving the first two strategies that has the symmetry of the Ising model and one that involves the last three strategies and has the symmetry of the Potts model.

The results obtained using the TRG method are consistent with the expected properties (order, location, critical exponents, etc.) of the various order–disorder phase transitions of the two games, they corroborate and extend the existing literature of both models. [1, 2]

Related publications

- [1] B. Király: *A tensor renormalization group analysis of the Blume–Capel model inspired by game theory*, Physica A **630**, 129296 (2023) <https://doi.org/10.1016/j.physa.2023.129296>
- [2] B. Király: *A tensor renormalization group analysis of an evolutionary game of competing Ising and Potts subgames*, Phys. Lett. A **502**, 129392 (2024) <https://doi.org/10.1016/j.physleta.2024.129392>

EVOLUTIONARILY STABLE PAYOFF MATRIX IN HAWK–DOVE GAMES

B. Király, T. Varga*, Gy. Szabó, J. Garay**

* Bolyai Institute, University of Szeged, ** Institute of Evolution, HUN-REN Centre for Ecological Research

The classical evolutionary models of game theory typically assume that the interactions are fixed and the players can only alter their payoffs by adapting their behaviour. Most real decision situations are not like this, as their outcomes clearly depend on not only the behaviour but also the abilities of the players involved, which may also change over time. To study the effects of this broader decision space, we introduced a modified version of the hawk–dove game in which each player phenotype is defined through two independent attributes, one that describes behaviour and one that quantifies a trait that determines interaction outcomes. In the original hawk–dove game, two players contest a resource using one of two strategies: A player who chooses the “dove” strategy will avoid conflict at all cost, while a player who chooses the “hawk” strategy will always escalate conflict, to the point of causing or receiving grievous injury, if necessary. When both players choose the same pure strategy, the winner is chosen randomly. In our modified version, the players have an additional evolving phenotypic trait called fighting ability, which determines the probability of winning and the cost of losing escalated hawk–hawk conflicts. (Fig. 1 shows a hawk–hawk payoff function constructed in this manner.)

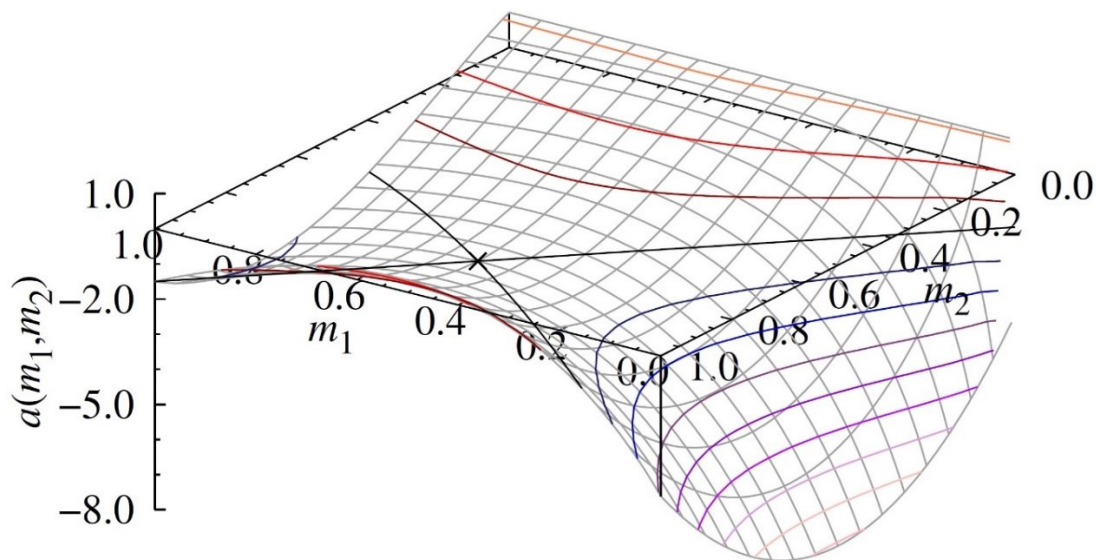


Figure 1: An example of a trait-dependent hawk–hawk interaction payoff function whose corresponding game has a non-trivial evolutionarily stable phenotype. \times evaluates the payoff function at the evolutionarily stable phenotype.

We studied the modified game in a framework consistent with the monomorphic model setup of Maynard Smith and Price. Applying the classical verbal definition of evolutionary stability (“a strategy such that, if most of the members of a population adopt it, there is no ‘mutant’ strategy that would give higher reproductive fitness”, J. Maynard Smith, G. R. Price, *Nature* 248 (1973) 15), we defined evolutionarily stable phenotypes as consisting of an evolutionarily stable strategy and an evolutionarily stable trait (and a corresponding evolutionarily stable payoff matrix), and determined the sufficient conditions for their existence in our modified hawk–dove game. We found that the maximal possible cost of escalating conflicts remains constant in the limit of fast behavioural and slow trait evolution. [1]

Related publication

- [1] B. Király, T. Varga, Gy. Szabó, J. Garay: *Evolutionarily stable payoff matrix in hawk–dove games*, *BMC Ecology and Evolution* **24**, 65 (2024) <http://dx.doi.org/10.1186/s12862-024-02257-8>

ABBREVIATIONS

2DEG	2-Dimensional Electron-Gas
AC	Alternating Current
Ac	Acinar
ACP	Amorphous Calcium Phosphate
AE	Acoustic Emission
AEKI	Institute for Atomic Energy Research (Hungarian acronym)
AES	Auger Electron Spectroscopy
AFM	Atomic Force Microscopy
AHP	Analytic Hierarchy Process
ALD	Atomic Layer Deposition
ALLEGRO	Experimental Helium Gas Cooled Fast Reactor Developed by the European V4G4
ANN	Artificial Neural Network
AOI	Angle Of Incidence
ATF-TS	Testing and Simulation for Advanced Technology and Accident Tolerant Fuels
ATOMKI	Institute for Nuclear Research, Debrecen (Hungarian acronym)
BCC	Body Centred Cubic
BCF	Boda Claystone Formation
BDD	Boron Doped Diamond
BES	Beam Emission Spectroscopy
BF	Bright Field
BFKH MMFF	Government Office of the Capital City Budapest - Metrological and Technical Supervisory Department (Hungarian acronym)
BME	Budapest University of Technology and Economics
BMGE NTI	Budapest University of Technology and Economics Nuclear Technology Institute
BNC	Budapest Neutron Centre
BOD	Biochemical Oxygen Demand
Br	Bronchial
BRR	Budapest Research Reactor
BSA	Bovine Serum Albumin
BU	Burnup
BWR	Boiling Water Reactor
CA	Chronoamperometry
CAD	Computer Aided Design
CANS	Compact Accelerator-based Neutron Sources
CBP	Capillary Bridge Probe
CCD	Charge Coupled Device
CCRS	Composite Common Risk Segment
CD	Critical Dimension
CDD	Context Definition Documents
CDR	Critical Design Review
CEFET-MG	Brazilian Federal Centre for Technological Education of Minas Gerais
CERIC	Central European Research Infrastructure Consortium
CFD	Computational Fluid Dynamics
CFP	Cladding Failure Prediction
CH	Cultural Heritage
CI	Cascade Impactor
CMOS	Complementary Metal-Oxide Semiconductor
CMTF	Cold Moderator Test Facility
CNC	Computer Numerical Control
CNN	Convolutional Neural Network
COD	Chemical Oxygen Demand

CODEX	COre Degradation Experiment
CoS	Chance of Success
CP	Chronopotenciometry, converse piezoelectric
CPE	Controlled Potential Electrolysis
CRP	Coordinated Research Project
CRS	Common Risk Segment
CSD	Control and Shutdown Device
μ -CT	micro-Computed Tomography
CV	Cyclic Voltammetry, Central Vector
CVD	Chemical Vapour Deposition
DBA	Design Basis Accident
DC	Direct Current
DCC	Direct Current Converter
dCP	dicalcium phosphate
DDAB	Didodecyldimethylammonium Bromide
DEMO	DEMONstration Power Plant
DFT	Density Functional Theory
DHR	Decay Heat Removal
DHW	Domestic Hot Water
DLR	German Aerospace Centre
DMS	Disruption Mitigation Systems
DOS	Density Of States
DPA	Displacement per Atom
DRM	Dry Reforming of Methane
DRIFTS	Diffuse Reflectance Fourier Transform Infrared Spectroscopy
DSC	Design Safety Calculation, Differential Scanning Calorimetry
DSD	Diverse Shutdown Devices
DT	Digital Twin
EAD	European Active Dosimeter
EB	Electron Beam
EBS	Engineered Barrier System
EC	Elemental Carbon, European Commission
ECB	Ethanol-monochlorobenzene
ECCO	European Cell COde
ECM	Electrochemical Migration
ECR	Electron Cyclotron Resonance, Equivalent Cladding Reacted
ECSA	Electrochemically Active Surface Area
ECSS	European Cooperation for Space Standardization
ED	Electron Diffraction
EDM	Electric Discharge Machine
EDS	Energy Dispersive X-ray Spectroscopy
EDX	Energy-dispersive X-ray Spectroscopy
EFPY	Effective Full Power Year
EGFET	Extended Gate Field Effect Transistor
EGSE	Electrical Ground Support Equipment
EIS	Electrochemical Impedance Spectroscopy
EK	Centre for Energy Research (Hungarian acronym)
ELI ALPS	Laser Research Institute, Hungary, Szeged
ELTE	Eötvös Loránd University, Budapest (Hungarian acronym)
EM	Electromagnetic, Engineering Model
EMA	Effective Medium Approximation
EOC	End of Cycle
EOT	Extended Operating Time
EPR	Electron Paramagnetic Resonance, Evolutionary Power Reactor
ERS	Electronic Raman Scattering
ESA	European Space Agency
ESIS	European Structural Integrity Society

ESS	European Spallation Source (Lund)
ET	Extrathoracic
EU	European Union
EU BSS	EU Basic Safety Standards Directive
EURAD	European Joint Programme on Radioactive Waste Management
EURATOM	European Atomic Energy Community
EVs	Electric Vehicles
EXAFS	Extended X-ray Absorption Fine Structure
FC	Faraday Cup
FCC	Face Centred Cubic
FE	Finite Element
FEA	Finite Element Analysis
FEM	Finite Element Method
FEN	[Fe(4-ety)2(N3)2]n
FIB	Focus Ion Beam
FIDES	Framework for Irradiation Experiments (NEA)
FKKL	EK Laboratory of Surface Chemistry and Catalysis (Hungarian acronym)
FL	MFA Photonics Laboratory (Hungarian acronym)
FluidFM	Fluidic Force Microscopy
FPGA	Field Programmable Gate Array
FPL	Fusion Plasma Physics Department, EK (Hungarian acronym)
FS	Fused Silica
FTL	Fusion Technology Department, EK (Hungarian acronym)
FT-IR	Fourier-transform Infrared Spectroscopy
FTO	Fluorine-doped Tin Oxide
FWHM	Full width at half maximum
GC	Glassy Carbon, Gas Chromatograph
GCI	Grating-Coupled Interferometry
GE	General Electric Company
GEM	Gas Electron Multiplier
GFP	Green Fluorescent Protein
GFR	Gas-Cooled Fast Reactor
GHI	Global Horizontal Irradiance
GIS	Geographical Information System
GPU	Graphics Processing Unit
GRS	Gesellschaft für Anlagen- und Reaktorsicherheit, Hamburg, Germany
HA	Hyaluronic Acid
HAADF	High-angle Annular Dark-field
HALO	Habitation and Logistics
HCP	Hexagonal Closely Packed
HEMT	High-Electron-Mobility Transistor
HEOs	High Entropy Oxides
HER	Hydrogen Evolving Reaction
HERA	High Burnup Experiment in Reactivity Initiated Accident
HiPIMS	High-Power Impulse Magnetron Sputtering
HK	House Keeping
HNHM	Hungarian Natural History Museum
HOPG	Highly Oriented Pyrolytic Graphite
HOT	Highly Optimized Tolerance
HPGe	High-purity Germanium
HRGS	High-Resolution Gamma-ray Spectrometry
HRTEM	High Resolution Transmission Electron Microscopy
HSA	Human Serum Albumin
HV	High Voltage
HZP	Hot Zero Power
IAEA	International Atomic Energy Agency
IC	Ion Chromatography

ICL	Imperial College London
ICP-MS	Inductively Coupled Plasma Mass Spectrometry
ICP-OES	Inductively Coupled Plasma Optical Emission Spectrometry
IDA	Internal Dosimeter Array
IL	Ion beam-induced Luminescence
ILL	Institute Laue-Langevin, Grenoble , France
INAA	Instrumental Neutron Activation Analysis
INSC	International Nuclear Safety Cooperation
IPCE	Incident Photon-to-Current Efficiency
IPERION HS	Integrating Platforms for the European Research Infrastructure ON Heritage Science
IQ	Installation Qualification
IR	Infrared, Induced Repair
ISFET	Ion-Selective Field Effect Transistor
ISS	International Space Station
ITER	International Thermonuclear Experimental Reactor
ITO	Indium Tin Oxide
JAXA	Japan Aerospace Exploration Agency
JET	Joint European Torus
JoFET	Josephson Field-Effect Transistor
JUICE	Jupiter ICy moons Explorer
KFK	West German Karlsruhe Laboratory
KIKO3DMG	Nodal Reactor Physics Calculation Code Developed in the EK
KR	Kretschmann-Raether
KRSE	KR Spectroscopic Ellipsometry
LDM	Low-Dimensional Neutron Moderator
LDOS	Local Density of States
LED	Light Emitting Diode
LENS	League of advanced European Neutron Sources
LINAC	Linear Electron Accelerator
LLD	Load Line Displacement
LOCA	Loss of Coolant Accident
LPE	Liquid Phase Epitaxy
LPU	Law of Propagation of Uncertainties
LSC	Liquid Scintillation Counting
LSPS	Large-Scale Pressure System
LSES	Large-Scale Engineering System
LSV	Linear Sweep Voltammetry
LTCC	Life-Time Considering Control
LTO	Long-Term Operation
LV	Low-Voltage
LWR	Light Water Reactor
MAE	Mean Absolute Error
MCA	Multi Channel Analyzer
MCDA	Multi-Criteria Decision Analysis
MCM	Monte Carlo Method
MCNP	Monte Carlo N-Particle Transport
MCP	Multi-Channel Plate
MD	Molecular Dynamics
MEMS	Microelectromechanical System
MFA	Institute of Technical Physics and Materials Science (Hungarian acronym)
MGI	Massive Gas Injection
MHX	Main Heat exchangers
MIC	Minimum Inhibitory Concentration
MIS	Minimally Invasive Surgery
ML	Machine Learning, Monolayer
MLP	Multi-Layer Perceptron

MO	Methyl orange
MOFs	Metal–Organic Frameworks
MOOCs	Massive Open Online Courses
MOVPE	Metal–Organic Vapour Phase Epitaxy
MOX	Mixed Oxide
MQ-water	Ultrapure Grade 1 water
MP	Microwave Power
MPCB	Materials and Processes Control Board
MS	Mössbauer Spectroscopy, Mass Spectrometry
MSE	Mean Squared Error
MTAB	Mercaptohexadecyl cetyltrimethylammonium bromide
MTEST	Material test
MVM	Hungarian Power Companies (Hungarian acronym)
MWCNT	Multiwalled carbon nanotube
NAA	Neutron Activation Analysis
NASA	National Aeronautics and Space Administration, USA
ND	Neutron Diffraction
NDA	Non-Destructive Assays
NEMS	Nanoelectromechanical System
NDT	Non-Destructive Testing
NDIR	Non-Dispersive Infrared
NF	Nuclear Forensics
NIPS	Neutron-Induced Prompt Gamma-ray Spectroscopy
NIPS-NORMA	Neutron-Induced Prompt Gamma-ray Spectroscopy - Neutron Optics and Radiography for Material Analysis
NIR	Near InfraRed
NLR	Non-Linear Regression
NMR	Nuclear Magnetic Resonance
NMX	Macromolecular Diffractometer
NORM	Naturally Occurring Radioactive Materials
NPP	Nuclear Power Plant
NRAs	National Nuclear Regulatory Authorities
NSD	Nuclear Security Department (AEKI)
NUBIKI	Nuclear Safety Research Institute (Hungarian acronym)
OAH	Hungarian Atomic Energy Authority (Hungarian acronym)
OC	Organic Carbon
ODI	Open Data Interface
ODS	Oxide Dispersion-Strengthened
OECD NEA	Organisation for Economic Co-operation and Development Nuclear Energy Agency
OER	Oxygen Evolving Reaction
OoC	Organ-on-Chip
OPD	Optical Pellet Diagnostic, Oxygen Packing Density
OQ	Operational Qualification
ORC	Organic Rankine Cycle
OSM	OpenStreetMap
OTKA	Hungarian Scientific Research Fund (Hungarian Acronym)
OWLS	Optical Waveguide Lightmode Spectroscopy
Paks NPP	Paks Nuclear Power Plant
PAS	Positron Annihilation Spectroscopy
PCA	Principal Component Analysis
PCB	Printed Circuit Board
PDADMAC	poly(diallyldimethylammonium chloride)
PEC	Photoelectrochemical
PEG	Polyethylene Glycol
PEIS	Potentiostatic Electrochemical Impedance Spectroscopy
PEM	Proton Exchange Membrane

PEP	Particle Environment Package
PFM	Proto-Flight Model, Positive Matrix Factorization, Piezoresponse Force Microscopy
PGA	Phosphoglycolate
PGAA	Prompt-gamma Neutron Activation Analysis
PGAI	Prompt-gamma Activation Imaging
PLC	Pressure Loss Coefficients
POC	Point-of-Care
PQ	Performance Qualification
PS	Pressureless Sintering, Polystyrene
PSA	Probabilistic Safety Analysis
PSF	Point-Spread Function
PTB	German National Metrology Institute
PtG	Power-to-Gas
PTFE	Polytetrafluoroethylene
PUMMA	Plutonium Management for More Agility
PV	Photovoltaic
PVA	Polyvinyl Alcohol
pXRF	Portable XRF Spectrometer
PWR	Pressurized Water Reactor
QCM	Quartz Crystal Microbalance
R&D	Research & Development
RAFM	Reduced Activation Ferritic Martensitic
RAPID	Repeated Analyte Pulses of Increasing Duration
RBC	Red Blood Cell
REEs	Rare Earth Elements
RF	Random Forest, Radio Frequency
RFQ	Radio Frequency Quadrupole
RG	Rhombohedral Graphite
RHA	Radiation Hardness Assurance
RHE	Reversible Hydrogen Electrode
R _L	load resistor
RMC	Reverse Monte Carlo
RN	Radionuclide
ROI	Return on Investment
RPV	Reactor Pressure Vessel
RR	Research Reactor
RTA	Rapid Thermal Annealing
RUBA	Rapid Urine Bacteria Analyser
SAED	Selected Area Electron Diffraction
SALICIDE	Self-aligned-silicide
SANS	Small Angle Neutron Scattering
SBO	Station Blackout Transient
sCMOS	scientific-grade Complementary Metal-Oxide Semiconductor
SCRAM	emergency shutdown of the reactor
SCs	Semiconductors
SCT	Small Compact Tension
SD	Sessile Drop
SE	Spectroscopic Ellipsometry
SECURE	Strengthening the European Chain of sUpply for next generation medical RadionuclidEs, EU-funded project
SEFOR	South-West Experimental Fast Oxide Reactor
SEM	Scanning Electron Microscopy
SEM-EDS	Scanning Electron Microscopy with Energy Dispersive Spectroscopy
SEM-EDX	Scanning Electron Microscopy with Energy Dispersive X-Ray microanalysis
SFP	Spent Fuel Pool
SI	Structural Integrity

SICs	Structural Integrity Computations
SL	Service-Lifetime
SLM	Stochastic Lung Model
SMSI	Strong Metal-Support Interaction
SMU	Source-Measure-Unit
SOC	Self-Organized Critical, Science Operation Centre
SPI	Shattered Pellet Injection
SPM	Streaming Potential Measurement
SPN	Simplified Spherical Harmonics
SPND	Self Powered Neutron Detector
SPP	Surface Plasmon Polariton
SQUID	Superconducting Quantum Interference Device
SRD	System Requirement Documents
SSTT	Small Specimen Test Techniques
STEM	Scanning Transmission Electron Microscope
STM	Scanning Tunnelling Microscopy
SVR	Support Vector Regression
SWV	Square Wave Voltammetry
TBG	Twisted Bilayer Graphene
TC	Total Carbon, Technical Cooperation
TEM	Transmission Electron Microscopy
TEMPO	2,2,6,6-tetramethylpiperidine-1-oxyl
TERA	Thunderstorm Energetic Radiation Array
TES	Thermal Energy Storage
TÉT	Bilateral Research Program (Hungarian acronym)
TFC	Trilateral Flash Cycle
TL	Thermoluminescent
TLV	Threshold Limit Value
TMM	Thermal Mathematical Models, Transfer Matrix Method
TMY	Typical Meteorological Year
TOC	Total Organic Carbon
TPR	Temperature Programmed Reduction
TRG	Tensor Renormalization Group
TSA	Tryptone Soya Agar
TSB	Tryptone Soya Broth
TSD	Third Shutdown System
TSO	Technical Support Organization
TXRF	Total-reflection X-Ray Fluorescence analysis
T&T	Training & Tutoring
UOX	Uranium Oxide
UV	Ultraviolet
vdW	van der Waals
VERONA	VVER On-Line Analysis
VVER	Water-Cooled Water-Moderated Energetic Reactor, Russian acronym
XANES	X-ray Absorption Near-Edge Structure
XPS	X-ray Photoelectron Spectroscopy
XRD	X-ray Diffraction
XRF	X-ray Fluorescence Analysis
XTEM	Cross-sectional Transmission Electron Microscopy
WEEE	Waste Electrical and Electronic Equipment
Wigner FK	Wigner Research Centre for Physics (Hungarian acronym)
WLM	Working Level Month
WPRM	Work Package Remote Maintenance

IMPRINT

Editor

László Redler

Lector

Ferenc Szlávik

Publisher

Ákos Horváth

Tamás Belgya

Béla Pécz

*HUN-REN Centre for Energy Research
H-1121, Budapest, Konkoly Thege M. út 29-33.
Hungary*

Design

Zsófia Zsarnay

Picture credits

HUN-REN Centre for Energy Research

Accessibility

<http://www.ek.hun-ren.hu/>

Contact

HUN-REN Centre for Energy Research

Location: KFKI Campus, Budapest Konkoly-Thege Miklós street 29-33., H-1121 Hungary

Phone: (+36 1) 395 91 59

E-mail addresses: info@ek.hun-ren.hu



**HUN
REN**



Centre for
Energy Research

KFKI Campus, Konkoly-Thege Miklós út 29-33.
Budapest H-1121, Hungary
Phone: +36 1 395 9159
www.ek.hun-ren.hu

